CONTROLS AND DISTRIBUTION PATTERNS OF GOLD MINERALISATION IN THE MANICA-MUTARE-ODZI GREENSTONE BELT, (WESTERN MOZAMBIQUE AND EASTERN ZIMBABWE)

BY

SALVADOR MONDLANE JUNIOR

2005

UNIVERSITY OF ZIMBABWE

Department of Geology, Faculty of Science

Controls and distribution patterns of Gold mineralisation in the Manica – Mutare – Odzi greenstone belt (western Mozambique and eastern Zimbabwe)

By

Salvador Mondlane Junior

Thesis submitted in fulfilment of the degree of Doctor of Philosophy

June 2005

Declaration

This work has not been submitted previously for any other degree. The thesis is the result of my own investigations done wholly in registered postgraduate candidature, except where otherwise stated. This thesis was submitted for examination in June 2005.

To my family

Acknowledgements

Late Dr. H. Munyanyiwa (UZ), Dr. M. Lupankwa (UZ), Prof. P. Dirks (UWits), Dr. H. Jelsma (De Beers Exploration) are sincerely thanked and gratefully acknowledged for their supervision, patience, constructive criticisms and encouragement without which it could not have been possible to materialise this project,

My gratitude also goes to Prof. Dr. Tom Blenkinsop for his support, comments and suggestions and provision of computer programs on the Fry and Fractal analysis.

Mr. D. Chatora and the Management of Redwing Mine (Zimbabwe) are thanked and gratefully acknowledged for support and permission to use their report files and to map their ground property.

Mr. H. Gumbo (private consultant) is thanked for allowing the use of his geophysical data from Redwing mine.

Mr. George Pybus and the De Beers Exploration Geoscience Centre (Johannesburg) are thanked and gratefully acknowledged for guidance, comments, suggestions and assistance on the spectral geology Chapter and the logistical support and permission to use the PIMA SP spectrometer.

Prof. S. White and Dr. Hugo de Boorder (Utrecht University) for their guidance and valuable discussions at early stages of project drafting; Dr. Mac Goossens (private consultant in the Netherlands) for his early stage fieldwork guidance, suggestions and image processing supervision; Dr. O. Maponga, Dr. D. Shoko, Dr. T. Sithole and Mr. C. Ngorima for their willingness in proof-reading, commenting, and contributing in the sections on statistical analysis and GIS modelling, are all thanked and acknowledged.

Prof. Lopo de Vaconcelos (Head of Geology Department – UEM and project co-ordinator) is thanked for his unconditional and unlimited help and support; Dr. Rien Dam, Drs. Berthe Schoonman and Drs. Hetty Winkel (project co-ordinators at Utrecht University) for their commitment and support.

NUFFIC is gratefully acknowledged for financial sponsorship and for allowing my family to join me from time to time in the Netherlands and in Zimbabwe.

HEP1_UEM is thanked for financial support for the last year of this study, it is gratefully thanked.

I thank and acknowledge all my colleagues (academic and technical) in the Geology Department UEM for their substantiated support; my colleagues (academic and technical) in the Geology Department – UZ for their help at several stages of the project; the sample preparation units in the Geology Departments (UEM and UZ); the friends in particular those of MOZ-Net for their unlimited moral support.

Mr. Daude (National Director of the Geological Survey) is thanked for allowing the use of confidential open files.

Mr. S.P.S. Joaquin (CENACARTA) is gratefully acknowledged for his help during early stages of satellite imagery rectification.

Eng. Abduremane (Provincial Director of the Ministry of Mineral Resources and Energy in Manica), Eng°. Mario Deus, Mr. F. Matos are all thanked for their help during the fieldwork in Manica.

Mr. Neves and Mr. Salomao (Hon's students from UEM), Mr. Zacarias and Mr. Matola (technicians, MIREM Manica), Mr. Jimy (Redwing mine) are all acknowledged for their help during the fieldwork.

The patience, understanding, encouragement and moral support of my family, especially my wife, are deeply appreciated.

I also thank the Mozambican community in Zimbabwe and my friend and brother (Tirso Dos Santos and family) for their support and social integration.

The research reported here benefited from assistance of many people along the four years of the study. Those, who directly or indirectly contributed to the success of this study and are not mentioned above, are gratefully acknowledged.

UNIVERSITY OF ZIMBABWE
Department of Geology, Faculty of Science

Abstract

Doctor of Philosophy

Controls and distribution patterns of Gold mineralisation in the Manica – Mutare – Odzi greenstone belt, (western Mozambique and eastern Zimbabwe)

By Salvador Mondlane Junior

The Manica - Mutare - Odzi (MMO) greenstone belt is a late Archaean linear structure that was formed around 2,74 Ga. The belt has produced up to 1995 c. 84 tonnes of Au mainly from shear zone/fault hosted and quartz vein hosted deposits. Gold deposits are arranged in corridors, which seem to control their localisation. These corridors are oriented at an angle to the known main orientation of the structures that host mineralisation in the belt.

The distribution of known gold deposits reflect a pattern of the structures controlling mineralisation to an extent that depends on the degree of mining in the MMO belt, and are important requisite to the design of exploration models and better understanding of gold genesis in the Archaean.

This study sought to understand the distribution patterns of gold deposits and the controls that influenced the Au mineralisation localization in the MMO greenstone belt. The study has established criteria for gold deposit recognition, built a database for structuring, easy retrieval, update and manipulation of the captured data, it also performed spatial association analysis to generate maps of evidence and finally it produced gold prospectivity maps for the MMO greenstone belt.

The study has reached among others the following results:

(i) Surface and concealed structures, granodioritic intrusions and mafic and ultramafic rocks of Bulawayan age mainly control gold mineralisation in the study area.

(ii) Gold deposits in the study area are fractal. The fractal dimension suggests a single event process or synchronous harmonic set of geological processes acting as one, probably related to hydrothermal systems that transported and deposited gold in favourable sites, governed the gold mineralisation distribution.

(iii) Autocorrelation analysis shows presence of important gold deposits at the intersections between known and the newly interpreted crypt structures.

(iv) According to Fry analyses gold deposits cluster at distance ranges between 2 and 30 km.

(v) The shear zones and zones of BIF were successfully mapped using iron parameter from PIMA (Portable Infrared Mass Analyser) data.

(vi) The gathered information on controls and distribution patterns of the gold occurrences were spatially related to the known gold occurrences in the area and, weights of evidence were calculated and optimum distance of influence established for each parameter. The cutoff distances are 500 for felsic and intermediate intrusions, 400 for shear zones and quartz veins, 700 for Shamvaian/Bulawayan contact, 900 for BIF, 800 for greenstone/granite contact, 500 for the Fry interpreted lineaments and 900 m for the Bulawayan lithologies.

(vii) In the contingency table for calculated chi-square two binary predictor patterns (the Fry lineaments and the BIF) did not meet the criteria for conditional independence and they were discarded from the model.

(viii) The gold prospectivity model as designed depicts 54% of the deposits within high and very high prospectivity areas and only 16% of the deposits fall within low prospectivity area.

(ix) Using the validation dataset, 51% of the deposits are distributed within the high and very high prospectivity areas and only 20% of the gold occurrences fall within low prospectivity area.

(x) The 30% of gold occurrences falling within area of moderate prospectivity index for both designing and validation datasets shows that the model is consistent.

(xi) The prospectivity maps highlight areas of high, very high prospectivity which can be used to guide future gold exploration programs.

Content Pages

Chapter 1

Chapter 2

Chapter 3

Chapter 4

Chapter 5

Chapter 6

Chapter 7

Chapter 8

Chapter 9

Chapter 10

List of Figures **Pages**

Chapter 1

Chapter 2

Chapter 3

Chapter 4

Chapter 5

Chapter 6

Chapter 7

Chapter 8

Chapter 9

List of Tables **Pages**

Chapter 2

Chapter 4

Chapter 5

Chapter 6

Chapter 7

Chapter 8

Chapter 9

Chapter 1

1 Introduction

1.1 Background summary to the Project

The project was initiated in 1998 at Utrecht University in the Netherlands as part of capacity building and staff development at the Geology Department of the Eduardo Mondlane University in the auspices of the MHO project funded by NUFFIC. The project was first supervised and based at Utrecht University Faculty of Earth Sciences and then it was transferred to University of Zimbabwe Geology Department in late 1999.

The Manica Mutare Odzi greenstone (MMO) belt area was selected because the geology, gold mineralisation and structure in this belt have not been studied in detail, except for the Mutare section of the belt where Chenjerai (1996) documented the gold mineralisation. Selected areas were mapped and logged in detail in order to resolve structural and geological relationships and to obtain a better understanding of the tectonic of greenstone belts in general.

1.2 General information (access, climate, vegetation and geomorphology)

1.2.1 Access

Mozambique and Zimbabwe share the 140 km long Manica Mutare Odzi (MMO) greenstone belt which extends for 35 km in Mozambique and for105 km in Zimbabwe (Fig. 1-1). It constitutes one of marginal belts within the Zimbabwe Archaean craton and is bordered to the west, north and south by the Archaean granites and gneisses and to the east by the Proterozoic Bárue granite gneisses of the Mozambique orogenic Belt. The MMO greenstone belt is approximately 20 km wide along the eastern side and gradually narrows down to about 3 km wide near the western end of the belt.

The belt is subdivided into three sections on the basis of geology and geographic position, the Manica section (in Mozambique), the Mutare section (the central zone of the belt running from the Zimbabwe/Mozambique border to parallel 32°30°) and the Odzi section (to the west of parallel 32° 30°).

Access is by a well-developed network of tar and dust roads. The main access is via the highway Beira (Mozambique) – Harare (Zimbabwe). During the rainy season, however, most of the dust roads can only be negotiated by a 4-wheel drive vehicle.

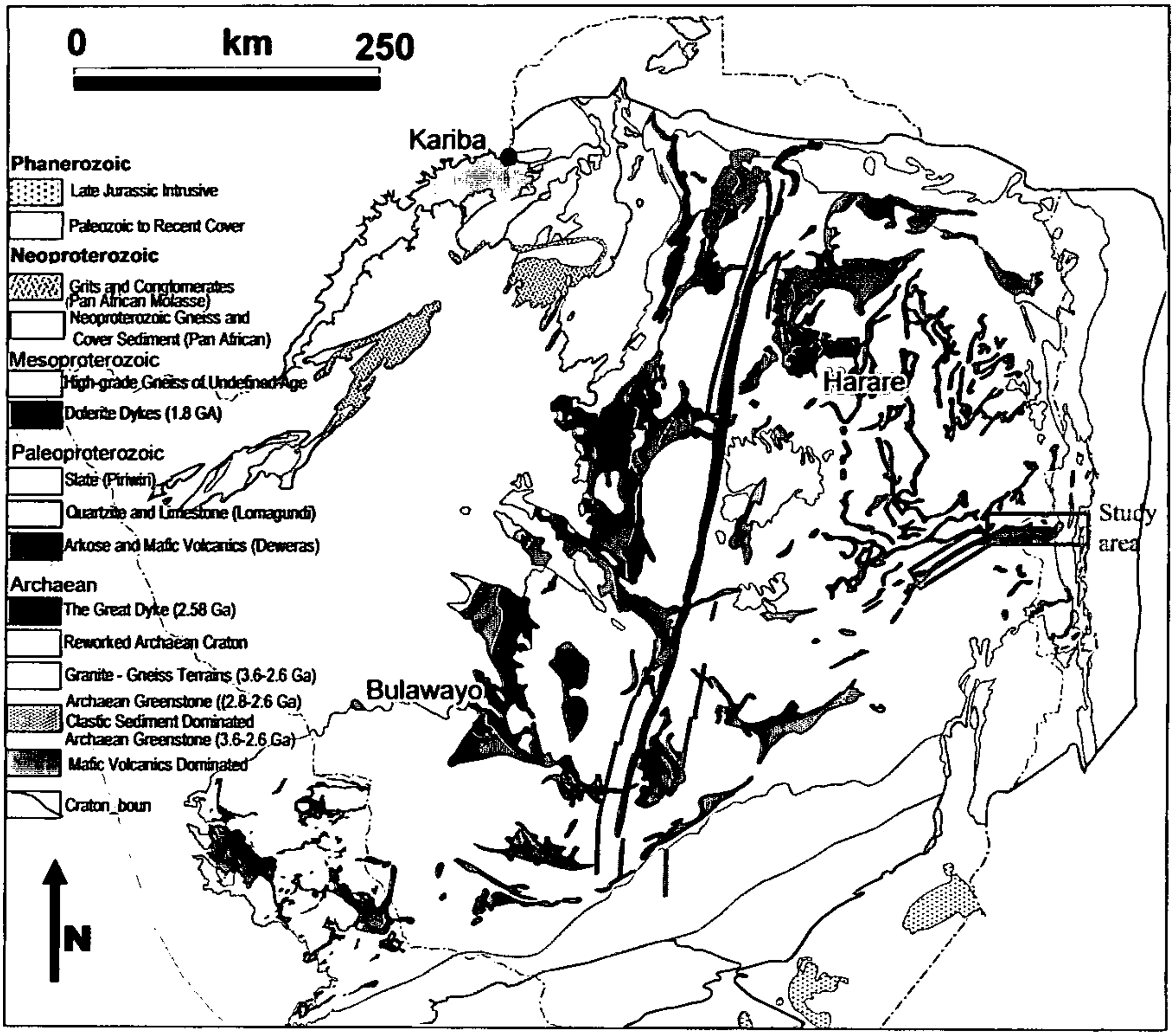

Figure 1-1. Simplified geological map of Zimbabwe showing the study area (Stagman, 1994)

1.2.2 Climate, Drainage and Vegetation

The study area is of a high altitude region with highest elevation peak at Cecil Kop with 1735 m above sea level, valleys and plateaus dissect it with elevations between 900 and 1200 m above sea level. The variable relief is to some extent an advantage because it enhances topographic and large morphologic features, which are of help to structural and lithological mapping.

Forests and dense shrubs are found on the eastern side and low vegetation on the western side of the study area. The vegetation remains a limiting factor for lithological mapping based on spectral differences.

The indigenous vegetation is characterised by Bracystegia species (msasa and mpfuti) covering most of the greenstone belt together with plantation of eucalyptus and pine. The Uapaca kirkiana is found on the granites (Chenjerai, 1996).

Long rainy seasons usually distributed throughout the year, mist and light showers occurre at intervals during winter.

The drainage system is dominated by a number of main rivers such as Mutari, Mbeza, Revue, and Munene with tributaries in a semi-dendritic pattern that suggest structural control in the drainage pattern.

1.3 Exploration History in the Manica Mutare Odzi area

The Manica Mutare Odzi greenstone belt is famous for its numerous gold workings and mines (c. 243). Gold mining in the Manica area started as early as the 10th century by the Monomotapa Empire who used to exchange gold for fabrics and jewellery from Arabs. In 1510 the Portuguese took over the gold market from the Arabs. It was only in 1888 that the first prospecting concession was granted to European prospectors in the *Campo Mineiro de Macequece*. From 1900 several companies prospected and mined gold in the Manica Mutare Odzi greenstone belt. In 1911 Andrada Mines Limites (AML) initiated systematic exploration at Chua, Revue, Zambuzi and nearby riverbeds.

The degree of exploration between the Zimbabwean and the Mozambican sides of the belt is different with the former being more explored than the later. This can be discerned by the comparatively large number of large deposits (produced more than 100 kg of gold) in the Mutare and Odzi section of the belt. The main difference is that Zimbabwe enjoys a well-established exploration and mining tradition while Mozambique lags behind in the level of exploration activities and mine development.

In Zimbabwe, there is regional coverage of airmagnetic and radiometric and more detailed (at concession level) geophysical (e.g. Induced Polarization (IP)) surveys, while in Mozambique only detailed scattered geophysical and geochemical surveys have been carried out.

In most cases the prospecting methods were restricted to soil geochemistry accompanied by geological mapping, pitting, trenching and diamond drilling and, occasionally, geophysical methods were used for follow up programs. These exploration methods were found to be appropriate for the MMO greenstone belt specially because of the deep weathering profile.

1.4 Rationality and scientific justification

Most of the gold exploration programs carried out in the Zimbabwe Craton are restricted to ancient workings. This shows the thoroughness of the ancient prospectors, who undoubtedly sought for surface expression of the mineralisation. It lends credibility to the use of known deposits as in this study for characterization of distribution patterns of gold mineralisation. However, absence of surface expression of concealed ore bodies also leads exploration programs to rely more on indirect methods for target delineation. The traditional indirect methods (geochemistry, geophysics and mapping) coupled recently by satellite imagery are the only ways for targeting new discoveries of mineralisation.

The rate of discoveries of new gold deposits in the Zimbabwe Craton has been very low in the last 30 years (Campbell and Pietfield, 1994).

The present study develops new exploration approaches for gold exploration in the Manica Mutare Odzi greenstone belt in particular and in the Zimbabwe Craton in general. This approach may increase the rate of discoveries. The proposed approach relies on understanding the tectonic and controls of known gold deposits as a base to model the position of unknown gold occurrences.

The distribution patterns of gold deposits and of controlling structures are tested using statistical methods of Autocorrelation (Fry) and Fractal analysis (Chapter 5) and are supported by satellite imagery interpretation (Chapter 8) and spectral geology (Chapter 6 and 7). Geographical Information Systems are used to integrate and relate entities by analysing the clustering and proximity to relevant features, e.g. shear zones (Chapter 9).

Gold mineralisation in the Zimbabwe Craton is mainly controlled by secondary and tertiary structures (Chapter 3) that occur within or close to the Archaean greenstone belts. This suggests that the combination of knowledge on structural controls, the geometry of individual deposits, and understanding of the tectonics of the greenstone belts (Chapter 2) will improve the exploration strategies for targeting concealed gold deposits.

The structures observed at a mine scale are usually trapping structures and they have to be modelled with care because, there are potentially several good trapping structures within and near greenstone belts, but not all of them are mineralised. Mineralisation is only found in specific parts of structures that meet optimum combinations of factors leading to gold deposition (Chapter 2). Thus the understanding of the main factors that lead to gold deposition in specific environments is key to the exploration model to be adopted.

The distribution patterns of gold deposits controlled by shear zones and faults suggest clusters occurring at regular intervals (Chapter 5). The reasons of clustering are far from being understood. However, if a pattern can be statistically or mathematically described, then undiscovered clusters can be predicted (Chapter 9).

The Manica – Mutare – Odzi area is dominated by a complex geological history, characterized by early accretionary structures and later folding and shearing. Various types of brittle-ductile fractures truncated this sequence before the introduction of gold mainly in the late Archaean. Several potential good trapping sites can be identified in the MMO greenstone belt and its vicinity, but very few of them are mineralised. This suggests that gold exploration should be directed to a description of the distribution patterns of gold mineralisation rather than to a search for trapping structures. The existence of trapping structure is necessary but not deterministic for gold deposition.

Geological interference of optimum-parameters increases the probability of gold deposition. Although it is recognised the importance of these interference sites for gold exploration, it is also known that they are not the only key factor for gold deposition. The MMO greenstone belt is an example of such inconsistencies of nature where the Chazuca granite intrudes similar set of lithologies that are intruded by the Penhalonga granodiorite, but the former is not mineralised.

The present study goes beyond interference of optimum parameters and biased geological interpretation and uses non-interpretative factors such as position of gold deposits, size, grade and presence of sulphides for proposing an exploration model where distribution patterns play an important role.

1.5 Objectives of this study

1.5.1 General objectives

The main objective is to understand the distribution patterns of gold deposits and the tectonic setting in which Au mineralisation has occurred and use such knowledge for generation of a predictive gold mineralisation model in the Manica-Mutare-Odzi (MMO) greenstone belt.

1.5.2 Specific objectives

The specific objectives of the project are focussed on the construction of a GIS-remote sensing based exploration model for gold mineralisation in the MMO greenstone belt and are as fellows:

1. Understand the mineralising processes in the MMO Greenstone Belt in relation to its structural evolution.
2. Design and compile a comprehensive database on all gold occurrences in the Mutare-Manica greenstone belt.
3. Characterise the economic mineralisation and the geological/tectonic setting through direct detailed field observations of gold occurrences, and spectral characterisation of gold occurrences.
4. Test of the spectral geology for characterisation of the spectral response of the mineral deposits (hydrothermal alteration) or groups of them.
5. Manipulate the database in order to derive a classification of gold deposits in the MMO belt.
6. Perform spatial analyses on the gold distribution patterns (e.g. cluster analysis, Fractal and Fry analysis).
7. Subdivide geological maps in geological units consisting of lithological or structural domains, including units expressed on maps as polygons and lineaments. Again this subdivision requires field verification (e.g. separate different generation shear zones).
8. Design statistical tests to quantify relationships between gold occurrences and geological units.
9. Design and present a GIS based gold predicting model for Manica Mutare Odzi area.

1.6 Study methodology

Airphoto (1:40 000 and 1:50000 scale) and satellite imagery (digital and hardcopies at 1:100 000 scale) were visually interpreted for geological lineaments, lithological mapping and pattern recognition on the trend map.

Computer aided interpretation of Landsat TM (Thematic Mapper) and ETM (Enhanced Thematic Mapper) and SPOT XS (multispectral) and PAN (panchromatic) frames were used to delineate regional structures, lithologies and hydrothermal alteration zones that reflect gold mineralisation.

A mosaic of the airphotos was digitally assembled and resampled to 10-m pixel size and afterwards fused with SPOT XS and PAN and TM in order to improve both spatial and spectral value of the imagery.

The fieldwork aimed at mapping mineral deposits and occurrences in the MMO greenstone belt in order to establish the main geological control of the gold deposits.

Mapping of selected areas was carried out in three field seasons of 40-days each, where the photo and satellite image interpretation was used to distinguish the different signatures (spectrum) of the geological units and mineral deposits played the main role.

Samples were collected to support the spectral identification of main features and for mineralogical and micro-structural analysis.

Structural mapping was accomplished by field mapping along random accessible outcrops at relevant lithologies and in three belt-scale N-S profiles in order to work out the geological/structural relationships of the area.

Remote sensing played a major supporting role in geological mapping of regional structures and subtle spectrum differences due to hydrothermal alteration related to mineralisation. Satellite images were interpreted pre-field work, the resulting sketches of the geology and structures were field-checked during the field work.

Landsat TM and ETM images at 100,000 scale were used and for selected areas larger scale and high-resolution images (SPOT XS and PAN) were also used.

The remote sensing approach assured the computer aided image interpretation where the following procedure was followed:

(i) data extraction,

(ii) data transformation (image correction and geocoding),

(iii) data enhancement (applying different filters to enhance certain features), and

(iv) data analysis and interpretation

Airmagnetic and radiometric anomalies were spatially compared with geological features and satellite image features to provide possible explanation.

A laboratory spectral analysis of soil samples was carried out using a Portable Infra-red Mineral Analyser (PIMA) and results were used to enhance the satellite image interpretation.

Finally, because satellite images, airmagnetic and geological data are only separate entities in exploration program, it was necessary to compare and combine them. This requires the ability to display all types of data at the same scale and in the same coordinate system. The first pre-requisite was to geocode the images, i.e. transform the coordinate system to a standard map projection.

Afterwards two approaches were followed, the first and simplest one was the independent production of maps and image displays, with a common origin and grid reference, which allowed a preliminary superposition of separate entities. The second and more complex was to assign an attribute to each type of information and combine them using ILWIS-GIS software (Chapter 9).

1.7 Thesis structure

The design of a GIS-based global exploration model requires that the input information to the model is well understood and that it is of high accuracy. In order to understand the tectonic setting of the mineralisation in the Archaean Greenstone belts a review of literature was carried out as discussed in Chapter 2.

The geology, gold mineralisation, structures and tectonic of the Manica Mutare Odzi greenstone belt are presented in Chapter 3.

The description of gold mineralisation and its classification is detailed in Chapter 4 using a GIS-based DataBase, which included existing information (reports, mine positions, mine descriptions, ore mineralogy, grade, production, controls and other), field data collected during this study (structural, geological and samples), and spectral data (Fig. 1-2).

The statistical manipulation, autocorrelation (Fry) and fractal analysis is presented in Chapter 5.

In Chapters 6 and 7 the spectral data acquired from PIMA spectrometer are presented, discussed and results are compared to satellite imagery.

In Chapter 8 the image processing methodology is described.

The design of the GIS based gold prediction model is presented in Chapter 9. This chapter also presents the exploration model/criteria for the MMO greenstone belt and prioritises the area in terms of prospectivity.

Finally, a discussion, conclusions and recommendations are presented in Chapter 10.

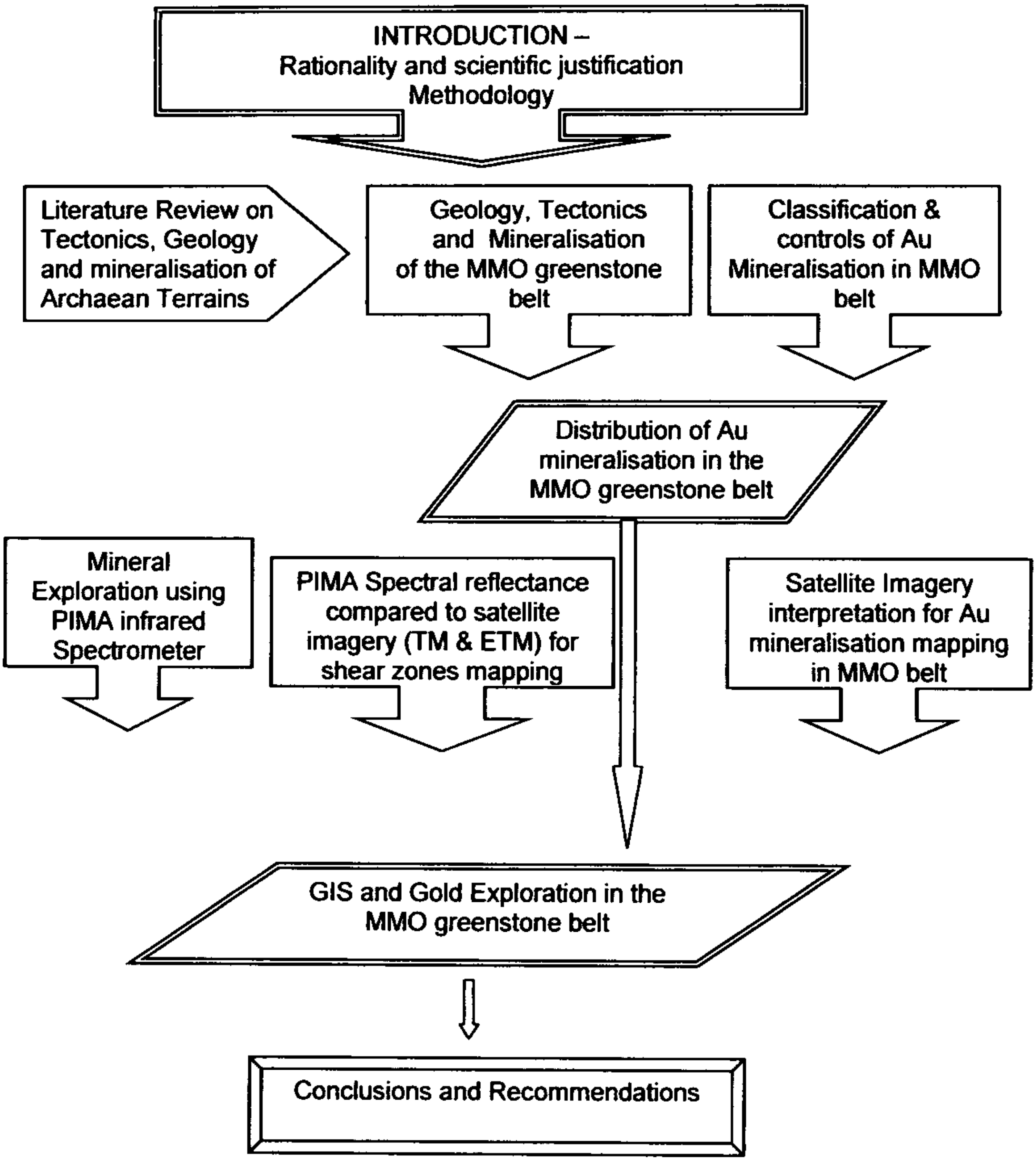

Figure 1 – 2. Thesis structure flow diagram, showing the development of the study themes

CHAPTER 2

2 TECTONIC SETTING OF THE ARCHAEAN GREENSTONE BELTS

2.1 Introduction to Archaean granite greenstone terrains

Greenstones are linear to arcuate low-grade volcano-sedimentary belts (ranging in age from 2.500 to 3.500 Ma) enveloped by tonalite- trondhjemite - granodiorite, generally intruded by later granitoid masses (e.g. Shackleton, 1995; de Wit and Ashwall, 1997; Kusky and Vearncombe, 1997; Kusky and Polat, 1999). Linear zones of high deformation (mobile belts) are largely responsible for the present outlines of Archaean Cratons.

Contacts between the greenstone belts and the surrounding gneisses and granitoids have structural breaks, intrusive contacts and unconformable contacts (e.g. Kusky, 1991; Tsomondo et al., 1992; Chadwick et al., 1992; Horwitz, 1992; Nisbet et al., 1993; Bickle et al., 1994; Wilson et al., 1995; Chenjerai, 1996; Ridley et al., 1997).

2.1.1 Greenstone terrains: Tectonic Setting and Origin

The greenstone belts include linear and anastomosing networks of upright synforms and accretionary geometries bordered by granitoid-gneiss batholiths (Kusky and Vearncombe, 1997). The Early Archaean greenstone belts are represented in the Kaapvaal Craton (e.g. Barbeton greenstone belt, c. 3.5 Ga) and the Late Archaean greenstone belts can be exemplified by the Migori belt in Kenya (2.9 – 2.7 Ga) (Shackleton, 1995). The differences between the Early and Late Archaean greenstone belts can be illustrated by observing the proportion of volcanic rocks in the greenstone belts as shown by Shackleton (1995) in Table 2-1.

Table 2-1. Proportions (by percentage area) of different volcanics in greenstone belts

Approx. age (Ga)	Barberton 3.5	Pilbara, West Australia 3.5	Upper Bulawayan, Zimbabwe 2.7	Migori-Kendu, SW Kenya 2.9 – 2.7	Sekuku-maland Tanzania 2.8	Superior Province, Canada 2.8
Felsic	<5	c.40	30	50	20	15
Intermediate	<5		20	30	30	30
Mafic	>80	c.60	50	20	40	55
Ultramafic	<10	c.60	minor	-	-	-

Source: Adapted from Shackleton, 1995

Table 2-1 has to be interpreted with care because these proportions depend also on the level of erosion of the Craton. It suggests that from Early to Late Archaean there was a decline in the proportion of ultramafic volcanic rocks. This must have been a result of tectonic processes and the evolution of the greenstones. The tectonics of the Archaean Greenstone belts has been widely discussed by several authors (see Table 2-2). The greenstones generally consist of thick, pillow - basalt sequences with or without subordinate komatiitic volcanic rocks, felsic volcanic rocks, and sedimentary rocks (de Wit, 1982; Kusky & Polat, 1999, Bickle et al., 1994 and references therein)

Table 2-2. Different models for the origin and tectonic of the greenstone belts

Location	Greenstone belts Model	Mode of formation	References
e.g. Yilgarn and Pilbara blocks	Intracratonic basins	Developed on upper crust in an intracratonic basin. They exhibit some characteristics of arc and marginal basin systems of an active continental margin. Resulted from lower crustal extension dominated by development of a regionally continuous volcanic pile.	Groves (1982)
e.g. Superior Province and Zimbabwe Craton	Oceanic crust	Ensimatic, oceanic crust with Ultramafic-mafic greenstone sequences regarded as obducted oceanic plateaux	Glikson, 1972; Annhaeusser, 1971; Hoffman, 1989; Card, 1990; Kusky and Kidd, 1992; Windley, 1993; Stott, 1997
e.g. Zimbabwe Craton	Continental crust	Greenstones were deposited on upper crust in the interval between 3.500 and 2.5 Ga as shield volcanoes.	Viljoen and Viljoen (1970); Windley (1973); Gorman et al (1978)
e.g. Zimbabwe;	Intracontinental rifts	Deposited onto 3.2 Ga – 2.8 Ga basement gneisses, in ensialic, continental basins. Regarded as typical example for vertical accretionary processes, relating magma under-and overplating in intracontinental rifts or similar settings above hot-spots or mantle plumes	Campbell and Hill, 1988; Bickle et al., 1994; Jelsma et al., 1996, Jelsma and Dirks, 2002; Blenkinsop et al., 2000
e.g. Zimbabwe Craton	Continental and Oceanic coexistence	Detailed structural and geochronological studies suggest contemporaneous coexistence of oceanic and continental crust and the operation of plate boundary processes during the Archaean.	de Wit (1982); Kusky & Polat (1999); Jelsma & Dirks (2000)
Abitibi; Yilgarn Block, Zimbabwe, Superior and Kaapvaal	Horizontal accretion	As the horizontal accretion involving near uniformitarian models with lateral amalgamation of mafic oceanic and felsic (island arcs) crustal fragments during a subduction-accretion related	Card, 1990; de Wit, 1982; Swager and Griffin, 1990; Myers, 1995

Craton		process	
Dharwar and Pilbara Cratons	Vertical accretion	Vertical accretionary processes, relating magma accretion and subsequent deformation of the greenstones and the underlying felsic basement due to vertical processes including melt segregation from a convective mantle, or underplating liquid and solid state diapirism in the evolving crust.	Bouhallier et al., 1993; Hickman, 1984

From the Table 2-2 it is clear that there is no consensus on Craton evolution and origin of the greenstone belts. On the other hand there is less controversy regarding the basements of the greenstone belts, which is mainly associated to sialic gneisses (Table 2-3). The contact between the basement and the greenstone is usually tectonic (Shackelton, 1995). The process responsible for overplating above mantle plumes is mainly the rifting.

Table 2-3. Examples of basement and supracrustal sequences for the greenstone belts

Craton / greenstone belts	Basement of the greenstone belts	Supracrustal Sequence	References
Canada Point Lake, Central Superior Province	Anton gneiss terrain: 3152±2 Ma [1]	Point Lake greenstone belt Mafic pillowed volcans, Conglomerates, siltstones ca. 2.7 Ga	Stockwell (1933) Henderson (1975) Kusky (1991)
Hearne Lake area S. Slave Province	Sleepy Dragon gneiss complex 2829 +40/-31 Ma [2]	Conglomerates, Cameron River volcanics-pillowed basalts ca. 2.7 Ga	Henderson (1995) Kusky (1990)
Steep Rock Superior Province	Marmion Complex Tonalitic gneiss 2991 Ma [3]	Conglomerate, carbonate (stromatolites), ironstone, mafic volcanics, >2.69 Ga	Wilks and Nisbet (1988)
South Africa Pongola	Kaapvaal granitoids	Fluvial, tidal and shelf, conglomerate, sandstone, silts & muds. Calc-alkali tholeiitic basalts. 2940± 22 Ma [4]	Mathews and Scharrer (1968)
Kaapvaal Barbeton greenstone	Oceanic floor ophiolites		De Wit, 1982 Kroner and Tegtmeyer, 1994
Zimbabwe Shurugwe area greenstones	Tokwe gneiss (c. 3.5 Ga) overlain by obducted ophiolite of ocean-floor origin	Upper Bulawayan conglomerate, ironstone and komatiitic and pillowed mafic volcanics, ca 2700 Ma	Stowe, 1974 Shackelton, 1995 Cotterill (1979) Tsomondo et al. (1992)

Belingwe area greenstone belts	3.5 Ga gneisses 2.9 Ga greenstones	Upper Bulawayan clastic sediments, limestone, ironstone, komatiitic and basaltic volcanics, ca 2.7 Ga [5]	Bickle et al., (1975) Nisbet et al. (1993)
Australia Pilbara Craton Whim Creek	Gneisses and, Warrawoona and Gorge Creek Groups ca. 3450 – 3300 Ma granite-greenstone terrain	Clastic sediments, komatiitic and mafic volcanics, felsic volcanics ca. 2990 ± 7 Ma McNaughton et al. cf [6]	Fitton et al. (1975) Barley (1987) Horwitz)1992)
Southern India Bababundan-Ranibennur Tract	Peninsular Gneisses 2900 – 3300 Ma [5]	Bababundan Group, clastic sediments, mafic and felsic volcanics, >2600 Ma [7]	Ramakrishnan et al., 1976; Chadwick et al. (1985); Chadwick et al. (1992); Viswanatha et al., 1982; Shackelton, 1995

Geochronology sources: [1] U-Pb zircon, Krogh and Gibbins (1978); [2] U-Pb zircon, Henderson et al. (1978); [3] U-Pb zircon, Davis and Jackson (1985); [4] U-Pb zircon, Hegner et al. (1984); [5] Pb- Pb thin slice, Chauvel et al. (1993); [6] Horwitz and Pidgeon (1993); [7] Pb – Pb whole-rock, Taylor and Chadwick. (1984).

The table 2 – 3 suggest that the greenstone sequences were definitely deposited above older continental crust and according to Bickel et al. (1994) there are no greenstone sequences exhibiting sufficient features to warrant definitive classification as an ophiolite. The tectonics of the greenstone belts depend much on the understanding the basement and the nature of the contact between the basement and the supracrustal sequences. The next section discusses the structures in the greenstone belts and their relationship to mineralisation.

2.1.2 Structures in the greenstone belts

The Archaean granite greenstone terrains present different types of structures in a variety of geometries. The thrust faults, synforms associated with either interference folding or domal/diapiric granitoids (e.g. Pilbara and Zimbabwe Craton), and late strike slip shear zones (e.g. Superior Province) are some of the dominant structures in greenstone belts (Kusky and Vearncombe, 1997).

The contacts between granitoid and greenstone belts are structural breaks or shear zones (e.g. Barberton in South Africa and Shurugwe in Zimbabwe) (Shackleton, 1995), or unconformities (e.g. Belingwe in Zimbabwe (Bickle et al., 1994) and India (Viswanatha et al., 1982 and Shackleton, 1995)). There has been controversy in the interpretation of these contacts, the stratigraphers consider them basin margin faults while the structural analysts argue that they are either thrust or strike-slip faults and/or younger structures not related to initial basin geometry (Kusky and Vearncombe, 1997).

Early extensional fault structures have been mapped in many greenstone belts (e.g. Barberton) and are associated with originally flat-lying structures associated with an early schistosity or they may represent transform faults (Platt, 1980; de Wit, 1986; Shackleton, 1995; Kusky and Vearncombe, 1997).

Early contractional structures are usually related to thrust faulting and recumbent folding as observed in the Zimbabwe and Kaapvaal Cratons (Tsomondo et al., 1992; de Wit 1982 and Jackson, 1984), Yilgarn Craton (Archibald, 1987 and Swager and Griffin 1990), Pilbara Craton (Bickle et al., 1985), Slave Province (Kusky, 1991) and Superior Province (Ayres and Corfu, 1991). These structures and the stratigraphy are interpreted as responsible for the overall distribution of rock types in the greenstone belts (Kusky and Vearncombe, 1997).

The non-linear pattern and cuspate outlines of some greenstone belts in the Zimbabwe and Dharwar Cratons suggest an influence of diapirs in the early stages of the greenstone belt evolution. Blenkinsop et al., (1993) and Jelsma and Dirks (2002) argue that the cuspate nature Zimbabwean greenstone belts reflect a true deformation patterns. This deformation is related to diapiric and ballooning plutons, which caused strong compression, and shortening of the inter-diapir greenstone belts with steep dips into the inter-diapir synclines (mainly in Pilbara, Dharwar and Zimbabwe Cratons) (Shackleton, 1995). The linearity of some greenstone belts (e.g. Yilgarn block in west Australia, eastern part of Dharwar Craton in India) is mainly a result of subduction-driven, along craton margin collision, or within-plate tectonics might be attributed to the deformational pattern (Shackleton, 1995).

In Zimbabwe context both processes may have operated. The ENE trending belts on the south of the craton are parallel to the Limpopo mobile belt trend whereas there are in the central west of the craton belts that have linear trends which are not readily related to craton margin events.

Early structures in greenstone belts were reactivated because they represent zones of weakness where late intrusive rocks intruded (de Wit et al., 1987) or might have been used as ascending path for mineralising fluids.

The structures in the greenstone terrains can be summarised in:

(i) Structures resulting from pre-diapiric gravity slides, thrusts (obductional?) and related compressional structures,

(ii) Structures resulting from the diapiric rise of plutons,

(iii) And post-diapiric compressional structures (Shackleton, 1995).

The next section discusses the mineralisation in the Archaean granite-greenstone terrains.

2.2 Gold Mineralisation in the Archaean Greenstone belts

Archaean greenstone belts are major sources of gold in the world. The explanation of what controls the distribution of gold in a greenstone belt is key to the development of any exploration model at mine, belt, or on a Craton wide scale.

Most of the gold in Archaean greenstone belts is confined to the vicinity of re-activated ductile shear zones (e.g. Groves et al., 1988; Colvine et al., 1984, 1988; Sibson et al., 1988; Groves and Foster, 1993; Campbell and Pitfield, 1994; Herrington, 1995; Dirks and van der Merwe, 1997). According to Colvine et al. (1984); Groves et al. (1987 and 1988); Groves and Foster (1993); and Campbell and Pitfield (1994) the precipitation of gold occurs in the brittle-ductile regime at 2±0.5 kbar and 350°C where fluid flow is localised and fluids are pumped up shear zones of sufficient scale.

Brittle-ductile shear zones, especially those with a reverse component, are regarded as extremely important in focusing fluid flow and acting as depositional centres (e.g. Sibson, 1987; Sibson et al., 1988; Boulier and Robert, 1992; Schmidt Mumm et al., 1994; Dirks and van der Merwe, 1997).

Authors such as Foster et al. (1986), Foster (1988a, b), Groves and Foster (1993), Campbell and Pitfield (1994), Dirks and van der Merwe (1997), Groves et al. (1998), and Blenkinsop et al. (2000), have shown that shear hosted gold deposits in greenstone belts are not within the primary shears, but within secondary structures (e.g. fault splays and duplexes) associated with them.

The changes in chemistry, pressure and temperature are the main factors that are responsible for the precipitation of gold. The chemistry is related to changes in mineralogy and composition of the host rock. The pressure variation may be due to presence of structures (e.g. dilational jogs) competence contrast and low stress at crustal level. The changes in temperature are mainly associated with crustal level, thermal conductivity of the host rock and nature of the geothermal gradients.

Lithologies related to greenstones (mafic, ultramafic and felsic volcanics, volcaniclastics, epiclastics, and BIF) and granodiorite/tonalite (associated with intensely sheared zone, Rezende gold fields in the MMO greenstone belt) and granitoid gneisses, with associated amphibolites, epiclastic metasediments that include shale/greywacke successions and banded iron formations are commonly associated with gold mineralisations in Archaean.

Gold is mainly associated with sulphides (pyrite (50 – 95 vol.% of opaque minerals), galena (e.g. at Rezende mine: 1 – 40 vol.%), arsenopyrite (0 – 40 vol. %) with accessory minerals such as pyrrhotite, and sphalerite (Schmidt Mumm et al., 1994)) and quartz veins. Most of this gold is primary and formed at the same time or from the same fluid as sulphides. The reactivation of fault structures leads to second or even third gold mineralising event.

On a Craton wide scale (e.g. Zimbabwe Craton, and Superior Province, Canada) there is a relationship between the location of gold deposits and the crustal or greenstone belt scale corridors (see Chapter 5). Despite this large-scale association, the first order structures rarely host gold deposits at any structural level for example in the Yilgarn (Groves et al., 1995) and Zimbabwe Cratons (Campbell and Pitfield, 1994).

Gold mineralisation is mainly deposited at structural collapses such as intersections of shears, inflections of shears, fault-splays and dilation shears, where there is increased permeability, and low stress fields that constitute an ore fluid focus. These sites are seldom continuous along a shear zone or structure. They are localised within distinct segments of these structures where permeability and or gradients in hydraulic head are highest (Cox, 1999).

The development of secondary structures, gold bearing veins and shear zones, is a sequential process representing an initial phase of synthetic R and antithetic R1 riedel shears which give way to transfer movement on principal shears (D or Y) striking parallel to the main vector of strike-slip (Fig. 2- 4) (Campbell and Pitfield, 1994). This process may repeat itself at higher levels of the crust, signifying more complexity of structures in the brittle regime (superficial) compared to the ductile (deeper) ones (Figs. 2-1 and 2-2).

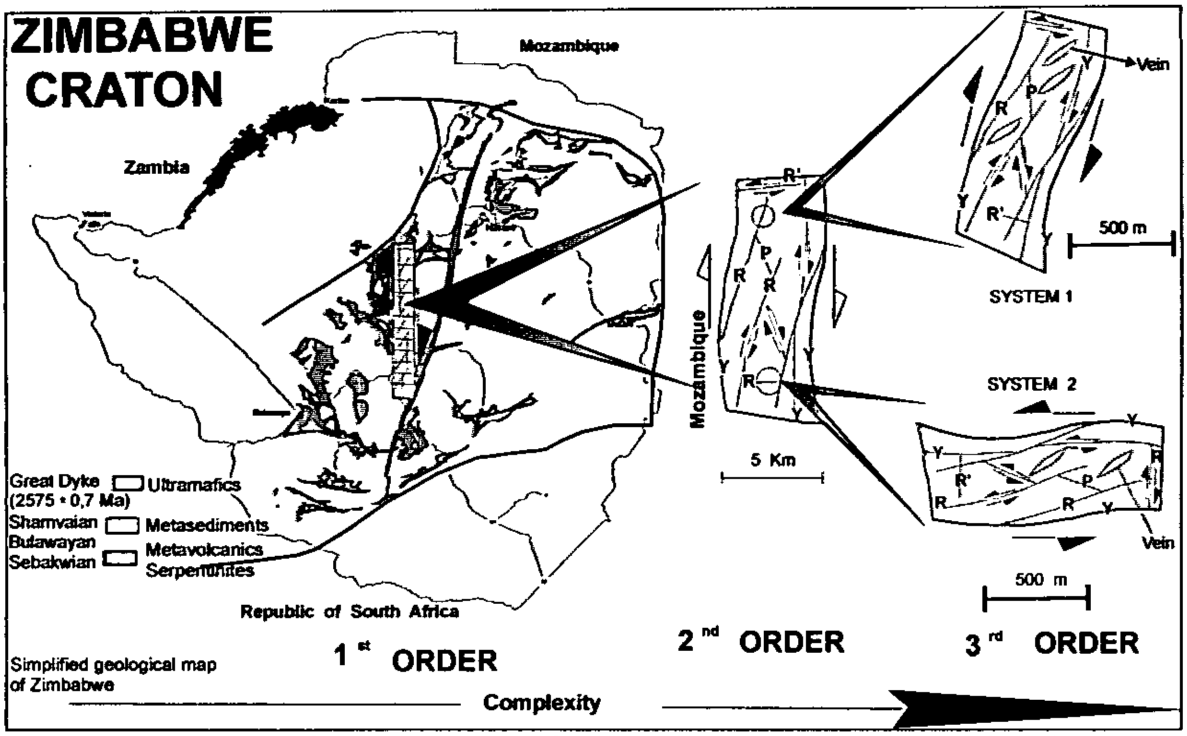

Figure 2-1. An example of scale dependency of gold bearing structures in the Zimbabwe Craton. The increase in complexity is accompanied by transition from pure ductile regime to pure brittle regime (see also figure 2-2) (after Dirks et al., 2001)

The Au-bearing structures are also scale dependent suggesting repeatability of structures with increasing complexity towards secondary and tertiary structures (Figure 2-1). Most conclusions are drawn on the basis of descriptions at the mine scale, which are extrapolated to the greenstone belt level and to Craton-scale. This evidently raises the question of the overall nature and scale of structural control of gold mineralisation in the Archaean, associated with multiple reactivations of structures by different tectonic events (regional and local).

The next session discusses the controls of gold mineralisation.

2.2.1 Controls of Gold Mineralisation in Archaean granite-greenstone Terrains

Archaean gold deposits share common characteristics, which are important to consider before discussing the controls of mineralisation. These common characteristics include; according to Cox (1999):

(i) Deposits occurring in, or adjacent to, low displacement faults or shear zones,

(ii) The host faults and shear zones form part of larger crustal scale shear systems,

(iii) High fluid flux that was localised along the faults and shear zones during ore formation,

(iv) Gold deposition occurring during deformation within the host structures,

(v) Depths of formation predominantly range between 4 and 15 km, and at temperatures between 250° and 500° (Kerrich & Cassidy, 1994),

(vi) The hydrothermal fluids were low salinity, predominantly H_2O- CO_2 fluids (McCuaig & Kerrich, 1994),

(vii) Deposits formed in near-lithostatic to transiently supra-lithostatic fluid pressure regimes (Sibson et al., 1988; Cox et al., 1991, 1995), and

(viii) Deposits formed typically in post-peak metamorphic regimes in convergent accretionary orogens (Kerrich & Cassidy, 1994).

In several regions within Australia, Canada, Zimbabwe and other Archaean terrains, gold deposition within banded iron formations and mafic rocks is enhanced relatively to other host rocks (Groves and Phillips, 1987; Colvine et al., 1988). These rocks might be more favourable because, when gold is transported as sulphur complexes (Phillips and Groves, 1983) the iron from the mafic and ultramafic rocks would facilitate the breakdown of Fe-Mg-bearing silicates (chlorite, actinolite) to form pyrite, and consequently destabilise the gold complexes in solution (Neall and Phillips, 1987) as illustrated on the reaction 1 (Phillips et al., 1996), using end-member chlorite.

$$Fe_6Si_4O_{10}(OH)_8 + 6HAu(HS)_2 + 1.5O_2 = 6Au + 6FeS_2 + 4SiO_2 + 13H_2O \qquad \text{(Eq. 1)}$$

$$\text{Chlorite} + \text{Au} - \text{S complex} + O_2 = \text{Au} + \text{pyrite} + \text{quartz} + H_2O$$

This reaction is just one of many possibilities for the liberation of gold, i.e. the changes in chemistry of the host rock, for example the presence of magnetite or more oxidising conditions would vary the end-members and consequently the results (see also Phillips et al., 1996).

In contrast chemical reactions between felsic-rich lithologies and gold bearing fluids mainly produce small amounts of gold, whereas those between mafic and andesitic types produces elevated values of gold. This has been shown to be the case where a shear zone traverses siltstones and andesites and gold is precipitated within the andesites (e.g. Stawell, Western Victoria, Phillips et al., 1996).

The thickness and geometry of the host lithology are other constraining factors that control the localisation of gold deposits because it allows more surface area for the fluid to interact.

The tectonically induced permeability conjugated with strain of the lithology has to accommodate large volumes of high-pressure fluid flux, and the stress gradient has to be high.

Besides the lithology the mineralisation is also controlled by the contacts between competent units adjacent and non-competent units (e.g. porphyry intrusions), or at the contact between units of contrasting competency which become highly mineralised (e.g. Phillips and Groves, 1983) while the incompetent units are rarely mineralised, except in fold hinges.

The development of hydrothermal systems responsible for the formation of economic deposits appears to be linked to the formation of deeply penetrating crustal shear systems (Cox, 1999). If the crust already contains these major structures, and other mechanical heterogeneities, they may control the development of areas of enhanced fluid flow and hence the structures themselves may be the sites (Sanderson & Zhang, 1999). Figure 2-2 illustrates the development of such sites from a pure ductile to pure brittle regime.

All gold mines in most greenstone belts world-wide (Canadian shield – Superior and Slave Provinces, Zimbabwe Craton, Kaapvaal Craton, Yilgarn and Pilbara Cratons) are influenced, to varying degrees, by structural disturbances that may be regional (crustal scale strike slip shear zones), or local, or both (e.g. Sibson 1990, 1996; Campbell and Pitfield, 1994, Groves et al., 1997; Sanderson & Zhang, 1999). In Zimbabwe, for example, 20% of total production is derived from mineralised shear zones (Campbell and Pitfield, 1994). Gold in the Zimbabwe Craton typically occurs either in second order shears, including conjugate sets within, or adjacent to the first-order shear zones which transect the greenstone belts, or, at particular sites along the shear zones associated with duplexing, inflections, en echélon segmentation, lithological contrasts, pressure shadows, shear-related folds, and dilational jogs (Campbell and Pitfield, 1994).

The high permeability sites represent areas of stress shadows around intrusions, releasing bends along shear bands which are related to brittle fractures that are important conduits for fluid flow and both tensile and shear failure, are mainly promoted by low effective stresses (Sibson, 1996; Sanderson and Zhang, 1999).

The mineralisation in Archaean greenstone belts is spatially and temporally consistent in its position, having formed during syn-to post-peak metamorphic event and emplaced at c. 3.2 - 2.6 Ga, as illustrated on Table 2-4. The available ages from Zimbabwe, Yilgarn, Slave, and Superior Cratons support this view. According to Barley and Groves (1992) the gold deposits in any Archaean terrain may well all be a part of the same supercontinent cycle.

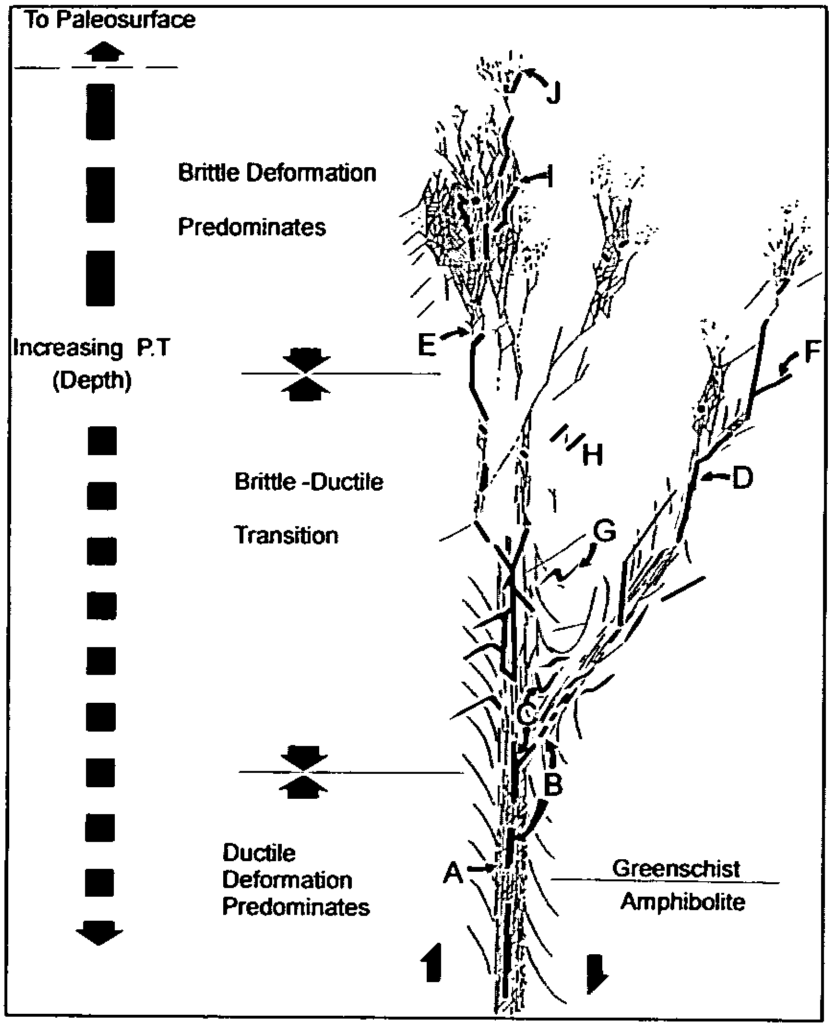

Figure 2- 2. Schematic representation of an ideal ore zone. Vein systems are interpreted as widening, and becoming increasingly complex with elevation: A. replacement veins; B. boudinaged veins; C. saddle reef veins; D. Riedel shear veins; E. “break ore” veins; F. undeformed tension veins; G. deformed tension veins; H. breccia veins; J. pervasive silicification. Source: Colvine et al., 1988

The presence of numerous granitic intrusions or cupolas, within greenstone belts is responsible for the formation of concentric or radial strike slip faults and normal faults, and shears that host mineralisation world-wide (e.g. Powell et al., 1991 and Campbell and Pitfield, 1994). After syntectonic plutonism (diapirism) further far field stress is accommodated by strike-slip shearing. The areas around the granitic body become fractured to an extent of creating high permeability zones and low stress fields allowing fluid focusing during mineralisation (Campbell and Pitfield, 1994). This is probably the case of the large number of deposits located around and within the Penhalonga granodiorite in the MMO greenstone belt.

The granites also supply the heat flux necessary to trigger the upward migration of fluids by increasing the fluid pressure.

Table 2-4. Showing the timing of Archaean mineralisation.

Province	Age of veining	Age of host Terranes	Spatially Associated Magmatism	Metamorphic Events	References
Zimbabwe Craton, Zimbabwe	2670, 2659	Early and Late Archaean	2700-2600, 2460 (Great Dyke at 2575±0,7)	2,69 Ga (?)	Foster and Piper (1993), Darbyshire et al (1996), Vinyu et al. (1996).
Yilgarn Craton, W. Australia	2640 – 2620	2750 – 2685	2690-2660, 2650-2630	2,69 –2,66 Ga, 2,65 - 2,63 Ga	Kent and McDougall (1995), Kent et al. (1996), Kent and Hagemann (1996), Cox (1999)
Slave Craton, NWT, Canada	about 2670 – 2660	Middle and Late Archaean	2663, 2640-2585	about 2,69 Ga	Abraham and Spooner (1995), MacLachlin and Helmstaedt (1995)
Superior Province, Canada	2720-2670, 2633-2404 (?)	Middle and Late Archaean	2720-2673, 2645-2611	2,69 – 2,643 Ga	Kerrich (1994), Kerrich & Cassidy (1994), Jackson & Cruden (1995), Powell et al. (1991)
Kaapvaal Craton, South Africa	3200-3064 (Barberton belt); >2700 with perhaps some at 2850 (Murchison belt)	3600-3200 (in Barberton belt)	3437, 3106, 3000 – 2700, 2600-2500	>3,2 Ga, some at 2,85 Ga	deRonde et al. (1991), Foster and Piper (1993)

(?) age not consistent with general pattern. *Adapted from:* Groves et al., 1998

In Zimbabwe, 23% of the mines are spatially related to felsic porphyries and felsic – intermediate intrusions and have produced over 800 tonnes of gold (Dirks et al., 2000). Other important parameters that control gold mineralisation are the physical and thermal factors, which are recognised as main contributors to fluid flow regimes and precipitation of metals in the upper crust. Researchers (e.g. Sibson, 1990 and Holyland et al., 1993) indicate that fluid migration in a tectonically active environment occurs dominantly in response to a physical, rather than chemical or thermal, driving mechanism. A sudden fluid pressure drop can drive phase separation processes and gold precipitation, leading to preferential gold deposition in veins, and especially at dilatant jogs where fluid pressure reductions at failure are most severe (Cox , 1999).

The change from ductile to brittle regime causes variations in physico-chemical conditions of the ore fluids and may be conducive to gold precipitation.

2.3 The Zimbabwe Craton

The Zimbabwe Archaean Craton contains granite-greenstone terrains of different ages whose broad subdivisions are distinguished on the basis of field relationships and age determinations (e.g. Macgregor, 1951, Snowden and Bickle, 1976, Wilson, 1979, Snowden, 1984, Jelsma et al., 1993, Bickle et al., 1993, Wilson at al., 1995, Jelsma et al., 1996, Blenkinsop et al., 1997, Dirks & Jelsma 1998a, Horstwood et al., 1999, Dirks et al., 2000, Jelsma & Dirks, 2000). It covers an area of 400000 km^2 and at surface, it is characterised by distinct greenstone belts with a ratio of greenstone belt to granite and granite gneisses being one to five (1:5) (Blenkinsop et al., 1997).

The evolution of greenstone belts is controversial with some consensus around models that advocate the intracratonic extensional basins with deformation associated to non-uniformitarian vertical tectonic processes. Related to this model is the vertical accretion process advanced for the Zimbabwe Craton (Blenkinsop et al., 1997) and Dhawar Craton in India (Bouhallier et al., 1993). The second model advocates that the greenstone belts are formed as result of plate tectonics similar to the present processes. The so-called horizontal accecretion is clamed to be responsible for the formation of greenstones in the Yilgarn Block of western Australia (Myers, 1995), the Kaapvaal Craton in South Africa (de Wit et al., 1992) and the Superior Province, Canada (Card, 1990). Researcher such as Dirks and Jelsma (1998), Dirks et al. (2000) and Kusky (1998) have reinterpreted the Zimbabwe Craton on the basis of field evidence and concluded that the evolution of the greenstone belts represents an amalgamation of various crustal fragments that accreted due to plate tectonic like processes.

2.3.1 Geological Setting and Stratigraphy

The Zimbabwe Craton comprises sedimentary and volcanic rocks of the greenstone belts, the associated granitoids and granitoid gneisses together with certain dyke swarms (Wilson, 1979).

The stratigraphic nomenclature for the greenstone belts of the Cratonic Basement Complex is based on the work by MacGregor (1951), Wilson (1979) and more recently Jelsma and Dirks (2002) and Wilson et al. (1995). MacGregor (1951) explained the distribution of the greenstones enveloping the granites as result of vertical movements due to diapirism. The greenstone belts can be broadly divided into three Supergroups – the Sebakwian, which is overlain by the Bulawayan and finally capped by the Shamvaian Supergroups. Generally the Shamvaian Supergroup is the final major sedimentary unit underlain by the widespread Bulawayan Supergroup, which consists of a volcanic pile together with some minor sedimentary rocks. The Sebakwian Supergroup is at the bottom of the succession and is considered the oldest unit and comprises supracrustal rocks and mafic and ultramafic rocks that broadly developed coeval with regional metamorphism and synkinematic granitoid emplacement.

Since the seventies researchers have concentrated their effort on studying the stratigraphy of Zimbabwe (e.g. Nisbet et al., 1977; Orpen, 1978; Bickle et al., 1975; Martin, 1978; Kusky, 1991; Kusky and Kidd, 1992; Bickle et al., 1993; Kusky and Winsky, 1995; Wilson et al., 1995). The stratigraphy of Belingwe greenstone belt as described by Martin (1978) comprised two major units, the Upper and Lower greenstones of the Bulawayan separated by an unconformity. These terms have subsequently been applied craton-wide to greenstone belts around the country, and Wilson et al 1995 retained the term Bulawayan for the upper succession and the volcanics to the Lower greenstones as the Belingwean (e.g. Bickle and Nisbet, 1993, Bickle et al., 1993, Kusky and Winsky, 1995) (Table 2 – 5 and Fig. 2 - 3). The stratigraphy at Belingwe greenstone belt has lateral variations from southeast to the west of the belt.

The Lower Greenstones at Belingwe, to the southeast, are represented by the Brooklands Formation, which consists of basaltic, and komatiitic lavas interbedded with phyllites and banded iron-stones, also with quartzites, chloritic grits and conglomerates (Martin, 1978, Martin et al., 1993). And to the west of the belt the Lower Greenstones comprise three formations, the Hokonui (Intermediate to felsic volcanics, mostly pyroclastic, and mafic volcanics), Bend (Komatiite, komatiitic basalt and ironstone) and the Koodoovale (Conglomaret, felsic agglomerate). The Hokonui formation consists of lateral variations of dacitic pyroclastic rocks, andesitic flows and pyroclasts, amphibolites, tremolite-chlorite schist and some banded calc-silicate rocks. The Bend Formation is inferred to overlie unconformably the Hokonui Formation and consists of alternating pillowed mafic lavas, spinifex-textured flows and sills, and intercalated-banded iron-formation. The Koodoovale Formation conglomerates of the Lower Bulawayan Group with boulders of banded iron-formation, tremolite-chlorite rocks, felsic volcanic rocks and granite caps these rocks (Wilson et al., 1995).

The Upper Greenstones of Wilson (1979) and Forster et al.(1996) is equivalent to the Upper Bulawayan and comprise of, from base to top, Manjeri Formation, the Reliance Formation, the Zeederbergs Formation, and the Cheshire Formation.

The Manjeri Formation consists of clastic shallow-water sediments and limestone, overlain by a sulphide facies banded iron-formation (Wilson, 1979). It rests unconformably on different formations of the Lower Greenstones and on the basement of the Shabani Gneiss. On top of it is the Reliance Formation made up of ultramafic rocks, komatiitic basalts, basalts, and pyroclastic units. The Zeederbergs Formation overlay the Reliance Formation and consists of tholeiitic basalts with massive and pillowed flows, and minor pyroclastic rocks.

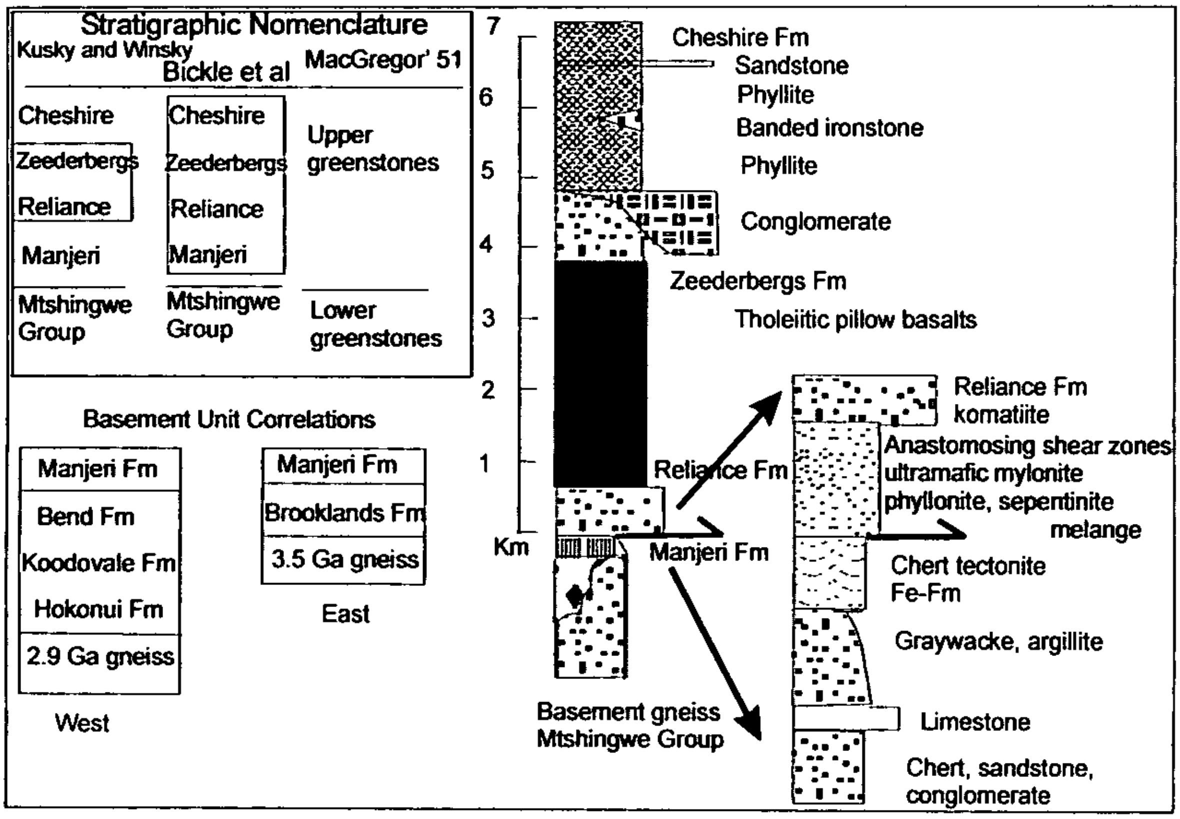

Figure 2 – 3. Stratigraphic columns of the Belingwe greenstone belt, showing also stratigraphic nomenclature of various workers and possible correlations of different units. (After Kusky and Winsky, 1995)

Conformably capping the volcanic pile is the Cheshire Formation that consists of shallow water pelitic sedimentary rocks (Martin, 1978 and Hofman et al., 2001). In places it develops stromatolitic limestones (Martin et al., 1980, Wilson et al., 1995) and a locally derived conglomerate at the base. Wilson et al., 1995 summarises the Zimbabwe stratigraphy adopting part of Bickle and Nesbit, (1993). In this summary the Belingwean and Bulawayan, each contains a number of greenstone volcanic cycles (Table 2-5). The Belingwean, divided into Lower (Hokonui and Bvute Formations) and Upper Belingwean (Bent Formations) is equivalent to the lower portion of the Lower Greenstone belts and to the lower part of the Lower Bulawayan (Wilson et al., 1995). These units are ultramafic – mafic in their lower parts and mafic-felsic in their upper parts and can be coupled to episodes of syn-volcanic to late –tectonic .tonalite-granodioritic plutonism.

Table 2 - 5. Summary of Major Events in the Zimbabwe Archaean terrane

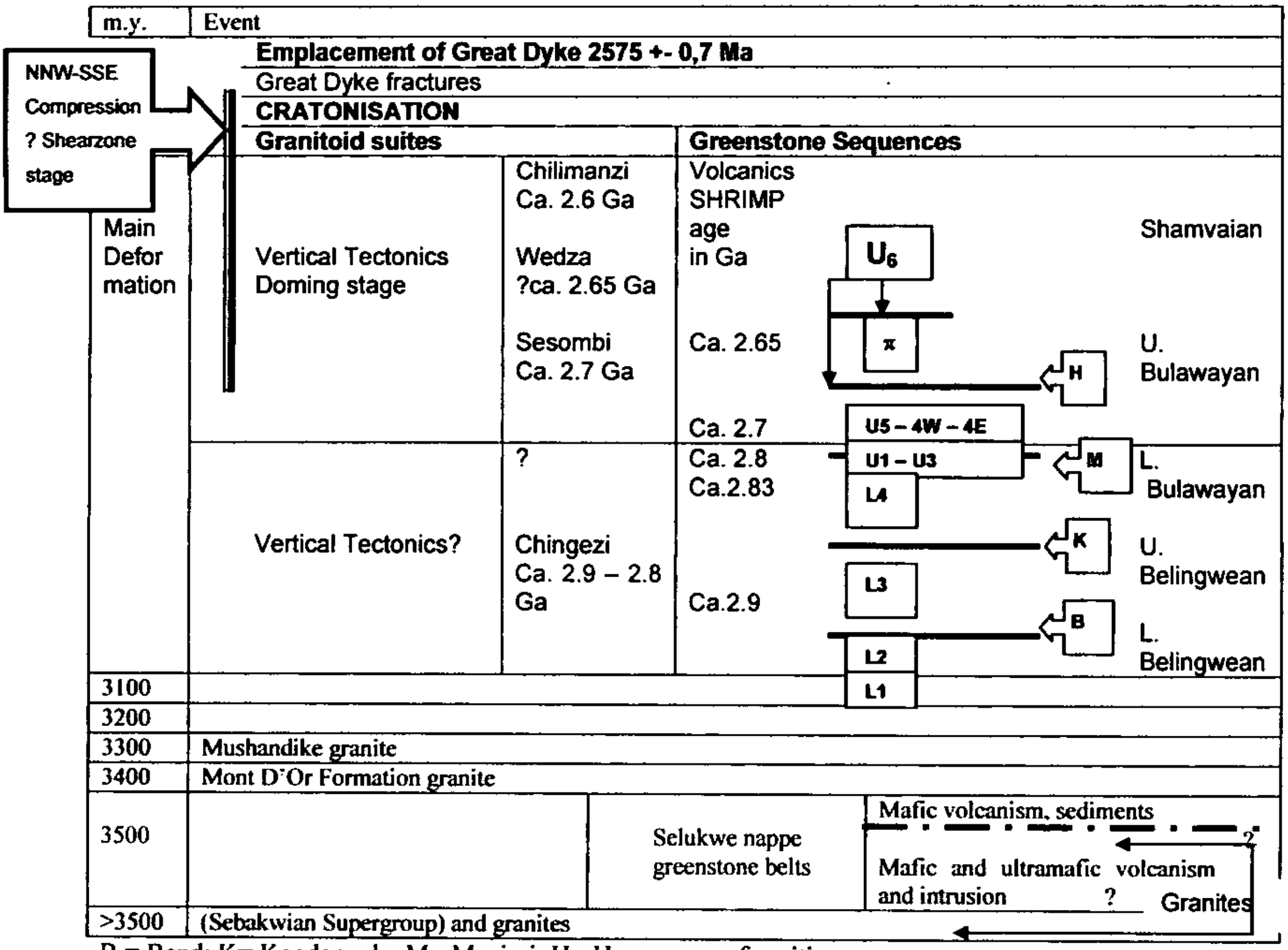

NNW-SSE Compression ? Shearzone stage

m.y.	Event					
	Emplacement of Great Dyke 2575 +- 0,7 Ma					
	Great Dyke fractures					
	CRATONISATION					
	Granitoid suites		**Greenstone Sequences**			
Main Defor mation	Vertical Tectonics Doming stage	Chilimanzi Ca. 2.6 Ga	Volcanics SHRIMP age in Ga	U₆		Shamvaian
		Wedza ?ca. 2.65 Ga				
		Sesombi Ca. 2.7 Ga	Ca. 2.65	π	H	U. Bulawayan
			Ca. 2.7	U5 – 4W – 4E		
	Vertical Tectonics?	?	Ca. 2.8 Ca.2.83	U1 – U3 L4	M	L. Bulawayan
		Chingezi Ca. 2.9 – 2.8 Ga			K	U. Belingwean
			Ca.2.9	L3		
				L2	B	L. Belingwean
3100				L1		
3200						
3300	Mushandike granite					
3400	Mont D'Or Formation granite					
3500		Selukwe nappe greenstone belts		Mafic volcanism, sediments Mafic and ultramafic volcanism and intrusion ?		Granites
>3500	(Sebakwian Supergroup) and granites					

B = Bend; K= Koodoovale; M= Manjeri; H= Harare unconformities

π = Harare sequence; A cycle indicates the full development of a lower ultramafic-mafic sequence which passes upwards into a mafic-felsic sequence. The felsic volcanics are dominantly dacites but may also include andesites and rhyolites. Unit U5 is andesite dominant. The Shamvaian Supergroup occurs unconformably above the Harare sequence and also on the eastern and western successions of the ca. 2.7 Ga Upper Bulawayan cycle. In the Masvingo greenstone belt, felsic volcanics from the Upper Shamvaian give age of 2661± 17 Ma. L_1 - L_4 and U_1 – U_4E are respectively the Mtshingwe and Ngezi Groups of Bickle and Nisbet (1993); L – Low Belingwean and U – Upper Belingwean. Adapted from Wilson, 1979 and Wilson et al., 1995.

2.3.2 Tectonic Evolution of the Zimbabwe Craton

Macgregor (1951) suggested that vertical movements due to diapirism and the formation of domes were responsible for the configuration of a number of granitic bodies with an ovoid shape and sheared margins across the Craton. Snowden and Bickle (1976) and Snowden (1984) later re-interpreted the Macgregor's model in terms of fold interference. More recently, Ramsay, (1989) and Jelsma et al., (1993), invoked ballooning plutonism or diapiric granite-gneiss dome, with remobilized older plutonic components on the basis of detailed studies of strain patterns around the Chinamora batholith. The diapiric models for emplacement of granites has been criticised on the basis of rheological, thermal and mechanical experiments (Clemens & Mawer 1992 and references therein). The granitic emplacement models tend to support more the idea of space creation through faulting in the upper crust (e.g. Hutton et al. 1990 and Grocott et al. 1994 and references therein).

A different view on the tectonic models was advanced by Coward & Daly (1984 and references therein), which hinges on the recognition of major strike-slip shear zones of large strike length. These structures suggest that Cratonic tectonics is dominated by horizontal displacements (Treloar & Blenkinsop, 1995). Jelsma and Dirks (2000) claimed that these earlier shear zones are linear zones of extreme flattening and transposition of earlier fabrics. Earlier workers (e.g. Treloar et al., 1992; Rollinson, 1993) related these shear zones to accretion of crustal fragments against the Kaapvaal Craton. This accretion culminated at 2.6 –2.7 Ga with collision of the Zimbabwe Craton and the Kaapvaal Craton. This collision of Zimbabwe and Kaapvaal Cratons caused crustal thickening, lower crust partial melting and emplacement of large, sheet-like plutons in the upper crust.

The southern part of Zimbabwe was explained in terms of a kinematic model by Coward & Daly (1984). They reported that the granite-gneiss terrain of east Midlands had been displaced towards the WSW along ENE-trending sinistral shears (Treloar and Blenkinsop, 1995). This block was then deformed approximately during the emplacement of the Chilimanzi granite suite as demonstrated by variable deformation of these granites and by the ductile nature of the deformation, which implies that the granites were not cold and brittle (Treloar and Blenkinsop, 1995).

The MMO greenstone belt lies in one of these ENE-trending crustal boundaries, hence the importance on the understanding the tectonic setting and its metallogenesis (see also Chapter 3). Crustal growth of the Zimbabwe Craton at ca. 2.7 –2.6 Ga is recorded by the widespread emplacement of granitoids and deposition of the Upper Bulawayan and Shamvaian greenstones. The stabilisation of the Craton was achieved around 2.6 Ga after the emplacement of the Chilimanzi granites (2.6 Ga) and the intrusion of 2575±0.7 Ma Great Dyke (Wilson et al., 1995).

The evolution of the Zimbabwe Craton is still far from being understood, and proper description of the events in the Craton hinges not only on the research on the stratigraphy of the greenstones belts but also in finding answers to questions such as, are they, in general, thick coherent sections with repeated stratigraphic alternations of felsic and ultramafic – mafic volcanic rocks and sedimentary rocks which underwent little deformation before late granitoid emplacement as claimed by Hamilton, (1998) or are they merely complexly deformed rock assemblages juxtaposed during collisional orogenesis as suggested by Kusky and Vearncombe (1997). Further problems on the stratigraphy of the Zimbabwe Craton can be illustrated by overturned stratigraphy from high-resolution SHRIMP ages on zircons from felsic volcanics of the Midlands greenstone belt (Wilson et al., 1995). The suggested presence of a major detachment zone in the Belingwe belt implies that a whole sequence of volcanics may have been transported from elsewhere (Kusky and Kidd, 1992; Kusky and Winsky, 1995; Shackleton, 1995).

2.3.3 Structures in the Zimbabwe Craton

Late Archaean faults and major shear zones focussing strain (Fig. 2-5) have been noted in various parts of the Zimbabwe Craton and its margins (e.g. Wilson, 1979; Coward et al., 1976; Stowe 1980; Herrington, 1995; Treloar and Blenkinsop, 1995).

In the Zimbabwe Craton there three types of important structures identified by different authors as shown in the Table 2 -6.

Table 2 – 6. Main structural types in the Zimbabwe Craton

Layer-parallel shear zones	**Concentric dome parallel shears**	**Regional ENE shears**	**Authors**
Accommodation structures	n.a.	n.a.	Blenkinsop et al., 1993
n.a	Doming related structures	n.a.	Jelsma et al., 1993
Thrusts	n.a.	Strike slip	Stowe, 1984
n.a.	Doming related structures	Strike slip	Campbell and Pietfield 1994
Accommodation structures	Doming related structures	Strike slip	Treloar and Blenkinsop 1995
Thrusts	Doming related structures	Strike slip	Dirks and Jelsma, 1998b
Thrusts	Doming related structures	Strike slip	Jelsma and Dirks, 2002

n.a. = no information available

The layer-parallel shear zones associated with low-angle stratigraphic truncations and silicified chert or BIF horizons have also been reported in the granite-greenstone terrains of the Yilgarn, Superior and Kaapvaal Cratons (de Wit et al., 1992; Swager and Griffin, 1990; Card, 1990; Myers, 1995) and are regarded as responsible for the overall distribution of the rock types as well as the thickening of the stratigraphic sequences.

The structural map (Fig. 2- 4) emphasises the presence of ENE trending moderately to steeply dipping crustal shear zones often with complex kinematics (Campbell and Pitfield, 1994).

The above described shear zones are known to control Au mineralisations in several greenstone belts of the Zimbabwe Craton (Campbell and Pitfield, 1994, Treloar and Blenkinsop, 1995), which include the Manica-Mutare-Odzi greenstone belt (see next section).

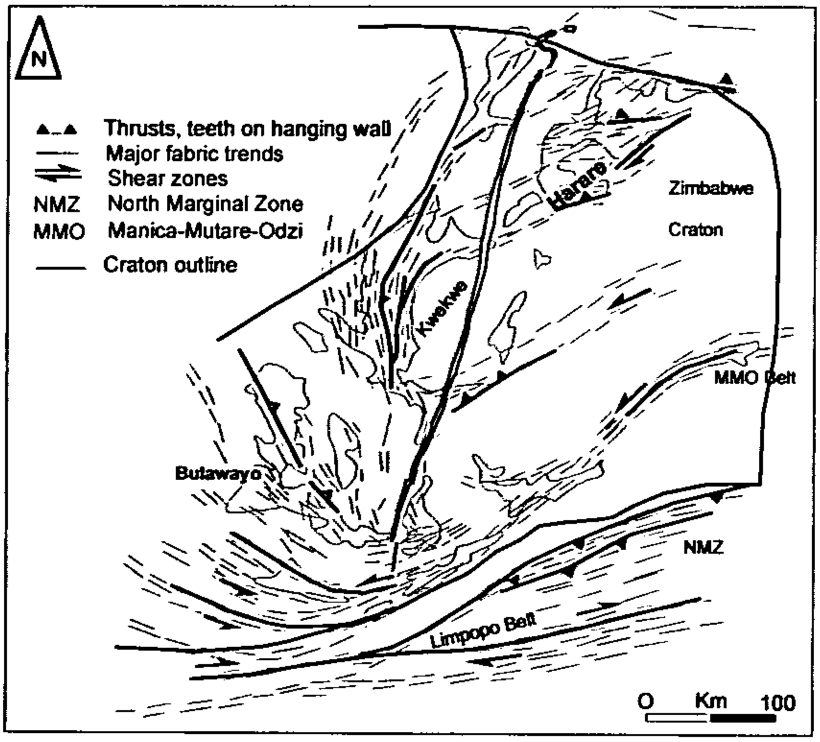

Figure 2-4. Revised map of major Archaean structures in the Zimbabwe Craton showing, in particular, the conjugate ENE-striking shear zones. Adapted from Treloar & Blenkinsop, 1995 and Geological Survey of Zimbabwe, 1980.

2.3.4 Archaean Gold Mineralisation in the Zimbabwe Craton

In the Zimbabwe Craton ca. 279 important deposits with production in excess of 1000000 ounces of Au have been recorded (Bartholomew, 1990; Oberthur, 1994). Most of the largest deposits occur within the Upper Bulawayan Supergroup, followed by the Shamvaian. Few large gold deposits are hosted in granite or diorite (e.g. Freda Rebecca mine). The majority of large deposits are concentrated in the Midlands greenstone belt between Chegutu and Kadoma in the north and Gweru and Shurugwi in the south.

Gold deposits in the Zimbabwe Craton are controlled by several factors, which can be categorised into structural, stratigraphic, metamorphic and granitic intrusions. Herrington (1995 and references therein), has dealt in detail with factors that influence the deposition of gold mineralisation in the Zimbabwe Craton.

Strike slip dislocation, dip-slip faulting and fault reactivation are evident in several deposits in the Zimbabwe Craton and, according to Foster (1989) it is also evident that the auriferous lodes are developed within a wide range of compressional, dilational, and ductile to brittle regimes (see Fig. 2-2). Forster (1989) notes that the geometry of the individual lodes was largely controlled by stress pattern, ductility of the rocks, lithologic inhomogeneities, and presence or absence of pre-existing structures.

Structures are only mineralised when cutting across lithologies with specific characteristics such as chemical, competence or sufficient thickness. That is the case of the Elvington mine and the Connemara group of mines. In both deposits the mineralisation is confined to a highly sheared banded iron-formation. In this case the BIF meets the competency criteria and probably the chemical conditions.

Shear zones in diorite host the current largest Au producer deposit in Zimbabwe, the Freda - Rebecca mine, and in the western Australia the giant Kalgoorlie and Golden Mile deposits. The lodes are often confined to the interface between rocks of different competence such as basalt-greywacke in the Cam & Motor and Globe & Phoenix mines in the Midlands greenstones (Collender, 1964; and Herrington, 1995), Dias Perreira mine in the MMO greenstone belt and the felsic (porphyritic) sill-basalt couple, which is a common control in many deposits in Zimbabwe (Foster and Wilson, 1984, Foster et al 1986; Foster, 1989). Foster et al. (1986) on the basis of observations at Redwing mine indicated that a considerable number of non-stratabound gold deposits are directly associated with intrusive "porphyries" or "felsites".

The metamorphic grade and intensity of deformation vary Craton-wide from lower greenschist facies to upper amphibolite facies. The high Mg-rocks when intruded by mineralised lodes tend to develop an aureole of carbonatization (e.g. Kwekwe ultramafic Complex, Foster et al., 1986), chloritization, sericitization and some silicification. These aureoles commonly exhibit outer zones of talc (Legion mine) or talc and chlorite (Germania mine), which pass into Mg-rich assemblages where the alteration is most intense (Foster, 1989 and references therein).

The metasomatism in metabasaltic rocks have typical assemblages: for example, in the greenschist facies, they involve actinolitic amphibole + chlorite + epidote + albite+ calcite+ quartz + pyrite (Powell et al., 1991). The ultramafic rocks are characterised by serpentine + talc + magnesite + pyrite at greenschist facies. And their alteration usually produced an actinolite-carbonate assemblage together with talc (e.g. Legion mine and Germania mine) (Foster et al., 1986).

Siderite and ankerite are located immediately adjacent to the lodes as invoked by Carter (1988) and Foster (1989). Fuchsite also occurs in intensely altered and deformed ultramafic units (e.g. in Manica portion of the MMO greenstone belt). Carter (1988) has identified hydrothermal albite in the alteration zone around the main ore body at Dalny mine west of Chegutu in Midlands greenstone belt. Sulphides are also common in the few millimetres of the wallrock adjacent to the veins. Wall rock alteration, though intense, may only extend for several meters from the veins (Foster et al., 1986), which makes it difficult to use satellite imagery direct mapping of hydrothermal alteration.

The main mineralisation event is a Craton-wide, probably worldwide, episode that occurred at time span between 2670 – 2620 Ma (see also Table 2-2 and Vinyu et al., 1996). This event correlates with the main deformation phase (D_1) with NW-SE, or E - W compression and sinistral transpression across the Craton (Campbell & Pitfield, 1994).

2.4 Discussion

It is puzzling why the late Archaean is particularly highly mineralized in gold. What is so special about the late Archaean that could explain its anomalous richness in gold? Where does gold come from and how was it concentrated in the known deposits? These and other questions that can be asked about Archaean gold mineralisation particularly in greenstone belts, their answers lie in understanding the tectonic evolution and stratigraphy of the Archaean terrains.

In this study, the identification of focus structures for gold mineralisation is believed to be able to lead to gold deposits. It is evident from present knowledge that deep-seated shear zones acted as focussing structures for gold in the Archaean terranes. This is supported by fluid inclusions studies, which revealed that the source of mineralising fluids is deep (Chenjerai, 1996, Huizenga, 1995, Jelsma et al., 1993). It is also a fact that gold is trapped in the secondary and tertiary structures rather than primary ones. These facts are demonstrated in the MMO greenstone belt (see Chapter 3).

The development of structurally controlled gold mineralisation in the Zimbabwe Craton is similar to mineralisation elsewhere in Archaean terranes (e.g. Kaapvaal Craton, Nutt et al., 1988, Pilbara Craton of west Australia, Bickle et al. 1985).

The combination of appropriate structure, lithology, favourable stress field, appropriate mineralogy and chemistry of the host rock and enough fluid provides a favourable environment for gold deposition. Lithological contacts such as granite-greenstone or banded iron formation-ultramafic rocks, metassediments – ultramafic units serve as appropriate sites for gold mineralisation. The orientation of the lithology in relation to the dominant stress field is also important for the formation of adequate structures, which might act as fluid focus.

This discussion leads us into understanding the global tectonic and structural framework of the Zimbabwe Craton. As discussed earlier there is no consensus on the tectonic setting and evolution of the Zimbabwe Craton. However, it is evident that the collision of the Zimbabwe Craton and the Kaapvaal Craton is an important stage in the Zimbabwe Craton evolution. The existence of ENE-trending zones of high deformation associated with shear zones is another important fact in the evolution of the Zimbabwe Craton. These structures are probably crustal block boundaries as claimed by several authors (e.g. Coward & Treloar, 1990 and Treloar and Blenkinsop, 1995 and references therein) or detachment fronts (Coward & Daly 1984), which are crucial, particularly where they are known to be mineralised (Monarch mine in the MMO greenstone belt). The MMO greenstone belt lies in one of these ENE-trending shear zones, hence the importance in understanding its tectonic setting for a validation of tectonic models for the Zimbabwe Craton.

2.5 Conclusions

The review presented in this Chapter shows that although there is little consensus about the origin of gold and the reason for its anomalous concentration in the late Archaean, it is a fact that greenstone belts worldwide are highly mineralised in gold. That fact makes the greenstone belts high prospectivity regions for gold mineralisation.

The universally accepted concept that zones of low mean stress or shear zones could have focused fluid (e.g. Groves et al., 1995), and hence controlled the setting of gold deposits, seems to apply to the MMO greenstone belt gold mineralisation. This explains the location of important gold deposits near or within shear zones in the Zimbabwe Craton (e.g. Dalny Mine) and in the MMO greenstone belt (e.g. Monarch mine, Guy Fawckes mine, Dot's Luck mine, Toronto mine, Champion mine, Reliance mine; Mondlane et al. 2001).

The most significant controls of gold mineralisation in the Zimbabwe Craton are structural; where gold is associated with sulphides or occurs as free gold in moderately-steep dipping (c. 50° ± 20°) reverse or oblique-reverse shear veins or shear zones that traverse the granite-greenstone belt.

The contacts of contrasting competency lithologies offer a potential host for gold mineralisation in the greenstone belts.

Chapter 3

3 Geology, Structure, Tectonic Setting and Mineralisation in the MMO greenstone belt

3.1 Introduction

In the previous chapter the Archaean granite greenstone terrains with particular emphasis to mineralisation controls and evolution of the Zimbabwe craton were discussed. In the present chapter a review of the geology, structure, tectonics, and metallogenesis of the Manica Mutare Odzi (MMO) greenstone belt in the light of the field evidence of the present study and satellite imagery interpretation is carried out. Emphasis is placed on the central and western part of the belt, which includes the best preserved, exposed and relatively well studied section of the belt.

The MMO greenstone belt lies in the eastern part of the Zimbabwe Craton and is shared between Mozambique and Zimbabwe. It is an important gold mining area with combined historical production and estimated reserves of 128 t of gold (Forster et al., 1996).

3.1.1 Previous geological work in the MMO greenstone belt

The majority of Zimbabwean greenstone belts have been described in a number of Geological Survey publications. However only the Midlands, Belingwe and Harare-Shamva greenstone belts where researchers such as Jelsma et al. (1993), Blenkinsop et al. (1993), Bickle and Nisbet (1993), Herrington (1995), Hoppner (1994), Wilson et al. (1995), Jelsma and Dirks (2000) and Hofmann et al. (2001), contributed towards a more detailed understanding of these belts.

The MMO greenstone belt is one of the least studied belts in the Zimbabwe Craton, despite its large gold production of around 84 tonnes up to 1995 (Forster et al., 1996). The central part of the belt is the best studied and the eastern section (Mozambican part of the belt) is the least investigated.

The early researchers (e.g. Swift, 1956) produced the first manuscripts on the geology of the belt, and described the mineral deposits (gold, copper, nickel, asbestos and magnesite) occurring within the belt. The geological map by Phaup (1937) for the Mutare section and by Swift (1956) for the Odzi section are by far the most comprehensive maps of the central and western sections of the belt to date.

The next period is characterised by works of Obretanov (1977), Stagman (1978), D'Orey (1978), Harrison (1979, and Fabiani (1980), who in general agreed with Phaup's observations, especially with respect to the intrusive nature of the felsite, quartz-diorites and the hydrothermal origin of the gold mineralisation. A different view is presented by Roberts (1979) and seconded by Chenjerai (1996) who suggested that the felsite is a pyroclastic horizon while the sulphide mineralisation is exhalative. They also report that the quartz-diorites are metasomatised greenstones that have been silicified due to migration of SiO_2 from the felsite.

Recent works include Manuel (1992), Chenjerai et al. (1994), Schmidt Mumm et al. (1994), Koenemann and Forster (1994), Treloar & Blenkinsop (1995), Wilson et al., (1995), Chenjerai (1996), and Forster et al. (1996). These authors concluded that the MMO is a late Archaean linear structure, anastomosing, deep seated, zone that was formed around or before 2.74 Ga. The ENE - trending belt is roughly synformal, with ultramafic metavolcanic rocks along the margins and coarse clastic metasedimentary rocks in the core. Volcanism was temporally associated with emplacement of early granitoids (Mondlane et al., 2000). Shear zones commonly separate individual lithological units. The whole sequence was intensely folded and later intruded by dolerite sheets and dykes of 1830 m.y. and Pan-African age (c.f. Wilson et al., 1987, Schmidt-Mumm et al., 1994, Forster et al., 1996).

The Manica section of the belt has been mapped at 1 to 5 000 and 10 000 scale by students of the Eduardo Mondlane University – Geology Department since 1987. Between 1991 and 1994, several groups sponsored by the BGR (Federal Institute for Geosciences and Natural Resources, Hannover, Germany) studied the MMO greenstone belt and the results are presented in Oberthür (1994) and Forster et al. (1996).

The greenstone sequence has been intruded to the north by an unsheared granite dated 2522 ± 36 Ma (Rb-Sr whole rock; Schmidt-Mumm et al., 1994) and to the south (in the Manica section) by the Vumba granite dated at 2527 ± 32 Ma (Rb-Sr whole rock; Manuel, 1992). To the east, the belt is bound by N-S trending Proterozoic gneisses of the Bárue Complex and quartzites and pelites of the Frontier Formation.

3.2 Regional Setting of the MMO Greenstone belt

The age of the MMO belt is constrained on the basis of Penhalonga granodiorite age (2742 ± 3 Ma) (U/Pb dating of individual zircon grains; Schmidt-Mumm et al., 1994), which gives the minimum age for the Bulawayan in the MMO belt. The ENE - trending MMO greenstone belt is roughly synformal, with Bulawayan Supergroup ultramafic metavolcanic rocks (serpentinites, talc schists, and komatiites) with intercalated lenses of banded iron formation, overlain by mafic metavolcanic rocks (pillow lavas and lapilli tuffs) along the margins and Shamvaian Supergroup coarse clastic metasedimentary rocks (acidic agglomerates, polymict conglomerate) in the core.

The Mbeza sediments are considered to predate the major phase of greenstone belt deformation and to be specific depositional response to the regional extension during ultramafic/mafic volcanism and sedimentation (Chenjerai, 1996).

The supracrustal sequences of the greenstone belt are intruded by granitoids of the Sesombi and Chilimanzi suites, which have overlapping ages of approximately 2800 to 2500 m.y. Gold mineralisation is known to be related to tonalitic intrusions (Forster et al., 1996).

Lithological units are intensely folded and a regional penetrative foliation has developed. Fold axes generally plunge shallowly either to the east or to the west and are parallel to the regional trend.

The main deformation phase include the NNW – SSE compression coeval with granite emplacement and characterised by shearing. This phase occurs during the doming stage related to granite emplacement and represents vertical tectonics.

3.3 Geology of the MMO Greenstone belt

This study utilised remote sensing images (frame TM169/073, ETM 169/73, SPOT - Xs and SPOT-Panchromatic), aerial photographs (1: 50000 scale) and geological map interpretation and was supported by ground truthing, mapping of selected portions of the belt, detailed logging of N-S traverses (Fig. 3 – 5) and detailed structural and geological mapping of mines.

A summary geological map at 1:50000 scale is presented in Figure 3-1. The geology of the MMO greenstone belt is characterised by an ENE – WSW trending volcanic sequences, which on lithological similarity has been assigned to the Lower (Koodoovale Formation) and Upper (Manjeri, Reliance, Zeederbergs and Cheshire Formations) Bulawayan of Wilson et al. (1995) (Table 2 – 5). The Bulawayan Supergoup are overlain by Mbeza and Mbeza Vengo sedimentary rocks of mainly polymict conglomerate at the base, the siltstones, and phyllites underlie the capping upward-coarsening sequence of clastic acidic agglomerates with meta-arkoses and grits.

The relationships between the Bulawayan and the overlying Mbeza and Mbeza Vengo sedimentary units is controversial and evidence by different authors suggest two possible interpretations:

i) The Mbeza and Mbeza Vengo sediments were deposited on a previously tectonised greenstone substrate (Obretanove, 1977, Koenemann and Forster, 1994, Forster et al., 1996), which implies major time break and presence of an unconformity. This would assign the Mbeza and Mbeza Vengo sedimentary rocks to Shamvaian.

ii) The presence of greenstone pebbles, and andesitic agglomerates, but no granitic pebbles, in the Mbeza and Mbeza Vengo succession (Scmidt Mumm et al., 1994) suggest that there was not apparent major time break between the Upper Bulawayan and the deposition of the Mbeza and Mbeza Vengo and, the absence of field evidence of early deformation in volcanics that did not affect the sediments (Chenjerai, 1996), implies that this thick unit of sediments and acidic agglomerate is conformable with the underlying Bulawayan rocks. Thus the Mbeza and Mbeza Vengo sedimentary rocks would be assigned to Upper Bulawayan, and equivalent to Cheshire Formation.

The assertion by Scmidt Mumm et al.(1994) that there are no granitic pebbles in the Mbeza sediments is not correct as these do exist. Therefore, the thesis of existence of unconformable relationships between the Bulawayan and the Mbeza and Mbeza Vengo groups is preferred.

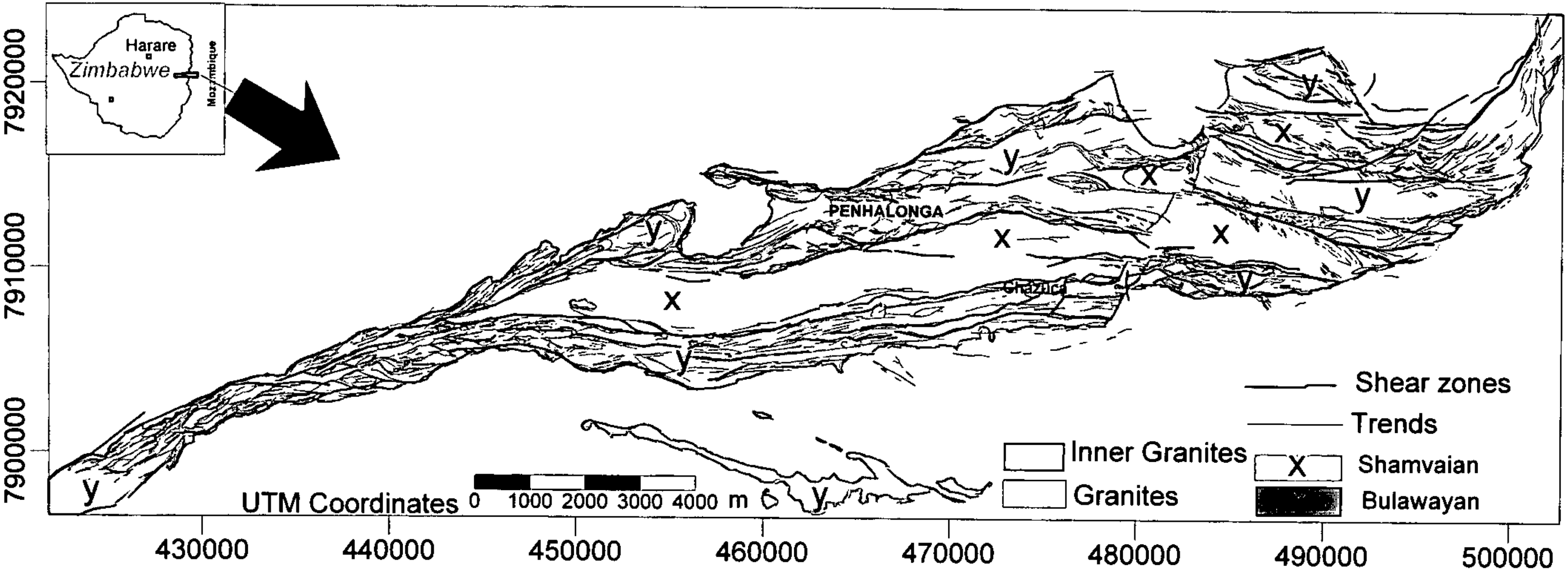

Figure 3 - 1. Geological map showing domains separated by anastomosing shear zones. The trends represent the foliation cleavage or bedding as interpreted from satellite imagery (TM169/73, ETM 169/73, SPOT - Xs and SPOT-Panchromatic) and mosaic of airphotos with geological map as reference.

3.3.1 Stratigraphy

The stratigraphy of the Zimbabwe craton greenstone belts is based on the Belingwe greenstone belt and is summarised by Wilson et al. (1995). The MMO greenstone belt does not expose the entire stratigraphic sequence (Fig. 3-2). Stagman (1978) correlated the Mbeza sediments to the Shamvaian Supergroup and Wilson et al. 1995 have confirmed this correlation. The major development of the Shamvaian is in the Shamva-Bindura area of the Harare greenstone belt and in the Masvingo greenstone belt. The Shamvaian Supergroup as described elsewhere occurs in basins generated syntectonically with deformation affecting the greenstone belts (Wilson et al., 1995). For example in the Shamva-Bindura area the basins and their infillings are believed to relate to vertical tectonic induced by the emplacement of the Wedza suite (Jelsma et al., 1993), whereas in the Masvingo greenstone belts, the basins are related to strike-slip (pull apart) basins related to major shears (see also Fig. 2-5) (Treloar and Blenkinsop, 1995, Wilson et al., 1995, Chenjerai, 1996).

In the MMO belt there is no evidence of Belingwean type lithologies. The mafic and ultramafic rocks have been assigned to the Bulawayan Supergroup but geochronological data on the ultramafic and mafic rocks are required in order to constrain the age of the rocks. In the Manica section of the belt these lithologies are referred to as the Macequece Formation. The Macequece Formation comprises peridotites, serpentinites, talc and chlorite schists, komatiitic and picritic metabasalts with discontinuous intercalations of BIF. The clastic rocks have been assigned to the Shamvaian Supergroup and are referred to as the Mbeza-Vengo Formation. The Mbeza-Vengo Formation is composed of basal conglomerate, polimict coglomerate/sandstone, siltstones, greywackes, slates, phyllites and grits. The presence of komatiitic basalt pebbles, BIF and minor granitic clasts in the basal conglomerate (Fig. 3 – 10) suggests that the Mbeza – Vengo metasedimentary rocks mainly originated from erosion of immediately underlying greenstone lithologies and old basement. The preservation of ultramafic clasts strongly supports the thesis that the ultramafic source was close by and that both erosion and deposition were rapid. This would imply that the beginning of the Mbeza sediments was related to a sudden increase in relief energy, probably due to basin margin uplift at early stages of syncline development. In the Manica section, the stratigraphy is not well constrained, therefore the thick sequence of basalts flanking the central tract of Mbeza metasedimentary rocks can probably be assigned to Upper Bulawayan (Campbell and Pitfield, 1994).

	Granitoid suites	*Age (Ma)*	*Greenstones Formations* *this study*	Inferred stratigraphic equivalent	*Orpen91 and Stagman 78*	*Direcçao Nacional de Geologia 87*
Main Deformation	Northern granites	2522 ± 36				
	Vumba granite	2527 ± 32				
	MINERALISATION EVENT (2650 ± 10)				**Basement Complex**	**Manica Group**
	Wedza Suite	2650				
	Inferred	2661± 17*	**Mbeza and Vengo Sediments**		**Mbeza Series of Mutare**	**Mbeza Vengo Formation**
			Clastic acidic agglomerates	Shamvaian	Metasediments	Metagreywackes
			Siltstones/phyllites/argillites		Felsic metavolcanics	and other sediments
			Polymict conglomerate		Basal conglomerate	Basal conglomerate
	??UNCONFORMITY					
	Inferred	2700**	**Macequece Formation**	Upper Bulawayan	**Odzi-Muatare succession**	**Macequece Formation**
	Penhalonga tonalite	2742 ± 3♦	Basalts (Manica section)		Andesitic dacitic metavolcanics	Picritic basalts
		2800 ?	**Mafic/ultramafic**		Basaltic metavolcanics	Komatiites
			Pillow Lavas			
			Basalts, Peridotitic Komatiite	Lower Bulawayan	Metasediments	Talc and chlorite schists
			Serpentinite, Talc schists		Ultramafic lavas and intrusions	Peridotites, serpentinites
			Tremolitic schists			
	Archaean granitic rocks				Younger intrusive granites	Cratonic granite-gneisses
					Older gneisses	

Figure 3 - 2. Summary of the main events in the Manica Mutare greenstone belt based on Wilson et al. (1995) and Jelsma et al. (1996), Orpen (1991), Stagman (1978), DNG (1987), ♦Schmidt Mumm et al. (1994).

*Felsic volcanics age –Upper Shamvaian (Masvingo greenstone belt)

** Upper Bulawayan cycle age, from Harare greenstone belt (Wilson et al., 1995);

The description of the individual lithologies in the MMO greenstone belt was attempted by Obretanov (1977) and Chenjerai (1996). The polymict conglomerate overlies the ultramafic sediments with a sharp contact. The conglomerate consists of BIF, quartz, ultramafic and mafic pebbles, felsic and granitic clastics. Chenjerai (1996) described areas where this unit is overlain by a poorly exposed sandstone unit. Siltstones or sandstones overlie the polimict conglomerate. The contact between the siltstones or sands and polimict conglomerated is sheared and dips 50° towards south (Chenjerai, 1996).

The depositional environment is debatable; Forster et al. (1996) suggest that the basins and the transverse ranges are a result of transcrustal sinistral shearing and shear-related imbrications. They also suggest that the sediment filled basin was folded together with the previously tectonized greenstone substrate. Koenemann and Forster (1994) have suggested a strike-slip of the Mbeza depository and ascribed such tectonics to pre-Mbeza deformation. Chenjerai (1996) argue that the greenstone belt including the Mbeza sediments has undergone the same progressive metamorphism and cleavage forming deformation. Furthermore he suggests a regime of extensional tectonics in which stepwise down faulting of the volcanic basin was an ongoing process. Hence the same tectonic event that controlled the ultramafic/mafic volcanism is likely to have persisted throughout the sedimentation period, culminating in the eruption of the andesitic agglomerate. The Chenjerai's view suggests that the Mbeza and Mbeza Vengo sediments and andesitic agglomerates are part of the Bulawayan.

The author has mapped neptunian dyke (Fig. 3 – 16) showing younging towards south within the basal conglomerate on Vengo sediments, which suggests that the conglomerate was deposited under water and the presence of sub-angular to well rounded pebbles implies that the source of the pebbles was not very far.

3.4 Structure of the MMO greenstone belt

The structural mapping is divided in two subsections; the existing structural framework and the field observations.

3.4.1 The existing structural framework

The present knowledge of the structure based on the Phaup (1937)' simple syncline structure, later on explained in detail by Koenemann and Forster, (1994), Forster et al., (1996), and Chenjerai (1996) as tightly folded synform made up of at least three east-west striking en echelon synforms gently plunging eastward at 25 – 30° and separated by tight antiforms. Chenjerai (1996) identified at least 4 phases of deformation: D_1 is mainly regional folding accompanied by cleavage formation and regional shearing with deformation intensity increasing towards the west to southwest. Forster et al. (1996) concluded that D_1 was accompanied by thrusting and the event reworked primary structures such as lava pillows and komatiites with spenifex textures and igneous mineral phases were largely destroyed. The ultramafic rocks and basalts were transformed into serpentinite, amphibole schist and talc schist. This deformation phase developed foliation, which is sub-parallel to the belt. D_2 is characterised by NNE-SSW and NW-SE striking faults of high to moderate angle reverse faults with a transcurrent dextral component, which displace the D_1 shears and the MMO greenstone belt lithologies.

Dolerite dykes intruded along D_2 structures; D_3 faulting is dominated by ENE-WSW striking faults occurring only in the granites and displace the D_2 faults with a sinistral sense of movement; a D_4 faulting phase displaces, in E-W sinistral sense, the D_2 faults and they are well developed underground at Redwing Mine.The interpretation by Chenjerai (1996) is based on structural data collected in the central and western zones of the belt. There is no coherent regional structural work in the eastern part of the belt.

Orpen (1982) and Koenemann & Forster (1994) suggested that prior to D_1 and deposition of the Mbeza metasedimentary rocks there was an older deformation event. Chenjerai (1996) refuted this suggestion due to lack of field evidence.

3.4.2 Field data

Considering the tectonic, metallogenic and structural importance of the shear zones along the contacts between Upper Bulawayan and Shamvaian, the structures of the belt have been mapped with the aim of explaining the structural model of the MMO greenstone belt. Special attention was paid to younging indicators, $S_0 - S_1$ relationships (Fig. 3 – 3b and Fig. 3 – 3c), intersection and stretching lineations (Fig. 3 – 3a), and shear sense indicators (see also appendix III-B).

The mapping of lineations (mineral stretching, elongation or slickenside) in the entire belt suggests a gentle (<30°) to moderate (<60°) plunge of the lineation towards the east or west (Fig. 3-3a). Related kinematic indicators (delta clasts and S-C relationships) consistently suggest thrusting from the south towards NW after unfolding the greenstone belt. This is true within the southern block of the greenstones and the entire sedimentary block up to the major silicified shear zone that makes the contact between the Mbeza sediments and the greenstones to the north.

The kinematic indicators (S-C fabrics) in the northern block of the greenstones show the northern block moving towards south. The foliation within the belt is steep and dips to the north or to the south (Fig. 3-3b). The bedding planes measured mainly within the Shamvaian metasedimentary rocks suggest an east west trend and dips mainly towards north and sometimes towards south (Fig. 3-3c).

Further analysis of the data by combining the structural field data and the trend map (Fig. 3-4) interpreted from satellite images and aerial photographs reveals that there are at least four distinct blocks within the belt. These blocks are named structural domains and are described in the next section (Fig. 3 – 5).

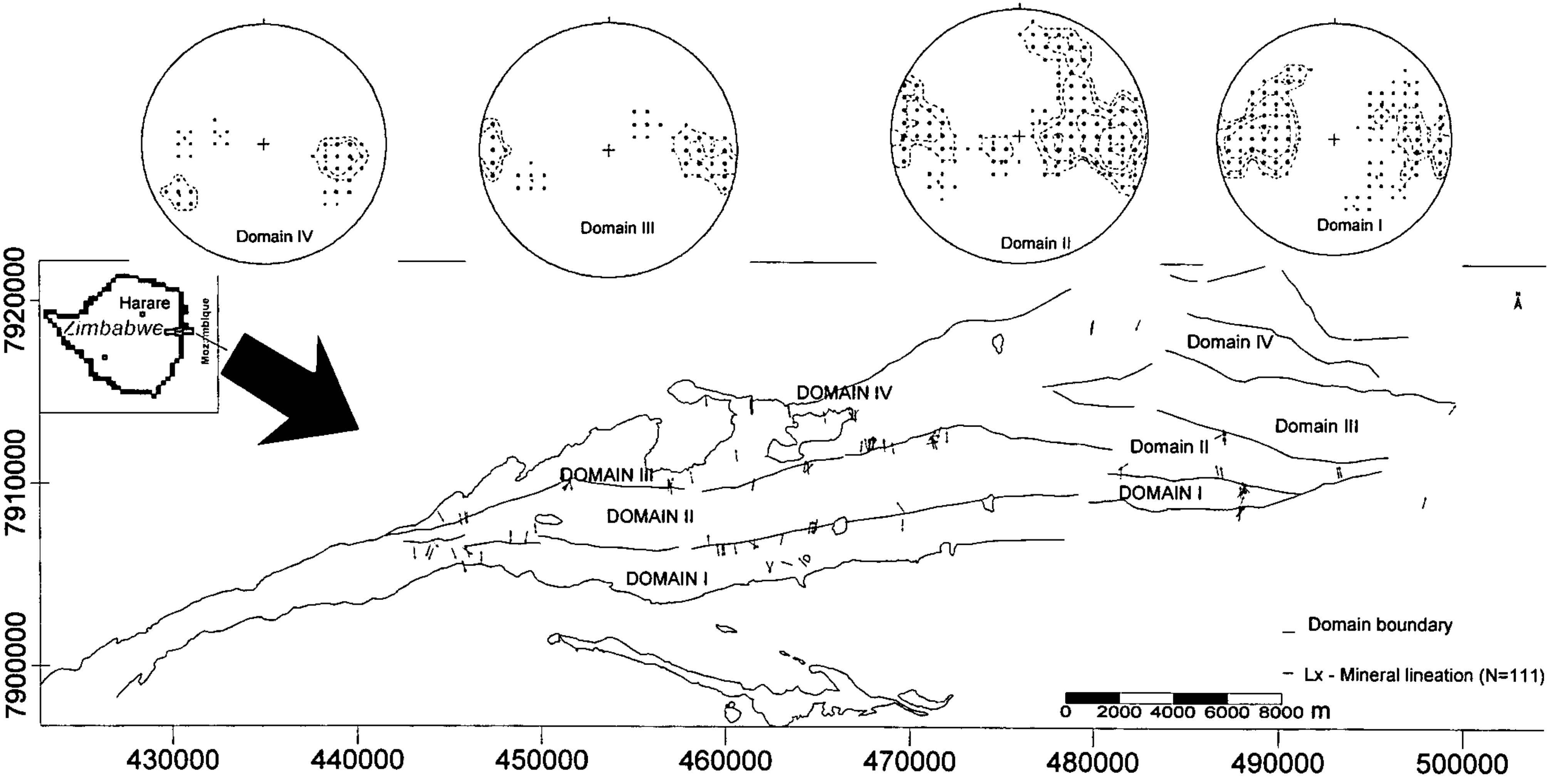

Figure 3 – 3a. Map of the structural domains showing mineral lineation. Domains defined from satellite imagery interpretation combined with field and literature reference data.

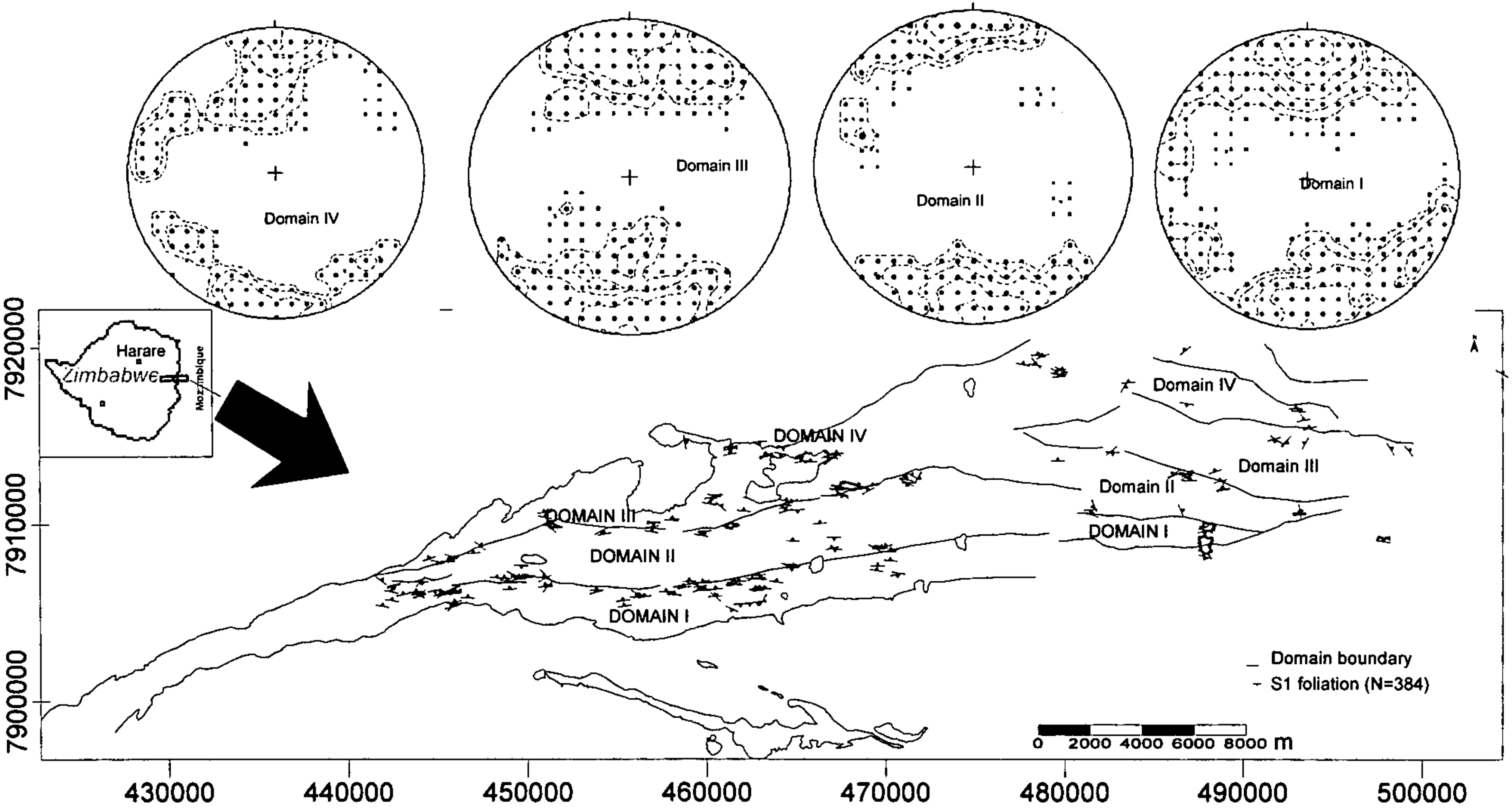

Figure 3 – 3b. Map of the structural domains showing foliation (S_1) and contours to the poles of foliation for domains I to IV. Domains defined from satellite imagery interpretation combined with field and literature reference data.

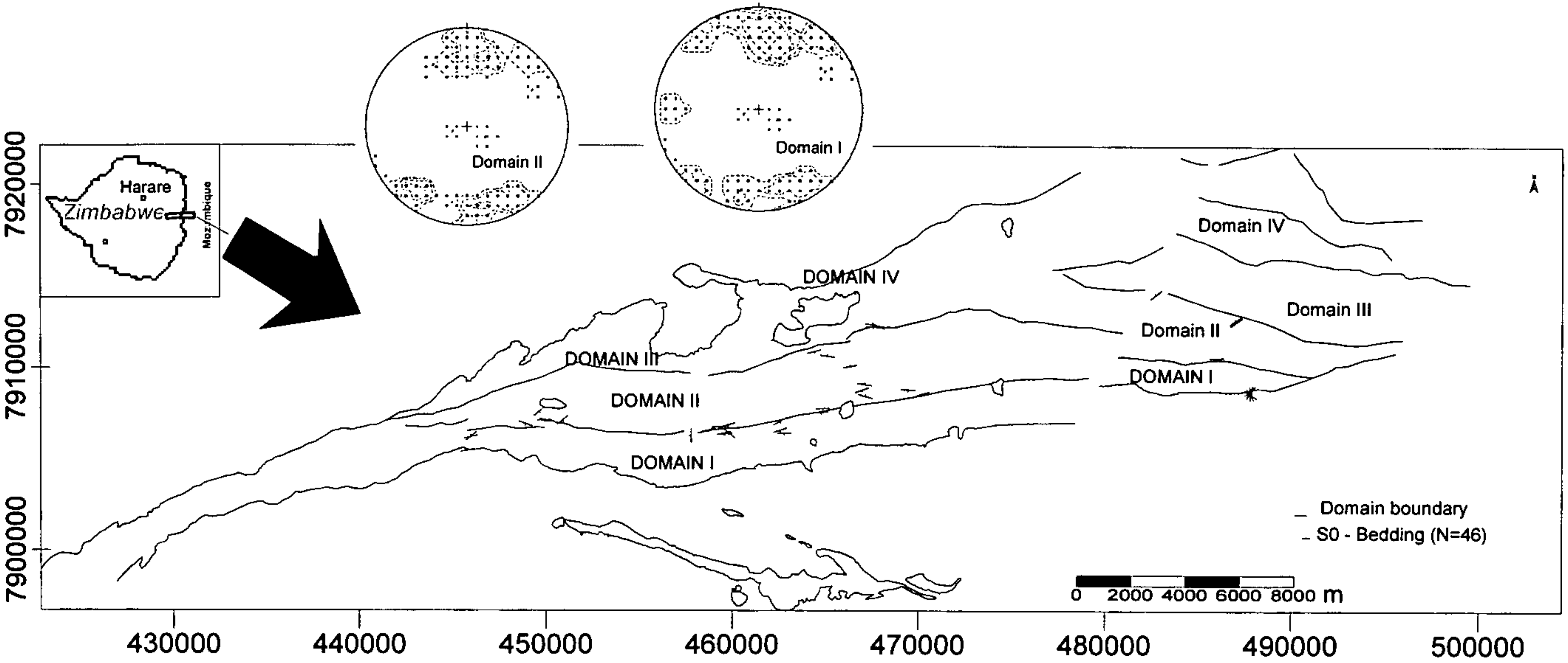

Figure 3 – 3c. Map of the structural domains showing bedding (S_0) and contours of poles to bedding for domains I and II. Domains defined from satellite imagery interpretation combined with field and literature reference data.

The synclinal structural model for the MMO is not supported here because it is found to be rather simplistic and based only on the latest and most obvious structures (e.g. orientation of S_1). Field measurements show that the foliation is near vertical throughout the belt and generally strikes parallel to the lithological contacts, which make its use inadequate for definition of the original structure in the belt. Mineral stretching and elongation lineations plunge shallowly to moderately either to the east or to the west. Younging direction and $S_0 - S_1$ relationships were used for the definition of the early structure of the belt.

The following sections describe the different parts of the MMO belt.

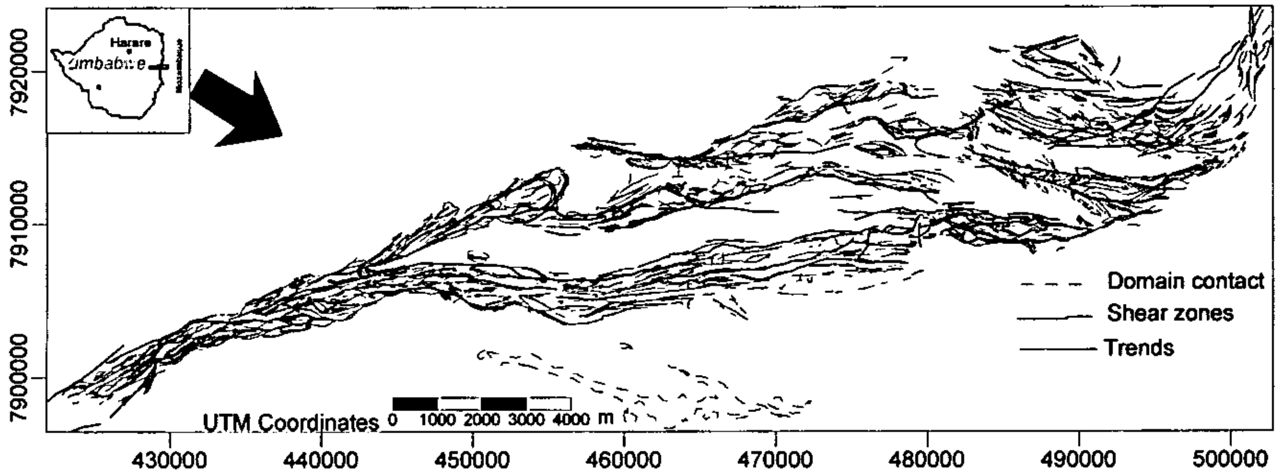

Figure 3 - 4. Trend map of the MMO greenstone belt showing also the main shear zones and domain contacts. The trends represent the foliation cleavage or bedding as interpreted from satellite imagery (TM169/73, ETM 169/73, SPOT - Xs and SPOT-Panchromatic) and mosaic of airphotos with geological map as reference.

3.4.2.1 The Mutare and Odzi area (central and western zone)

Major shear zones, sub-parallel to the main foliation and along the trend of the linear belt, separate the four domains that are recognized on the basis of younging directions, $S_1 - S_0$ relationships, and stretching lineation. These different litho structural domains are as follows (see Figure 3-5):

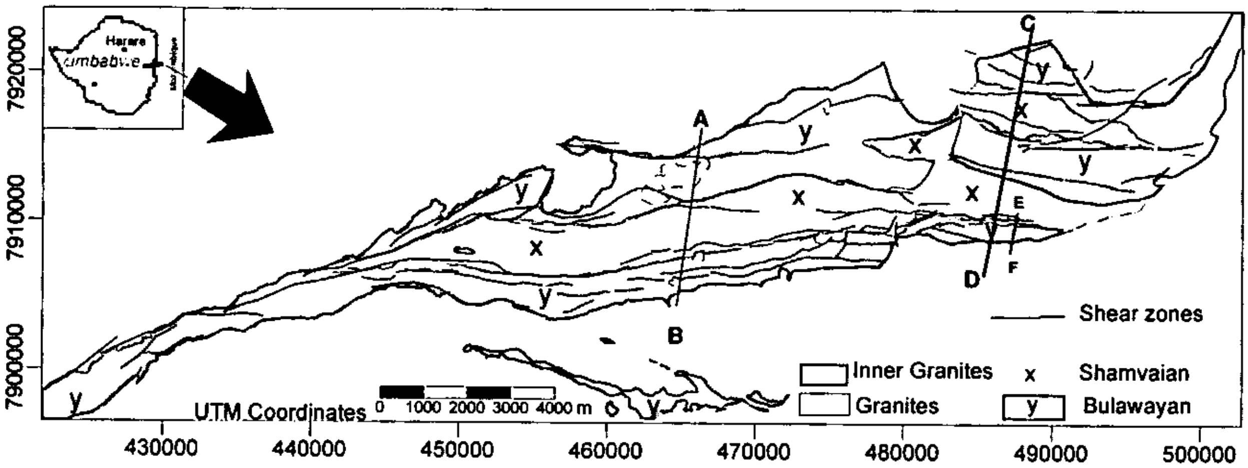

Figure 3 - 5. Geological map of the MMO greenstone belt showing the main litho stratigraphic units. The cross section AB, CD and EF are presented in figures 3-11, 3-12 and 3 - 13 respectively.

Domain I, covers the southern area, consisting of serpentinite, and talc-schists, and makes the southern contact with the granite gneiss terrain. The contact with granitoids is steeply dipping with down-dip stretching lineation. Within this domain a moderate to steep mineral elongation lineation which plunges towards the south and southwest (200°-260°/25-50°) is developed, suggesting a component of strike slip (e.g. Fig. 3 – 7). Foliations dip mainly southward at moderate to steep angles (160°-195°/30° – 77°) (also in Campbell and Pitfield, 1994). The younging directions are very difficult to map in this domain and, the directions in basaltic lavas are very poor, however, Chenjerai (1996) reported younging directions towards north. The S-C fabrics along the shear-boundary at Dot's Luck mine, for example, indicate a reverse sense of movement (Fig. 3 – 6). The Dot's Luck and Toronto deposits are the typical examples of mineralisation within and near the northern contact of this Domain (Appendix III-A and III-B). At Dot's Luck mine, a strongly developed, steep, stretching lineation plunging towards WSW (224°-70°) and in places towards the east is developed.

Kinematic indicators (delta clasts) and within the southern contact of the domain suggest thrusting accompanied by strike slip movement with southern block up. Treloar and Blenkinsop (1995) mapped the southern contact and report steeply dipping with down-dip stretching lineation.

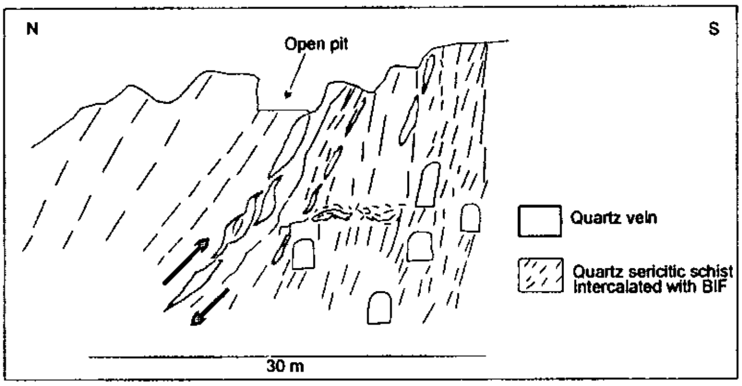

Figure 3 - 6. Section of the Dot's luck showing the concentration of adits on the footwall (southern part) of the E-W shear zone.

The contact of this domain with Domain II to the north comprises sheared conglomerates showing elongated clasts (Fig. 6 – 7); at places BIF lenses are reported along the contacts.

Figure 3-7. Location: UTM 0448279 - 7907074; Deformed conglomerate with E-W vertically dipping pebbles elongated and giving a 270°/35° orientation.

Domain II consists mainly of Mbeza sediments deformed to flattened pebble conglomerates, phyllites with slate cleavage, and siltstones and agglomerates with cleavage-bedding ($S_1 - S_0$) relationships suggesting a vergence towards north. The slickenside lineation is shallow and plunges to the west or to the south-west. Sedimentary cross bedding and grain fining up sequences suggest younging towards the north.

The shear zone that borders the domain to the north is represented by a BIF-rich deformed sedimentary breccia that is well exposed for at least 100 m along the Penhalonga road cut (Fig. 3 – 8).

Figure 3 – 8. Exposure of the shear zone represented by a deformed polymict conglomerate along the northern margin of domain II. Evidence of shearing that was delineated by the trend map in Fig. 3 – 4. Location: UTM 0484213 - 7917746

This shear zone dips 190°/ 75°, the S_2 trends E-W dipping either to the north or to the south and S-C relations suggest a dominantly reverse component of shear. Along this shear zone gold mineralisation is reported at Guy Fawckes (Fig. 3 - 9), Monarch, Howat's Luck and Boa Esperança mines for example.

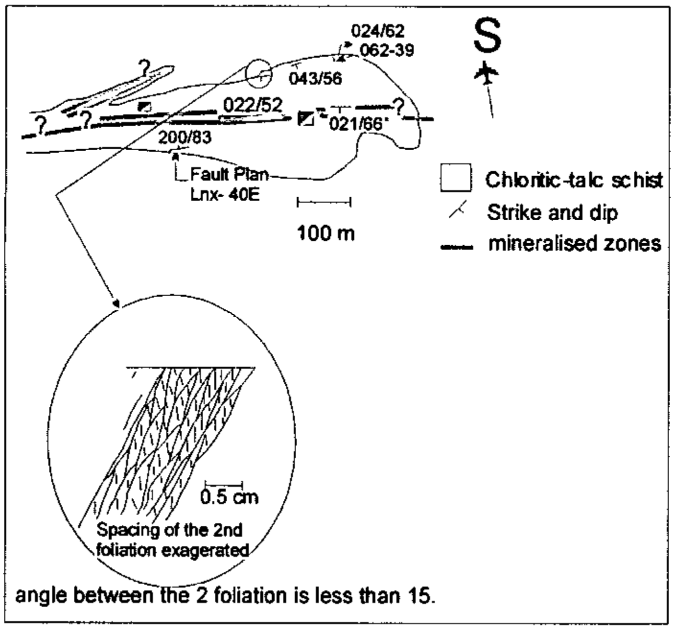

Figure 3 – 9. Schematic representation of the geology around Guy Fawckes mine situated on the north of the domain II.

Domain III contains tonalite (Penhalonga), diorite, rhyolite intrusions, komatiitic basalts and talcschists. The mineral elongation lineations plunge shallowly (25° - 30°) to the east or to the west, S_1 trends E-W and the younging direction (best observed underground at Rezende and Redwing Mines) is towards the south on the basis of pillow lavas (e.g. Fig 3 – 10). These younging indicators are consistent with Chenjerai (1996)'s findings.

This domain contains more than 60% of the gold deposits and has produced more than 90% of the total production in the belt.

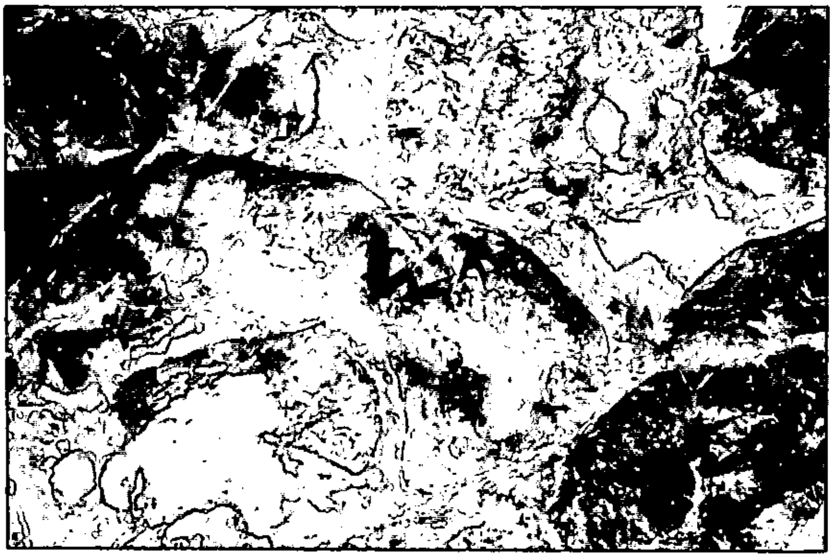

Figure 3 – 10. Pillowed basaltic lavas showing younging upwards. Photo looking south. Location: Redwing mine – Underground. 0465865 - 7914052

Domain IV is the northernmost domain and forms the northern contact of the belt with granitic gneisses and is composed mainly of ultramafic rocks and basalts. No mineral lineation or any other indicators of non-coaxial strain were recorded in the field for this domain, but the domain is sandwiched between two granites, which indicates that non-coaxial strain did occur. The northern greenstone belt – granite contact has mineral lineation (fibre growth) plunging moderately towards the northeast suggesting a sinistral sense of movement with a component of dip slip.

Treloar and Blenkinsop (1995) identified kinematic indicators for sinistral movements at the northern contact of this domain with granites.

Figure 3 -11 shows a simplified N-S cross-section in the Mutare section of the belt.

This interpretation contradicts previous structural models of mainly simple synformal structure or multiple en echelon synclines as proposed for the Manica area of the belt.

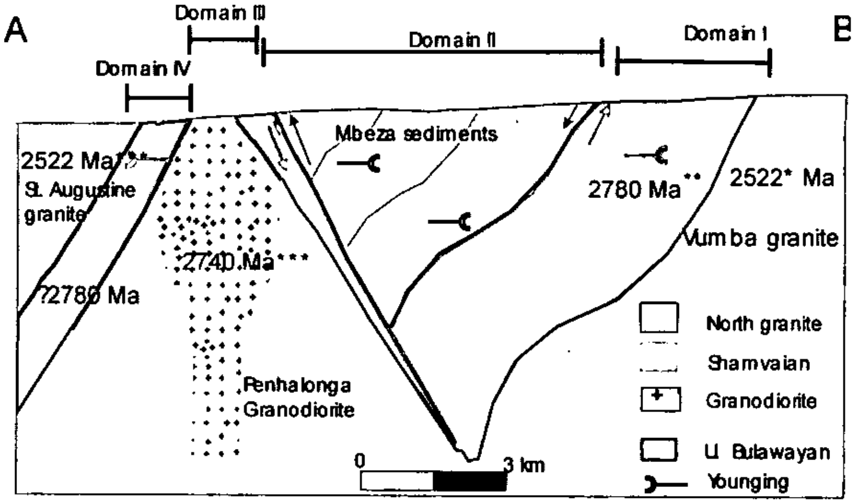

Figure 3 - 11. N-S (A-B on Fig. 3 - 5) cross-section of the MMO greenstone belt through Penhalonga granodiorite showing the litho-structural domains and approximate age of the domain. All ages are inferred on the basis of lithological similarities with type area in the Belingwe greenstone belt. The younging is based on $S_0 - S_1$ relationships and on the pillow lavas stacking. Vertical scale exaggerated. *Manuel (1992), **Wilson et al. (1995), ***Schmidt Mumm et al.(1994)

3.4.2.2 The Manica Area (eastern zone)

The geology of this area is dominated by shear zones occurring at the contacts between upper Bulawayan and the Mbeza metasedimentary rocks here regarded as Mbeza-Vengo and within ultramafic units (Fig. 3-12).

The sheared boundaries are (sub) parallel to the main foliation and separate the MMO greenstone belt in five different domains on the basis of younging directions, shear zones, $S_1 - S_0$ relationships, and mineral lineation orientation. These litho structural domains are shear-zone or unconformity bounded and are as follows (Figure 3-12):

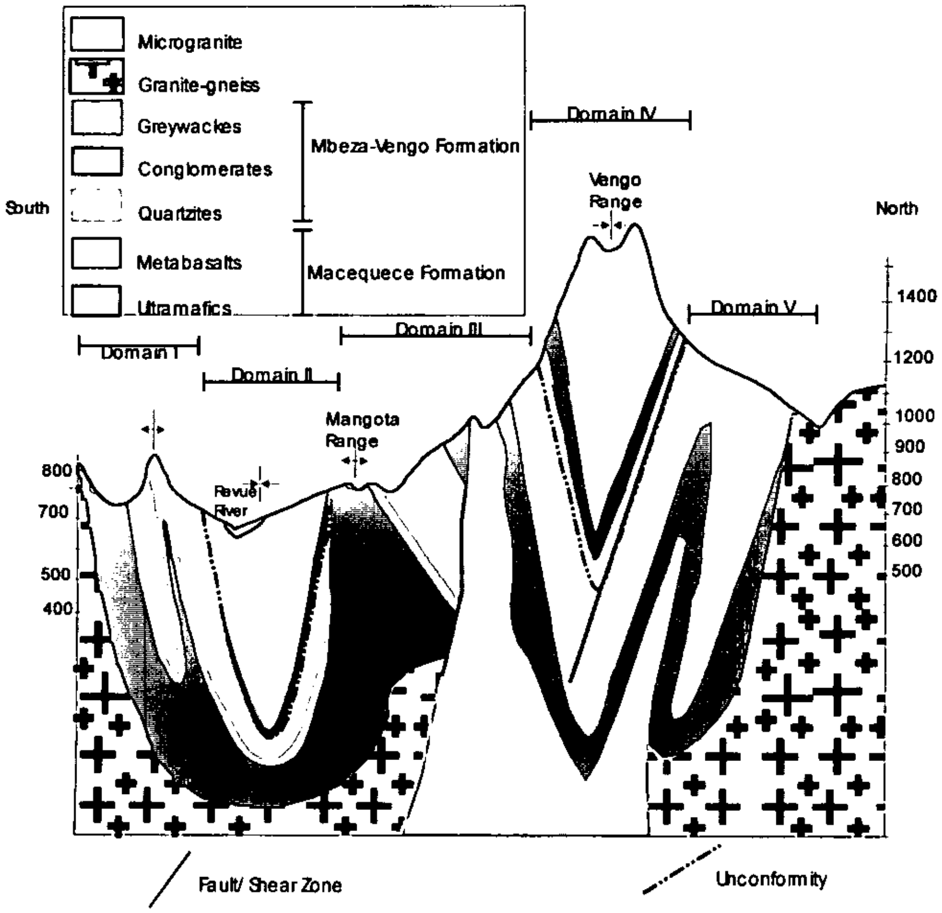

Figure 3 - 12. Schematic representation of S-N (D-C on the Fig. 3 – 5) cross-section through Mangota mountain in Manica section (based on Geological map 1:1000000 scale, satellite imagery interpretation and field evidence) showing the five litho-structural domains. Vertical scale in meters.

Domain I in the Manica area is similar to the Domain I in the Mutare Section of the belt (see section 3.4.2.1). Figure 3-13 shows a detailed cross-section in Domain I. Field observations within this domain show intense folding and shearing. Within this domain the bedding is quite evident as illustrated by Fig. 3 – 14.

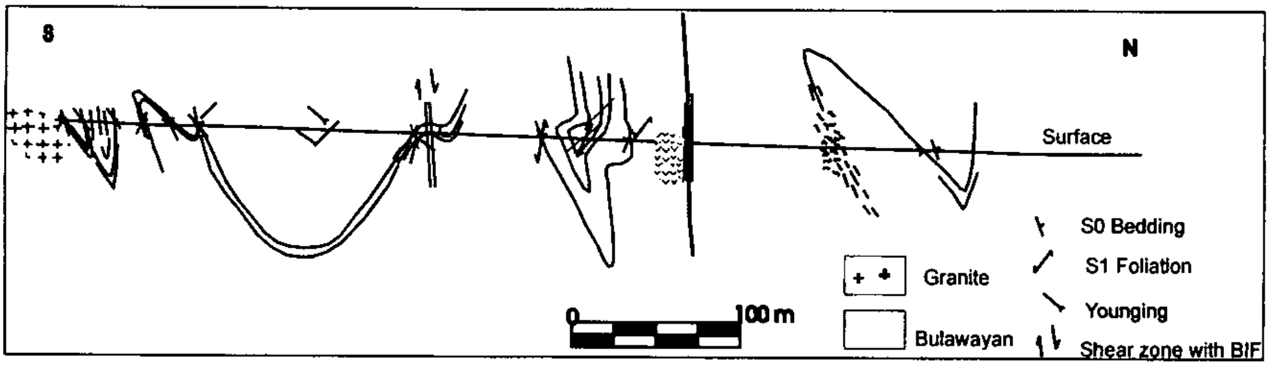

Figure 3 - 13. Schematic representation of S-N (E-F on the Fig. 3 – 5) Cross-section and interpretation of the domain I in the Manica part of the MMO belt.

The Try Again, Dot's Luck and Fair Bride are typical gold deposits within this domain. They are BIF hosted situated near the northern contact of this domain.

Figure 3 – 14. Water lain tuffs within domain I. Location: 0487843 - 7908730

Domain II is represented by the Mbeza-Vengo sediments and is similarly bound to the north by a shear zone expressed by BIF breccia. In the Manica section, this shear zone crops out on top of the Penhalonga range and at the valley of the Muza River. Here the conglomeratic breccia is sheared and is composed of 80-90% sub-rounded to angular BIF fragments in an ultramafic matrix (Fig. 3 - 15). The mineral elongation lineation plunges towards the east at 30°. The bedding dips towards the south (60°/195°) while cleavage dips steeply towards the north-east (70°/020°).

There is no reported mineralisation within this domain, except for mineralisation related to the domain boundaries to the north (e.g. Guy Fawckes, Boa Esperanca, Munhene and Monarch mines) and to the south (see domain I).

Figure 3-15. Location: 0464401 - 7910860; Shear zone represented by deformed banded chert breccia. The Chert fragments are angular to well rounded and generally oriented along strike of the shear zone (E - W). Fragments elongation orientated 30° - 095.

Domain III is dominated by ultramafic and mafic schists with intercalation of massive serpentinite and BIF lenses. This domain is bound to the north by a sheared contact (Fig. 3-12) at the base of the Vengo sediments represented by BIF breccias (Fig. 3 – 16). The mineral lineation plunges steeply to the east or to the west. Erosional surface suggests younging southwards (south of the granite intrusion) and locally towards north at the north of the granite.

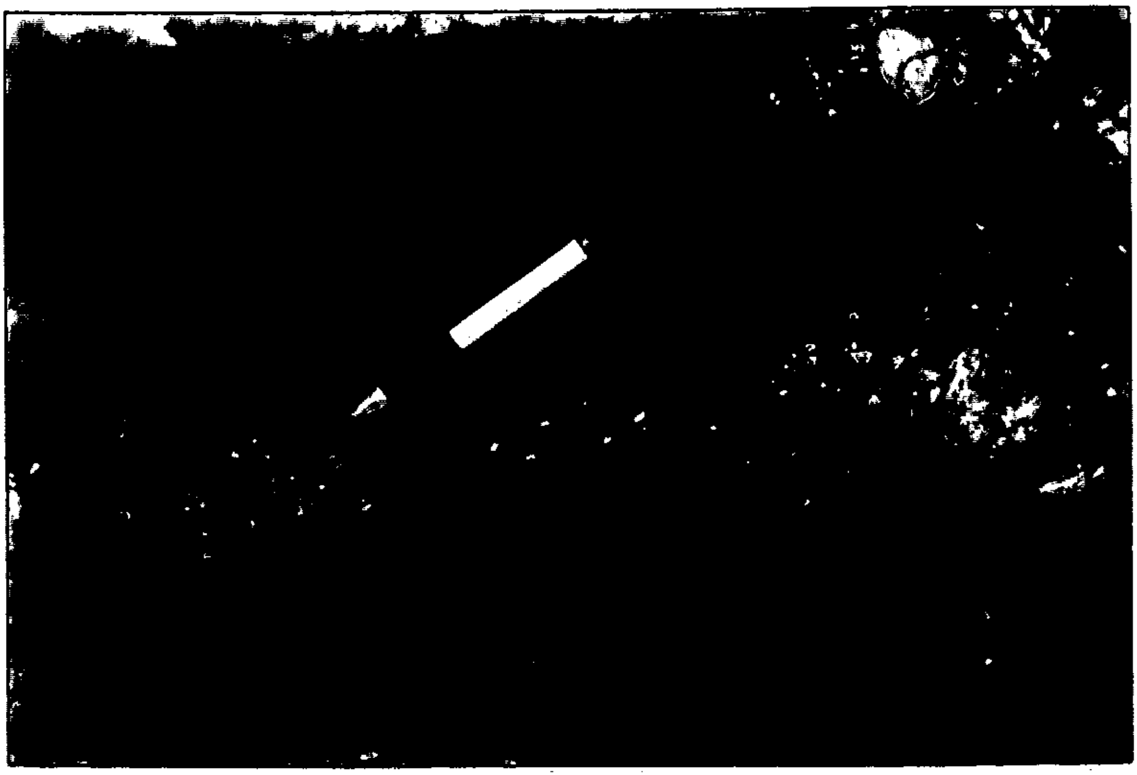

Figure 3 – 16. Base of Vengo metasediments represented by coarse conglomerate overlain by a fine grained greywacke which at the western side of the photo illustrates a Neptunian dyke. From this structure it was interpreted a younging direction towards south. Photo looking south. Location: UTM 0484082 – 7917762.

Mineralisation within this domain is confined to sheared quartz veins in serpentinite associated with BIF e.g. Muza Reef, Munhene reef, Guy Fawckes, Monarch, Boas Esperanca (e.g. Fig. 3-17 and 3 – 20; see also section 3.6)

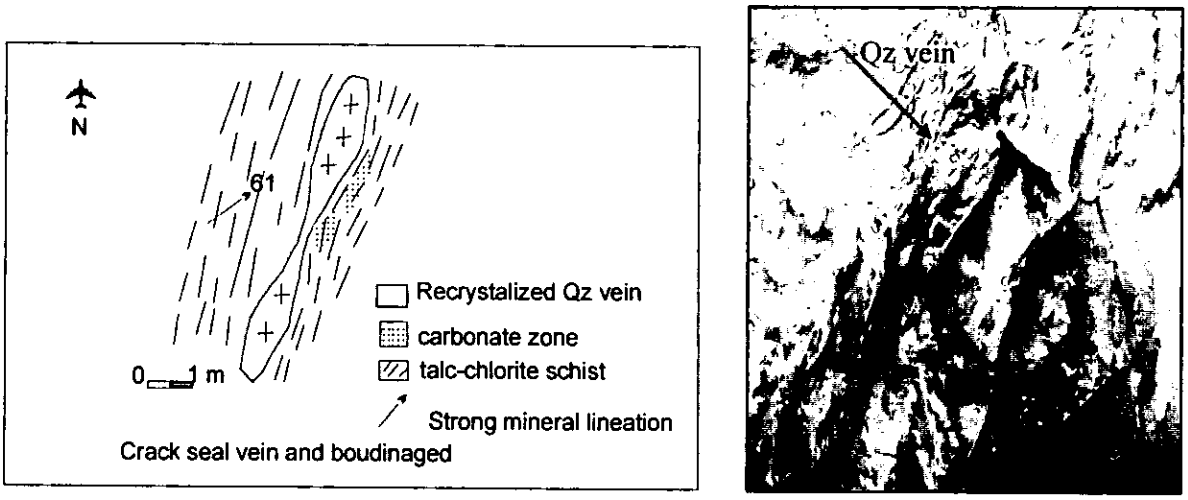

Figure 3 – 17 left and right. Mineralised quartz in sheared carbonate ultramafic rock at Muza Reef mine, showing also the zone of carbonate alteration. Location in UTM: 0499330 - 7914250

Figure 3 – 18 illustrates the mineralised zone of horizontal BIF lenses related to recrystalized quartz vein. Mineralisation is related to galena, arsenopyrite, pyrite and marcasite in quartz sericite schist confined to ultramafic schists and serpentinites.

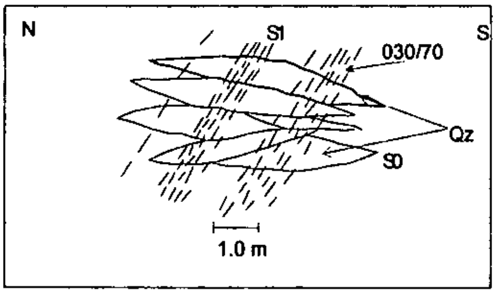

Figure 3 - 18 Schematic representation of the mineralised horizontal lenses of BIF crosscut by NNE dipping cleavage at Boa Esperança mine.

Domain IV is represented by the Mbeza-Vengo Formation composed of quartzites, a basal conglomerate underlying greywacke, phyllites, arkoses and manganiferous black shales.

The basal conglomerate crops out to the south and to the north of the Vengo sediments, it is 10 - 20 m thick and composed of quartz sericite-schist pebbles, BIF, granite and basalt pebbles in a fine chloritic-sericitic-quartz matrix.

The black shales, sericitic and argillaceous schists form the largest sedimentary component of the Vengo Formation. These schists are intensely folded at micro and mesoscopic scale suggesting strong deformation of the sediments either by shearing or by N-S bulk compressional strain.

Domain IV is deformed to a sub-vertical position with down dip lineations. A thrust zone trending E-W borders the domain to the north and branches into the domain itself (Fig. 3 – 19) and to the south a fault boundary is also reported (Manuel, 1992).

This domain is presumably a different sedimentary facies of the Mbeza sediments. The sediments are less metamorphosed, preserving sedimentary structures such as fining upward sequences in greywackes and arkoses. Earlier researchers referred to it as a thrust remnant of a group of sediments, which accumulated in a small separated basin or a detached block of Mbeza metasediments (Obretanov 1977; Hunting Geology and Geophysics, 1984; Sheeran & Venter, 1990). This unit forms an en-echelon basin north of the Mbeza unit.

Mineralisation is only related to the northern contact where silicified BIF is sheared, as an example it hosts the Dias Pereira mine (Fig. 3 – 19).

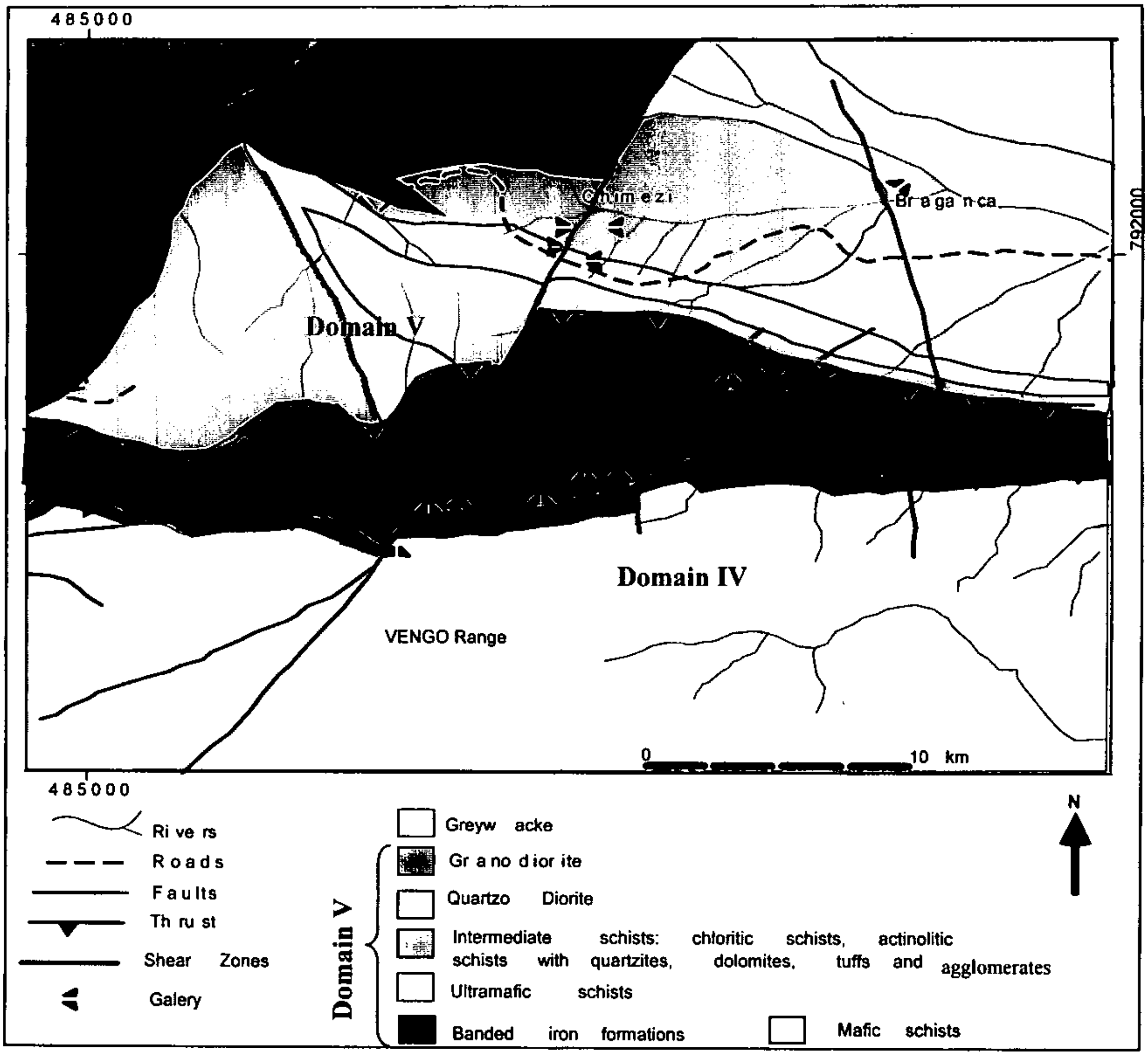

Figure 3 – 19. Simplified geological map of the Bragança mineralised zone, showing also the Dias Perreira and Chimedzi mines (after Sheeran et al., 1990).

Domain V is characterised by mafic and ultramafic schists, and BIF (Sheeran & Venter, 1990) trending E-W and extending from the northern slope of the Vengo Range (domain IV) to the northern contact with deformed granites.

The Macequece Formation (equivalent to Upper Bulawayan) greenschists, BIF, serpentinites and talc schists form the basement and are unconformably overlain by the argillaceous schists and conglomerates of the Vengo formation (domain IV).

A strong foliation is developed close to the contact with northern granite. A major southward dipping, E - W trending thrust fault, represented by BIF breccia, trends nearly parallel to the contact at the base of domain IV (Fig. 3 – 19). It is along this structure where the Dias

Pereira and Richmond gold deposit are situated (Fig. 3 – 19). This domain also hosts the Braganca mine, one of the largest deposits in the Manica area.

These field data trigger a new question, is the MMO belt a simple synform as claimed by earlier authors?

3.5 Tectonic framework of the MMO greenstone belt

A number of models have been proposed for the tectonic evolution of the MMO greenstone belt (Phaup, 1937; Orpen, 1982; Chenjerai, 1996) and all suggest that the MMO belt is a shallowly eastward plunging belt, exposing different crustal levels from Odzi (the deepest part) to Manica (the shallowest part). Orpen (1982) suggested a tectonic model where the greenstone lithologies were metamorphosed, folded and thrusted to different crustal levels (see also Chenjerai, 1996).

The linearity of the MMO greenstone belt is attributed to regional NNW – SSE shortening (Treloar and Blenkinsop, 1995).

Chenjerai (1996) also showed that the lateral and vertical escape of the central crustal block is due to shortening, with the Manica and Mutare sections being subjected to lower compressive strain compared to the Odzi section of the belt. Regional shearing and folding, probably due to lateral escape that accompanied the tectonic process. However, this model considers shortening as the only mechanism driving tectonism and explains neither the existence of crustal shear boundaries in the belt nor the tectonic repetition in two en-echelon synforms (Forster et al 1996) in the Manica section of the belt.

Forster et al. (1996) postulated that the first tectono-metamorphic event in the greenstone succession involved horizontal thrusting, shearing and mineral texture reworking under low-grade metamorphic conditions (chlorite-schist facies). The tectonic model suggested by these authors combines the synformal characteristics of the belt with strike-slip aspects explained by subsidence of Mbeza sediments in shear bounded tectonic grabens and the uplift of ultramafic units in en echelon configuration with sinistral component of movement. Forster et al. (1996) concluded that extensional regimes, expressed at the surface as pull-apart basins in anastomosing transcurrent faults, were important in the tectonic-structural evolution of the MMO greenstone belt.

The models presented earlier lack field evidence. In this study on the basis of field data, it is proposed that after the first deformation that developed belt parallel to sub-parallel foliation (D_1), a NNW – SSE shortening (D_2) is the oldest event and is triggered by granitic doming around 2.742 ± 3 Ga (? Penhalonga granodiorite) and active crustal faulting that results in ENE shear bounded graben domains. This process occurred under greenschist facies to lower to middle amphibolite facies conditions and favoured the development of complex folding within individual domains (D_3) (see section 3.4.2). The entire belt has been subjected to the same metamorphic conditions; however, tectonic processes such as uplift and consequent erosion have exposed different crustal levels of the belt. The Manica section of the belt represents shallower levels of the crust characterised by greenschist facies while the Odzi section represents the deeper exhumed levels of the crust with middle amphibolitic facies. The mineral lineations in the entire belt are predominantly sub-horizontal and parallel to the belt, however, in localised zones it is sub-vertical, down-dip. Lineation distributions in the MMO belt support the existence of a component of strike slip tectonics (Fig. 3-20; see also section 3.4.2).

The deposition of Mbeza metasedimentary rocks started with turbiditic conglomerate above an erosional surface and progressed from the margins towards the centre of the belt (e.g. Chenjerai, 1996; Forster et al., 1996). The presence of serpentinitic, komatiitic and granitic fragments in the conglomerate shows that the Mbeza sediments are a result of erosion and deposition of greenstones and granitoid terrains and that probably both erosion and sedimentation occurred in an active tectonic environment characterised by rapid basin subsidence. This is explained by the presence of angular fragments of BIF within the conglomerate. Overlying the conglomerate are chloritic white mica slates, quartzites and minor dolomitic marbles. The top of the Mbeza metasedimentary rocks is made up of dacitic volcaniclastics (agglomerates).

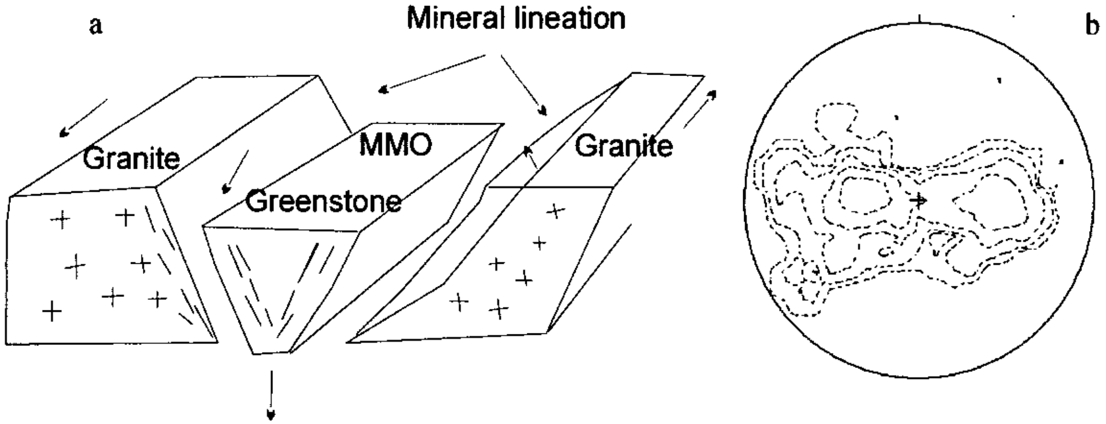

Figure 3 - 20. a) Sketch showing the tectonic setting, on the basis of mineral lineations, of the MMO greenstone belt. b) Stereogram of 111 lineations in the MMO greenstone belt

The whole sequence of Mbeza sediments was deposited in a tectonically active graben with progressive crustal scale faulting and shearing accompanied by internal folding (D3).

Folding in the sediments is rarely observed, probably due to competency of the sediments, which accommodated strain without significant folding (Fig. 3-21). However, along strike (E - W direction) the argillites were deformed into phyllites with bedding parallel foliation (assigned to D_2) (Fig. 3 – 22) while the clasts of the conglomerate were deformed into flattened and elongated pebbles of same composition of the matrix (Fig. 3-7). And the BIF shows complex fold geometries.

Figure 3 - 21. Open folds in Mbeza sediments; the fold axis is oriented 30° - 240°. Location: UTM 0449994 - 7907092

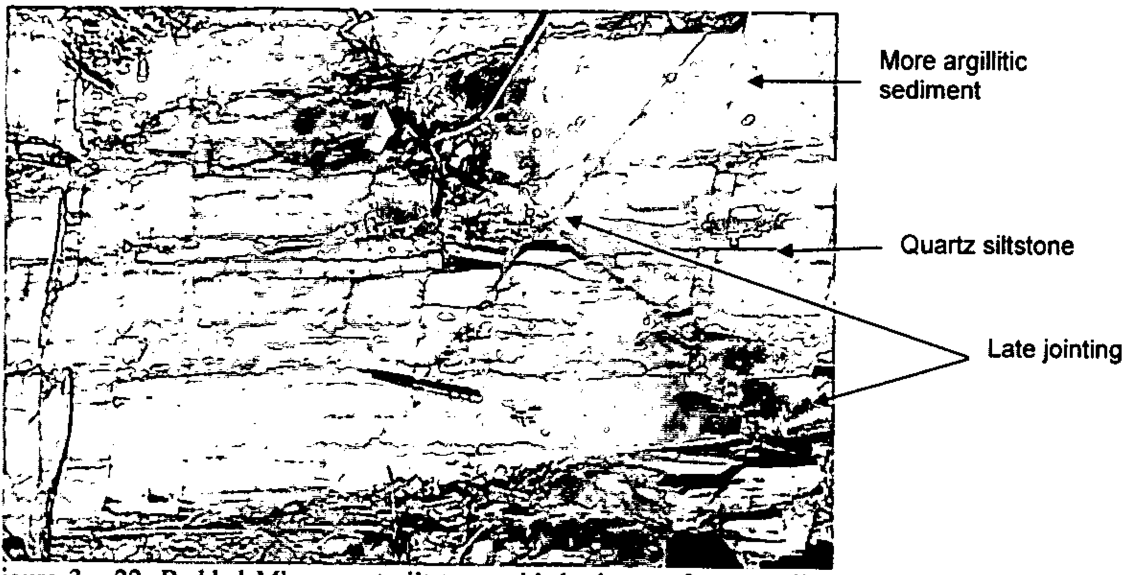

Figure 3 - 22. Bedded Mbeza metasiltstone with horizons of quartz siltstone interlayered with coarse argillaceous material (dark). Repetition]of layers suggests a cyclic depositional environment. S_0 - 50°/188° and S_1: 70°/ 192° S0:S1 relationship indicate synform to the north. Location: UTM 0458732 – 7906537

The active tectonic setting is supported by presence of a 50 to 100 m-wide zone of brittle deformation composed of banded chert breccia (Fig. 3- 8 and 3 - 15) that makes the northern contact between the Mbeza sedimentary rocks and the greenstones and trending continuously from Manica to Mutare sections of the belt.

The entire sequence was deformed (D4) by intrusion of post tectonic granites, which caused contact metamorphism in the greenstones, and probably local growth of biotite in the Mbeza sediments (Forster et al., 1996). The intrusion of late granites and the related metamorphism represent the last significant deformation phase in the Archaean. In the Proterozoic, the MMO greenstone belt and surrounding granites were fractured and intruded by dolerite dykes (570 - 799 Ma, Wilson et al., 1987) and mainly north-westerly trending and related sills (D5).

3.6 Gold Mineralisation in the MMO greenstone belt

3.6.1 Mineralisation at belt scale

Gold mineralisation in the MMO greenstone belt is mainly related to dilational quartz veins. Usually gold occurs as free gold in veins that rarely exceed 1.2 meters in width within the oxidation zone and in auriferous sulphide veins (pyrite, pyrrhotite, arsenopyrite, chalcopyrite). Gold mineralisation can also be found in slates and other metasedimentary rocks. For example at Dot's Luck mine (Fig. 3-23) where gold occurs in pebbly metagreywacke in contact with ultramafic schists. In Guy Fawckes (Fig. 3-23), gold occurs in BIF interfingered within talc-actinolite schists which are overlain by the Shamvaian rocks. Mineralisation in the MMO greenstone belt is mainly controlled by second and third order structures related to crustal shear zones and also by lithological contacts of rocks of different competence (see also Chapter 5). The fact that mineralised quartz veins at Dot's luck, for example, are perpendicular to slicken fibre growth indicate that the mineralisation and the host structure are coeval.

The significant gold deposits in greenstone belts elsewhere are restricted to the brittle-ductile transition zone (Forster et al., 1996). These structures are splays (e.g. Champion mine - Fig. 3-24), dilational veins (e.g. Redwing mine - Fig. 3-23), shear intersections (e.g. Guy Fawckes mine) and inflections of shears (Boa Esperança mine- Fig. 3-23).

Penetrative deformation, and the formation of suitable structures followed by the intrusion of tonalitic magmas (e.g. Penhalonga granodiorite), are important factors in gold concentration in MMO greenstone belt.

The mineralising fluids in the MMO region are characterised by a CO_2-bearing aqueous fluid (0-12% CO_2) at 250-350°C and 1-3 kbar, near neutral to slightly alkaline under reduction conditions (Groves and Forster, 1991, Forster et al. 1996, Saeze, 2000).

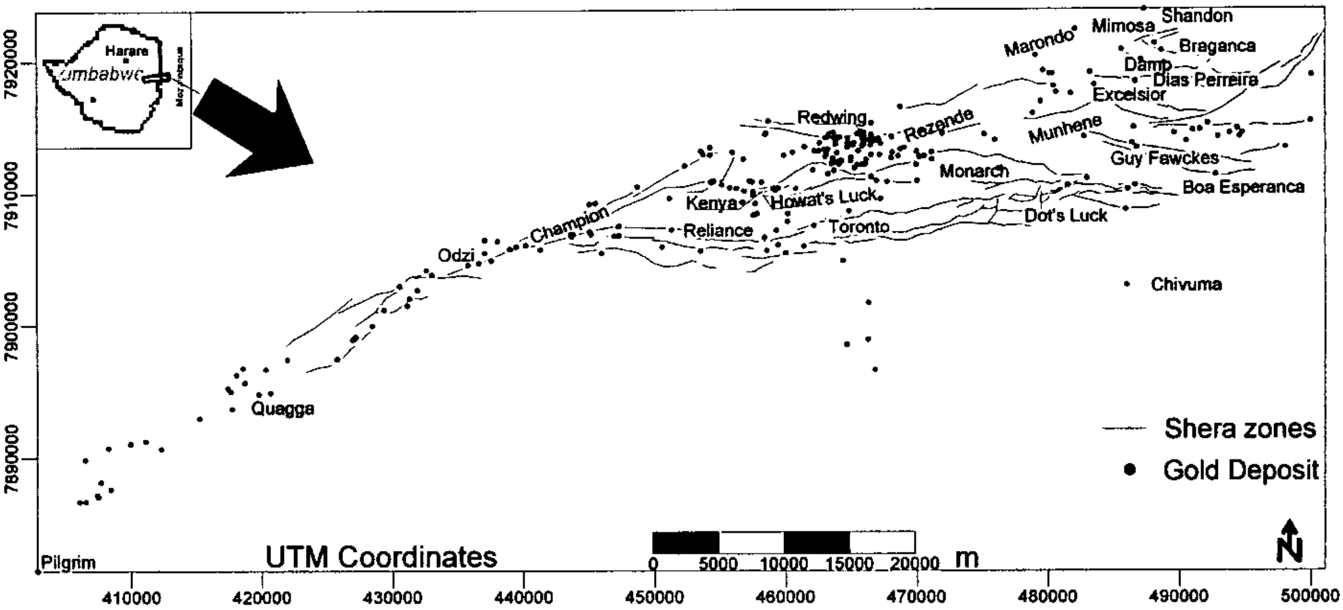

Figure 3-23. Distribution of gold deposits in the MMO belt, and their spatial relationship with structures (Shear zones).

The main alteration processes were carbonatization (evident at Redwing mine underground – Fig. 3- 24), silicification (e.g. Cantão mine), alkali metasomatism (K_2O and locally, Na_2O) and sulphidation (e.g. Marondo mine) (see also Chapter 6).

The wallrock alteration in MMO region is dependent on the lithology type and hydrostatic gradient between the conduit and the wallrock, it is restricted from few centimetres up to a maximum of few metres (e.g. Schmidt-Mumm et al., 1994).

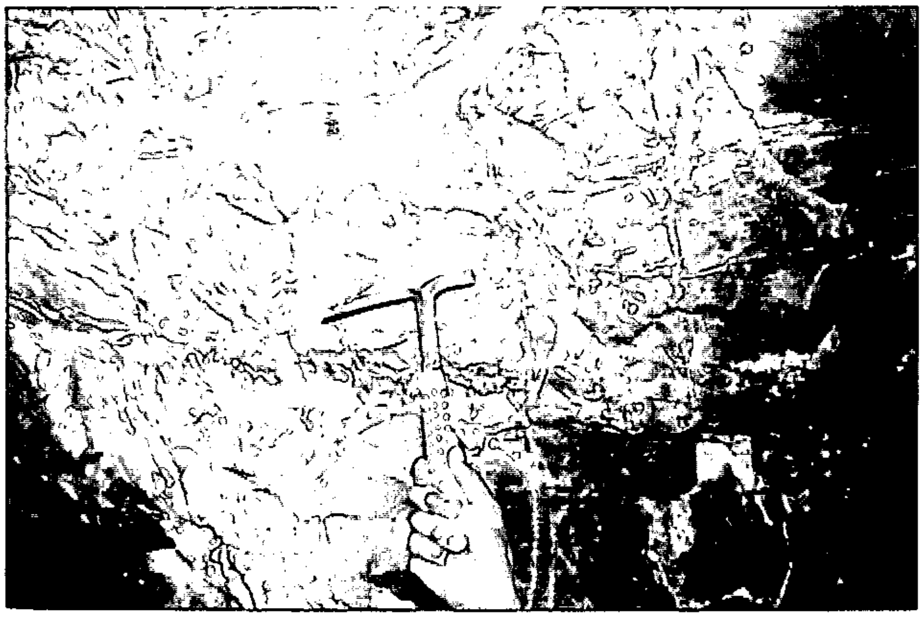

Figure 3-24. Carbonate alteration (white) at Redwing Mine underground. Location: UTM 0465865 - 7914052

Hydrothermal processes during the carbonatization and serpentinization of ultramafic and mafic rocks were responsible for depositing gold and for the 'hydrothermal overprinting of BIF and felsic rocks'.

The mineralisation is dated at 2650± 10 Ma (Pb-Pb dating of the galena at Redwing mine, Schmidt Mumm et al., 1994), post peak metamorphism, which is older than young granites (~2500 Ma) and younger that the Penhalonga granodiorite (2742 ±3 Ma) (U/Pb dating of individual zircon grains; Schmidt-Mumm et al., 1994), and probably younger than Mbeza-Vengo sediments. This is consistent with late Archaean main mineralisation event in the Zimbabwe Craton (Forster et al., 1996).

In order to investigate whether gold mineralisation in the MMO greenstone belt is uniform or varies from place to place, each section of the belt (Manica, Mutare and Odzi) was studied separately in terms of controls of mineralisation and type of mineralisation and is presented in the next sections.

3.6.1.1 Odzi section

The Odzi section is believed to represent a lower crustal-level section of rocks defined by the low to middle amphibolite mineral assemblages facies. This section of the belt is less mineralised compared to the rest of the belt, with 61 mines producing a total of c. 3,5 t of gold (Forster et al., 1996). It is in this section of the belt where production of 80 t of WO_3 has been reported from scheelite mining (Forster et al., 1996).

3.6.1.2 Mutare section

In the Mutare section, mineralisation is dominated by the highly anomalous cluster of gold deposits represented by the Rezende group (e.g. Rezende, Redwing, Penhalonga, Old West, King's Daughter, Liverpool, Kent, Elgin, Violet, Golden Gate, Magog, Umtali and Iona West) (Fig. 3-25) with a production of 68 t of Au and c. 75 t of Ag (Forster et al., 1996) while the rest of the section produced only 6 t of Au. Figure 3-25 represents a simplified structural geological map, showing gold reefs with their orientations in the area around Penhalonga granodiorite.

Mineralisation in the Mutare section is controlled by pre-existing structures such as the Rezende shear zone, which controls the localisation of the Rezende and subsidiary deposits.

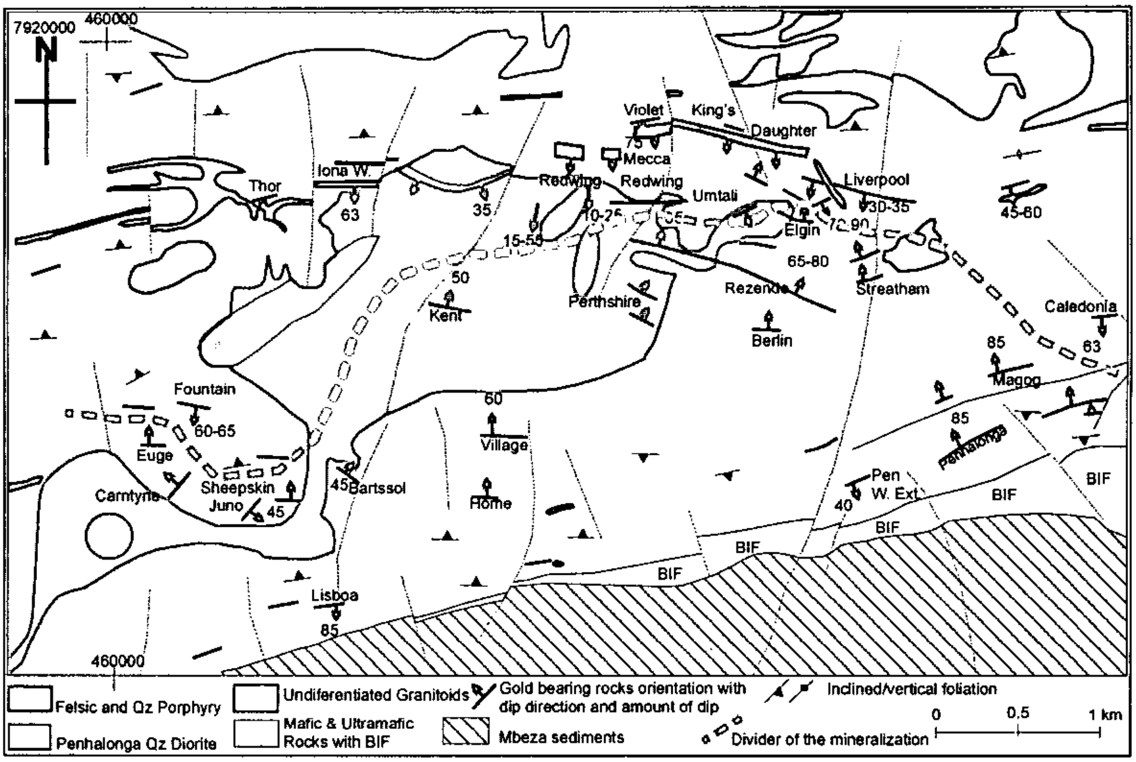

Figure 3-25. Simplified geological map of the Penhalonga area (Mutare section of the MMO greenstone belt) showing the distribution and orientation of gold reefs (Adapted from Campbell and Pitfield (1994)).

On the basis of spatial relationships between gold deposits and the Penhalonga granodiorite, and its age, it seems that the intrusion could have played an important role in supplying the heat source for the migration, remobilisation and deposition of gold along favourable structures, it also could have influenced in creating fractures where mineralisation was later deposited.

The orientations of the gold reefs dipping either to the north or to the south suggest the existence of an east-west central structure cutting across the Penhalonga granodiorite. This structure must be earlier than the mineralisation and it seems to have acted as the main mineralisation focus structure, which at depth (probably at ductile-brittle transition zone) branched complexly in a more fractured zone parallel to the main channel (Figure 3- 26). This event (D_2) might have occurred between 2700 Ma and 2661 Ma, probably related to the emplacement of the Penhalonga granodiorite or during the deposition of the Shamvaian sediments.

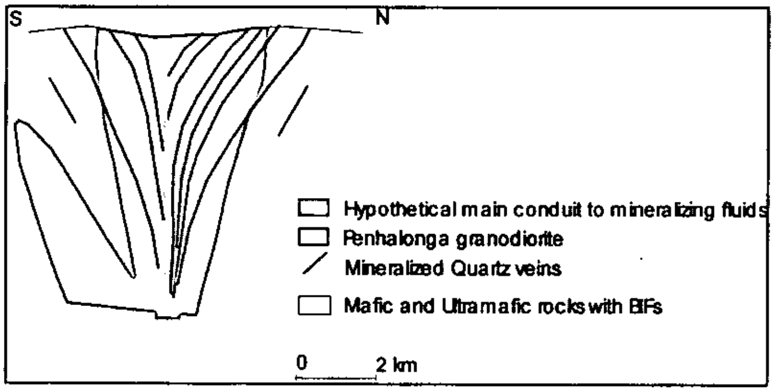

Figure 3-26. Schematic representation of hypothetical situation for the mineralising event in the Penhalonga area of the Mutare section of the MMO greenstone.

3.6.1.3 Manica section

The Manica section has produced c. 12 t of gold, between 1889 and July 1994, (Forster et al., 1996) mainly from alluvial mining. The primary gold in the section has been recovered mainly from supergene zones; exceptions are the lodes at Bragança and Guy Fawckes, which were mined down to c.150-200m. The strike of the quartz veins is mainly E-W although N-S oriented veins are observed in the granites adjacent to the belt. There is also a clustering of gold deposits near the contact or embayment of granites into schists (Fig. 3 – 27), which is dominated by a lobe of the late/post tectonic granite in the north of the belt. These include Cantão, Two Fools, Old Wednesday, Excelsior, Estrela and Morgan (Fig. 3 – 27).

The ore minerals consist of gold, auriferous pyrite, arsenopyrite, together with magnetite, hematite and scheelite (Excelsior mine). Other minerals that can be found in the gold mines are ankerite and dolomite, sericite, calcite, chlorite, limonite, crocoite and anglesite.

Ferruginous quartzites and BIF are sub-vertical and contain magnetite, hematite, limonite, carbonates, and auriferous pyrite, pyrrhotite and arsenopyrite, as well as free gold.

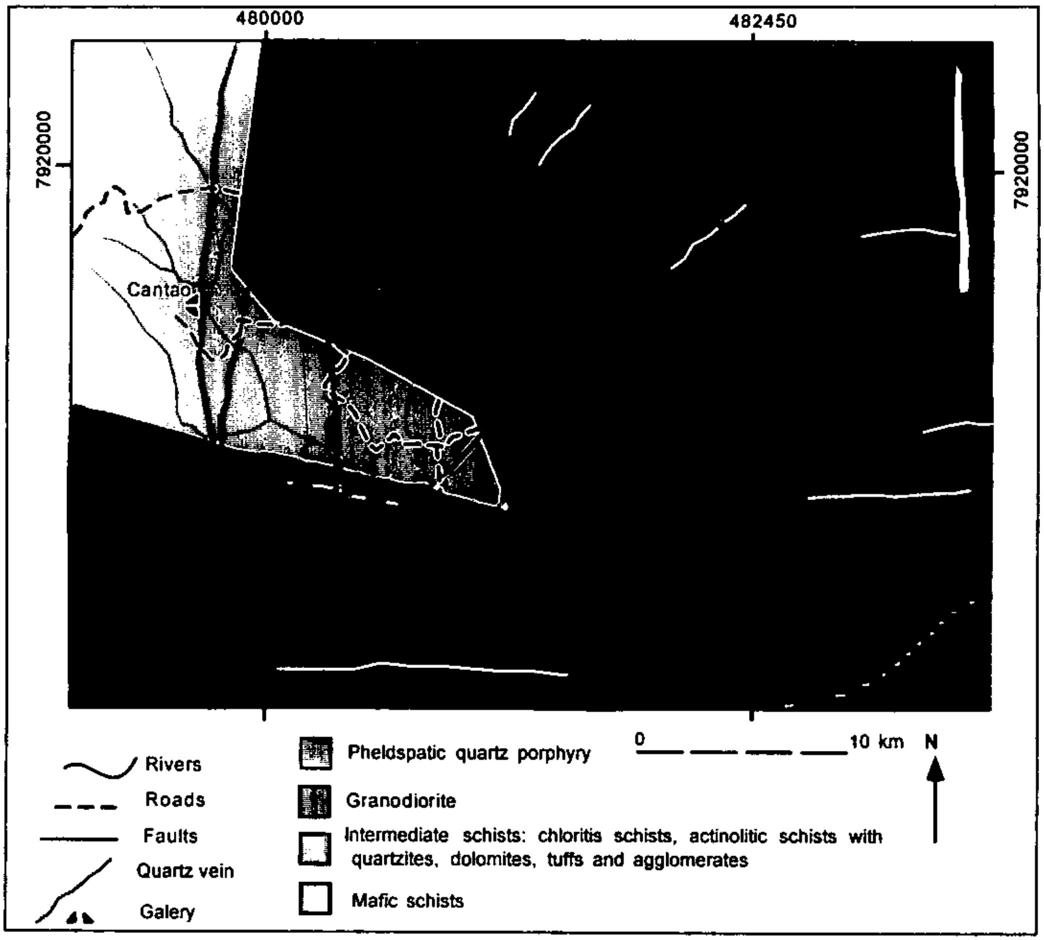

Figure 3 – 27. Simplified geological map of the area around Cantão, Two Fools, Old Wednesday, Morgan and Chua mines, showing also the position of the main adits (after Sheeran et al., 1990)

3.6.2 Gold mineralisation at mine scale

Detailed geological and structural mapping on a mine scale revealed that besides the structural control of the mineralisation there is lithological control. In general, mineralisation can be grouped in:

- Deposits related to the contact between greenstones and sedimentary rocks associated with BIF
- Deposits hosted in granites or at the contact between granites and mafic or ultramafic units
- Deposits hosted in BIF (silicified shear zones) within mafic and ultramafic rocks
- Fault/shear zone hosted deposits

3.6.2.1 Deposits related to contacts between greenstones and sediments associated with BIF

Dot's Luck Mine

It is located (481537; 7910650) on the northern slope of Duque Mountain, 7 km NW of Manica. Gold associated with silver at 4.3 g/t Au in average and had been mined in the oxidation zone. The mineralisation is confined to a sequence of pebbly, tuffaceous metagreywackes close to the contact with the ultramafic (talc) schists to the south (Fig. 3 – 28). The mineralised body is laminated ferruginous micaceous quartz lens of 700x30x3 m striking E –W and steeply dipping towards the south (194°/84°). The wallrock lineation plunges at steep angles towards the WSW (224°/70°) and at places toward east. The mineralised zone represents a sheared tectonic contact zone that dips at (170°-185° /30° – 50°) and of lensoidal shape (c. 20 m wide). The shear zone has been crosscut by post mineralisation N-S striking faults and shears steeply dipping towards NE (034°/88°) (Fig. 3 – 29). The kinematic indicators (shear bands) suggest a movement of the hanging wall block (south over north block). Dot's Luck deposit is structurally controlled by a sheared contact, which appears to have been active over a long period of time, and is confined to the lensoidal dilational feature.

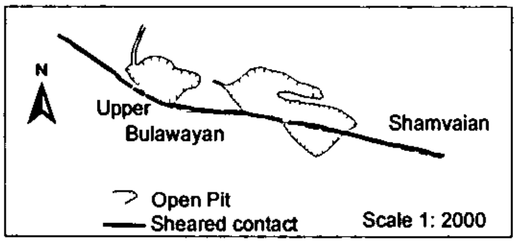

Figure 3 – 28. Geological map around the Dot's Luck gold deposits in Manica. Location: 481537; 7910650

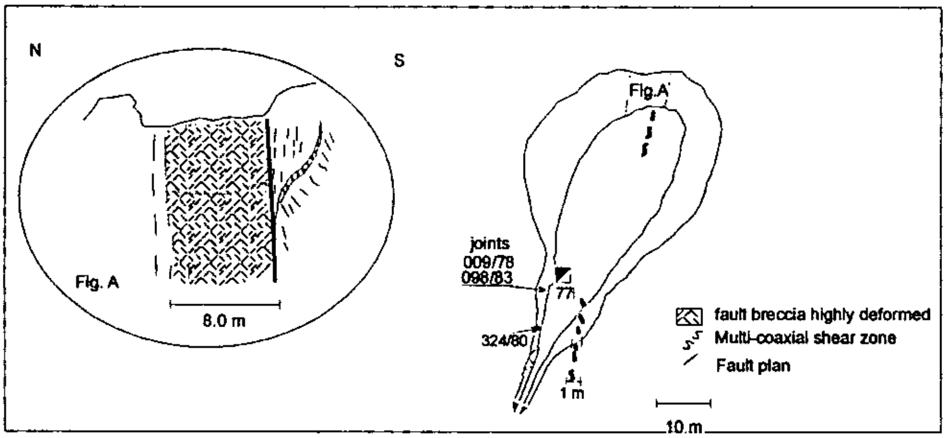

Figure 3 – 29. Schematic representation of the Dot's Luck open pit showing the mineralised shear zone. Note that the structure is 1 meter wide to the far west and is 8 meters to the east (figure A). Location: 481537; 7910650

Earlier authors suggested that the quartzite unit formed the cap of an anticline structure or a set of shears developed along contacts between high competency and low competency rocks and, the lensoidal dilational feature being related to initial warping of the southern limb of the MMO belt (e.g. Obretanov, 1977). Field evidence at the outcrop in the open pit (Fig. 3 – 6) shows that the richest mineralised part of the deposit is at the footwall near the south contact with ultramafic schists.

The gold mineralisation is related to sulphides, mainly pyrrhotite, pyrite and arsenopyrite, and rarely chalcopyrite, galena and sphalerite. The deposit also contains magnetite, chlorite and hematite (Forster et al., 1996, Obretanov, 1977).

The deposit presents an apparent thermal zoning of the sulphides from peripheral pyrrhotite, intermediate pyrite, and central arsenopyrite (e.g. Forster et al., 1996). In this deposit, there are indications of silicification and pyritisation of what appears to have been originally BIF (e.g. Forster et al., 1996).

The mineralised felsic intrusion located some 200 m south of the deposit may have played a significant role (e.g. ignition of the thermal flux that remobilised Au to its present location) in controlling the mineralisation at Dot's Luck.

The right dihedra method of Angelier & Mechler (1977) was used to reduce the orientation fields containing $\sigma 1$ and $\sigma 3$ (Lisle, 1987) (Fig. 3-30). The maximum principal stress direction lies at 342°/24° (P - shortening) and the minimum principal stress lies at 227° /44° (T - extension).

Stress analysis at mine scale reveals that gold is trapped by structures that resulted from an event of maximum compression ($\sigma 1$) oriented N-S, which could explain the distribution pattern of deposits in the NE-SW shear fracture patterns. This is the event responsible for the distribution of quartz vein hosted deposits. Fracture/fault orientations considered to be related to mineralisation together with slickenside lineation orientations and the estimation of the sense of movement were measured. These fractures are related to mineralisation because they control the orientation of the mine (pit), and quartz veins in places are perpendicular to slicken fibre growth which suggest that they must be coeval.

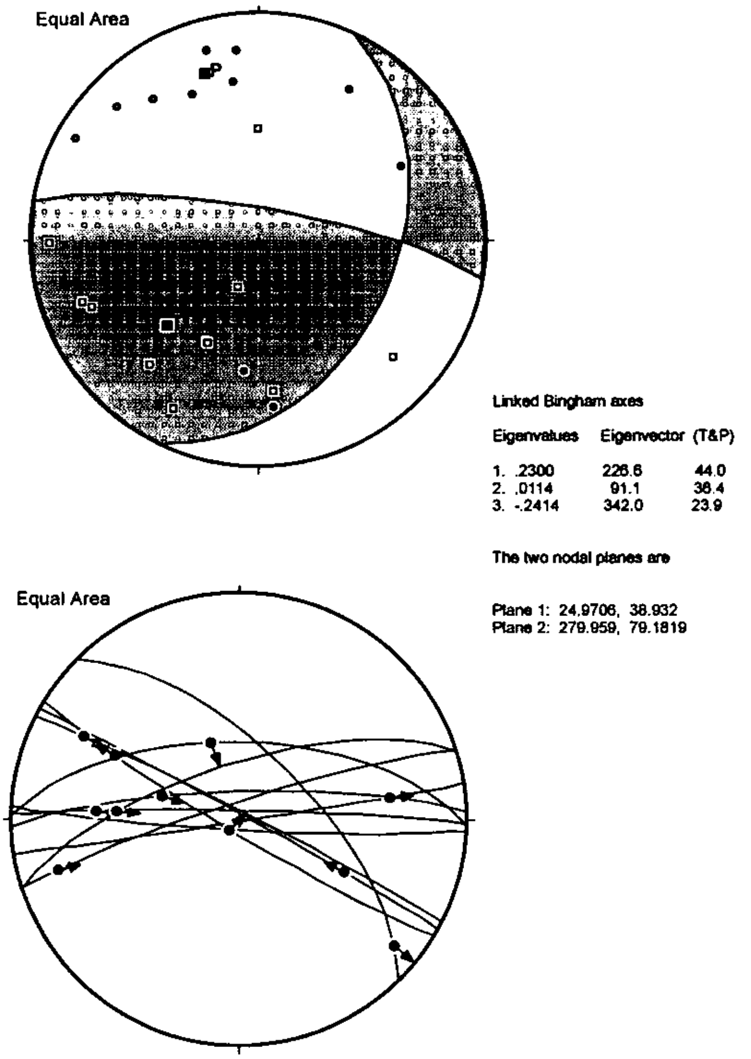

```
Linked Bingham axes

Eigenvalues    Eigenvector  (T&P)

1.  .2300       226.6        44.0
2.  ,0114        91.1        38.4
3.  -.2414      342.0        23.9

The two nodal planes are

Plane 1:  24,9706,  38.932
Plane 2:  279.959,  79.1819
```

Figure 3-30. Fault planes and striation lineation direction with arrow pointing towards movement direction of the hanging wall. P represents the direction of maximum compression and average compression direction; T represents the direction of minimum compression and average extension direction.

Boa Esperança mine

This deposit is located to the east of the Manica region on the northern margin of Revue River (0493160; 7910720).

The orebody consists of a banded iron quartzite (highly sheared quartz sericite schist) oriented E - W and has dimensions of 150 x 25 x 2 m. The average grade of this deposit is 6.0 g/t (Obretanov, 1977, Forster at el., 1996)

The deposit is located near the sheared contact of conglomerate (serpentinite bearing and quartz pebbles in a micaceous matrix) oriented at 82°/172° and 78°/190°. Conglomerate pebbles are prolate with long axes plunging at 110°/22°- 58°).

Underground and main pit observations suggest complex fold interference structures with an early foliation oriented at 321°/85°, seemingly to have been affected by later deformation concentrated in specific zones mainly oriented at 026°/60°. In places, boudinaged structures (Fig. 3 – 31) with an envelope oriented at 110°/55° are observed. Faults with orientation of 096°/70° locally cut earlier fabrics.

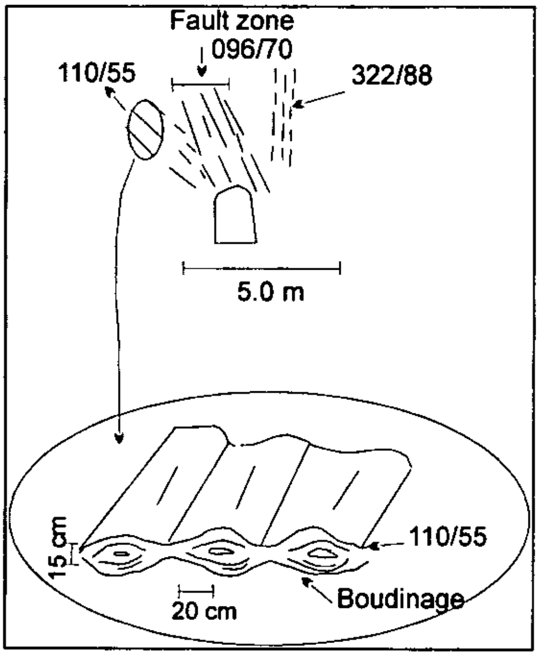

Figure 3 – 31. Complex interference structures with boudinage at Boa Esperança mine.

The presence of horizontal to sub-horizontal lenses of BIF (Fig. 3 - 18) may reflect asymmetric folding.

Re-crystallised, laminated and highly deformed quartz veins of up to 30 cm wide represent one of the hosts of the mineralisation. Samples collected at the dumpsite show that the mineralisation is related to sulphides (mainly galena, arsenopyrite, pyrite, marcasite) present in quartz sericite schist, ultramafic schist and highly weathered serpentinite host rocks.

3.6.2.2 Deposits hosted in granites or at the contact between granites and mafic / ultramafic units

Excelsior Mine

Excelsior is situated on the western side of the Vengo range in the valley of the river Pimentel Pinto close to the Manica – Inhamcurara road (Fig. 3 – 27). The deposit occurs at the contact between granodirite and schists of the Macequece Formation. The ore body is a mineralised quartz vein hosted in both the granite and the schists. Veinlets of quartz 1 - 2 cm thick in different orientations are sometimes mineralised.

The exploited veins are oriented E-W and dip at 60° north. They are on average 224 m long and 38 cm wide at an average grade of 10.5 g/t Au (Forster et al. 1996).

Field observations suggest the existence of two conjugate quartz veins in a weathered quartz porphyry microgranite.

The first vein is oriented at 320°/65° and the sense of movement along the brittle ductile shear plane suggest a sinistral sense. The quartz vein is laminated and the Au mineralisation is related to sulphides. A network of small veinlets of quartz with sericite alteration up to 1 – 2 meters away from the shear is present. The foliation is oriented at 85°/240° and mineral lineation vary between 153°/02° and 085°/60° suggesting a normal faulting (Fig. 3 – 32).

The second vein is oriented at 340°/72° and the sense of movement as observed along the brittle ductile shear is dextral. The quartz vein is of crack seal type. The main foliation (040°/65°, 030°/73) and mineral lineation (355°/60°) suggest SW over NE block. Secondary veins (dilational veins) are oriented at 272°/40° and 265°/39°.

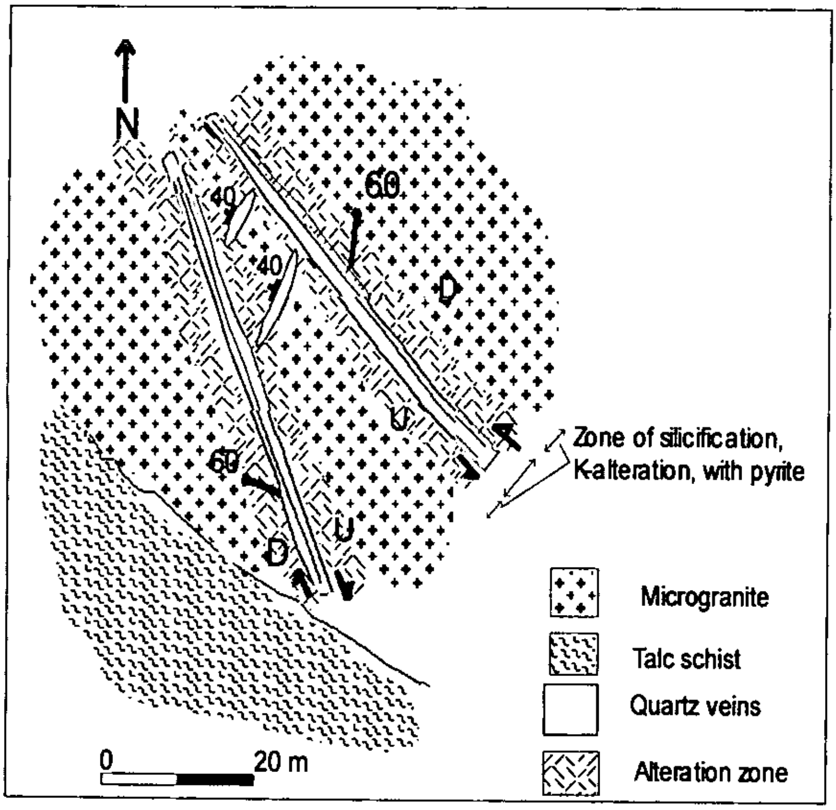

Figure 3 – 32a. Schematic representation of the geology at Excelsior mne.
D= down; U = up; P= p shear; R= Riedel shear; σ_1= main compression direction

The Fig. 3-32 gives an ilustration of the interpetation possibilities and, according to field observations the dextral Riedel system is more appropriate.

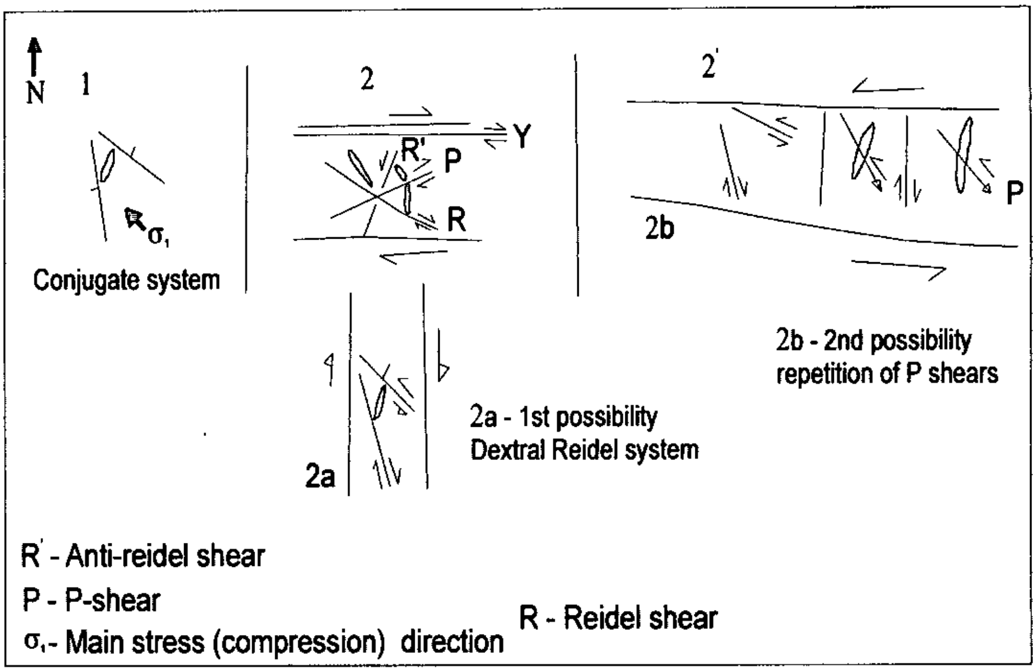

Figure 3 – 32b. Interpretation possibilities of the mineralisation setting at Excelsior mine
1. Probably a conjugate system; 2. Probably a dextral Riedel system; 2'. Probably a sinistral

3.6.2.3 Deposits hosted in BIF within mafic and ultramafic rocks

Monarch Mine

This deposit is located to the west of Manica close to the Zimbabwe boarder on the Penhalonga range (c. 471505; 7912863; 1461m).

The ore body strikes E -W and dips 55°- 80° north. It is hosted in chlorite – talc - schist with hematite. An S-C cleavage is very pronounced and indicates south block up. The intersection lineation is flat to sub-horizontal towards SE (160°- 03°) while the mineral lineation plunges steeply towards the NE (053°/74°). Some carbonate and silica alteration are visible on outcrop scale in form of patches. At the open pit, a N-S shear zone is exposed with a fibre growth lineation plunging 21° towards 020° in laminated carbonaceous (graphitic) schist impregnated with sulphides (Fig. 3-33). The deposit is intruded and offset by N-S dolerite dykes and a set of N-S faults (Fig. 3 - 34).

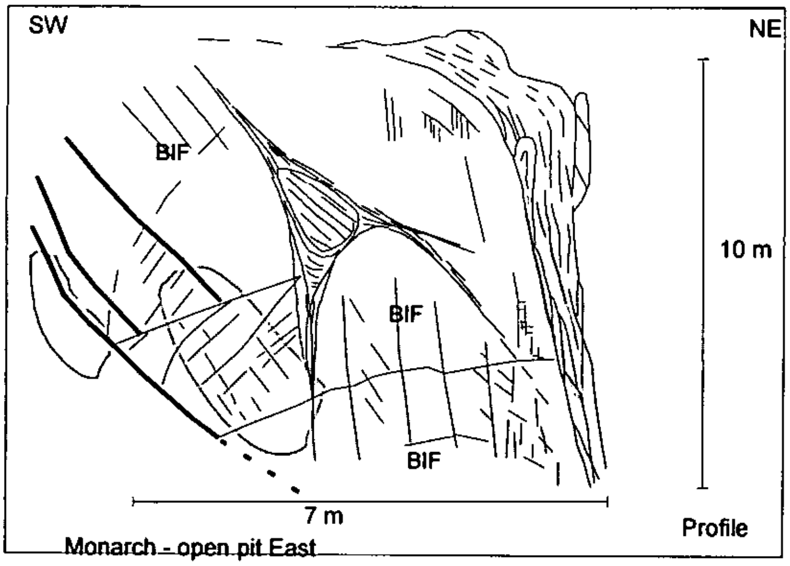

Figure 3 – 33. Schematic representation of the geology at the open pit (Monarch Mine), showing the sulphide impregnation (coloured brown)

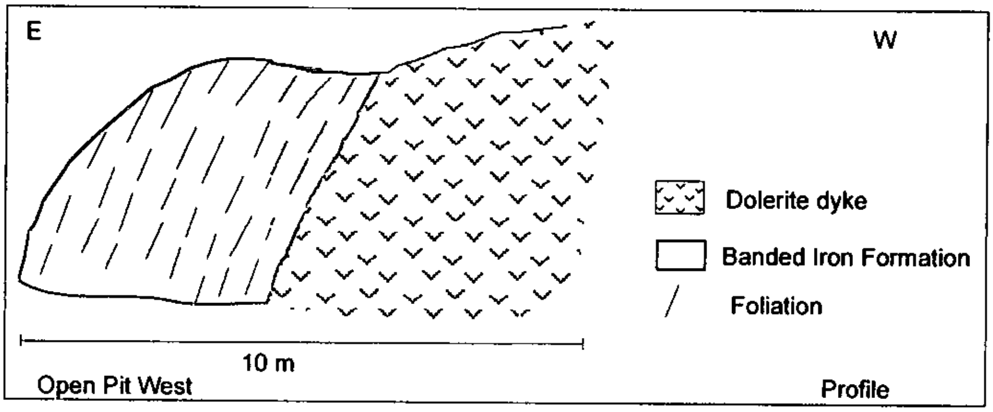

Figure 3 – 34. N – S intrusive contact between the dolerite and mineralised BIF at Monarch mine open pit.

The mineralisation is within a highly silicified banded (at places brecciated) chert impregnated with sulphides (pyrite, pyrrhotite, arsenopyrite, galena, sphalerite.). Au is within sulphides and is found also as very fine-grained free Au in the oxidation zone (Sheeran et al., 1990). The sulphides are irregularly disseminated or they form stringers (veinlets) of 1 - 10 mm thick. The sulphides may constitute around 17% of the banded chert. According to Vicente & Camarinhas (1949) and Obretanov (1977) the average grade is c. 9.7 Au g/t, but Forster et al., 1996 worked out a more conservative grade of 6.4 g/t.

Field observations suggest that the Monarch deposit is controlled by a combination of at least three factors, the N-S fault, the sinistral - sheared tectonic contact (talc-schist and the laminated chert) and the quartz vein (see main shaft position – Fig. 3 - 35).

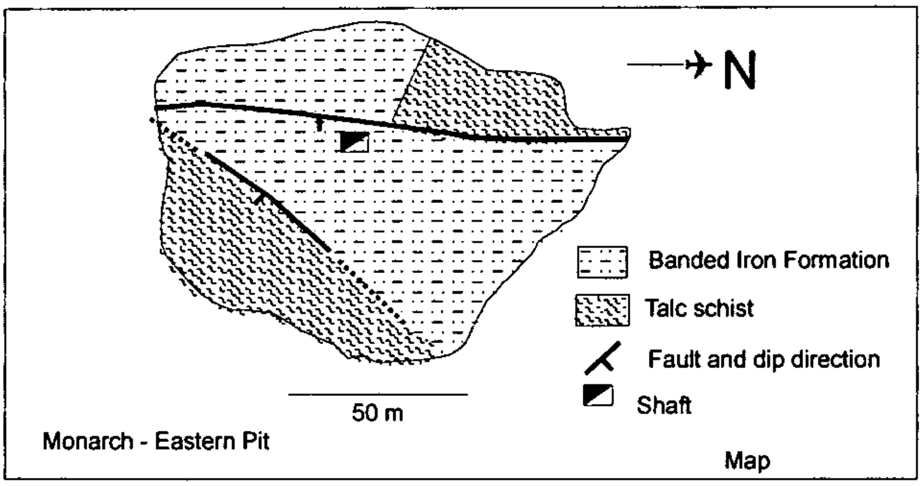

Figure 3 – 35. Schematic representation of the geology and structure at Monarch mine open pit showing the position of the main shaft.

Guy Fawckes

The mine is located in the northern hills of the Revue valley (0486990; 7912920). The host lithologies are talc schists, chloritic talc schist (highly sheared and intensely foliated in places with anastomosing foliation), and BIF breccia.

Field observations show that the main foliation is oriented at an average 193°/87° and a spaced cleavage at 046°/70°. The mineral growth lineation plunges 62° east. Poorly developed kinematic indicators suggest south up.

Locally, for example in the main open pit, there is development of a secondary foliation at a very small (5° - 15°) angle to the main foliation (022°/52°). The exposures at the main open pit suggest a fault-hosted ore in a highly sheared extensional quartz vein oriented E – W.

Underground observations indicate that the deformation is more intense in the footwall of the shear zone and gradually decreases towards the hanging wall (Fig. 3 - 36). The adits are developed consistently on the footwall of the hosting structures.

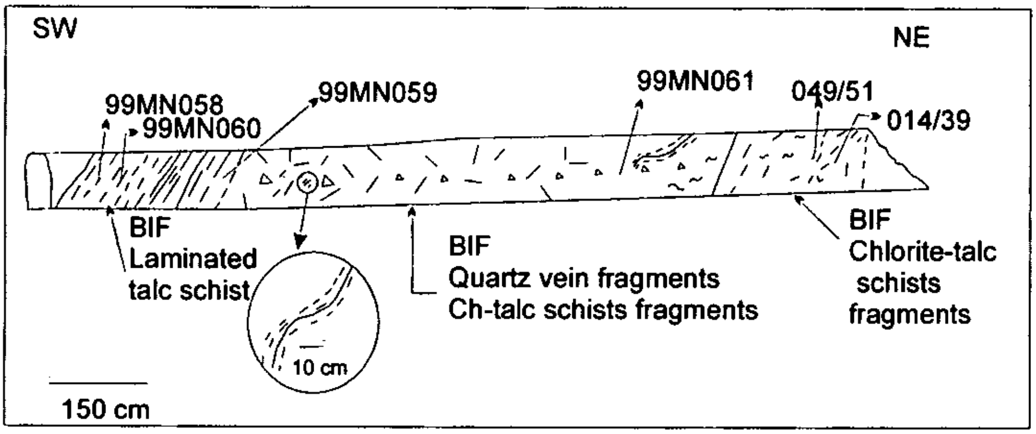

Figure 3 – 36. Main adit at Guy Fawckes, simplified geology.

In summary, the shearing (E-W), faulting associated with quartz veins (E –W to NW – SE) and brecciated BIF and quartzites control the mineralisation at Guy Fawckes. The different foliation orientations (to the south or to the north), mineral lineations (towards east) and small scale folding suggest that the area has been affected by several ductile - brittle deformation phases.

The Guy Fawckes mine comprises four recognised ore zones with different ore types: the breccia ore (BIF fragments, mineralisation restricted to sites where quartz veins cut the breccia), the quartz vein (dipping at 80° to the north), the brecciated quartzite (highly pyritic brecciated white quartzite) and the quartzite (NW striking quartz vein, which dips steeply to the east) (Sheeran et al., 1990).

3.6.2.4 Fault/Shear zone hosted deposits

Bragança Mineralised zone

The Bragança zone is located to the ENE of the Chimedzi mine (main shaft 0488134; 7920129). It is developed in an approximately N - S fault, cutting through oriented granite to the north into the greenschists, serpentinites and talc schists of the Macequece formation to the south. The zone comprises the Bragança, the Marianas, the Damp and the Richmond deposits (Fig. 3 –19 for relationship between gold deposits and geology).

Gold mineralisation is developed within a complex, N-S trending quartz vein that was emplaced in a sequence of metavolcanics (talc-chlorite and chlorite schists) with thin bands of banded ironstone near the contact with a quartz diorite to the east. It also appears that the vein development and mineralisation are confined to parts of the fracture that cut the metavolcanics, although the fracture post-dates the emplacement of the quartz diorite (Sheeran & Venter, 1990). Old plans and maps show a parallel, mineralised zone 40-m east of Bragança deposit that is described as a quartzite, but Sheeran and Venter (1990) suggested a mylonitized quartz vein with an average grade of 9 g/t Au, whereas Forster et al., (1996) reported an average grade of 15 g/t Au.

Marondo Mine

The mineralisation at Marondo mine (0478533; 7919663) occurs within NE trending sugary quartz veins which varies in thickness from 0.2 to 3.0 m over a strike of 300 m. Grab sampling from the open pit yielded values around 3.33 g/t Au (Sheeran & Venter, 1990). The foliation in the ultramafic schists is oriented, in average, 190°/35° - 40. Some quartz veins are steep and strike mainly SW - NE (287°/68° in average). The mineral growth lineation plunges 40° towards 212°. Some sub-vertical fault planes were measured and gave strike of 010°-190°. The fold axes in the ultramafic schist plunge shallowly towards 210°. The quartz veins are highly sheared and recrystalised. There are at least two generations of quartz veins in the area. Sulphidation is extensively developed. Fault zones with component of shearing seem to control the mineralisation in the Marondo Mine.

Cantão Mine

This deposit is located (0478723; 7918652) within the Chua river valley and the ore body is a quartz vein of 0.6 - 0.8 m thick in mafic schists (Fig. 3 – 27). The lenticular quartz vein representing a N – S fault zone that strikes ESE - WNW and dips 25°- 30° north (Obretanov 1977). Gold mineralisation is associated with sulphides (arsenopyrite, pyrite, and -+ chalcopyrite) impregnation (Sheeran et al., 1990).

The foliation is oriented mainly east or southeast at moderate to steep angles. Fault planes are oriented towards east to southeast at steep angle (e.g. 096°/70°, 160°/50° and 065°/80°) (Fig. 3 – 39). The mineral lineation plunges 10° towards 278° or 40°towards 094°, 082° and 108°. Silicification, sericitisation and carbonatisation are common in the deposit.

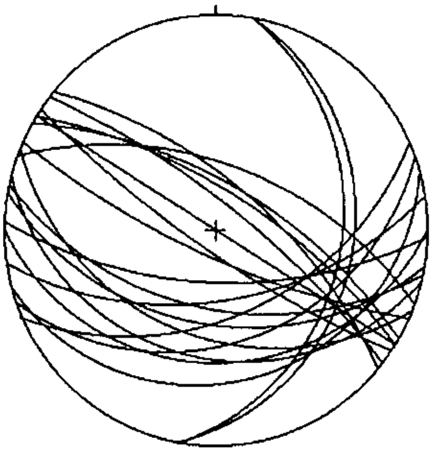

Figure 3 - 37 Poles to foliation in chloritic schist at Cantão mine.

Musa Reef Mine

This mine is located on the eastern part of the MMO greenstone belt on the southern slope of the Muza River valley (099330; 7914250) The main lithological units include serpentinites, talc-chloritic-carbonate schists, chloritic schists and some felsites, microgranites and dolerite dykes on the core of the Mangota range.

The highly sheared sub-vertical quartz vein (140°/75° – 85°) in the Macequece Formation serpentinites and talc-chlorite-carbonate schists in contact with chloritic schists (Fig. 3 - 17) constitute the main orebody. The mineralised quartz vein is located on the contact between chlorite and talc-chlorite-carbonate schists. The strong mineral lineation (065°-61°) and striation lineation towards 030° and plunging 76° suggest a normal sense of movement, which might result from late reactivation of the shear zone.

The alteration (Fig. 3 –17) is mainly pervasive carbonatization in the talc-chlorite carbonate schist. Pervasive alteration is very difficult if not impossible to detect from remotely sensed images. The presence of sulphides in the wall rock supports a phase of sulphidation that may or may not be related to the mineralisation.

Field observations suggest at least three generations of quartz veins. The first (probably the oldest) oriented parallel to the main foliation (E – W), the second one is oriented at small angle to the first foliation and the last is oriented N-S and cuts the main foliation at right angle.

The mineralisation is related to the first and second generation of quartz veins, which are recrystalised, and boudinaged (Fig. 3 - 17), it is a crack-seal (laminated) quartz vein (75°/124°) and corresponds to an early E -W shear zones (Upper Bulawayan) reactivated by late deformations. The grade is reported to be between 0.3 and 1 g/t Au (Forster et al. 1996).

3.7 Discussion

The geology, tectonic and structural geometry of the MMO greenstone belt is not yet well understood. The same applies for the rest of the Archaean greenstone belts (Jelsma and Dirks, 2002). The main problems lie on the tectonic reconstruction and understanding of the relationships between geometry of structures and mineralisation. Data obtained in this study indicates that the MMO belt consists of at least 4 distinct structural domains separated by layer parallel shear zones as shown in Fig 3-12, each domain is structurally complex with internal deformation. This interpretation shows that the stratigraphy of the MMO greenstone belt is not a coherent sequence of greenstone synclines with sediments filling up the basins.

But it is also true that there is stratigraphic repetition such as the formation of at least three E-W striking en echelon basins separated by tight antiforms in the Manica part of the belt (Forster et al. 1996) and the silicified shear zones that separate the domains may suggest that some of the terrains were accreted.

The presence of komatiitic basalt fragments and granitic clasts observed (Chenjerai, 1996) within the basal conglomerate of the Mbeza sediments implies that the environment in which parts of the MMO greenstone belt were deposited was an active tectonic basin in proximity to granitic basement.

Observations at mine scale suggest a structural control of gold deposits combined with lithological control since there are no large deposits within Shamvaian in the MMO belt.

At mine scale the mineralisation tends to be controlled by secondary structures mainly related to crustal shear zones and also by lithological contacts between rocks of different competence.

Gold mineralisation in the MMO belt was found to be contemporaneous with the formation of hosting structures because the mineralised veins are perpendicular to slicken fibre growth at the mine scale. This implies that the mapping, description of the distribution patterns of structures and characterisation of known gold deposits (see also Chapters 4, 5 and 9) can lead us to new gold mineralisation.

The mineralisation event in the MMO greenstone belt post-dates the peak metamorphism and is synchronous with a cratonwide event that occurred at ~ 2.65 Ga (Mondlane et al. 2000). The distribution of gold in the MMO belt shown in Fig. 3 - 24 is controlled by surface (visible) trapping structures (e.g. Schmidt-Mumm et al. 1994; Chenjerai, 1996; Forster et al., 1996). The next chapter discusses in detail the controls of mineralisation and the classification of gold deposits in the MMO greenstone belt.

3.8 Conclusions

The following conclusions can be drawn from this chapter:

- The MMO belt is a late Archaean linear structure controlled by deep-seated first order shear zones. The minimum age of the belt is constrained by the Penhalonga granodiorite, which yielded an age of 2742±3.
- Parts of the MMO belt were deposited in active tectonic basins in the proximity to granitic crust.
- The southern contact between the greenstone belt and the adjacent gneiss is steeply dipping with a down-dip stretching lineation. The northern contact is characterised by asymmetric S-kink bands that plunge moderately towards the west suggesting sinistral movement (e.g. Treloar and Blenkinsop, 1995).
- Contacts between the Upper Bulawayan and the Shamvaian, in sections, show shearing and silicifition related to BIFs. These contacts are mineralised as it is the case of

Toronto, Dot's Luck, Reliance, Try Again, Fair Bride mines which are located within or very close to the southern contact and Guy Fawckes, Monarch, Howat's Luck, and Munhene located within or close to the northern contact.

- Gold mineralisation in the MMO belt is coeval to the formation of the hosting structure.
- Early shear zones trend ENE and are found at the greenstone margins and the contacts between Upper Bulawayan and Shamvaian Supergroups. Late shear zones crosscut the early shear zones at a high angle and mainly trend NNW and N-S.
- At a mine scale the mineralisation shows both a structural control and a lithological control. Four main groups of mineralisation can be identified on the basis of hosting structure in the MMO greenstone belt: (i) Deposits related to contact between greenstones and sedimentary rocks associated with BIF; (ii) Deposits hosted in granites or at the contact between granites and mafic or ultramafic units; (iii) Deposits hosted in BIF (silicified shear zones) within mafic and ultramafic rocks; (iv) Fault/shear zone hosted deposits.

Chapter 4

4 Controls and Classification of Au Mineralisation in the MMO greenstone belt

4.1 INTRODUCTION

The information about gold mineralisation in the MMO belt is diverse such that it needs to be compiled in a systematic relational database, which allows easy search, retrieving and manipulation. The main parameters that were used to classify the deposits included the controls of the gold mineralisation, host rocks, grade and production, sulphides assemblages and geometry of the deposits. On the basis of the common parameters that could be identified in the dataset the deposits were classified in four main groups: - fault/shear zones, quartz veins, BIF hosted, and felsic and intermediate intrusions related deposits. Each group may accommodate subgroups (see also Chapter 3).

This chapter deals with the above parameters beginning with controls of mineralisation through database design and classification of gold deposits. The chapter also forms the foundation for the distribution patterns analysis presented in subsequent chapters.

4.2 Controls of Au mineralisation in the MMO Greenstone belt

Gold mineralisation in the MMO greenstone belt is controlled mainly by secondary and tertiary structures (e.g. Campbell and Pitfield, 1994) linked to layer-parallel regional shear zones that separate geological-structural domains as shown in Fig. 3-4. In general, gold is confined to sections of possibly reactivated, sub-vertical shear zones where favourable conditions for gold precipitation were met, such as pressure drops during reverse faulting within favourable host rocks (e.g. Cox et al., 1991, Gates, 1991, Sibson, 1992). The optimum combination of these conditions leads to formation of large deposits. These conditions may include the presence of a felsic intrusion (e.g. Rezende group of deposits), specific lithology (e.g. in banded iron formations), or a competence contrast between lithologies (e.g. Dot's Luck deposit; Fig. 3 – 31; located near the contact between mafic-ultramafic rocks and metasedimentary rocks) in the MMO belt. The felsic intrusions are commonly either earlier (e.g. Penhalonga granodiorite), coeval or postdate the mineralisation event. The structures that trap mineralisation in the MMO greenstone belt are planar or linear penetrative fabrics mainly oriented north - south and northeast - southwest.

Strong deformations, and formation of suitable structures followed by the intrusion of tonalitic magmas (e.g. Penhalonga granodiorite), are probably the most important factors in gold concentration in MMO greenstone belt.

Significant gold deposits in greenstone belts elsewhere worldwide are restricted to the brittle-ductile transition zone (e.g. Groves, 1993, Forster et al., 1996). This study suggests that these structures in the MMO greenstone belt are represented by fault splays (e.g. Champion mine (Phaup, 1937, Campbel and Pitfield, 1994)), dilational quartz veins (e.g. Redwing mine (e.g. Schmidt Mumm et al., 1994, Chenjerai, 1996), shear intersections (e.g. Guy Fawkes mine; (Fig. 4-1) and inflections of shears (Boa Esperança mine, Fig. 4-1).

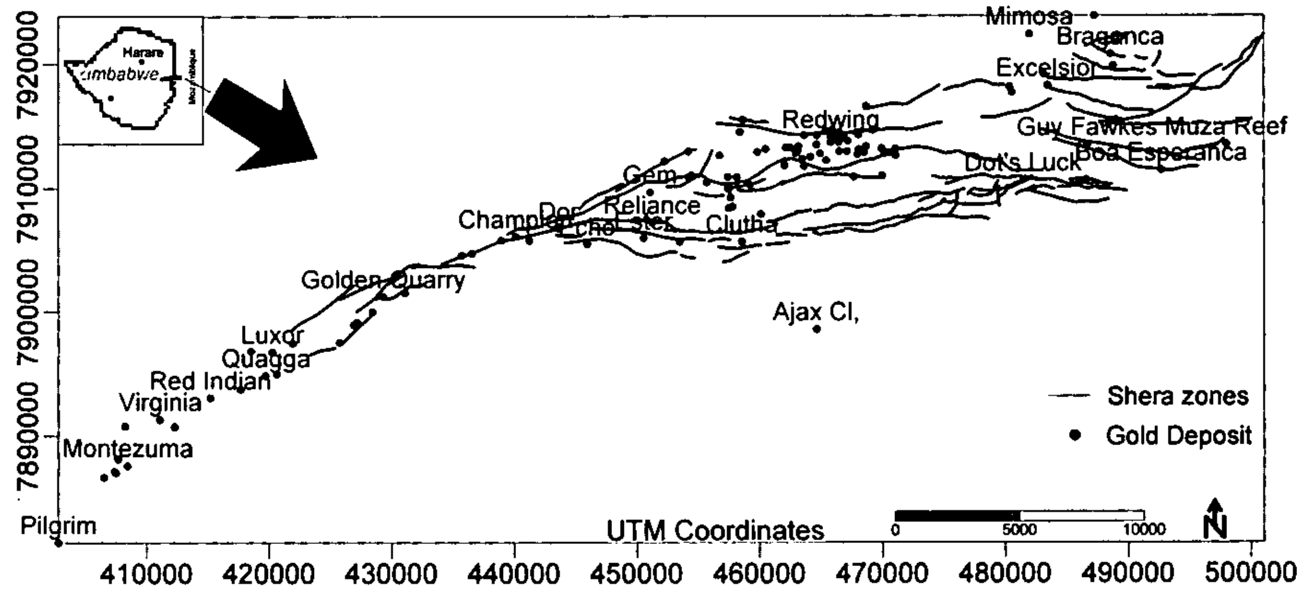

Figure 4-1. Distribution of shear zone hosted deposits in the MMO belt and its spatial relationship with main shear zones.

The gold deposits in the Manica Mutare Odzi greenstone belt can be subdivided in the following categories on the basis of lithology and sulphides association:

1. Deposits associated with the Penhalonga granodiorite
    - Deposits hosted by and/ or in the immediate vicinity of the Penhalonga granodiorite, e.g. Old-West, Redwing, Rezende, and Liverpool.
2. Deposits hosted by ultramafic schists (talc, tremolite, actinolite schists) or BIF
3. Deposits associated with sheared contact between rocks of contrasting competency. In this case, the mineralisation is mostly in the form of As - Sb sulphide replacements (Campbell and Pitfield, 1994) in talc and actinolite schists which are in contact with either felsite (Toronto mine) or serpentinite (Reliance mine)
4. Deposits hosted either by biotite granite, within mica schist/ tremolite schist xenoliths within granite, or localised along the sheared contact between granite and ultramafic schist

In a more structural and stratigraphic approach the above categories can be simplified on the basis of descriptions of known gold deposits in the MMO greenstone belt as follows:

- i) Felsic and intermediate intrusions in the greenstone sequence (e.g. the Penhalonga granodiorite) including the northern and southern granites with xenoliths of schists
- ii) BIF
- iii) Shear zones and sheared lithological contacts
    - a) contact ultramafics/metabasalts
    - b) contact Mbeza sediments/felsite or serpentinite
    - c) contact granite/ultramafic schists
    - d) early (crustal) and late shear zones mainly located in tholeitic basalts (high magnesium) of extrusive (pillow lava and spinifex texture). These shear zones are usually silicified and are associated with BIFs.
- iv) Quartz veins
- v) Shamvaian lithologies
- vi) Bulawayan lithologies

Table 4 - 1. Summary of the main characteristics of the groups of deposits

Group	No. deposits	No. Deposits with information	Main Sulphides	Total Production [kg]	Ave. grade [g/t]
i)	65	60	Py (18), Gn (16), Po (8), Ccp (7)	30741	9,11
ii)	42	39	Py (18), Po (14), Gn (14) and Ccp (8)	7325	15,1
iii)	122	111	Py (40), Po (21), Ccp (19), Gn (37), Asp (9)	39847	14,17
iv)	170	143	Py(41), Gn (34), Ccp (18), Po (17)	35825	11.93
v)	31	28	Py (13), Gn (13), Po (4), Ccp (7), Aspy (3)	7023	12,60
vi)	114	105	Py (37), Gn (31), Po (21), Ccp (16), Aspy (9), Bism (4), Sph (3), Pn (2)	37309	8,83
	1	Rezende mine	Py, Po, Ccp, Gn	23505	15,52

Py = pyrite, Po = pyrrhotite, Ccp = chalcopyrite, Gn = galena, Sph = sphalerite, Asp = arsenopyrite, Bism = bismuthinite. (13) or 13 - number of deposits recorded within the parameter. (i) Felsic and intermediate intrusions; (ii) BIF; (iii) Shear zones/faults; (iv) quartz veins, (v) Shamvaian and (vi) Bulawayan.

The way the groups can be recognized in the field is very important, for example the shear zones are distinguished on the basis of cross cutting relationships into: early shear zones, late shear zones and sheared contacts. The early shear zones are laterally continuous on tens of kilometre scale and are associated with BIF. These shear zones trend ENE parallel to the long axis of the MMO belt. Stretching lineation along these shear zones plunge towards east at ~ 30°. The sense of movement, based on field observations of stretching lineation, fibre growth directions and shear bands or rotated boudins where present, is characteristically sinistral with south over north and with dip slip component.

The late shear zones are characterised by more limited strike lengths (km scale). In general, the sense of movement along these shears is sinistral and the stretching mineral lineation plunge towards east at ~ 20°. The shear zones associated with lithological contacts are mainly as a result of competence contrasts between different lithologies. The deposits related to these shear zones tend to be small in size but high grade (Table 4 – 1). Commonly, they are associated with quartz veins. Some of these gold deposits seem to be influenced by proximity of felsic intrusions (e.g. Dot's Luck mine - Fig. 4 - 1) and in places, these deposits may be associated with BIFs.

4.3 Database design and statistics

The present study is entirely based on a GIS based digital database. The database was created with the objective of organising, standardising, structuring and allowing efficient management (sorting, calculating, retrieving, and sharing) of the multidata required for the study. This Chapter and Chapters 5, 8 and 9 require information generated from the database, which turn input for visualisation and modelling exercises.

The design of a database is guided by its objective (Frizado, 1992). In this study a straightforward structure that allows for calculating, sorting and retrieving information efficiently has been designed. The database structure includes primary entities (see Appendix IV-A) such as location, name of the deposit, associated sulphides, ore type, structure, veining, host rocks, alteration, production, grade and mining period. The primary entities were subdivided into second order entities, third order entities and so on in a hierarchical structure (see Appendix IV-A).

The database was originally created in Excel and linked to ILWIS 2.2, Surfer 7.0 and Arcview 3.2 for visualisation and calculation of spatial relationships and modelling (see Chapter 9).

4.3.1 Data-source and data-quality

The database was based on information from literature, fieldwork, satellite imagery and aerial-photography interpretation.

The position of the mines was obtained from 1:100000 and 1:50000 geological maps (Phaup, 1937) and 1:100000 geological map by Swift (1956) for the Zimbabwean part of the belt (Dirks et al., 2000) and from a Russian database (ING, 1986) assembled from field measurements in the late 70's and early 80's for the Mozambique part of the belt. The gold deposits descriptions were gathered from geological bulletins (e.g. Phaup, 1937; Swift, 1956, Campbell and Pietfield, 1994), publications (e.g. Chenjerai, 1996; Manuel, 1992; Schmidt-Mumm et al., 1994), mines and companies' reports (e.g. Sheeran and Venter, 1990), student reports and dissertations (e.g. Nyama, 1999; Saeze, 2000). Each mine or data point was described in terms of sulphides, deposit type, controlling structure, vein orientations, size, geometry and type, host lithology, alteration type, grade, production, pit volume, and mining period. The descriptions were not complete for all mines, for example some mines did not have production information probably because their productions were declared at a different mine.

The quality of the data was assessed by comparing earlier descriptions with more recent ones and by field check where 60 mines (25% of the total of the deposits) were visited and checked in regard to position, ore type, orebody orientation, pit volume and orientation, number of pits, host lithology, controlling structure, alteration type and sulphide assemblages (Appendix IV-A and IV-B).

The descriptions acquired from the literature (Phaup, 1937, Swift, 1956) regard fault-hosted deposits as a generic term that includes faults (s.s.), shear zones and contact reefs deposits. In general, the descriptions were good enough for the study although the positions of mines were more difficult to ascertain, and errors between 50 and 100 meter were recorded. This error is deemed acceptable because a deposit may be represented by a number of adits, pits and ore-bodies extending for more than 500 meters (e.g. Guy Fawkes mine) and also because it is not known exactly where the first position was (first adit, main shaft or centre of the claim).

The ore mineralogy analysis was carried out for selected deposits during this study because the data available (e.g. Phaup, 1937, Schmidt-Mumm et al., 1994 and Chenjerai, 1996) did not cover all deposits in the belt.

4.3.2 Nature of the data

The gold mines in a mining district may represent a random or non-random sampling of the most accessible part of the mineralisation. This sample may be statistically representative of the mineralisation present in the district, but it is more likely to be under representative. The question of representativeness of samples such as the one under investigation has been explained by roll-off effect in fractal analysis (e.g. Blenkinsop and Sanderson, 1999). These authors attributed the roll-off effect to undersampling of small features due to limits of measurement precision (c.f. Walsh et al., 1991), suggesting that more deposits are still likely to be discovered in a particular district. This problem of sample representativeness is not clearly understood and is beyond the scope of this discussion. In this thesis, on the basis of number of deposits (241), number of deposits per km^2 (~5) (Forster et al., 1996, Mondlane et al., 2000) and the spatial distribution, it is inferred that the known gold deposits are a representative sample of the mineralisation in the MMO belt.

The satellite imagery (SPOT, ETM and TM), aerial photos, geological and structural maps, gold deposits maps, mine plants and exploration maps in the study area were projected in UTM coordinate system on the Clarke 1866 ellipsoid. This standardization of the coordinate system in the data introduced a residual error due to the polynomial transformations involved. The residual error in the satellite imagery was 60 m, this error is constant and it affects the data in the same way throughout the study area, thus it can be neglected. The other reason for ignoring this error is that the size of a normal deposit is usually larger than 60 meters, thus being 60 meters away one is still within the deposit's area. Fact which may not be ignored is that a point represents the location of each deposit on the map regardless of the number of small orebodies, shown by different pits or adits, which constitute the deposit or its extension. This is well solved by the minimum fractal distance defined in chapter 5, in which a 1.0 km is defined as significant for the distribution pattern analysis. A deposit is considered to be truly represented by a single point when analysing the data set between 1 and 20 km scale interval, in which the distribution of gold deposits is considered to be truly fractal in the MMO greenstone belt (see also chapter 5). Below 1 km the data is mainly affected by the complexity of surface brittle structures that control the trapping of gold and the undersampling (e.g. Blenkinsop and Sanderson, 1999). Beyond 20 km, the analysis is strongly affected by the NE – SW linearity of the MMO greenstone belt (Mondlane, et al., 2001).

4.3.3 Data classification

On the basis of grouping patterns identified in the 241 gold occurrences in the study area, the data were grouped into the categories of shear zones/faults/contact reefs, quartz veins, BIF-hosted, felsic and intermediate intrusion related deposits.

The shear zones group consists of three subgroups i.e. early shears, late shears, and sheared contacts. The early and late shear zone distinction is based on crosscutting relationships. The gold deposits related to early shear zones have variable grade, for example e.g. Guy Fawckes, Kenya, Howat's Luck are low grade while Monarch mine and Munhene deposits are high grade. In the late shear zones, mineralisation is locally associated with scheelite and the deposits have higher grade (e.g. Rezende mines group) compared to deposits associated with early shear zones. A possible explanation for the association of these structures with large deposits could be the reactivation of structures, remobilisation and re-concentration of gold.

The quartz veins represent the most important group in terms of total production in the MMO belt (c. 35825 kg of gold produced at an average grade of 12 g/t, and from a singular deposit 7162 tons of lead (Table 4-1)) (Mondlane et al., 2000). These deposits are mainly oriented north – south and are related to the latest deformation phase in the late Archaean (? D_4). The deposits are usually small and high grade (table 4-1), with exceptions such as Rezende mine which represent a large deposit with a production of 23.5 t. Quartz vein deposits may occur in association with shear zones, stockwork/disseminated deposits in the majority of lithologies particularly near felsic intrusions.

The above classification is the key to the analysis and description of distribution patterns of gold deposits in the MMO belt (chapter 5). In this regard, it is useful to understand each group as composed of deposits truly representing the specific type of deposit but also a significant overlap of other types of deposits. This overlap is because a deposit is not made up of a single homogeneous type of mineralisation, but usually by several types and is controlled by multiple factors. For example, in the total of 122 shear zones /fault hosted deposits, 94 are also quartz veins (Mondlane et al., 2000). Thus, the interpretation and statistical analysis based on the type of deposit carried out in the next section should be done with care.

4.3.3.1 Data presentation and statistics

The diversity of the records in the database makes its presentation statistically complex. The abundance of each parameter is initially investigated individually and later on relationships are worked out. In the data presentation, interpretative parameters such as type of deposit are not considered because they could bias the data. Non-interpretative parameters, which include the position of the deposit, grade, production, ore mineralogy and host lithology are presented following the diagram presented in Fig. 4-2. There are several crosscut relationships that can be derived from the five parameters, thus a simplification was introduced interactively. Grade is used as a baseline, i.e. low grade deposits hosted in Shamvaian with production less than 100 kg and associated with pyrite and galena.

On the basis of the historical records on grade, it is feasible to say that deposits with grades below 5 g/t are low and otherwise are high grade. In the database there are 73 low-grade deposits and 123 high-grade deposits and 45 deposits without information on grade.

The host lithologies in the MMO greenstone belt (see appendix IV-A) were not use particularly because it was found acceptable to use stratigraphic division such as Shamvaian and Upper Bulawayan and, due to its particular importance in the MMO belt the felsic and intermediate intrusions. Considering these three subdivisions the total records show that the Shamvaian hosts 31 deposits, Bulawayan rocks host 114 and 65 deposits are related to felsic and intermediate intrusions (Fig. 4-2) and 31 deposits have no information on lithology.

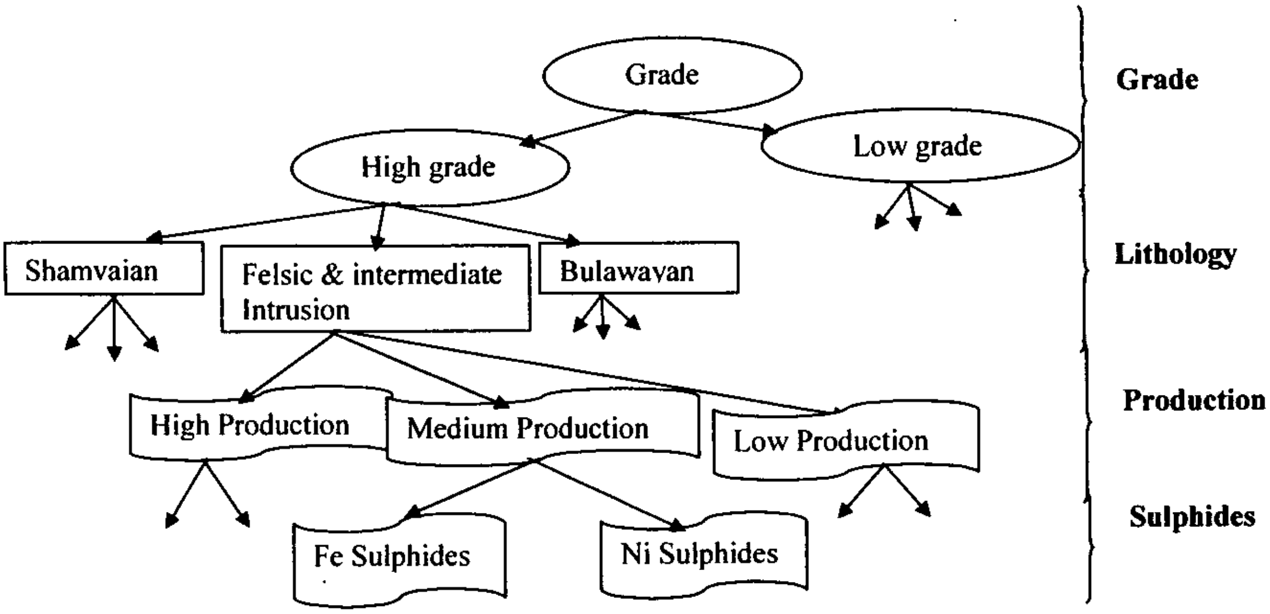

Figure 4 - 2. Flow chart for data analysis and interpretation. The open arrows mean that the next class is the same for other entities of the same category.

On the basis of statistical analysis of the historical records the production can be divided into high (>100kg (37)) medium (10 - 100 kg (50)) and low (<10 kg (110)), and 44 deposits have no information on production (Table 4-2).

Table 4-2. Statistical summary of the gold deposits in relation to production, grade, lithology and sulphides.

Production	Ave. Grade [g/t]	Low/ High grade	Deposit Type	Main Sulphide	Main Stratigraphic unit	Total Production [kg]
>100 kg (37)	8,96	Low 7 High 30	(i). 9 (ii). 8 (iii). 10 (iv). 10	Py (18), Gn (17), Ccp (10), Po (8), Aspy (7), Sph (3)	Shamvaian (1) Intrusions (15) Bulawayan (21)	40887
10 - 100 kg (50)	16,39	Low 17 High 33	(i). 10 (ii). 3 (iii). 15 (iv). 22	Py (13), Po (10), Gn (8), Ccp (8), Bism (5), Aspy (3)	Shamvaian (1) Intrusions (20) Bulawayan (29)	1995
<10 kg (110)	10,93 (6 without information)	Low 47 High 57	(i). 16 (ii). 14 (iii). 25 (iv). 55	Py (12), Po (5), Gn (15), Ccp (2), Sph (1)	Shamvaian (7) Intrusions (28) Bulawayan (69)	255

Py = pyrite, Po = pyrrhotite, Ccp = chalcopyrite, Gn = galena, Sph = sphalerite, Asp = arsenopyrite, Bism = bismuthinite. (13) or 13 - number of deposits recorded within the parameter. (i) Felsic and intermediate intrusions; (ii) BIF; (iii) Shear zones/faults; (iv) quartz veins.

The deposits that produced more than 100 kg are typically high grade and occur within the Upper Bulawayan and/or near felsic intrusion (Table 4-2 and Fig. 4-3).

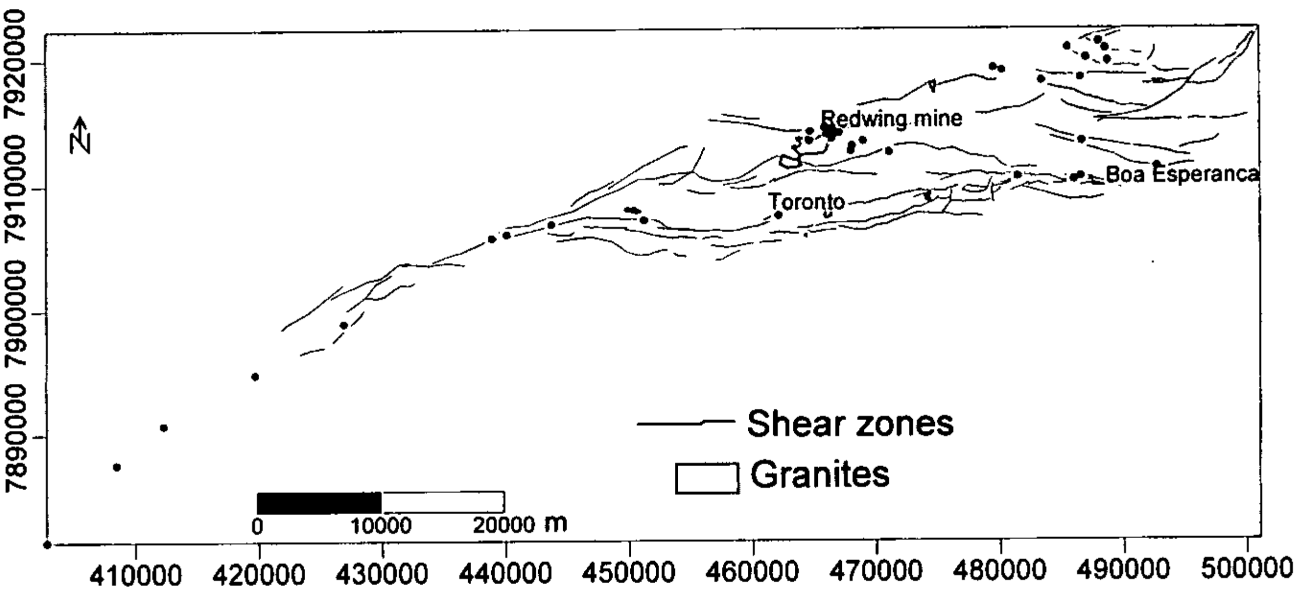

Figure 4 - 3. Relationship between gold deposits that produced more than 100 kg and shear zones

The historical records on gold deposits in the MMO belt, also show that shear zone/fault hosted deposits that produced more than 100 kg are mainly related to the early shear zones (Fig. 4-1) with few exceptions such as the Rezende deposit which is related to a shear zone that crosscuts the main trend of early shears. These deposits have produced over 40 tons of gold at an average grade of 8,96 g/t (Table 4-2). Upper Bulawayan and felsic intrusions host most of these deposits (Table 4-2).

The geometry of shear zone deposits is dominantly lensoidal in a crack seal type of ore body. The mineralised shear zones in the belt dip mainly towards north and to less extent south (Fig. 4 – 4).

The most common sulphides within the shear zone deposits are pyrite and galena. Other sulphides in descending order of occurrence are pyrrhotite, chalcopyrite, arsenopyrite, crocoite and bismuthinite (Table 4-2).

The quartz vein deposits are mainly hosted in the Upper Bulawayan and felsic intrusions. They are primarily associated with shear zones/faults, which constitute up to 55% of the quartz vein deposits.

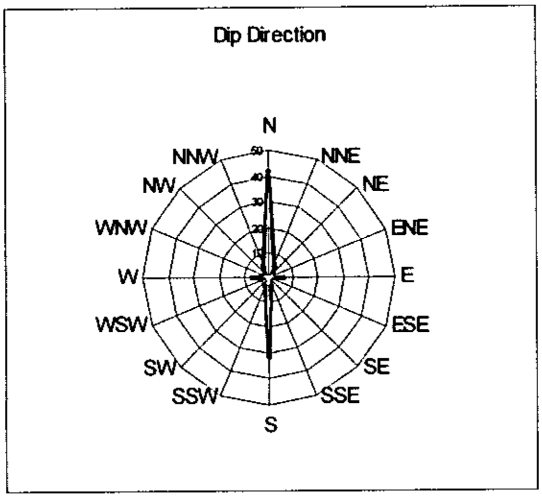

Figure 4 – 4. Rose diagram showing dip directions of the mineralised shear zones in the MMO greenstone belt.

The geometry of the orebody is lensoidal (Fig. 4 – 5) in stockwork and crack seal type (e.g. Munhene deposit in the Manica part of the belt). The quartz veins deposits are, in general, small deposits with 99 deposits out of 170 having produced less than 10 kg and only 29 deposits with production higher than 100 kg (Table 4-2).

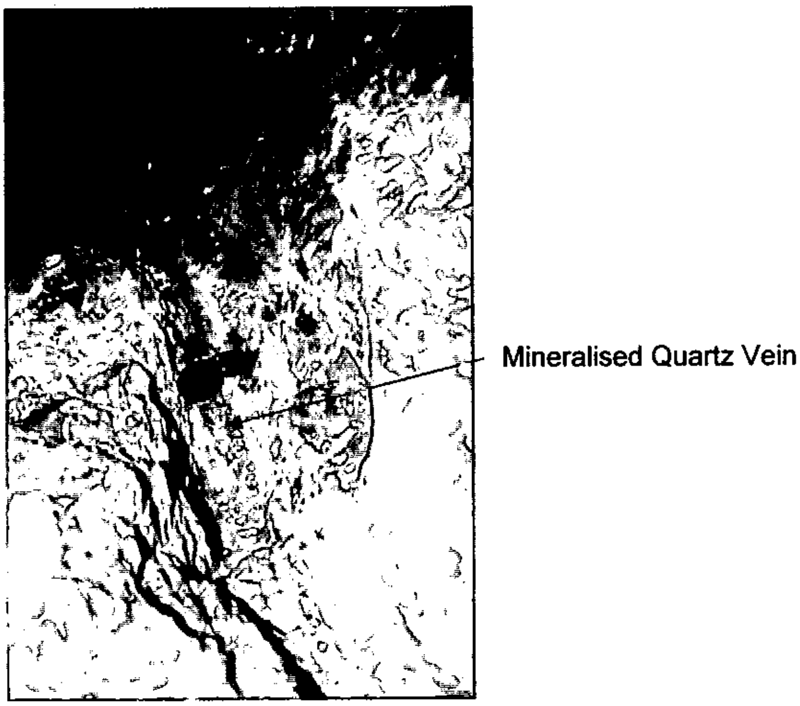

Figure 4 – 5. Mineralised lensoidal quartz vein in the Munhene mine. Photo looking west. Location in UTM 0482691 - 7914282
hfvhj

Pyrite and galena are the dominant sulphides within quartz vein deposits followed by pyrrhotite and chalcopyrite (Table 4-3). The rest of minerals such as arsenopyrite, sphalerite, bismuthinite, and pentlandite are present in small quantities.

The deposits hosted by felsic and intermediate intrusions comprise 29 deposits of low production, 20 of medium and 16 high production deposits. The most abundant sulphides are galena, pyrite and pyrrhotite.

The type of sulphides associated with gold mineralisation gives an indication on the type of mineralizing fluids, such as iron rich fluids (A) or nickel rich fluids (B). The abundance of sulphides in the MMO greenstone belt is shown on Table 4-3 where it is also evident that the majority of sulphides are iron type, suggesting mineralising fluids of metamorphic origin. The shear zones and quartz-vein deposits show a wide variety of sulphides and higher abundance compared to felsic intrusions and BIF deposits. This large diversity of sulphides can be explained by reactivation of the shear zones and channel ways of the metamorphic fluids.

Table 4-3. Abundance in % and number of deposits of sulphides in gold deposits types and their host rocks. Table a) represents the abundance as recorded in the literature and compile in the database and b) shows normalised percentage of the sulphides.

a)	Py	Po	Apy	Ccp	Gn	Sph	Bism	Pn	Total mines
Shears/Faults (iii)	40	21	9	19	38	3	5	2	147
BIF (ii)	18	14	4	8	14	3	1	0	66
Qtz vein (iv)	41	20	5	18	34	4	5	2	137
Totals	99	55	18	45	86	10	11	4	350
Felsic and intermediate Intrusions (i)	18	8	0	7	16	1	1	0	52
Bulawayan (vi)	37	21	9	16	31	3	4	2	133
Shamvaian (v)	13	4	3	7	13	2	1	0	46
	68	33	12	30	60	6	6	2	231

b)

	Py	Po	Apy	Ccp	Gn	Sph	Bi	Pn	%
Shears/Faults	27.21	14.29	6.12	12.93	25.85	2.04	3.40	1.36	100.00
BIF	27.27	21.21	6.06	12.12	21.21	4.55	1.52	0.00	100.00
Qtz vein	29.93	14.60	3.65	13.14	24.82	2.92	3.65	1.46	100.00
									%
Felsic and intermediate Intrusions (i)	34.62	15.39	0.00	13.46	30.77	1.92	1.92	0.00	100.00
Bulawayan (vi)	27.82	15.79	6.77	12.03	23.31	2.26	3.01	1.50	100.00
Shamvaian (v)	28.26	8.70	6.52	15.22	28.26	4.35	2.17	0.00	100.00

Py = pyrite, Po = pyrrhotite, Ccp = chalcopyrite, Gn = galena, Sph = sphalerite, Asp = arsenopyrite, Bism = bismuthinite, Pn = pentlandite. (13) or 13 - number of deposits recorded within the parameter. (i) Felsic and intermediate intrusions; (ii) BIF; (iii) Shear zones/faults; (iv) Quartz veins. (Source: database – appendix IV-A)

4.4 Discussion

The quality of data is acceptable for the purpose of this study. The inaccuracy in position of the deposits that was revealed by fieldwork is of up to 50 meters on X direction and 100 meter on Y direction. Considering the size of the deposits, which range from 100 to 1000 meters, the position inaccuracy is within the tolerance of the deposit size.

The statistical analyses of the historical records suggest that groups can be formed on the basis of grade, production, host lithology and sulphides. This classification is not unique and is not perfect, i.e. a deposit can be classified into both as quartz vein and shear zone thus creating an overlap. The overlap can be as high as 75% in the case of shear zone deposits and quartz vein deposits, which explains the positive correlation between these two deposits. For the purpose of this study the quartz vein and the shear zones are combined in one group because separating them would bias the final exploration model for gold mineralisation (chapter 9).

The stratigraphic classification is more distinctive and allows clear separation of the groups.

Intrusive deposits are also considered as deposits near an intrusion even if they are within a stratigraphic class.

The records on sulphides suggest that the ore fluids were iron-rich in the whole belt. The main sulphides are pyrite and galena and chalcopyrite or pyrrhotite (Table 4-3).

In general, early shear zones control gold mineralisation in the MMO greenstone belt. The production and number of gold deposits related to felsic and intermediate intrusions in Bulawayan lithology suggest that they are promising exploration targets. BIFs in the MMO belt are commonly silicified to an extent of forming ridges that are easy to map using remote sensing or air photos and they also control gold mineralisation specially where they crosscut Bulawayan lithologies.

The following Chapter will discuss the spatial distribution patterns of the classes of gold deposits in relation to controls of gold mineralisation. Basically the next chapter will show whether the controls of mineralisation or the surface or subsurface expression of these controls can be detected using spatial and lineament analysis.

4.5 Conclusions

This chapter has shown that use of GIS oriented database is adequate for systematisation of the MMO belt gold deposits descriptions.

The nature and quality of the existing data in the MMO belt is adequate for designing a GIS based database for use in exploration modelling in the area.

The description of the controls of mineralisation in the MMO belt allow the following classification of the deposits:

- Felsic and intermediate intrusions in the greenstone sequence (e.g. the Penhalonga granodiorite) including the northern and southern granites with xenoliths of schists
- BIF
- Shear zones, quartz veins and sheared lithological contacts
- Shamvaian lithologies
- Bulawayan lithologies excluding BIFs

Chapter 5

5 Distribution patterns of Gold mineralisation in the MMO Archaean Greenstone belt

5.1 Introduction

Structures control mineralisation at a mine scale and regional scale such as greenstone belt scale (Forster et al., 1996). Blenkinsop et al. (2000), based their arguments on field observation in the Mazowe area, within the Harare-Bindura-Shamva greenstone belt of Zimbabwe, and noted that the regional structures are not particularly important in the control of mineralisation. Dirks et al. (2001) argued that gold mineralisation is strongly controlled by transcrustal regional structures. The aim of this Chapter is to show the importance of structures in the control of Late Archaean gold mineralisation at regional scale, and mine scale with special emphasis on the Manica Mutare Odzi greenstone belt. This Chapter also aims at proving that not all mineralisation is controlled by surface structures (structures visible on the surface); hidden structures at regional (belt scale) and probably global scale (cratonwide) also seem to control gold mineralisation in the Manica Mutare Odzi greenstone belt.

It has been established that surface structures control the trapping of gold mineralisation in the Manica Mutare Odzi greenstone belt (e.g. Chenjerai, 1996, Forster et al., 1996). Data obtained during this study show that groups of mines are not randomly distributed within these structures (Fig. 5 – 1). Some gold deposits are aligned (by drawing a line between the deposits) in certain directions that are not directly related to the observed surface structures.

In a structurally controlled mineralisation province such as MMO belt, the distribution of known deposits may reflect the distribution pattern of the controlling structures. The veracity of this statement is dependent on the degree of mining in the geological province. The known deposits may represent a sample of the mineralisation on the ground and its representativity is generally uncertain.

Generally gold mineralisation is controlled by multiple factors including the scale (local or belt, region or province, and craton or orogeny) of the controlling phenomenon. This complexity is due to interaction of all three scales in one area where each controls specific type of deposits in particular geological setting. The main problem in this case hinges on ability to separate the different events by scale of occurrence and also by considering their overprinting relationships.

In this Chapter spatial distribution patterns of known gold deposits are described and relationships between these patterns and mineralised structures are investigated. This is done by finding groups of deposits that reflect coherent spatial patterns at different scales, which can be enhanced by applying autocorrelation methods, fractal and lineament analysis.

The data were first analysed as a full set and then subdivided into the categories of shear zones/faults/contact reefs, quartz veins, BIF and felsic to intermediate intrusions related deposits, production (<10, >10<100, and >100 [kg]), high (>5 g/t) and low (<5 g/t) grade, sulphides, stratigraphic (Shamvaian and Upper Bulawayan) and combinations such as high grade quartz veins or high grade quartz veins in Upper Bulawayan. In all cases, different scales were tested for autocorrelation and lineament analyses.

5.2 Distribution patterns of Gold Deposits in the MMO Greenstone belt

The map of deposits in the MMO (Fig. 5 – 1) shows alignments in N-S and NW-SE directions that are not directly related to any discernable feature or geological association. Figure 5 - 1 shows the distribution of gold deposits where prominent alignments of deposits in N – S, WNW - ESE, NE - SW directions are suggested. The N -S direction for example, congregates deposits hosted in granites (e.g. Chivuma mine, Shandon mine), BIF in ultramafics (e.g. Guy Fawckes mine), BIF (e.g. Dias Perreira mine) and in mafic schists (e.g. Damp mine). These deposits are associated with pyrite, galena and sphalerite (e.g. Guy Fawckes and Damp mines), and quartz veins (e.g. Chivuma mine).

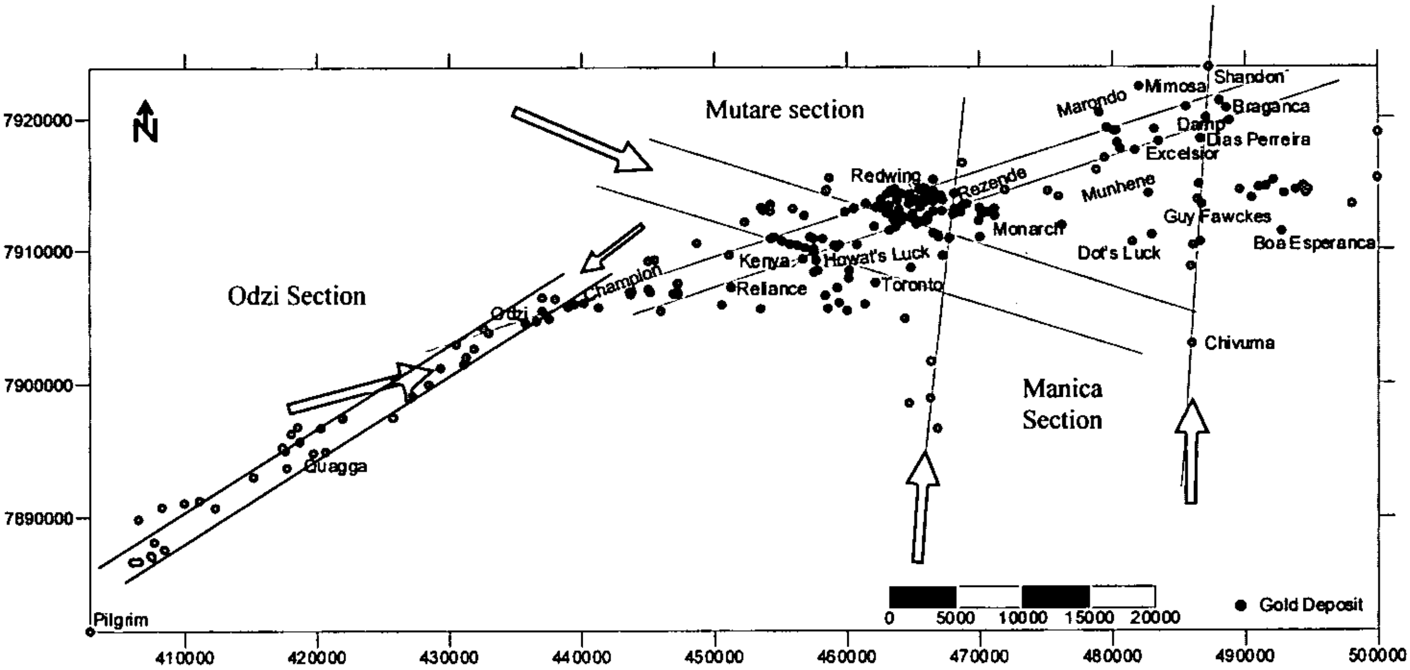

Figure 5 – 1. Map showing all known gold deposits in the Manica Mutare Odzi Greenstone belt. The arrows and the lines show some alignment of gold deposits in N-S, WNW - ESE, NE-SW directions.

These alignments suggest some sort of control apart from the lithology and surface structures. If alignments like the ones represented in Figure 5 - 1 have a geological significance, then they may not be an isolated case, and more such cases must be presented at different scales within the greenstone belt. The description and enhancement of such "lineaments" (discrete corridors consisting of alignment of gold deposits in a map) is important for understanding the controls and characterization of gold mineralisation in the study area. The integration of the "lineaments" in a powerful tool such as GIS-based database clearly relate spatially these parameter with gold deposits in the MMO belt (Chapter 9).

5.3 Lineament enhancement techniques

The main pattern that generally arises from an analysis of the distribution patterns of gold deposits in a structurally controlled mineralisation district like MMO greenstone belt is a linear pattern. A lineament is an alignment of gold deposits in a linear array reflecting a line or a corridor adjoining these deposits. Lineaments can be enhanced statistically, graphically or geometrically by means of autocorrelation methods and variography. In this study, autocorrelation analysis was selected due to its simplicity, sensitivity to subtle changes in linear patterns, ability to analyse limited data points and the fact that it uses only geometrical considerations in the first instance (Vearncombe and Vearncombe 1999; Mondlane et al., 2001). The method has the disadvantage of overemphasing the long axis of a linear belt. Despite this, it remains better than variography hence its adoption here.

5.3.1 Fractal Analysis

5.3.1.1 Introduction

The principle of Fractal Analysis was introduced many years ago by Lewis Fry Richardson (1961), who found out that the relation between the measured length of a coastline and the scale of mapping increases logarithmically with increase of scale of mapping. This implies that with the increase in the scale, more and more features are resolved and can be delineated.

Mandelbrot (1967) used the findings of Richardson and incorporated what he called the "theory of fractals". Mandelbrot (1982) recognised that for most naturally occurring phenomena the amount of resolvable detail is a function of scale. Increasing the map scale does not result in an absolute increase in precision, but only reveals variations that had hitherto passed unnoticed (c.f. Burrough, 1986). According to Burrough (1986) the fractal principle has two main characteristics: firstly, it embodies an idea of self-similarity; that is the manner in which variations at one scale are repeated at another; secondly, it has the peculiar property of fractional dimension, from which it derives its name. A fractal curve is defined as one where a mathematical parameter known as the "Hausdorff-Besicovitch dimension" exceeds the topological dimension. This means that a continuous linear series such as a polynomial tends to look more and more like a straight line as the scale at which it is examined increases (Burrough, 1986).

Fractal objects or sets are irregular, but the degree of irregularity is highly ordered: it is the same on all scales, or scale invariant. Scale invariance can be expressed mathematically by a power law such as:

$$N(r) = Cr^{-D} \qquad (5.1)$$

Where $N(r)$ is the number of objects in a fractal set with a linear dimension greater than r, and C and D are constants (c.f. Turcotte, 1991, 1992, Blenkinsop, 1995)

The level of variation present at all scales can be described by a single parameter, the fractal dimension, defined by Mandelbrot (1982) as:

$$D = \log Cr / \log N(r) \qquad (5.2)$$

Where N is the number of steps used to measure a pattern unit length, and r is the scale ratio.

The value of D for a linear fractal curve can vary between $D = 1$ (the Euclidian dimension of a line) and $D = 2$ (the Euclidian dimension of a surface). $D = 1$ implies that the curve is so smooth that it can be fully approximated by a polynomial relation; a tangent can be drawn at any point along its length. When D is larger than 1, it implies that the line has an associated band of "fuzziness" or uncertainty that "eats up" a little of the second spatial dimension. For $D = 2$, the fuzziness is so large that the line, in fact, becomes an area. For surfaces, the D-values range between **2** (completely smooth) and **3** (infinitely crumpled).

Mandelbrot (1982) was the first to suggest that mineral distribution in the earth could be considered in fractal terms (c.f. Blenkinsop, 1994). If ore deposits have a fractal distribution, they are clustered to some degree, and they can be treated as fractal dusts and are clearly distinct from random or Poisson distribution.

In the last two decades several authors have dedicated research to proving fractal distributions in many areas of geoscience. Turcotte (1986) showed that the relationship between ore grade and tonnage is fractal for mercury and copper production and uranium reserves in USA. Barton and Scholz (1995) demonstrated that hydrocarbon accumulations have fractal size and spatial distributions. Carlson (1991) proved that hydrothermal precious metal deposits in the western USA have a fractal distribution and drew important implications for exploration. Blenkinsop (1994) showed that gold mines in the Masvingo-Mashava and Shamva areas of Zimbabwe Craton have fractal distributions. Blenkinsop (1995) discussed the fractal size distributions of mines in the entire Zimbabwe Craton. Sanderson et al. (1994) applied fractal relationships to vein-hosted gold deposits in Spain. Blenkinsop (1994) applied the fractal measures for size and spatial distributions of gold mines in Zimbabwe and discussed their economic implications. Fractal relationships have been used to describe the spatial distribution of gold deposits as a function of grade, production, deposit type and the presence of sulphides.

This section discusses fractal analysis application for gold mineralisation in the Manica-Mutare-Odzi Archaean greenstone belt as a fuction of gold production and grade and, compares the results with those obtained by, for example Blenkinsop (1994) on the Zimbabwe craton.

5.3.1.2 *Fractal Distribution of Gold Deposits in the MMO Greenstone belt*

It was assumed that the gold mineralisation in the MMO greenstone belt is co-eval and synchronous with cratonwide event at 2.65 Ga. This suggest that all gold deposits in the MMO belt can be treated as fractal dust and can be compared with similar results elsewhere in the Zimbabwe Craton (see Table 5 – 4). The data for the fractal analysis namely, locations of the deposits, gold production statistics, grade, deposit type and type of sulphides are extracted from the GIS based Database (see also Chapter 4 and appendix IV-A and B).

The first method used to define fractal dimension was the so called "ruler method" (Turcotte, 1992) although, it is not the most generally applied method. The second method, "box-counting method" has a much wider range of applicability than the ruler method (Pfeiffer and Obert, 1989).

The approach in this study follows the "box-counting method" as applied by Blenkinsop (1994). The "box counting" method was selected for this study due to its simplicity and its sensitivity to variations in fractal dimension with length scale as demonstrated by Blenkinsop (1994) and Blenkinsop & Sanderson (1999).

The method consists of counting the number of squares (n) of side length ***d*** necessary to cover all deposits. The parameters are linked in the following manner:

$$n\,(d)\ \alpha\ d^{-D} \tag{5.3}$$

Where ***d*** is the side length of the square, ***n*** is the number of squares of side ***d*** and ***D*** is the fractal dimension.

An alternative method for evaluating the fractal dimension is by counting the number of deposits ***N(r)*** in a circle of radius ***r***, which are related by the expression:

$$N(\,r) = Cr^{-D} \tag{5.4}$$

Where ***C*** is a constant.

N(r) is evaluated for each deposit in turn and the results are averaged over all deposits to give the final relationship. This procedure was applied to the data that is subdivided into gold deposit types, variation in grade, presence of specific sulphides, and production in the Manica-Mutare-Odzi greenstone belt. The fractal dimension ***(D)*** has been evaluated by standard linear regression (Excel) and the error is given as the standard error of the regression.

5.3.1.2.1 Results of Fractal analysis applied to MMO gold deposits

The gold deposits have been box counted with a 1st square of circa 100 by 100 km, which covers all deposits of the belt. The box sizes are divided by an arithmetic progression using an unpublished macro program developed by Blenkinsop (pers. comm., 2000).

This section presents selected plots of the fractal analysis (e.g. Figs. 5 – 2 and 5 – 3) and parameters extracted from this analysis (Table 5 - 1).

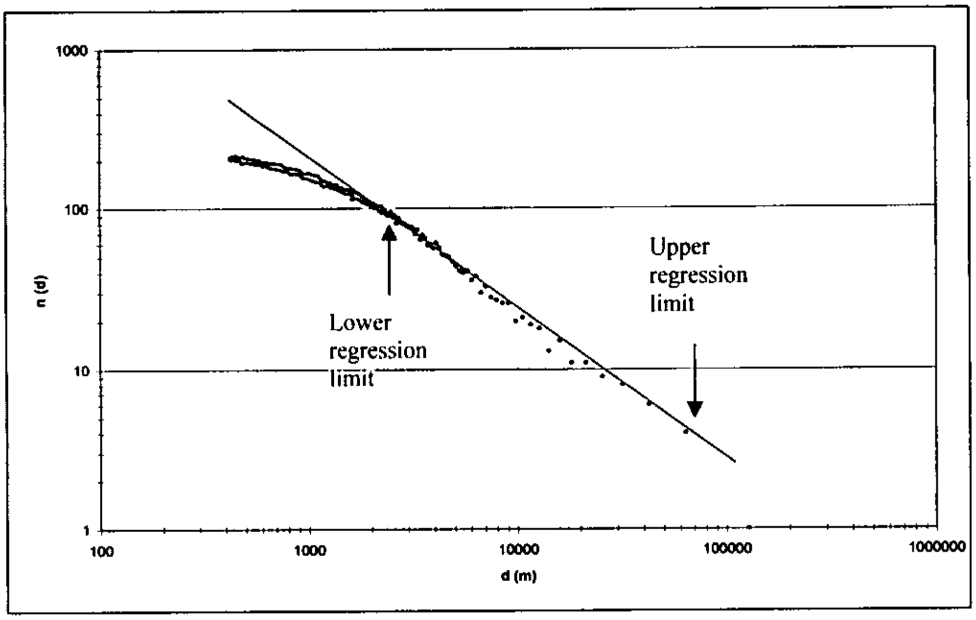

Figure 5 – 2. Number of squares n (d) of length d (meters) necessary to cover all (241) gold deposits as a function of d for the MMO greenstone belt. Note the bimodal population in the curve.

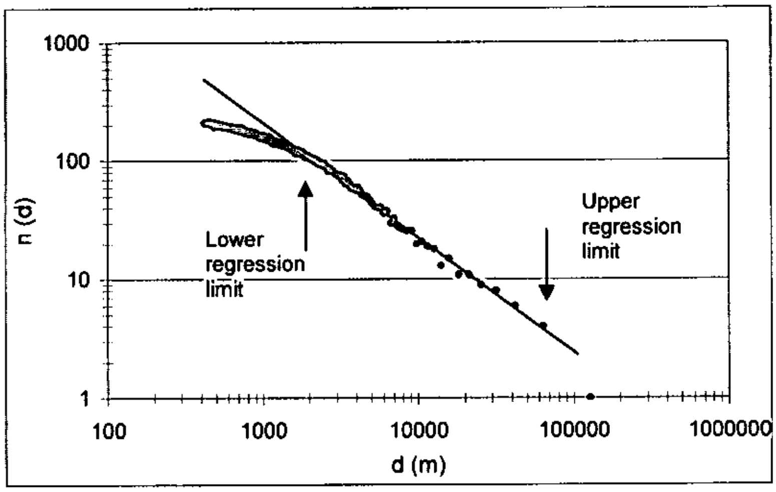

Figure 5 – 3. Number of squares n (d) of length d (meters) necessary to cover all (47) gold deposits as a function of d for the Manica section of the MMO greenstone belt. Note the bimodal population in the curve.

Table 5 – 1. Fractal dimension (D) (slope) of line joining gold deposits by the square counting method for different ranges of length of square, d (km). R – correlation coefficient (regression), E – standard error of the slope, N – number of mines, M – number of observations within regression line.

Area	**Range of r (km)**	**D**	**R**	**E**	**N**	**M**
MMO	1,74 – 63,5	0,997	-0,977	0,0089	241	300
Manica	2,5 – 17,15	0,991	-1,00	0,0260	47	30
Muatre	0,58 – 1,99	0,992	-1,000	0,0252	136	22
Odzi	1,43 – 22,24	0,992	-0,958	0,0233	58	30

5.3.1.2.2 Data analysis and interpretation

The results of fractal analysis applied to all deposits in the entire belt show that the deposits obey a fractal relationship at $1,7 < r < 64$ km (Table 5 - 2) and D is ≈ 1.0. This suggests that there is higher density of deposits at small r, i.e. more squares are needed to cover all deposits at minimum r =1,7 km and fewer squares of maximum r = 63 km are required to cover all deposits.

The true fractal relationship for the Manica section of the MMO greenstone belt is observed at $2, 5 < r < 17,5$ km while for the Mutare and Odzi sections of the belt, the relationship occurs at $0,58 < r < 2$ km and at $1,4 < r < 22$ km, respectively. These limits suggest that in the Mutare section there is a higher density of deposits for small length scales compared to Odzi and Manica sections of the belt. The high concentration of deposits in the Mutare section can be explained by the presence of many (circa 60) deposits around Penhalonga granodiorite in an area of c. 2 km^2. The Odzi section presents a higher density of deposits for small length scales than the Manica section of the belt.

The table 5 – 1 shows that there are two important fractal dimension within the MMO greenstone belt; one related to areas where exploration effort has been high and more deposits are known at small range or high clustering of gold deposits (Mutare section of the MMO belt) with clustering range between 0,58 – 1,99 km corresponding to a fractal dimension of 0,996, and a second range between 1,5 and 22 km observed at Odzi and Manica sections of the MMO belt with fractal dimension around 0,99. The overall result is a compound of these two fractal dimensions and cluster range between c. 2 and 60 km corresponding to a fractal dimension of 0,997.

The values of the minimum fractal limits for each of these sections are interpreted as evidence of spatial distribution or clustering of all deposits in the MMO greenstone belt and can be explained by a single process and the small variation result from the differentiated exploration efforts. This is supported by the fact that the three sections of the belt have similar fractal dimension (≈ 1.0) within acceptable error for the box counting method. This suggests that a unique process for the spatial distribution of gold deposits could have operated in the entire belt. Along that line it was also important to test fractal analysis for the different mineral deposits categories also used for autocorrelation (see subsequent sections).

The geological evidence supports a structural control where gold was transported by hydrothermal fluids and deposited as large or small deposits as supported by field observations as discussed in previous Chapters. Observations at Excelsior, Monarch, Guy Fawkes, Rezende, Toronto mines support this view.

The structural control can be considered to be a unique process that operated for the spatial distribution of gold mineralisation in the MMO greenstone belt. The other geological evidence for a unique process is that there is no unique lithological control on mineralisation.

Fractal analysis was carried out as a form of evaluate whether other fractal distribution patterns arise from subgroups defined in Chapter 4. Results are presented in next section (5.3.1.3).

5.3.1.3 Fractal Distribution of Gold Deposits types in Space

The gold deposits were grouped into shear zone and fault hosted, quartz vein hosted, BIF related deposits, high and low grade deposits, high, medium and low production deposits, deposits hosted by felsic and intermediate intrusions, by Shamvaian metasediments and Upper Bulawayan lithologies. The distribution of gold deposits types, and plots of the fractal analysis appear as Figs. 5 – 4 to 5 – 9. Parameters are shown in Table 5 - 2.

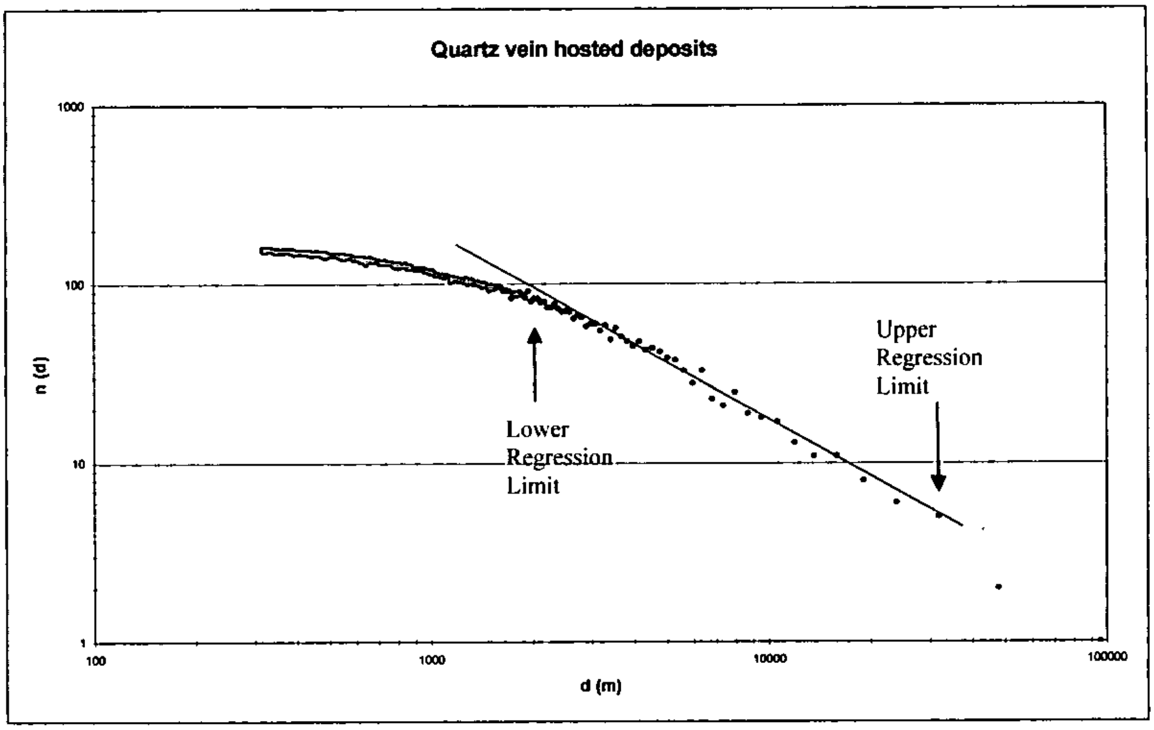

Figure 5 – 4. Number of squares n (d) of length d (meters) necessary to cover all (170) Quartz vein hosted gold deposits as a function of d for the MMO greenstone belt. Note the bimodal population in the curve.

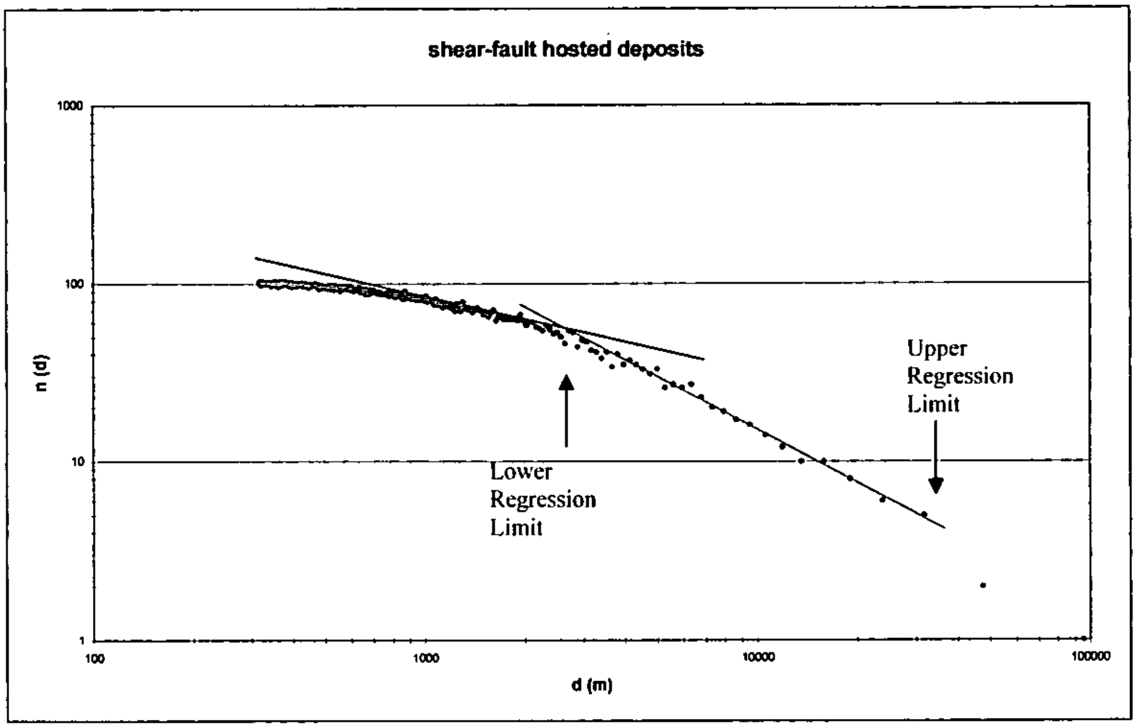

Figure 5 – 5. Number of squares n (d) of length d (meters) necessary to cover all (116) shear-fault hosted gold deposits as a function of d for the MMO greenstone belt. Note the bimodal population in the curve.

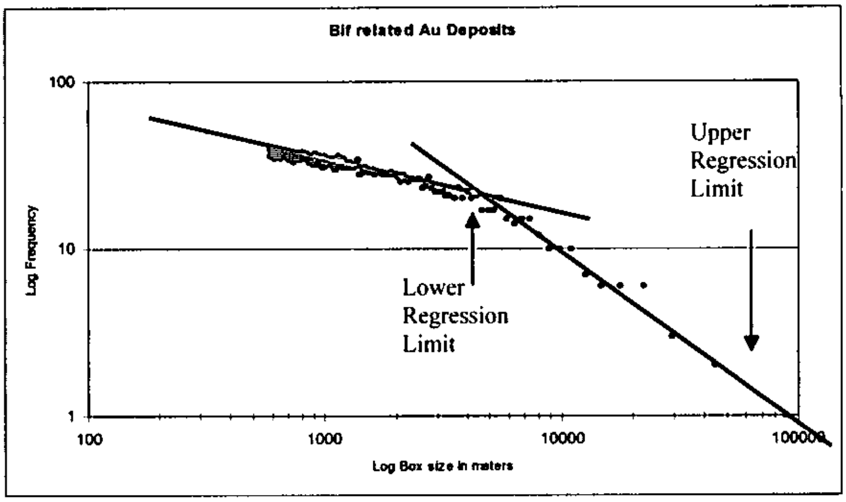

Figure 5 – 6. Number of squares n (d) of length d (meters) necessary to cover all (42) BIF related gold deposits as a function of d for the MMO greenstone belt. Note the bimodal population in the curve.

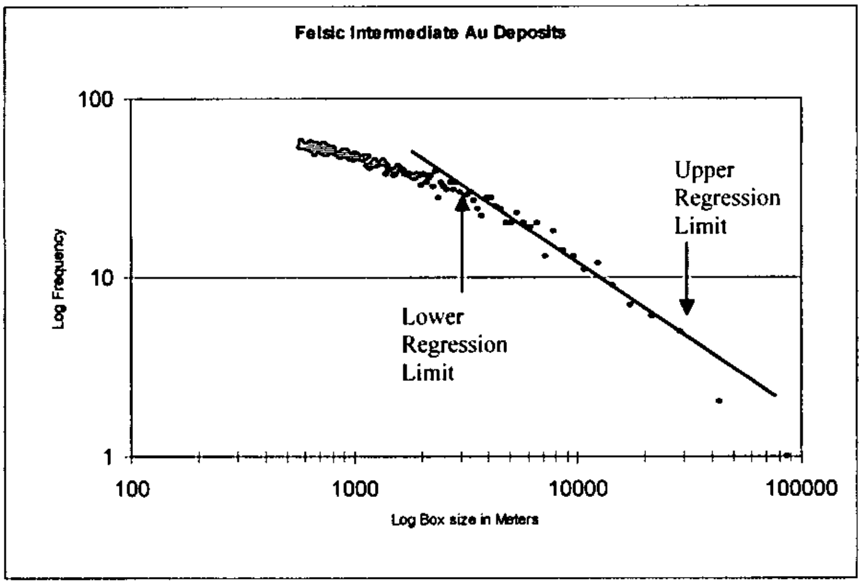

Figure 5 – 7. Number of squares n (d) of length d (meters) necessary to cover all (65) gold deposits hosted by felsic and intermediate intrusions as a function of d for the MMO greenstone belt. Bimodal

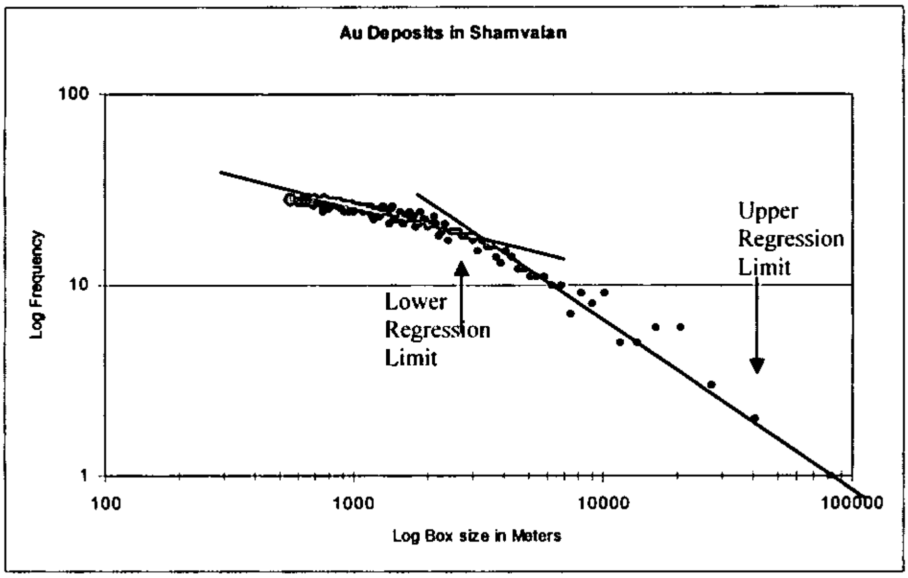

Figure 5 – 8. Number of squares n (d) of length d (meters) necessary to cover all (31) gold deposits hosted by Shamvaian lithologies as a function of d for the MMO greenstone belt. Note the bimodal population in the curve.

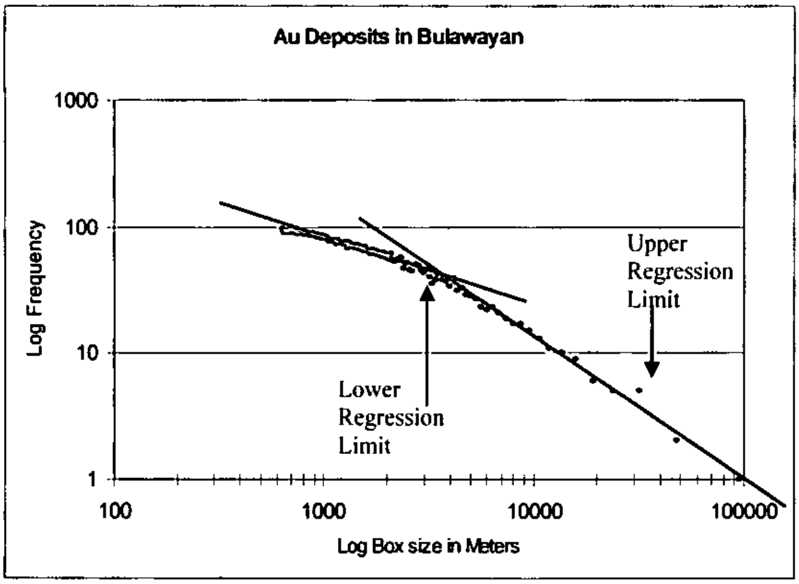

Figure 5 – 9. Number of squares n (d) of length d (meters) necessary to cover all (114) gold deposits hosted by Bulawayan lithologies as a function of d for the MMO greenstone belt. Note the bimodal population in the curve.

Table 5 – 2. Fractal dimension (D) (slope) of gold deposits by the square counting method for different ranges of length of square, d (km). R – correlation coefficient (regression), E – standard error of the slope, N – number of mines, M – number of observations within the regression line.

Deposit type	**Range of r (km)**	**D**	**R**	**E**	**N**	**M**
Shear zone/faults	2,50 – 31,74	0,994	-0,947	0,0179	116	36
Quartz vein	2,57 – 31,73	0,994	-1,000	0,0213	170	35
BIF hosted	3,60 – 29,4	0,981	-0,914	0,0380	42	22
Felsic-intermediate intrusions	3,4 – 28,6	0,961	-0777	0,0488	65	23
Shamvaian hosted	3,30 – 27,2	0,948	-0,662	0,0466	21	25
Bulawayan hosted	2,57 – 23,8	0,990	-0,976	0,0231	114	37

Data Analysis and Interpretation

The results of fractal analysis summarised in Table 5 - 2 suggest that there is a clear change in the fractal dimension at r = 2.5 km for the shear zone/fault hosted deposits, quartz veins and deposits hosted by Bulawayan rocks. The 2.5 km change in fractal dimension is consistent with the entire Zimbabwe craton in general and with Shamva and Masvingo - Mashava greenstone belts in the Zimbabwe craton in particular (Blenkinsop, 1994). This suggest a significant importance of the type of geology at deposit scale, although, Blenkinsop (1994) explained this change as being related to exploration efforts being greater in the immediate vicinity of pre-existing mines.

The fractal dimension and the minimum range agree with the idea of a unique process operating for the spatial distribution of the shear zone/fault hosted and quartz vein hosted deposits. This is also supported by the structural control of these types of deposit. The structural control is evident at regional scale and at mine-scale as observed in detailed field observations at Excelsior, Dot's Luck and other mines as discussed in Chapters 3 and 4.

5.3.1.4 Fractal Distribution of Gold Deposits grades and productions in space

The gold deposits with grades higher than 5 g/t are considered high-grade and those with less than 5g/t are considered low grade. The fractal analysis for gold deposit grades distribution in space may contribute towards refining of exploration objectives in terms of areas to cover when searching for specific deposit (grade and tonnage).

The production record is a good indicator of the size of the deposit. The application of fractal analysis to different gold production intervals is sensitive to deposit size in space. This principle can be used successfully in exploration. The use of gold production is biased towards on-going mining and unknown or non-economic reasons for mine closures. The influence of the first constraint is minimised by the number of deposits being mined within the MMO greenstone belt, which is only three. The problem related to reasons for closure of the mines is more complex and for this study it was assumed that all mines had ceased production due to economical reasons, mainly lack of economic reserves at the time of closure. Thus production records until time of closure of a mine are treated here as economic reserves and so are the sizes of the deposits. The deposits that had produced more than 100 kg of gold were considered large deposits and those that had produced less than 10 kg as small.

The distribution of gold deposits' grades in space are presented in plots of the fractal analysis (Figs. 5 – 10 and 5 - 11) and parameters used in these plots are shown in the Table –5-3.

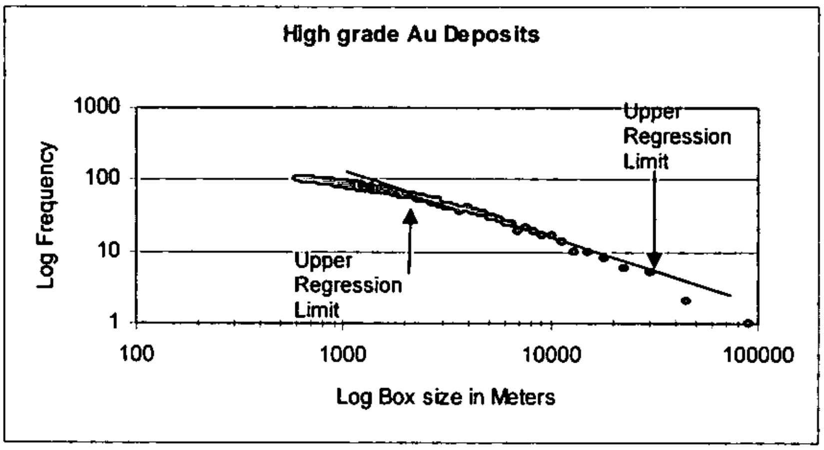

Figure 5 – 10. Number of squares n (d) of length d (meters) necessary to cover all (123) high-grade gold deposits as a function of d for the MMO greenstone belt.

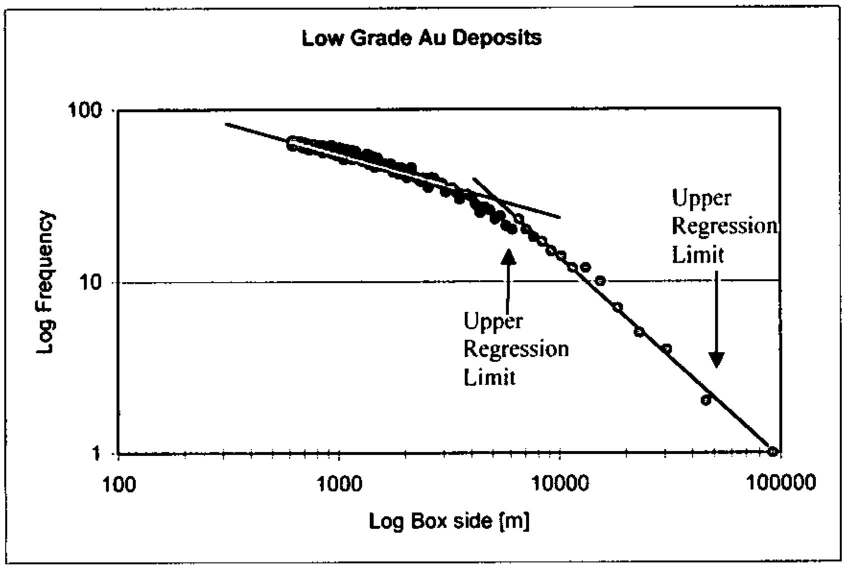

Figure 5 – 11. Number of squares n (d) of length d (meters) necessary to cover all (73) low-grade gold deposits as a function of d for the MMO greenstone belt. Note the bimodal population in the curve.

Table 5 – 3. Fractal dimension (D) (slope) of gold deposits by the square counting method for different ranges of length of square, d (km). R – correlation coefficient (regression), E – standard error of the slope, N – number of mines, M – number of observations within the regression line.

Grade Interval	**Range of r (km)**	**D**	**R**	**E**	**N**	**M**
<5,0	4,4 – 30,7	0,983	-0,776	0,0341	73	20
>5,0	3,3 – 30	0,988	-0,894	0,0289	123	25

The distribution of gold production in space was studied by fractal analysis and the results are presented in Table 5 - 4. Figures 5 – 12 to 5 - 14 represents the fractal plots of a number of deposits with specific production interval as a function of the length of squares needed to cover them.

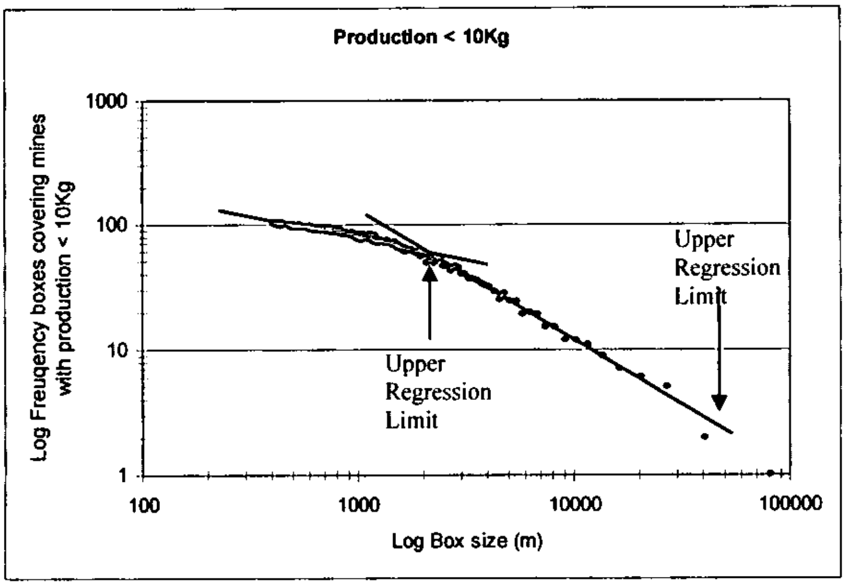

Figure 5 – 12. Number of squares n (d) of length d (meters) necessary to cover all gold deposits that produced less than 10 kg of gold. Note the bimodal population in the curve.

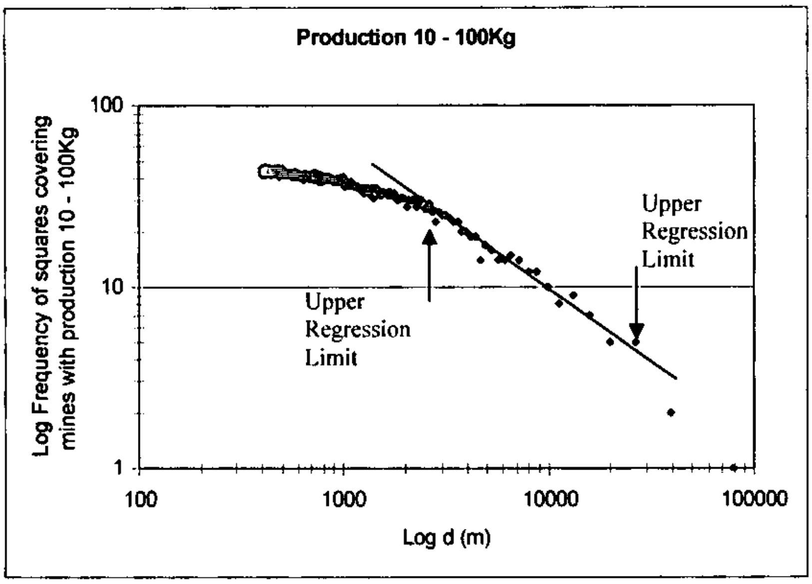

Figure 5 – 13. Number of squares n (d) of length d (meters) necessary to cover all gold deposits that produced between 10 and 100 kg of gold. Note the bimodal population in the curve.

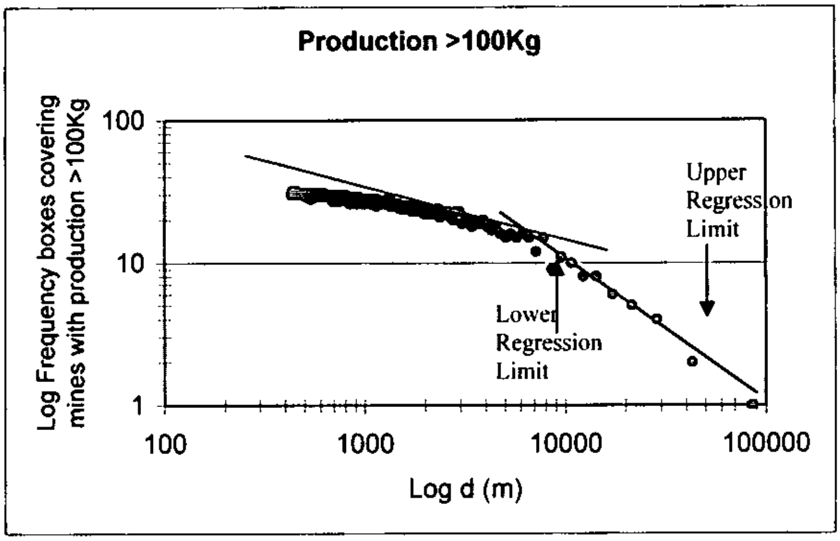

Figure 5 – 14. Number of squares n (d) of length d (meters) necessary to cover all gold deposits that produced more than 100 kg of gold. Note the bimodal population in the curve.

Table 5 – 4. Fractal dimension (D) (slope) of gold deposits by the square counting method for different ranges of length of square, d (km). R – correlation coefficient (regression), E – standard error of the slope, N – number of mines, M – number of observations within the regression line.

Production (kg)	Range of r (km)	D	R	E	N	M
< 10	2,03 – 27,1	0,996	-0,985	0,0152	110	38
10 - 100	2,3 – 26,33	0,986	-0,761	0,0240	51	29
> 100	5,4 – 28,6	0,938	-0,760	0,0806	33	14

Data Analysis and Interpretation

The results summarised in Table 5 - 3 suggest that high-grade deposits obey a fractal distribution within the distance range between 3,3 and 30 km. And the low-grade deposits obey a fractal distribution between 4,4 and 30 km. The fractal dimension for both high and low grade deposits is equal which suggests that these deposits are spatially controlled by the same factor.

The spatial distribution of gold deposits that produced a certain quantity of gold as studied by fractal analysis (Table 5 – 4) revealed that most of the deposits (production <100 kg) are spatially distributed at distance ranges of between circa 2 and 27 km. The lower regression limit of 2 km suggests that the deposits that produced less than 100 kg cluster at shorter distance range compared to those that produce more than 100 kg. It is expected that large deposits cluster at large distance range (5,4 km) because large deposits are harder to find compared to small deposits. The upper regression limit of all gold deposits with recorded production is circa 27 - 28 km suggesting that the productive districts and sub-districts are not larger than 28 km in diameter if the mineralisation event obey a power law and behave as fractal dusts with fractal dimension (D) of circa 1.

5.3.2 Discussion on Fractal Analysis

The gold deposits in the Manica-Mutare-Odzi greenstone belt, as a whole, and for the three distinct areas (Manica, Mutare and Odzi) obey a fractal distribution at a range of distances between circa 2,0 and 20 to 30 km with **D** approximately equal to one.

The fractal dimention and overall results from fractal analysis agree to a certain degree with other similar studies carried elsewhere in the Zimbabwe Craton (Table 5 – 5).

Table 5 – 5. Fractal dimension (D) (slope) of gold deposits by the square counting method for different ranges of length of square, d (km). R – correlation coefficient (regression), E – standard error of the slope, N – number of mines, M – number of observations within the regression line. Data from this study are compared to results from Blenkinsop (1994), (1995), Blenkinsop and Sanderson (1999) and Carlson (1991).

Author	Area	Fractal Dimension (**D**)	Range of **r** (km)	Correlation Coefficient	Recorded number of mines
Blenkinsop (1995)	Masvingo - Mashava	1.21	1,0 – 10	-0,999	147
Blenkinsop and Sanderson (1999)	Craton	0.92	10 – 60	-0,999	651
	Harare	0.98	10 – 60	-0,992	288
	Bulawayo	0,97	10 – 60	-0,994	321
	Masvingo	1,06	2.5 – 20	-0,998	147
	Shamva	1,18	2,5 - 20	-0,995	122
Blenkinsop (1994)	Masvingo	0,32	0,3 – 2,5	-0,947	147
		1,12	2,5 – 29	-0,995	147
	Shamva	0,28	0,3 – 2,5	-0,988	122
		1,18	2,5 – 29	-0,999	122
Carlson (1991)	Basin and Range	0,50	1 – 15		4775
		1,51	15 - 1000		4775
This Study	MMO	0,997	1,74 – 63,5	-0,977	241
	Mutare	0,996	0,58 – 1,99	-1,00	136
	Manica	0,991	2,5 – 17,15	-1,00	47
	Odzi	0,992	1,43 – 22,24	-0,958	58

The table 5 – 5 shows that if the main population within fractal dust of all deposits is considered a consistent range between c. 2 and 20 to 30 km corresponding to a fractal dimension between 0,99 and 1,18 are observed in all greenstone belts. This is a clearer evidence of existence of a common factor that control de distribution of gold deposits within the greenstone belts of the Zimbabwe Craton.

The analysis of fractal distribution of, not only 'deposit' positions but also the deposit type, host lithology, grade interval and production levels of the deposits was meant to probe the hypothesis that the "control of gold deposits distribution can be explained by single process".

In general, the use of grade is expected to be more sensitive to geological factors than production, because the later is highly influenced by economic factors while the grade is intimately related to geological aspects. The use of grade in this study for analysing the spatial distribution of deposits suggested a fractal relation at square length range of 4,4 – 30,7 and 3,3 - 30 km for low-grade and high-grade respectively has shown that there is no significant difference between the deposits distribution controlling factor for both high and low grade deposits. These ranges are considerable high compared to the distribution pattern suggested by other authors (e.g. Blenkinsop, 1994, Blenkinsop, 1995 and Blenkinsop and Sanderson, 1999) when using deposits positions, however the fractal dimension is very similar, fact which encourage the general idea of explaining the fractal distribution of deposits by a unique mineralisation event.

Furthermore the study shows that different types of deposits such as quartz vein deposits and deposits hosted in Bulawayan correlate with pattern suggested by Blenkinsop (1994) for the Zimbabwe Craton in terms of fractal dimension close to one. This implies that the single event explanation is also valid for the quartz vein/ fault deposit type.

The fractal analysis for gold deposits that produced < 100 kg follow a fractal distribution pattern for a distance range between circa 2,3 and 27 km and a fractal dimension equal to 0,99. This finding agrees with the general conclusions made on the greenstone belts in Zimbabwe (Blenkinsop, 1995) and for Mesozoic hydrothermal precious metal deposits in the western USA (Carlson, 1991). Ord (1994) studied the fractal spacing of shear zones while Blenkinsop (1993), Kruhl (1994), Zhang and Sanderson (1994) studied the fractal spacing of brittle fractures. All these authors invoked a single mineralisation event to explain the fractal distribution of gold deposits as 'a hydrothermal system with channeled flow in deformation zones'.

Evidence from this study show that gold mineralisation in the MMO greenstone belt obeys a fractal distribution in a range between circa 2 km and circa 20 – 30 km. Thus, fractal analysis can be used to explain distribution patterns of gold deposits in the MMO greenstone belt and, such distribution is considered to be controlled by a single event, most probably related to structural control.

5.3.3 Autocorrelation analysis (or Fry analysis)

Autocorrelation (Fry) analysis is used in this study to determine the spatial relationships among the gold deposits. Fry analysis was first applied to determine the bulk strain in rocks, which arises from changes in the inter-grain's distances due to tectonic activity (e.g. Fry, 1979; Hanna & Fry, 1979; Crespi, 1986; Dunne et al., 1990). Fry analysis was extended to applications such as analysis of description of distribution patterns of data points representing mineral deposits by Vearncombe and Vearncombe (1999).

Successful examples of application of autocorrelations analyses for mineral exploration include the kimerlites in West Africa, hydrothermal and porphyry copper deposits in Arizona, gold deposits at Mount Pleasant (northwest of Kalgoorlie), Western Australia, advanced exploration drilling in the Jundee gold mine, Western Australia, and exploration drilling and grade control from the Bronzewing gold mine, Western Australia (Vearncombe and Vearncombe, 1999).

The method involves placing a transparent medium over the map of the deposits with the centre of the transparent paper on one of the deposits, and then marking the positions of each deposit on the transparent medium. After that, the centre of the transparent medium is moved to the next deposit (the overlay is to be kept in the same orientation) and again, all the positions are marked on the transparent medium; the procedure is repeated until all deposits' positions on the map have acted as centre of the plot. In this study, the autocorrelation analysis was performed using a computer program developed by Blenkinsop (pers. comm., 2000). The resulting plot is commonly called translation map or fry plot or autocorrelation plot (e.g. Fig. 5 - 15) and it shows trends in different directions and visually the trends suggest a repeated pattern in a specific direction.

The autocorrelation analysis visually enhances geometrically linear trends in the X Y direction, calculating spatial autocorrelation for **n** data points that result in $\mathbf{n}^2 - \mathbf{n}$ point data (Vearncombe and Vearncombe, 1999). Subtle linear patterns in the data points become more pronounced in the autocorrelation analysis results. The results are presented as histograms of the frequency of the length of the segments linking two data points versus the length of the segments (translation vectors), and in rose diagrams of azimuth distribution of the segments linking each two data point.

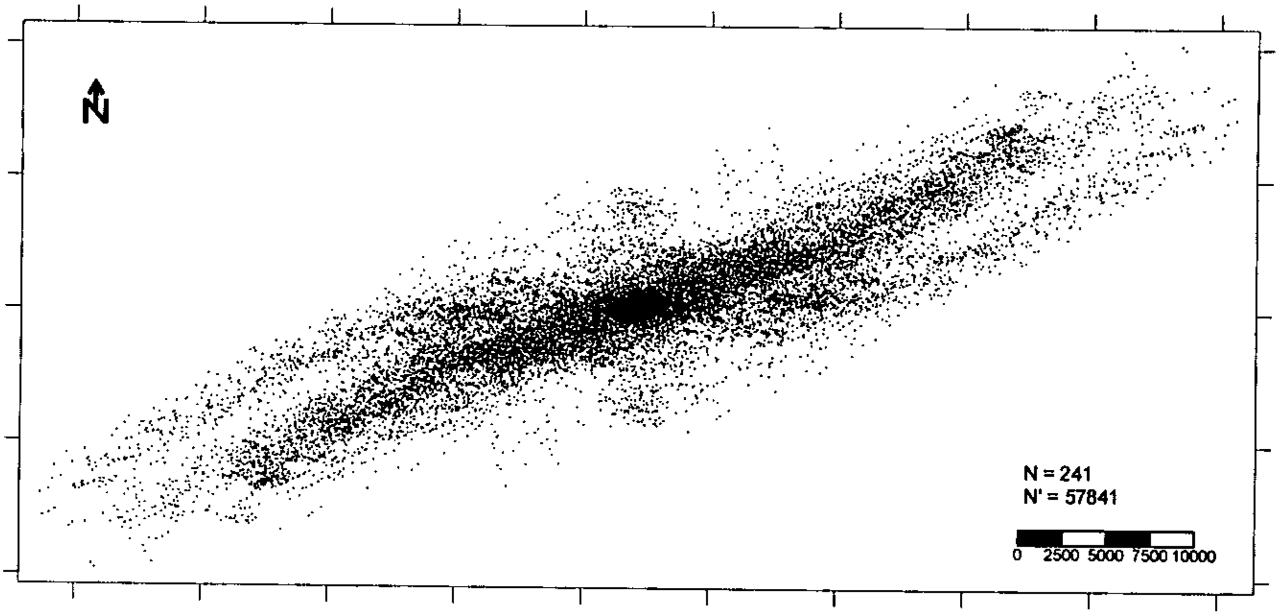

Figure 5 – 15. Results of autocorrelation analysis for the MMO greenstone belt presented in a translation map of N = 241 deposits, which resulted in 57841 points here called **N'**. The X and Y direction are in UTM co-ordinates zone 36K, Clarke 1866.
Translation map is plotted for an average point of every three points for computation efficiency. This simplification does not visually affect the final appearance of this plot.

5.3.3.1 Methodology

A lineament in the present context can be regarded as an alignment of gold deposits in a linear array reflecting a line or a corridor adjoining deposits. Lineaments can be enhanced statistically, graphically or geometrically by means of autocorrelation methods and variography. The geological complexity of the data require processing methods that privilege the scale dependency of the data where each scale in a different data set is estimated from histograms (e.g. Fig. 5 - 16) plotting the frequency of the length of the segments linking each segment of two data points (translation vectors) in the autocorrelation analysis result. Each break (maximum) in the histogram represents a change in grouping size at a specific distance segment search, which can be calculated as a half width at the maximum frequency position.

The main pattern of gold deposits in the MMO belt is linear.

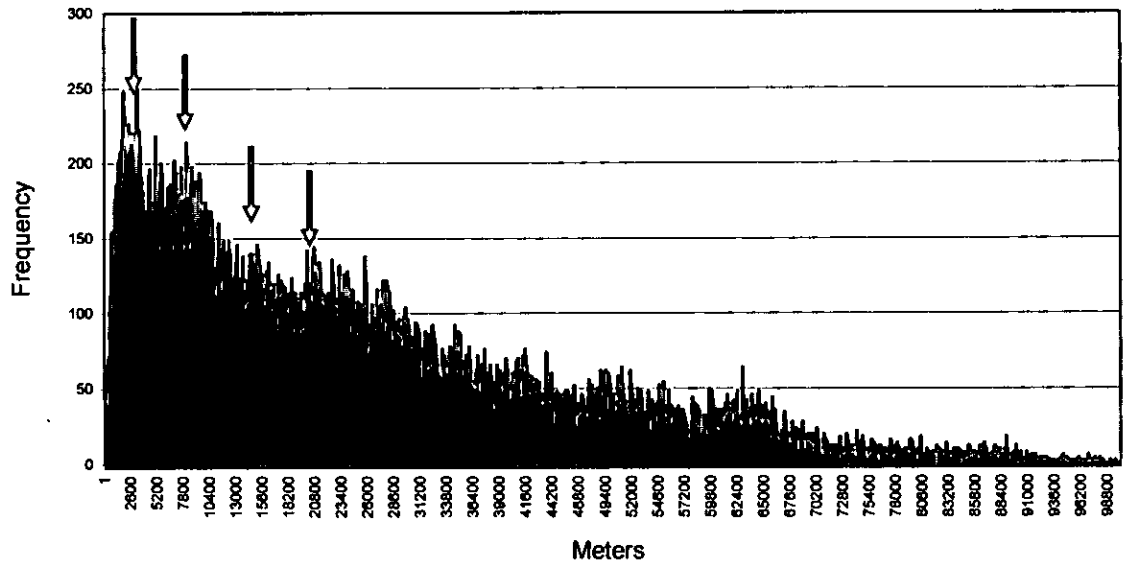

Figure 5 – 16. Histogram of segment frequency per length of the segments in meters at average of 100 m spacing for all deposits in the MMO.
Note the clustering that can be estimated by the *mode* of the class in the graph at 3 km, 9 km, 15 km and 20 km. The *Mode* is the length that occurs with greatest frequency in the data (Davis, 1973) and is equivalent to the maximum of each class.

Possible scale dependency is assessed from histograms (e.g. Fig. 5-16) of the lengths of the translation vectors. Figure 5 - 16 shows that individual populations with *modes* at 3-km, 9-km, 15-km and 20-km radius represent a degree of clustering of gold deposits estimated by the half width at the *mode*. The resulting grouping presented in this figure can be obtained by calculating interactively the distance search.

The *mode* of each population was used to test the distribution patterns of the data-points.

As noted in (Mondlane et al., 2001) the entire data set of the MMO greenstone belt was tested using the autocorrelation method. Firstly it was applied to all gold deposits and then segments based on the presence of distinct populations defined by the histogram shown in Fig. 5 – 16. The autocorrelation plot of the entire data set (241 mines) is presented in figure 5 - 15, and the equivalent rose diagram is shown on Fig. 5 – 17A.

The autocorrelation analysis for the distance search at *modes* of sub-populations 3-km, 9-km, and 20-km are shown as rose diagrams in Figs. 5 - 17B, 5 - 17C, and 5 - 17D.

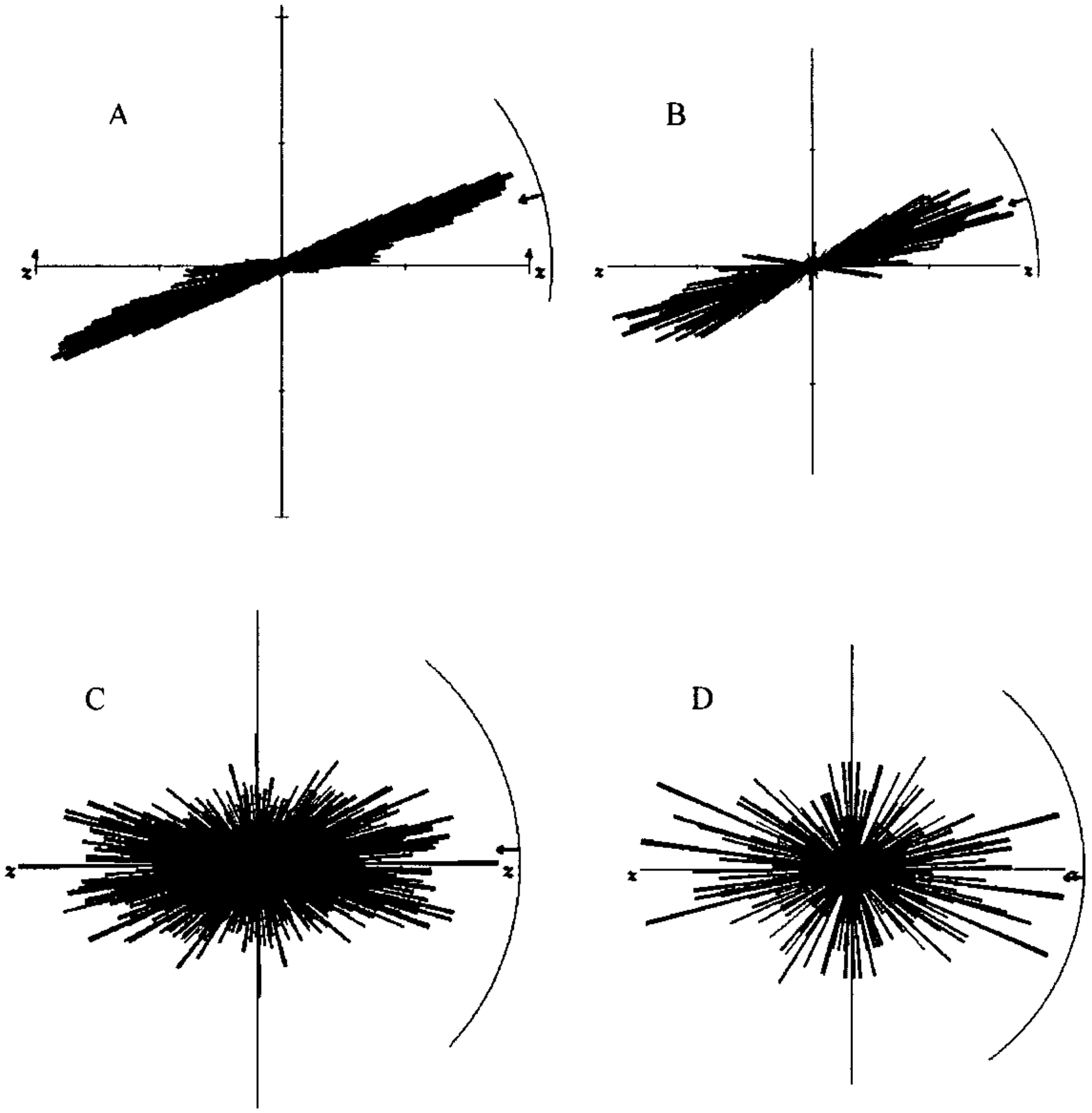

Figure 5 – 17. Rose diagrams of the MMO greenstone belt representing the azimuth frequency of the point data resulting from the autocorrelation analysis exercise.
A) Rose diagram of all deposits in the MMO greenstone belt with no limit on the distance search. B) Rose diagram showing all deposits within 20-km distance search limit. C) Rose diagram of all deposits within 9-km distance search limit. D) Rose diagram of all deposits within 3-km distance search limit.

5.3.3.2 Interpretation of the results

The interpretation of the trends and patterns from autocorrelation is done by comparing results with trends on the structural-geological maps and satellite imagery. In order to be able to recognise patterns and trends on maps, a semi-quantitative approach is adopted.

The semi-quantitative analysis of the distribution patterns involves manual tracing of the lines linking aligned points or clusters of points in the autocorrelation plots considering the geological controls of the deposits. When finalised, the traced lines indicate a pattern in the directions identified by rose diagrams with an additional parameter of spacing between parallel lineaments. The distance between lines is calculated and is used for predicting similar alignments in other areas.

The first stage of the spatial analysis is to compare the trends from gold deposits with lineaments that can be drawn from the autocorrelation plot (Fig.5 - 18).

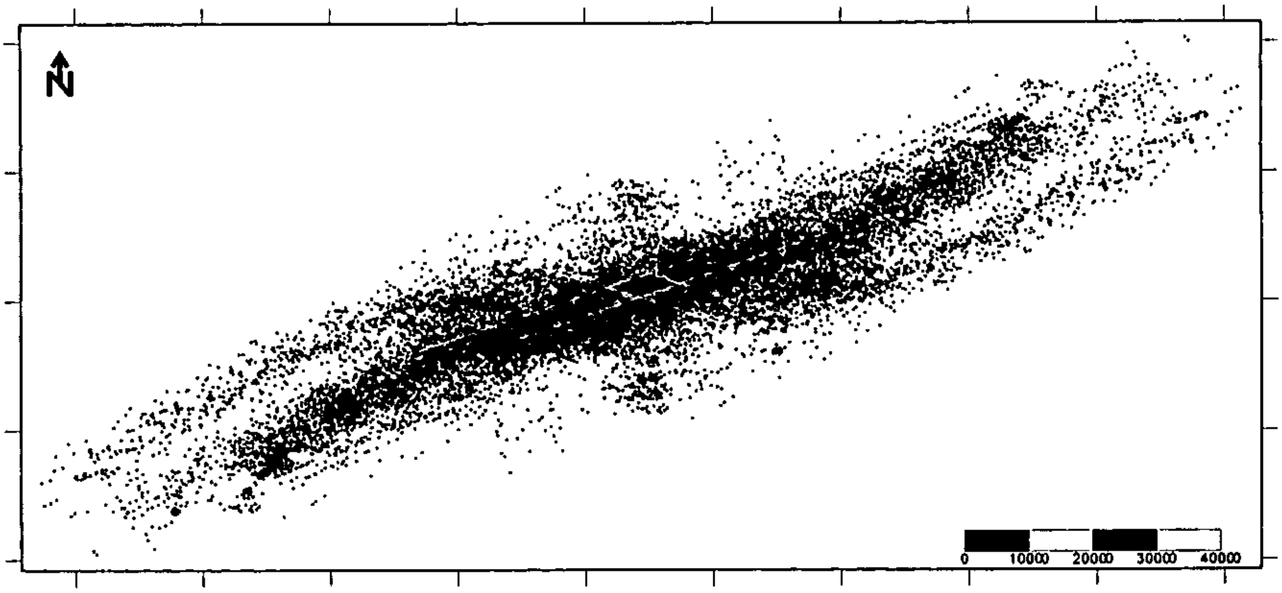

Figure 5 – 18. Results of autocorrelation analysis for all deposits in the MMO greenstone belt presented on a translation map overlain on a map of all deposits (red dots).
The X and Y directions by solid lines are in UTM co-ordinates zone 36K, Clarke 1866. Some alignments of gold deposits are traced for illustration of the method.

The next step involves overlaying the mineralised structures on the trend pattern generated from the autocorrelation plot as shown in figure (Fig. 5 - 19).

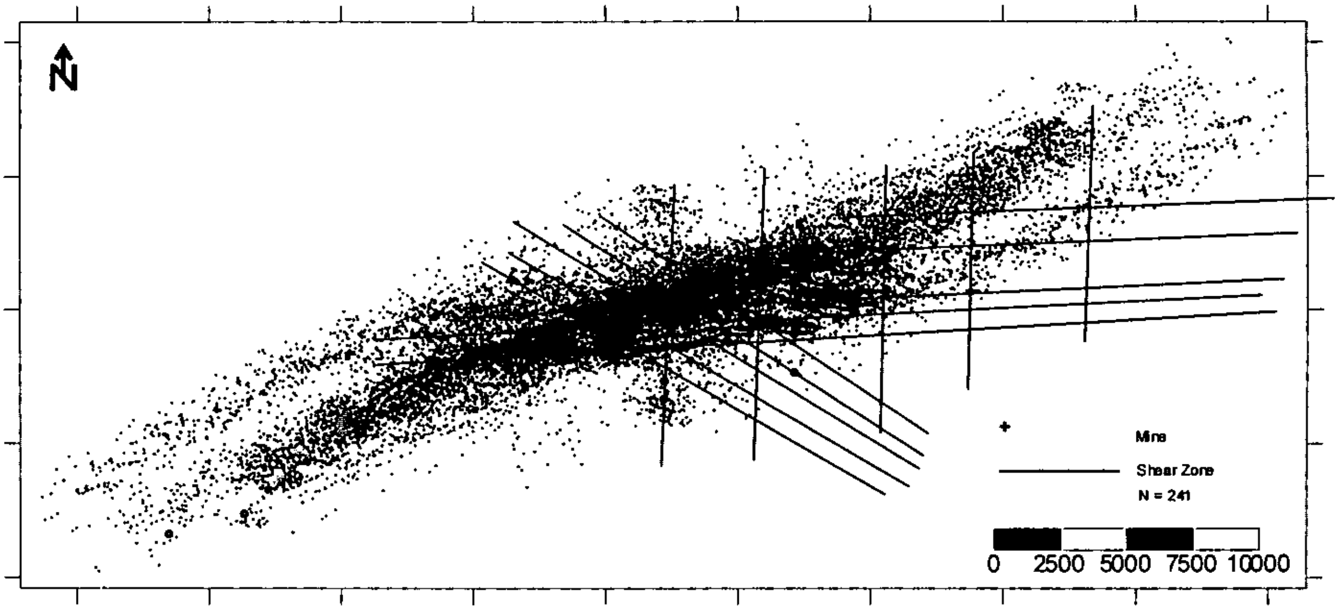

Figure 5 – 19. Results of autocorrelation analysis for all deposits in the MMO greenstone belt presented on a translation map. The X and Y direction are in UTM co-ordinates zone 36K, Clarke 1866.
The translation map is superimposed on a map of structures related to gold mineralisation and a map of gold deposits. Note the blue line represent alignments positioned parallel to the structures and away from it. Note also the potential alignments oriented at an angle to the known structures.

The final stage is to compare gold deposits, structures and lineaments generated from autocorrelation. The final result is to be interpreted considering genetic models for gold mineralization in the region.

5.3.3.3 Analyses of the Results

The autocorrelation plot of all gold deposits presented in Fig.5 - 15 suggests a dominant NE - SW trend which can be interpreted as a reflection of the bias due to NE-SW linearity of the MMO belt. The same plot shows also a prominent secondary trend WNW-ESE and E –W. The rose diagram of all gold deposits shows mainly the NE-SW and E-W trends (Fig. 5 – 17A), the WNW-ESE is not evident. The analysis of all deposits is only recommended when a general idea of the regional linear trends of the data is required (Mondlane et al., 2001). For more detailed analysis, it is important to separate the gold deposits on the basis of the clustering dimension, which is defined by the *mode* as distance limit search of each grouping shown in Fig. 5 - 16. In this analysis, the rose diagrams in Fig. 5 - 17 show different patterns at different scales. The 20-km distance limit search rose diagram in Fig. 5 – 17B shows a primary trend oriented NE-SW and subsidiary trends oriented E-W and ESE-WNW, the N-S trend direction is comparatively insignificant. The 9-km and the 3-km distance limit search rose diagrams show trends oriented NW-SE, NE-SW, N-S and E-W. Note that the bias due to NE-SW linearity of the belt has no effect at these detailed scales.

A closer analysis of the autocorrelation analysis lineaments suggests that at their intersection lies a big deposit. This is true in the case of Rezende, Dias Pereira, Boa Esperanca and Howat's Luck deposits for example.

The trends traced on the basis of the known gold deposits produced an indistinct pattern with dominant NE-SW and N-S directions (Fig.5 - 1 and Fig. 5 - 18). The spatial relationships between lineaments generated from aligned deposits and the lineaments derived from autocorrelation plot suggest a more comprehensive pattern in three main directions, ENE-WSW and NW-SE at 3-km spacing and, NNE-SSW at 9-km spacing (Fig. 5 - 18). This interpretation suggests that when exploring for new gold deposits in the MMO greenstone belt, effort should be concentrated within 3-km radius from known ENE or NW alignments of deposits and within 9-km radius of known alignments in the NNE direction.

The relationships between lineaments derived from autocorrelation plot and the mineralised regional structures favour the E - W structures that are traditionally known to host mineralisation while on the other hand, patterns with trends at an angle to these structures represent a new breakthrough on the controls of mineralisation. It is not clear whether or not these directions represent a sort of structural control. One may argue that in any group of points there is always more than one direction of trends. This argument is valid, but if the trend direction is persistent at different scales and for different groups of deposits, then it is something to look at carefully, because it might be an important control of mineralisation. Thus in order to confirm the validity of trend directions and patterns, the data set was divided into the categories of shear zones/faults/contact reefs, quartz veins, felsic and intermediate intrusion and BIF related deposits. Further subdivision into production (<10, >10<100, and >100 [kg]), high (>5 g/t) and low (<5 g/t) grade, sulphides, stratigraphic units (Shamvaian and Upper Bulawayan) and their combinations such as high grade quartz veins or high-grade quartz veins in ultramafics was made. In all cases different scales were tested for autocorrelation and lineament analyses (Appendix V-A). An example is the consideration of the search for distribution patterns of "large" deposits (i.e. production larger than 100 kg up to 1995) in the MMO greenstone belt, whose results are illustrated in Figures 5 - 20 and 5 - 21.

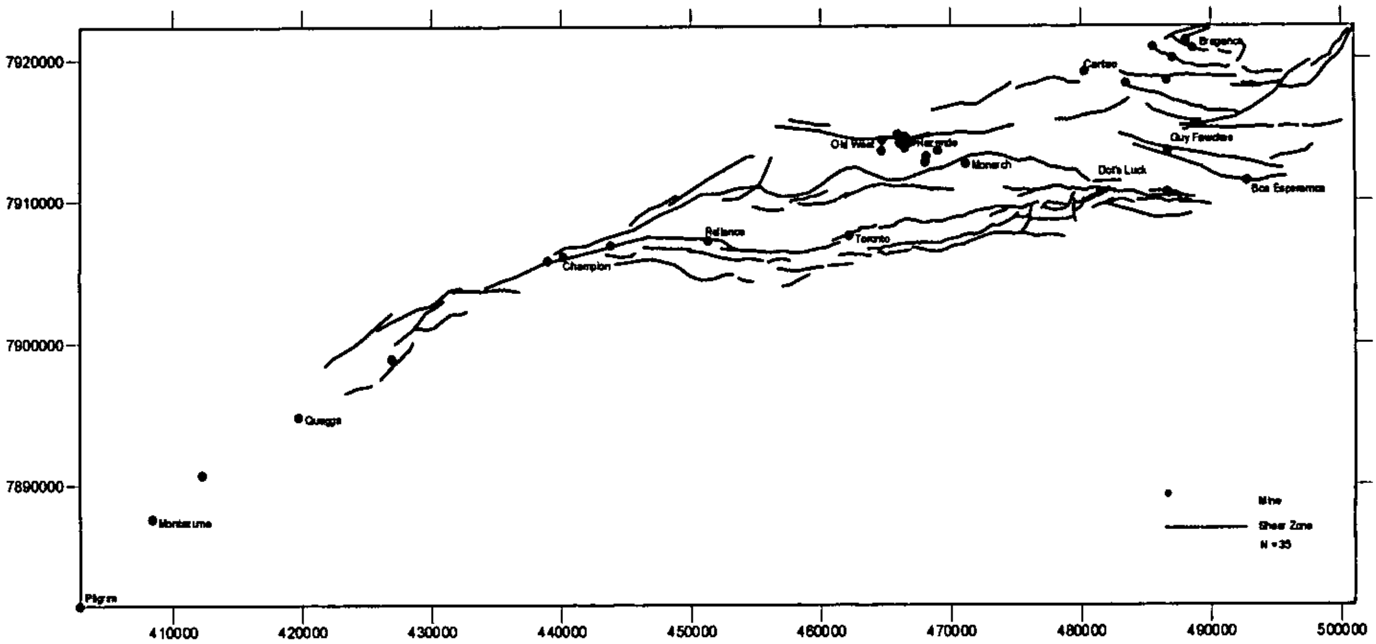

Figure 5 - 20 - Gold deposits that produced more than 100 kg and all structures known to control mineralisation in the MMO greenstone belt.

Note the high structural control of this type of deposits, with exception of the Rezende group of deposits that seem to be highly influenced by the presence of the Penhalonga granodiorite. The X and Y direction are in UTM co-ordinates zone 36K, Clarke 1866.

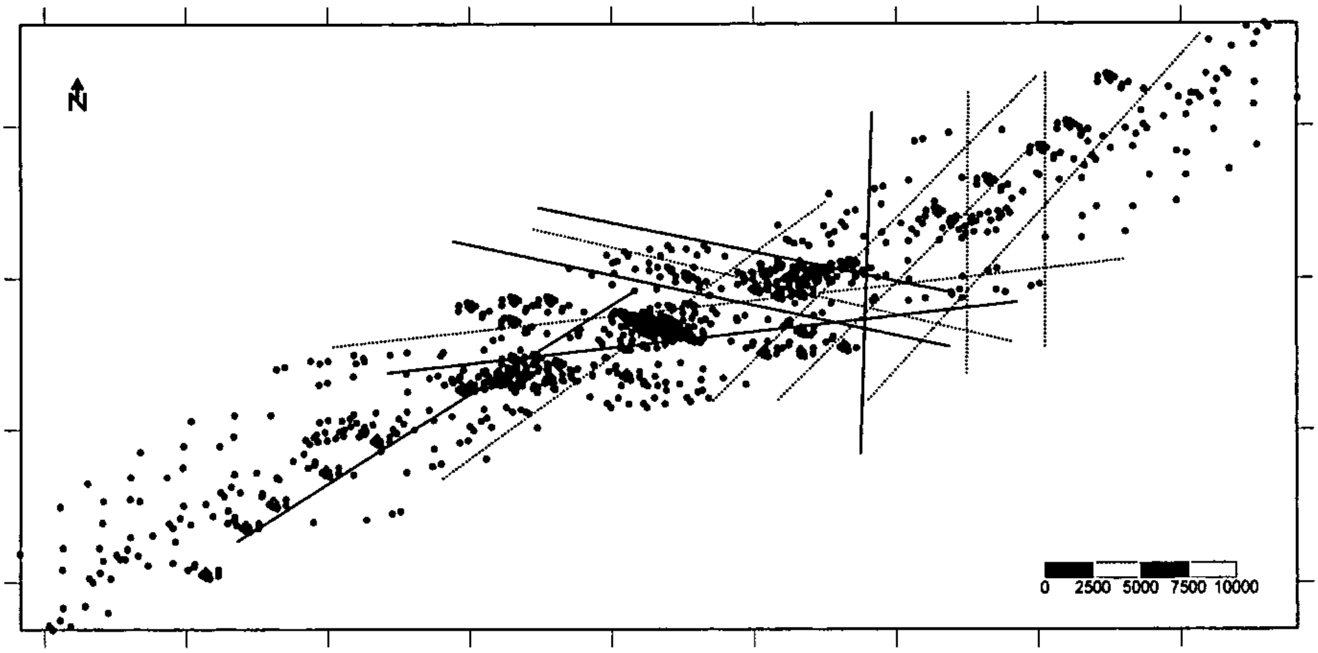

Figure 5 – 21. Results of autocorrelation analysis for deposits that produced more than 100 kg in the MMO greenstone belt presented in a translation map is superimposed on a map of deposits that produced more than 100 kg (red dots).

Alignments of gold deposits are traced in full lines and the predicted alignments resulting from Autocorrelation plot are traced in dotted lines. The X and Y direction are in UTM co-ordinates zone 36K, Clarke 1866.

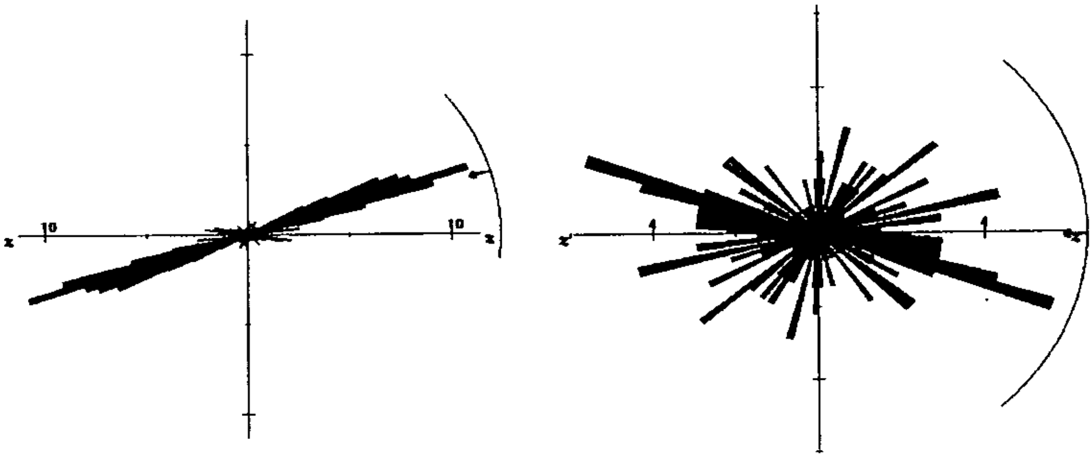

Figure 5 – 22. Rose diagrams of the gold deposits that produced more than 100-kg of gold representing the azimuth frequency of the point data that resulted from autocorrelation analysis.
5 - 22A) Rose diagram of all deposits that produced more than 100 kg in the MMO greenstone belt with no limit on the distance search. 5 - 22B) Rose diagram showing all deposits that produced more than 100 kg in the MMO within 9-km distance search limit.

The rose diagram (Fig. 5 - 22A) of all deposits that produced more than 100 kg shows a prominent NE-SW trend and a subsidiary WNW-ESE trend. When considering the 9-km distance limit search the rose diagram (Fig. 5 - 22B) it is dominated by WNW–ESE trends while the other directions are relatively less important (<10 %).

The interpretation of these results by spatial comparison with gold deposits trends (Fig. 5 - 21) reveals that in general, large deposits do not cluster, but are distributed, in this case, in a 9-km spacing pattern oriented mainly WNW. This result also suggests that the structural control dominant for this class (>100 kg) of deposits at a scale of 9-km is not very different from the E -W orientation of the mineralised structures in the belt.

The results of all classes obtained following the methodology described above are summarised in the table 5 - 6.

Table 5 – 6. Main direction obtained from lineament and rose diagram analysis. The number in brackets is of deposits in each class or group or type.

		Manica (46)	**Mutare (136)**	**Odzi (59)**	**MMO (241)**
All deposits	All deposits (241)	N-S	N-S; NW- SE	E-W	N-S; E-W NE - SW
	<3 km inter-distance				N-S; E-W; NE-SW; NW-SE
	<9 km inter-distance				NW-SE, NE- SW, N-S
	<20 km				WNW-ESE, NE - SW
Deposit Type	Shear-fault- (122)				ENE - WSW
	20 km search limit				ENE – WSW, E -W
	15 km search limit				ENE – WSW, E -W
	9 km search limit				ENE – WSW, E –W, WNW - ESE
	3 km search limit				ENE – WSW, E –W, WNW – ESE, N - S
	Quartz vein (170)				ENE – WSW, E - W
	20 km search limit				ENE – WSW, E - W
	15 km search limit				ENE – WSW, E - W
	9 km search limit				E – W, NE – SW, WNW, ESE, N - S
	3 km search limit				E – W, NE – SW, WNW, ESE, N - S
	BIF related (42)				ENE – WSW, E - W
	20 km search limit				ENE – WSW, E - W
	15 km search limit				ENE – WSW, E – W
	9 km search limit				ENE – WSW, E – W, N - S
	3 km search limit				ENE – WSW, E – W, N - S
	Undefined (45)				N - S; NW - SE
Grade	Low Grade (<5 g/t) (73)				ENE - WSW
	20 km search limit				ENE – WSW, E - W
	15 km search limit				ENE – WSW, E – W, NE - SW
	9 km search limit				ENE – WSW, E – W, NE – SW, N - S
	3 km search limit				N – S, NE – SW, NW - SE
	High grade (>5 g/t) (123)				ENE - WSW
	20 km search limit				ENE – WSW, E - W
	15 km search limit				ENE – WSW, E - W
	9 km search limit				ENE – WSW, E – W, WNW – ESE, N - S
	3 km search limit				N – S, E – W, NE – SW, NW - SE
Production	Low <10 kg (110)				E – W, ENE - WSW
	20 km search limit				E – W, ENE - WSW
	15 km search limit				E – W, ENE – WSW, N - S
	9 km search limit				E – W, ENE – WSW, WNW – ESE, N - S
	3 km search limit				E – W, ENE – WSW, NW – SE, N - S
	Medium (10-100 kg) (50)				ENE - WSW
	20 km search limit				ENE - WSW
	15 km search limit				ENE – WSW, NE - SW
	9 km search limit				ENE – WSW, NE - SW
	3 km search limit				ENE – WSW, NE – SW, N - S
	High, > 100kg (37)				ENE - WSW
	20 km search limit				ENE – WSW, WNW - ESE
	15 km search limit				N – S, NE – SW, WNW – ESE, E - W
	9 km search limit				N – S, NW – SE, NE – SW, E - W
	3 km search limit				N – S, NW – SE, ENE - WSW

Lithology Stratigraphy	Felsic and intermediate Intrusion (65)		ENE - WSW
	20 km search limit		E – W, ENE – WSW, N - S
	15 km search limit		E – W, ENE – WSW, N – S, NE - SW
	9 km search limit		E –W, NE - SW
	3 km search limit		E – W, ENE – WSW, N - S
	Shamvaian (31)		E - W
	20 km search limit		E - W
	15 km search limit		E - W
	9 km search limit		E – W, NE – SW, ENE – WSW,
	3 km search limit		E – W, NE – SW, NW - SE
	Bulawayan (114)		ENE – WSW
	20 km search limit		ENE – WSW, E - W
	15 km search limit		ENE – WSW, E - W
	9 km search limit		ENE – WSW, E – W, WNW - ESE
	3 km search limit		ENE – WSW, E – W, N – S, NE - SW

(114) Number of deposits in specific group

5.3.3.4 Discussion on the Autocorrelation analysis

Very little work has addressed the description of patterns in point distributions resulting from gold deposits or the factors that control these patterns. The understanding of the distribution patterns and the controlling factors are required for improving gold exploration models. This section has made a step towards such understanding particularly of the lineaments not directly related to known surface structural trends or geological associations.

The assumptions such as "the known gold deposits correspond to a representative sample of the mineralisation" and "the mineralisation is structurally controlled" are a pre-requisite for the interpretation of autocorrelation maps.

Interpretation of the autocorrelation maps show that the ENE – WSW direction at more than 20 km scale is related to the linearity trend of the MMO greenstone belt. Thus, the Fry plots should be analysed with care, in case of linear belts such as the MMO because the method can be biased by the linearity of the belt, which is reflected as continuity in the translation maps (e.g. Verncombe and Verncombe, 1999).

The fact that the intersections of the autocorrelation analysis lineaments coincide with presence of a large deposit make the method a powerful exploration tool for MMO belt.
Autocorrelation analysis has shown the existence of linear patterns oriented NW-SE and N-S directions, which are not directly related to surface structures such as, shear zones, lithological contacts and veins in the MMO greenstone belt.

The NW-SE and N-S directions controlling gold distribution have also been identified in other greenstone belts on the Zimbabwe craton, e.g. the Mashava area (Blenkinsop, 1994). This could mean that the mineralising event at MMO belt and the Mashava area were simultaneous, suggesting a craton wide scale event.

Rose diagrams in the MMO greenstone belt show different patterns at different scales. These scales are defined by a histogram of segment (translation vectors) frequency per length of the segments linking each two deposits. The break points that represent change in deposit spacing are estimated at 3-km, 9-km, 15-km and 20-km. The changes in patterns at different scales may suggest that different mechanisms were dominant during the emplacement of gold mineralisation at each scale. Each group of deposits defined by common spacing is characterised by different deposit type, deposit size, grade and ore mineralogy.

The deposits at 3-km and 9-km spacing in high production (>100 kg) and low grade (<5 g/t) are typically quartz vein hosted and are controlled by surface trapping structures. While the 15 and 20-km spacing deposits are dominantly shear zone-hosted deposits associated with BIF and the N-S and NW – SE are the subsidiary patterns. The N-S and NW- SE pattern are also present at 3 and 9-km scale showing mainly the orientation of the quartz veins.

In general it seems that the N-S event that opened transcrustal regional fractures was active before the mineralising event and was responsible for the emplacement of late granites. During the mineralising event (2,65 Ga) the transcrustal fractures were partially or totally reactivated (fault valve behaviour, laminated veins and fractal results showing more than one population) and acted as focussing structures for the mineralisation fluids in specific segments. Gold mineralisation could then be trapped in several types of brittle structures near surface and are oriented in all directions that give the surface pattern drawn by Autocorrelation analysis of gold deposits at 3 and 9-km scale.

The presence of N-S deep-seated transcrustal structures have been discussed (e.g. Dirks pers. comm., 2001) in the light of rotation of main compressional stress field from E-W to N-S during the cratonization of the Zimbabwean Archaean basement.

The existence of deep seated structures oriented at high angle (± 80° - 90°) to the surface structures e.g. N-S and WNW-ESE is a very important concept for gold exploration in the area, hence the actual exploration models need to concentrate efforts in searching for optimum sites favourable for trapping mineralisation. These models are easily supported by lineament analysis from surface structures visible on satellite imagery and aeromagnetic survey maps. They neglect the fact that surface structures are not the focussing structures as they only trapped mineralisation. In our interpretation future exploration in the Archaean terrains should go beyond understanding trapping structures into underlying focussing structures.

5.4 General discussion on Fry and Fractal Analyses

Although the Fry analysis or the autocorrelation methods are not recommended to linear belts due to over representation along the main axes of the belt it constitute an alternative to variography for directional studies and allows easy handling of large point databases and to analyse data within specified distance range (Vearncombe and Vearncombe, 1999). The autocorrelation methods by nature yield more noise due to the specificity of the data points, which are less sorted, and this fact is inflated by the uncertainties and errors, introduced during collection and inputting of the data. The effect of the linearity of the MMO belt was minimised by dividing the belt in geographical units (Manica, Mutare and Odzi). The comparison of the results yield in this study (specially the fractal analysis) with those from other authors has demonstrated that the effect of linearity of the MMO belt was not significant.

The advanced data analysis in the MMO belt, such as directional distribution of gold deposits associated with specific parameters (e.g. production, grade, deposit type or lithological control) has shown ability to describe patterns not evident in whole set data analysis.

The fractal analysis has the advantage of being a logarithmical or exponential distribution, which by nature allow a smoothing of the data. The results of the two methods show clearly this effect. For example the well-sorted data such as structurally controlled deposits treated by the two methods did yield the same result in terms of cluster size. In the MMO greenstone belt the cluster size of 2 – 20 km maximum obtained earlier by the autocorrelation method, is proved to be supported also by the fractal analysis (cluster size of 2 – 30 km).

The use of gold deposits position for fractal analysis has been discussed by Blenkinsop (1994 and 1995) who showed that the mines were only a random sample which suggests that more deposits are to be discovered in the Zimbabwe craton.

The gold deposits are affected by multiple factors, which are represented by presence of more than one population in fractal analysis. The main focus is oriented to the population that yield the highest correlation coefficient, and for this populations, one can confidently conclude that the main controlling factor is unique.

The application of the two methods (fry and fractal analysis) to similar data sets proved that the two methods converge to a certain degree.

5.5 Conclusions

Distribution patterns of gold deposits and controls of gold mineralisation in the Manica-Mutare-Odzi greenstone belt have been determined by statistical, autocorrelation and Fractal analyses.

From a basic consideration that the known gold deposits reflect a representative sampling of the mineralisation, it has been shown that the controls of gold mineralisation in the Manica Mutare Odzi greenstone belt goes beyond the surface trapping structures (discernible on surface). The orientations of regional structures that control mineralisation do not, in most cases, coincide with orientation of surface trapping structures.

The study has also demonstrated that autocorrelation analysis has potential in the characterisation of regional distribution patterns, which is important for gold exploration and for understanding the metallogenic evolution of MMO greenstone belt.

The correlation and consistency of the direction of the mineralisation controlling structures at different scales and in different subsets prove the high capacity of the autocorrelation analysis in explaining the spatial relationships of complex data sets such as gold deposits in the MMO Archaean greenstone belt.

Autocorrelation analyses of lineament intersections represent high probability of finding new gold mineralisation in the MMO belt. This is supported by the fact that the known large deposits fall on these intersections.

Based on the distribution patterns of known gold deposits, this study has shown that the gold deposits are fractal and the mineralisation has been transported and deposited in favourable geological structures by hydrothermal systems.

There is a clear relationship between mineralisation and shear zones of different generations with evidence of reactivation proved by crosscutting relationships and enrichment in gold of the second generation shear zones (see also chapter 4 and 9).

The autocorrelation analysis suggests a structural control of gold mineralisation in a pattern mainly oriented N-S and WNW - ESE at a regular 5 km spacing of maximum width. These corridors might have constituted the deformation zones where the hydrothermal systems acted to emplace the gold deposits.

The autocorrelation analysis can be used as exploration tool for new deposits in the MMO where field evidence should be gathered within 3-km radius from known ENE or NW alignments of deposits and within 9-km radius of known NNE alignments.

The fractal relationship has proved that the gold deposits in the MMO greenstone belt can be explained by a single event, as already suggested by earlier author Blenkinsop (1994 and 1995) for the Shamva and Masvingo - Mashava greenstone belt.

Autocorrelation and fractal analyses have shown that the gold deposits in the MMO greenstone belt cluster at distance ranges between 2 and ~30 km with the exception of deposits spatially related to the Penhalonga granodiorite where the cluster size is between 0,58 and 2 kms.

The lower regression limit of 2 km on fractal analysis suggests that the deposits that produced less than 100 kg cluster at shorter distance range compared to those that produce more than 100 kg. It is expected that large deposits cluster at large distance range (5,4 km) because large deposits are harder to find compared to small deposits.

Chapter 6

6 Mineral Exploration using infrared Spectroscopy

6.1 Introduction

The most challenging problem in mineral exploration is finding method or methods that easily map mineralised structures in greenstone belts. In previous chapters gold mineralisation was characterised and its relationship with shear zones was established. The next step is to check whether the shear zones have particular reflectance signature (e.g. mineralogical alteration pattern) that can allow its mapping using remotely sensed data. For this purpose soil and rock samples where collected across the mineralised shear zones. The samples were analysed using infrared spectrometer (PIMA SP) (Appendix VI-A).

The PIMA results provide better understanding on how mineralised shear zones can be mapped using remote sensing by supplying digital values of the spectral reflectance of the shear zones.

The other objective is to obtain spectral inputs from different lithologies, which will be used to improve the satellite imagery (TM, ETM and SPOT) interpretation. The comparison between the ETM or TM reflectance and the PIMA spectrum is only valid for the infrared bands (bands 5 and 7).

These goals are achieved by characterising spectrally the alteration assemblages and their compositional variations along traverses across the shear zones and the analysis of chip samples of several lithological units (Fig. 6 - 1).

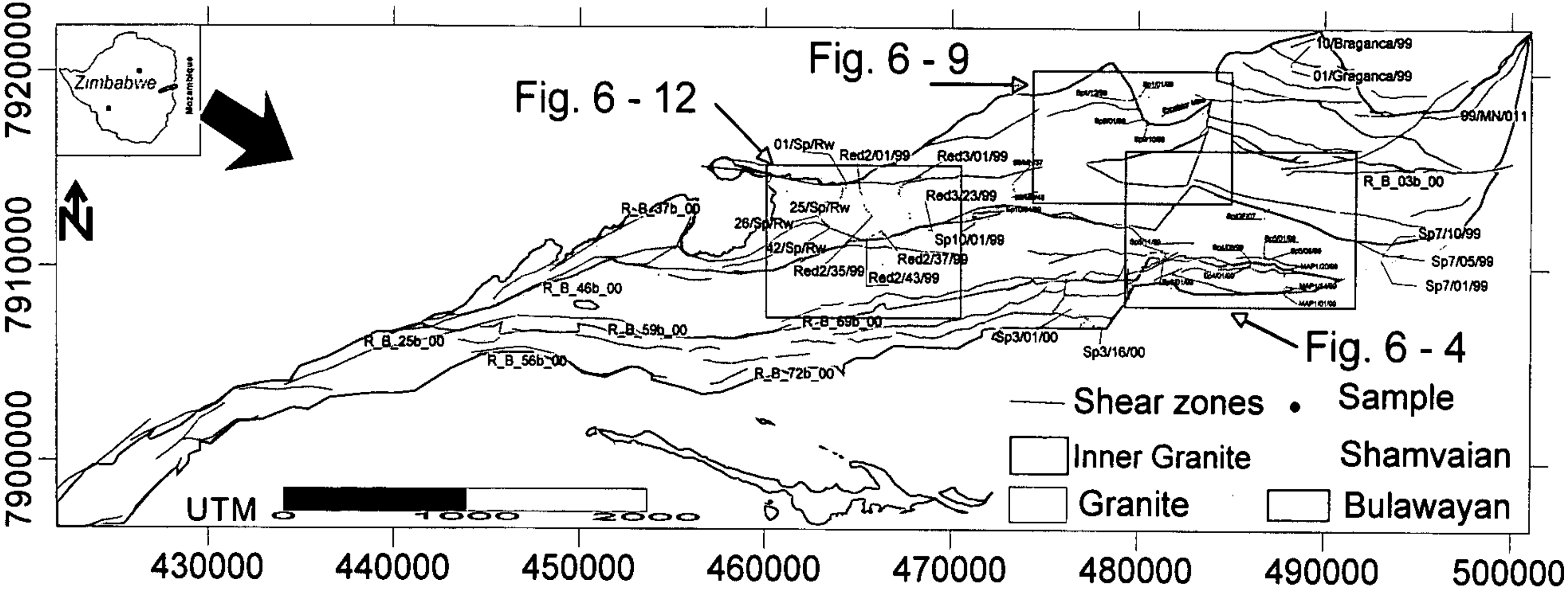

Figure 6 – 1. Simplified geological map showing the rock and soil samples locations in the MMO greenstone belt. The geological units are interpreted from satellite imagery (TM169/73, ETM 169/73, SPOT - Xs and SPOT-Panchromatic) and mosaic of airphotos with geological map as reference. The inserts show detailed sample profiles.

The use of Short Wavelength Infrared (SWIR) spectrometry for geologic studies, especially for mineral exploration has increased dramatically in recent years (Clark and Roush, 1984). The reflectance spectrum of a particular mineral in the SWIR (Fig. 6 - 2) is characteristic of that mineral. This is because mineral spectrum is dependent on composition and crystallinity of the mineral, which is unique to each mineral.

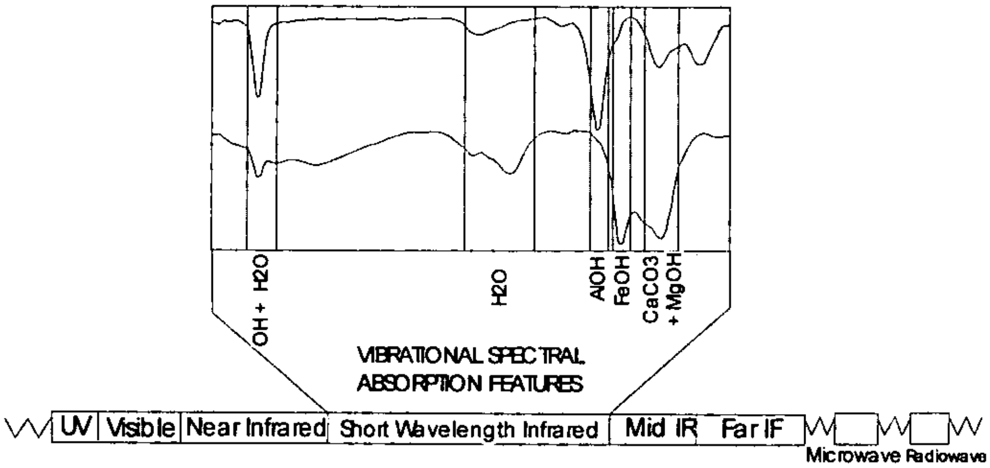

Figure 6 – 2. Short Wavelength Infrared position in the electromagnetic spectrum

The minerals, when irradiated by a source of light, selectively absorb and reflect light in different amounts at specific wavelengths due to the bending and stretching of molecular bonds (Clark, 1999).

According to Pontual et al. (1997a), the bonds giving rise to absorption features in SWIR include those in hydroxyl (at 1400nm), water (1400 and 1900nm), carbonate (2300-2350nm) and between Al-OH (2200nm), Mg-OH (2330nm), and Fe-OH (2200nm). These molecules are major components in phyllosilicates (including clay, chlorite and serpentine minerals) hydroxylated silicates (e.g. epidote and amphiboles) and sulphates (alunite, jarosite and gypsum), and carbonate minerals. Table 6 - 1 and Fig. 6 - 3 summarise the dominant diagnostic absorption features in the SWIR.

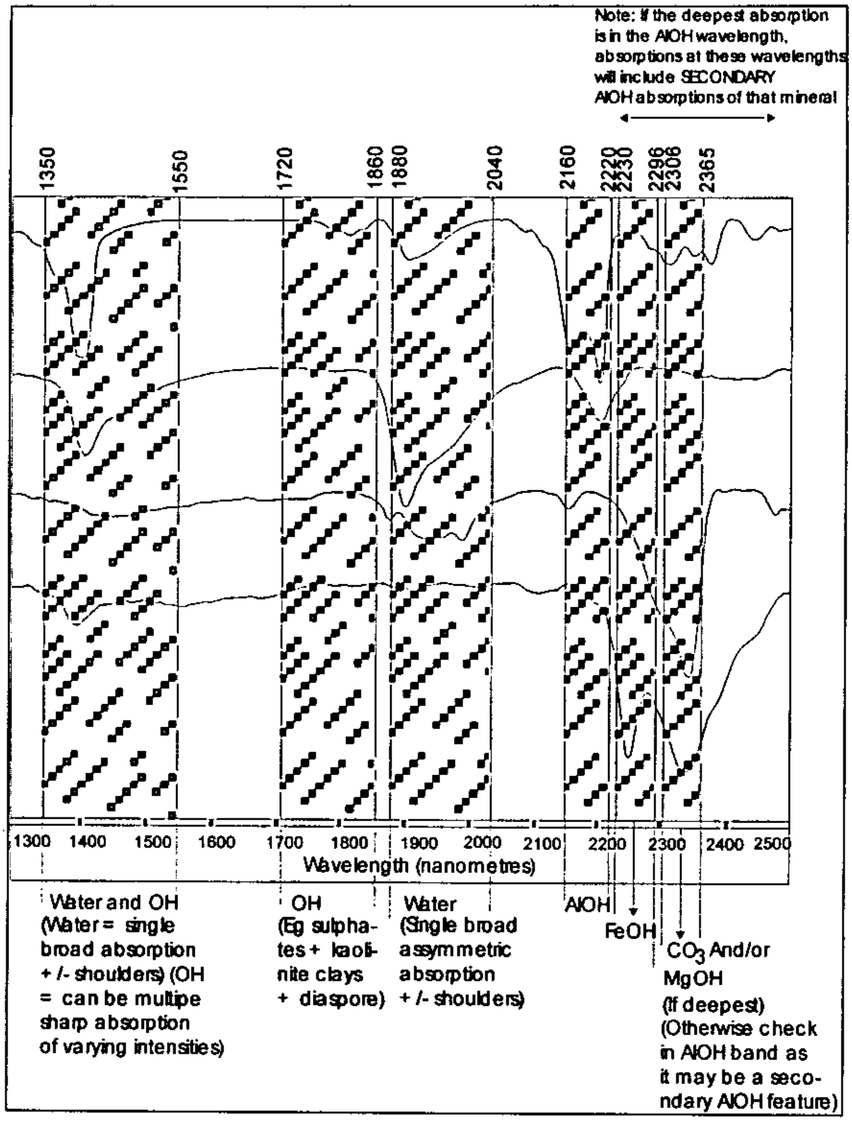

Figure 6 – 3. Major spectral absorption bands in the SWIR for different clay minerals (Source: Pontual et al. (1997a))

Table 6 – 1. Wavelength positions of dominant absorption features in the SWIR

Mineral group/composition	Wavelength in nm
OH (structurally bound)	1400 (also 1550 and 1750-1850 in some minerals)
Water	1400 and 1900
Al-OH	2160-2220
Fe-OH	2230-2295
Mg-OH	2300-2360
CO_3	2300-2350 (and also at 1870, 1990 and 2155)

The diagnostic absorption features may also reflect variations in crystallinity of the minerals due to changes in the shapes. They also provide useful information for discrimination of compositional variations within mineral groups (Pontual et al., 1997a). For example the shift in the wavelength positions of the diagnostic absorption features may reflect variations due to alteration. They are also important for mapping mineralisation/alteration relationships.

The PIMA SP principles, the PIMA spectrum, PIMA measurements and data processing, and feature extraction from PIMA are explained in the Appendix VI-A.

6.2 Data Collection and Sample Preparation for PIMA Analysis

6.2.1 Data Collection

The samples were collected from areas selected on the basis of existing information, airphotographs, geological maps mainly compiled during this study and gold deposits database with information on control of the deposits, production, and geology. Orientation fieldwork was carried out before commencing sample collection so as to establish the main structures (shear zones), deposits and sites to be included in the sampling program. It was concluded from the orientation field study that the soil samples are the most useful sample types for spectral analysis due to dense vegetation, poor exposure (Manica section) and thick soil profile.

Soil samples were collected along profiles at 10 to 25 m sample-spacing across mineralised shear zones, main felsic intrusion and known structurally controlled gold deposits as illustrated in Fig. 6 - 1. The option of collecting surface samples and not the horizon B or C as recommended in most geochemical soil studies was supported by the need to compare the spectral results with Landsat TM and ETM whose scanning penetrability is superficial (less than 30 microns). The spacing of 10 to 25 m was an effort to warrant the detection of the mineralogical changes that may not be discernible on Landsat due to its broad spatial-resolution (30 by 30 m) on bands 5 and 7. Efforts were made to collect samples from places with minimum vegetation in order to allow direct comparison to Landsat images and reduce the effect of vegetation. Two hundred and fifteen (215) soil samples each weighing c.200 g were collected. At each sample point, information on type of vegetation, main lithology, size and type of floats present were recorded (Appendix VI – B). The list of samples, location and description are given in the Appendix VI-B.

A total of one hundred and forty five (145) rock samples (chips) were collected from different lithological units ranging from basalts to granitoids (Appendix VI-B). It was expected from rock samples to characterise the spectral reflectance of the lithological units in the SWIR range in order to improve the interpretation of the satellite imagery and resolve image features not previously detected.

6.2.2 Sample preparation

The soil samples were split in halves in order to retain duplicates and thus a portion of about 100 g was used for PIMA analysis. The samples were not oven dried because the main objective was to measure the samples in their most approximate natural conditions which are the same or similar to the conditions during the acquisition of the Landsat TM and ETM. Soil and powder samples are measured in glass petri dishes. The finer part of the sample was concentrated at the bottom of the petri dish by manually shaking it. The petri dishes are about 2.5 cm in diameter and 0.5-cm height.

The collected rock samples were split in three; the first part of the sample was used for thin section analysis, the second part of the sample was for PIMA and the third was for reference. The rock samples were pulverized to 150 microns and powder was scooped by petri dish and shaken in order to settle the finer particles to the bottom. The powder samples are needed to cross check the reflectance spectra from the rock (chip) samples which is more affected by scattering of the light and there is a high chance to measure only one mineral rather than the several minerals that constitute the rock. The cut surfaces of the rock samples were also used to place the sample on the PIMA SP optical port to obtain the reflectance spectra.

The explanation on mineral identification and feature extraction procedures on PIMA SP data are presented in Appendix VI-C. The interpretation of spectra using a spectral library can be summarised in the seven steps suggested by Pontual et al. (1997a), (see Appendix VI – D).

6.3 Mapping the degree of alteration in the mineralised shear zones and granite intrusions using PIMA

The soil samples profiles Sp3, Sp4, Sp5, Sp/GF, Sp7, Sp10 were drawn perpendicular to shear zones that crosscut different rocks. Profiles Red2, Red3 and Sp/Rw were designed to crosscut the Penhalonga granodiorite and the shear zones to the south and to the north of it as shown in Fig. 6 – 1.

The profile Sp1 crosscuts the northern contact between the MMO greenstone belt and the granite and the profile MAP1 crosscuts the southern contact. Soil samples were preferred due to the need to correlate the PIMA analysis with Landsat TM and ETM (see discussion in Chapter 7).

The chemical compositions of the lithologies and equivalent soils were kindly supplied by previous authors (e.g. Chenjerai, 1996). Generally, soils are a complex mixture of newly formed clay minerals and iron hydroxides and minerals inherited from the underlying bedrock. The following minerals are usually present in variable proportions: hornblende or actinolite ± chlorite (typical of upper grenschist and lower amphibolite facies, metabasites), talc and serpentine (present in ultramafic rocks), nontronite, saponite, montmorillonite (smectite group), kaolinite (kaolinite group) (common weathering products near surface), muscovite, illite and or phengite, and sericite (illite group) (present in felsic and some metasediments). The above minerals can be divided into chlorite, carbonate and muscovite zones.

The next subsections presents the spectra of the soil samples and the mineralogical variations imposed by the presence of different type of shear zones in the MMO belt.

6.3.1 Shear zones near the contact between the Bulawayan and Shamvaian Supergroups

The shear zones near the contact between the Bulawayan and the Shamvaian host c 40 deposits in the MMO greenstone belt.

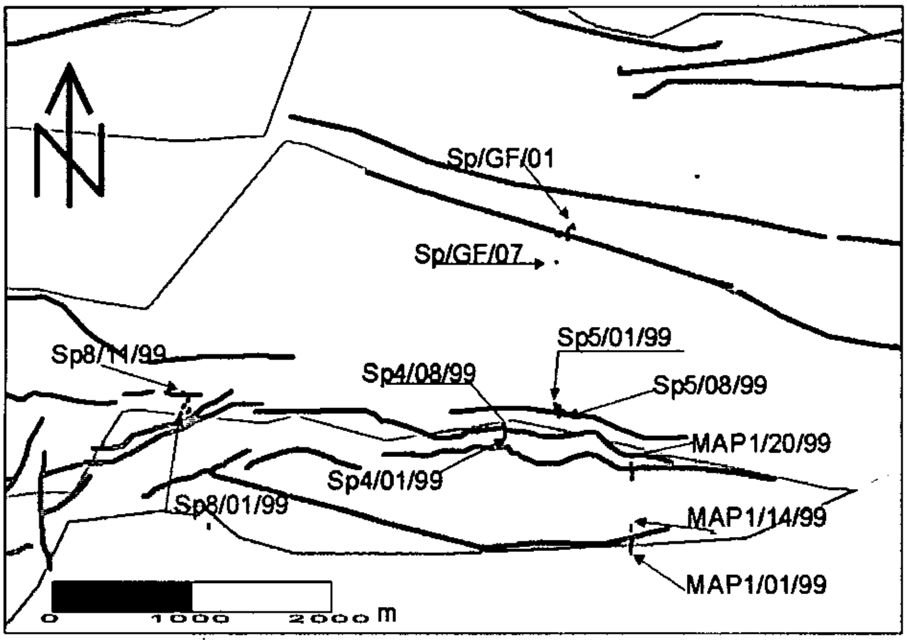

Figure 6 – 4. Simplified geological map showing the sample location for the profiles Sp/GF, Sp5, Sp4, Sp8 and MAP1. For geological legend refer to Fig. 6 – 1.

In the Figure 6 – 5a, reflectance spectra for the soil samples obtained by PIMA are shown. These spectra show that the samples Sp8_1 to Sp8_3 are dominated by the same minerals, namely anhydrite, halloysite/kaolinite and talc in different proportions and are characterized by low reflectance compared to sample Sp8_4.

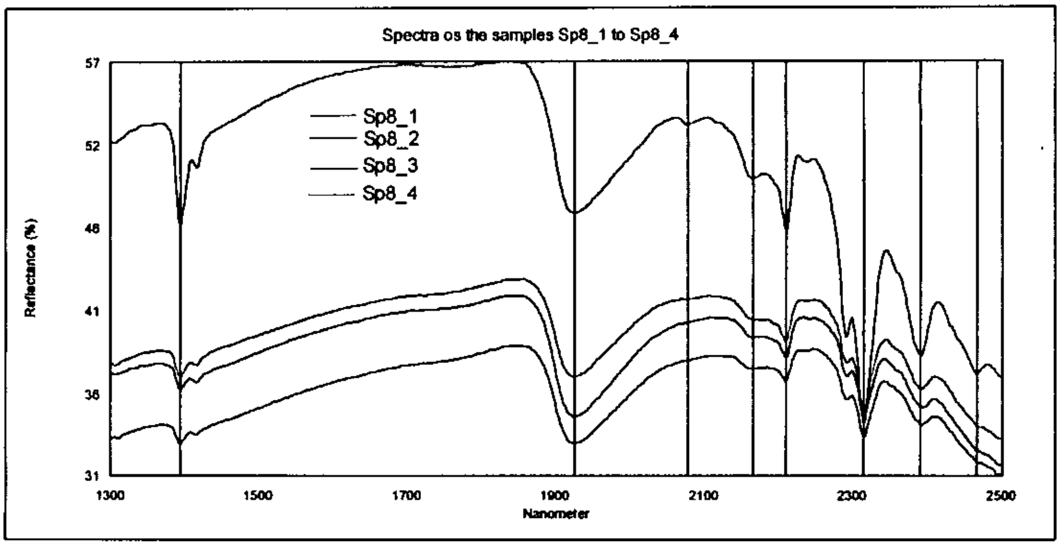

Figure 6 – 5a. Reflectance spectra of the samples Sp8_1 to Sp8_4.
Note the similarity of the spectra representing mainly talc (absorption at 2312nm) and halloysite/kaolinite (absorption at 2208nm doublet and smaller doublet at 1393nm). The 1900 absorption feature is due to the presence of free water. (For location refer to Fig. 6 – 4)

Figures 6 – 5b and 6 – 5c show that the reflectance remains relatively high for the samples Sp8_5 to Sp8_9 and drops slightly for the samples Sp8_10 and Sp8_11. The samples have similar minerals with proportion varying from talc being dominant and followed by kaolinite in the samples Sp8_5 to Sp8_7. In the samples Sp8_9 to Sp8_11 there is no talc and the samples are dominantly kaolinite/halloysite and anhydrite.

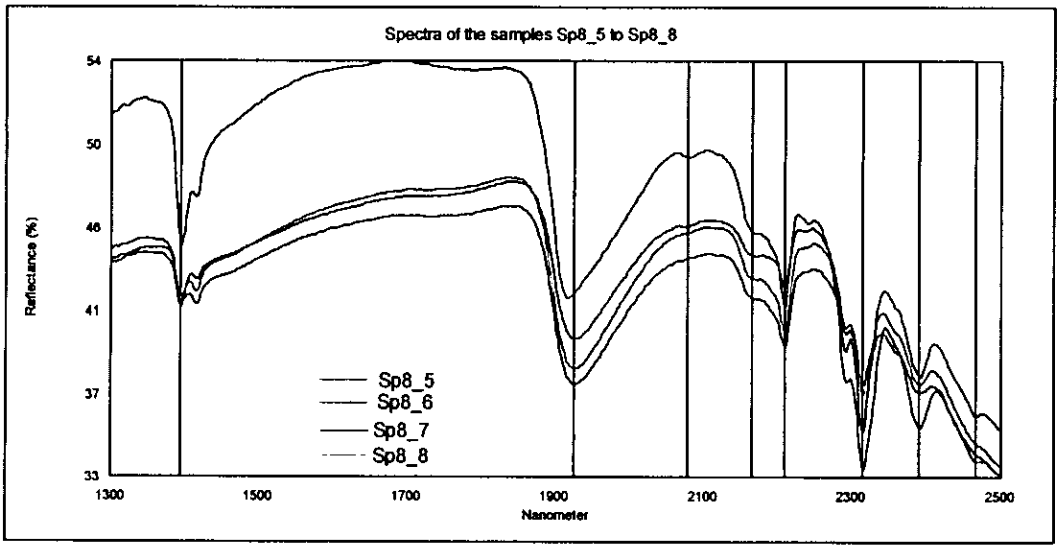

Figure 6 – 5b. Reflectance spectra of the samples Sp8_5 to Sp8_8.
Note the similarity of the spectra representing mainly talc (absorption at 2312nm) & halloysite/kaolinite (absorption at 2208nm doublet and smaller doublet at 1393nm). The 1900 absorption feature is due to the presence of free water. (For location refer to Fig. 6 – 4)

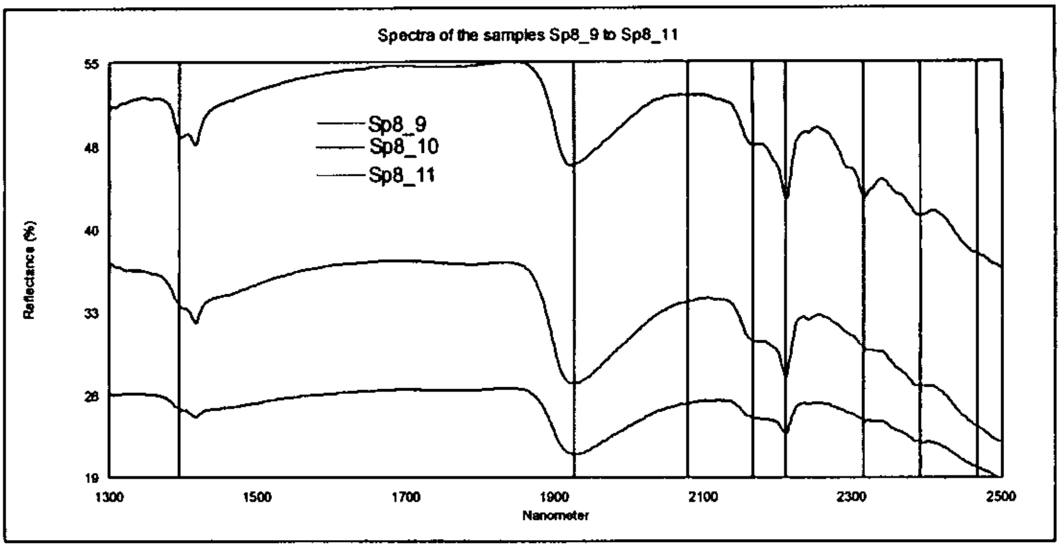

Figure 6 – 5c. Reflectance spectra of the samples Sp8_9 to Sp8_11.
Note the similarity of the spectra representing halloysite/kaolinite (absorption at 2208nm doublet and smaller doublet at 1393nm). The 1900 absorption feature is due to the presence of free water. (For location refer to Fig. 6 – 4)

Figure 6 - 6 represents the mineralogical fields identification using the absorption features mapping and the asymmetry index for the profile Sp8.

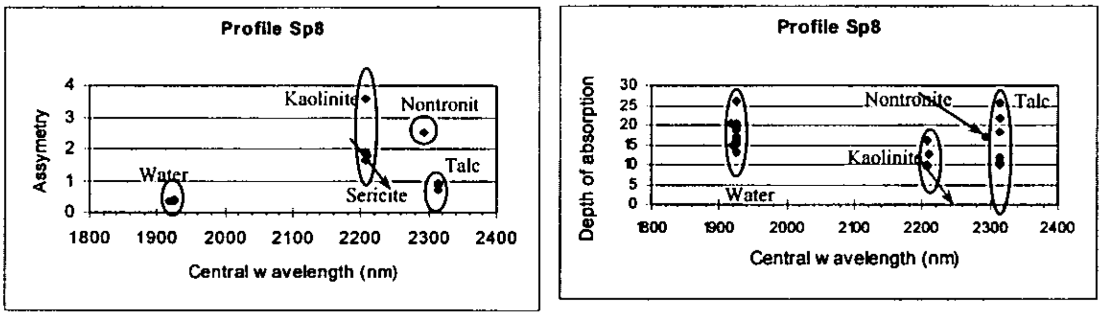

Figure 6 – 6. Mineral-field identification using the asymmetry index and absorption features of the profile Sp8. For distribution of these samples across the profile refer to Fig. 6 – 18. The arrows indicate the position of specific mineral.

In Fig 6 – 7, the spectra along the profile Sp/GF across Guy Fawckes deposits (see chapter 4) indicate that according to reflectance percentage there are three groups of samples; the low reflectance (Sp/GF/01), the middle reflectance (Sp/GF/02, Sp/GF/04 and Sp/GF/05) and the relatively high reflectance of samples Sp/GF/03, Sp/GF/06 and Sp/GF/07. The low reflectance of the sample Sp/GF/01is explained by the presence of free water. The mineralogy along this profile is presented in the Appendix VI – E. The relatively high reflectance seems to be associated with presence of kaolinite without free water. In general the reflectance increases with increasing kaolinite proportion in the sample (Pontual et al., 1997a).

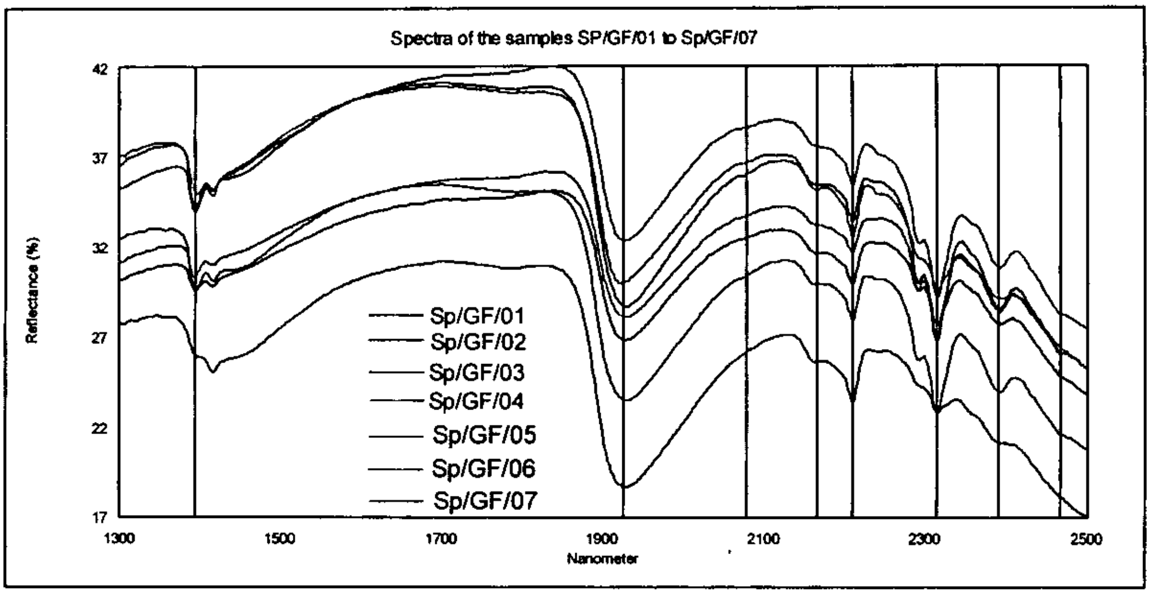

Figure 6 – 7. Reflectance spectra of the samples Sp/GF/01 to Sp/GF/07.
Note the similarity of the spectra representing mainly talc (absorption at 2312nm) & Halloysite (absorption at 2208nm doublet and smaller doublet at 1393nm). The 1900 absorption feature is due to the presence of free water. (For location refer to Fig. 6 – 4)

Figure 6-8 shows the mineral field mapping using the absorption features and the asymmetry index. In this particular case the two methods give similar results.

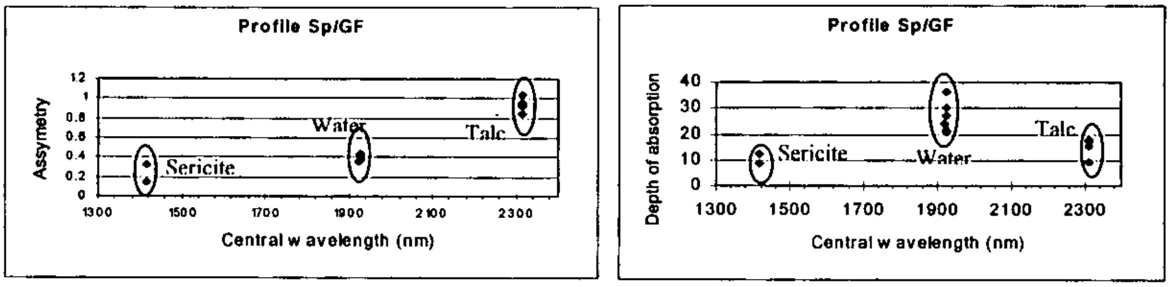

Figure 6 – 8. Mineral-field identification using the asymmetry index and absorption features of the profile Sp/GF. For distribution of these samples across the profile refer to Fig. 6 – 18.

6.3.2 Shear zones on the contact between Bulawayan Supergroup and granites

Some portions of the sheared contact between the Bulawayan and the granites are significantly mineralised. These shear zones were also sampled (Fig. 6 – 9) for PIMA analysis.

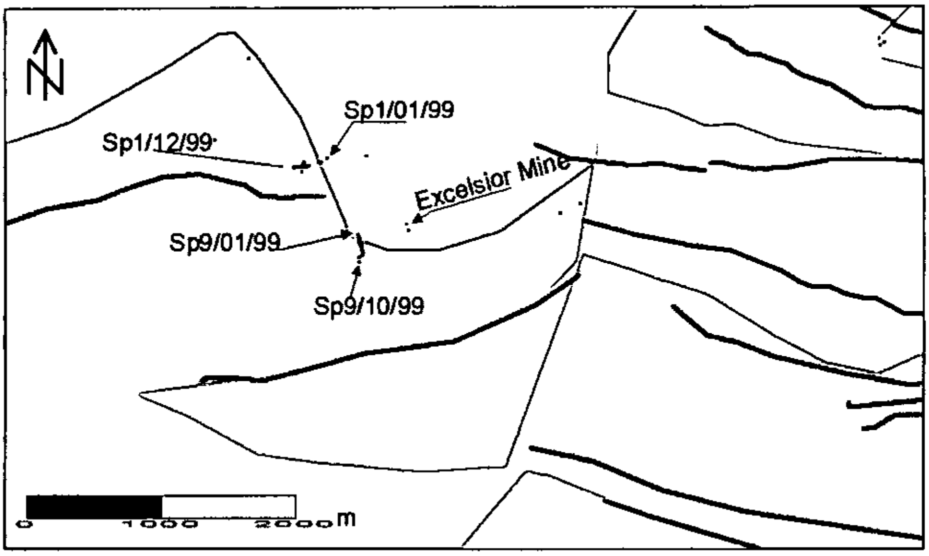

Figure 6 – 9. Simplified geological map showing the sample location for the profiles Sp9 and Sp1. For geological legend refer to Fig. 6 – 1.

The spectral response shown in Figs. 6 – 10a and 6-10b suggest that the samples collected on the granite side of the profile have higher proportion of kaolinite compared to the ultramafic rocks as would be expected.

The samples Sp1_1 to Sp1_04 contain halloysite as the dominant mineral followed by kaolinite and anhydrite, hence the relatively low reflectance. The samples Sp1_5 to Sp1_07 have higher proportion of kaolinite compared to anhydrite and halloysite, which explains the relatively high reflectance. The samples Sp1_08 and Sp1_10 have free water, which reduces significantly their reflectances. The last two samples on the profile (Sp1_11 and Sp1_12) have halloysite and anhydrite dominant compared to kaolinite.

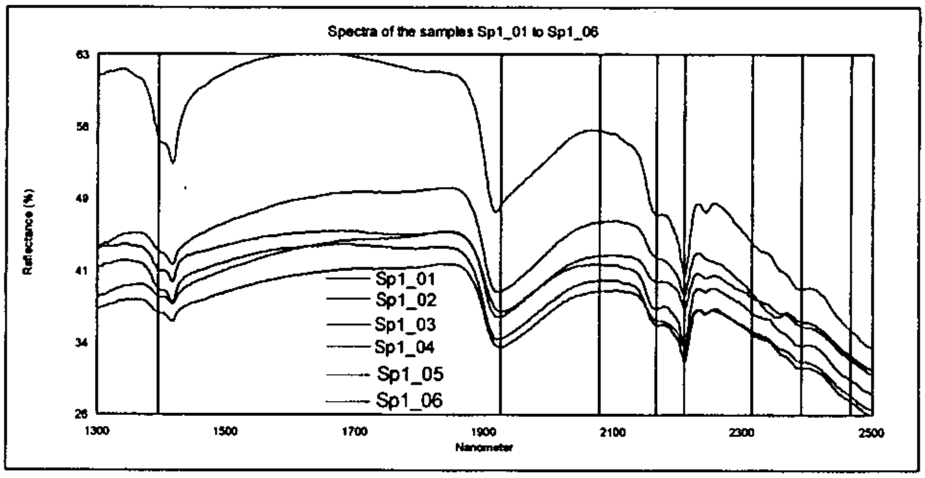

Figure 6 – 10a. Reflectance spectra of the samples Sp1_01 to Sp1_06.
Note the similarity of the spectra representing mainly halloysite/kaolinite (absorption at 2208nm doublet and smaller doublet at 1393nm). The 1900 absorption feature is due to the presence of free water. (For location refer to Fig. 6 – 9)

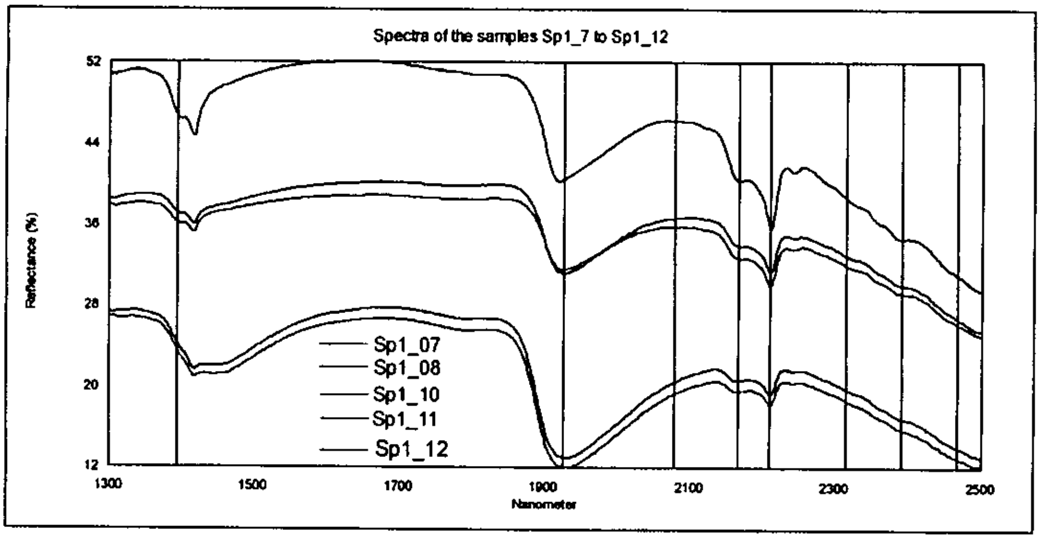

Figure 6 – 10b. Reflectance spectra of the samples Sp1_07 to Sp1_12.
Note the similarity of the spectra representing mainly halloysite/kaolinite (absorption at 2208nm doublet and smaller doublet at 1393nm). The 1900 absorption feature is due to the presence of free water. (For location refer to Fig. 6 – 9).

The mineralogical fields shown in Fig. 6 – 11 as mapped by asymmetry index and deepest absorption features suggest three distinctive fields representing kaolinite and sericite.

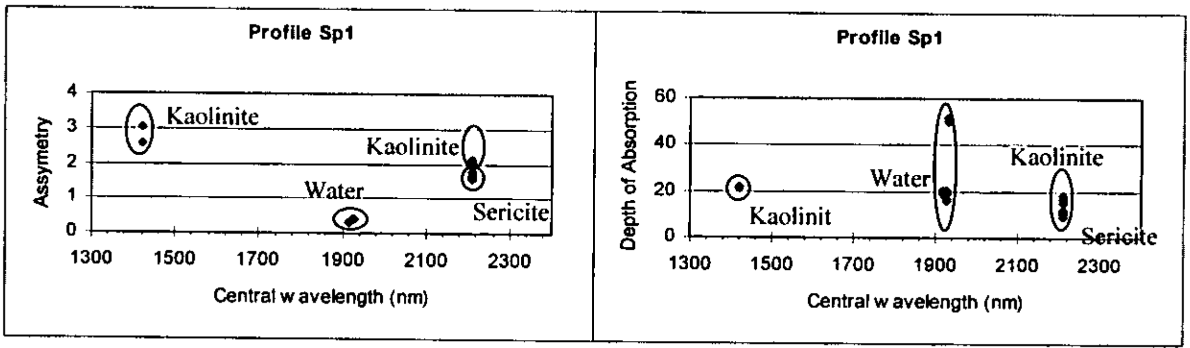

Figure 6 – 11. Mineral field identification using the asymmetry index and absorption features or the profile Sp1. For distribution of these samples across the profile refer to Fig. 6 – 19.

6.3.3 Shear zones near the Penhalonga granodiorite

Other sets of mineralised shear zones in the study area are situated to the north and to the south of the Penhalonga granodiorite (Fig. 6 – 12). The samples collected across these shear zones show in general low reflectance (less than 40%), which may be attributed to the dominance of talc (Figs 6 – 13a, to 6 – 13c).

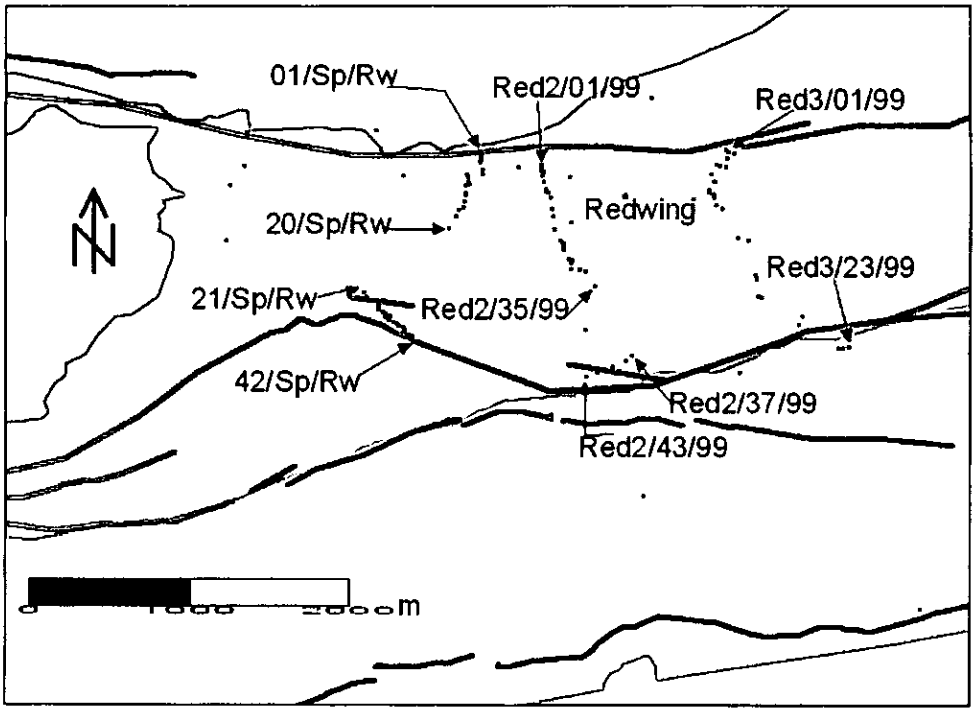

Figure 6 – 12. Simplified geological map showing the sample location for the profiles Sp/Rw, Red2 and Red3. For geological legend refer to Fig. 6 – 1.

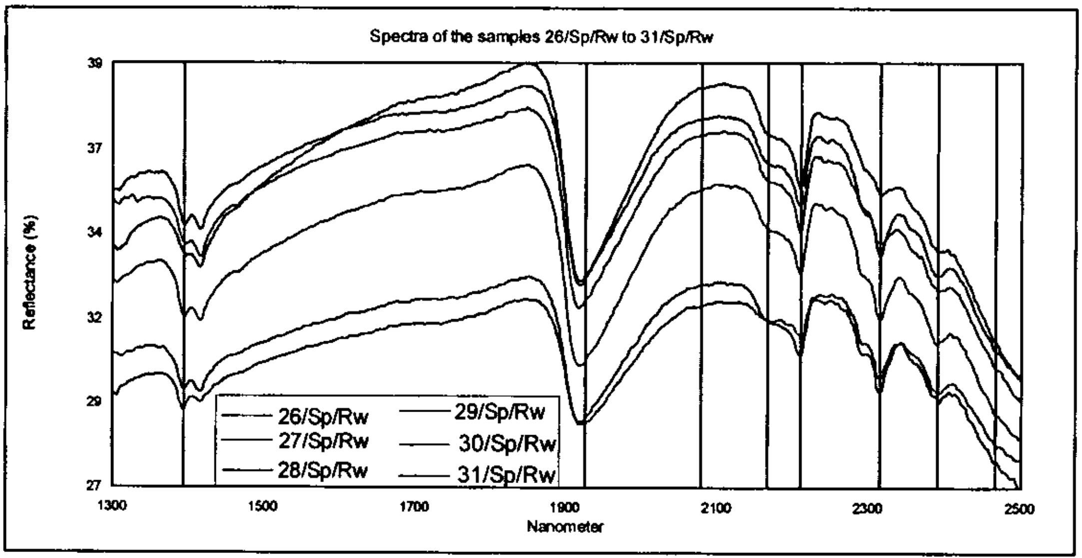

Figure 6 – 13a. Reflectance spectra of the samples 26/Sp/Rw to 31/Sp/Rw.
Note the similarity of the spectra representing mainly talc (absorption at 2312nm) & Halloysite (absorption at 2208nm doublet and smaller doublet at 1393nm). The 1900 absorption feature is due to the presence of free water. The presence of sericite and kaolinite is not expressive. (For location refer to Fig. 6 – 12).

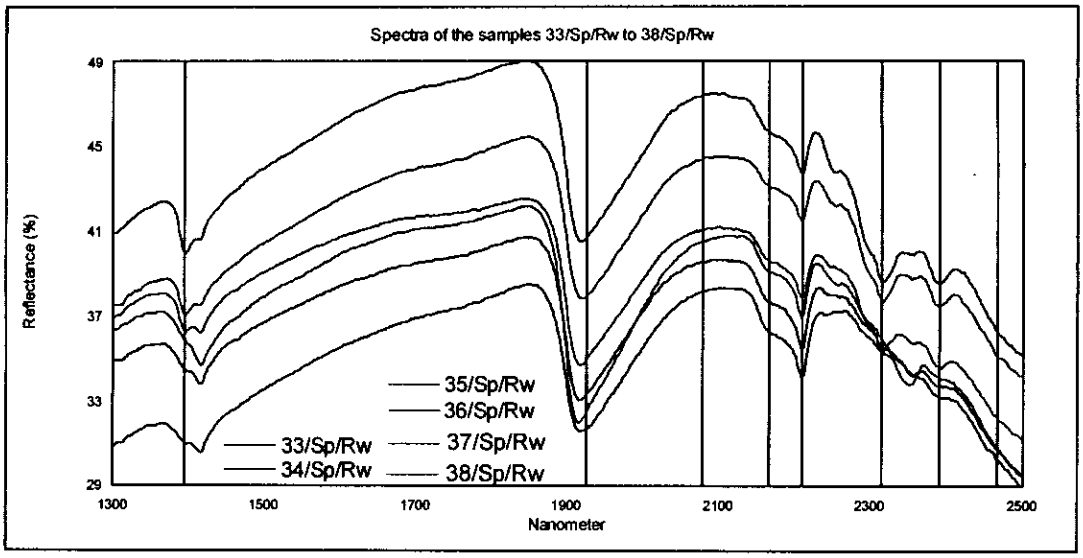

Figure 6 – 13b. Reflectance spectra of the samples 33/Sp/Rw to 38/Sp/Rw.
Note the similarity of the spectra representing mainly talc (absorption at 2312nm) & Halloysite (absorption at 2208nm doublet and smaller doublet at 1393nm). The 1900 absorption feature is due to the presence of free water. The presence of sericite and kaolinite is not expressive. (For location refer to Fig. 6 – 12).

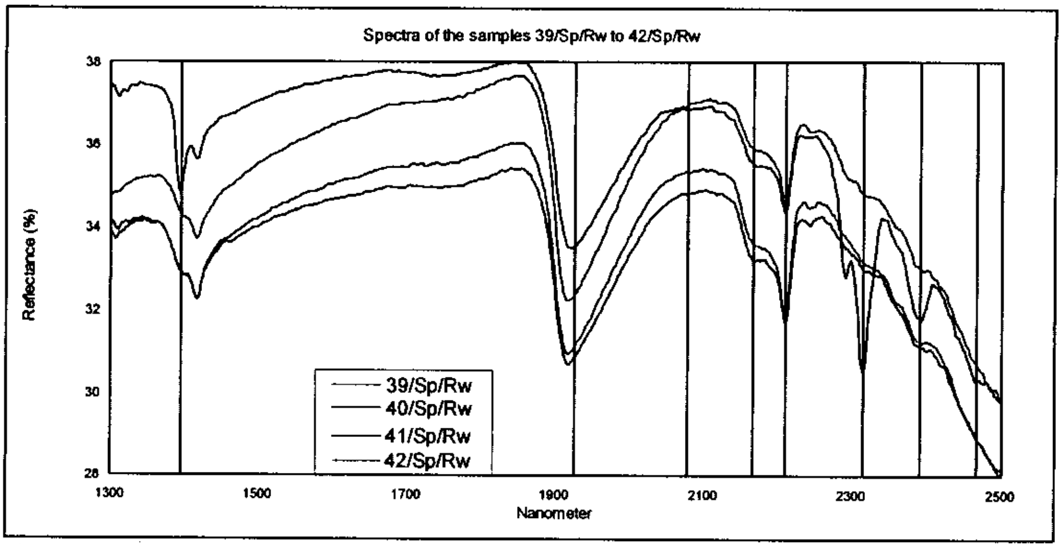

Figure 6 – 13c. Reflectance spectra of the samples 39/Sp/Rw to 42/Sp/Rw.
Note the similarity of the spectra representing mainly talc (absorption at 2312nm) & Halloysite (absorption at 2208nm doublet and smaller doublet at 1393nm). The 1900 absorption feature is due to the presence of free water. The presence of sericite and kaolinite is not expressive. (For location refer to Fig. 6 – 12)

The Fig. 6 – 14 indicates that four mineral fields are present in the samples from the profile Sp/Rw, namely kaolinite, talc, sericite and water.

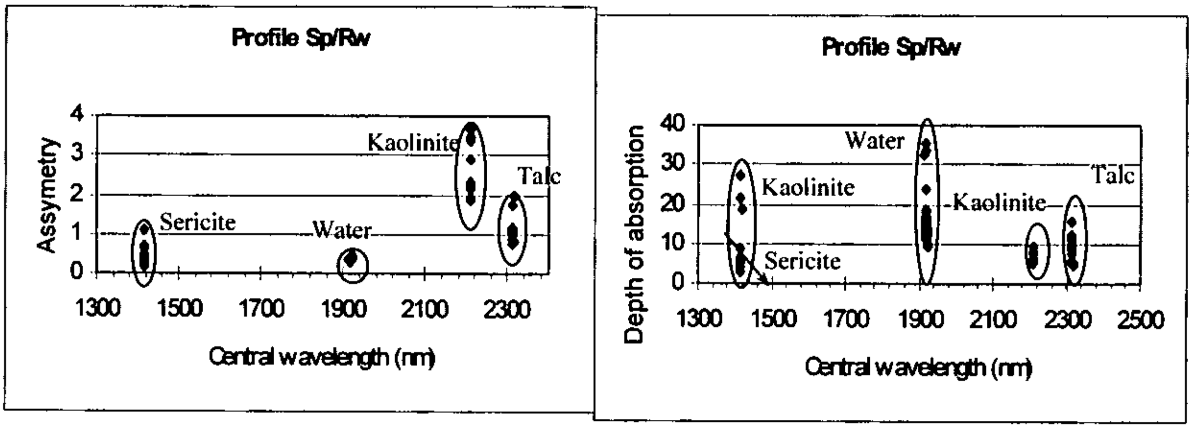

Figure 6 – 14. Mineral field identification using the asymmetry index and absorption features or the profile Sp/Rw. The arrows indicate the position of specific mineral. For distribution of these samples across the profile refer to Fig. 6 – 20.

6.3.4 Felsic intrusions within the Bulawayan Supergroup

As shown in Figs. 3 – 23 and 3 - 25, the majority of gold deposits in the MMO belt are located within or in the vicinity of the Penhalonga granodiorite. Fig. 6 – 12 shows location of samples around Penhalonga granodiorite and Figures 6 - 15a to 6 - 15f show the reflectance spectra of different samples.

The spectral response of the intrusion and its contact with Bulawayan metabasalts show little mineralogical variation from the soils suggesting that the soils are probably transported from elsewhere.

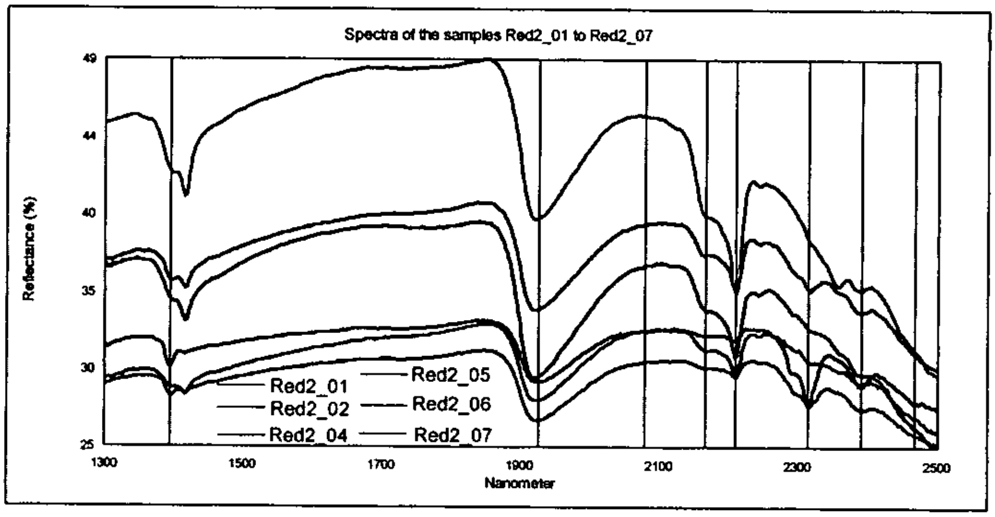

Figure 6 – 15a. Reflectance spectra of the samples Red2_01 to Red2_07
Note the similarity of the spectra Red2_04 to Red2_07 representing mainly halloysite/kaolinite (absorption at 2208nm doublet and smaller doublet at 1393nm). The spectra Red2_01 and

Red2_02 have the main doublet at 2315 nm and the smaller one at 1395 nm showing the presence of talc and tremolite. The 1900 absorption feature is due to the presence of free water.

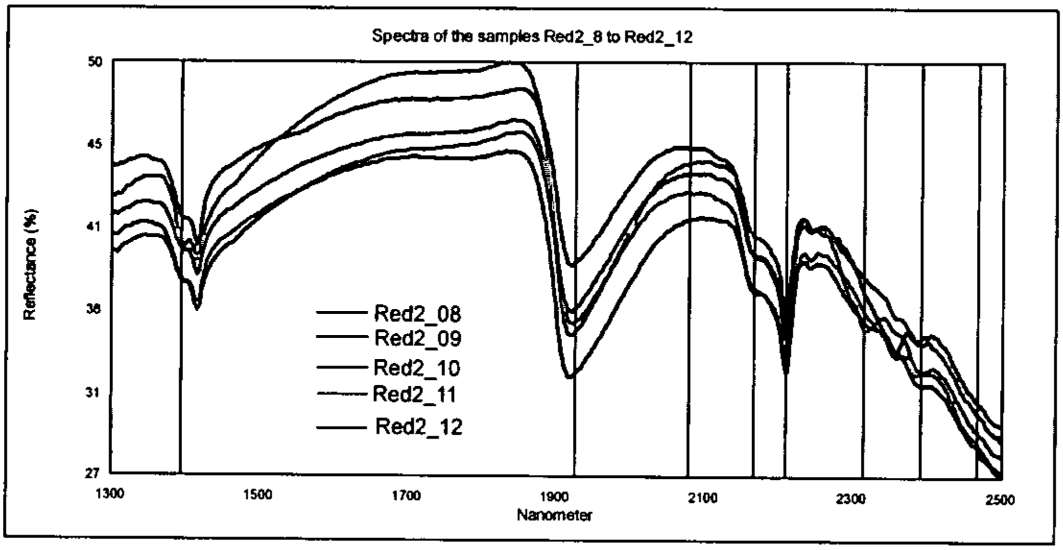

Figure 6 – 15b. Reflectance spectra of the samples Red2_08 to Red2_12.
Note the similarity of the spectra Red2_08 to Red2_10 representing mainly halloysite/kaolinite (absorption at 2208nm doublet and smaller doublet at 1393nm). The sample Red2_11 has an extra absorption at 2317nm for the tremolite. The 1900 absorption feature is due to the presence of free water.

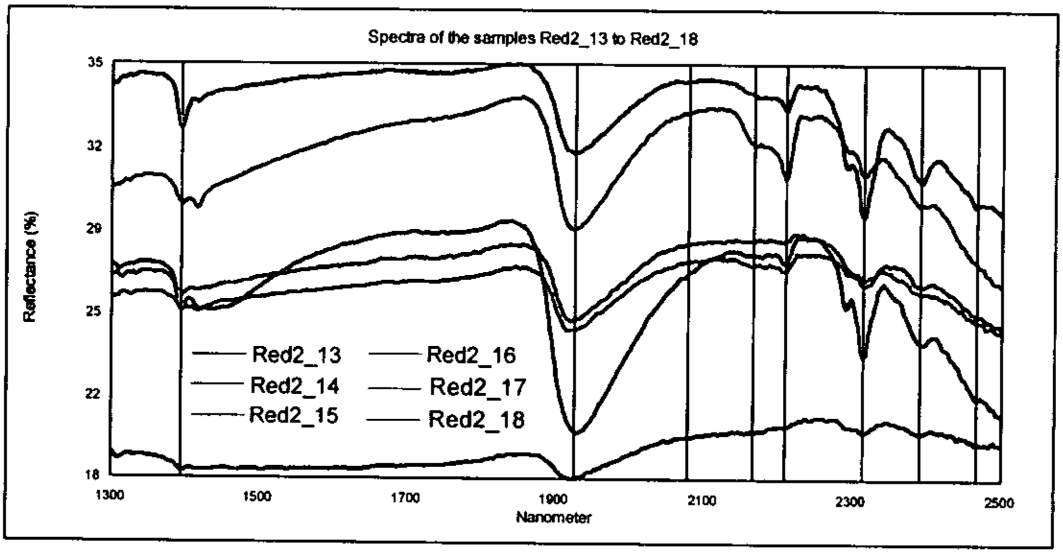

Figure 6 – 15c. Reflectance spectra of the samples Red2_13 to Red2_18
The sample 13 was not spectrally identifiable. Note the similarity of the spectra Red2_14 to Red2_16 representing mainly talc and tremolite (absorption at 2313 to 23 17 nm doublet and smaller absorption at 1395nm). The samples Red2_17 and Red2_18 are dominated by halloysite and Anhydrite. The 1900 absorption feature is due to the presence of free water.

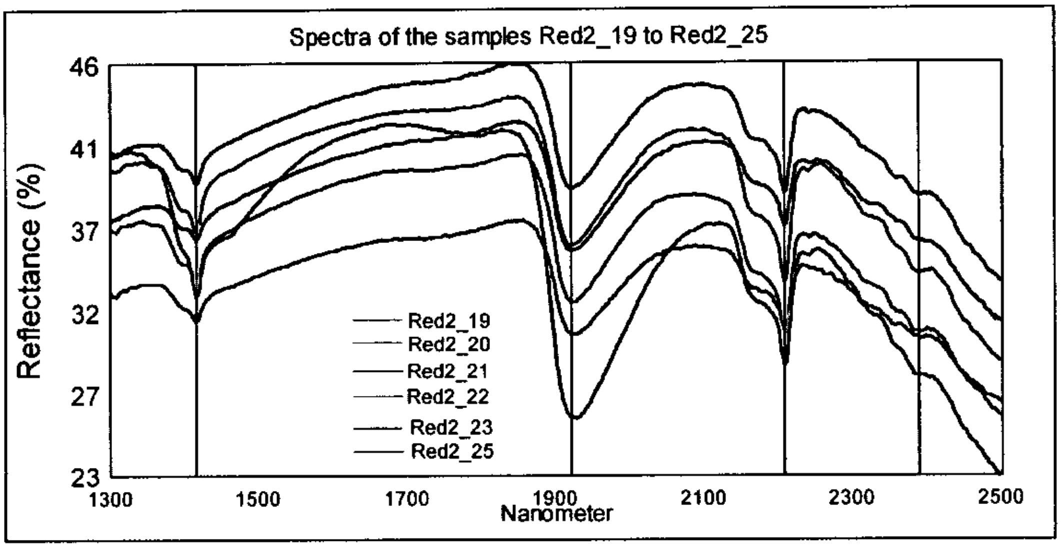

Figure 6 – 15d. Reflectance spectra of the samples Red2_19 to Red2_25
Note the similarity of the spectra representing mainly halloysite/kaolinite (absorption at 2208nm doublet and smaller doublet at 1393nm). The presence of sericite, alunite and kaolinite is not significant. The 1900 absorption feature is due to the presence of free water.

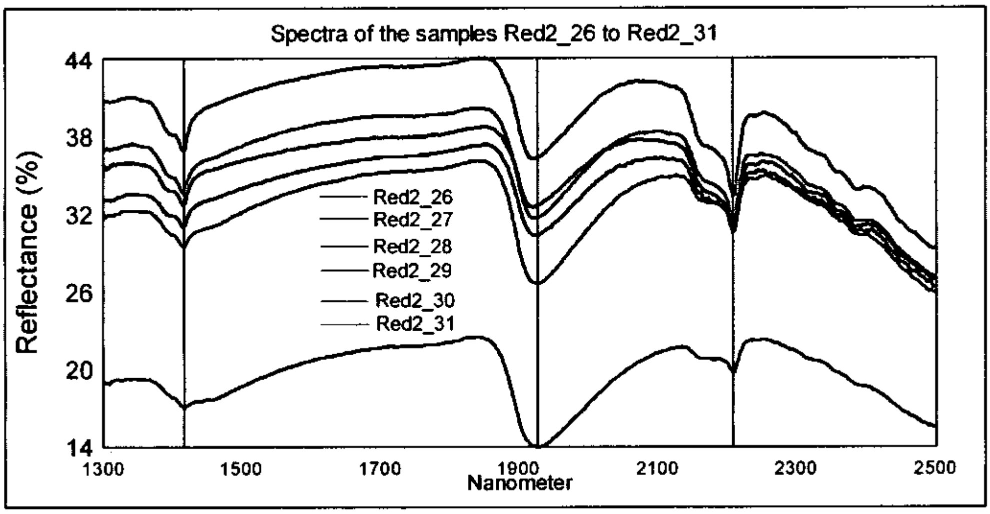

Figure 6 – 15e. Reflectance spectra of the samples Red2_26 to Red2_31
Note the similarity of the spectra representing mainly halloysite/kaolinite (absorption at 2208nm doublet and smaller doublet at 1393nm). The presence of sericite, alunite and kaolinite is not significant. The 1900 absorption feature is due to the presence of free water.

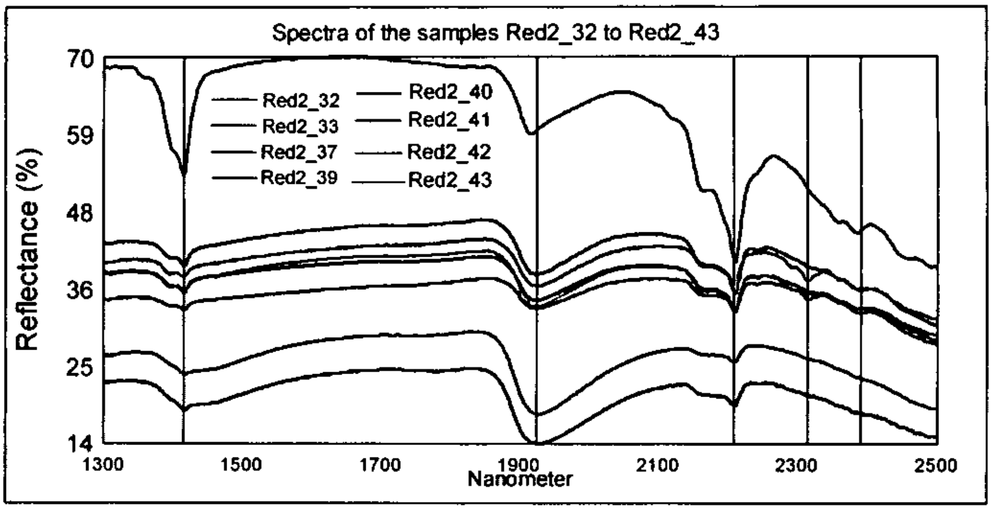

Figure 6 – 15f. Reflectance spectra of the samples Red2_32 to Red2_43

Note the similarity of the spectra Red2_32 to Red2_43 representing mainly halloysite/kaolinite (absorption at 2208nm doublet and smaller doublet at 1393nm). Exception is the sample Red2_41 that contain phengite (absorption at 2210 and 1412 nm). The presence of sericite, alunite and kaolinite is not expressive. The 1900 absorption feature is due to the presence of free water.

Figure 6 – 16 indicates that five mineral fields are present in the samples from the profile Sp_Red2, which are kaolinite, talc, sericite, alunite and water.

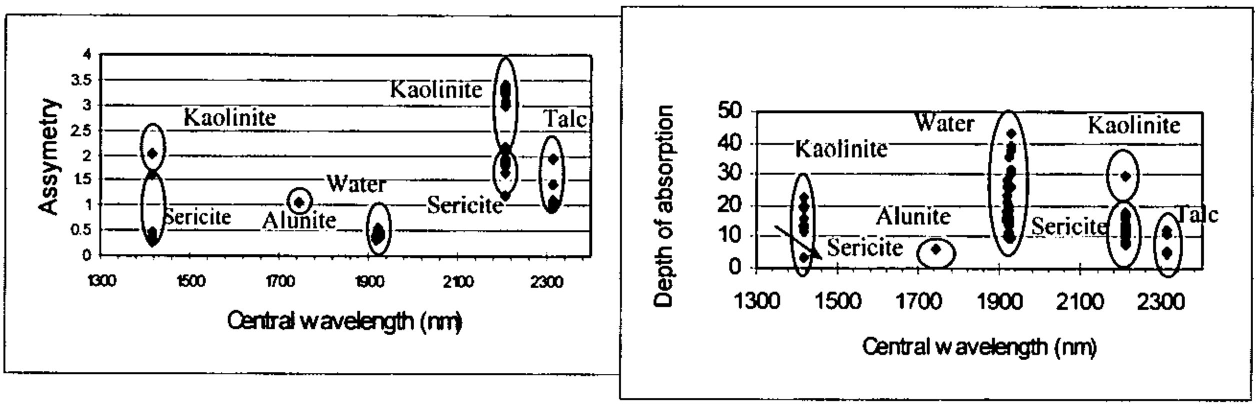

Figure 6 – 16. Mineral field identification using the asymmetry index and absorption features or the profile Sp_Red2. The arrows indicate the position of specific mineral. For distribution of these samples across the profile refer to Fig. 6 – 21.

6.3.5 Interpretation of the Results

The reflectance parameters (e.g. absorption feature) and the asymmetry index are important parameters for the identification of the minerals in each sample but have proved to be of less significance when it comes to map shear zones and associated alteration, mainly due to mineralogical mixture reflected in the spectrum and to the limited amount of minerals revealed by this technique. Therefore, a different approach was adopted which considers the percentage of each mineral in the mixture in order to identify differences in proportion and distribution of minerals resulting from the presence of shear zones. Fig. 6 - 17 shows that samples Sp8/04/99 and Sp8/8/99 are anomalous compared to the rest of the profile. These samples were collected next to the Dots Luck open pit, which may suggest a contamination from the mining activity.

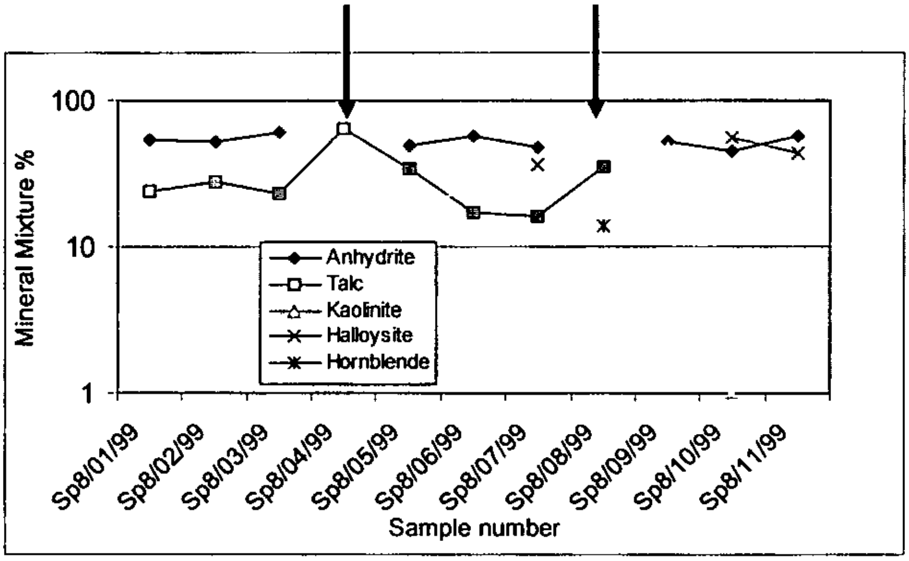

Figure 6 –17. Mineralogical variations across the profile Sp8
Note the presence of anomalies on Sp8/04/99 and Sp8/08/99 and Sp8/09/99. Black arrow shows the position of the shear zones

The profile Sp/GF (Fig. 6 – 18) illustrates that the sample Sp/GF/04 is mineralogically anomalous, presenting only talc and kaolinite. Considering that the sample was collected next to the Guy Fawckes open pit mine, it may suggest a contamination of the soil due to mining, thus the absence of anhydrite, a typical mineral in highly sulphurdised deposits such as Guy Fawckes. Some of the incompatible minerals shown in the samples suggest contamination presumably by mining activity or agriculture.

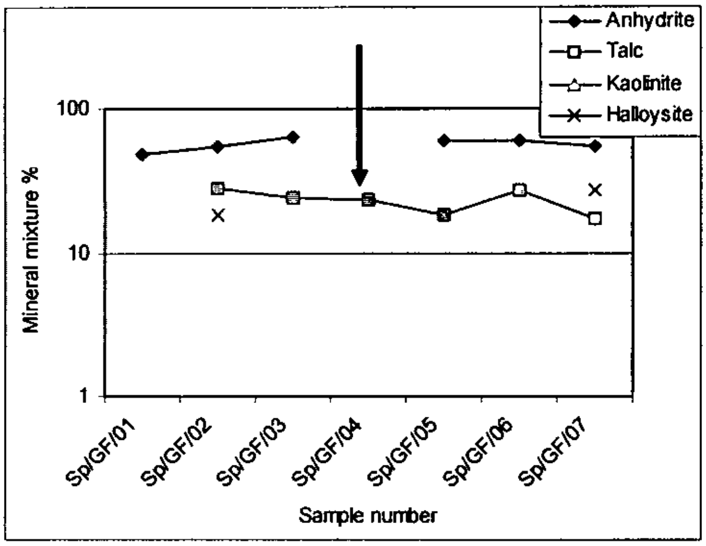

Figure 6 – 18. Mineralogical variations across the profile Sp/GF
Note the presence of an anomaly on the sample Sp/GF/04. Black arrow shows the position of the shear zone as mapped by previous authors

The soils above of the contact between the granites and the Bulawayan rocks were expected to have a combination between these two lithologies. The samples (Fig. 6 – 19) Sp1/01 to Sp1/04 were collected on the granitic side of the contact and the sample Sp1/05 on the expected contact, samples Sp1/06 to Sp1/09 were collected from basaltic soil, and the rest of the samples come from the old mine dump.

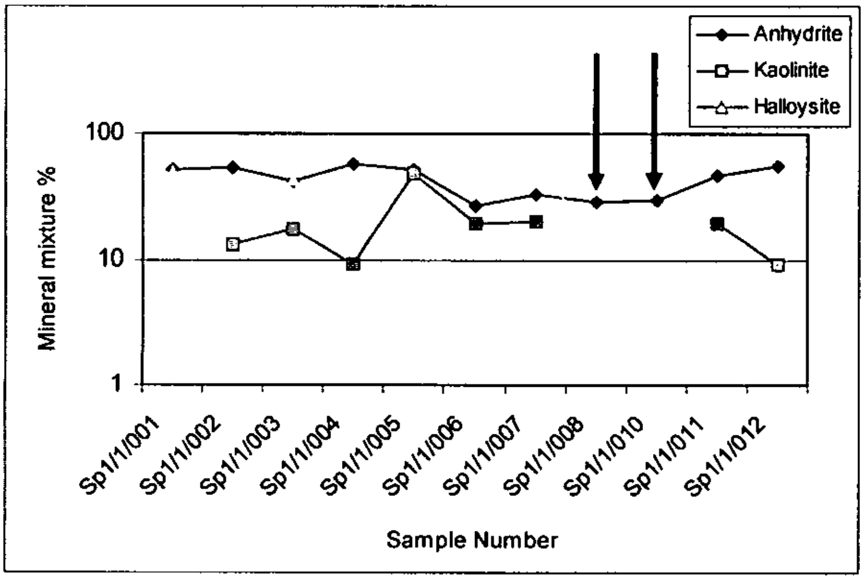

Figure 6 – 19. Mineralogical variations across the profile Sp1
Note the presence of anomalies on samples Sp1/1/005, Sp1/1/010 and Sp1/1/11. Black arrow shows the position of the shear zone as mapped by previous authors

The samples 34/Sp/Rw to 36/Sp/Rw were collected above the shear zone (see also Fig. 6 – 1) and according to the profile Sp/Rw shown on Fig. 6 – 20 these samples have different mineralogical composition. It is not clear at this stage whether this difference is due to presence of shear zone or to other influences. The sample 41/Sp/Rw to 43/Sp/Rw were collected over the Penhalonga granodiorite.

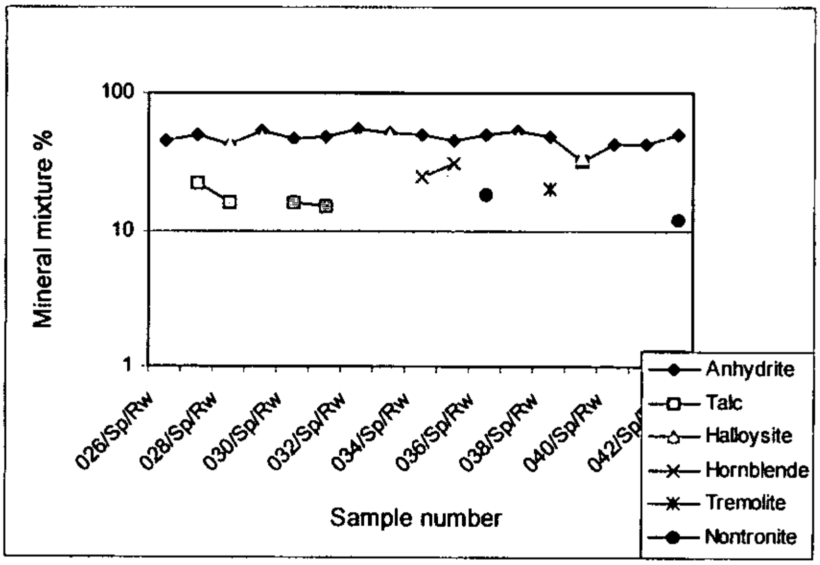

Figure 6 – 20. Mineralogical variations across the profile Sp/Rw

The profile Sp_Red2 (Fig. 6 – 21) transect different rocks ranging from northern ultramafic schists (Sp_Red2_1 to Sp_Red2_15), Penhalonga granodiorite (Sp_Red2_17 to Spr_Red2_32), southern ultramafic schists (Sp_Red2_37 to Sp_Red2_43), a disturbed mine area including old mine dump (Sp_Red2_34 to Sp_Red2_36) and a contact between granodiorite and the ultramafic schists (Sp_Red2_16). All these sections of the profile present different minerals at varying proportions, which probably can be related to the lithologies underneath.

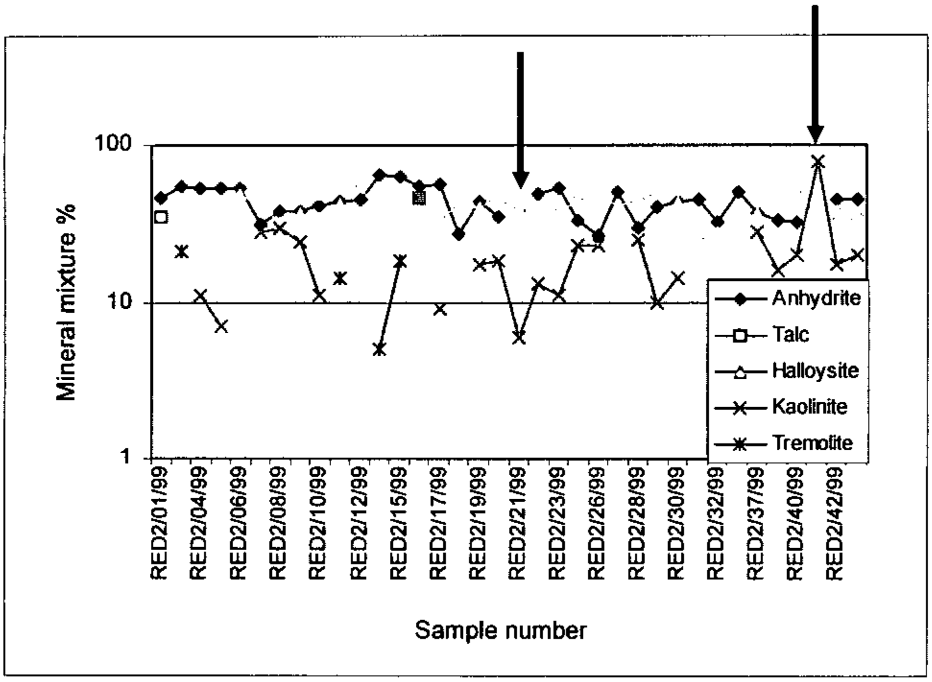

Figure 6 – 21. Mineralogical variations across the profile Sp_Red2.
Black arrow shows the position of the shear zone as mapped by previous authors.

6.4 Discussion

Three methods on how to identify minerals using PIMA were presented. The first method identifies minerals by comparing the spectrum generated by PIMA for each sample with USGS reference library spectrum. The best match resolves the sample spectrum and provides a semi quantitative analysis where the proportion of each mineral is given in percentage.

The second method considers the deepest absorption feature of the spectrum and its wavelength position. In this method minerals are identified on the basis of their field position on scatter plot. Although this method can successfully discriminate the main fields of talc, chlorite, nontronite, and actinolite, it fails to discriminate overlapped fields such as kaolinite – sericite fields.

A third method was devised to resolve overlapping fields. This method uses the scatter plot of asymmetry versus wavelength.

In this chapter it was shown that scatter plots could be used to characterise fields of occurrence of specific minerals although overlaps may occur. The absorption features and the asymmetry index demonstrated to be valid instrumental techniques for mineral identification. However, it also proved to be of little use for mineral mapping and illustration of the mineralogical trend across the shear zones. This is mainly due to the mineral fields overlap that occurs on the scatter plots, which depend on the several element ratios that influence the position of specific mineral in the plot. For example the position of the main absorption features that diagnose kaolinite partially overlap with the main absorption features that identify the sericite/illite (see also Figs. 6 - 10, 6 – 15, 6 – 18 and 6 – 21). These two minerals could only be distinguished on the basis of the asymmetry index because the sericite tend to have low asymmetry indices (usually less than 2).

The PIMA results do not quite agree with the petrological studies of thin section mainly because the PIMA analysis is performed in a single point of 2 mm by 10 mm, which can be a single mineral while the thin section is much larger area. And the fact that the PIMA only characterize the mineral in the SWIR region of the spectrum, which means it leaves many minerals such as quartz unidentified, these minerals may constitute the main elements in the rocks. Researchers have been arguing the need for carrying out PIMA analysis instead of collecting samples and making thin sections for petrological analysis. This view is not correct so is any attempt to validate the PIMA results using petrological analysis because the idea of field spectrometer is to have quick analysis of specific important minerals during the field exploration while the petrological studies are expected to be carried out at late stages of the exploration program. The petrological studies will provide both quantitative and qualitative data while the PIMA data are indicative and provisional.

In the MMO greenstone belt the presence of pervasive talc and anhydrite as main weathering products makes their use for characterisation of mineralised shear zones very difficult. These minerals interfere on the spectra in such a way that the identification of other minerals present in smaller quantities is difficult.

Profiles of spectral data crosscutting perpendicularly the shear zone is a powerful instrumental method that allows characterization of the spectral changes caused by the presence of the shear zones. In this study some indicative anomalies are observed on the profiles Sp1, Sp8, Sp/Rw, Sp_Red2 and Sp/GF. The observed changes in the profiles Sp8, Sp_Red2 and Sp/GF may be a result of the disturbance due to mining. However, the spectral and mineralogical variations shown in the profiles Sp1 and Sp/Rw are due to different causes, which could be, among other reasons, the presence of the shear zones. It is interesting to understand that the differences observed on the mineral assemblages profiles are not evident on the spectral profiles presented in the section 6.3.2.

The mapping of shear zones, felsic intrusions, Bulawayan – Shamvaian contact, Bulawayan – granites contact was performed using the three methods described in the section 6.3.1. The mineralogical variations occurring due to presence of shear zones or due to presence of a contact are plotted in Figs 6 – 17, 6 – 18, 6 – 19, 6 – 20 and 6 – 21.

The Fig 6 – 17, samples Sp8/04/99 and Sp8/09/99, and Fig.6 – 18 (sample Sp/GF/03) show that the shear zones are characterized by anomalies of kaolinite and talc with absence of anhydrite and halloysite.

The Fig. 6 – 19 shows an anomaly of kaolinite and anhydrite without halloysite on the sample Sp1/1/005. While the anomalies in the profile Sp/Rw (Fig. 6 – 20) are characterised by presence of talc, as seen in the samples number 027/SP/Rw, 028/Sp/Rw, 030/Sp/Rw, and 039/Sp/Rw. The presence of talc suggests anomaly in the profile Sp_Red2 (Fig. 6 – 21) as shown in samples RED2/01/99 and RED2/16/99.

The results shown in the profiles Sp1, Sp8, Sp/Rw, Sp_Red2 and Sp/GF suggest two types of anomalies related to shear zones, one characterised by presence of talc and kaolinite (e.g. Sp8 and Sp/GF) and the other characterised by presence of talc only (e.g. Sp/Rw and Sp_Red2). This shows clearly that the soil profile plays an important role in the type of anomaly because the first type of anomaly is related to the samples collected in the Manica part of the belt and the second type of anomaly is from samples collected in the Mutare part of the belt. As already mentioned elsewhere in this thesis that the Manica and Mutare parts of the belt are different in the weathering profile. This simply means that the PIMA analysis are to be conducted separately for the two parts of the belt.

The next chapter discuss how the PIMA results can be used to improve satellite imagery interpretation for mapping of mineralised structures such as shear zones.

6.5 Conclusions

- Most of the common mineral assemblages occurring in the soils or rocks of the MMO greenstone belt can be distinguished on the basis of the interpretation of spectral information on the SWIR and using the scatter plot of asymmetry index and deepest absorption feature percentage reflectance.
- The study has shown that the use of mineralogical assemblages in the MMO greenstone belt and probably in most greenstone belts situated in the tropics, is not conclusive due to weathering which produces minerals such as talc, kaolinite, chlorite, anhydrite and little sericite at the surface. Minerals such as alunite, important for the mapping of shear zones are present in very small amounts, and in general all spectra are affected negatively by presence of organic matter, lime, iron oxides and vegetation (e.g. roots).

- The PIMA analysis supports the fact that the Manica and the Mutare parts of the MMO greenstone are different in regard to soil profile. In the Manica the anomalies related to the shear zones are characterised by presence of talc and kaolinite without halloysite or anhydrite, while in the Mutare the shear zones are characterised by presence of talc.

- Profiles of spectral data crosscutting perpendicularly the shear zone have shown to be an important instrumental method that allows characterization of the spectral changes caused by the presence of the shear zones. The changes observed in the profiles Sp1, Sp8, Sp/Rw, Sp_Red2 and Sp/GF are not conclusively known to be related to hydrothermal activities in the shear zones, but the fact that they are there suggest that it is worth checking on the ground during exploration.

- The study showed that the PIMA spectrometer could particularly be used in the field for mapping of mineralised shear zones during exploration programs in the MMO greenstone and similar environments. The study proved that PIMA analysis could be important for validation of the existence or not of shear zones, which could have been defined on the basis of satellite imagery interpretation. This was observed in all profiles that crossed known shear zones which have shown anomalies on top of the shear zones.

- The study has also shown that PIMA data are only provisional for preliminary stages of exploration programs and this type of data bear the advantage of fast mineralogical results in the field.

Chapter 7

7 PIMA Spectral reflectance compared to satellite images (ETM and TM) for shear zones mapping in gold exploration

7.1 Introduction

This chapter discusses the comparison between Landsat imagery and the Portable Infrared Mass Spectrometer (PIMA) spectral reflectance. Emphasis is placed on understanding whether or not PIMA results can be used to improve the quality of interpretation of Landsat TM or ETM by resolving the mixture of the material represented in a pixel.

Several studies have been carried out on the development of multispectral scanners (e.g. Landsat TM or ETM) separated from the development of the hyperspectral scanners (e.g. PIMA, Airborne Visual and Infra-Red Imaging Spectrometer (AVIRIS)). Less work has been done on the combination of the two systems or use of the hyperspectral data to improve the spectral and spatial quality of the multispectral data.

Clark (1999) has shown that the spectrometry identifies more accurately minerals such as alunite than the Landsat Thematic Mapper (TM) or Moderate Resolution Imaging Spectroradiometer (MODIS) (Fig. 7 - 1). An important factor when comparing the spectra is the resolution of the spectrometers. PIMA spectrometer has a resolution of 7nm, which gives enough precision to record details in the spectrum.

The principal difference between multispectral scanners like TM and spectrometers like PIMA is that with PIMA and similar spectrometers can identify materials (e.g. minerals) whereas with multispectral scanners could only discriminate between materials (e.g. sandstone being different from basalt). The PIMA measures single point in a sample and its result generally is not displayed as an image. The combination of ETM and TM images with PIMA data has also the disadvantage imposed by restriction to SWIR bands (band 5 and band 7) due to spectral bandwidth of the PIMA spectrometer (1,3 μm to 2,5 μm). The PIMA produces a continuous spectrum between 1,3 μm and 2,5 μm which is an advantage for mineral identification. Spectrally the Landsat

TM or ETM pixel represents an average reflectance of specific bandwidth at resolution of approximately 100nm.

In general the spectroscopy has an added advantage of being sensitive to both crystallinity and amorphous materials and the capability of being used in the laboratory or from space. Nevertheless the spectroscopy has the disadvantage of being too sensitive to small changes in the chemistry and/or structure of materials (Clark, 1999). This disadvantage is nowadays turning into a major advantage, allowing analyses of more detailed changes due to chemical variations, which might be related, in the case of geology, to hydrothermal alteration.

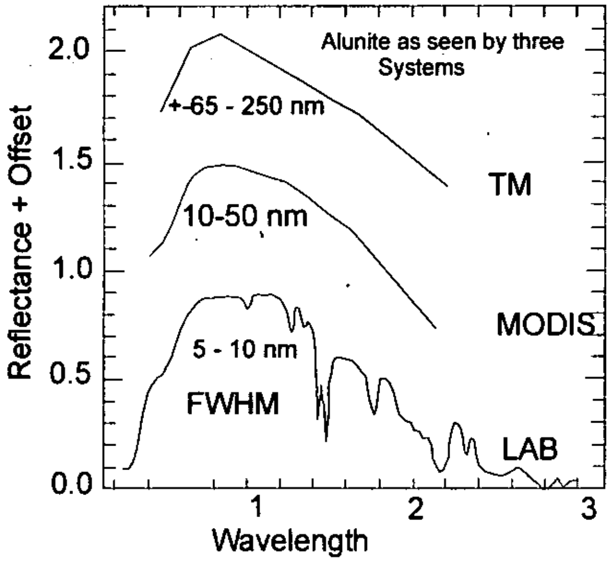

Figure 7 – 1. Spectra of the mineral alunite are shown as measured in the laboratory and for broadband remote sensing instruments (TM and MODIS).
The FWHM is the Full Width at Half Maximum. Sample HS295.3B from the USGS spectral library. Each spectrum is offset upward 0.6 units from the one below it for clarity (Clark, 1999).

The satellite imagery contrary to the PIMA data is affected by presence of vegetation and atmospheric conditions (e.g. % of humidity).

7.1.1 Effect of Vegetation on Satellite imagery

Vegetation influences the satellite imagery in two distinct forms, which can be considered end-members, dominate a spectrum of vegetation: green and wet (photosynthetic), and dry (non –photosynthetic) (Clark, 1999). He also argued that there is a seemingly continuous range between these two end-members. Clark (1999) justified the similarity of the spectra as caused by all plants being made of the same basic components.

For a typical spectrum of green vegetation (Fig. 7 - 2), reflectance increases drastically (from visible to near-infrared light) at about 0.7 µm (band 4 TM; 0.76 – 0.90 µm).

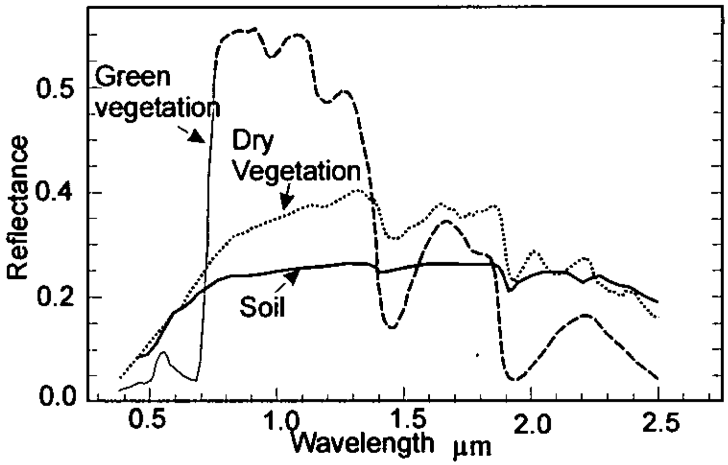

Figure 7 – 2. Reflectance spectra of photosynthetic (green) vegetation, non-photosynthetic (dry) vegetation, and soil.
The green vegetation has absorptions shot at 1 µm due to chlorophyll. Those at wavelengths greater than 0.9 µm are dominated by liquid water. The dry vegetation shows absorptions dominated by cellulose, but also lignin and nitrogen. These absorptions must also be present in the green vegetation, but can be detected only weakly in the presence of the stronger water bands. The soil spectrum shows a weak signature at 2.2 µm due to montimorillonite (after Clark 1999).

Considering that about 15% of the study area is covered by pine forest; bands TM 3 (visible – 0.63 – 0.69 µm), band TM4, band TM5 (1.55 – 1.75 µm) and band TM7 (2.08 – 2.35 µm) have been combined in order to distinguish vegetated-areas from soil and rocks in the area. The mathematical expressions that relate TM or ETM bands 3, 4, 5 and 7 is based on maximising the reflectance of vegetation in band 4 where it yield high values and minimise its reflectance in band 3 where vegetation produce low reflectance are as follows:

(TMb4 * TMb5)/(TMb3 * TMb7) (this study) (7 – 1)

and

(TMb4 – TMb3)/(TMb3 + TMb4) (ILWIS Users Guide) (7 – 2)

Where, TMb3 is Landsat TM band three

The expression (7 - 2) is regarded as Normalised Difference Vegetation Index (NDVI), which yield results between –1 and 1. Typically, vegetated areas will have high values due to relatively high reflectance in the near infrared (TMb4) and low reflectance in visible light (TMb3) (Fig. 7 - 3). The rocks and bare soil areas will have values, which are near zero due to similarity in reflectance of these materials in the visible and near infrared range. Finally the negative values will represent water bodies and clouds due to their high reflectance in the visible band compared to near infrared. Expressions 7 – 1 could be used to give similar results as long as the principle of comparing visible (red band) and near infrared spectra is observed and when spectral differences can be strengthened. In the MMO greenstone belt, the highly vegetated zones (Fig. 7 – 3) were excluded from the search for alteration patterns or mineralised shear zones because it was observed that the artificial plantations were not related to particular lithology. Another reason for not using these zones relates to thick soil profiles associated with these areas of plantations, which made it difficult to map for structures using remotely sensed data or ground spectrometry.

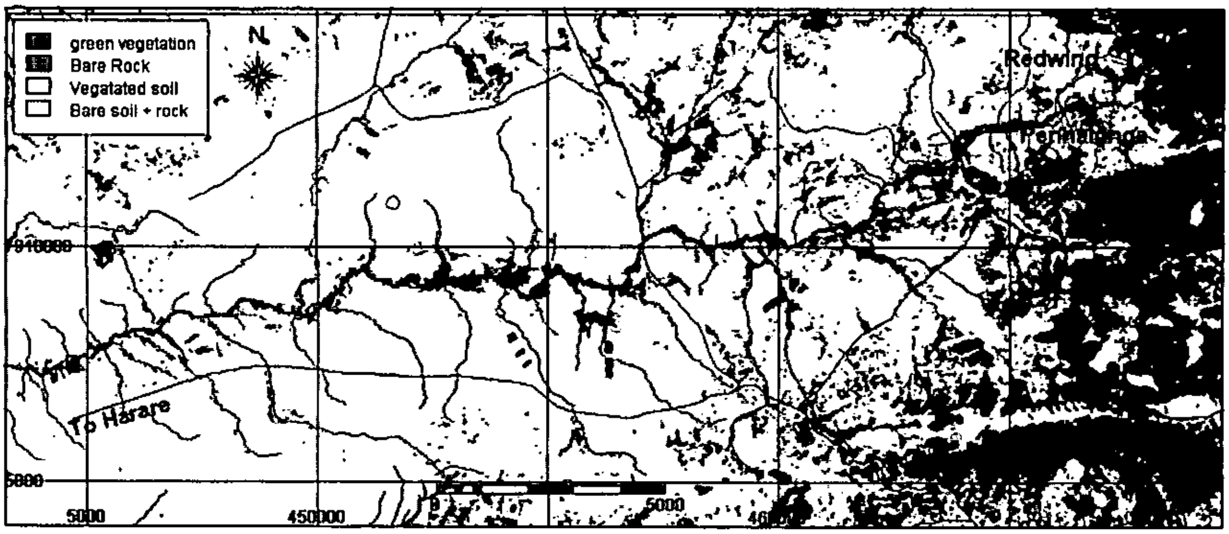

Figure 7 – 3. Image showing highly vegetated areas in green (pine plantation and dense vegetation along the rivers) in the MMO region. Map calculated from expression 7 – 1 (ETM4*ETM5)/(ETM3*ETM7), and the result was sliced in order to improve the visual impression of the image as <0.4 green vegetation, 0.4 – 0.9 Bare rock; 0.9 – 0.97 Vegetated soil; 0.97 – 1.0 Bare soil or rock.

The NDVI is widely used in the qualitative estimation of vegetation using the satellite imagery (e.g. Townsend and Justice, 1986). The application of NDVI for quantitative analyses requires corrections, especially the conversion of digital numbers into apparent reflectance (Guyot and Gu, 1994, Lupankwa, 1999).

NDVI gives a qualitative indication of the amount of vegetation present in each pixel. This indication is important for the assessment of reflectance due to vegetation and that resulting from soil or rock obtained by PIMA spectrometer. The fact that the NDVI is partially a difference and partially a ratio gives an added advantage of reducing the spectral variations of the incoming radiation. The main disadvantage in the use of NDVI lies in the pixel cover mixture where the influence of soil and rock affect its result. Several authors (e.g. Elvidge and Lyon 1985; Huete et. al., 1985, Lupankwa, 1999) have studied this influence and concluded that its complexity is mainly due to collateral factors such as moisture content, surface roughness, relief and organic matter content which contribute significantly to the scattering of the incoming radiation, and the partial coverage of the pixel by vegetation which originate mixed pixels. The topic is so complex that Huete (1988) introduced the Soil Adjusted Vegetation Index as a way to minimise the problem of soil background in the NDVI. The Huete index introduces a constant factor dependent on the Leaf Area Index (LAI) that is calculated from tables.

In this study it was not quantified the amount of vegetation per pixel, thus the problems of soil background which would require the use of Soil Adjusted Vegetation Index (SAVI) are not addressed. Interested readers may refer to Huete (1988) for more detail.

7.1.2 Effect of Humidity on satellite imagery

The other important factor for the estimation of the true reflectance of the samples (soils or rocks) or ground is the amount of moisture contained in the atmosphere and on the ground. The water reduces the spectral reflectance especially on the wavelengths greater than 700 nm, which are the most important for PIMA analyses (i.e. 1300 to 2500 nm). The effect of water on the atmosphere was reduced during the atmospheric correction performed on the satellite imagery is such a way that the satellite data represent real reflectance of the ground surface. The atmospheric correction was not done for the PIMA samples because the analyses were carried out in the laboratory. The effect of water (moisture) on the ground can be qualitatively evaluated from rainfall data during the period of collection of the samples. Table 7 - 1 shows rainfall data for the study area for the months when the remotely sensed data was collected. The Table 7 –1 indicate that throughout the acquisition period the area did not receive any rainfall.

Table 7 – 1. Rainfall at the date of the acquisition of the satellite imagery and monthly average for the fieldwork days, in mm. The monthly average is arithmetic mean of the daily rainfall.

	Oct. 94	***Jul-99***	***17-Nov-99***	***25-Apr-00***	***Jul-00***
TM	0mm				
ETM			0mm	0mm	
Fieldwork		0mm			0mm
Rainfall ave.	0mm	0mm	0mm	0mm	0mm

Table 7 - 2 shows the average daily Relative Humidity (%) based on the hourly Synoptic(1) observations and the date of acquisition of the satellite imagery and field data (samples) month are highlighted.

Table 7 – 2. Rusape daily Relative Humidity (%) based on the hourly Synoptic Observations

	1994	1994	1999	1999	2000	2000
Day	Jul	Oct	Jul	Nov	April	July
1	73	60	54	57	86	78
2	85	58	53	53	91	90
3	77	45	64	56	85	74
4	63	47	73	51	80	75
5	59	80	74	39	80	75
6	59	71	74	51	89	73
7	72	62	74	58	90	76
8	60	46	73	53	78	75
9	57	46	79	83	72	84
10	55	40	74	75	82	77
11	66	42	63	74	80	73
12	70	52	73	62	77	76
13	64	74	92	55	72	64
14	70	84	76	58	72	71
15	65	86	58	42	87	63
16	74	98	53	47	88	55
17	66	93	48	42	79	54
18	74	89	46	48	77	47
19	66	78	75	70	80	40
20	67	64	75	89	75	39
21	65	48	76	82	78	56
22	61	57	63	85	74	71
23	56	70	58	85	67	77
24	50	67	58	82	59	71
25	40	58	61	81	58	65
26	37	55	63	74	54	73
27	38	46	59	62	47	66
28	76	50	54	60	79	65
29	69	59	53	56	91	58
30	75	72	52	67	80	58
31	71	88	44			61
Average	64	64	64	63	77	65

(1) The synoptic hours are 02:00, 06:00, 08:00, 11:00, 14:00, 17:00 and 20:00 hours

Source: Actual readings from the monthly records of the meteorological stations in Russape

Thus, deducing qualitatively the influence of rainfall and relative humidity during the acquisition of the satellite data and the vegetation index values, theoretically reflectance values (on the band TM5 and TM7) close to the real values of the ground without vegetation could be obtained. This reflectance would be similar to the one obtained from PIMA if the spectral and spatial resolution of the two systems (Landsat and PIMA) were similar.

7.2 Method, Data presentation and analyses

To properly compare the PIMA reflectance spectra with the conventional satellite imagery (e.g. Landsat TM or ETM) data, the data sets must be sampled at the same wavelengths and resolution.

The hull quotient PIMA spectra were stretched, gridded and resampled to TM or ETM with bandwidth centred at 2225 nm and 1650 nm for band 7 and 5 respectively. Gridding of a spectrum is to fit a square grid on the spectrum in order to reference all spectra to the same co-ordinate system. The resampling operation involved proportional weighted-average of the bandwidth wavelength and assigning the value to the band centre, and the transformation of reflectance values in a range between minimum and maximum wavelength of the TM or ETM bands 5 and 7 equivalents on the PIMA spectrum. The results of resampled PIMA spectrum are two values corresponding to TM band 5 and 7 equivalent bands.

Data from October1994 TM, November 1999 and April 2000 ETM images band 5 and 7, the equivalent Normalised Difference Vegetation Index (NDVIs), the resampled PIMA spectral reflectance values for the equivalent band 5 (band centre 1650nm) and 7 (band centre 2250nm) are retrieved and displayed simultaneously through the "pixel information window" in ILWIS v.2.2. This information is entered into the database and is further processed in Excel (Appendix VIIA). The TM or ETM bands 5 and 7 are selected due to their position (SWIR) on the spectrum and they mainly detect the following (Sabins, 1987):

- TM band 5 (1,55 µm – 1,75 µm) detects moisture content of soil and vegetation and it allows good contrast between vegetation types.

- TM band 7 (2,08 µm – 2,35 µm) coincides with an absorption band caused by hydroxyl ions in minerals (see also Chapter 7 section 7.1 and 7.2).

The ratio of bands 5 and 7 is potentially useful for mapping hydrothermally altered rocks associated with mineral deposits (e.g. Herrmann et al., 2001).

To minimise the effect of the spectral and spatial differences between Landsat and PIMA, band ratios were used to compare the two systems. As shown in Clark et al. (1990) band ratios are sensitive to the relative absorption in a spectrum at two wavelengths. The ratio approach has the advantage of compensating for the brightness variations caused by variations on illumination conditions and topography for the TM and ETM imagery and, by lithological mixing for the PIMA (Herrmann, et al., 2001). Other analysts including Sabins, 1987, Lillesand and Kiefer, 1987 contend that the ratio also emphasises differences in slopes of the spectrum. Band ratios are affected by the amount of organic carbon in the soils (e.g. Stoner and Baumgartner, 1981 and Goossens, 1992).

The figure 7 – 4 shows TM and ETM band 5 and band 7 ratio for the 8 soil sample profile (see Fig. 6 – 1) in the MMO greenstone belt stack plotted together with NDVI and absorption ratio from resampled PIMA values.

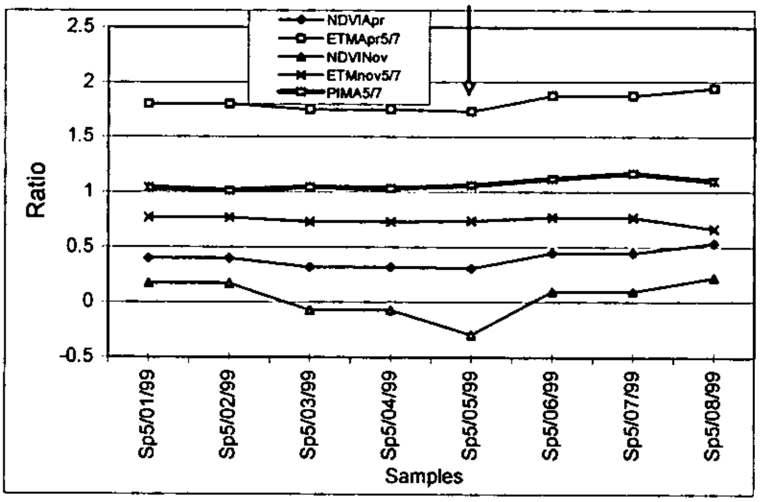

Figure 7 – 4. Graphical representation of the ratios ETM Nov. 99, ETM Apr. 00 and PIMA bands 5 and 7 and, NDVI April and November for the soil profile SP5. The red arrow represents the position of interpreted BIF.

The reflectance percentage of the same profile (Sp5) was plotted as shown in Fig. 7 – 5 for comparison with ratio method and it proved to be significantly less consistent compared to the ratio method.

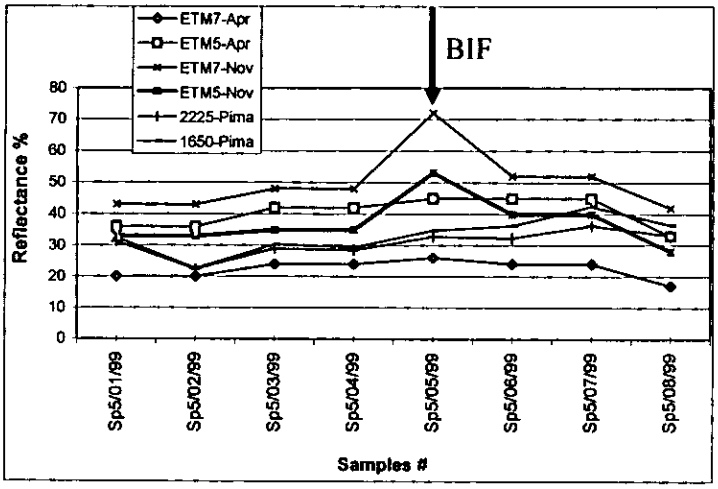

Figure 7 – 5. Graphical representation of the comparison of the radiance of the Landsat images ETM Nov., ETM April and PIMA bands 5 and 7 for the soil profile SP5.

The other analyses that was used to detect shear zones, particularly those associated with ironstones, was the iron parameter plotted against sample numbers as appears in Fig. 7 – 6. The iron parameter is equivalent to weighted average absorption (%) in the wavelength between 1350 and 1700 nm, for each sample that were used for PIMA analyses. Pontual et al. (1997c) demonstrated that the iron parameter could be used to map iron rich minerals (actinolite and Fe-carbonate) in either side of shears zones in greenstone belts. High index of the iron parameter suggest presence of iron rich minerals (e.g. actinolite, Fe-Carbonate). The background values for this index depend on the lithology type present, thus the importance of presenting this results in graphic form (e.g. Fig. 7 – 6).

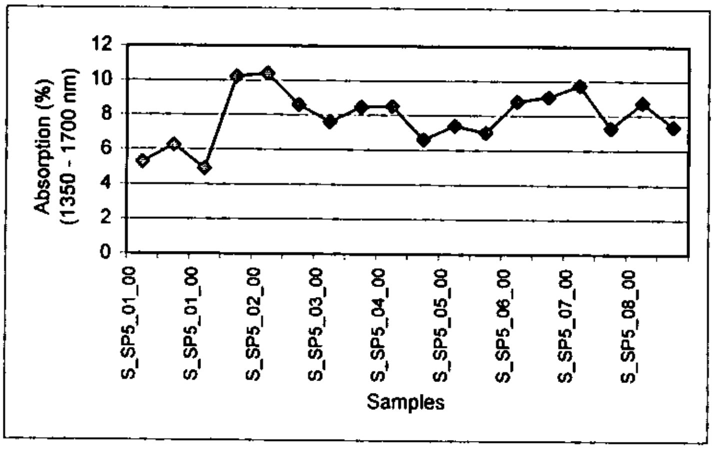

Figure 7 – 6. Graphical representation of the iron parameters for each sample in the soil profile SP5.

The fact that the Iron parameter is calculated from a wavelength that does not coincide with any Landsat band. The Landsat band 5 (5 (1550 – 1750 nm) has only an overlap of 41.7% with iron parameter zone fact which prevent the use of this parameter to improve satellite imagery data.

7.3 Results and Interpretation

7.3.1 Results

Figure 7 - 4 is an example of a typical soil sample profile across a gold deposit in the Manica area and represents the ratios ETM Nov. 99, ETM Apr. 00 and PIMA bands 5 and 7 and, NDVI April and November for the soil profile SP5. The graph shows that the PIMA ratio is always higher than the ETM November ratio and lower than the April ratio. The November NDVI is always lower than the April ratio (see also Appendix VII), and this is because in November there is less fresh vegetation compared to April.

Ratio comparison of Landsat imagery and iron parameter analyses were carried out for the other shear zones including the shear zones near the contact between Bulawayan and the granite (e.g. Figs. 7 – 7 and 7 - 8), the shear zones near the Penhalonga granodiorite (e.g. Fig. 7 – 9 and 7 - 10) and the presence of the Penhalonga granodiorite (e.g. Fig. 7 – 12 and 7 - 13).

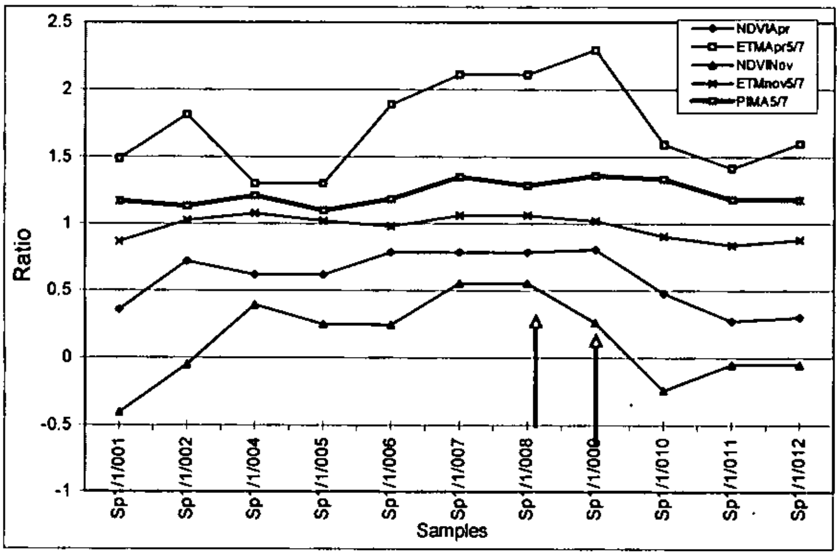

Figure 7 – 7. Graphical representation of the ratios ETM Nov. 99, ETM Apr. 00 and PIMA bands 5 and 7 and, NDVI April and November for the soil profile SP1. The red arrows show the position of shear zones as mapped by earlier authors.

The Fig. 7 – 8 shows the Fe^{2+} response and highlights the spatial occurrence of Fe-carbonate on one side of the interpreted shear zone.

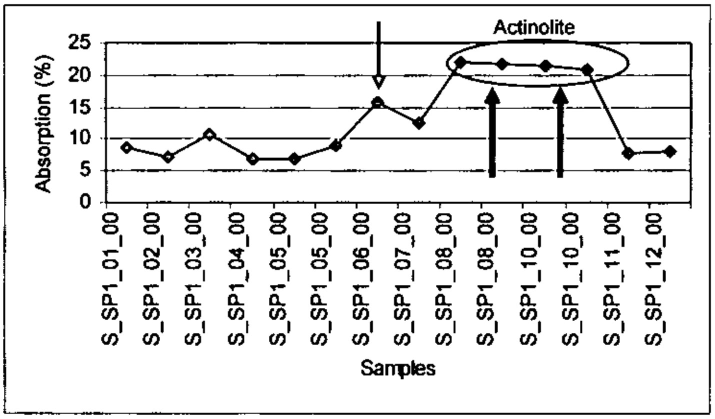

Figure 7 – 8. Iron parameters for the profile Sp1 in the Manica part of the MMO belt. The red arrow represents the interpreted BIF. The black arrows show the position of shear zones as mapped by earlier authors.

The example of integrated data ratio illustrated in Fig. 7 – 9 demonstrate the accuracy of the method in mapping shear zones as interpreted on Fig. 6 – 12.

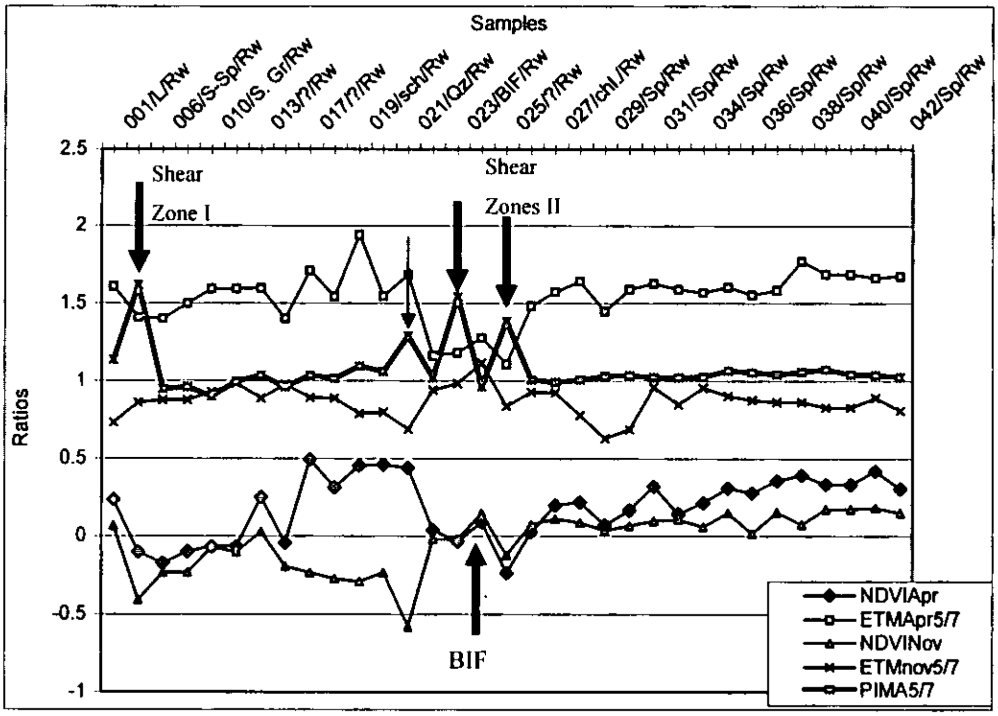

Figure 7 – 9. Graphical representation of the ratios ETM Nov., ETM Apr. and PIMA bands 5 and 7 and, NDVI April and November for the soil profile SP_Rw1.

A spectral parameter has been calculated to show the Fe^{2+} response in all samples considered in Fig. 7 – 9. The result presented in Fig. 7 – 10 illustrate that the shear zones interpreted in position around sample 23 have high Fe^{2+} response. The high expression of this anomaly minimised the response of the other shear zones previously interpreted on Fig. 7 – 9 position sample 3 to 4. A second anomaly is observed on position around sample 34, which has not been mapped by the integrated ratio method, regardless to its interpretation on the geological map (Fig. 6 – 12). This aspect demonstrates that the iron parameter method is more sensitive to presence of Fe-carbonate minerals, which can be associated to shear zones than the ratio method.

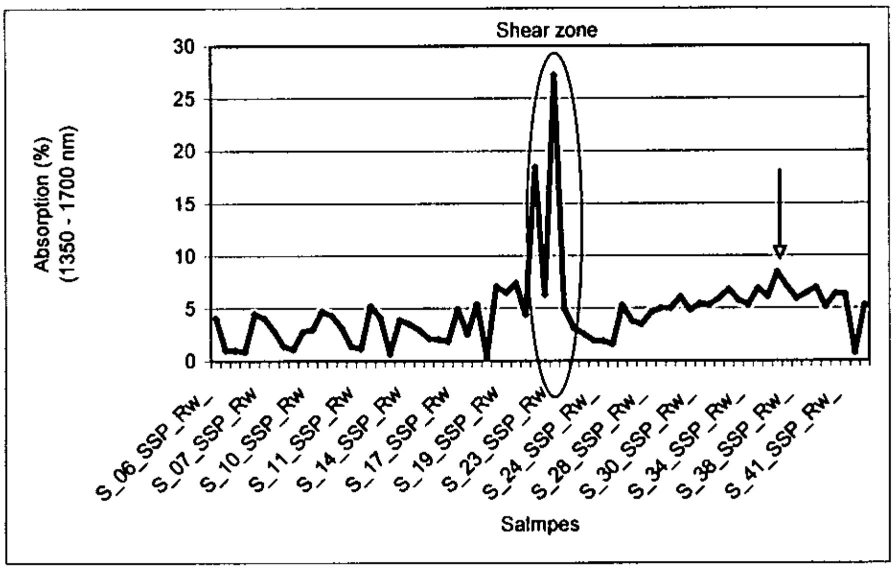

Figure 7 – 10. Iron parameters for the profile Sp/Rw in the Mutare part of the MMO belt. The red arrow points to an interpreted shear zone position.

The profile RED02 was drawn is such a way that it would map the contact between the Bulawayan basalts and the Penhalonga granodiorite (Fig 6 – 12). The result shows that the contact zone positioned around sample 10 – 12 is characterised by change in iron response from high to low and similar pattern is observed in the ratio analyses of the PIMA data. This result demonstrates that the iron parameter and integrated ratio methods can be used for mapping lithological contacts. The anomalies in Fe^{2+} observed in plot (Fig. 7 – 12) position around sample 18, 22, 33 and 41 are interpreted as enrichment of Fe-carbonate minerals along known (samples 41 and Fig 6 - 12) and unknown (samples

18, 22, 33) fracture zones. The ratio method only distinguishes the samples 18, 22 and 41 as anomalous (Fig. 7 – 11).

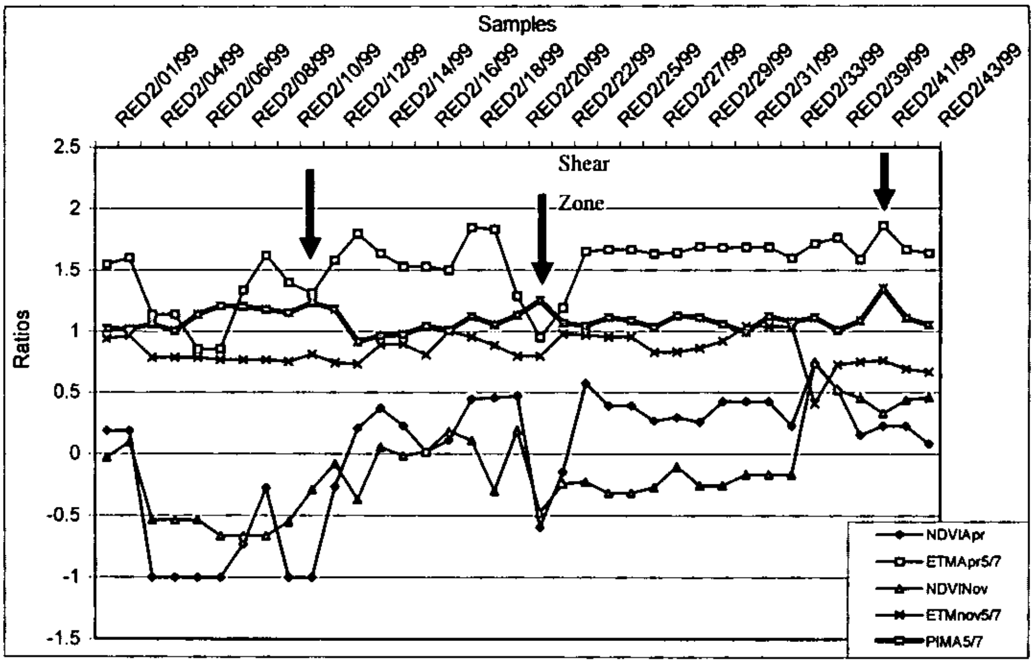

Figure 7 – 11. Graphical representation of the ratios ETM Nov., ETM Apr. and PIMA bands 5 and 7 and, NDVI April and November for the soil profile SP_Red2.

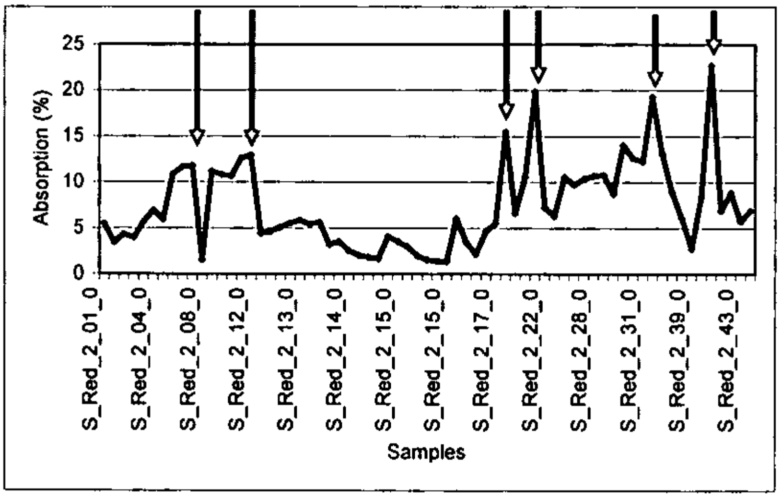

Figure 7 – 12. Iron parameters for the profile Sp1 in the Mutare part of the MMO belt

The presented data and Figs. 7 – 4, 7 – 7, 7 – 9 and 7 - 11 suggest that shear zones have relatively high ratio on PIMA and low ratio on the ETM_April, and only occasionally the ratios are high on the ETM_Nov as seen in Fig. 7 – 9 and Fig. 7 – 11. This interpretation is more consistent for the samples collected on the Zimbabwean part of the MMO greenstone belt than the results obtained on the Mozambican part of the belt.

This is presumably because of the thin soil profile in the Zimbabwean side compared to the Mozambique part of the belt where the thick soil profile dilutes the signature. The figures 7 – 4 and 7 – 7 show these differences.

The iron-parameter analyses results highly correlate (e.g. profiles Red02, 6 out of 3, Rw 2 out of 3, Sp01 1 out of 1 anomalies for iron parameter and ratio methods, respectively) with known or interpreted and confirmed in the field shear zones and has proved to be more sensitive to changes in Fe^{2+} proportion compared to integrated ratio method, plots (as shown in Figs. 7 – 8 and 7 – 10, 7 – 12) and geological map on Figs 6 - 12.

7.3.2 Interpretation

The use of radiance for the comparison between the conventional scanners (e.g. Landsat TM or ETM) and the infrared hyperspectrometers (e.g. PIMA) is less reliable due to several externalities influencing the scattering of the incident radiance as illustrated in the Fig. 7 - 5. Fig. 7 - 4 represents the same profile (Sp5) but it can be noted that the interpretation of Fig. 7 - 5 does not give a clear understanding of the comparison between the two systems. However, the PIMA results are very consistent despite little, if any, externality related to scattering of the incident radiance.

These results suggest that the main variations in ratio between different images must be related to different acquisition dates and sample collection periods. One of the most challenging problems is still the use of PIMA reflectance spectra to improve the multispectral satellite imagery fact, which hinds on development of scanner channels that overlap within the required wavelength (1350 – 1750 nm for iron parameter versus the TM or ETM band 5 (1550 – 1750 nm)). The ratio method, although its merit on resampling the PIMA data to 1650 nm equivalent to the centre of the ETM or TM band 5 and 2250 nm equivalent to the centre of the ETM or TM band 7, it has the disadvantage of living out the region around 1300 nm which is important for the iron absorptions.

The results arising from the ratio and iron parameters methods can be used, with care, to reinterpret the satellite imagery by assigning real reflectance values to shear zones and train pixels for supervised classification. The next section discusses the mapping of the shear zones using satellite imagery and PIMA data.

7.4 Discussion

As can be observed from the results of the comparison between ETM and PIMA spectrometer, the overall shapes (Fig. 7 – 4, 7 – 5, 7 – 7, 7 – 9, 7 – 12 and Appendix VII) are quite similar. This can be interpreted as an indication of correlation to some extent. If all data were acquired (satellite imagery and field samples) at the same period it would significantly increase the chances of correlation between the PIMA spectral reflectance and the fully corrected and vegetation removed ETM and TM reflectance data.

April is characterised by high humidity (~77%), some rain and high vegetation. This implies high values on band 5 and low values on band 7. The ratio 5/7 will yield relatively high values.

The scenario is opposite with November frame, where there is low rain, low vegetation and low humidity (~63%). This implies that the ratio band 5 and 7 will yield relatively low values due to high values of the band 7.

The PIMA values are collected in July, just after the rainy season, the rains are scarce and the average relative humidity is ~64% in Manica and Mutare and there is in general relatively low vegetation. These results are relatively high ratio values in comparison to November but lower than April. This would be expected in the multispectral satellite imagery and the fact that it is also observed with PIMA reflectance values show that there is correlation between the two systems. This leads to conclude that the PIMA reflectance values can be used, with care, to improve the spectral and spatial reflectance data of the multispectral satellite imagery. However it is recognised that there is a need for more exercises involving different soil types (grain size, texture, sorting etc.) under different climatic conditions for further validation of this hypothesis.

The iron parameter is a powerful method for mapping silicified shear zones and BIF related zones (e.g. Fig. 7 – 10). The zones of high iron parameter were field checked and compared with geological maps and proved to be related to presence of BIF. The BIF zones were confirmed by Landasat band ratio 5 and 7 image.

Ten out of fifteen shear zones fall within areas of high iron parameter, which give a positive results for this analyses.

The structural interpretation of the satellite imagery based on the digital numbers of shear zones calculated here is presented in the next chapter.

7.5 Conclusions

In this chapter, the comparison between satellite imagery and the PIMA spectral reflectance was studied and the following conclusions are drawn:

- The PIMA results can be used, with care, to improve the interpretation of the Landsat imagery by providing details that are not easily observable at first sight but once the interpreter knows that they are present, become much easier to locate.
- The results presented in this chapter show that PIMA and remotely sensed data, when properly processed, enhanced and interpreted, offer an alternative approach to traditional geological and or structural mapping methods.
- The plotting of ratios band5/band7 for the ETM_April, ETM_November and Pima map adequately shear zones. This conclusion is supported by iron parameter plot and field observations.
- The use of PIMA data and Landsat imagery as supplementary methods to each other has proved to be an adequate mapping base for interpreting major structural elements (e.g. shear zones through the alteration associated to it). The Landsat data can be used in preliminary stages of studies in order to give general information on the existence or absence of hydrothermal minerals. While the PIMA spectrometer can be used at later stages in the studies with the aim of providing detailed mineralogical, crystallographic and compositional variations in specific area or set of samples.
- The use of PIMA data and Landsat imagery does not substitute fieldwork; it only reduces the amount of time for it by focusing the fieldwork to specific and smaller areas of interest.

Chapter 8

8 Satellite Imagery Interpretation for gold mineralisation mapping in the MMO greenstone belt

8.1 Introduction

Studies in digital image processing have successfully used remotely sensed data for spectral differentiation of lithologic units in arid to semiarid environments of well-exposed rocks and little vegetation. But areas of dense vegetation and poor exposure, such as the MMO region, have attracted very little attention from researchers.

Remotely sensed data are highly influenced by local conditions of climate, land use and geomorphology, which do not allow direct application of techniques and models developed for other different regions. This is a major weakness with using remotely sensed data.

For this study satellite images (Landsat Thematic Mapper (TM) October 1994 and Enhanced Thematic Mapper (ETM) April 2000 and November 1999 Scene, SPOT multispectral (XS) 1994, SPOT panchromatic (pan), air photographs (1:40 000 scale), Topographic maps at 1: 50 000, and several geological maps were used to map structures that may control gold mineralisation in the MMO belt. These structures have been proved in earlier chapter to be shear zones. Thus this chapter addresses and test techniques for structural mapping and alteration associated with mineralised structures. Some lithologies, such as granitic intrusions and Bulawayan mafic and ultramafic rocks have been identified has important host to gold mineralisation in the MMO belt, hence their mapping using mainly reference geological maps and satellite imagery manipulation. The positions of the gold deposits are extracted from the database developed in chapter 4. The airphotographs were scanned at 400 dpi and rectified and geo-coded, and the geological maps were scanned and fed to a computer for digital image comparison.

The digital image processing techniques are described in Appendix VIII-B with relevant references.

8.2 Results of Digital Image Processing

Digital image processing involved the manipulation and interpretation of digital images with aid of a computer. The multiple data processing procedures for the MMO greenstone belt followed the diagram in Appendix VIII - A and are described in detail on Appendix VIII - B with relevant citations.

8.2.1 Lithological mapping

This study has concentrated in distinguishing between major and minor rock units, such as banded ironstones of few metres wide (10 – 30m) and ultramafic rocks of Upper Bulawayan.

Fieldwork was undertaken to check interpretations of the image processing (Appendix VIII-B) and the structural and lithological field observations and measurements are summarised on Appendix III – A and Fig. 3 – 3 as part of ground truthing of the satellite imagery interpretation. Phaup (1937) geological map at 1: 50000 scale for the Mutare section of the belt, the Sheeran et al. (1990)'s geological map at 1: 25000 scale for Manica section of the belt and, the Swift (1956)'s geological map at 1: 100000 for Odzi section of the belt were used as reference maps for the satellite imagery interpretation (e.g. Fig. 3 – 1, Fig. 3 – 4, Fig. 6 – 1, Fig. 8 – 3 and Fig. 8 – 7d).

Granites and granite gneisses

The intrusive rocks include the Penhalonga granodiorite, gneisses (syn-tectonic granites) and K-rich granites. The gneisses occur on the margins of the belt. According to Chenjerai (1996), they have intruded the greenstone belt supracrustals and have been deformed together with the greenstone lithologies. The K-rich granites occur on both the northern and southern margins of the greenstone belt and have intruded both the greenstone belt and gneissic lithologies. The Penhalonga granodiorite, which has an emplacement age of 2742±3 Ma, is the oldest intrusion in the area (Schmidt-Mumm et al., 1994).

Intrusive lithologies were mapped by a colour composite (R = Pc1; G = Pc2; B = Pc3) image of principal component of the three bands in the visible range of the spectrum (see Appendix VIII – B). The colour composite (R = ETMb1; G = ETMb3; B = ETMb7) image successfully distinguished small granitic intrusion within mafic volcanic and sedimentary rocks (e.g. Chazuca granitic plug of 800 X 2000 m as in Fig. 8 – 1). The gneisses are mapped from a colour composite (R = ETMb7; G = ETMb4; B = ETMb3) image.

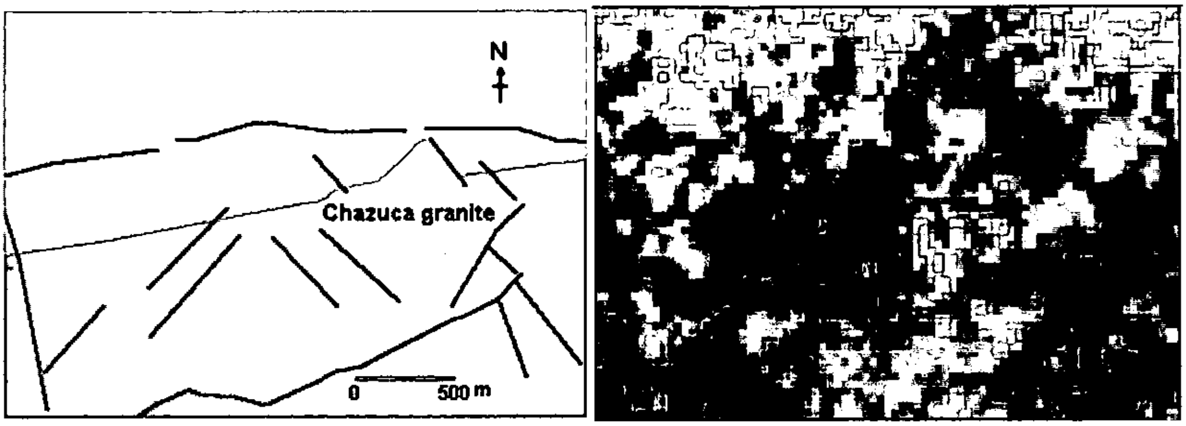

Figure 8 – 1. Chazuca granite intrusion at the contact between metassediments to the north metabasalts to the south. Colour composite ETM bands 1-3-7 as RGB and simplified geological interpretation. The red lines are faults. Coordinates at the centre of the granitic plug UTM X = 477206, Y = 7909052

Ultramafic and mafic metavolcanic rocks

The metavolcanic units consist mainly of serpentinites, komatiites, komatiitic basalts and high-Fe tholeiites and constitute the majority of rocks of the greenstone belt succession.

The outline of the greenstone belt is mapped using the colour composite image (R = ETM7; G = ETM4; B = ETM3); (R = ETM1; G = ETM3; B = ETM7, Fig. 8 – 2c); (R = Pc1; G = Pc2; B = Pc3, Fig. 8 – 2b). The colour composite (R = ETM7; G = ETM4; B = ETM1, Fig. 8 – 2a) image was the best band combination for mapping serpentinite units even when interfingered with other volcanic rocks (e.g. see the area west of Old Umtali) (Fig.8 – 2a, 8 – 2c and 8 – 2d), and for the SPOT images, the colour composite 321 as RGB (Fig. 8 – 2e) aerial photos mosaic (Fig. 8 –2f) and geological maps were used for mapping. On Fig. 8 – 2a the active dumps are shown in blue and reddish and in yellow bluish (Fig. 8 – 2c). The same colours are observed in the cultivated fields. Fig. 8 – 3 is the geological interpretation of Fig. 8 – 2.

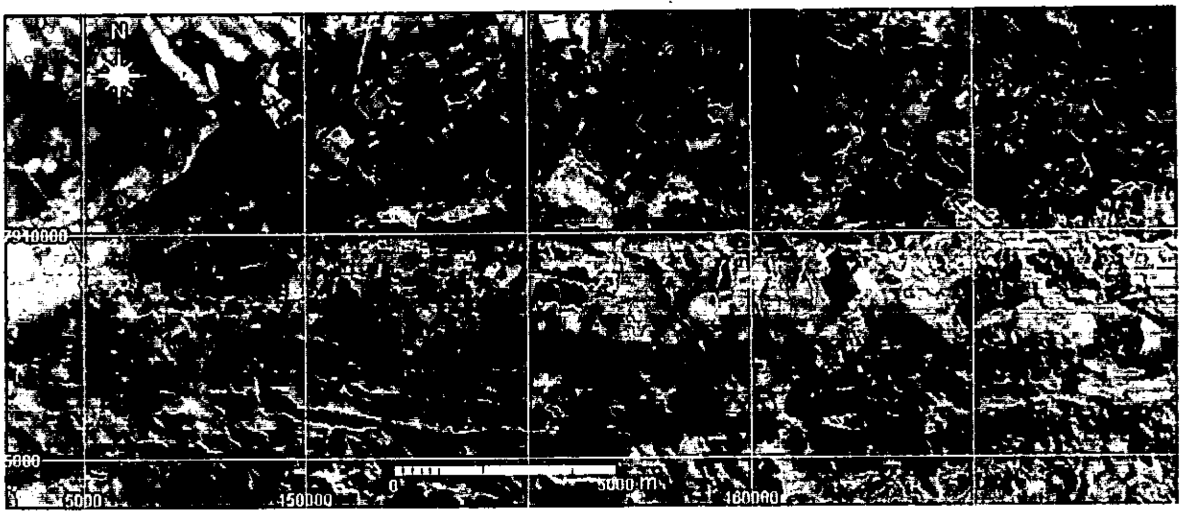

Figure 8 – 2a. Colour composite of April 00 ETM image bands 741 as RGB. UTM coordinates

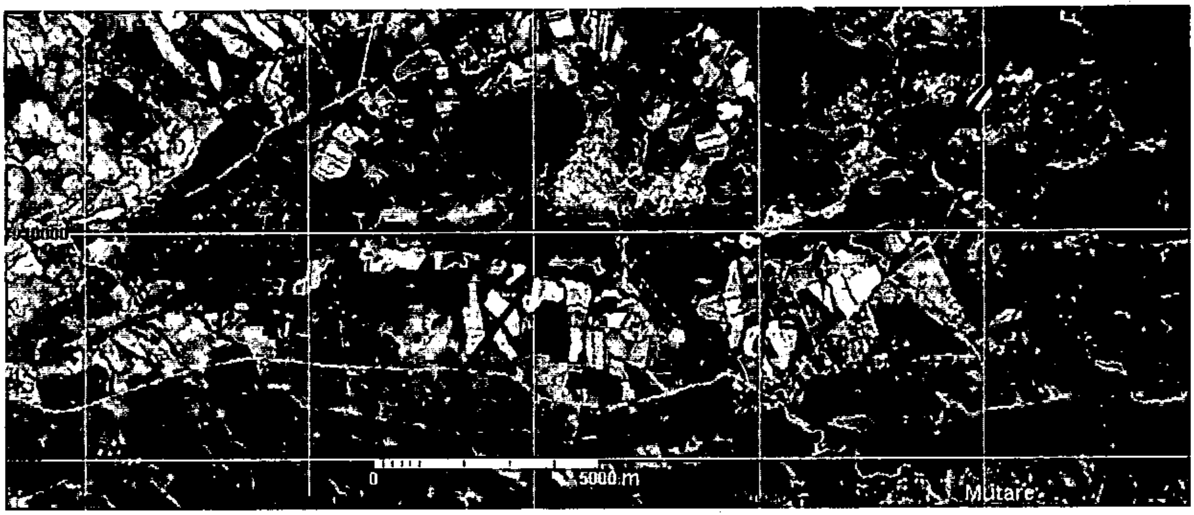

Figure 8 – 2b. Colour composite of April_00 ETM image bands 137 as RGB. Note the ultramafic units pointed by red arrows. UTM coordinates

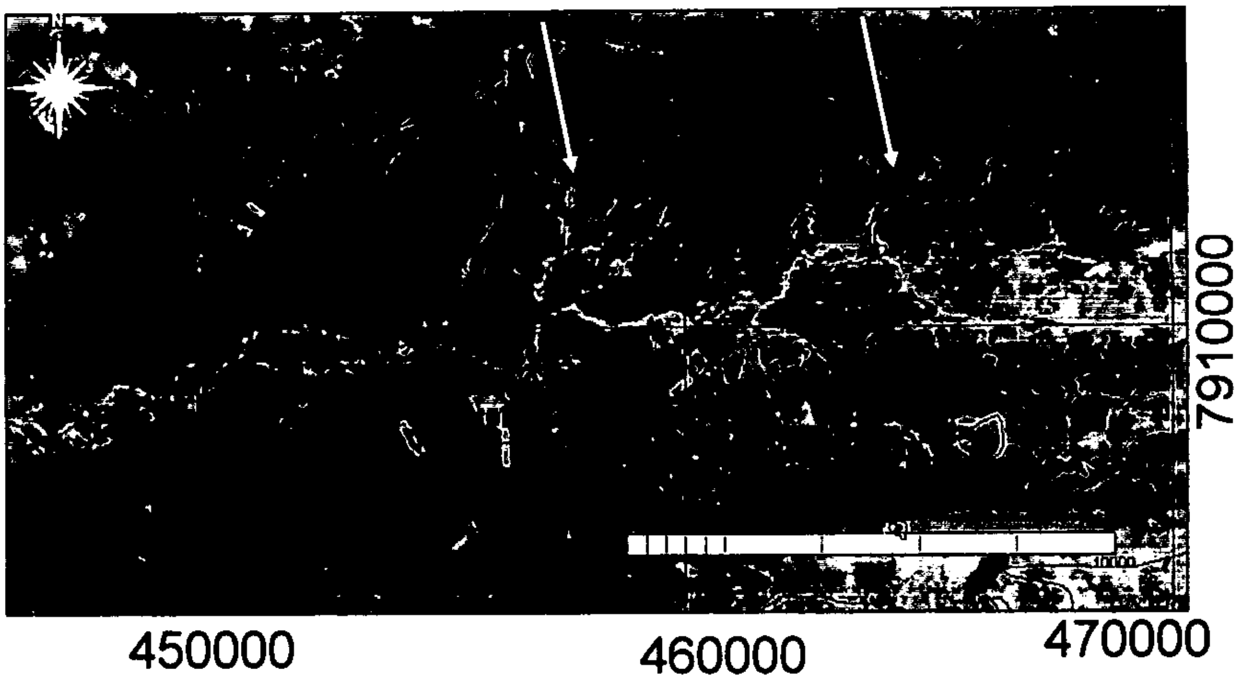

Figure 8 – 2c. Colour composite of Principal Component PC1, PC2 and PC3 as RGB of the November_00 ETM image. Note the granite intrusions pointed by white arrows. UTM coordinates

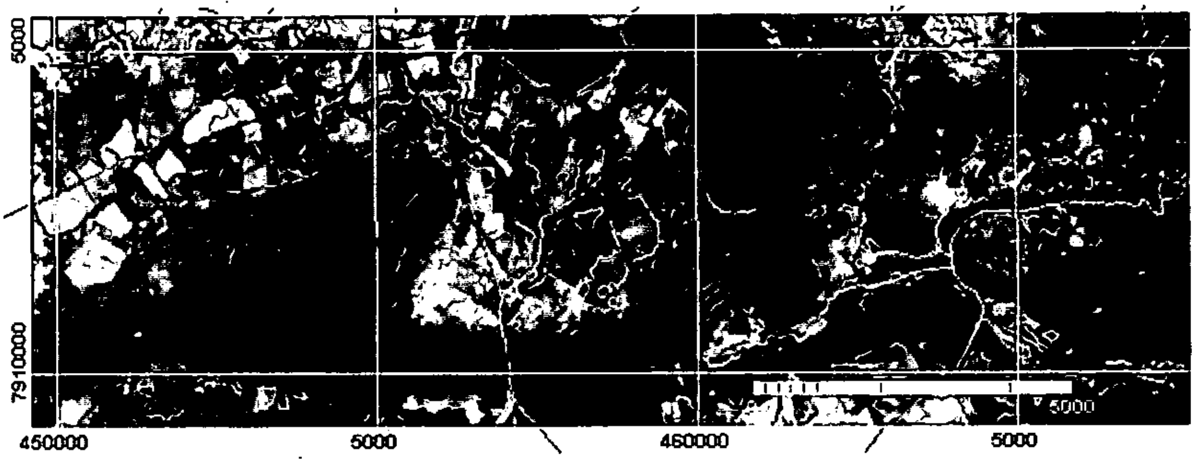

Figure 8 – 2d. Colour composite of November image Ratio ETMb5/7, ETMb7, ETMb3 as RGB. Note the ultramafic units and linear structures pointed by red arrows. UTM coordinates.

Figure 8 – 2e. Colour composite of SPOT-xs image bands 321 as RGB, Mutare section of the belt. UTM coordinates

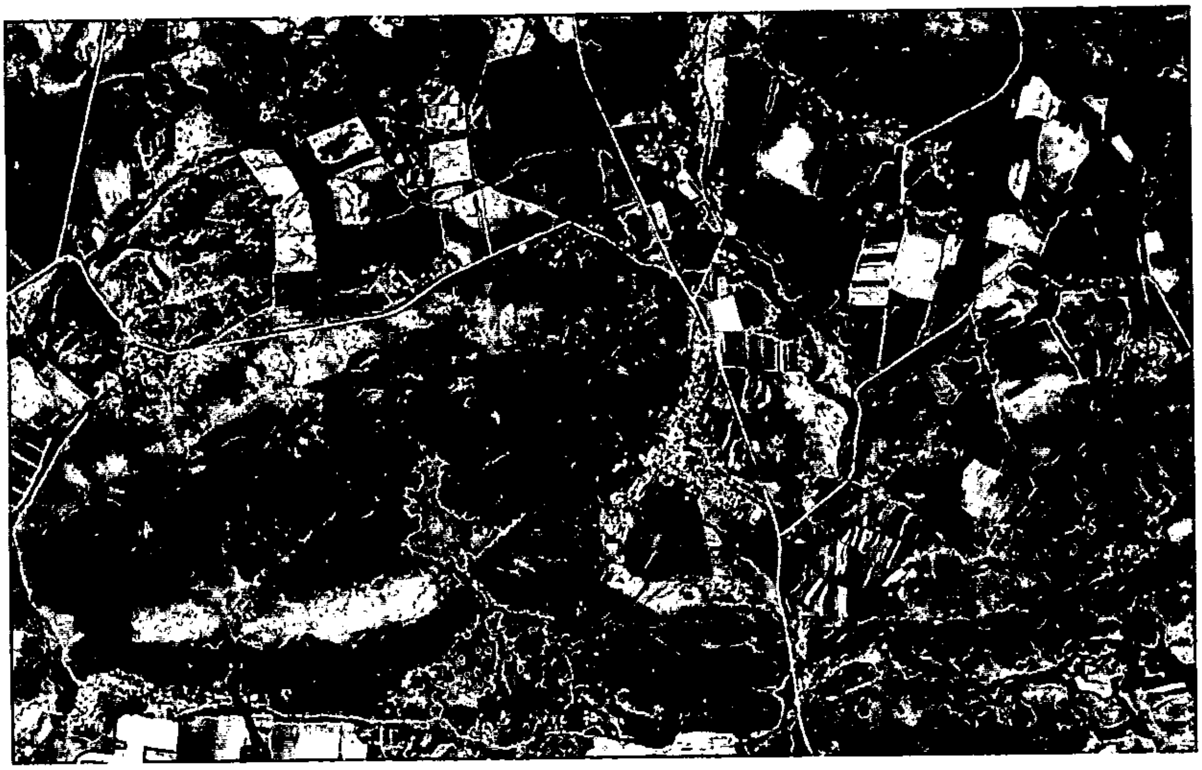

Figure 8 – 2f. Mosaic of aerial photos in the Mutare area. UTM Conner coordinates Upper left 450210;7915791 and lower right 460200; 7909520

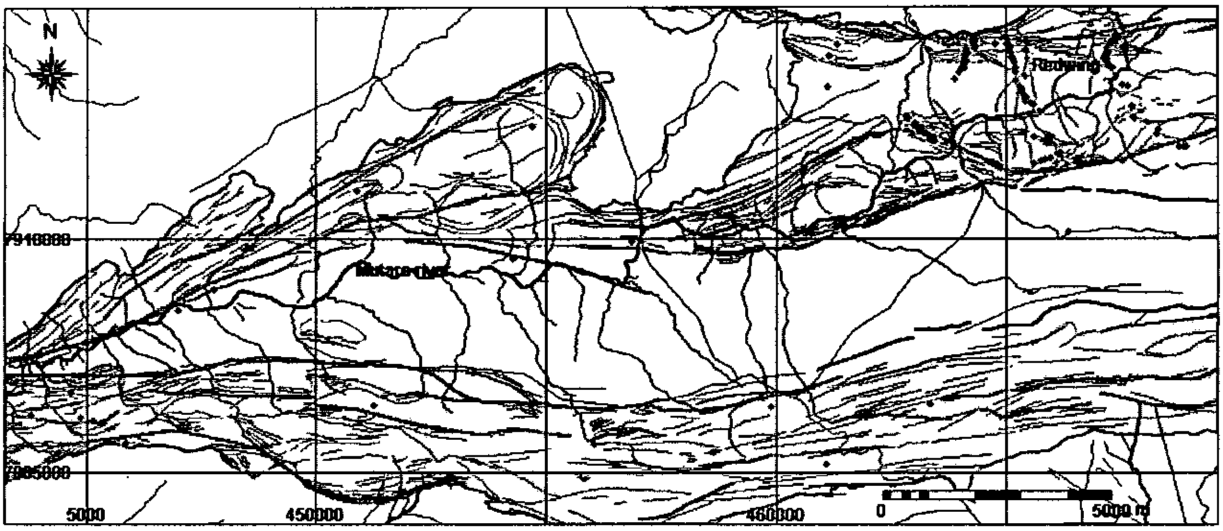

Figure 8 – 3. Geological interpretation of the Fig. 8 – 2. The red lines are shear zones and the black dots are sample points for PIMA analyses; the black thin lines are trends representing the foliation cleavage or bedding as interpreted from satellite imagery (TM169/73, ETM 169/73, SPOT - Xs and SPOT-Panchromatic) and mosaic of airphotos with geological maps as reference.

The secondary iron enrichment areas were also mapped using the iron ratio images (ETM_00 band3/ETM_00 band1) as shown in Fig. 8 – 4.

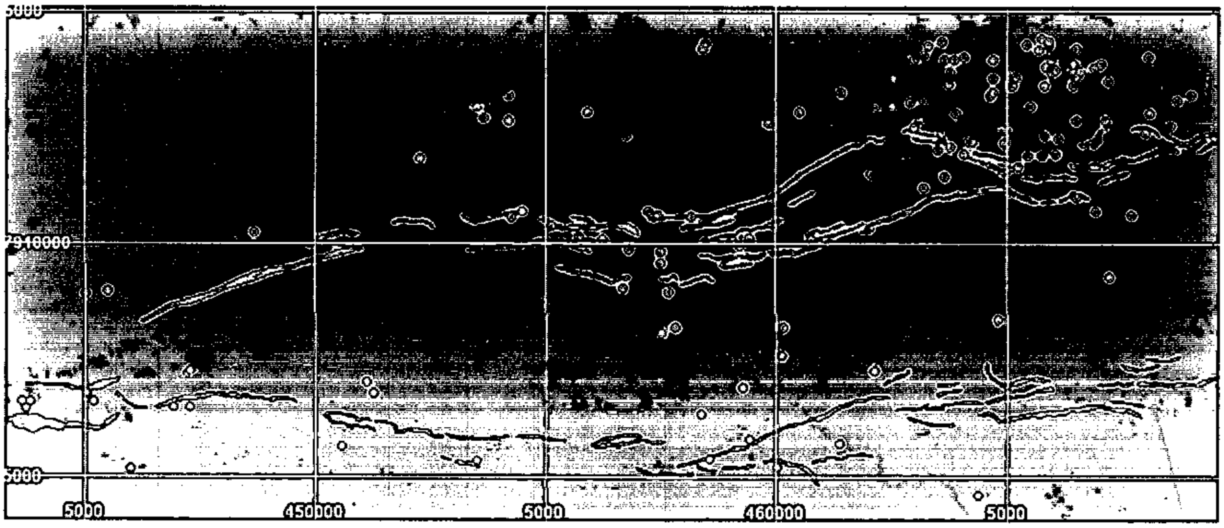

Figure 8 – 4. Binary map of ratio image ETM 00 b3/b1, showing areas of secondary iron enrichment (red), the green dots are gold deposits and the black tracing are the silicified ironstones.

Metasedimentary rocks

The sediments comprising essentially conglomerates, sandstones, siltstones and banded ironstones occupy the central part of the belt. The banded ironstones (BIF) occur as discontinuous units following mainly the regional shear zones (Fig. 8 – 4). The outcrop width varies from 10 m to 30 m and strike-lengths ranges from a few metres to 5 km (Chenjerai, 1996).

The metasedimentary rocks in general are difficult to distinguish among them from satellite imagery due to lack of prominent spectral difference and due to intense homogenisation resulting from farming. The sediments may be mapped indirectly using the land use patterns, because they form valleys where appropriate soil for agriculture may be accumulated.

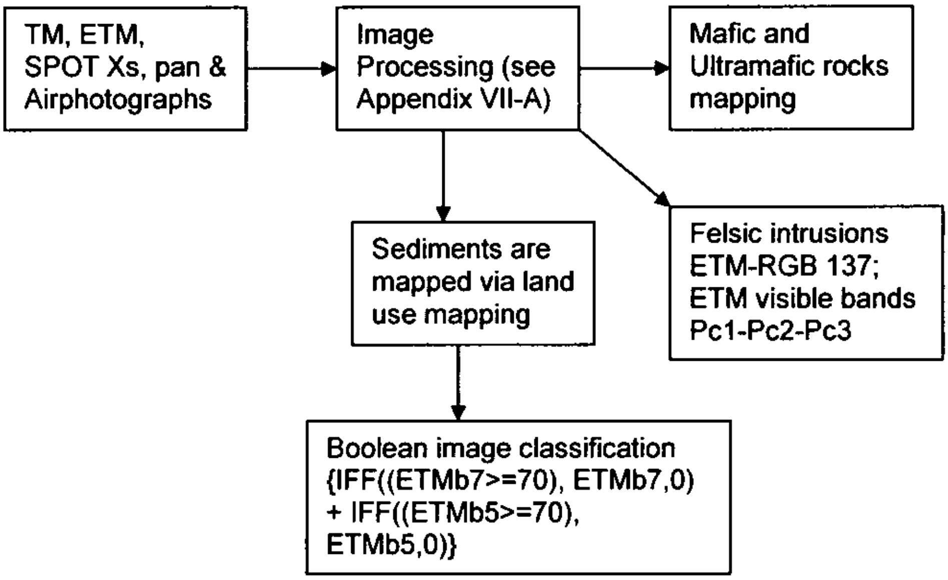

Figure 8 - 5. Schematic representation of data flow for lithological mapping in the MMO belt

8.2.2 Alteration and Image Manipulation for shear zones mapping

It is the objective of this chapter to detect features on the satellite images that relate directly or indirectly to the mineralised structures in the MMO greenstone belt. Economic gold mineralisations in the MMO belt occur spatially related to sections of shear zones (Fig. 8 - 6) within zones of alteration confined to them (Table 8 – 1 and Fig. 8 – 8).

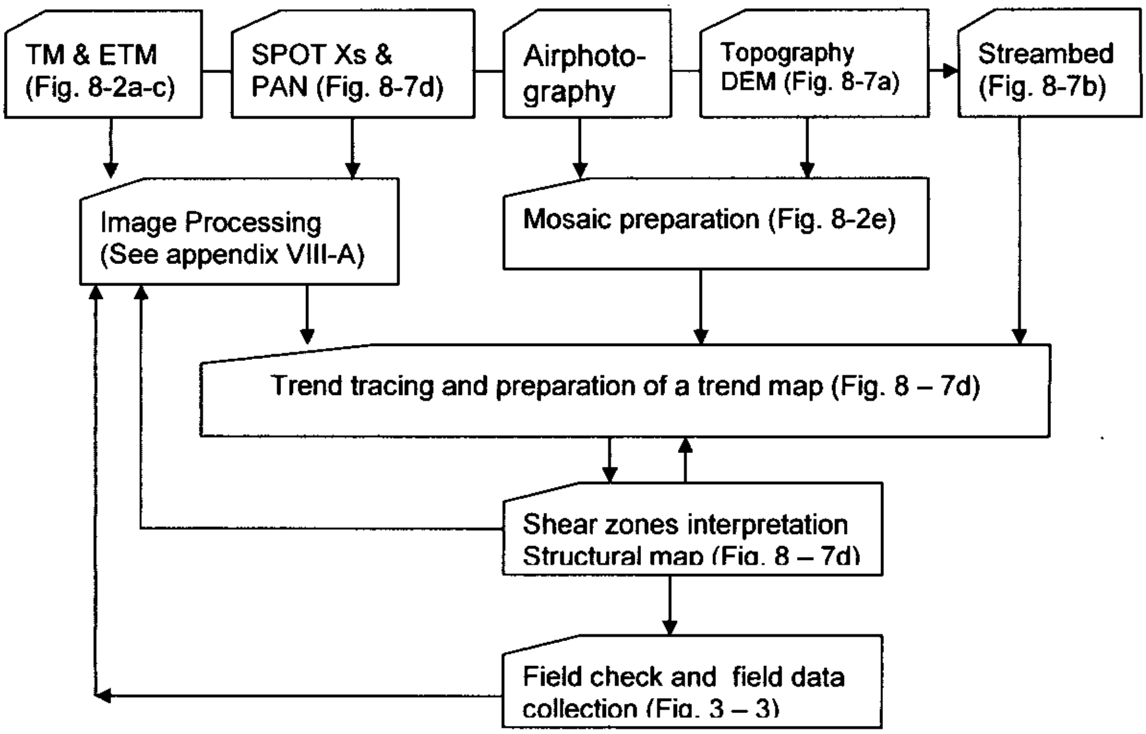

Figure 8 - 6. Schematic representation of the data flow for shear zone mapping in the MMO belt.

Field observations show that the orebodies in most cases are quartz veins associated with vein-type and disseminated sulphide mineralisation. Alteration minerals vary from sericite to calcite – chlorite away from the orebodies. The alteration expressions around shear zones are narrow extending at most up to 10 metres away of the structures. The mapping of such narrow alteration zones on the basis of remotely sensed data is rather complex (Fig. 8 – 8). Thus the mapping of alteration was centred in mapping alteration in known gold deposits (Table 8-1) and by mapping linear zones on the satellite imagery. The linear zones can extend to up to 1000 metres along strike.

The silicified shear zones are mainly banded ironstones, and they have positive topographic expressions, which ease its detection when poorly vegetated.

Table 8 – 1. Summary of geological characteristics of selected shear zone hosted Archaean gold deposits in the MMO greenstone belt

Depo-sits	Produ-ction (kg Au)	Description and Structure	Host rocks	Nature of ore	Alteration	Ore minerals
Kenya	32	Shear/fault	Upper Bulawayan	Disseminated in quartz veins	?	Py, Gn, Ccp, Bis
Ester	8	Crack seal steep shear zone associated with BIF	Shamvaian	Quartz stockwork	?	Py, Gn
Reliance	226	Crack seal sheared quartz vein zone associated with BIF	Upper Bulawayan	Quartz stockwork	Carbonate and chlorite alteration	(Au, Ag) Py, Po, Gn,
Try Again	100	Steep sheared contact, Quartz sericite schist associated with BIF	Contact Upper Bulawayan and Shamvaian	Au associated with sulphides in quartz sericite schist	Sericitic, sulphidation	Py, Po, Aspy, Ccp
Clutha	80	Moderately dipping Sheared quartz vein	Upper Bulawayan	Au associated with sulphides in quartz sericite	Sericitic, sulphidic alteration	Au and Ag with Py, Ccp, Gn, Sph
Fair Bride	201	Steep sheared contact consisting of Quartz sericite schist associated with BIF	Contact Upper Bulawayan and Shamvaian	Quartz veins and stringer zones, and sulphide-bearing silicified zones within the southern shear zone	Sericitic, sulphidation, and Carbonate	Py, Po, Aspy, Ccp
Dot's Luck	181	Steep sheared contact consisting of Lensoidal quartz vein associated with BIF	BIF in the Upper Bulawayan in contact with Shamvaian	Au associated with sulphides in banded ferruginous quartzite	Sericitic, sulphidation, carbonatization	Py, Aspy, Ccp, Gn,
Boa Esperanca	507	Reverse shear zone; Lensoidal	BIF in Upper Bulawayan	Quartz veins and stringer zones, and sulphide-bearing silicified zones within the reverse shear zone	Sericitic, sulphidation, silicification	Py, Aspy, Gn
Muza Reef	106	Vertical shear zone; Sigmoidal quartz vein associated with BIF	Upper Bulawayan	Sheared quartz vein	Carbonate and chlorite alteration	
Guy Fawckes	494	Steep Sheared contact zone; Quartz vein in a lensoidal quartz vein associated with BIF	Contact (Upper Bulawayan and Shamvaian)	Quartz veins and stringer zone, and sulphide-bearing silicified zones within 200 m wide shear zone; Breccia veins	Sericitic, sulphidation and silicification	Py, Ccp, Gn

Dias Perreira	500	Steep sheared contact	Contact (Shamvaian and Upper Bulawayan)	Quartz veins and stringer zone, and sulphide-bearing silicified zones; Breccia veins	Sericitic, sulphidation, carbonatization	Py, Ccp, Gn
Magog	125	Shear zone; Highly faulted lensoidal quartz vein associated with BIF	BIF in Upper Bulawayan	Sheared quartz vein	?	Py, Gn,
Champion	301	Steep sheared contact zone			Pervasive Silicic alteration	Aspy
Monarch	261	Steep faulted lensoidal quartz vein and sheared contact associated with BIF	BIF in the Upper Bulawayan basalts	Stockwork Au associated with sulphides in silicified BIF	Carbonate alteration and silicification	Py, Po, Aspy, Ccp, Gn, Sph
Pension	61	Flat dipping sheared hinge fold; Stockwork	Upper Bulawayan	Parallel quartz veins	?	Au and Ag with Py, Po, Gn
Midas	25	Fault hosted quartz vein	Upper Bulawayan		?	Au, Ag with Py, Gn. Croc
Penha-longa	25	Sheared lensoidal quartz veins associated with BIF	BIF in Upper Bulawayan	Quartz stockwork zones, en echelon and crack seal shear zone	?	Au, Pb, Ag. Py, Ccp, Gn, Croc

It was assumed as first indicator for the presence of regional shear zones, the topography (Fig. 8 – 7a), the streambed pattern may reflect the bedding trends (Fig. 8 – 7b), the truncation surfaces of the primary trends mapped from the air photographs mosaic, SPOT panchromatic, SPOT xs (Fig. 8 – 7c), TM, ETM images and field work (e.g. Fig. 3 - 3).

The second indicator was the spatial relationship of these truncation surfaces with BIFs. The mineralised shear zones were interpreted on the basis of its spatial relationship to gold deposits as discussed in Chapters 7 and 9. Based on field evidence interpretation two types of shear zones namely northern and southern shears were identified (Fig. 3 – 3). These shear zones are mainly deep-seated fault zones marking boundaries between lithologically contrasting domains within the greenstone or along its margins (as discussed in Chapters 3). It was not possible to distinguish these shear zones on the basis of associated alteration, which would be important for their mapping from remotely sensed data (Table 8 – 1).

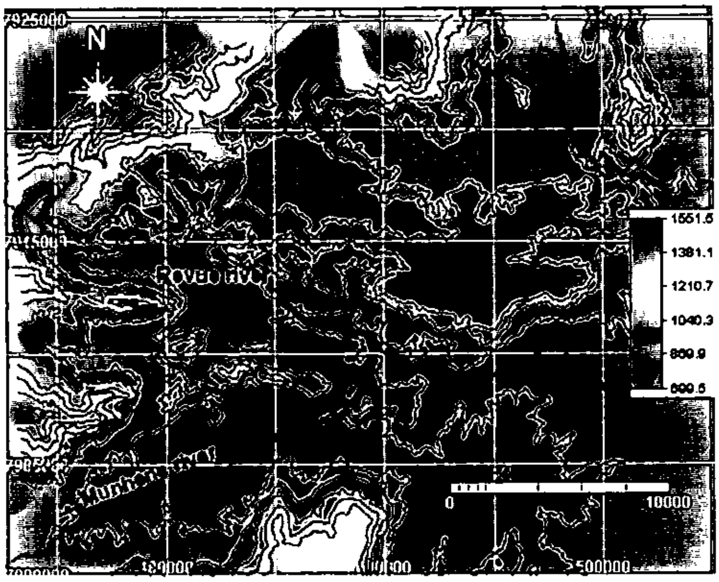

Figure 8 – 7a. Digital Elevation Model (DEM) for the Manica section of the MMO belt. The pink dots are gold deposits. For geological interpretation refer to Fig. 8-7d.

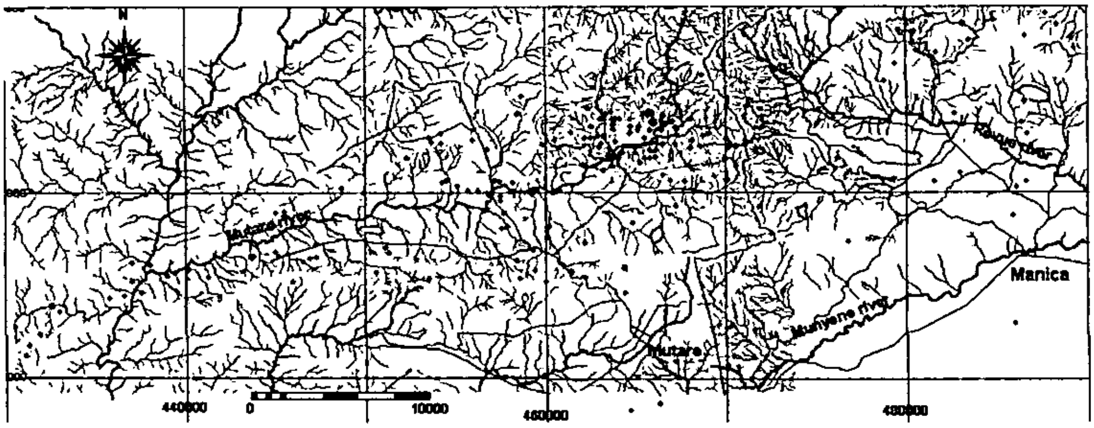

Figure 8 – 7b. Map of 1st, 2nd, 3rd, and 4th order of streambed in the MMO. The red dots are gold deposits. For geological interpretation refer to Fig. 8-7d.

Figure 8 – 7c. Colour composite of SPOT-xs image bands 321 as RGB, entire MMO belt. For

geological interpretation refer to Fig. 8-7d.

The silicification is an increase in the proportion of quartz or cryptocrystalline silica in the rock. Usually the silica is introduced by hydrothermal solutions or it may be the by-product of the alteration of feldspars and other minerals during the leaching of bases (Evans, 1998). The sulphidation, divided into pyritization and hematization, is a process by which sulphur is introduced in the altered rocks attacking both iron oxides and mafic minerals. The most common sulphidation in the MMO greenstone belt is the pyritization (e.g. Eq. 8 – 1 (Evans, 1998)), which occur along shear zones associated to gold mineralisation.

$$\underset{\text{(Magnetite)}}{Fe_3O_4} + 6H_2S + O_2 \Rightarrow \underset{\text{(Pyrite)}}{3FeS_2} + 6H_2O \qquad \text{Eq. 8 - 1}$$

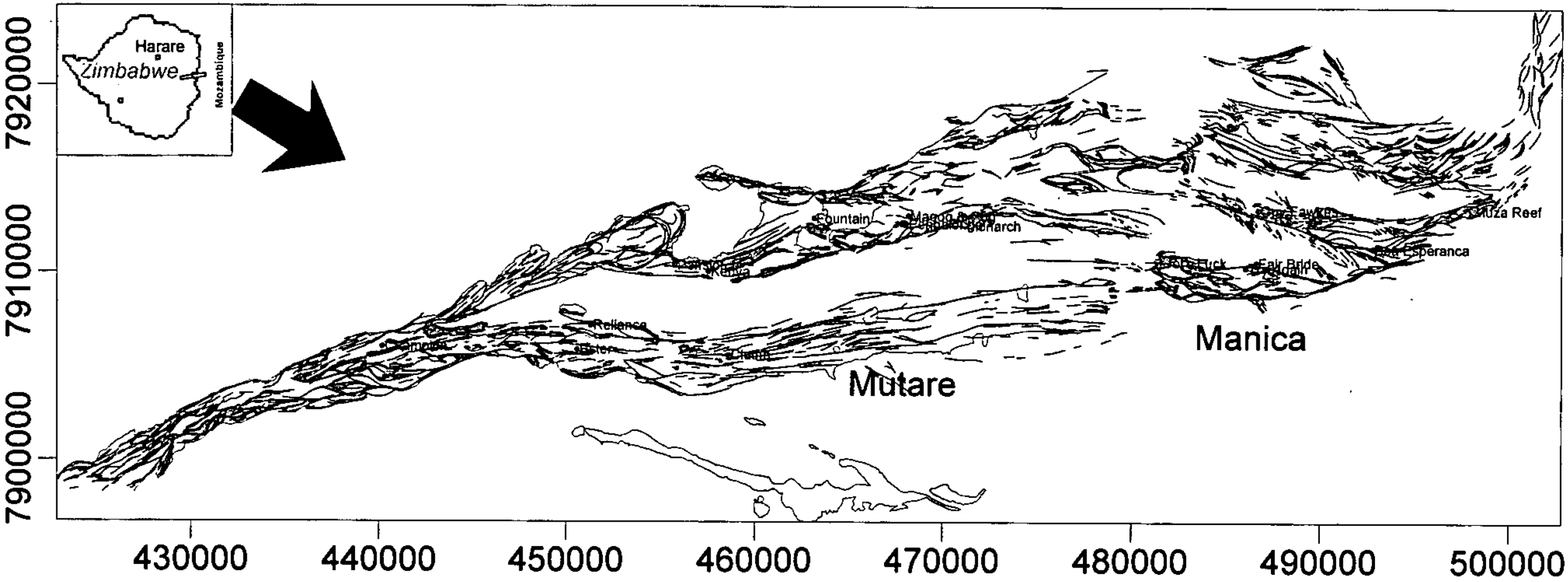

Figure 8 – 7d. Illustration of the main shear zones on the basis of trend map and their spatial relationship to the gold mineralisation as a result of satellite imagery interpretation. The thin black lines are trend lines traced from satellite imagery (different colour composite, single band images and aerial photos).

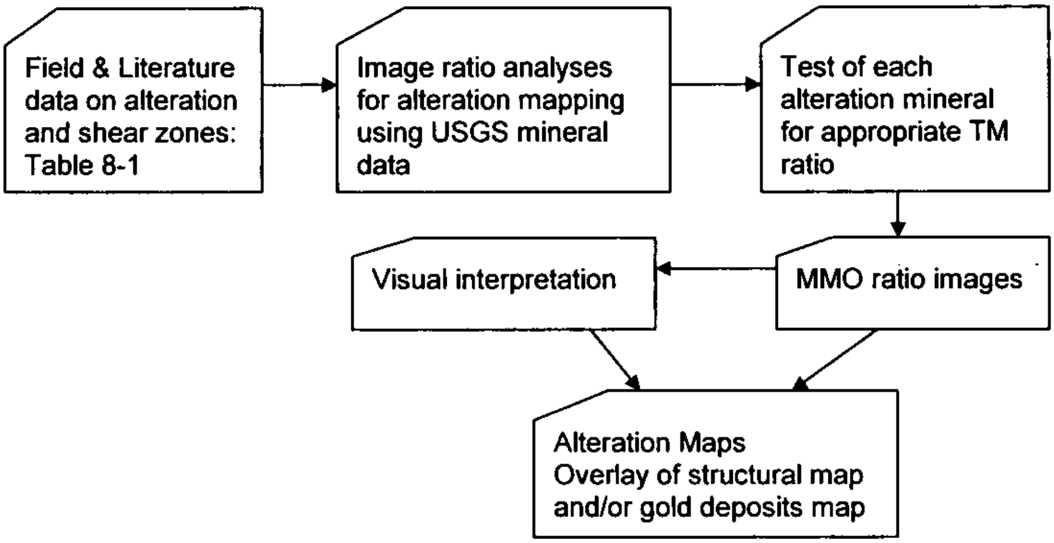

Figure 8 -8. Schematic representation of the data flow for mapping alteration in the MMO belt

After the identification of the main alteration process in the MMO greenstone belt, the following stage consisted of testing the spectral ratio for clay minerals in order to detect pixels that are likely to represent alteration soils overlaying shear zones. Laboratory spectra show that the mineralogical variations due to silicification and sulphidation can be detected using band ratios TM2/TM3, TM2/TM7, TM3/TM4, TM4/TM7 and TM5/TM7. For example, the alunite presents ratios higher than illite/sericite, hematite or kaolinite in the ratio TM5/TM7 (Fig. 8 – 9). The ratio band 5 and band 7 TM images is selected due to its susceptibility to alteration and the possibility of comparing the results with PIMA data (Chapter 7).

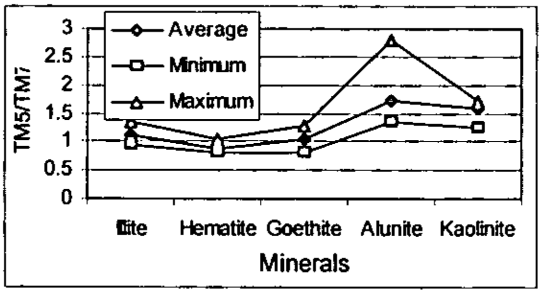

Figure 8 – 9. TM band ratio (TMband5/TMband7) plot for the different alteration minerals - Note that the ratio value is on average higher than one. TM data source: Spectral library USGS (1998).

The final consideration for mapping the shear zones is to bring these results into the satellite images. The ratio images were calculated and reclassified for the presence of specific alteration minerals. The supervised classification was mainly based on ground spectral data collected across mineralised shear zones (e.g. Guy Fawckes shear zone) and across the mineralised Penhalonga granodiorite (see Chapter 6).

Figure 8 – 10 shows that the ratios TM5/TM7, TM4/TM7 and TM2/TM7 present values relatively higher than the other ratios and on that basis can be used to detect kaolinite in the soils. From the best three ratios, only the ratio TM5 by TM7 is presented in form of classified image (Fig. 8 – 11), this is because the results of the three ratios were similar and because the two bands are in the SWIR which allow its comparison with PIMA data.

The presence of kaolin is generally part of the argillic alteration of plagioclase and can be found in many environments including soils accompanied by allophane clays. In MMO belt the kaolin is widely distributed in the farming fields and in the granite-gneiss zones as illustrated by the Fig. 8 – 11 and supported by field observation.

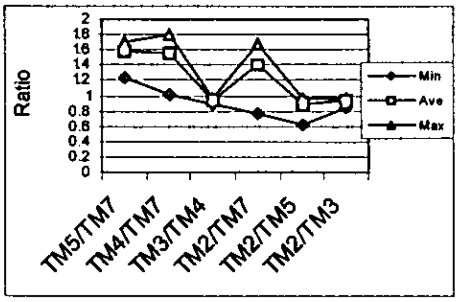

Figure 8 – 10. TM band ratios (TM5/TM7, TM4/TM7, TM3/TM4, TM2/TM7, TM2/TM5 and TM2/TM3) for kaolinite. TM data source: Spectral library USGS (1998).

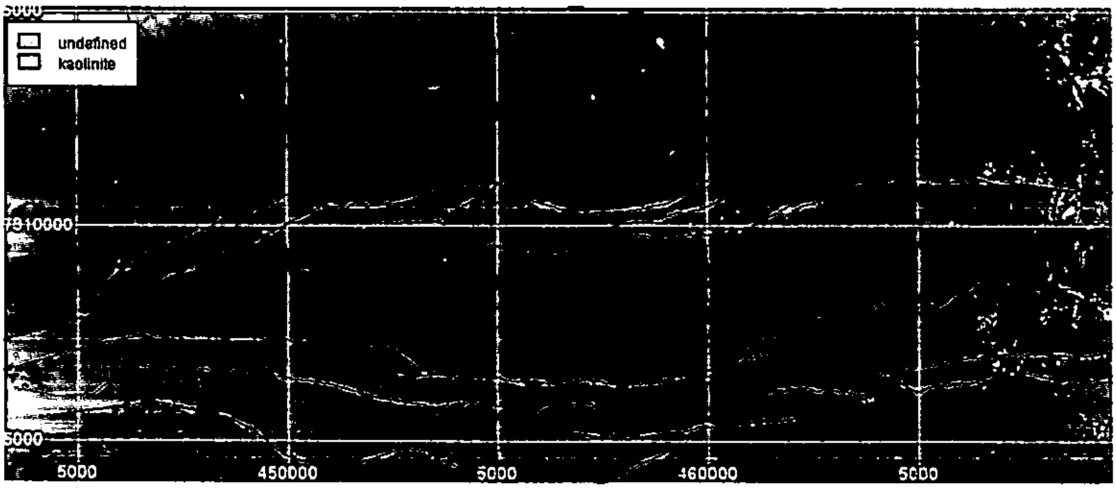

Figure 8 – 11. Classified ratio band 5 / band 7 ETM April_00 image showing areas of high concentration of kaolinite, also goethite or hematite in the MMO greenstone belt. Image threshold as follows: iff(Image 5/7>=1.6,1,0). The threshold of 1.6 was determined on the basis of statistical representation (Fig. 8-10) and geological knowledge of the area. The black lines are shear zones. White pixel correspond to area without information on band 5 and 7.

The ratios TM5/TM7, TM3/TM4 and TM2/TM3 can potentially detect the presence of illite, goethite and hematite in the soils (Fig. 8 – 12, 8 - 14).

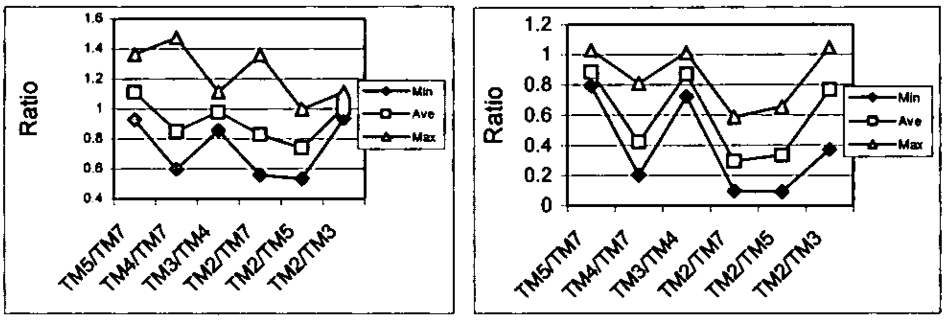

Figure 8 – 12. TM band ratio (TM5/TM7, TM4/TM7, TM3/TM4, TM2/TM7, TM2/TM5 and TM2/TM3) for illite (a) and hematite (b). TM data source: Spectral library USGS (1998).

The satellite image mapping the illite in the MMO belt (Fig. 8 - 13) show that the ratio ETM3 by ETM4 detect the presence of illite in the late faults and in K - Al rich lithologies, and correlate with some sections of known shear zones (Fig. 8 – 13).

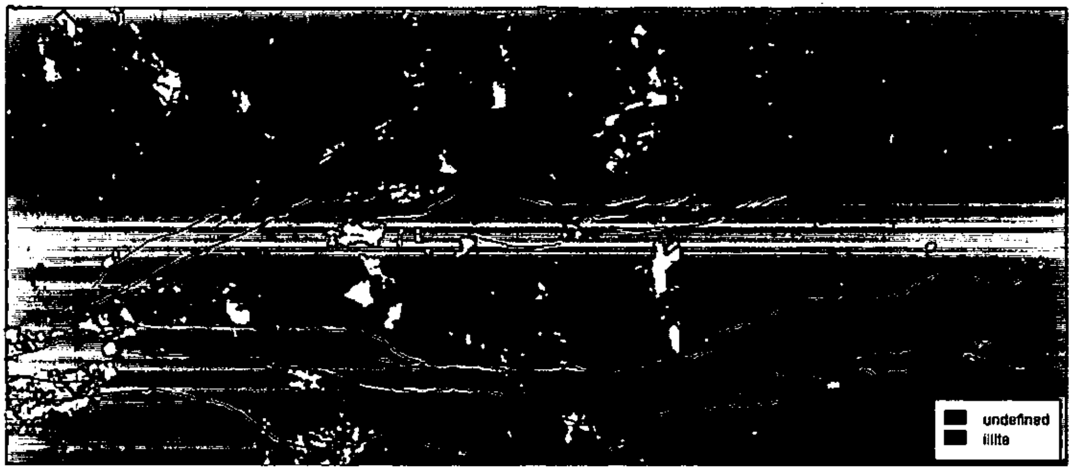

Figure 8 – 13. Classified band ratio 3/4 ETM April_00 image showing areas of high concentration of Illite or Hematite or Goethite in the MMO greenstone belt. Image threshold as follows: iff(image 3/4>=1,1,0). The threshold of 1 was determined on the basis of statistical representation (Fig 8-12) and geological knowledge of the area. White pixels correspond to area without information on band 3 and 4.The black lines are shear zones.

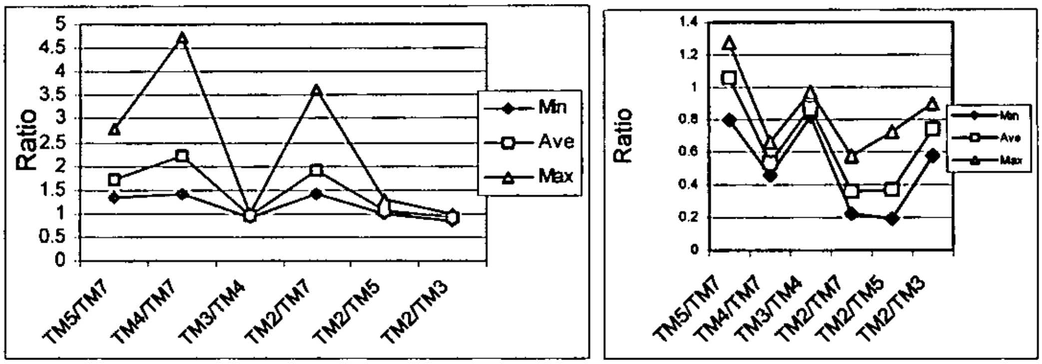

Figure 8 – 14. TM band ratio (TM5/TM7, TM4/TM7, TM3/TM4, TM2/TM7, TM2/TM5 and TM2/TM3) for goethite (a) and Alunite (b). TM data source: Spectral library USGS, 1998.

Alunite is better mapped using the ratios TM4/TM7 and TM2/TM7 as shown in Fig. 8 – 14b. The classified image (Fig. 8 - 15) of ratio ETM2/ETM7 suggests that the mapping of alunite using the above ratio is highly affected by presence of vegetation. Thus, in the MMO belt, due to dense vegetation it is not possible to map the alunitization. In the Fig. 8 – 14 it is most likely that all the anomalies represent areas of high vegetation as illustrated by the extreme east of the image (Fig. 8 – 15).

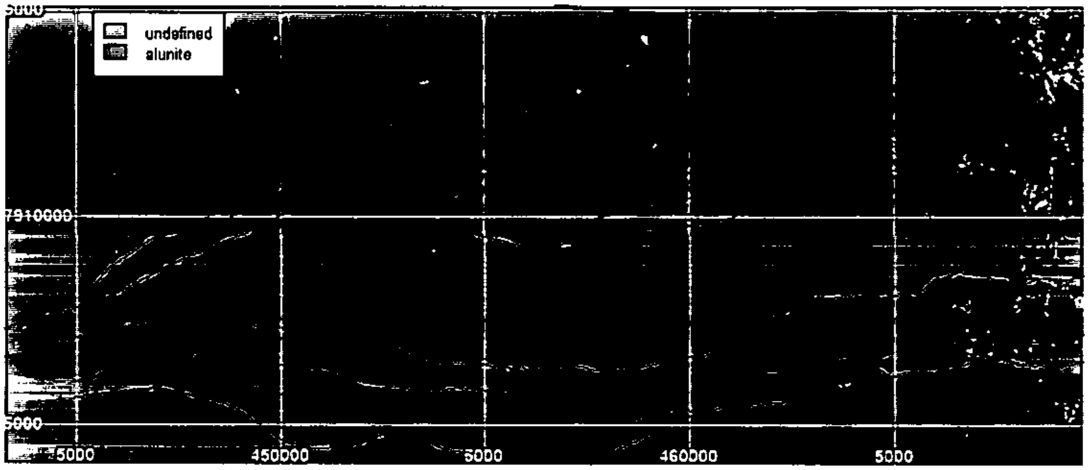

Figure 8 – 15. Classified band ratio 2/7 ETM April_00 image showing areas of high concentration of Alunite in the MMO greenstone belt. Image threshold as follows: iff(Image 2/7>=2,1,0). The threshold of 2 was determined on the basis of statistical representation (Fig. 8-14) and geological knowledge of the area. White pixels correspond to area without information on band 2 and 7.The black lines are shear zones.

Carbonatization in the MMO greenstone belt involves chemical alteration of chlorite into ankerite – dolomite according to equation (eq. 8 – 2; after Evans (1998))

$(Mg,Fe)_6Si_4O_{10}(OH)_8 + 6CaCO_3 + 6CO_2 \Rightarrow 6(Mg,Fe)Ca(CO_3)_2 + 4SiO_2\ 4H_2O$

(Chlorite) (Ankerite or Dolomite) (Eq. 8 – 2)

The hydrothermal chlorites often show a change in their Fe:Mg ratio with distance from the orebody, usually being richer in iron adjacent to the sulphides (Evans, 1998).

The normalised intensity on TM bands show that the chlorite is brighter in the infrared bands and darker in the visible and near infrared bands.

This implies that the ratio between reflected infrared and visible bands should enhance the detection of chlorite bearing rocks on the satellite images as shown in Fig. 8 – 16 (e.g. ratio TM7/TM3 and TM5/TM2).

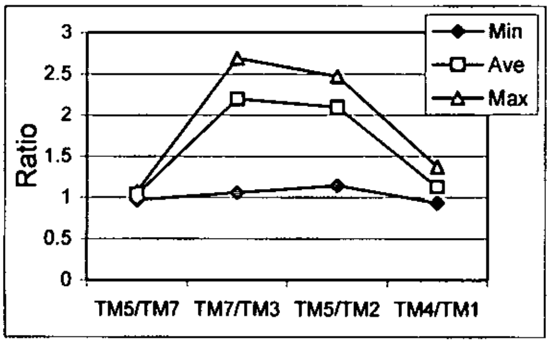

Figure 8 - 16. TM band ratio for chlorite (TM5/TM7, TM7/TM3, TM5/TM2 and TM4/TM1). TM data source: Spectral library USGS, 1998.

Chlorite may result from the alteration of mafic minerals or from the introduction of magnesium and iron or can grow as low-grade metamorphic mineral in a variety of environments including metasedimentary. In the MMO belt the mapping of chlorite shows both type of chlorites, one resulting from the alteration of mafic minerals (e.g. patches around 450259; 79102000) and the other occur along fractures (Fig. 8 - 17). Some portions of the known shear zones coincide with areas of chlorite anomaly. However, the nature of the anomalies do not allow exclusive positive correlation.

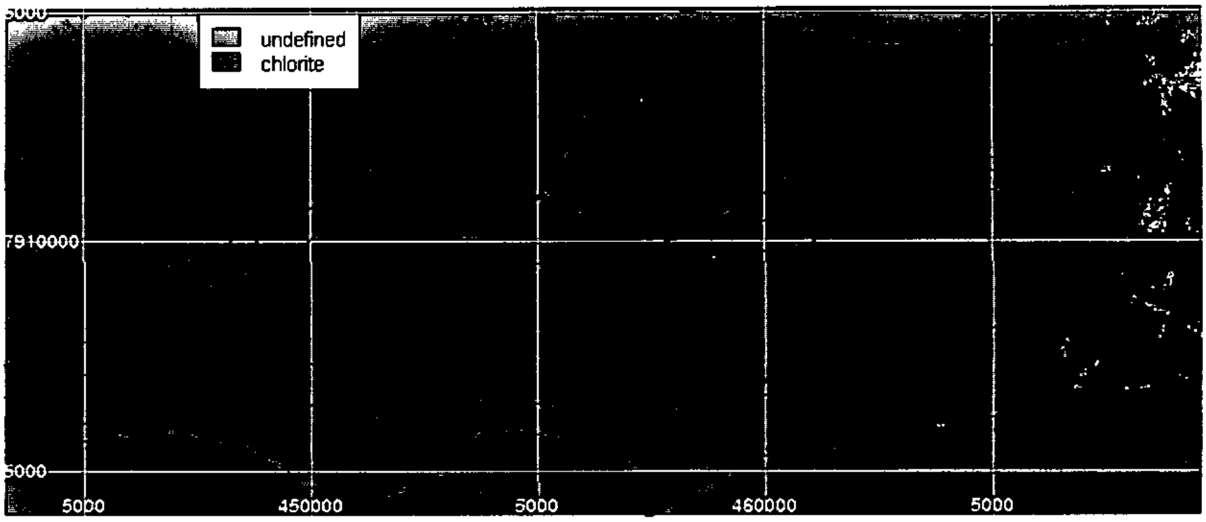

Figure 8 – 17. Classified ratio band 7/ band 3 ETM April_00 image showing areas of high concentration of chlorite in the MMO greenstone belt. Image threshold as follows: iff(Image 7/3>=2.3,1,0). The threshold of 2.3 was determined on the basis of statistical representation (Fig. 8-16) and geological knowledge of the area. White pixels correspond to area without information on band 7 and 3.The black lines are shear zones.

8.2.3 Mapping of shear zones using combined PIMA and ETM or TM images

The combination of the ETM and TM images with PIMA data revealed capable of improving the interpretation of the satellite imagery by adding a ground component of the true reflectance of the shear zones and geological lithologies.

Reflectance spectra of the different rocks and soils recorded from PIMA in the MMO greenstone belt do not show much difference in configuration, but do show significant differences in the intensity as already shown in Chapter 6. These differences are not apparent in the individual bands of the Landsat TM or ETM and SPOT XS or panchromatic, probably because of the spectral resolution associated to spectral bandwidth.

On the basis of the ratio values and iron parameter obtained in the chapter 7, it appear that the image ETM_April band ratio 5 over 7 should give values between 1.11 and 1.28, and reach values of 1.86 for the shear zones or hydrothermally altered zones. For the image ETM_November, the band ratio 5 over 7 yields values between 0.84 and 1.11. The PIMA spectral values band ratio (equivalent) 5 over 7 bear values between 0.97 and 1.54 (Fig. 8 – 18). These ratio value intervals are very broad to allow specific mapping of the single and narrow zones corresponding to phyllitic alteration. However, after image classification (slicing) continuous zones can be detected as shown in Fig. 8 – 19.

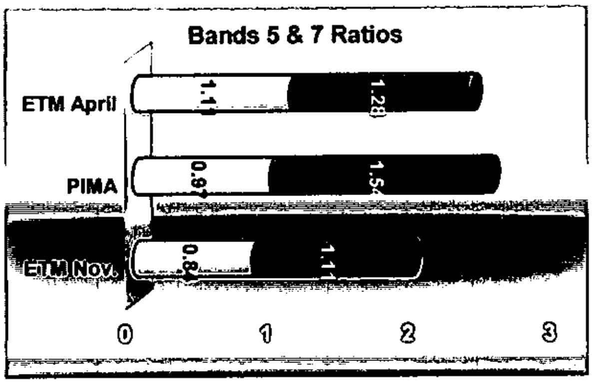

Figure 8 – 18. Graphical illustration of the PIMA, ETM April and ETM November minimum and maximum ratios. Note that the PIMA ratio is higher than all other.

The Fig. 8 – 19 shows that shear zones can be mapped by combined PIMA and Landsat ETM or TM ratios.

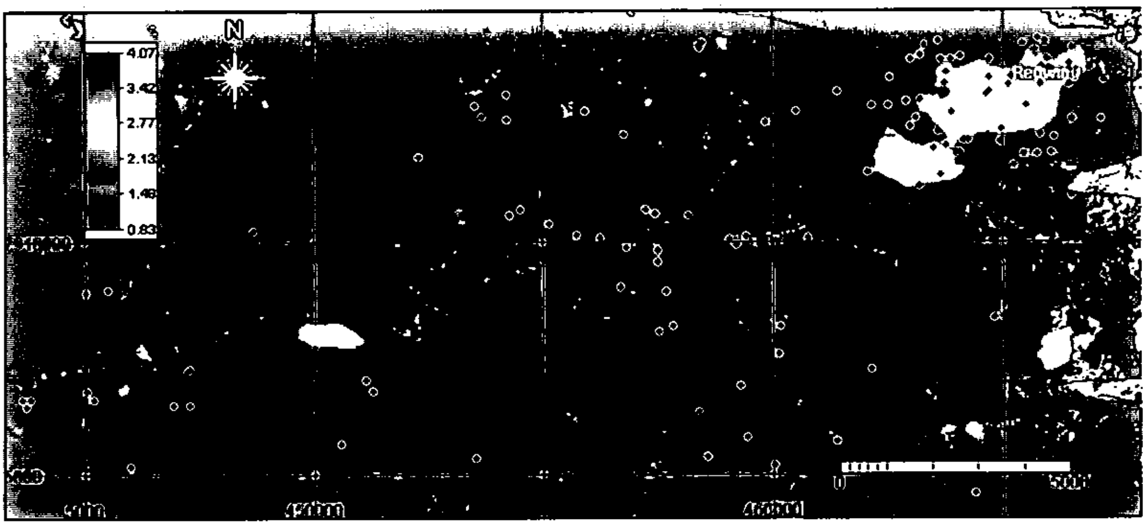

Figure 8 – 19. Landsat ETM ratio image (ETM_00 Band 5/ETM_00 Band 7) calibrated by PIMA ratio on the basis of data represented on Fig. 8-18. The colour scheme goes from blue to red corresponding to low and high alteration. The red lines correspond to interpreted shear zones. The black dots correspond to gold deposits in the Mutare area.

By comparing the shear zones and the BIF zones, which resulted in high anomalies in iron parameter analyses of PIMA data, it is evident that most of the shear zones coincide with zones of BIF (Fig. 8 – 19 and Fig. 8 - 20). This is also supported by field observations at the main northern shear zone along the road to Penhalonga, and along the profile Sp/Rw, for example.

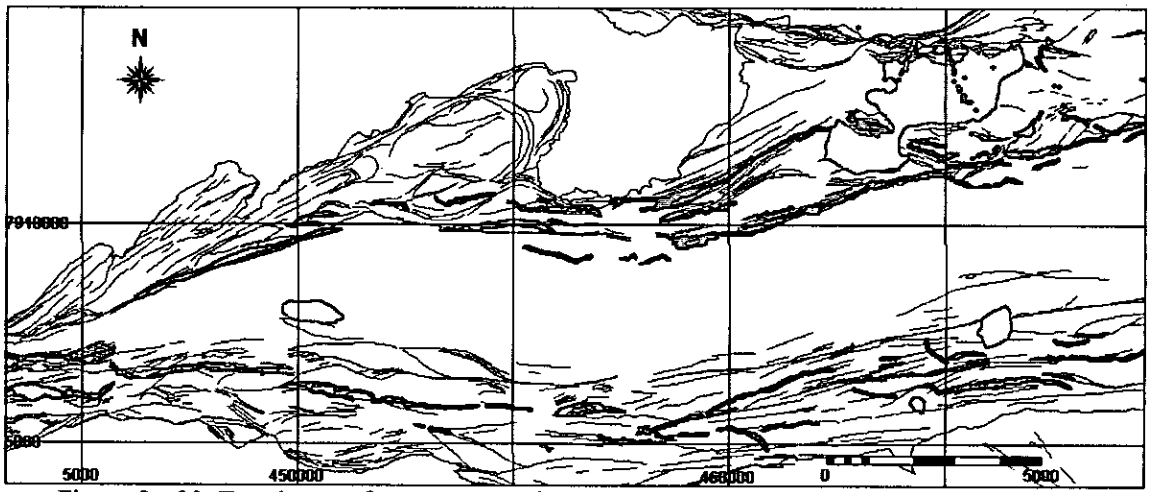

Figure 8 - 20. Trend map of Mutare part of the MMO superimposed the BIF in red and green dots represent the location of samples for PIMA analyses. The thin red lines are lithological boundaries between ultramafics and granites and ultramafics and metasediments. The brown polygons represent the granites. The thin black lines are trends representing the foliation cleavage or bedding as interpreted from satellite imagery (TM169/73, ETM 169/73, SPOT - Xs and SPOT-Panchromatic) and mosaic of airphotos with geological map as reference. UTM coordinates.

The shear zones, specially those within ultramafic units are distinguished on the Landsat ETM images by composite images of their ratio 5/7 April image, 5/7 November image, and 7, in R-G-B (Fig. 8 – 21).

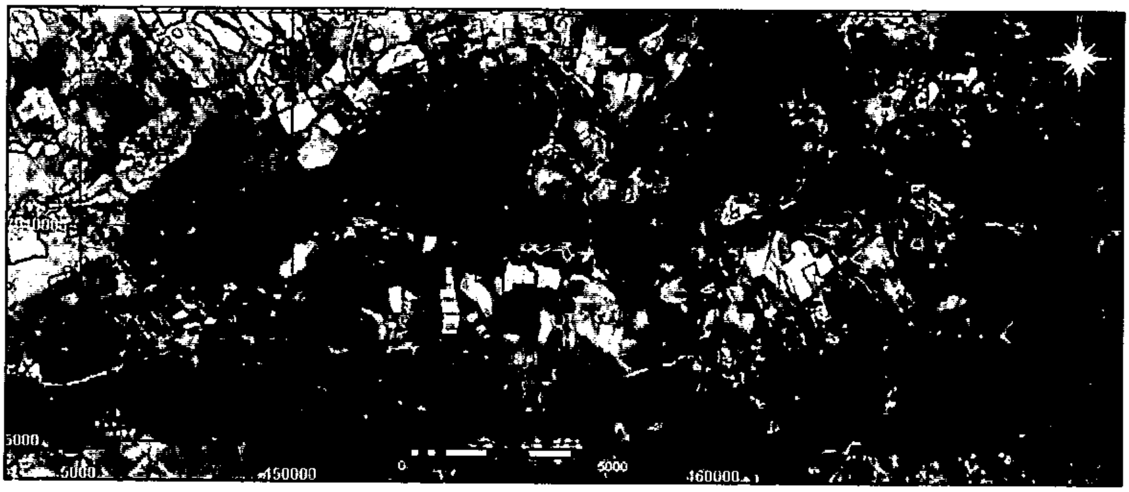

Figure 8 - 21. Landsat ETM ratio images (5/7 April image, 5/7 November image, ETM_April band 7, in R-G-B) illustrating linearity of ultramafic units (interpreted as shear zones in Fig. 8- 22) to the north and to the south of the belt.

The Fig. 8 – 22 show the structural interpretation based on Landsat imagery, PIMA results interpretation and field observations. Most of the interpreted shear zones coincide with zones of discrete alteration shown in Fig. 8 – 19.

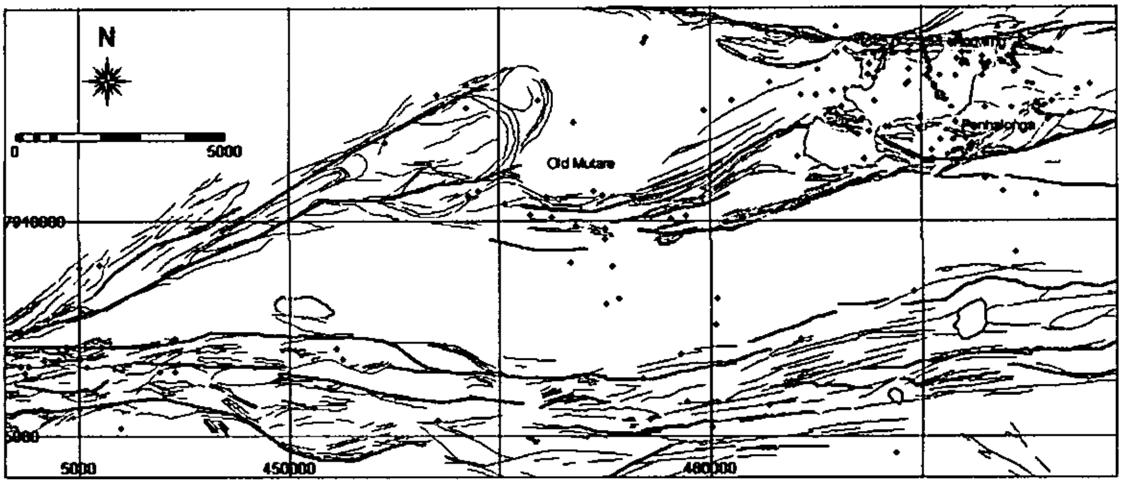

Figure 8 - 22. Structural interpretation of satellite imagery of the Mutare section of the MMO, the shear zones in red and the green dots representing the location of samples for PIMA analyses. The thin black lines are trends representing the foliation cleavage or bedding as interpreted from satellite imagery (TM169/73, ETM 169/73, SPOT - Xs and SPOT-Panchromatic) and mosaic of airphotos with geological map as reference. The brown polygons represent the granites. The black dots represent the location of gold deposits. UTM coordinates.

8.3 Discussion

The mapping of mineralised structures hinges in the mapping of shear zones which are already known to be associated to BIF. The BIFs have positive topographic expressions and linear on E-W strike, which ease its detection when poorly vegetated. Field evidence shows that deposits related to contact between Shamvaian and Upper Bulawayan are associated with BIF. Thus combining the structural interpretation of the satellite and aerial photography and field data it was possible to map the BIF.

Band ratios were used to evaluate the applicability of standard clay and iron ratio to MMO belt. It was found that the standard clay and iron ratio had to be customised to the local conditions. This was achieved following two main approaches, which firstly consisted of identification of the ratios that can potentially map the alteration minerals by plotting the ratio using the USGS 1998 spectral library data, and the second involved the testing of the anomalous ratios for the MMO data (ETM_00 or ETM_99 images).

Various ratios were tested using first the spectral library of the USGS (1998) (Figs. 8 – 9, 8 – 10, 8 – 12, 8 – 14 and 8 – 16). After that only the anomalous ratios were tested using MMO data (Figs. 8 – 11 (band 5/band 7), 8 – 13 (band 3/ band4), 8 – 15 (band 2/ band 7), and 8 – 17 (band 7/ band3)).

The ratio images were then classified and sliced for better visualisation. The ratio maps show anomalies in the areas of high concentration of alteration minerals (Figs.8 –

11, 8 – 13, 8 – 15 and 8 – 17). These anomalies correlate with sections of known shear zones as expected. The fact that only sections of shear zones coincide with alteration patterns revealed by the ratio images is explained by the fact that not all shear zones are associated with alteration and for those which are, it is not the entire shear zone that is expected to be mineralised. The alteration maps correlate well with distribution of lithology and vegetation.

The poor correlation between ratio images and shear zones required testing of spectral ground data collected in profiles across known mineralised shear zones using Pima, as discussed in the Chapter 6.

Relating spatially the shear zones and the mineral deposits made it possible to identify the mineralised shear zones (as discussed in Chapters 3 and 4). The shear zones that were not related to mineralisation were considered non-mineralised, among these shear zone some undiscovered mineralisation may be present (Chapter 9).

The satellite imagery processing performed in the study area followed the diagram presented in appendix VIII-A. These proceedings are specific to the MMO data; their use in different data set would require necessary testing. This is because the satellite imagery data are influenced by local climatic conditions, which reduce the chances of direct importing of image processing techniques that work elsewhere into a different area.

As seen in the Fig. 3 - 3, the field data corroborate with satellite imagery interpretation (Fig. 8 – 22) for mapping of geological structures in the MMO greenstone belt, which demonstrates that satellite imagery is a useful tool for structural mapping in greenstone belts.

8.4 Conclusions

The following conclusion could be drawn from this chapter:

- The image processing approach used for the study of the Manica Mutare Odzi greenstone belt data set has proved to be valid for lithologic and structural mapping.
- The manipulation of satellite imagery based on the PIMA data has mapped some shear zones associated with gold.
- Shear zones could be mapped on the basis of topography (when associated with BIF), truncation surfaces of primary layering and trend surfaces on the SPOT-Panchromatic images and air-photograph mosaic and are supported by field observations (Appendix VIII-B).
- Alteration zones that coincide with shear zones to a large extent are (i) phyllitic; (ii) chloritization; (iii) sulphidation and (iv) silicification.
- The structures and alteration patterns mapped with remote sensing corroborate with field observation.
- Band ratios TM3/TM4, TM5/TM7, TM2/TM3 proved to be important for mapping illite, goethite and hematite. The band ratio TM5/TM7 was useful for mapping argillitic alteration, while the band ratio TM7/TM3 was appropriate for mapping chlorite.
- The mapped alteration minerals such as chorite, illite, pyrite, kaolinite, alunite, hematite and sericite are supported PIMA and field observations (Appendix III-A).
- The manipulation of satellite imagery in combination with PIMA data has proved to be a powerful tool for mapping shear zones associated with gold deposits.

Chapter 9

9 GIS and Gold Exploration in the MMO greenstone belt

9.1 Introduction

Mineral exploration has always benefited from combination of spatial and non-spatial data for target delineation. Since early times of cartography the georeferencing of the spatial data has been important. Before Geographical Information System (GIS) techniques, the advents of maps were physically overlaid on lamp tables in order to find the areas of high prospectivity or targeting anomalies. The overlay of spatial data requires that the data are from the same area and that the scale is the same.

The digital *era* brought the GIS, which relate vertical and lateral multiple spatial and associated non-spatial data sets. GIS is defined as a set of tools for collecting, storing, retrieving at will, transforming, and displaying spatial data from the real world for a particular set of purposes (Burrough, 1986). The data set feeding the GIS is described in terms of position (e.g. X – Y UTM coordinates), attributes that are unrelated to position, and spatial interrelations within the data.

In this chapter, the role of GIS as a prospectivity mapping tool is presented, with relevance to regional-scale gold exploration in the Manica Mutare Odzi greenstone belt. The aim is to identify under-explored areas which are considered to be geologically favourable or similar to those known to contain mineralisation, or which satisfy specific requirements on genetic models of gold mineralisation in the MMO greenstone belt. The GIS will combine Fry and fractal results, structural and lithological data generated by image processing and field work, and gold deposits types, in order to generate prospectivity maps.

9.1.1 Review of GIS applications in mineral exploration

Since its establishment, GIS proved to be a useful and important tool for mineral exploration. Work in GIS applications in mineral exploration produced elements relevant for making predictions about the mineral potential of selected areas. These works are driven by supervised and non-supervised decisions (Wyborn et al., 1994). The supervised decisions in the GIS based data is an analyses where the opinion of the geologist is important whereas in non-supervised analyses the predictions are based on measured parameters in well known mineralised system (e.g. Reddy and Bonham-Carter 1991).

In most cases of GIS application in mineral exploration a hierarchical sequential decision-making is adopted. The initial stage has been always to build a GIS based database (as shown in Chapter 4) with diverse lithological, structural and mineral deposits data coupled by geocoded satellite imagery (Landsat TM, ETM and SPOT XS and Panchromatic). The typical analyses is conduced by producing binary maps (Boolean operations) showing areas of presence or not of specific parameter (see section 9.4.3). These maps are usually a result of optimised criteria of selection of specific factors in the controls of mineralisation. One of most used criteria is a spatial relationship between the controlling parameter and known gold deposits.

Bonhan-Carter et al. (1988) investigated the integration of geological datasets (geological map data, lake-sediment geochemical data; airborne geophysics; and mineral occurrence data) for gold exploration in Nova Scotia and come up with overlaying procedures. Bonham-Carter et al. (1995) conducted a study adopting the following processing procedure: (i) map generalization; (ii) selection of the contacts between map classes using raster-to-vector transformations; iii) generation of proximity maps; iv) overlay modelling on the basis of user defined operators; v) displaying new probability maps. The decision model used Boolean operations and Bayesian probability functions to evaluate hypotheses in terms of one or more pieces of evidence. They first described the deposits in terms of association to quartz veins, usually confined to the Goldenville Formation; the veins are concordant and occur at or near the crests of folds; gold occurs within quartz-carbonate veins with associated arsenopyrite and/or pyrrhotite and minor amounts of chalcopyrite, sphalerite, pyrite and locally scheelite and stibnite; the occurrences are commonly confined to pyrite-arsenopyrite-rich black shale horizons; in some cases the gold occurrences are related to NW-SE oriented faults.

On the basis of the above descriptions proximity maps were generated around fold axes, northwest trending lineaments, granite contact, Halifax-Goldenville contact. The proximity maps were then combined using weights of evidence to evaluate how important the presence, or absence of a characteristic is, based on the mineral occurrences present in the area.

The final product was a map showing the known occurrences and new target areas coupled with the probability of finding gold occurrence calculated using Bayesian rules.

Tighe et al. (1995) studied the surface expression of basement faults and their relationship to gold deposits adjacent to the Chedabucto Fault in Nova Scotia using satellite images, airborne gamma ray spectrometer data, ground sample geochemical data and digital geological and topographic maps.

GIS was used to examine empirically the spatial relationships of the following factors to known gold occurrences: (i) multi-element ground and lake sediment geochemistry; (ii) radiometrics; (iii) lithology; and (iv) distance to contacts and distance to lineaments.

Different weights were allocated to the different factors, which were then used to calculate a score for each location representing the gold mineral potential of the area. This procedure has produced a map that shows favourable mineral potential where no mineral occurrences have been found previously.

The delineation of high prospective target areas using GIS in mineral exploration has attracted the attention of many researchers in the 1990's and various methods have been presented (e.g. Boolean logic, index-overlay, weights of evidence). For example Reddy and Bonham-Carter (1991) portrait that decision tree approach of spatial and non-spatial data integration (in GIS) provides a way of identifying target areas for gold exploration, Gettings and Bultman (1993) applied the probability theory from fuzzy logic to the quantification of favourableness of quartz-carbonate vein deposits in southeast Arizona, Bonham-Carter *et al.*, 1988, Agterberg *et al.*, 1990, Bonham-Carter (1997), Carranza and Hale (2000), favour the use of Bayesian probability theory for predicting mineral potential for districts where a number of representative mineral occurrences are known. The later method is particularly valid for modelling the spatial correlations between geological features and known mineral occurrences, this is the method that was used in the MMO greenstone belt.

The above review shows that in general, GIS is progressing in relation to mineral exploration and can only be useful when the genetic models of mineralisation are well constrained. The use of GIS in non-supervised approach (Bonham-Carter et al., 1988 and Tighe et al., 1995) should be handled with care or supported with very good statistics and extensive field validation.

The GIS is worth applying when it is assumed that mineralisation in certain area is not depleted and other deposits of the same type exist but are yet to be discovered.

9.2 Rationality of GIS in the gold exploration

GIS is used to manipulate spatial data by querying, analysing and defining critical parameters to the mineralisation process that lead to the deposition of specific gold deposits within particular geological environment. GIS produces not only the exploration procedures, but also maps of prospectivity, which minimise the exploration costs.

GIS is used in Archaean gold exploration because the Archaean gold mineralisation is considered to be a single event related to late Archaean orogenesis that preceded cratonization and that mineralisation is late in the tectonic evolution, and most of the deposits are formed from structurally focussed hydrothermal fluids (e.g. Grooves et al., 1998); This suggests that the geological observations in Archaean terrains reflect the relationships during the time of gold deposition, and that gold deposits are direct or indirectly controlled by structures. Most known deposits are located in sites of interference of optimum multiple factors that control the deposition of gold in large amounts. The controls of mineralisation have proved to be complex in nature and its interrelations. The large number of known deposits in the MMO Archaean greenstone belt implies that the sample of the mineralisation from known deposits might be representative. However, the degree of depletion of gold mineralisation due to mining remains unknown.

This discussion supports the use of GIS for establishing the relationships between critical controlling factors of known gold deposits and predicting areas of high probability of occurrence in the region. The discussion illustrates that gold mineralising systems are complex, and a complex and powerful inference system (GIS) tested with known gold deposits and other mineral occurrences is required to obtain convincing results.

9.3 The GIS pool for Manica Mutare Odzi Greenstone belt

9.3.1 Data Input

The data used in the GIS study were extracted from the digital GIS based database of the MMO belt as noted in Chapter 4. The data consisted of a geological map, a map of structures, satellite images (Landsat TM and ETM, SPOT XS and Pan), aerial photographs, alteration maps generated from Landsat imagery, spectral data from soil and rock samples, streambed patterns, DEM (digital elevation models), field data (e.g. younging direction, mineral lineation, shear indicators), descriptions from literature (e.g. production, grade, host lithology, mineralogy, host structure and location) and gold deposits positions.

Other data that fed proceeding stages were generated along the process of data evaluation, manipulation and interactive interpretation.

In summary the 241 gold deposits in the Manica Mutare Odzi greenstone belt share the following general characteristics:

(i) they occur mainly related to dilational quartz veins and to banded ironstones (BIF), usually in all Bulawayan lithologies;

(ii) they are trapped by secondary and tertiary structures linked to layer-parallel regional shear zones;

(iii) the contact between Bulawayan and Shamvaian lithologies is an important control of mineralisation

(iv) strong deformations, and formation of suitable structures followed by the intrusion of tonalitic magmas, were important factors in gold concentration; and

(v) the main gold mineralisation event occurred in late Archaean;

The vector map of the lithological contacts provided the vector maps to feed the vector-raster operation. Likewise, the lineament maps derived from satellite imagery, air photographs, streambed and trend map interpretation provided the extraction of north-south and northwest -southeast trending used for proximity analyses.

9.3.2 Quality of Data

Spatial and non-spatial geological data are rarely perfect. The uncertainties arise from every processing stage, from data collection to data interpretation and output generation.

The quality of the MMO greenstone belt data hinges on the accuracy of the position of the deposits, the limited knowledge at the time of most of the geological descriptions (e.g. principle of shear zones was not known, the description of less common sulphides is difficult even nowadays), the mapping details which differ from place to place within the belt, and the need for homogenisation (coordinate conversions) of the projection systems that would allow cross maps and table operation in a GIS environment. Most of these inaccuracies result from the age of the data. It is known that the reliability of geological data decreases with age and, the mathematical polynomial operation for projection systems changes.

The quality of the data was assessed by comparing earlier descriptions with more recent ones and by ground truthing, during which 60 mines (25% of the total of the deposits) were visited and checked with regards to position, ore type, mineralised body orientation, pit volume and orientation, number of pits, host lithology, controlling structure, alteration type and sulphide assemblages. The descriptions taken from literature present fault-hosted deposits as a generic term that also includes shear zones and contact reef deposits (Phaup, 1937). In general, the descriptions were good enough for the study although the positions of mines were more difficult to ascertain, and errors between 50 and 100 m were recorded. This error is deemed acceptable because a deposit may be represented by a number of adits, pits and mineralised bodies extending for more than 500 m (e.g. Guy Fawckes mine) and also because it is not known exactly where the recorded position was taken (first adit, main shaft or centre of the claim).

The geological maps were field checked in selected profiles and supported by air photography and satellite imagery interpretation. The final geological map used for the purpose of this chapter was the one presented in Fig. 3 – 1.

It is not within the scope of this Chapter to elaborate on the errors and uncertainties, but it is important to highlight that when uncertainty is present in a dataset, the decision rule needs to accommodate the propagation of the uncertainty through a rule that replaces the hard decision procedures of certain data with soft-data of uncertainty.

Bayesian probability theory are extensively used for decision making in mineral exploration projects where uncertainties are present (Bonham-Carter et al., 1995), Dempster-Shafer theory (Campbell et al., 1982) and fuzzy set theory (Duda et al., 1977). In this study the Bayesian probability theory was used (Appendix IX – A).

9.4 Methodology

9.4.1 Data set and Analyses

Data analyses consisted of the extraction of relevant information and its patterns from the GIS based database. The querying in GIS allows rapid interactive spatial visualization of phenomenon being analysed. This module in a GIS package relates spatial and non-spatial data and may show the result in a map or table with details that the naked eye would not distinguish. The spatial query of a GIS database involves two principal types of questions (Bonham-Carter, 1997):

1) What characteristics exist at some location? and
2) At what locations do certain characteristics exist?

The first question concerns details on, for example, structure, mineralogy, distance to an intrusion, deposit type, distance to the major deposits, production and grade of the deposit, gold content in specific lithology, and distance to the nearest deposits. The second type of query uses detailed attributes (requirements) of the features and searches for the location where preconceived characteristic (s) are satisfied. Conditional query may be like "find all occurrences of gold with production between 1g and 25g" or "find all gold deposits occurring in ultramafics and with production less than 100kg at 5g per ton". The query may be more complex involving more than one attribute and several types of features in a single operation.

In the MMO belt maps of structures (shear zones and selected lithological contacts), lithology maps and map of gold deposits were rasterised at 30m by 30m pixel size for the computation of the weights of the binary predictor maps, and then co-registered on a base of air photograph mosaic, topographic maps and acquired ground control points. The rasterization pixel size was particularly chosen to ensure that only one gold deposit is found within one pixel (Agterberg, 1992). Clusters of deposits in the

MMO belt, particularly around the Penhalonga tonalite intrusion, are as small as 1 km diameter with deposits located at less than 100 meters apart.

Several binary maps were generated. During processing stage, mineralised shear zones and main lithological contacts were selected from structural maps on the basis of their spatial relation to gold deposits, the geological map was regrouped in map domains to generalize, overlay modelling, and displaying new maps after slicing the out put range into convenient and discrete intervals for visualization. Vector-raster operation was used to transform the vector maps into binary raster maps. Constructing buffers around the main lineaments generated proximity maps. The distance to the following features were buffered:

- distance to the nearest Archaean shear zone;
- distance to the nearest granite and porphyry intrusions
- distance to the contact between the greenstones and the external granites;
- distance to the nearest contact between highly contrasting lithologies (Bulawayan and Shamvaian)
- distance to the nearest Fry analyses trend, and
- distance to the nearest BIF

The above maps were combined using weighted algorithms to evaluate the importance of presence, or absence of specific characteristic, with mineral occurrences present in each buffer area.

The optimisation is carried out through a decision-tree analyses, which partitions the dataset, using one variable at a time, to produce mutually exclusive subsets as tested by studentised contrast.

9.4.2 Spatial relationship between gold deposits and controlling factors

The distance between the gold deposit and the critical parameter was measured in such a way that spatial correlation is optimal. The optimum distance is estimated from analyses of the graph of contrast (C) versus cumulative distance as presented in Bonham-Carter, (1997). The highest C is obtained at optimum distance which the predictive power of the binary pattern is maximized Bonham-Carter et al., (1988).

The algorithms for buffering operation have been developed for a variety of data structures, both raster and vector. Discussion of this substance is beyond the scope of this study, interested reader may refer to Bonham-Carter et al., (1988) and references therein.

The binary maps are generated using conditional probability. The proximity maps were created by constructing buffers at successive radii in 100 m intervals. The maps produced show distance to the nearest lineament. The buffers referring to one shear zone continue until it encounters another buffer of neighbouring shear zone, then the buffer with the shortest radius takes priority, ensuring that the resulting map (Fig. 9-1) shows the nearest distance to the shear zone in question.

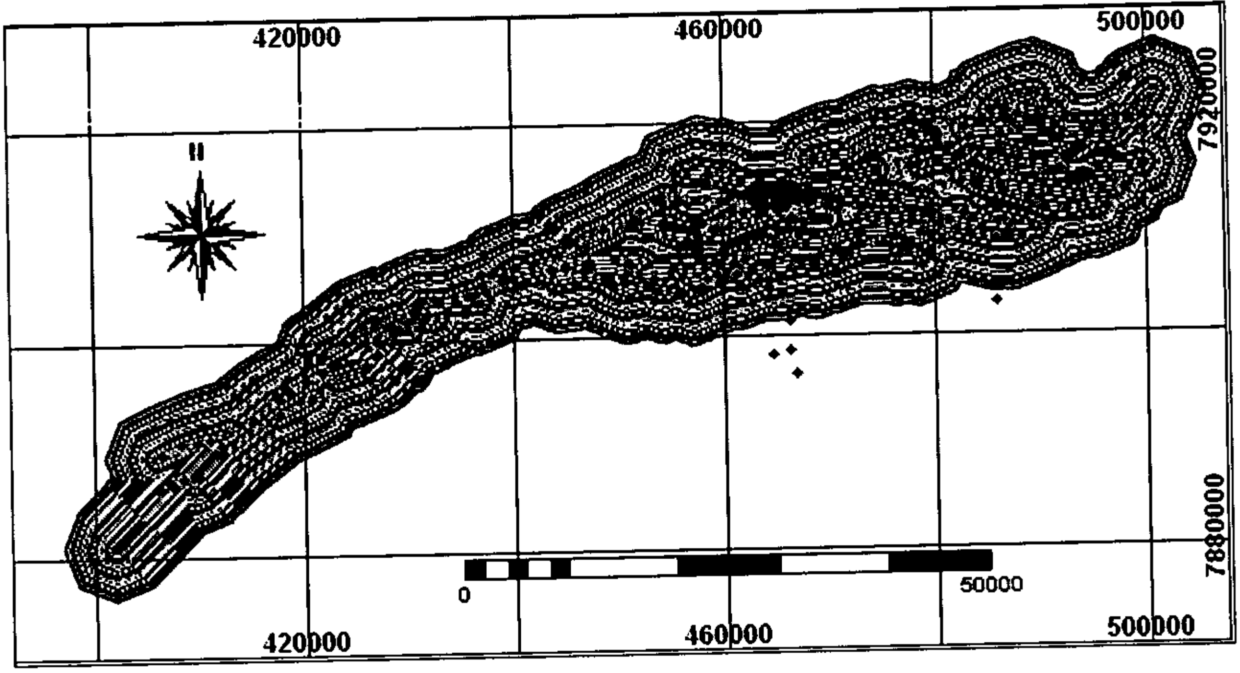

Figure 9 - 1. Proximity map showing shear zones (red lines), gold deposits (black dots). The shear zones were dilated at 100 m interval and the buffer zones are cumulative outwards. Coordinates in UTM.

9.4.2.1 Proximity analyses

In order to quantify the spatial relationship of gold deposits to the shear zones, distribution of distances of the deposits to the nearest shear zone is calculated and statistical analyses was carried out. The figure 9 –1 is used to calculate the distance of gold deposits to the nearest shear zone or the frequency of gold deposits in a 100 m buffer interval. The distribution was obtained by rasterizing the shear zones map followed by creation of buffers at 100 m interval. The following stage was to rasterize the map of gold deposits using the same georeference system as the raster map of the shear zones. The distance between the gold deposit and the nearest shear zone was obtained by crossing the raster map shear zones with the raster map gold deposits. The result is a map representing the intersection of the point map and the bufferėd shear zones; this result can also be displayed as a table containing all intersection points, the distance to the nearest shear zone and the area of influence of the point. The table information was exported into spreadsheet software and the frequency histograms presented in the next sections were generated.

Figure 9 – 3 suggests that over 90% of the gold deposits in the MMO belt are situated within a km from shear zone over 65% are within 500 m and 35% are located within 200 m from shear zones. These results indicate that shear zones are important factors in the control of gold mineralisation in the MMO belt.

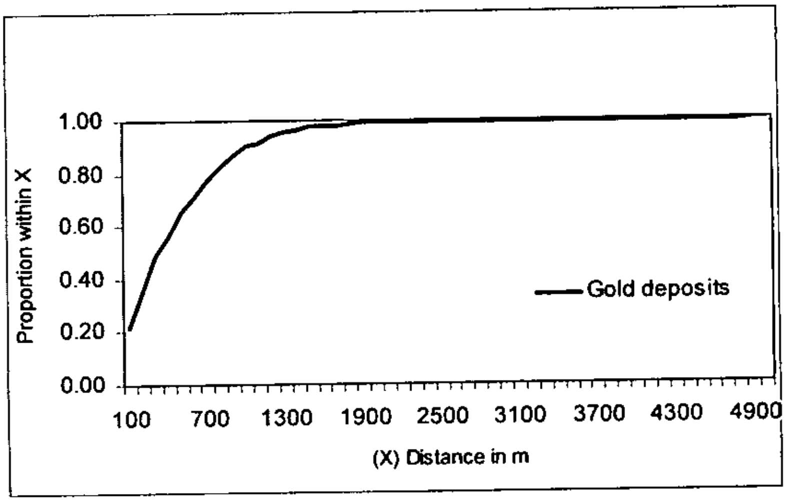

Figure 9 – 2. Observed distribution of gold deposits (occurrences) from nearest shear zone, calculated from the proximity map as described in the text. Represented as cumulative percentage of gold deposits versus distance from the nearest shear zone.

The next analyses carried out was to see whether the general distribution pattern reflected in all deposits is reflected or not at gold deposit type scale. The proximity to the nearest shear zone is estimated for quartz vein (Fig. 9 – 3), high grade (Fig. 9 – 4) and low (Fig. 9 - 5) grade, high (Fig. 9 - 6), medium (Fig. 9 – 7) and low (Fig. 9 – 8) production deposits.

The Fig. 9 – 3 point out that more than 86% of quartz veins hosted deposits are situated within 1 km and 33% within 200 m.

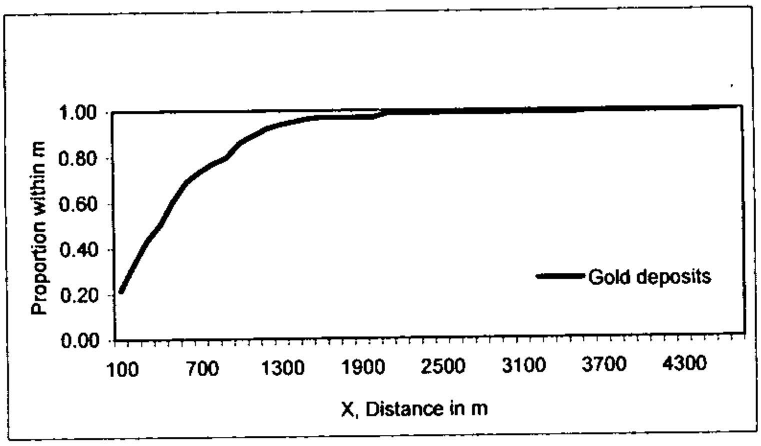

Figure 9 – 3. Observed distribution of quartz vein gold deposits (occurrences) from nearest shear zone, calculated from the proximity map as described in the text. Represented as cumulative percentage of gold deposits versus distance from the nearest shear zone.

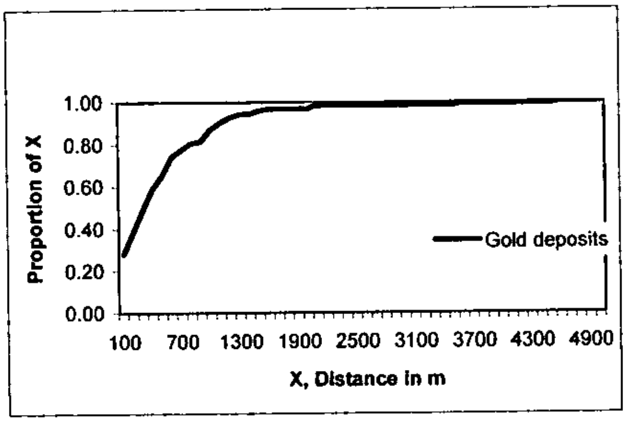

Figure 9 – 4. Observed distribution of high-grade gold deposits (occurrences) from nearest shear zone, calculated from the proximity map as described in the text. Represented as cumulative percentage of gold deposits versus distance from the nearest shear zone.

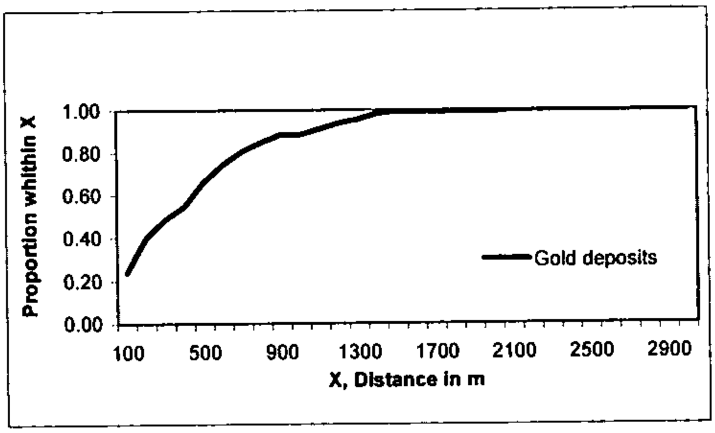

Figure 9 – 5. Observed distribution of low-grade gold deposits (occurrences) from nearest shear zone, calculated from the proximity map as described in the text. Represented as cumulative percentage of gold deposits versus distance from the nearest shear zone.

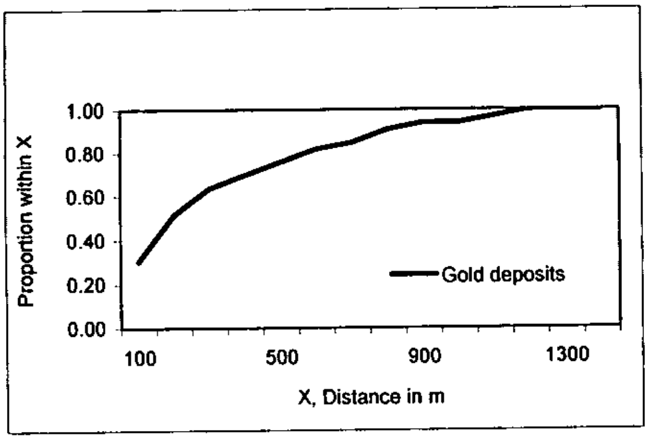

Figure 9 – 6. Observed distribution of high production gold deposits (occurrences) from nearest shear zone, calculated from the proximity map as described in the text. Represented as cumulative percentage of gold deposits versus distance from the nearest shear zone.

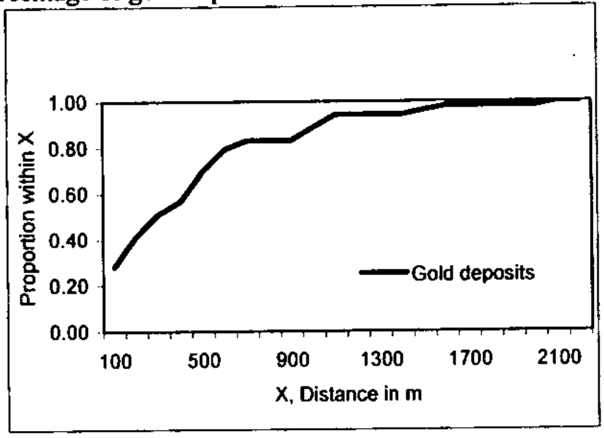

Figure 9 – 7. Observed distribution of medium production gold deposits (occurrences) from nearest shear zone, calculated from the proximity map as described in the text. Represented as cumulative percentage of gold deposits versus distance from the nearest shear zone.

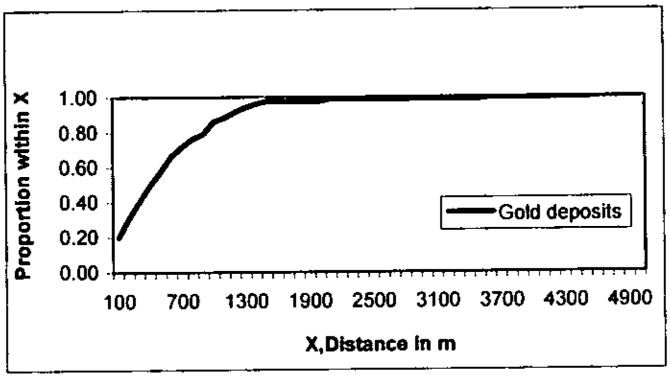

Figure 9 – 8. Observed distribution of low production gold deposits (occurrences) from nearest shear zone, calculated from the proximity map as described in the text. Represented as cumulative percentage of gold deposits versus distance from the nearest shear zone.

Table 9 – 1 summarises the distribution of gold deposits in the MMO belt in relation to the distance from the nearest Archaean shear zone. From Table 9 – 1 it can be seen that the deposits hosted in Shamvaian (35.7%) and the high production deposits (30.3%) are spatially the most related to the shear zones followed by the BIF hosted (28.6%), the medium production (28.3%) and the high grade (28.2%) deposits, which are within 100 m from the shear zone.

Table 9 –1. Summary of the relationship between the Archaean shear zones and distribution of gold deposits in the MMO belt

% of gold deposits & distance to the nearest shear	Number of deposits	1 km {%}	500 m {%}	200 m {%}	100 m {%}
All deposits	241	90	65	35	21.5
Quartz veins	166	86	61	33	21.7
High grade	125	87.1	65.3	49.2	28.2
Low grade	113	88.5	66.4	39.8	23.9
High production	33	93.9	75.8	51.5	30.3
Medium production	53	88.7	69.8	41.5	28.3
Low production	151	86.1	57.6	31.1	19.9
Felsic and Intermediate	61	88.5	59	26.2	18
Shamvaian	28	85.7	60.7	57.1	35.7
BIF	42	85.7	59.5	40.5	28.6

In order to find out the importance of each lithology in the control of gold occurrences related to the nearest shear zone characteristic analyses was carried out. This analysis suggests that most of the Shamvaian host deposits are spatially (35.7% of the deposits are within 100 m and 57.1% are within 200 m from the nearest shear zone, the highest percentage in this range) related to the shear zones (as shown in Table 9 - 1, Fig. 9 – 12). Over 40% of BIF related deposits are located within 200 m from the nearest shear zone (see Table 9 - 1, Fig. 9 – 9). The high correlation between the shear zones and BIF explain the presence of 29% of BIF related deposits within 100 m and 86% within a km from any shear zone. In total 90% of all deposits, 94% of the high production, 89% of felsic – intermediate and 86% of quartz vein deposits in the MMO belt are located within a Km from any shear zone (Table 9 – 1, Fig. 9 – 10). The shear zones are interpreted as major controller to medium to high production deposits (42% of medium and 52% of high production deposits are located within 200 m) and relatively high grade, 49% within 200 m and 94% within a km to the nearest shear zone. These figures rate the shear zones as the most important control of gold mineralisation in the MMO greenstone belt.

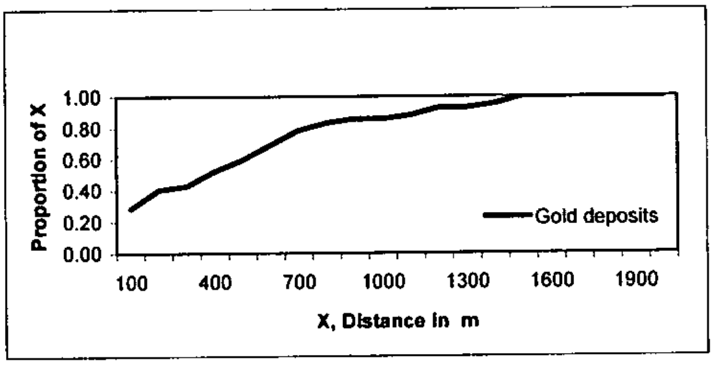

Figure 9 – 9. Observed distribution of quartz vein gold deposits (occurrences) from nearest shear zone, calculated from the proximity map as described in the text. Represented as cumulative percentage of gold deposits versus distance from the nearest shear zone.

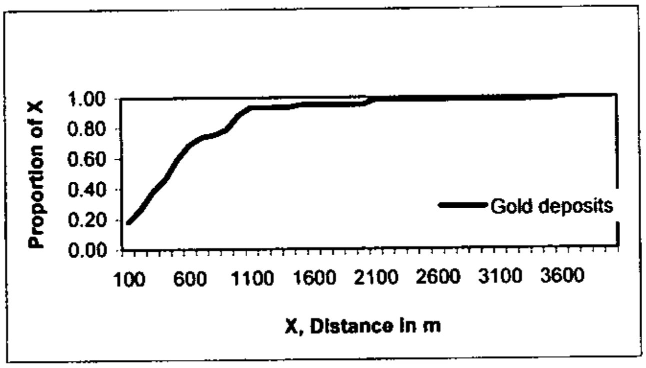

Figure 9 – 10. Observed distribution of Felsic and Intermediate hosted gold deposits (occurrences) from nearest shear zone, calculated from the proximity map as described in the text. Represented as cumulative percentage of gold deposits versus distance from the nearest shear zone.

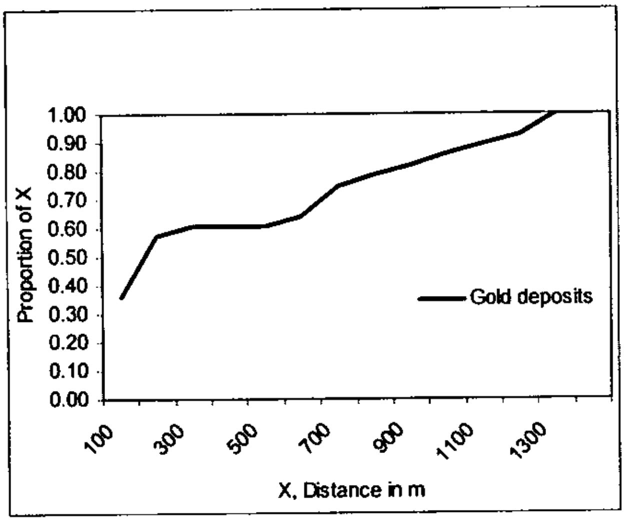

Figure 9 – 11. Observed distribution of Shamvaian gold deposits (occurrences) from nearest shear zone, calculated from the proximity map as described in the text. Represented as cumulative percentage of gold deposits versus distance from the nearest shear zone.

Similar analyses was carried out for the felsic and intermediate intrusion (Fig. 9 – 12), the contact between greenstone belt and the surrounding granite gneiss (Fig. 9 – 13), the contact between Shamvaian and Bulawayan (Fig. 9 – 14), and the lineaments generated from Fry analyses in Chapter 5. In each analysis spatial relationships between each factor and the different types of gold deposits and the main lithologies were estimated and are shown in Figs 9 – 12, 9 - 13 and 9 – 14. The results are summarised in Tables 9 – 2, 9 – 3, 9 – 4 and 9 – 5.

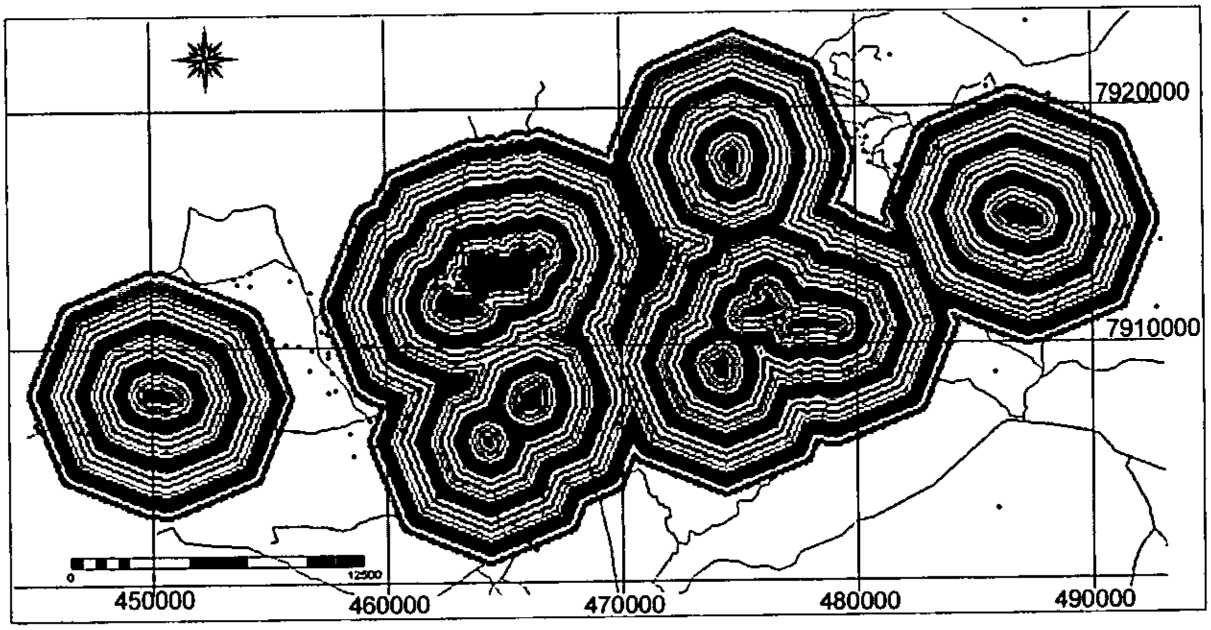

Figure 9 - 12. Proximity map showing granitic intrusions (grey polygons) and gold deposits (red dots) in the MMO belt. The granitic intrusions were buffered at 100 m interval and are cumulative outwards. Coordinates in UTM.

The outcrops of tonalitic intrusions and granitoids mapped from geological map 1:50000 were recognised as important control of gold mineralisation in the MMO belt (see also Fig. 3 – 25 and 3 – 26) due to its contribution to hydrothermal mineralisation system as heat source. The granitoids and granitic intrusions were digitised and polygonised and converted into distance maps that were discretised at 100 m buffering (Fig. 9 – 12). The overlaying of the image on Fig. 9 – 12 with gold deposits allowed the estimation of relative importance of the granitic and granitoid intrusions in the spatial distribution of the deposits. The Table 9 – 2 shows hat 28% of medium production, 17% of high grade and only 12% of high production deposits occur within the granitoids. Within a km from the outer limit of the granitoids occur 32% of quartz vein, 38% of felsic intermediate, 27 of BIF and 28 of all deposits in the MMO belt. Among all deposits located within a km from the intrusion there is 36% of medium and 30% high production, and 30% are high grade.

Table 9 –2. Summary of the relationship between felsic and intermediate intrusions and distribution of gold deposits in the MMO belt

% of gold deposits & distance to the nearest granite intrusion	Number of deposits	1 km {%}	500 m {%}	200 m {%}	100 m {%}	Within granite {%}
All deposits	241	27.8	24.1	19.5	16.6	11.6
Quartz veins	166	31.9	26.5	19.3	17.5	13.9
High grade	125	30.4	27.2	21.6	20.0	16.8
Low grade	113	26.6	20.3	14.2	9.7	6.2
High production	33	30.3	27.3	15.1	15.1	12.1
Medium production	53	35.8	35.8	32.1	30.2	28.3
Low production	151	25.8	19.2	13.2	11.3	8.6
Felsic Intermediate	61	37.7	32.8	26.2	26.2	21.3
Shamvaian	28	7.1	3.6	3.6	3.6	3.6
BIF	42	28.6	19.0	16.7	16.7	14.3

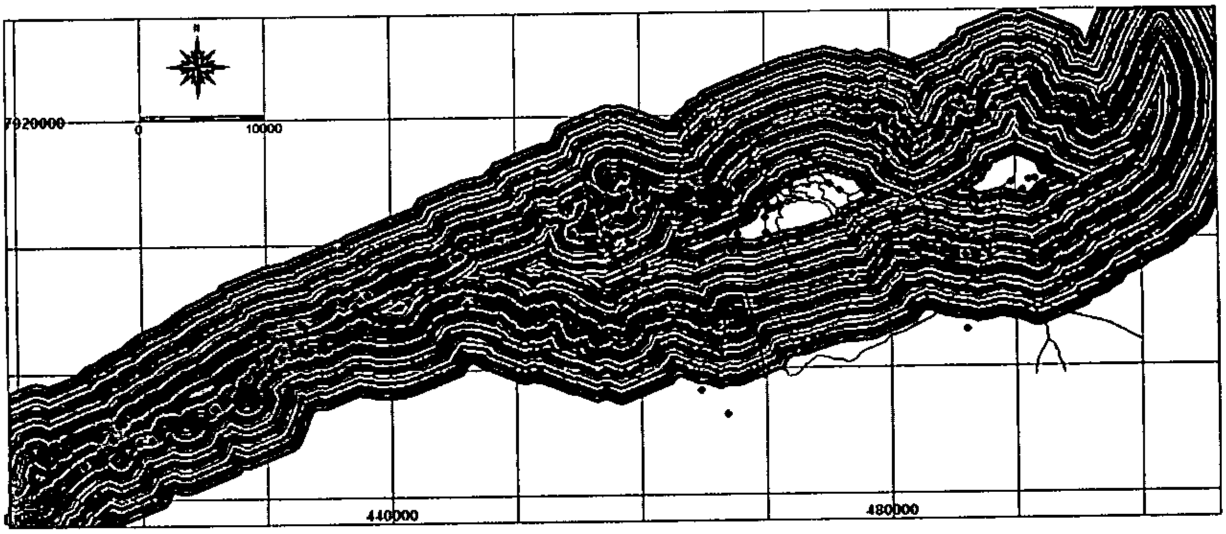

Figure 9 - 13. Proximity map showing the contact between (red line) greenstone belt and the surrounding granite gneiss terrain and gold deposits (black dots) in the MMO belt. The contact was buffered at 100 m intervals and the buffer zones are cumulative outwards. Black lines is the road network. Coordinates in UTM.

The lithological contact between greenstone belts and the surrounding granite-gneiss terrains is known to be spatially associated with gold mineralisation in the Manica and Odzi sections of the MMO belt. The table 9 – 3 shows that 42% of all deposits, 42% of quartz vein type, 62% of felsic Intermediate type, 42% high grade and 42,5% high production deposits in the MMO belt are located within a km from the contact. It is confirmed (Table 9 – 3) that the Shamvaian host deposits are the least influenced by the contact between greenstone belt and the surrounding granite gneiss terrains, because of the stratigraphic position of the Shamvaian sediments (Fig. 3 – 1).

Table 9 –3. Summary of the relationship between the greenstone – granite gneiss terrain contact and distribution of gold deposits in the MMO belt

% of gold deposits & distance to the nearest contact granite - greenstone belt	Number of deposits	1 km {%}	500 m {%}	200 m {%}	100 m {%}
All deposits	241	42.0	26.6	14.5	8.6
Quartz veins	166	41.9	26.4	14.9	10.8
High grade	125	42.4	25.6	14.4	8.8
Low grade	113	41.6	27.4	15.1	11.6
High production	33	42.5	21.2	12.1	6.1
Medium production	53	42.5	25.9	13.0	11.1
Low production	151	41.7	27.8	15.9	10.6
Felsic Intermediate	61	62.3	42.6	24.6	18.0
Shamvaian	28	7.1	3.6	0.0	0.0
BIF	42	23.8	14.3	7.2	2.4

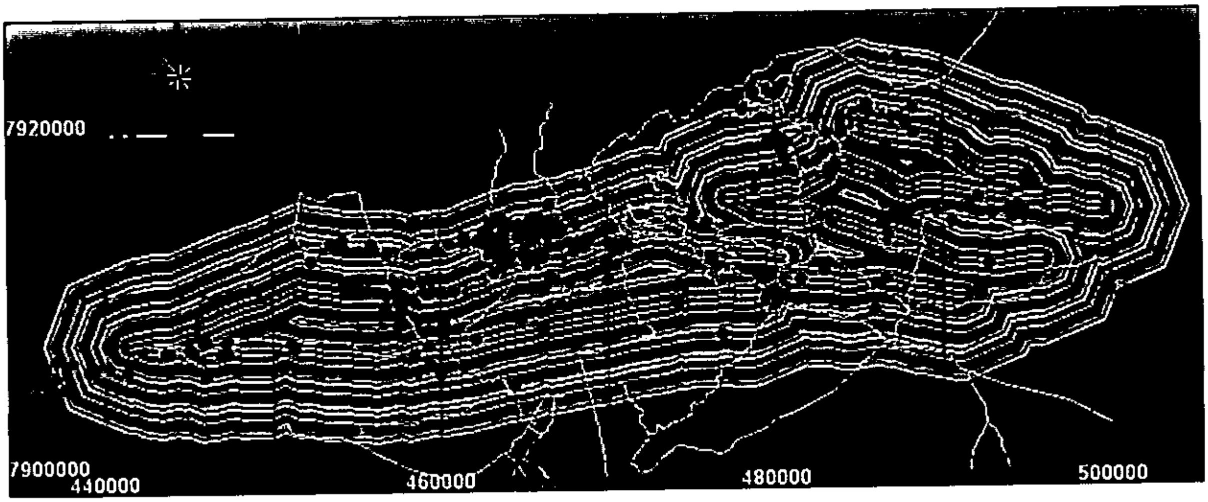

Figure 9 - 14. Proximity map showing the contacts between the Shamvaian and the Bulawayan (red lines), and gold deposits (black dots) in the MMO belt. The contacts were buffered at 100 m interval and the buffer zones are cumulative outwards. The white lines is the road network. Coordinates in UTM.

The contact between Shamvaian and Bulawayan is sheared at places and is known to be associated with gold mineralisation in the MMO belt as exemplified by the Dot's Luck deposit (see section 3.6.2.1). The Table 9 – 4 shows the spatial relationship between the Shamvaian and the Bulawayan contacts and demonstrates that 75% of Shamvaian host deposits, 52% of BIF, 33% of high production and 34% of all deposits in the MMO belt are located at less than a km from this contact. The analysis also proves the non-association of the above contact with felsic intermediate host deposits.

Table 9 – 4. Summary of the relationship between the Shamvaian – Bulawayan contact and distribution of gold deposits in the MMO belt

% of gold deposits & distance to the nearest contact Shamvaian - Bulawayan	Number of deposits	1 km {%}	500 m {%}	200 m {%}	100 m {%}
All deposits	241	34.0	18.6	9.2	5.8
Quartz veins	166	25.9	13.2	5.4	3.7
High grade	125	28.0	15.2	8.0	5.6
Low grade	113	31.0	14.2	7.1	3.6
High production	33	33.3	21.2	12.1	6.0
Medium production	53	24.5	15.1	9.4	5.6
Low production	151	30.4	13.3	6.0	4.6
Felsic Intermediate	61	3.3	0.0	0.0	0.0
Shamvaian	28	75.0	50.0	14.3	10.7
BIF	42	52.4	30.9	16.6	7.1

9.4.3 Creation of binary maps (weights of evidence) of the geological features controlling gold mineralisation

This method was favoured instead of the multiple regression method because it avoids the need to subdivide the area into cells, each cell associated with its own attributes. These would create large attribute files and a complex degree of spatial autocorrelation, which in fact would not improve the quality of the analyses (e.g. Wackernagel, 1995). The weights of evidence probability analysis for quantification of relationships between known mineral deposits and deposits recognition criteria using Bayesian rule is extensively described by Bonham-Carter et al. (1998) and Bonham-Carter (1997). Appendix IX describes the Bayes' rule for binary maps creation. The binary maps are actually themselves probability maps which take into account the architecture of the geology of the MMO belt. The binary model was calculated on the basis of half of the dataset in all categories. The data splitting method was such that every deposit had the same chance to belong to one or other set. This was achieved by selecting in the randomly listed deposits every other deposit to belong to one group and the rest to the other group set.

The rasterised lithological map or any other geological pattern was reclassified into a binary map of favourable lithologies (assigned 1) and non-favourable lithologies (assigned 0).

In the case of MMO region where there are known gold occurrences with gap areas in between, the potential of the whole region including the gap areas, can be calculated statistically. The assessment of this potential requires that relationships between gold mineralisation and the controlling factors (granitic intrusions, Shamvaian – Bulawayan contact, granite – greenstone belt contact, BIF, quartz veins and shear zones) be established. Such relationships were established in the previous sections by constructing buffers around the parameters and relating this to the gold occurrences. Because these relationships are complex and overlap among themselves it is important to establish the distance up to which the influence of each controlling factor is optimum. This optimum distance can be called cut-off or threshold distance and is defined by calculating and interpreting the contrast (C) at successive cumulative distances away from the controlling factor. The highest contrast usually indicates the optimum threshold distance at which the predictor power of the binary pattern is maximized (Bonham-Carter et al., 1998, Caranza and Hale, 2000). The Studentized C was used to determine the threshold distance due to its high sensitivity to small changes and because it takes into account the certainty (and uncertainty) of the contrast. The mathematical formulas for the weights of evidences, contrast value, Studentized contrast value and conditional independence are well described in Bonham-Carter, (1997) and reproduced in Caranza and Hale, (2000).

Table 9 – 5 shows the weight of evidence, distance to the nearest granitic intrusion, contrast and Studentized contrast variation. The contrast and Studentized contrast variation is also illustrated in Fig. 9 – 19 and the cutoff value, regarded as the highest value of the contrast and indicated by the black line. The 500 m threshold encompasses 32 gold occurrences out of 120. This is equivalent to 26% of the total deposits, which is supported by geological evidence of the region where it is known that granitic intrusions control around 25% of the gold occurrences in the MMO belt (see also the Chapter 4).

Table 9 - 5. Weight of evidences, distance to the nearest granitic intrusion, contrast and Studentized contrast for the gold deposits in the MMO belt

Distance Buffer	Deposits	W^+	$S^2(W^+)$	W^-	$S^2(W^-)$	C	sC	C/sC
0	16	7.436	0.063	-0.143	0.010	7.579	0.269	28.224
100	19	7.346	0.053	-0.172	0.010	7.518	0.250	30.065
200	23	7.280	0.043	-0.213	0.010	7.492	0.232	32.305
300	27	7.239	0.037	-0.255	0.011	7.494	0.219	34.280
400	30	7.171	0.033	-0.287	0.011	7.459	0.211	35.380
500	**32**	**7.066**	**0.031**	**-0.310**	**0.011**	**7.376**	**0.206**	**35.730**
600	32	6.886	0.031	-0.310	0.011	7.196	0.206	34.859
700	34	6.814	0.029	-0.333	0.012	7.147	0.203	35.278
800	34	6.693	0.029	-0.333	0.012	7.025	0.203	34.679
900	36	6.628	0.028	-0.356	0.012	6.984	0.199	35.061
1000	36	6.512	0.028	-0.356	0.012	6.869	0.199	34.480
1100	36	6.413	0.028	-0.356	0.012	6.769	0.199	33.980
1200	36	6.305	0.028	-0.356	0.012	6.661	0.199	33.438
1300	36	6.215	0.028	-0.356	0.012	6.572	0.199	32.989
1400	37	6.155	0.027	-0.368	0.012	6.523	0.198	32.997
1500	38	6.103	0.026	-0.380	0.012	6.483	0.196	33.037
1600	38	6.030	0.026	-0.380	0.012	6.410	0.196	32.661
1700	38	5.955	0.026	-0.380	0.012	6.335	0.196	32.283
1800	40	5.925	0.025	-0.405	0.013	6.330	0.194	32.688
1900	41	5.884	0.024	-0.417	0.013	6.301	0.192	32.737
2000	42	5.846	0.024	-0.430	0.013	6.276	0.191	32.792
2100	42	5.785	0.024	-0.430	0.013	6.215	0.191	32.471
2200	42	5.728	0.024	-0.430	0.013	6.158	0.191	32.174
2300	43	5.698	0.023	-0.442	0.013	6.140	0.190	32.253
2400	43	5.632	0.023	-0.442	0.013	6.075	0.190	31.909
2500	45	5.625	0.022	-0.469	0.013	6.094	0.189	32.318
2600	47	5.619	0.021	-0.496	0.014	6.115	0.187	32.698
2700	48	5.594	0.021	-0.509	0.014	6.103	0.186	32.754
2800	48	5.548	0.021	-0.509	0.014	6.057	0.186	32.507
2900	48	5.502	0.021	-0.509	0.014	6.011	0.186	32.261
3000	48	5.450	0.021	-0.509	0.014	5.959	0.186	31.982
3100	49	5.431	0.020	-0.523	0.014	5.954	0.186	32.057
3200	50	5.410	0.020	-0.537	0.014	5.947	0.185	32.119
3300	51	5.389	0.020	-0.551	0.014	5.941	0.185	32.171
3400	51	5.351	0.020	-0.551	0.014	5.903	0.185	31.964
3500	51	5.314	0.020	-0.551	0.014	5.866	0.185	31.764
3600	52	5.291	0.019	-0.566	0.015	5.857	0.184	31.792
3700	52	5.254	0.019	-0.566	0.015	5.820	0.184	31.592
3800	52	5.220	0.019	-0.566	0.015	5.786	0.184	31.408

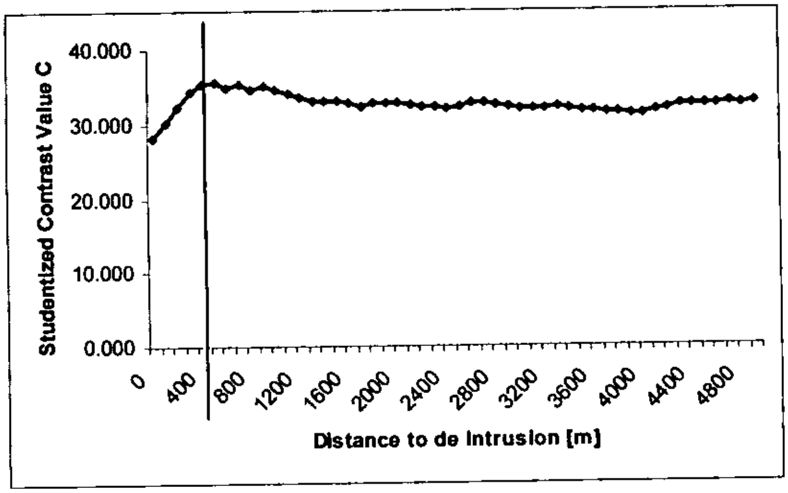

Figure 9 -15. Variation in Studentized contrast value (C) for cumulative distance to the nearest granitic intrusion in the MMO belt

Shown in table 9 – 6 and Fig. 9 – 16 is the variation in the weight of evidence, the contrast and the Studentized contrast for cumulative distance from the nearest Archaean shear zone in the MMO belt. The Studentized contrast is highest at 400 m while the contrast is not conclusive as shown in Fig. 9 - 16. The cutoff distance is set at 400m for the optimum influence of the Archaean shear zones. The table also shows that 74 deposits out of 120 are within the optimum area of influence of the shear zones.

Table 9 - 6. Weight of evidences, distance to the nearest shear zone, contrast and Studentized contrast for the gold deposits in the MMO belt

Distance Buffer	Deposits Number	W^+	$S^2(W^+)$	W^-	$S^2(W^-)$	C	sC	C/sC
Total	120							
100	28	5.798	0.036	-0.265	0.011	6.063	0.216	28.090
200	41	5.683	0.024	-0.417	0.013	6.100	0.192	31.689
300	56	5.655	0.018	-0.627	0.016	6.282	0.183	34.333
400	**65**	**5.592**	**0.015**	**-0.778**	**0.018**	**6.370**	**0.183**	**34.769**
500	74	5.560	0.014	-0.956	0.022	6.516	0.188	34.705
600	84	5.531	0.012	-1.201	0.028	6.732	0.199	33.795
700	90	5.490	0.011	-1.383	0.033	6.874	0.211	32.604
800	94	5.450	0.011	-1.526	0.038	6.977	0.222	31.485
900	96	5.399	0.010	-1.606	0.042	7.005	0.228	30.695
1000	102	5.391	0.010	-1.893	0.056	7.284	0.256	28.491
1100	106	5.364	0.009	-2.144	0.071	7.509	0.284	26.405
1200	109	5.336	0.009	-2.385	0.091	7.721	0.316	24.407
1300	111	5.312	0.009	-2.586	0.111	7.898	0.347	22.788
1400	113	5.288	0.009	-2.837	0.143	8.125	0.389	20.861
1500	114	5.257	0.009	-2.991	0.167	8.248	0.419	19.692
1600	115	5.235	0.009	-3.173	0.200	8.408	0.457	18.405
1700	115	5.206	0.009	-3.173	0.200	8.379	0.457	18.342
1800	115	5.175	0.009	-3.173	0.200	8.348	0.457	18.273
1900	115	5.145	0.009	-3.172	0.200	8.318	0.457	18.207

2000	115	5.121	0.009	-3.172	0.200	8.293	0.457	18.154
2100	117	5.115	0.009	-3.683	0.333	8.798	0.585	15.047
2200	117	5.090	0.009	-3.683	0.333	8.773	0.585	15.005

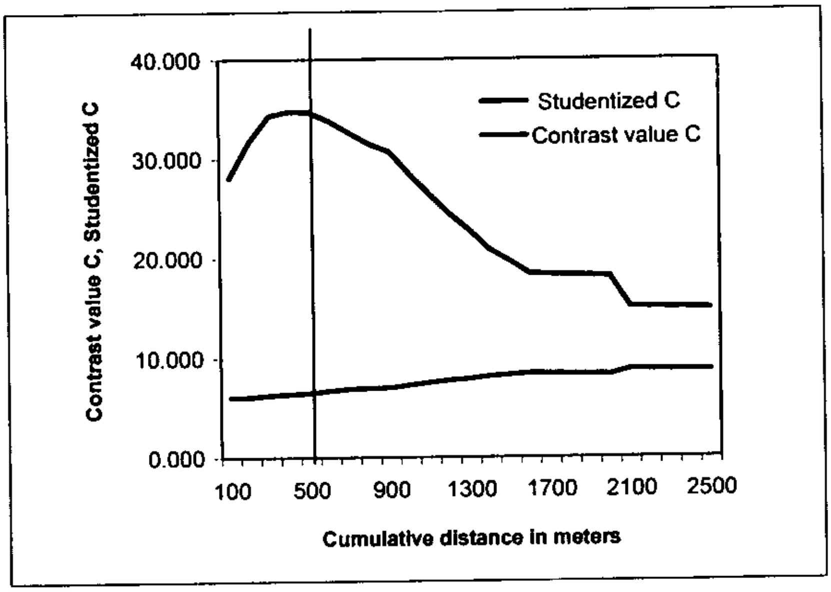

Figure 9 - 16. Variation in contrast value and Studentized contrast value for cumulative distance to the nearest Archaean shear zone intrusion in the MMO belt

The Table 9 – 7 and illustrated in the Fig. 9 – 17 Summarise the weights of evidence, contrast values and Studentized contrast value for cumulative distances from the nearest Shamvaian – Bulawayan contact in the MMO belt.

Table 9 - 7. Weight of evidence, distance to the nearest Shamvaian – Bulawayan contact, contrast and Studentized contrast for the gold deposits in the MMO belt

Distance Buffer	Deposits Total (120)	W^+	$S^2(W^+)$	W^-	$S^2(W^-)$	C	sC	C/sC
100	5	5.232	0.200	-0.042	0.009	5.274	0.457	11.545
200	7	5.049	0.143	-0.060	0.009	5.109	0.389	13.117
300	11	5.149	0.091	-0.096	0.009	5.245	0.316	16.578
400	14	5.136	0.071	-0.123	0.009	5.259	0.284	18.494
500	18	5.186	0.056	-0.162	0.010	5.347	0.256	20.916
600	20	5.108	0.050	-0.181	0.010	5.289	0.245	21.592
700	**28**	**5.301**	**0.036**	**-0.265**	**0.011**	**5.565**	**0.216**	**25.786**
800	28	5.180	0.036	-0.264	0.011	5.445	0.216	25.227
900	31	5.176	0.032	-0.297	0.011	5.473	0.209	26.244
1000	35	5.201	0.029	-0.343	0.012	5.544	0.201	27.604
1100	38	5.194	0.026	-0.379	0.012	5.573	0.196	28.400
1200	45	5.276	0.022	-0.468	0.013	5.744	0.189	30.462
1300	53	5.374	0.019	-0.581	0.015	5.955	0.184	32.393
1400	57	5.387	0.018	-0.642	0.016	6.029	0.183	32.980
1500	60	5.384	0.017	-0.691	0.017	6.075	0.183	33.272
1600	60	5.336	0.017	-0.691	0.017	6.027	0.183	33.012
1700	62	5.328	0.016	-0.725	0.017	6.052	0.183	33.132
1800	63	5.305	0.016	-0.742	0.018	6.047	0.183	33.078

1900	64	5.288	0.016	-0.759	0.018	6.047	0.183	33.049
2000	68	5.319	0.015	-0.833	0.019	6.152	0.184	33.395
2100	69	5.306	0.014	-0.853	0.020	6.159	0.185	33.352
2200	71	5.309	0.014	-0.893	0.020	6.201	0.186	33.390
2300	71	5.283	0.014	-0.893	0.020	6.176	0.186	33.254
2400	75	5.314	0.013	-0.978	0.022	6.291	0.189	33.365
2500	75	5.285	0.013	-0.978	0.022	6.263	0.189	33.214
2600	77	5.288	0.013	-1.023	0.023	6.311	0.190	33.150
2700	78	5.278	0.013	-1.046	0.024	6.324	0.191	33.044
2800	80	5.281	0.013	-1.095	0.025	6.376	0.194	32.925
2900	82	5.283	0.012	-1.146	0.026	6.430	0.196	32.764
3000	84	5.285	0.012	-1.200	0.028	6.486	0.199	32.559
3100	90	5.323	0.011	-1.383	0.033	6.706	0.211	31.808
3200	92	5.325	0.011	-1.452	0.036	6.776	0.216	31.395
3300	93	5.315	0.011	-1.488	0.037	6.803	0.219	31.119
3400	93	5.295	0.011	-1.488	0.037	6.783	0.219	31.026

The Studentized contrast is highest for 700 m wherein 28 of the 120 gold occurrences are present and a second pick is at 1500 m where 50% of the deposits are included. The optimum cut off distance from the Shamvaian – Bulawayan contact is set at 700 m because is unrealistic for the geology of the region that 50% of the deposits would be influenced by this contact.

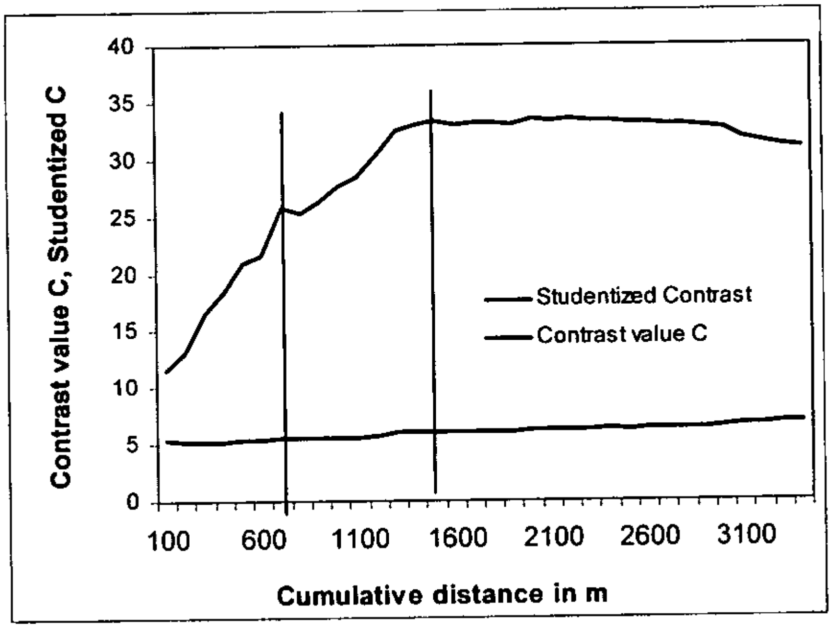

Figure 9 - 17. Variation in contrast value and Studentized contrast value for cumulative distance to the nearest Shamvaian – Bulawayan contact in the MMO belt

The variations of weights of evidence, contrast values and Studentized contrast values for cumulative distances from the nearest BIF in the MMO belt are shown in Table

9 – 8 and Fig. 9 – 18. The highest contrast and the cutoff distance are set at 900 m wherein 62 out of 120 deposits are present.

Table 9 - 8. Weight of evidence, distance to the nearest BIF, contrast and Studentized contrast for the gold deposits in the MMO belt

Distance Buffer	Deposits Total (120)	W^+	$S^2(W^+)$	W^-	$S^2(W^-)$	C	sC	C/sC
100	16	5.483	0.063	-0.143	0.010	5.625	0.269	20.947
200	21	5.371	0.048	-0.192	0.010	5.563	0.240	23.154
300	26	5.296	0.038	-0.243	0.011	5.539	0.222	24.997
400	32	5.315	0.031	-0.309	0.011	5.624	0.206	27.244
500	38	5.340	0.026	-0.379	0.012	5.719	0.196	29.142
600	44	5.351	0.023	-0.455	0.013	5.806	0.189	30.652
700	48	5.306	0.021	-0.509	0.014	5.815	0.186	31.206
800	55	5.349	0.018	-0.611	0.015	5.960	0.183	32.530
900	**62**	**5.386**	**0.016**	**-0.725**	**0.017**	**6.111**	**0.183**	**33.450**
1000	63	5.321	0.016	-0.742	0.018	6.062	0.183	33.164
1100	66	5.289	0.015	-0.796	0.019	6.084	0.183	33.158
1200	69	5.267	0.014	-0.853	0.020	6.120	0.185	33.142
1300	74	5.269	0.014	-0.956	0.022	6.225	0.188	33.153
1400	79	5.278	0.013	-1.071	0.024	6.348	0.192	32.982
1500	84	5.284	0.012	-1.200	0.028	6.484	0.199	32.550
1600	89	5.294	0.011	-1.350	0.032	6.644	0.209	31.859
1700	92	5.284	0.011	-1.451	0.036	6.736	0.216	31.208
1800	92	5.242	0.011	-1.451	0.036	6.693	0.216	31.009
1900	94	5.219	0.011	-1.525	0.038	6.744	0.222	30.434
2000	98	5.225	0.010	-1.692	0.045	6.917	0.236	29.321
2100	100	5.213	0.010	-1.787	0.050	7.000	0.245	28.577
2200	102	5.199	0.010	-1.892	0.056	7.092	0.256	27.739
2300	105	5.198	0.010	-2.075	0.067	7.273	0.276	26.348
2400	106	5.179	0.009	-2.143	0.071	7.322	0.284	25.750
2500	111	5.190	0.009	-2.585	0.111	7.776	0.347	22.435
2600	113	5.181	0.009	-2.836	0.143	8.017	0.389	20.583
2700	113	5.156	0.009	-2.836	0.143	7.992	0.389	20.518
2800	114	5.140	0.009	-2.990	0.167	8.130	0.419	19.411
2900	114	5.115	0.009	-2.990	0.167	8.105	0.419	19.350
3000	114	5.089	0.009	-2.990	0.167	8.079	0.419	19.289
3100	115	5.069	0.009	-3.172	0.200	8.241	0.457	18.040
3200	115	5.047	0.009	-3.172	0.200	8.219	0.457	17.992
3300	115	5.025	0.009	-3.172	0.200	8.197	0.457	17.942
3400	115	5.002	0.009	-3.172	0.200	8.173	0.457	17.891

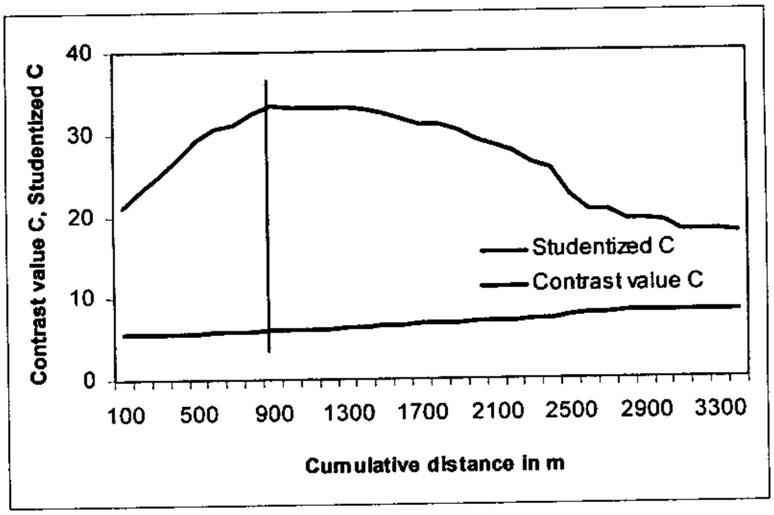

Figure 9 - 18. Variation in contrast value and Studentized contrast value for cumulative distance to the nearest BIF in the MMO belt

The fry analyses or autocorrelation analyses, discussed in Chapter 5 has shown that the translation maps of gold occurrences suggest alignments of dots which are regularly spaced. The main orientations of the alignments are NE – SW, N –S, and E – W. The relationships between the gold occurrences and the alignment identified by autocorrelation analyses are presented using 100 m spacing buffers, estimation of contrast value, Studentized contrast value, and weights of evidences in a Boolean model (Table 9-9).

Table 9 – 9. Weights of evidence analyses of the Autocorrelation analyses lineaments

Distance Buffer	Deposits Total (120)	W^+	$S^2(W^+)$	W^-	$S^2(W^-)$	C	sC	C/sC
100	18	5.508	0.056	-0.162	0.010	5.669	0.256	22.176
200	29	5.487	0.034	-0.276	0.011	5.763	0.213	27.024
300	46	5.571	0.022	-0.482	0.014	6.053	0.188	32.241
400	56	5.541	0.018	-0.627	0.016	6.167	0.183	33.706
500	**62**	**5.462**	**0.016**	**-0.725**	**0.017**	**6.187**	**0.183**	**33.867**
600	67	5.363	0.015	-0.815	0.019	6.178	0.184	33.607
700	75	5.321	0.013	-0.978	0.022	6.299	0.189	33.405
800	80	5.281	0.013	-1.095	0.025	6.377	0.194	32.929
900	83	5.226	0.012	-1.173	0.027	6.399	0.198	32.372
1000	90	5.210	0.011	-1.382	0.033	6.592	0.211	31.271
1100	93	5.152	0.011	-1.487	0.037	6.640	0.219	30.372
1200	95	5.108	0.011	-1.564	0.040	6.672	0.225	29.681
1300	96	5.056	0.010	-1.604	0.042	6.660	0.228	29.184
1400	99	5.022	0.010	-1.738	0.048	6.760	0.240	28.136
1500	101	4.980	0.010	-1.837	0.053	6.817	0.250	27.261
1600	103	4.953	0.010	-1.948	0.059	6.901	0.262	26.361
1700	104	4.919	0.010	-2.009	0.063	6.927	0.269	25.795
1800	106	4.889	0.009	-2.142	0.071	7.031	0.284	24.726
1900	107	4.851	0.009	-2.216	0.077	7.067	0.294	24.059
2000	108	4.826	0.009	-2.295	0.083	7.121	0.304	23.402
2100	108	4.794	0.009	-2.295	0.083	7.089	0.304	23.296
2200	109	4.768	0.009	-2.382	0.091	7.150	0.316	22.601
2300	110	4.749	0.009	-2.477	0.100	7.226	0.330	21.877
2400	111	4.731	0.009	-2.582	0.111	7.313	0.347	21.100
2500	111	4.698	0.009	-2.582	0.111	7.280	0.347	21.005
2600	111	4.670	0.009	-2.582	0.111	7.252	0.347	20.924
2700	113	4.665	0.009	-2.833	0.143	7.498	0.389	19.249
2800	113	4.642	0.009	-2.832	0.143	7.475	0.389	19.191
2900	114	4.627	0.009	-2.986	0.167	7.613	0.419	18.176
3000	114	4.603	0.009	-2.986	0.167	7.589	0.419	18.118
3100	114	4.573	0.009	-2.986	0.167	7.559	0.419	18.048
3200	114	4.554	0.009	-2.986	0.167	7.540	0.419	18.001
3300	114	4.533	0.009	-2.985	0.167	7.518	0.419	17.950
3400	115	4.521	0.009	-3.168	0.200	7.688	0.457	16.830

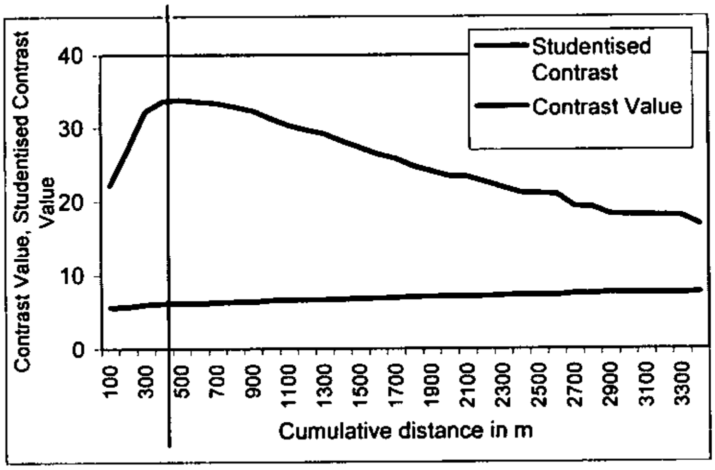

Figure 9 – 19. Variation in contrast value and Studentized contrast value for cumulative distance to the nearest Fry lineament in the MMO belt

At this stage there is one set of seven binary predictor maps (Table 9 –10) that can be integrated to map the gold potential in the MMO greenstone belt on the basis of known gold occurrences. The weights of evidences, contrast values and their standard deviations and Studentized contrast for each of the binary predictor maps are summarised in Table 9 – 10 and the seven maps are shown in Figs 9 – 20 to 9 – 26.

Table 9 - 10. Summary of the weight of evidence, threshold distance and contrast for the gold deposits in the MMO belt

Binary Predictor Pattern	Deposits within threshold	Threshold Distance in metres	W^+	sW^+	W^-	sW^-	C	sC	C/sC
Felsic and Intermediate intrusions	32	500	7,066	0,031	-0,310	0,011	7,376	0,206	35,73
Shamvaian – Bulawayan contact	28	700	5.301	0.036	-0.265	0.011	5.565	0.216	25.786
Granite – Greenstone contact	47	800	4.957	0.021	-0.494	0.014	5.452	0.187	29.151
BIF	62	900	5.386	0.016	-0.725	0.017	6.111	0.183	33.450
Shear zones	74	500	5,560	0,014	-0,956	0,022	6,516	0,188	34,705
Fry lineaments	62	500	5.462	0.016	-0,725	0.017	6.187	0.183	33.867
Bulawayan host rocks	106	900	5.289	0.009	-2.144	0.071	7.433	0.284	26.138

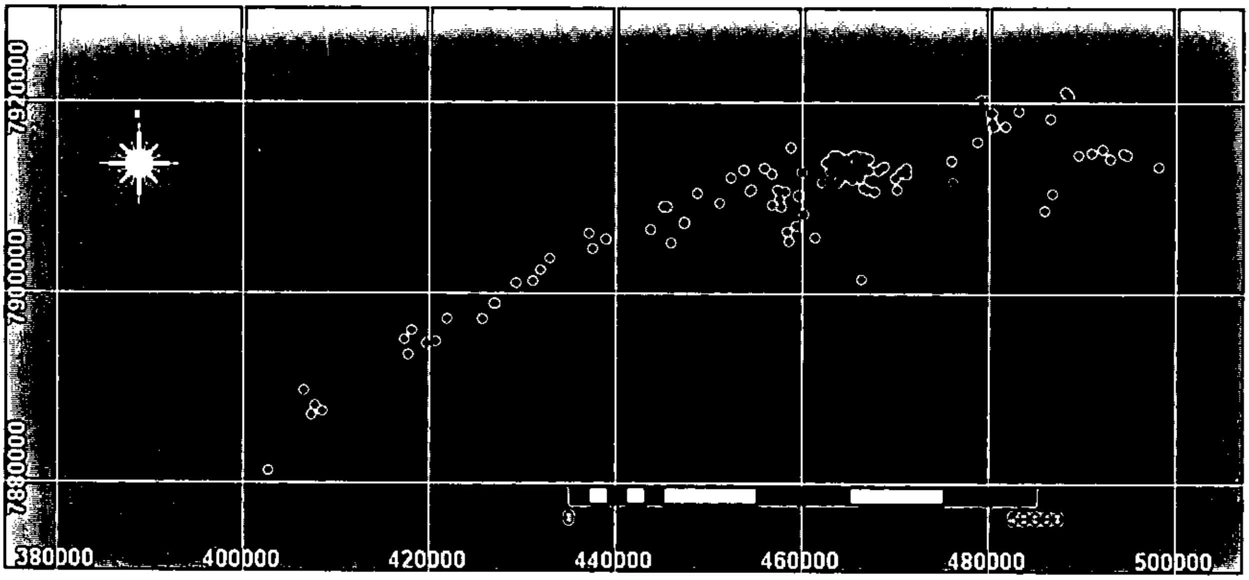

Figure 9 - 20. Binary geological pattern for buffered granitic intrusions (500 m cutoff) and positive and negative weights of 7,066 (red) and -0,310 (blue) respectively. The black dots correspond to all 120 gold occurrences in the MMO belt

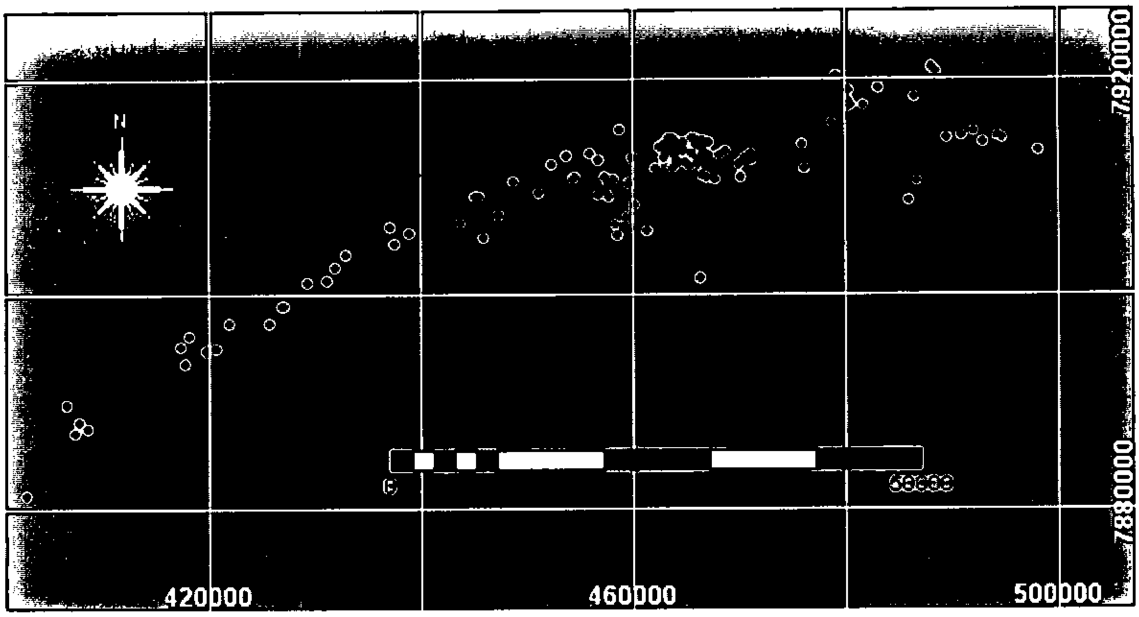

Figure 9 - 21. Binary geological pattern for buffered Shamvaian – Bulawayan contact (700 m cutoff) and positive and negative weights of 5.301 (red) and –0.265 (blue) respectively. The black dots correspond to 120 gold occurrences in the MMO belt

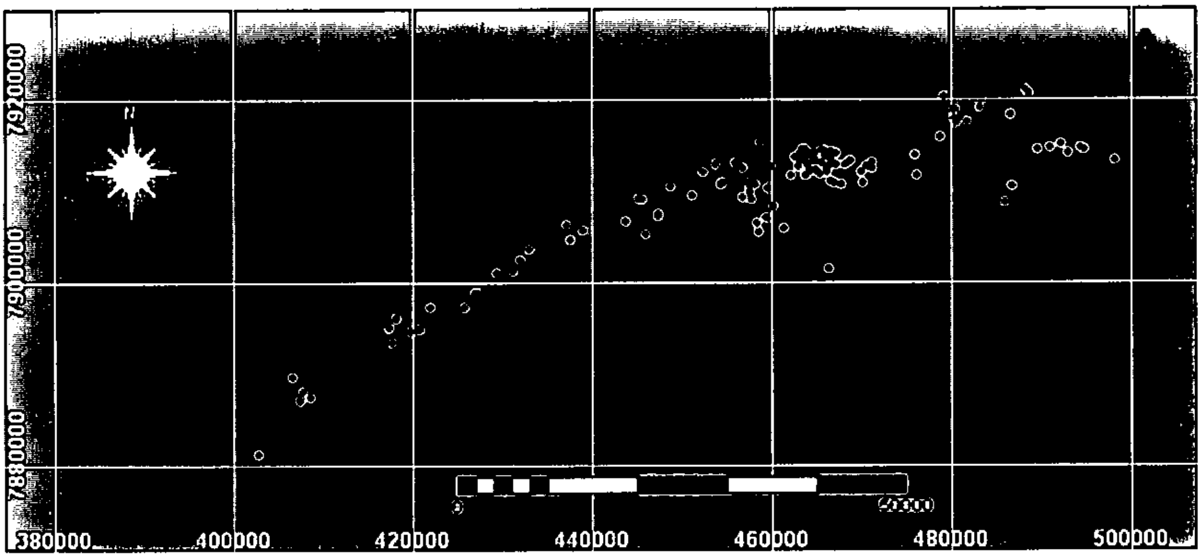

Figure 9 - 22. Binary geological pattern for buffered granite - greenstone contact (800 m cutoff) and positive and negative weights of 4.957 (red) and -0.494 (red) respectively. The black dots correspond to 120 gold occurrences in the MMO belt

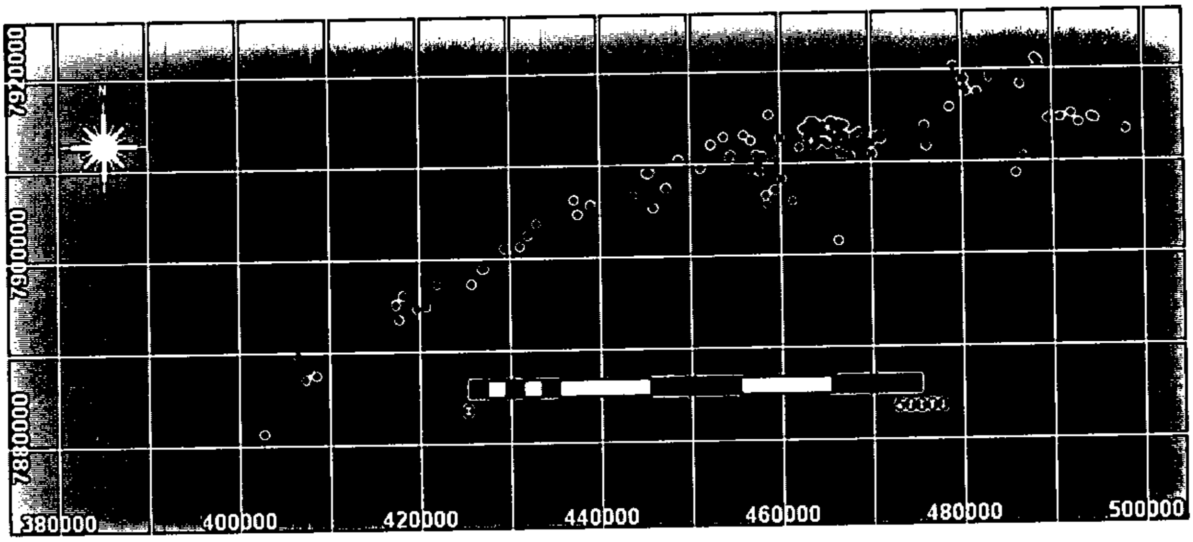

Figure 9 - 23. Binary geological pattern for buffered BIF (900 m cutoff) and positive and negative weights of 5.386 (red) and -0.725 (blue) respectively. The black dots correspond to 120 gold occurrences in the MMO belt

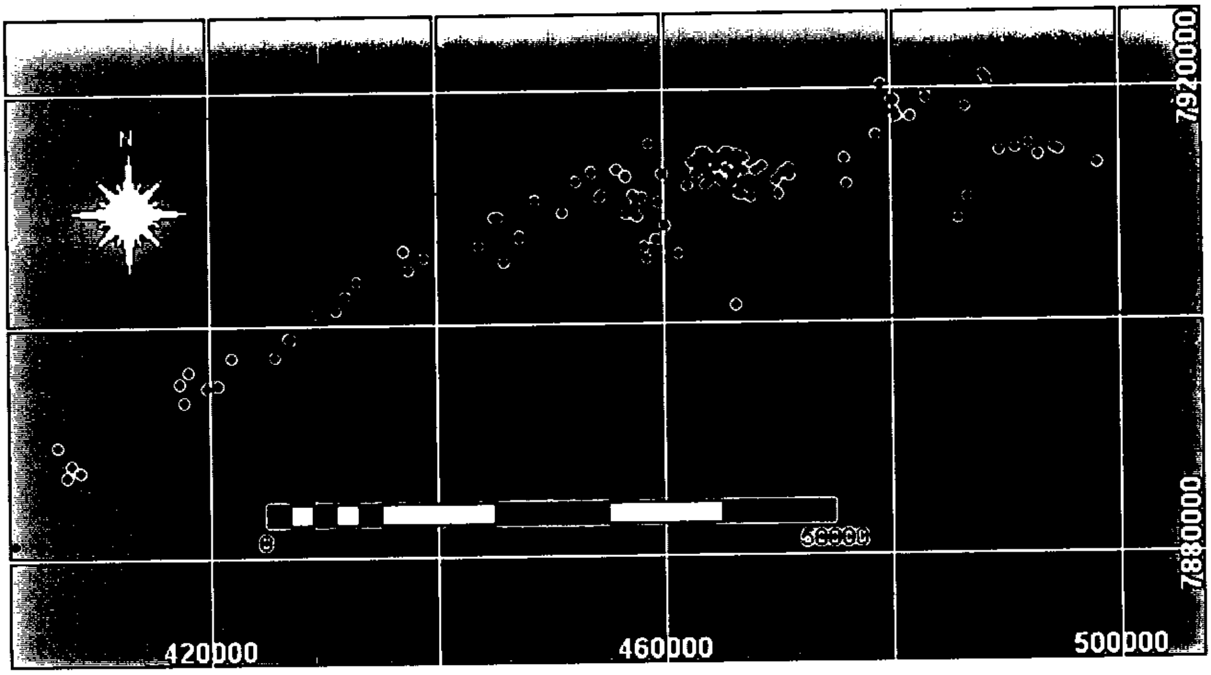

Figure 9 - 24. Binary geological pattern for buffered Shear zones (400 m cutoff) and positive and negative weights of 5,560 (red) and -0,956 (blue) respectively. The black dots correspond to 120 gold occurrences in the MMO belt

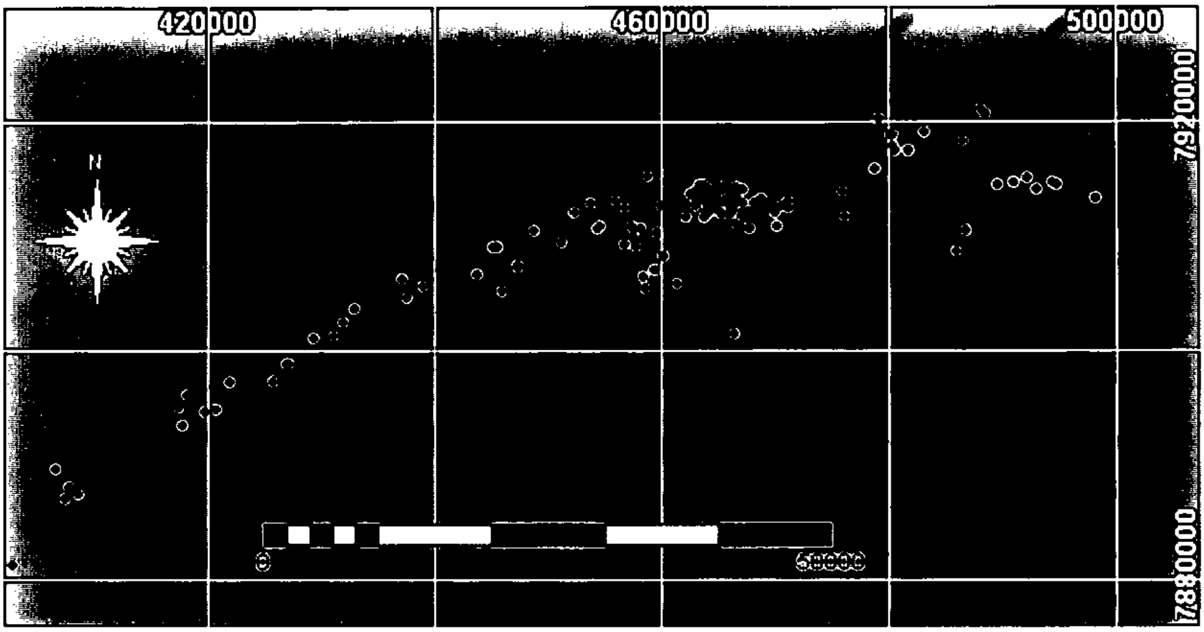

Figure 9 - 25. Binary geological pattern for buffered fry lineaments (500 m cutoff) and positive and negative weights of 5.462 (red) and -0,725 (blue) respectively. The black dots correspond to 120 gold occurrences in the MMO belt

The lithologies hosting more than 25% of the gold deposits in the belt are empirically considered favourable to mineralisation (Table 9 – 10). This condition makes the Bulawayan rocks and the granitic intrusions favourable lithologies and the BIF and Shamvaian lithologies unfavourable. But, if productivity of each lithology, defined per number of deposits per square km is used, the BIF (17465 oz/km^2) becomes favourable (Mondlane et al, 2000).

These lithologies were then integrated and binary maps were generated using conditional probability.

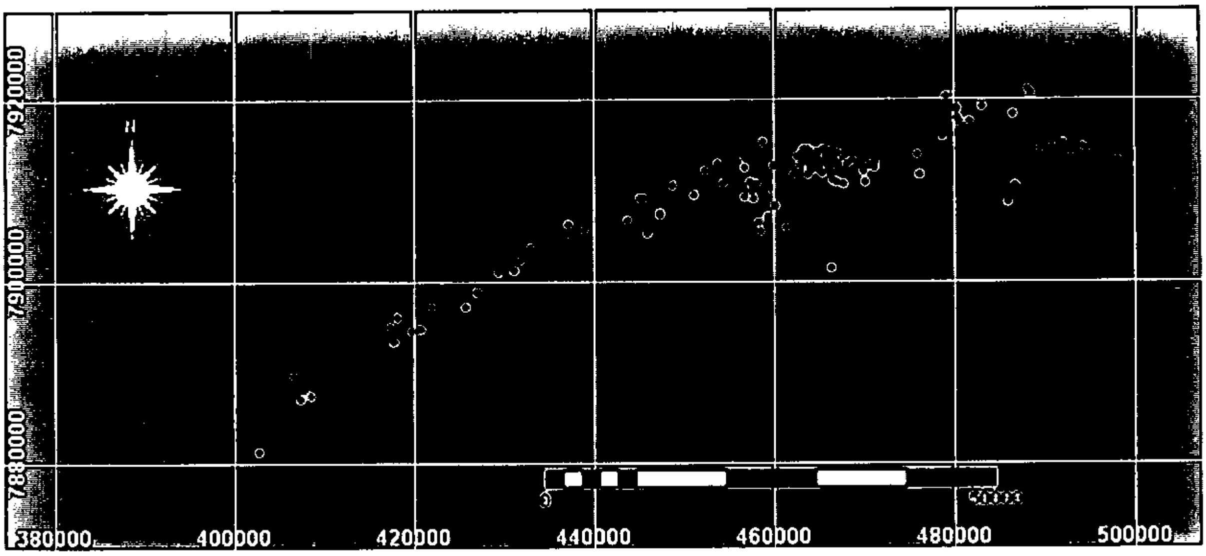

Figure 9 - 26. Binary geological pattern for buffered favourable host Bulawayan lithologies (900 m cutoff) and positive and negative weights of 5.289 (red) and -2.144 (blue) respectively. The black dots correspond to 120 gold occurrences in the MMO belt

9.5 Creation of a mineral potential map for MMO

9.5.1 Test of Conditional Independence

In the MMO region where there are known gold occurrences with gap areas in between, the potential of the whole region including the gap areas, can be calculated statistically. The assessment of this potential requires that relationships between gold mineralisation and the controlling factors (granitic intrusions, Shamvaian – Bulawayan contact, granite – greenstone belt contact, BIF, quartz veins and shear zones) be established.

The seven binary predictor maps created in section 9.4.3 can now be combined to produce a predictive map for the MMO belt. Prior this integration using the Bayesian probability model described by Bonham-Carter, (1997) and Asadi and Hale, (2001), it is necessary to test the conditional independence between all pairs of the maps to be combined.

The test of independence means that the conditional probability of binary pattern e.g. A_1 being present is independent of whether binary A_2 is present or not, and vice versa and can be calculated using the following equation (Bonham-Carter, 1997).

$$N\{A_1 \cap A_2 \cap D\} = \frac{N\{A_1 \cap D\}\, N\{A_2 \cap D\}}{N\{D\}} \qquad \text{Eq. 9 -1}$$

Where **A_1** and **A_2** are conditionally independent with respect to a set of mineral occurrence points **D**.

The left-hand side of the equation is the observed number of deposits in the overlap region where both binary patterns **A_1** and **A_2** are present. The right-hand side is the expected number of deposits in the overlap area. The result of the equation 9-1 can be represented as a contingency table (Table 9 – 11).

The conditional independence is valid only if $N\{A_1 \cap A_2 \cap D\}$ is not equal to zero. In the case where there is no spatial overlap between the patterns **A_1** and **A_2**, then $N\{A_1 \cap A_2 \cap D\}$ is equal to zero, thus there is no conditional independence. If a pattern has high spatial correlation with other, it will imply that the patterns are not conditionally independent and the right hand member of the equation 9 -1 will be greater than the left hand. According to Agterberg (1992), Bonham-Carter (1997) and Caranza (2002) in such cases one of the binary patterns must be discarded or possibly be combined with appropriate binary pattern before the weights of evidence analysis.

The spatial relationships between the binary patterns and the minerals deposit can be related according to a contingency table calculation for testing the conditional independece of every two binary predictor patterns (Table 9 – 11).

Table 9 – 11. Contingency table for testing conditional independence. The four values in the table are either the expected or calculated values according to Eq. 1, or observed values from the maps. (after Bonham-Cater, 1997)

	A_1 Present	A_1 Absent	Total
A_2 Present	$N\{A_1 \cap A_2 \cap D\}$	$N\{\bar{A}_1 \cap A_2 \cap D\}$	$N\{A_2 \cap D\}$
A_2 Absent	$N\{A_1 \cap \bar{A}_2 \cap D\}$	$N\{\bar{A}_2 \cap \bar{A}_2 \cap D\}$	$N\{\bar{A}_2 \cap D\}$
Total	$N\{A_1 \cap D\}$	$N\{\bar{A}_1 \cap D\}$	$N\{D\}$

The conditional independence is tested by calculating χ^2 as follows:

$$\chi^2 = \sum_{I=1}^{4} \frac{(\text{observed } d_i - \text{expected } d_i)^2}{\text{Expected } d_I} \qquad \text{Eq. 9 - 2}$$

The χ^2 can be used to calculate the conditional independence with at least 98% confidence level because the deposits are considered as points, which are not affected by unit area measurements (Walker and Lev, 1953, Bonham-Carter, 1997).

Other methods of testing the conditional independence between a pair of binary predictor patterns are described by Bonham-Carter et al. (1989) where they privilege the calculation of observed and predicted numbers of pixels with and without deposits in eight unique overlap possibilities.

With respect to all deposits in the MMO belt all pairs of binary geological parameters, except for the Fry lineaments and the BIF, are conditionally independent (Table 9 - 12). As proved by the comparison between the critical value of chi-square, which is equal to 15.98 for the probability level of significance of 1%, and degree of freedom is calculated as (number of rows -1) times (number of columns -1) (Levine et al., 2002). The bold values in Table 9 – 12 are those pairs for which the conditional independence is not violated.

Table 9 – 12. Calculated chi-square values for testing conditional independence between all pairs of 5 binary maps with respect to all gold occurrences in the MMO belt.

Binary Map	Shamvaian – Bulawayan contact	Granite – Greenstone contact	BIF	Shear zones	Fry lineaments
Felsic and Intermediate intrusions	**7,388**	**6.774**	**9,384**	**10,888**	23.135
Shamvaian – Bulawayan contact	-	**13,971**	28,297	**25,769**	**15,433**
Granite – Greenstone contact	-	-	**14,671**	**15,633**	17,731
BIF	-	-	-	27,580	52,053
Shear zones	-	-	-	-	29,000

The fact that the geological parametres are conditionally independent, suggest that the binary patterns can be combined using the weights assigned in Table 9 – 10 and the Fry lineaments and BIF must be discarded from the model (see next section).

9.5.2 Data Integration and Results

The final product of the analyses is a new map that should reflect the known occurrences and provides as well new target areas. The probability of finding gold occurrence is calculated using Bayesian rules (Appendix IX). The final maps showing probabilities of gold occurrences were prepared using ILWIS software.

The binary patterns that proved to be conditionally independent according the test described in previous section were assigned the positive weight for the pixels within the optimal spatial association with respect to gold deposits, and otherwise pixels were assigned the negative weight. The pairs of input binary predictor patterns that proved to be conditionally dependent according to the chi-square test were discarded. The overlying of the map is by itself a true geological and statistical test of validity of the predictor patterns. Thus, an overall test of conditional independence for probing the statistical validity of the posterior probability map was not performed in this study.

The GIS uses a query method to create a spatial model by superimposing all the weighted critical parameters in binary maps on to a single map and likewise comparing with known gold deposits and occurrences. The overlap of various evidences of the critical parameters on binary maps resulted in the areas with highest cumulative weights representing the highest probability of gold occurrence.

The Fig. 9 – 26 shows the prospectivity map considering five binary maps (granite-greenstone contact, Bulawayan – Shamvaian contact, shear zones, felsic and intermediate intrusions and the Bulawayan lithology) with predictive weights ranging from a maximum of 22.754 to a minimum of -3,991, providing a relative measure for prioritising areas of exploration potential for gold.

The prospectivity map is presented as discrete and threshold in terms of low, moderate, high and very high prospectivity areas for better visual impact.

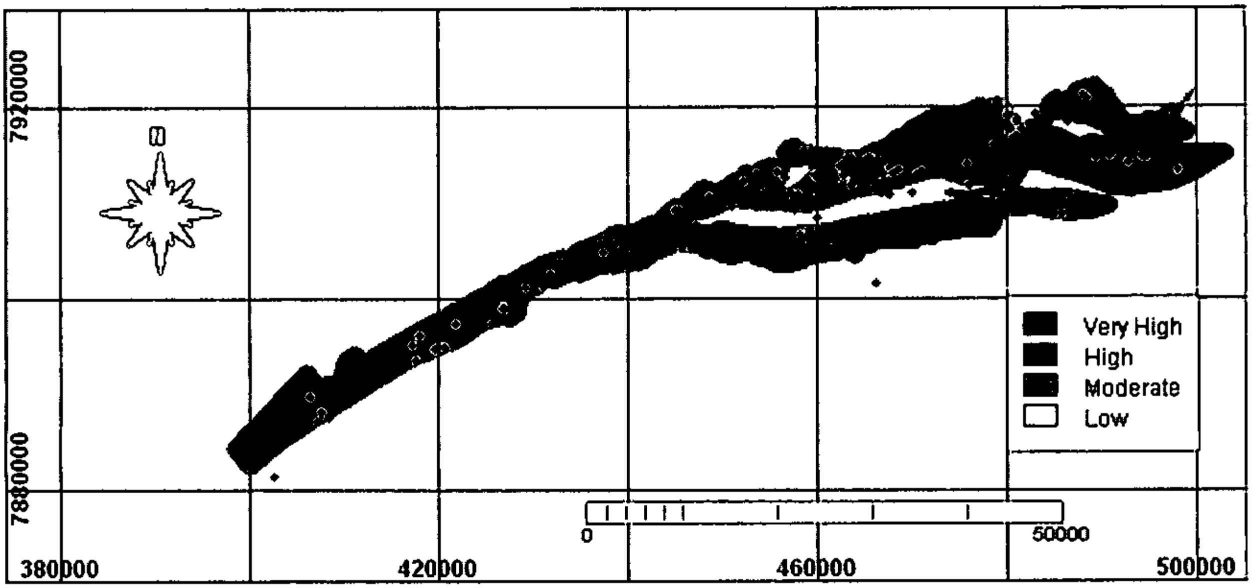

Figure 9 –27. Final map of gold potential based on binary predictor patterns whose weights were calculated for 120 deposits in the MMO belt. The black dots correspond to the 120 gold occurrences used to generate the model.

]

Threshold between low and moderate prospectivity zones is set by $W^+_1 + W^+_2 - W^-_1 + W^-_2$, where the subscripts refer to the predictor patterns with lowest **positive** weights, and is equal to 4.957 + 5.289 – (0,494) + (2,144) = 8.596 for low grade deposits in the MMO belt.

The threshold between the moderate and the high prospectivity areas is calculated using the three-predictor patterns with lowest positive weights, and thus is 13.632.

The threshold between the high and very high prospectivity areas are also calculated similarly using the four-predictor patterns with lowest positive weights, and in this case it is equal to 18.236. The threshold intervals as defined earlier correspond to 16% of the deposits falling in the low prospectivity area, 30% within moderate, 40% and 14.2% of the known deposits are in the high and very high prospectivity areas, respectively.

9.5.3 Analyses of the Results

The summary of the weights and contrast value used in the predictive model for all deposits (Table 9 – 10) of the belt has been illustrated on map of prospectivity Fig. 9 – 27. In the contingency table for calculated chi-square two binary predictor patterns did not meet the criteria for conditional independence and they were discarded from the model. These patterns are geologically related, for example, most of the BIF are within shear zones hence their high spatial correlation. The Fry lineaments are derived from alignments of known deposits which are controlled by one or another pattern in the model, hence its high correlation with all other patterns except for the contact between Bulawayan and Shamvaian. The discarding of these two binary predictor patterns did not affect the model.

The model as designed depicts 54% of the deposits within high and very high prospectivity areas (Fig. 9 – 28). The other strength of the model is that only 16% of the deposits are within low prospectivity area.

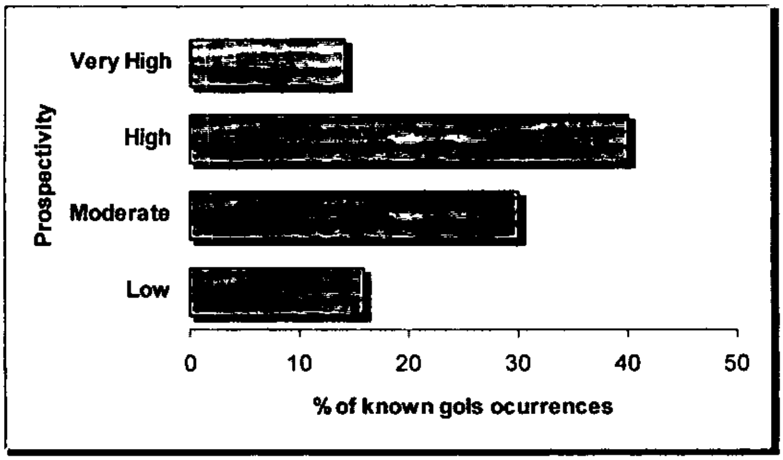

Figure 9 - 28. Distribution of all known deposits within the study area per Prospectivity Index. Note the dominance of deposits within the highly prospective zones.

9.5.4 Model Validation

In general, if more than or approximately 55% of known gold occurrences fall within the areas of high and very high probability one can consider the model correct and the areas of high and very high probability without known deposits may constitute the location of unknown deposits of same type. Table 9 – 13 summarise the distribution of deposits by the probability intervals as mean of model validation. The patterns are similar in all prospectivity index categories where 51% of the deposits are distributed within the high and very high prospectivity areas (Fig. 9 – 29). In the validation data set only 20% of the gold occurrences fall within low prospectivity area. The 30% of gold occurrences falling within area of moderate prospectivity index shows some consistency of the model for the designing and the validation datasets.

Table 9 – 13. Summary of the results of the predictive maps based on the original data (model generator) and the unknown data set (validation set) of gold occurrences in the MMO belt

Gold potential	**All deposits [Set one]**		**All deposits [Set two]**	
	Number	%	Number	%
Low	19	15.8	25	20.7
Moderate	36	30	35	28.9
High	48	40	43	35.5
Very High	17	14.2	18	14.9
Total	120	100	121	100

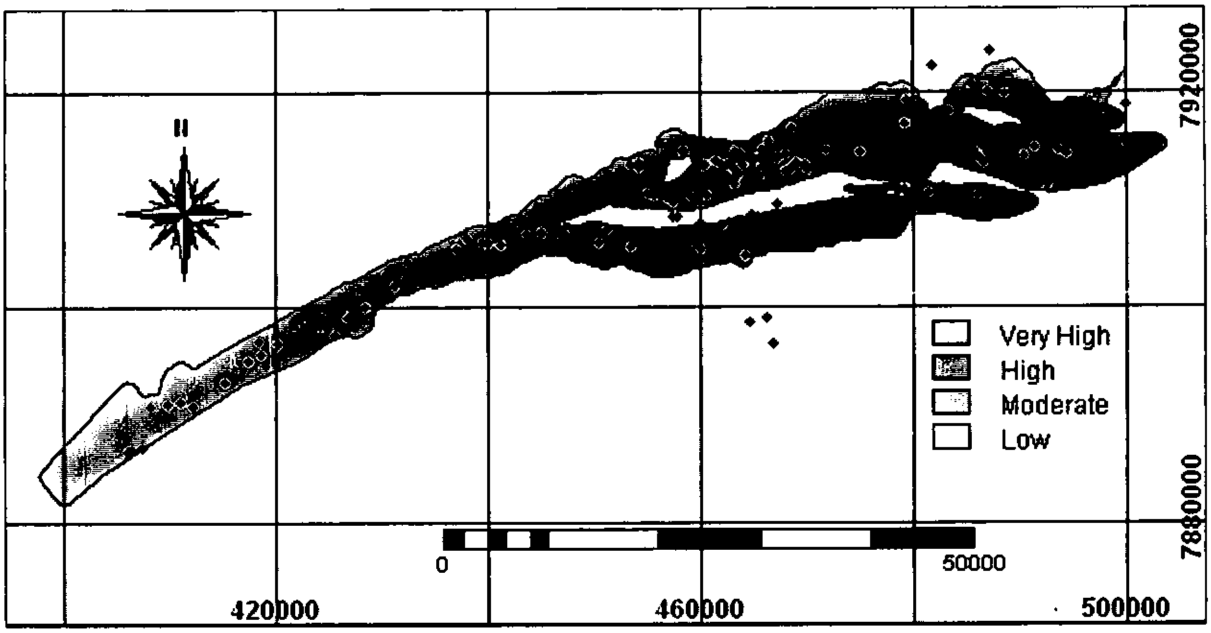

Figure 9 – 29. Final map of gold potential based on binary predictor patterns whose weights were calculated for 121 deposits in the MMO belt. The black dots correspond to the 121 gold occurrences which were not used in the model generation phase.

The Fig. 9 – 30 shows that 70% of the gold occurrences in the validation dataset are within moderate to very high prospectivity areas. This indicates that the assumptions of conditional independence discussed earlier are not seriously violated (Table 9 – 12). This facto, to some extent validates the splitting process used in dataset in order to obtain a model generating dataset and a validation dataset.

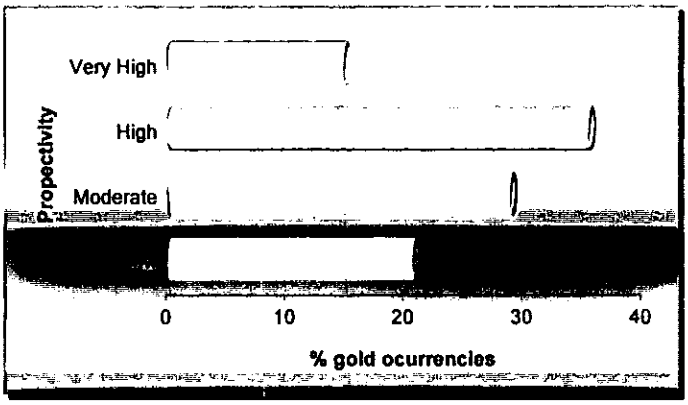

Figure 9 - 30. Distribution of all unknown deposits (Validation dataset) within the study area per Prospectivity Index. Note the pattern similarity between this Fig and the Fig. 9 – 28.

The Fig. 9 – 31 represent the data flow of the GIS model for gold mineralisation prediction in the MMO greenstone belt.

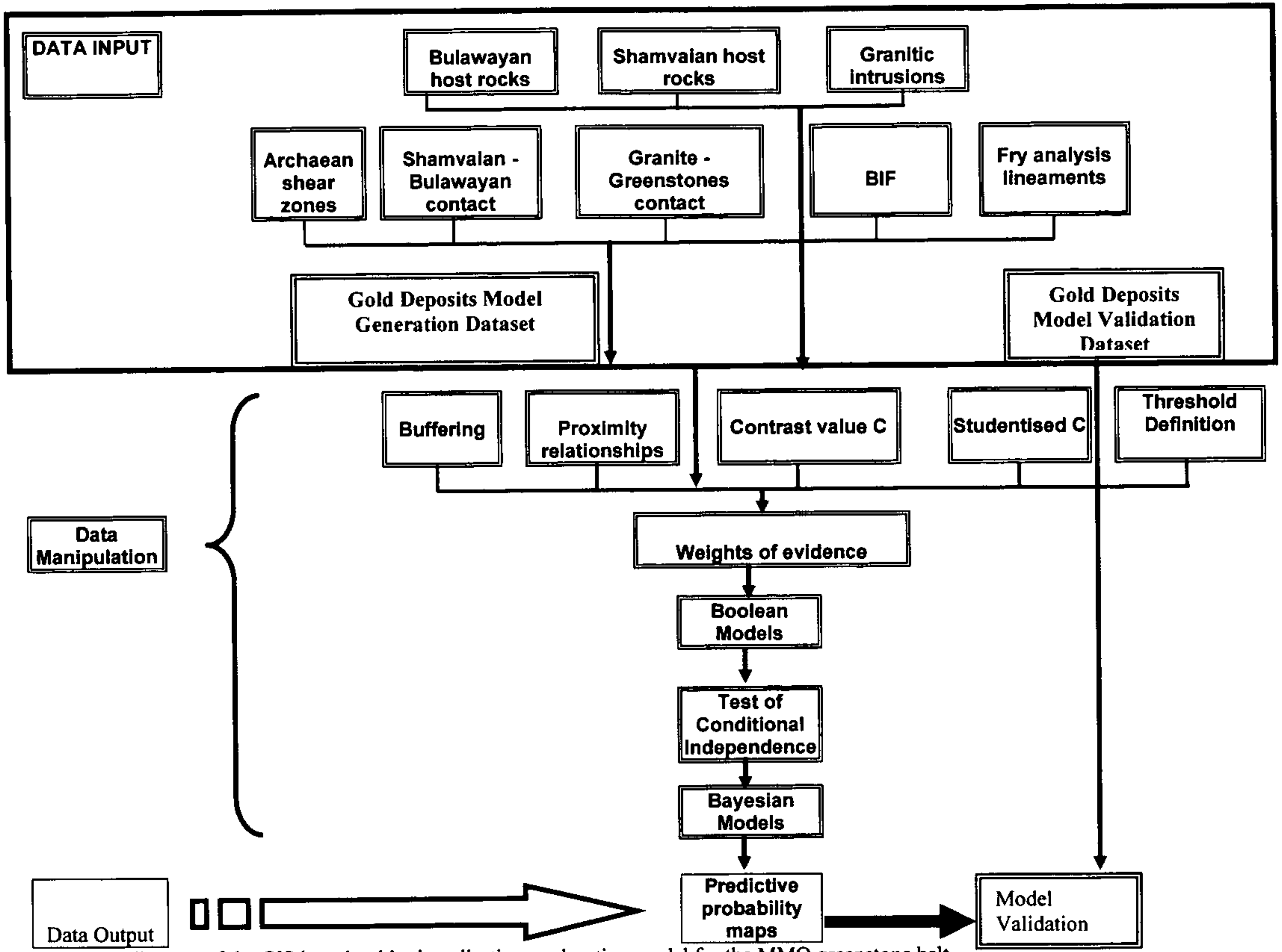

Figure 9 - 31. Schematic diagram of the GIS based gold mineralisation exploration model for the MMO greenstone belt.

9.6 Discussion

This chapter demonstrated the distribution of deposits within distance interval (buffer) to the nearest mineralisation-controlling factor (e.g. shear zones) and, it is seen in Fig 9 – 3 that 90% of the gold deposits in the MMO belt are situated within a km from Archaean shear zones for example. This is the pattern when considering all deposits in the belt. The subdivision of the gold occurrences in mineralisation categories (Figs 9 – 3 to 9 – 8 and Table 9 –1 – to 9 - 4) reveals that different categories present different distributions and proximity to the controlling factors, but all of them within 1.5 km. For example, the high production deposits are concentrated within 400 m to the nearest shear zone (Fig. 9 –6 and Table 9 - 1).

The study proved here that some patterns are spatially more related to mineralisation than others (Table 9 –1 to 9 - 4) e.g. 51,5% of high production deposits are located within 200 m to the nearest shear zone, while 53,3% of medium production deposits are situated within 100 m to the nearest felsic or intermediate intrusion (Table 9 – 2), 41.9% of felsic or intermediate occurrences are located within 500 m to the nearest greenstone – granite gneiss terrain contact (Table 9 – 3) and 50% of the Samvaian-host deposits are situated within 500 m to the nearest Shamvaian – Bulawayan contact. This example shows that there is need to harmonize the importance of each parameter before combining all of them in the predictive model. One way of harmonizing the influence of each parameter is by calculating their weights of evidence.

At this stage the gold occurrences dataset was split into two subsets of 120 and 121 occurrences. One set was used to generate the model of weight of evidence and the other was used to test the validity of the model. From the weights presented earlier, it has been seen that the presence of felsic and intermediate intrusions carries more weight of favourableness than any other factors, contrary, the granite – greenstone contact carries the least weight (Table 9 – 10). This finding is supported by geological evidences, fry analyses results and the known deposits distribution which show a cloud of deposits around the Penhalonga granodiorite, for example. This suggests that the felsic and intermediate intrusions statistically represent the most important parameter in terms of favourableness of occurrence of gold deposits. The use of weights of evidence for mapping gold prospectivity as main criteria has been applied by other researches (see for example, Sahoo et al. (2000), Carranza and Hale (2000), Ngorima (1999)), however none of these studies addressed gold mineralisation in greenstone bets. In general the results obtained by earlier authors compare favourably with results obtained in this study.

The magnitude of Studentized C (e.g. Tables 9 – 5 to 9 - 10, or Figs. 9 – 15 to 9 - 19) shows that based on cutoff distance of influence, input binary maps important for prediction of gold occurrences are (i) proximity to felsic and intermediate intrusions, (ii) proximity to Archaean shear zones, (iii) proximity to banded iron formations, (iv) proximity to Upper Bulawayan – Shamvaian contact, and (v) proximity to granite – greenstone contact. On the basis of Studentized C the felsic and intermediate intrusions is again the most significant predictor of all gold occurrences in the MMO belt. Studentized C for calculation of optimum cutoffs distance was also used by e.g. Bonham-Carter et al., (1988), Bonham-Carter (1997), Carranza and Hale, 2000. Bonham-Carter (1997) suggests that Studentized C must be used in a relative rather than an absolute sense, because of the assumptions required for a formal statistical test. He adds that it is nice to see values of Studentized C higher than 1,5 or even 2 because this will imply that the contrast is large compared with the standard deviation, and then the contrast is more likely to be "real". All of Studentized C values in this study are higher than 1,5, which according to Bonham-Carter (1997) would be more likely to be statistically "real".

As mentioned earlier, binary map analysis was selected due to its flexibility and it avoids the subdivision of the study area into cells, each cell with associated attributes. The binary maps were prepared using the optimum cutoffs determined by the Studentized C analyses. The positive and negative weights of evidence were used to produce the binary maps of mainly two values, positive or negative weight. The positive weight is assigned to the area within the cutoff distance and the negative weight of evidence is assigned to the area outside the optimum cutoff distance.

The conditional independence test carried out for all pairs of binary maps (Tables 9 – 12) shows that chi-square values for most of pairs do not violate the null hypothesis. The shear zones – BIF binary maps pair show high dependence in all pairs, i.e. the chi-square value is high than the critical chi-square value. This can be explained by the fact that most of the BIFs are shear zones. Thus, the decision to discard the binary predictor BIF was taken. The shear zones also show conditional dependence with Upper Bulawayan – Shamvaian contact, which is explained by the fact that large segments of this contact are highly sheared. Statistically, the shear zones were supposed to be removed from the analyses because they violate the conditional independence principle, but the removal of shear zones from the analyses would be "geologically" incorrect although statistically correct. The Fry lineaments show dependence to all other binary parameters except for the Shamvaian – Bulawayan contact, thus it was removed from the model.

From the exercise presented in this Chapter it has been shown that the presence of shear zones in general and surroundings, within 400 m, is a highly favourable to presence of gold deposits. The GIS model tested here depicts around 55% of the deposits within areas of high and very probability of occurrence. The model was then tested for validity using the other dataset and proved to be consistent and valid by depicting 51% of the deposits within high and very prospectivity areas and 80% within moderate to very high prospectivity. These observations mean that each dataset of gold deposits can be used to predict the location of the other gold deposits. This is evidence to support that the gold mineralisation in the MMO greenstone belt is genetically and spatially associated to a single event and to similar geological features. This observation corroborate with conclusion of Fractal analyses discussed in chapter 5.

9.7 Conclusions

From the discussion presented in this Chapter the following conclusions can be drawn:

- The establishment of quantitative and qualitative distribution of the spatial association between known gold occurrences and geological features in the MMO belt is important tool for mapping its mineral potential.
- The distribution of the deposits within distance intervals to the nearest mineralisation-controlling factor agree largely with results from the fractal analyses regarding the cluster size around the factors (e.g. shear zones).
- GIS modelling using Bayesian probability for gold potential assessment and prediction provided a useful tool for predicting gold potential in the MMO greenstone belt. The results obtained in the MMO greenstone belt can be considered representative because of the large number of gold occurrences within the belt and the number of occurrences per square km.

- The selection of the controls of mineralisation using geological principles was in general confirmed to be correct by statistical test of conditional independence for the pairs of predicting patterns.
- The Studentised contrast (C) has shown to be a powerful criterion for establishing the cut-off distances of influence for each controlling parameter which was later used for conversion of multi-class proximity maps into binary patterns.
- The magnitude of contrast (C) and the Studentised C proved to be a good indicator of the importance of each mineralisation-controlling factor, being high for all factors, suggesting the statistical validity of the binary predictors.
- The test of conditionality shows that chi-square values for most of the binary maps pairs do not violate the null hypothesis, thus could be combined.
- The crossing of validation dataset with resulting maps of posterior probabilities shows that the model is correct. This is evidence to support that the gold mineralisation in the MMO greenstone belt is genetically and spatially associated to a single event and to similar geological features.
- The posterior probability maps have identified unexplored gold potential zones in additions to the known gold potential zones. These maps can be used to direct exploration work to search for new deposits in the area.

Chapter 10

10 Discussion, Conclusions and Recommendations

10.1 Introduction

This thesis investigated mainly the design and use of a GIS based database for gold exploration in the MMO belt; the spatial distribution patterns of known gold deposits and their occurrences through statistical, autocorrelation and fractal analysis; the use of satellite imagery for mapping structures and alteration patterns related to mineralisation; the ground infrared spectral geology for mapping alteration and structures related to gold mineralisation; and the design of a GIS based gold mineralisation prediction model for MMO belt.

10.2 General Discussion

Discussions were presented at the end of each Chapter in order to highlight the main observations. In this section only few general problems of the study are discussed.

The design and testing of GIS based gold prediction model requires several parameters that feed into the model. The acquisition of these parameters is crucial for the quality and accuracy of the results. Earlier studies have generated these parameters mainly by traditional exploration methods, including geophysics, geochemistry and fieldwork coupled with laboratory studies and they are not usually compliant with digital database requirements. The main problem with such approach is that it is time consuming, laborious and ultimately expensive.

The main challenge in the digital exploration model design is to find entry parameters that are easy to gather, rapid to use and less laborious and still be of high quality to be able to produce reliable prospectivity maps. This study has contributed towards a GIS based exploration model that depends less on the traditional methods. The generation of entry parameters is based on the processing and systematisation of previous knowledge of the area in terms of geology, structure, and metallogenesis into a GIS based database backed and updated by ground truthing. Satellite imagery and airphotography interpretation supported by infrared spectral geology constitute the other source of information for the model.

The advantages of systemising the information in a database are, easy retrieval, access, storage, updating and processing. The distribution patterns, statistical, autocorrelation and fractal analysis were directly supported by the database.

Probably the most demanding problem for this study was trying to bring all different data sources into a common platform, which could allow comparison or overlay. The data, mainly geological and satellite imagery has different sources, different accuracy, different scale, age and purpose, such that to attempt a spatial relationship of all data was a complex exercise. The initial stage consisted of bringing all data into a similar coordinate system such as UTM. The following stages included systematisation of the data in such a way that areas with more detail are comparable to areas with less detail.

Other problems were related to representativity of the gold mineralisation sample. The gold deposits in the MMO belt may reflect a representative sample of the mineralisation because of their large quantity and the widespread distribution throughout the belt. Thus the distribution patterns and controls of known deposits should reflect the distribution pattern of the mineralisation in the belt. From this assumption it has been shown that the controls of gold mineralisation in the MMO belt goes beyond the surface trapping structures. The orientations of regional structures that control mineralisation do not, in most cases, coincide with orientation of the structure at mine scale.

The compilation of the GIS based database faced difficulties related to age, source and accuracy of the geological descriptions. In this study the interest was in studying the regional relationships between controls of mineralisation (structural, lithological, hydrothermal alteration, deformation event and metamorphism) and the distribution patterns of the gold deposits, mainly by statistical, autocorrelation and fractal analysis.

As discussed in Chapter 3 and 4, gold mineralisation in the Zimbabwe Craton is mainly controlled by secondary and tertiary structures that occur within or close to the Archaean greenstone belts. This suggest that the combination of knowledge on structural controls, the geometry of individual deposits, and understanding of the tectonic of the greenstone belts noted in Chapter 2 would improve the exploration strategies for targeting concealed gold deposits.

Several potential good trapping sites can be identified from satellite imagery in the MMO greenstone belt and vicinity, but very few of them are mineralised. This suggests that effort on the gold exploration should be devoted to description of distribution patterns of gold mineralisation rather than search for trapping structures. The existence of trapping structures is necessary but not deterministic for gold deposition.

The distribution patterns of gold deposits controlled by shear zones and faults suggest clusters at regular intervals. The discussion in Chapter 5 covers this extensively. The reasons of clustering are far from being understood. However, if a pattern can be statistically or mathematically described, then undiscovered clusters can be predicted (see Chapter 9).

Geological interference of optimum-parameters increases the probability of gold deposition. This has been the dogma in gold exploration for many years without measuring the effort of modelling several parameters mainly by static overlay. Yet the rate of discoveries did not improve significantly compared to use of traditional methods. This suggests that probably the interference of several optimum factors is important but not sufficient. For example in Manica the Chazuca granite (Fig. 8 - 1) intrude similar set of lithologies that are intruded by the Penhalonga granodiorite (Fig. 3 - 25), but the former one is not mineralised. Probably the explanation is more complex where aspects of amount of heat flux supplied by the granite and its size play a role in the mobilisation and deposition of gold. The thickness of the country rock is another factor that may influence the deposition of gold in specific structures near granitic intrusions.

This study combined parameters that control mineralisation and geological interpretative and non-interpretative factors such as position of gold deposits; size, grade and presence of sulphides for proposing an exploration model where distribution patterns play an important role. This integration is done in a GIS environment where entities (binary predictor or controls of mineralisation) are spatially related to known gold deposits. The model produces prospectivity maps, which result from the sum of weights of evidence of different controlling parameters. The highest values characterise the highest probability and the lowest values the lowest probability of finding gold deposits.

After generating the prospectivity maps, the next problem is related to how accurate this maps are? If the model depicts in the moderate, high and very high probability areas more than 80% of known deposits, then it is considered valid model for the study area. The model was validated by running it for a new dataset, which was not used during the model generation stage and, this showed that the model still depicts in the moderate, high and very high prospectivity areas 80% of the deposits.

10.3 Conclusions

The objectives of this study presented in Chapter 1 were achieved following the methodology summarised in the same chapter. The following main conclusions can be drawn from the study:

The nature and quality of the existing data is adequate for the designed GIS based database followed by its use for exploration modelling in the MMO belt.

The gold deposits are fractal and the mineralisation has been transported and deposited in favourable geological structures by hydrothermal systems. This assumption is based on the distribution patterns of known gold deposits,

The autocorrelation analysis can be used as exploration tool for new deposits in the MMO belt, where field evidence should be gathered within 3-km radius from known ENE or NW alignments of deposits and within 9-km radius of known NNE alignments.

Shear zones could be mapped on the basis of topography, truncation surfaces of primary layering and trend surfaces digitised from SPOT-Panchromatic images and air-photograph mosaic, and are supported by field observations.

The spectral geology using infrared spectrometer such as PIMA (used in this study) can positively contribute towards fine turning of satellite imagery interpretation by providing the ground spectral information, which is not affected by atmospheric conditions or by the mixing of radiance derived from spatial or spectral resolution of the satellite platforms.

The comparison between satellite imagery data and PIMA data shows that major structural elements (such as shear zones) identified by interpreting TM imagery can be confirmed by carrying out perpendicular profiles across them with PIMA.

The most significant controls of gold mineralisation in the Zimbabwe craton are structural where gold is associated with sulphides or occurs as free gold in moderately-steep dipping (c. 50° ± 20°) reverse or oblique-reverse shear veins or shear zones that traverse the greenstone belts.

Gold mineralisation in the MMO belt is controlled by the presence of:

(i) Felsic and intermediate intrusions within Bulawayan rocks,

(ii) Shear zones and associated second order shear veins and adjacent conjugate sets

(iii) Contact between Bulawayan and Shamvaian,

(iv) BIF,

(v) Quartz veins oriented N-S

(vi) and hidden lineaments that correspond to those lineaments generated by autocorrelation and fractal analysis.

(vii) Mafic and ultramafic rocks of Bulawayan

The selection of the controls of mineralisation for the GIS model using geological principles was generally confirmed to be valid by statistical tests of conditional independence (contrast value and studentised contrast value) for the pairs of predicting patterns.

The resulting maps of posterior probabilities based on two datasets of gold occurrences are similar. This implies that the model is statistically or/and geologically robust.

The various analytical methods including statistics, autocorrelations, fractal, spectral geology, satellite imagery interpretation, geological mapping applied are essential tools in mineral exploration yet they only contribute positively in the target delineation when combined in such a way that the prospectivity maps generated from there are of increased confidence to mining companies.

The GIS gold exploration model designed for the MMO greenstone belt which takes into account the fractal and autocorrelation lineaments, the structures interpreted from satellite imagery and checked in the field, depicted new areas of high prospectivity. The prospectivity maps of MMO belt can be used to direct exploration work in search for new deposits.

The use of GIS based exploration model reduces the time need for fieldwork and laboratory studies, and increases the efficiency of the search for new deposits. It also reduces the cost of the exploration programs because a reduced team does most of work and fieldwork is only conduced in limited pre-targeted areas.

10.4 Recommendations

The research reported here has contributed towards understanding the controls on the evolution of the distribution patterns of gold mineralisation in the MMO belt. Nevertheless, further studies are recommended specially towards testing the applicability of the autocorrelation and fractal analysis in more diversified geological setting.

Better understanding of the correlation between PIMA and TM or ETM imagery is needed when conducing gold exploration in Archaean terrains. The knowledge of this relationship is of great importance for the mapping of hydrothermal alteration within shear zones. More research is required in order to establish more precisely the limitations and capabilities of the PIMA data in relation to TM or ETM in regard to gold exploration in Archaean greenstone belts.

The GIS based exploration models are becoming increasingly popular at different levels of exploration. However, more research is needed for understanding the importance of the quality of the data entry and the need to test the conditional independence of the data by calculation of chi-square values.

The geological data input has many assumptions, which need to be quantified by assigning weights. However, assuming weights creates uncertainties as to the actual weighting involved due to the complex nature of mathematical formulations. Thus, more research on the field of GIS modelling for geoscientists is recommended.

References

Abraham A. P.G. and Spooner E. T. C., 1995. Late Archaean regional deformation and structural controls on gold-quartz vein mineralization in the northwestern Slave Province. N.W.T., Canada. Canadian Journal of Earth Science, **32**: 1132 – 1154.

Adams J. B. and Smith M. O., 1986. Spectral mixture modelling: a new approach to analysis of rock and soil types at the Viking Lander 1 site. J. Geophys. Res., **91**: 8098 – 8112

Agterberg F.P., 1989. Systematic approach to dealing with uncertainty of geosciences information in mineral exploration. Proceedings of the 21st APCOM Symposium, Las Vegas, Chapter 18: 165 – 178.

Agterberg F.P., 1992. Combining indicator patterns in weights of evidence modelling for resource evaluation. Non-renewable Resources, vol. 1: 39 – 50.

Agterberg F.P., Bonham-Carter G.F. and Wright D.F., 1990. Statistical pattern integration for mineral exploration. In: Gaal G., and Merriam D.F., (Eds.) Computer Applications in Resource Estimation. Pergamon Press, Oxford, pp. 1 – 21.

Albert N. R.D., 1975. Interpretation of Earth Resources Technology Satellite imagery of Nabesna quadrangle, Alaska: USGS misc. field studies map MF-655-J, sheets 1 and 2, scale 1: 250,000

Angelier J. and Mechler P., 1977. Sur une méthode graphique de recherche des contraintes principales également utilisable en tectonique et en séismologie: La méthode des diédres droits; Bulletin Societé Geologica des France; XIX (7), 1309 - 1318.

Anhaeusser C. R., 1971. Cyclic volcanicity and sedimentation in the evolutionary development of Archaean greenstone belts of shield areas. Special Publications Geological Society of Australia, **3**: 57 – 70.

Anhaeusser C. R, 1974. Precambrian tectonic environments. Annual Reviews Earth Palnetary Science, 3: 31 – 53.

Anhaeusser C. R., 1976. The nature and distribution of Archaean gold mineralisation in Southern Africa; Minerals Science Engineering, **8**: 46 – 84

Archibald N. J., 1987. Geology of the Norseman – Kambalda area. *In*: *Second Eastern Goldfields Geological Field Conference, Part A; Extended abstracts*. Geological Society of Western Australia Division, Perth. pp. 30 – 31.

Asadi H.H. and Hale M., 2001. A predictive GIS model for potential mapping of gold and base metal mineralization in Takab area, Iran; Computers and Geosciences 27: 901 – 912.

Ayres L. D. and Corfu F., 1991. Stacking of disparate volcanic and sedimentary units by thrusting in the Archean Favourable Lake greenstone belt, central Canada. Precambrian Research, **50**: 221 – 238.

Barley M. E., 1987. The Archaean Whim Creek Belt, an ensialic fault bounded basin in the Pilbara Block, Western Australia. Precambrian Research, **37**: 199 – 215.
Barley M. E. and Groves D. I., 1992. Supercontinent cycles and the distribution of metal deposits through time. Geology, **20**: 291 – 294.

Bartholomew D. S., 1990. Gold deposits of Zimbabwe. Zimbabwe Geological Survey Mineral Resources Series no. 23: 1 – 75.

Barton C. C. and Scholz C. H., 1995. The fractal size and spatial distribution of hydrocarbon accumulations: *In:* Barton C.C. and La Pointe P. R. (editors), *Fractals in Petroleum Geology and Earth Processes*: Plenum Press, New York, p. 13-33

Baumgardner M. F., Stoner E. R., Silva L. F. and Biehl L. L., 1985. Reflectance properties of soils. In: N. Brady (Ed.), Advances of Agronomy, Academic Press, New York: pp 1 – 44.

Berthelsen A., 1960. Structural studies in the Precambrian of Western Greenland. Part 2. Geology of Tovqussap Nuna. Meddr. Gronland. 123 (1): 223p.

Bickle M. J. and Nisbet E. G., 1993. (Editors) The Geology of the Belingwe Greenstone Belt, Zimbabwe: a study of Archaean continental crust. Geological Society of Zimbabwe Special Publications, **2**. Rotterdam, Balkema, 239p.

Bickle M. J., Martin A. and Nisbet E. G., 1975. Basaltic and peridotitic komatiites, stromatolites, and a basal unconformity in the Belingwe Greenstone belt, Rhodesia. Earth Planet Science Letters, **27**: 155 – 162.

Bickle M. J., Morant P, Bettenay L. F., Boulter C. A., Blake T. and Groves D. I., 1985. Archaean tectonics of the Shaw batholith, Pilbara block, Western Australia: structural and metamorphic tests of the batholith concept. *In*: L. D. Ayres, P.C. Thurston, K. D. Card and W.Weber (editors), *Evolution of Archaean supracrustal sequences.* Geological Association of Canada Special Paper, 28: 325 – 341.

Bickle M. J., Nisbet E. G., and Martin A., 1994. Archaean greenstone belts are not Oceanic Crust; The Journal of Geology, **102**; 121 – 138.

Bickle M. J., Orpen J. L., Nisbet E. G. and Martin A., 1993. Structure and metamorphism of the Belingwe greenstone belt and adjacent granite – gneiss terrain: The tectonic evolution of an Archaean craton. *In*: Bickle M. J. and Nisbet E. G. (Editors), *The geology of the Belingwe Greenstone Belt.* Geological Society of Zimbabwe Special Publications, **2**. Rotterdam, Balkema, pp. 39 - 68.

Binns R. A., Gunthorpe R. J. and Groves D. I., 1976. Metamorphic patterns and development of greenstone belts in the Eastern Yilgarn Block, Western Australia. *In*: Windley B. F. (Editor) *The Early History of the Earth.* John Wiley, London, pp 303 – 313.

Bishop M.M., Feinberg S.E. and Holland P.W., 1975. Discrete Multivariate Analysis: Theory and Practice. MIT Press, Cambridge, Massachusetts, 587p.

Blenkinsop T. G., 1993. Fracture spacing distributions in rock. Abstract, International Symposium on Fractals and Dynamic Systems in Geoscience, Johann Wolfgang Goethe – University, Frankfurt, Germany. pp 6 – 7.

Blenkinsop T. G., 1994. The Fractal Distribution of Gold Deposits: Two examples from Zimbabwe Archaean Craton. In J. H. Kruhl (ed.), Fractals and dynamic systems in geoscience: 247 – 258. Springer-Verlag. Berlin

Blenkinsop T. G., 1995. Fractal measures for size and spatial distributions of gold mines: Economic applications; *In*: Blenkinsop T. G. and P. L. Tromp (editors) Sub-saharan Economic Geology. A. A. Balkema, Rotterdam, 177 – 186.

Blenkinsop T. G., Bickle M. J., Martin A., Nisbet E. G., Wilson J. F., 1993. Ensialic origin for the Ngezi Group, Belingwe greenstone belt, Zimbabwe. Geology **21**: 1135 – 1138.

Blenkinsop T. G., Martin A., Jelsma H. A & Vinyu M. L., 1997. The Zimbabwe Craton. *In*: De Wit, M. J.& Ashwal, L. D.(editors) *Greenstone belts*. Oxford Univ. Press, 567 – 580, UK.

Blenkinsop T. G., Oberthur T. and Mapeto O., 2000. Gold mineralization in the Mazoe area, Harare-Bindura-Shamva greenstone belt, Zimbabwe: I. Tectonic controls on mineralization. Mineralium Deposits, **35**: 126 – 137.

Blenkinsop T. G and Sanderson D. J., 1999. Are gold deposits in the crust fractals? A study of gold mines in Zimbabwe craton. *In*: McCaffrey, K. J. W., Lonergan, L. & Wilsinson, J. J. (editors) *Fractures, Fluid Flow and Mineralization*. Geological Society, London, Special Publications, **155**: 141 – 151.

Bliss N. W., 1970. The geology of the country around Gatooma. Bulletin Geological Survey of Rhodes **64**:1 – 240.

Bloem E. J. M., Dalstra H. J., Groves D. I. & Ridley J. R., 1994. Metamorphic and structural setting of Archaean amphibolite-hosted gold deposits near Southern Cross, Southern Cross Province, Yilgarn Block, Western Australia. Ore Geology Reviews, **9**: 183 – 208.

Boardman J. W., 1993. Automated spectral unmixing of AVIRIS data using convex geometry concepts. In: Summaries, Fourth JPL Airborne Geoscience Workshop, JPL Pub. 93 – 26, **1**: 11- 14.

Bonham-Carter G.F., 1997. Geographic Information Systems for Geoscientists, Modelling with GIS. 3rd Ed. Pergamon, Ontario; 398p.

Bonham-Carter G.F., Agterberg F.P. and Wright D.F., 1989. Weights of evidence modelling: a new approach to mapping mineral potential. In: Agterberg F.P. and Bonham-Carter G.F. (Editors), Statistical Applications in Earth Sciences, Geological Survey of Canada, Paper **89-9**: 171 – 183.

Bonham-Carter G.F., Agterberg F.P. and Wright D.F., 1998. Integration of geological data sets for gold exploration in Nova Scotia. Photogrammetric Engineering and Remote Sensing **54**: 1585-1592.

Bonham-Carter G.F., Reddy R.K.T., and Galley A.G., 1995. Knowledge-driven modelling of volcanogenic massive sulphide potential with a geographic Information System. In Mineral Deposit Modelling. Geological Association of Canada, Special Paper **40**: 735-749.

Bonham-Carter, G.F., Agterberg, F.P. and Wright, D.F., 1988. Integration of geological datasets for gold exploration in Nova Scotia. *Photogrammetric Engineering and Remote Sensing*, **54**, no. 11, pp. 1585-1592.

Bouhallier H., Choukroune P. and Ballevre M., 1993. Diapirism, bulk homogeneous shortening and transcurrent shearing in the Archaean Dharwar craton: the Holenarsipur area, South India. Precambrian Research, **63**: 43 – 58.

Boullier A. M. and Robert F., 1992. Palaeoseismic events recorded in Archaean gold-quartz vein networks, Val d'Or, Abitibi, Quebec, Canada. Journal Structural Geology, **14**: 161 – 179.

Bridgwater D., McGregor V. R. and Myers J. S., 1974. A horizontal tectonic regime in the Archaean of Greenland and its implications for early crustal thickening. Precambrian Research, **1**: 179 – 197.

Browning P., Groves D. I., Blockely J. R. & Rosman K. J. R., 1987. Lead isotopic constraints on the age and source of gold mineralisation in the Archaean Yilgarn Block, Western Australia. Economic Geology, **82**: 971 – 986.

Buchholz P., Herzig, P., Friedrich G., & Frei R., 1998. Granite-hosted gold mineralization in the Midlands greenstone belt: a new type of low-grade gold deposit in Zimbabwe. Mineral. Deposita **33**: 437 – 460.

Buda R.O., Hart P.E., Nilsson N.J. Slocum J. and Sutherland H.I., 1977. Development of a computer-based consultant for mineral exploration. Stanford Research Institute International, SRI International, Artificial Intelligence Centre, Final Report for SRI Projects 5821 and 6415, Menlo Park, California, 193 p.

Burrough P. A., 1986. Principles of Geographical Information Systems for Land Resources Assessment; Oxford Science Publications; Monographs on Soil and Resource Survey no. 12. 193p, Oxford.

Campbell A.N., Hollister V.F., Buda R.O. and Hart P.E., 1982 – Recognition of hidden mineral deposits by an artificial intelligence program. Science **217**: 927 – 929.

Campbell I. H. and Hill R. I, 1988. A two-stage model for the formation of granite-greenstone terrains of the Kalgoorlie-Norseman area, Western Australia. Earth and Planetary Science Letters, **90**: 11 – 25.

Campbell S.D.G. and Blenkinsop T.G., 1994. A simple size-frequency basis for assessing the gold exploration potential of an area – The fractal dimension. In prep.

Campbell S.D.G. and Pitfield P. E. J., 1994. Structural controls of gold mineralisation in the Zimbabwe Craton – Exploration guidelines. Zimbabwe Geological Survey Bulletin **101**, 270p.

Card K. D., 1990. A review of the Superior Province of the Canadian Shield, a product of Archaean accretion. Precambrian Research, **48**: 99 – 156.

Carlson C. A., 1991. Spatial distribution of ore deposits. Geology **19**: 111 – 114.

Carranza E.J.M, 2002. Geologically constrained Mineral Potential Mapping; Examples from the Philippines. PhD thesis. ITC: 86; The Netherlands

Carranza E.J.M. and Hale M., 2000. Geologically constrained probabilistic mapping of gold potential, Baguio district, Philippines. Natural Resources Research, **9**: 237-253.

Carter A. H. C., 1988. The transport and deposition of gold within a major Archaean shear zone; Dalny mine, Zimbabwe. University of Southampton Report. **C12**, 52p.

Chadwick B., Ramakrishnan M. and Viswanatha M. N., 1985. Babubadan – a late Archaean intracratonic volcanosedimentary bain, Karnataka, South India, part 1: stratigraphy and basin development. Journal of Geological Society of India, **26**: 769 – 801.

Chadwick B., Vasudev V. N., Krishna Rao B. and Hegde G. V., 1992. The Dharwar Supergroup: basin development and implications for Late Archaean tectonic setting in western Karnataka, southern India. In: Glover J. E. and Ho S. E., (editors), *The Archaean Terrains, Processes and Metallogeny* (Proceedings volume 3rd International Archaean Symposium, Perth): Geology Department and Extension Service, University of Western Australia, 3 - 15.

Chauvel C., Dupre B., Arndt N. T. and Hofmann A. W., 1993. Pb and Nd isotopic correlation in Belingwe komatiites and basalts. In: Bickle M. J. and Nisbet E. G., (Editors), *The geology of the Belingwe Greenstone Belt, Zimbabwe: a study of Archaean continental crust*. Geological Society of Zimbabwe Special Publications **2**:167 – 174. Balkema, Rotterdam.

Chenjerai K. G., 1996. The Mutare Greenstone Belt, Zimbabwe: Geology, geochemistry and gold mineralisation. PhD Dissertation; Cuvillier verlag Gottigen; Gottingen, 184p.

Chenjerai K. G., Porada, H., Schmidt Mumm A. & Blenkinsop T. G., 1994. The Redwing Gold Deposit, Mutare Greenstone Belt, Zimbabwe: Geotectonic Setting and Regional Exploration Significance. Conference and Workshop: Metallogenesis of Gold in Africa, Hannover, Germany. Abstract Volume pp.9.

Clark M. E., Carmichael D. M., Hodgson C. J. & Fu M., 1989. Wallrock alteration, Victory gold mine, Kambalda, Western Australia: processes and P-T-XCO_2 conditions of metasomatism. *In*: Keays, R. R., Ramsay, W. R. H. & Groves, D. L. (editors) *The*

Geology of Gold Deposits – The Perspective in 1988; Economic Geology Monograph, 10: 445 – 459. Littleton.

Clark N. R., 1999. Spectroscopy of Rocks and Minerals, and Principles of Spectroscopy. *In*: A. Rencz (Editor) *Manual of Remote Sensing;* John Wiley and Sons, Inc; New York. p 3- 58; http//www. speclab.cr.usgs.gov/PAPERS.refl-mrs/refl4.html.

Clark R. N. and Roush T. L., 1984. Reflectance spectroscopy: Quantitative analysis techniques for Remote Sensing Applications; Journal of Geophysical Research, **89**. No. B7, p. 6329 – 6340.

Clark R.N. and King T.V.V., 1987. Causes of Spurious Features in Spectral Reflectance Data: *Proceedings of the Third Airborne Imaging Spectrometer Data Analysis Workshop,* JPL Publication 87-30, 132-137.

Clark R.N., Gallagher A.J. and Swayze G.A., 1990. Material Absorption Band Depth Mapping of Imaging Spectrometer Data Using a Complete Band Shape Least-Squares Fit with Library Reference Spectra, *Proceedings of the Second Airborne Visible/Infrared Imaging Spectrometer (AVIRIS) Workshop.* JPL Publication 90-54, 176-186.

Clark R.N., King T.V.V., Ager C. and Swayze G.A., 1995. Initial vegetation species and senescence/stress mapping in the San Luis Valley, Colorado using imaging spectrometer data. *Proceedings: Summitville Forum '95,* H.H. Posey, J.A. Pendelton, and D. Van Zyl Eds., Colorado Geological Survey Special Publication **38**: 64-69.

Clark R.N., King T.V.V., Ager C., Swayze G.A., 1997. Vegetation Species and Stress Indicator Mapping in the San Luis Valley, Colorado using Imaging Spectrometer data, Remote Sensing of Environment (submitted)

Clemens J. C. & Mawer C. K., 1992. Granitic magma transport by fracture propagation. Tectonophysics. **204**: 339 - 360.

Clout J. M. F., Cleghorn J. H. & Eaton P. C., 1990. Geology of the Kalgoorlie goldfield. *In*: Hughes, F. E. (editor) *Geology of the Mineral Deposits of Australia and Papua New Guinea.* Australasian Institute of Mining & Metallurgy, Monograph Series, **14**: 411 – 431.

Collender F. D., 1964. The geology of the Cam and Motor mine, southern Rhodesia. *In:* Haughton S. H. (Editor) *The geology of some ore deposits in southern Africa.* Geological Society of South Africa, Special Publications, **2**: 15 – 27.

Colvine A. C., Andrews A. J., Cherry M. E., Durocher M. E., Fyon A. J., Lavinge M. J., Macdonald A. J., Marmont S., Poulsen K. H., Springer J. S. and Troop D. G., 1984. An integrated model for the origin of Archaean lode gold deposits: Ontario Geological Survey Open-File Report 5524, 98p.

Colvine A. C., Fyon J. A., Heather K. B., Marmont S., Smith P. M. and Troop D. G., 1988. Archaean Lode Gold Deposits in Ontario. Ontario Geological Survey miscellaneous Papers, 139, 136pp.

Conel J. E., Abrams M. J. and Goetz A. F. H., 1978. A study of alteration associate with uranium occurrence in sandstone and its detection by remote sensing methods: JPL publ. 78-66, **v. 1**, 260p, and **v. 2**, 138 p.

Connlly P. & Cosgrove J., 1999. Prediction of static and dynamic fluid pathways within and around dilational jogs; *In*: McCaffrey, K. J. W., Lonergan, L. and Wilkinson, J. J. (editors) *Fractures, Fluid Flow and Mineralisation.* Geological Society special publications, **155**: 105 – 121.

Cotterill P., 1979. The Selukwe schist belt and its chromite deposits. Geological Society of S. Africa Special Publications **5**: 229 – 245.

Coward M. P., 1976. Archaean deformation patterns in South Africa. Philosophical Transactions of the Royal Society, London, **A283**: 313 – 331.

Coward M. P. and Daly M. P., 1984. Crustal lineaments and shear zones in Africa: their relationship to plate movements. Precambrian Research, **24**: 27 - 45.

Coward M. P. and Treloar P. J., 1990. Tibetan models for Archaean tectonics in southern Africa. *In*: Barton, J. M. (editor) *The Limpopo Belt: a field workshop on Granulites and deep crustal tectonics.* Department of Geology, Rand Afrikaans University, 35 - 38. Johannesburg.

Coward M. P., James P. R. and Wright L. I., 1976. The movement patterns across the northern margin of the Limpopo mobile belt, southern Africa. Geological Society of America Bulletin, **87**: 601 – 611.

Cox S. F., 1999. Deformational controls on the dynamics of fluid flow in mesothermal gold systems; *In*: McCaffrey, K. J. W., Lonergan, L. and Wilkinson, J. J. (editors) *Fractures, Fluid Flow and Mineralisation.* Geological Society special publications, **155**: 123 – 140, London.

Cox S. F., Sun S.-S., Etheridge M. A., Wall V. J. & Potter T. F., 1995. Structural and geochemical controls on the development of turbidite-hosted gold-quartz vein deposits, Wattle Gully Mine, central Victoria, Australia. Economic Geology, **90**: 1722 – 1746.

Cox S. F., Wall V. J., Etheridge M. A. & Potter T. F., 1991. Deformational and metamorphic processes in the formation of mesothermal gold deposits – Examples from the Lachlan Fold Belt in central Victoria, Australia. Ore Geology Reviews, **6**: 391 – 423.

Crampin S., 1994. The fracture criticality of crustal rocks. Geophysical Journal International, **118**, 428 – 438.

Crespi J. M., 1986. Some guidelines for the practical application of Fry's method of strain analysis. J. Struct. Geol., **8** - No. 7: 799 - 808.

Crowley J. K., 1991. Visible and near-infrared (0.4 – 2.5 μm) reflectance spectra of playa evaporite minerals. J. Geophys. Research, **96**: 16231 – 16240.

D'Orey F. L. C., 1978. A génese das mineralizações cupro-niqueliferas da Edmundian (Vila Manica, Moçambique). Tese, Universidade de Lisboa.

Darbyshire D. P. F., Pitfield P. E. J. and Campbell S. D. G., 1996. Late Archaean and Early Proterozoic gold-tungsten mineralization in the Zimbabwe Archaean craton: Rb – Sr and Sm – Nd isotope constraints. Geology, **24**: 19 – 22.

Davis D. W. and Jackson M. C., 1985. Preliminary U-Pb zircon ages from the Lumby Lake – Marmion Lake area, district of Kenora and Rainy River. Ontario Geological Survey Miscellaneous Paper **126**: 135 – 137.

Davis J. C., 1973. Statistics and data analysis in Geology. John Wiley & Sons, Inc. New York, 550pp.

De Ronde C. E. J., Kamo S., Davis D. W., de Wit M. J. and Spooner E. T. C., 1991. Field, geochemical and U/Pb isotopic constraints from hypabyssal felsic intrusions within the Barberton Greenstone belt, SA: implications for tectonic and the timing of gold mineralization. Precambrian Research, **49**: 261 – 280.

De Wit M. J., 1982. Gliding and overthrust nappe tectonics in the Barberton Greenstone Belt. Journal of Structural Geology, **4**: 117 – 136.

De Wit M. J., 1986. Extensional tectonics during the igneous emplacement of the mafic-ultramafic rocks of the Barberton Greenstone Belt. *In*: *Workshop on Tectonic Evolution of Greenstone Belts*. LPI Technical Report. **86 – 10**. Lunar and Planetary Institute, Houston, 84 – 85.

De Wit M. J. and Ashwal L.D., 1997. Greenstone Belts. Clarendon Press. Oxford, 809p.

De Wit M. J., Armstrong R., Hart R. J. and Wilson A. H., 1987. Felsic igneous rocks within the 3.3 – 3.5 Ga Barberton greenstone belt: high crustal level equivalents of the surrounding tonalite-trondhjemite terrane, emplaced during thrusting. Tectonics. **6/5**: 529 – 549.

De Wit M. J., Jones M. G. and Buchanan D., 1992. The geology and tectonic evolution of Pietersburg greenstone belt, South Africa. Precambrian Research, **55**: 123 – 153.

Direcçao Nacional de Geologia, Mozambique, 1987. Carta Geológica de Moçmbique1: 1 000 000; Maputo.

Dirks P. H. G. M and Jelsma H. A., 1998a. Horizontal accretion leading to stabilization of the Archaean Zimbabwe Craton. Geology, **126**: 11-14.

Dirks P. H. G. M and Jelsma H. A., 1998b. Silicic layers-parallel Shear Zones in a Zimbabwean Greenstone Sequence: Horizontal accretion preceding Doming. Gondwana Research, **1**: 177-193.

Dirks P. G. M., Jelsma H. A. and Hofmann A., 2000. Accretion of an Archaean greenstone belt in the Midlands of Zimbabwe. Journal of Structural Geology (Submitted)

Dirks P. H. G. M. and van der Merwe J. A., 1997. Tectonic stacking in an Archaean Greenstone sequence and its control on gold mineralisation in Zimbabwe. Journal of African Earth Sciences **24**: 603 – 620.

Dirks P. H. G. M., Jelsma H. A., Mikhailov A., and Barber B., 2001. Lithospheric lineaments and their control on the distribution of Archaean lode gold deposits. Unpublished MSc. Course notes handout, University of Zimbabwe, Harare.

Drury S. A., 1997. Image interpretation in geology; 2nd ed. Chapman & Hall 283p.

Duda R. O., Hart P. E., Nilsson N. J., Reboh R., Slocum J., and Sutherland G. I., 1977. Development of a computer-based consultant for mineral exploration. Stanford Research Institute International, SRI International, Artificial Intelligence Center, Final Report for SRI Projects 5821 and 6415, Menlo Park, California, 193p.

Dunne W. M., Onasch C. M. and Williams R. T., 1990. The problem of strain-marker centers and the Fry method. J. Struct. Geol. **12:** 933 - 938.

Elvidge C. D. and Lyon R. J.P., 1985. Influence of rock-soil spectral variation on assessment of green biomass. Remote Sens. Environ. 17:265 – 279.

Etheridge M. A., Wall V. J., Cox S. F. & Vernon R. H., 1984. High fluid pressure during regional metamorphism and deformation: implications for mass transport and deformation mechanisms. Journal of Geophysical Research, **89**: 4344 – 4358.

Evans A. M., 1998. Ore geology and Industrial Minerals – An Introduction; 3rd Ed. Blackwell Science; 389p.

Fabiani W. M. B., 1980. The geology of a felsite – intrusion in the Penhalonga valley – with special reference to the Old West mine. Unpublished Special Hons. Project. Univ. Zimbabwe.

Fitton M. J., Horwitz R. C. and Sylvester G., 1975. Stratigraphy of early Precambrian in the west Pilbara, Western Australia. CSIRO Mineral Reseach Laboratory Division Mineral Report, **FP11**, 24p.

Foster R. P., 1988a. Archaean gold mineralisation in Zimbabwe: Implications for metallogenesis and exploration.Bicentennial Gold 88, *Extended abstracts*. Geological society of Australia. Melbourne, pp. 62 – 72.

Foster R. P., 1988b. Major controls of Archaean gold mineralization in Zimbabwe, Transactions Geological Society South Africa 88: 109 – 133.

Foster R. P., 1989. Archaean gold mineralisation in Zimbabwe: Implications for metallogenesis and exploration. *In*: Keays R. R., Ramsay W. R. H. and Groves D. I. (Editors) *The geology of gold deposits: the perspective in 1988*; Economic Geology Monograph 6: 54 – 71.

Forster H., 1993. Lagerstatten-Inventar des Odzi-Mutare-Manica- Grunsteingurtels, Simbabwe/Mosambik. Unpbl. Report for BGR contract no. 2-106286 (Hannover: Federal Institute for Geosciences and Natural Resources (BGR), 108p.

Forster H, Koenemann F. H. and Knittel U., 1996. Regional framework for gold deposits of the Odzi-Mutare-Manica greenstone belt, Zimbabwe-Mozambique. Trans. Inst. Min. Metall. (Sect. B: Applied Earth Science) **105**: 60-73.

Foster R. P., Mann A. G., Miller R. G. and Smith P. J. R., 1979. Genesis of gold mineralization in the Gatooma area, Rhodesia. Special Publication of the Geological Society of S. Africa, **5**: 25 – 38.

Foster R.P. and Piper D. P., 1993. Archaean lode gold deposits in Africa: crustal setting, metallogenesis and cratonization. Ore geology Reviews, **8**: 303 – 347.

Foster R.P. and Wilson J. F., 1984. Geological setting of Archaean gold deposits in Zimbabwe. In: Foster R. P. (Editor) Gold'82 (The Geology, Genesis and geochemistry of gold deposits), A.A. Balkema Publications, Rotterdam, pp. 521 – 551.

Foster R. P., Mann A. G., Stowe C. W. and Wilson J. F., 1986. Archaean Gold mineralisation in Zimbabwe. *In*: Anhaeusser G. A. and Maske S. (Editors) *Mineral Deposits of Southern Africa*, Geological Society of South Africa, **1**: 43 – 112

Fripp R. E. P., 1976. Stratabound Gold Deposits in Archaean banded iron-formation, Rhodesia. Economic Geology, **71**: 58 – 75.

Frizado J., 1992. Management of geological databases; Computer methods in the geosciences, v. 11; Pergamon press; Oxford. 250p.

Fry N., 1979. Random point distributions and strain measurements in rocks. Tectonophysics **60**. 89 - 105.

Gates A. E., 1991. Shear zone control on mineral deposits in the state-line serpentine, Pennsylvania Piedmont. Ore Geology Reviews **6**, 171 – 184.

Gettings M.E. and Bultman M.W, 1993. Quantifying favourableness for occurrence of a mineral deposit type using fuzzy logic – an example from Arizona. USGS Open File Report 93-392, 23p.

Glikson A. Y., 1972. Early Precambrian evidence of primitive ocean crust and island nuclei of sodic granite. Geological Society of America Bulletin, **83**: 3323 – 3344.

Goetz A. F. H., 1992. Imaging Spectroscopy for Earth Remote Sensing. *In*: F. Toselli & J. Bodechtel (Eds.), *Imaging Spectroscopy: Fundamentals and Prospective Applications*. Kluwer Academic Publishers, Dordrecht: pp. 1 – 19.

Goetz A. F. H., 1992. Principles of narrow band spectrometry in the visible and IR: instruments and data analysis. In Imaging spectroscopy: Fundamentals and prospective applications (EURO courses: Remote Sensing v.2), F. Toselli and J. Bodechtel, eds., Dordrecht, The Netherlands: Kluwer Academic Pub., pp 21 – 32.

Goetz A. F. H., Billingsley F. C., Gillespie A. R., Abrams M. J., Squires R. L., Shoemaker E. M., Lucchitta I. and Elston D. P., 1975. Application of ERTS images and image processing to regional geologic problems and geologic mapping in Northern Arizona: Jet Propulsion Laboratory Tech. rep. 32 – 1597, 188 p., Pasadena, California.

Goodwin A. M., 1972. The Superior Province. *In*: Prince R. A. and Douglas R. J. W. (Editors) *Variations in Tectonic Styles in Canada*. Geological Association of Canada, Special Paper, **11**: 527 – 624.

Goossens M. A., 1992. Petrogenesis of the mineralised granitic intrusion near Los Santos, western-Spain, and remote Sensing and data integration as a tool in regional exploration for granite related mineralization. PhD. Thesis. Rijksuniversiteit te Utrecht. The Netherlans. 149pp.

Goosens M. A. and Kroonenberg S. B., 1994. Spectral discrimination of contact metamorphic zones and its potential for mineral exploration; Remote Sensing of the Environment. **47**: 331 – 344.

Gorman B. E., Pearce T. H., and Birkett T. C., 1978. On the structure of Archaean greenstone belts; Precambrian Research, **6**: 23 – 41.

Green A. A. and Graig M. D., 1985. Analysis of aircraft spectrometer data with logarithmic residuals. In: G. Vane & A. F. H. Goetz (Editors.), *Proceedings of the Airborne Imaging Spectrometer Data Analysis Workshop, Pasadena*, USA, NASA-JPL Publication **85-41**: 111 – 119.

Grocott J., Brown M., Dallmeyer R. D., Taylor G. K. & Treloar P. J., 1994. Mechanism of continental growth in extensional arcs: an example from the Andean plate boundary zone. Geology, **22**: 391 - 394.

Gross G. A., 1980. A classification of banded iron formations based on depositional environments. Canadian Mineralogy **18:** 215 – 222.

Groves D. I. and Forster, H., 1991. Archaean gold deposits. *In:* Forster R. P. (editor) *Gold metallogeny and exploration*; Blackie, London.

Groves D. I. And Foster R. P., 1993. Archaean lode gold deposits. *In*: Foster R. P. (Editor) *Gold metallogenesis and exploration*, pp. 63 – 103. Chapman and Hall, London.

Grove C. I., Hook S. J. and Paylor II E. D., 1992. *Laboratory reflectance spectra of 160 minerals, 0.4 to 2.5 micrometers*. NASA-JPL Publication 92 – 2, Pasadena: 300pp.

Groves D. I. and Phillips G. N., 1987. The genesis and tectonic control on Archaean gold deposits of the Western Australian Shield – A metamorphic replacement model. Ore Geology reviews, **2:** 287 – 322.

Groves D. I., 1982. The Archaean and earliest Proterozoic evolution and metallogeny of Australia; Revista Brasileira de Geociencias, **12**: 1 – 3.

Groves D. I., 1993. The crustal continuum model for late-Archaean lode-gold deposits of Yilgarn Block, Western Australia. Mineralium deposita, **28**: 366 – 374.

Groves D. I., Goldfarb R. J., Gebre-Mariam M., Hagemann S. G. and Robert F., 1998. Orogenic gold deposits: A proposed classification in the context of their crustal distribution and relationship to other gold deposit types. Ore Geology Reviews, **13**: 7 - 27.

Groves D. I., Golding S. D., Rock N. M. S., Barley M. E. & McNaughton N. J., 1988a. Archaean carbon reservoirs and their relevance to fluid source for gold deposits. Nature, **331**: 254 - 257.

Groves D. I., Philips N., Ho S. E., Houstouns S. M., and Standing C. A., 1987. Craton-scale distribution of Archaean greenstone gold deposits: Predictive capacity of the metamorphic model; Economic Geology, **82**: 2045 – 2058.

Groves D. I., Ridley J. R., Bloem E. M. J., Gebre-Mariam M., Hagemann S. G., Hronsky J. M. A., Knight J. T., McNaughton N. J., Ojala J., Vielreicher R. M., McCuaig T. C. & Holyland P. W., 1995. Lode-gold deposits of Yilgarn block: products of Late Archaean crustal-scale overpressured hydrothermal systems. *In:* Coward M. P. & Ries A. C. (editors.), *Early Precambrian Processes,* Geological Society Special Publication, **95**: 155 - 172. London.

Groves, D. I., Goldfarb, R. J., Gebre-Mariam, M. Hagemann, S. G. and Robert, F., 1998. Orogenic gold deposits: A proposed classification in the context of their crustal distribution and relationship to the gold deposit types; Ore Reviews; in press.

Guha P. K. and Venkataramana I., 1992. Extraction of geologic features by band combination of IRS-1A data; International Journal of Applied Earth Observation and Geoinformation. **3**: 234 – 238.

Guyot G. and Gu X., 1994. Effect of radiometric corrections on NDVI determined from SPOT-HRV and Landsat TM data. Remote Sensing Environment **49**: 169 – 180.

Hagemann S. G., Groves D. I., Ridley J. R. & Vearncombe J. R., 1992. The Archaean lode-gold deposit at Wiluna high-level, brittle-style mineralisation in a strike-slip regime. Economic Geology, **87**: 1022 – 1053.

Hamilton W. B., 1998. Archaean magmatism and deformation were not products of plate tectonics. Precambrian Research **91**, 143-179.

Hanna S. S. and Fry N., 1979. A comparison of methods of strain determination in rocks from south-western Dyfed (Pembrokeshire) and adjacent areas. Journal Structural Geology **1**:155 - 162.

Hapke B., 1981. Bidirectional reflectance spectroscopy 1. Theory, J. *Geophys. Research* **86**: 3039-3054.

Harrison N. M., 1970. The geology of the country around Que Que. Bull. Geological Survey of Rhodesia **67**: 1 – 125.

Harrison N. M., 1979. The geology of the Redwing gold mine, Penhalonga, Umtali District, Rhodesia. Special Publication of the Geological Society Africa, **5**: 66 – 71.

Hegner E., Kroner A. and Hofmann A. W., 1984. Age and isotope geochemistry of the Archaean Pongola and Usushwana suites in Swaziland, southern Africa: a case for crustal contamination of mantle-derived magma. Earth Planet Scientific Letters, **70**: 267 – 279.

Henderson J. B., 1975. Sedimentological studies of the Yellowknife Supergroup in the Slave Structural Province: Geological Survey of Canada paper **75-1A**: 325 – 330.

Henderson J. B., 1995. Geology of the Yellowknife-Hearne Lake area, District of Mackenzie: a segment across an Archaean basin. Geological Survey of Canada Memories **414**. 135p.

Henderson J. B., van Breeman O. and Loveridge W. D., 1978. Some U-Pb zircon ages from Archaean basement, supracrustal and intrusive rocks, Yellowknife – Hearne Lake area, district of Mackenzie. In: Radiogenic age and isotopic studies. Report 1, Geological Survey of Canada Paper **87 – 2**: 11 – 121.

Herrington R. J., 1995. Late Archaean structure and gold mineralization in the Kadoma region of the Midlands greenstone belt, Zimbabwe. *In*: Coward, M. P. and Ries, A. C. (editors) *Early Precambrian Processes*. Geological Society of London Special Publication No. **95**: 173 – 191, London.

Herrmann W., Blake M. D., Huston D., Kamprad J., Merry N., and Pontual S., 2001. Short wavelength Infrared (SWIR) Spectral Analysis of Hydrothermal Alteration Zones Associated with Base Metal Sulfide Deposits at Rosebery and Western Tharsis, Tasmania, and Highway-Reward, Queensland. Economic Geology **96**; pp. 939 – 955.

Hickman A. H., 1984. Archaean diapirism in the Pilbara Block, Western Australia, *In*: Kroner A. and Greiling R (Editors), *Precambrian Tectonics Illustrated.* IUGS, 113 – 127.

Ho S. E., Groves D. I. & Phillips G. N., 1985. Fluid inclusions as indicators of the nature and source of ore fluids and ore depositional conditions for Archaean gold deposits of Yilgarn Block, Western Australia. Transactions of the Geological Society of South Africa, **88**: 149 – 158.

Ho S. E., Groves D. I. and Bennett J. M., 1990. Gold deposits of the Archaean Yilgarn Block, Western Australia: Nature, Genesis and exploration guides. Geology Department (key centre) & University Extension, The University of Western Australia, Publication, 20.

Hoffman P. F., 1989. Precambrian geology and tectonic history of North America. *In*: Bally A. W. and Palmer A. R. (Editors) *The Geology of North America – an overview*. Geological Society of America VA: 447 – 512.

Hoffmann A., Dirks P. H. G. M. and Jelsma H. A., 2001. Late Archaean foreland basin deposits, Belingwe greenstone belt, Zimbabwe. Sedimentary Geology, **141 – 142**: 131 – 168.

Holloway J. R. and Ojala V. J., 1997. Computer aided structural targeting in mineral exploration: two and three-dimensional stress mapping. Australian Journal of Earth Science, **44**: 421 – 432.
Holloway J. R., 1976. Fluids in the evolution of granitic magmas: consequences of finite CO2 solubility. Bulletin of the Geological Society of America, **87**: 1513 – 1518.

Holyland P. J., 1995. Lode-gold deposits of the Yilgarn block: products of Late Archaean crustal-scale overpressured hydrothermal systems; *In*: Coward, M. P. & Ries, A. C. (editors) *Early Precambrian Processes*. Geological Society Special Publication, **95**: 155 – 172. London.

Holyland P. J. and Ojala V. J., 1997. Computer aided structural targeting in mineral exploration: two and three-dimensional stress mapping. Australian Journal of Earth Sciences **44**: 421 – 432.

Holyland P. W., Ridley J. R. and Vearncombe J. R., 1993. Stress mapping technology (STM^{TM}); in Geofluids '93: Contributions to an International Conference on Fluid Evolution, Migration and Interaction in Rocks, 272 – 275.

Höppner M., 1994. The Eureka gold deposit in northern Zimbabwe: an example of gold-quartz shear zone mineralisation derived from magmatic fluids. Geol. Jahrb. Reihe D. **100**: 391 – 422.

Horstwood M. S. A., Nesbitt R. W., Noble S. R. & Wilson J. F. 1999. U-Pb zircon evidence for an extensive early Archaean terrane in Zimbabwe: a reassessment of the timing of craton formation, stabilization, and growth. Geology **27**: 707 – 710.

Horwitz R. C. and Pidgeon R. T., 1993. 3.1 Ga tuff from the Sholl belt in the west Pilbara: further evidence for diachronous volcanism in the Pilbara craton of Western Australia. Precambrian Research, **60**: 175 – 183.

Horwitz R. C., 1992. The Archaean unconformity at Shay Gap, northeastern Pilbara Craton. *In*: Glover J. E. and Ho S. E., (editors), *The Archaean Terrains, Processes and Metallogeny* (Proceedings volume 3rd International Archaean Symposium, Perth): Geology Department and Extension Service, University of Western Australia, 51 - 57.

Huete A. R., 1988. A soil adjusted vegetation index (SAVI). Remote Sensing of Environment **25**: 295 – 309.

Huete A. R., Jackson R. D., Post D. F., 1985. Spetral response of a plant conopy with different soil backgrouns. Remote Sensing Environment, **17**: 37 – 53.

Huizenga J. M., 1995. Fluid evolution in shear zones from the late Archaean Harare-Shamva-Bindura greenstone belt (NE Zimbabwe): thermodynamic calculations of the C – O – H system applied to fluid inclusions. Ph.D. thesis, Vrije Universiteit Amsterdam, The Netherlands, pp 146.

Hunt G. R. and Salisbury J. W. and Lenhoff C. J., 1974. Visible and near-infrared spectra of minerals and rocks, IX. Basic and Ultrabasic igneous rocks. Modern Geology, **5**: 15 – 22.

Hunt G. R. and Salisbury J. W., 1970. Visible and near-infrared spectra of minerals and rocks, I. Silicate Minerals. Modern Geology, **1**: 283 – 300.

Hunt G. R. and Salisbury J. W., 1971. Visible and near-infrared spectra of minerals and rocks, II. Carbonates. Modern Geology, **2**: 23 – 30.

Hunt G. R., 1977. Spectral signatures of particulate minerals in the visible and near-infrared. Geophysics, **42**: 501 – 513.

Hunt R. G. 1979. Near infrared (1.3 – 2.4 μm) spectra of alteration minerals: potential for use in remote sensing. Geophysics **44**: 1974 – 1986.

Hunt R. G. and Ashley R. P., 1979. Altered rock spectra in the visible and near infrared: Economic Geology **74**: 1613 – 1629.

Hunt R. G., Salisbury J. W. and Lenhoff C. J., 1971a. Visible and near infrared spectra of minerals and rocks, III: Oxides and hydroxides: Modern Geology **2**: 195 –205.

Hunter D. R., 1974. Crustal development in the Kaapvaal Craton. Part 1: the Archaean volcanic rocks. Geochim. Cosmochim. Acta, **38**: 611 – 627.

Hunting Geology and Geophysics, 1984. Mineral Inventory Project in Tete Province and parts of Manica, Sofala and Zambezia Provinces; Final Report. Unpublished; DNG, Maputo.

Hunting Geology and Geophysics, 1994. Gold deposits in Mozambique, Unpublished Report; DNG, Maputo.

Hutton D. H. W., Dempster T. J., Brown P. R. and Becker S. M., 1990. A new mechanism of granite emplacement: intrusion in active extensional shear zones. Nature, **343**, 452 - 455.

Hyde, R. F. and Vesper, N. J. 1983 – Some effects of resolution cell size on image quality. Landsat Data Users Notes, **29**: 9 – 12.

ING 1986. Gold mineralisation inventory database in Mozambique, unpbl. Report, ING. Maputo.

Jackson M. P. A., 1984. Archaean structural styles in the Ancient gneiss complex of Swaziland. *In:* A. Kroner and R. Greiling (editors) *Precambrian tectonics illustrated.* E. Schweizerbart'sche Verlagsbuchhanlung, Stuutgart. pp. 1 – 18.

Jackson S. L. and Cruden A. R., 1995. Formation of the Abitibi greenstone belt by arc-trench migration. Geology, **23**: 471 – 474.

Janssen L. L. F., 2000. Principles of Remote Sensing, Vol. 2 of ITC Educational Textbook Series. International Institute for Aerospace Survey and Earth Science, Enschede, The Netherlands. 225p

Jelsma H. A. and Dirks P. H. G. M., 2000. Tectonic evolution of a greenstone sequence in northern Zimbabwe: sequential early stacking and pluton diapirism. Tectonics, **19**: 135 – 152.

Jelsma H. A. and Dirks P. H. G. M., 2002. Neoarchean tectonic evolution of the Zimbabwe Craton. *In*: C.M.R. Fowler, C. J. Ebinger and C. J. Hawkesworth (editors) *The Early Earth: Physical, Chemical and Biological Development*. Geological Society, London, Special Publications, **199**: 183 – 211.

Jelsma H. A., van der Beek P. R. and Vinyu M., 1993. Tectonic evolution of the Bindura – Shamva greenstone belt (northern Zimbabwe): progressive deformation around diapiric structures. Journal Structural Geology **15**: 163 – 176.

Jelsma H. A., Vinyu M. L., Valbracht P. J., Davis G. R., Wijbrans J. R. & Verdurmen E. A. T. 1996. Constraints on Archaean crustal evolution of the Zimbabwe craton: a U-Pb zircon, Sm-Nd and Pb-Pb whole-rock isotope study. Contrib. Mineral. Petrology, **124**: 55 – 70.

Johnson P. E., Smith M. O., Taylor-George S. and Adams J. B., 1983. A semi empirical method for analysis of the reflectance spectra of binary mineral mixtures. Journal of Geophysics Research, **88**: 3557 – 3561.

Johnson S. P. M. and Taylor-George S., 1983. A semi-empirical method for analysis of the reflectance spectra of binary mineral mixtures. *J. Geophys. Research* **88**: 3557-3561.

Kent A. J. R., Cassidy K. F. and Fanning C. M., 1996. Archean gold mineralisation synchronous with the final stage of cratonization. Yilgarn Craton, Western Australia. Geology 24: 879 – 882.

Kent A.J.R. and Hagemann S. G., 1996. Constrains on the timing of lode-gold mineralization in the Wiluna greenstone belt, Yilgarn Craton, Western Australia. Australian Journal of Earth Sciences, **43**: 573 – 588.

Kent A.J.R. and McDougall I., 1995. Constrains on timing of gold mineralization in the Kalgoorlie goldfield, Western Australia, from ^{40}Ar/^{39}Ar and U- Pb dating: Evidence for multiple mineralization episodes. Economic Geology, **90**: 845 – 859.

Kerrich R., 1994. Dating Archaean auriferous quartz vein deposits in the Abitibi greenstone belt, Canada: ^{40}Ar/^{39}Ar evidence for a 70 – 100 m.y.-time gap between plutonism-metamorphism and mineralization. A discussion. Economic Geology, **89**: 679 – 686.

Kerrich R. and Cassidy K. F., 1994. Temporal relationships of lode gold mineralisation to accretion, magmatism, metamorphism and deformation – Archaean to present. Ore Geology Reviews 9: 263 – 310.

Knight J. T., Groves D. I. & Ridley J. R., 1993. The Coolgardie Goldfield, Western Australia: district-scale controls on an Archaean gold camp in an amphibolite facies terrane. Mineralium Deposita, **28**: 436 – 456.

Koenemann F. H. and Forster H., 1994. Polyphase strike - slip origin of the Odzi - Mutare - Manica greenstone belt, Zimbabwe/Mozambique. Conference and workshop: Metallogenesis of Gold in Africa, Hannover, Germany. Abstract volume pp. 25.

Krogh T. E. and Gibbins W., 1978. U-Pb isotopic ages of basement and supracrustal rocks in the Point Lake area of the Slave Structural Province, Canada. Geological Association of Canada. Abstracts with program, **3**: 438.

Kroner A., 1977. The Precambrian geotectonic evolution of Africa: plate accretion versus plate destruction. Precambrian Research **4-2**: 163 – 213.

Kroner A. and Tegtmeyer A., 1994. Gneiss-greenstone relationships in the Ancient Gneiss Complex of Southern Swaziland, Southern Africa, and implications for early crustal evolution. Precambrian Research, 67: 109 – 139.

Kruhl J. H., 1994. The formation of extensional veins: An application of the Cantor-Dust Model. In: Kruhl (editor) Fractals and Dynamic systems in Geoscience. Springer, Berlin Heidelberg New York, pp 95 – 104

Kusky T. M., 1990. Evidence for Archaean ocean opening and closing in the southern Slave Province: Tectonics **9**: 1533 – 1563.

Kusky T. M., 1991. Structural development of an Archaean orogen, Western Point Lake, Northwest Territories: Tectonics **10**: 820 – 841.

Kusky T. M., 1991b. Are the upper greenstones at Belingwe (Zimbabwe) allochthonous?, *in* Proceeding of the Lunnar and Planetary Conference **22**: 769 – 770.

Kusky T. M., 1998. Tectonic setting and terrane accretion of the Archaean Zimbabwe craton. Geology **26**: 163 – 166.

Kusky T. M. and Kidd W. S. F., 1992. Remnants of Archaean oceanic plateau, Belingwe greenstone belt, Zimbabwe. Geology **20**: 43 – 46.

Kusky T. M. and Polat A., 1999. Growth of granite-greenstone terranes at convergent margins, and stabilisation of Archaean terranes. Tectonophysics **305**: 43 – 77.

Kusky T. M. and Ramadan T. M., 2002. Structural controls on Neoproterozoic mineralization in the South Eastern Desert, Egypt: an integrated field, Landsat TM, and SIR-C/X SAR approach. Jurnal of African Earth Sciences **35**: 107 – 121.

Kusky T. M. and Vearncombe J. R., 1997. Structural aspects. *In*: De Wit M. J. and Ashwal L. D (Editors) *Greenstone Belts*. Oxford University Press, pp 91 – 124.

Kusky T. M. and Winsky P. A., 1995. Structural relationships along a greenstone/shallow water shelf contact, Belingwe greenstone belt, Zimbabwe. Tectonics **14**: 448 – 471.

Levine D. M., Stephan D., Krehbiel T. C. and Berenson M. L., 2002. Statistics for managers using Microsoft Excel; 3rd Edition; Prentice Hall, New Jersey, 885p.

Lillesand T. M. and Kiefer R. W., 1987. Remote sensing and image interpretation. John Wiley & Sons, New York. 721pp.

Lillesand T. M. and Kiefer R. W., 1994. Remote Sensing and Image interpretation; 3rd Ed, John Wiley & Sons, New York 750 p.

Lisle R. J., 1987. Principal stress orientations from faults: an additional constraint. Annales Tectonicae **1**: 155 - 158.

Loéve M., 1955. Probability theory: D. van Nostrand Co., Prnceton, NJ

Lowe D. R. and Byerly G. R., 1986. The rock components and structures of Archaean greenstone belts: and overview. *In*: *Workshop on Tectonic Evolution of Greenstone Belts.* LPI Technical Report. **86 – 10**. Lunar and Planetary Institute, Houston, 142 – 146.

Lupankwa M., 1999. The use of remote sensing in the study of dambos in Zimbabwe; PhD Thesis, University of Zimbabwe, Zimbabwe. 233p.

Lusted L.B., 1968. Introduction to Medical Decision Making, Charles Thomas, Springfiel, 271p.
MacGregor A. M., 1951. Some milestones in the Precambrian of Southern Rhodesia. Proceedings of the Geological Society of South Africa **54**: 27 – 71.

MacLaughlin K. and Helmstaedt H., 1995. Geology and geochemistry of an Archaean mafic dike complex in the Chan Formation: basis of a revised plate tectonic model of the Yellowknife greenstone belt. Canadian Journal of Earth Science **32**: 614 – 630.

Mandelbrot B. B. 1967. How long is the coast of Britain? Statistical self-similarity and fractal dimension, Science **156**: 636 – 8.

Mandelbrot B. B. 1982. The fractal geometry of nature. Freeman, New York.

Manuel I. M. R., 1992. Geologie, Petrographie, Geochemie un Lagerstatten des Manica-Greenstone-Belt (Mosambik). Ph.D. thesis, University of Aachen, 210p, Aachen.

Mareschal J. C. and West G. F., 1980. A model for tectonism. Part 2. Numerical models of vertical tectonism in greenstones belts. Canadian Journal of Earth Sciences, **17**: 808 – 855.

Martin A., 1978. The geology of the Belingwe – Shabani Schist Belt. Rhodesia Geological Survey Bulletin, **83**, 213p.

Martin A., Nesbit E. G., Bickle M. J., 1980 – Archaean stromatolites of the Belingwe Greenstone Belt. Precambrian Research **13**: 337 – 362.

Martin A., Nesbit E. G., Bickle M. J. and Orpen J. L., 1993 – Rock units and stratigraphy of the Belingwe Greenstone Belt: The complexity of the tectonic setting. *In*: Bickle M. J. and Nisbet E. G. (Editors) *The Geology of Belingwe Greenstone Belt: a Study of the Evolution of Continental Crust*. Geological Society of Zimbabwe Special Publications, **2**:13 – 37.

Mathews P. E. and Scharrer R. H., 1968. A grade unconformity at the base of the early Precambrian Pongola system. Transactions of Geological Society of S. Africa, **71**: 257 – 272.

McCuaig T. C. and Kerrich R., 1994. P-T-t deformation-fluid characteristics of lode gold deposits: evidence from alteration systematics. In: D. R. Lenz (Editor), Alteration and alteration processes associated with ore-forming systems. Geological Association of Canada, Short Course Notes, **11**: 339 – 379.

McNaughton N. J., Cassidy K. F., Dahi H., Groves D. L., Perring C. S. & Sang J. H., 1990. Sources of ore fluid and ore components: lead isotope studies. *In*: Ho, S. E., Groves, D. I. & Bennett, J. M. (editors), *Gold deposits of the Archaean Yilgarn Block, Western Australia: Nature, Genesis and Exploration guides*. Geology Department (Key centre) and University Extension, The University of Western Australia, Publication, **20**: 226 – 236.

Mehliss A. T. M. and Goldberg I., 1961. Gold prospecting in southern Rhodesia. Rhodesian Mining Engineering, **26**: 24 – 31.

Mikucki E. J. and Ridley J. R., 1993. The hydrothermal fluid of Archaean lode-gold deposits – Constraints on its composition interred from ore and wallrock alteration assemblages over a spectrum of metamorphic grades. Mineral Deposita, **28**, 469 – 481.

Mondlane S., Dirks P., Jelsma H., and Blenkinsop T., 2000. A structural and metallogenic analysis for gold exploration in the Manica - Mutare - Odzi greenstone belt, West Mozambique and East Zimbabwe; the use of remotely sensed data. Poster abstract; 18th Colloquium of African Geology. Graz – Austria.

Mondlane S., Dirks P., Jelsma H., and Blenkinsop, T., 2001. Distribution patterns of Au mineralisation in the Archaean Manica Mutare Odzi greenstone belt (Zimbabwe – Mozambique); Extended abstract; International Symposium on the Assembly and Breakup of Rodinia and Gondwana, and Growth of Asia; Osaka; Japan; GRG/GIGE Miscellaneous Publication no. **12**.

Mustard J. F. and Pieters M. C., 1987. Quantitative abundance estimates from bi-directional reflectance measurements. Journal of Geophysics Research, **92**: 617 – 626.

Mustard J. F. and Pieters M. C., 1989. Photometric phase functions of common geologic minerals and applications to Quantitative analysis of Mineral mixture reflectance spectra; Journal of Geophysical research **94 - B10**: 13619 – 13634.

Myers J. S., 1995. The generation and assembly of an Archaean supercontinent: evidence from the Yilgarn craton, Western australia. *In*: Coward, M. P. & Ries, A. C. (editors), *Early Precambrian Processes*, Geological Society Special Publication, **95**: 143 - 154. London.

Nash D. B. and Conel J. E., 1974. Spectral reflectance systematics of mixtures of powdered hypersthene, labradorite, and ilmenite. Journal of Geophysical Research **79**: 1615 – 1621.

Neall F. B. and Phillips G. N., 1987. Fluid-wallrock interaction around Archaean hydrothermal gold deposits: a thermodynamic model. Economic Geology, **82**: 1679 – 1694.

Nelson D. R., 1998. Granite-Greenstone crust formation on the Archaean Earth: a consequence of two superimposed processes. Earth Planetary Letters **158**: 109 – 119.

Newhouse W. H., 1942. Ore Deposits as related to structural features. Princeton University Press. Princeton.

Ngorima C. F., 1999. Statistical modelling of spatial controls of mineralization in the Iberian Pyrite belt. MSc. Thesis; ITC-Delft, the Netherlands. 121p.

Nisbet E. G. and Fowler C. M. R., 1983. Model for Archaean plate tectonics. Geology **11**: 376 – 379.

Nisbet E. G., Bickle M. J. and Martin A., 1977. The mafic and ultramafic lavas of Belingwe belt, Rhodesia. Journal of Petrology **18**: 521 – 566.

Nisbet eE. G., Martin A., Bickle M. J. and Orpen J. L, 1993. The Ngezi Group: Komatiites, basalts and stromatolites on continental crust. *In*: Bickle M. J. and Nisbet E. G. (Editors) *The Geology of Belingwe Greenstone Belt: a Study of the Evolution of Continental Crust*. Geological Society of Zimbabwe Special Publications, **2**:121 – 165.

Nutt T. H. H. C., McCourt S and Vearncombe J. R., 1988. Structure of some antimony-gold deposits from the Kaapvaal and Zimbabwe cratons. *In:* Ho S. E. and Groves D. I. (Editors) *Advances in understanding Precambrian gold deposits*. **2**. Geological Department and University Extension, University of Western Australia, Publications, **12**: 63 – 80.

Nyama N., 1999. The geology and structure of the central part of the Mutare greenstone belt. Unpbl. BSc. Hons thesis, Univ. of Zimbabwe, Harare. 89p.

Oberholzer W. F., 1964. A geologia da Mancha de Manica, II plano de fomento, Unpublished report, Loureço Marques.

Oberthur T., 1994. Metallogenesis of selected gold deposits in Africa. Hannover. 679 p.

Obretanov N., 1977. Região mineira de Manica. Relatório sobre os resultados do estudo geologico e dos trabalhos da prospecção e pesquisa executados em 1976. Unpublished Report; DNG, Maputo.

Ord A., 1994. The fractal geometry of patterned structures in numerical models of rock deformation. *In*: Kruhl (editor) ***Fractals and Dynamic systems in Geoscience***. Springer, Berlin Heidelberg New York, pp 131 – 155.

Orpen J. J., 1978. The geology of the south-western part of the Belingwe greenstone belt and adjacent country – The Belingwe Peak area. Ph.D. thesis. Harare, Zimbabwe. University of Rhodesis, 242p.

Orpen J. L., 1982. Final Report on E.P.O. 584 – Geological Report (unpbl.), Geological Survey of Zimbabwe, Harare.

Orpen J. J., 1991. Provisional geological map of Zimbabwe, 1 : 1 000 000. Geological Survey of Zimbabwe; Harare.

Pfeiffer P. and Obert M., 1989. Fractals: Basic concepts and terminology. *In*: Avnir, (editor), ***The Fractal Approach to Heterogeneous Chemistry***. John Wiley, Chichester. pp. 11 – 43.

Phaup A. E., 1937. The geology of the Umtali Gold Belt. S. Rhod. Geological Survey Bulletin. **32**. 167p.

Phillips G. N., 1986. Geology and alteration in the Golden Mile, Kalgoorlie. Econ. Geol., **81**: 779 – 808.

Phillips G. N., 1993. Metamorphic fluids and gold. Mineral. Magazine, **57**: 365 – 374.

Phillips G. N. and Brown I. J., 1987. Host rock and fluid control on carbonate assembalges in the Golden Mile Dolorite, Kalgoorlie gold deposit, Australia. Canadian Mineralogy, **25**: 265 – 274.

Phillips G. N. and Groves D. I., 1983. The nature of Archaean gold-bearing fluids as deduced from gold deposits of Western Australia. Geological Society of Australian Journal, **30**: 25 – 39.

Phillips G. N., Groves D. I. & Kerrich R., 1996. Factors in the formation of the giant Kalgoorlie gold deposit; Ore Geology Reviews **10**: 295 – 317.

Phillips G. N., Groves D. I. And Brown I. J., 1987. Source requirements for the Golden Mile, Kalgoorlie: Significance to the metamorphic replacement model for Archaean gold deposits. Canadian Journal Earth Sciences **24**: 1634 – 1651.

PIMA SP, 1999. Users manual. 109p. Australia

Platt J. P., 1980. Archaean greenstone belts: a structural test of tectonic hypotheses. Tectonophysics, **65**: 127 – 150.

Pontual S., Merry N, and Gamson P., 1997c. Archaean greenstone Gold; Spectral analysis guides for Mineral Exploration – G-MEX, vol. 6; AusSpec International Pty.Ltd. Australia

Pontual S., Merry N. and Gamson P., 1997a. Spectral analysis guides for Mineral Exploration – G-MEX, vol. 1; AusSpec International Pty.Ltd; Australia

Pontual S., Merry N. and Gamson P., 1997b. Practical Applications Handbook; Spectral analysis guides for Mineral Exploration - G-MEX, vol. 2; AusSpec International Pty.Ltd; Australia.

Powell R., Will T. M. & Phillips G. N., 1991. Metamorphism in Archaean greenstone belts: calculated fluid compositions and implications for gold mineralisation. Journal of Metamorphic Geology, 9: 141 – 150.

Prema M. M. J. P. A., 1998. Spectral unmixing and the estimation of ground cover proportions in geology; MSc. thesis; ITC, Enschede, 81p.

Raines G. L., Offield T. W. and Santos E. S., 1978. Remote sensing and subsurface definition of facies and structure related to uranium deposits in the Powder River Basin, Wyoming: Economic Geology 73, no. 8.

Ramakrishnan M., Viswanatha M. M. and Nath J. S., 1976. Basement-cover relationships of Peninsular Gneiss with high-grade schists and greenstone belts of southern Karnataka. Journal of Geological Society of India, 17: 97 – 111.

Ramos Z. N. C., Phillips G. N. and Groves D. I., 1987. Alteration processes related to gold mineralisation in the Golden Mile, Kalgoorlie: a preliminary quantitative study, *In*: S.E. Ho and D. I. Groves (Editors) *Recent Advances in Understanding Precambrian Gold Deposits*. Geol. Dep. Ext., University of Western Australia Publications, 11: 161 –165.

Ramsay J. G., 1989. Emplacement kinematics of a granite diapir: the Chinamora batholith, Zimbabwe. Journal of Structural Geology, 11: 191 – 209.

Rast M., 1991. Imaging spectroscopy and its application in spaceborn systems. ESA SP-1144, ESTEC, Noordwijk, The Netherlands: ESA pub. Division, 144p.

Reddy R.K.T. and Bonham-Carter G.F., 1991. A decision-tree approach to mineral potential mapping in Snow Lake area, Manitoba. Canadian Journal of Remote Sensing 17: 191 – 200.

Renshaw C. E., 1997. Mechanical controls on the spatial density of opening mode fracture networks. Geology, 25: 923 – 926.

Richardson L. F., 1961. The problem of contiguity: An appendix of statistics of deadly quarrels. General Systems Yearbook 6: 139 – 87.

Richter F. M., 1985. Models for the Archaean thermal regime. Earth and Planetary Science Letters, 73: 350 – 360.

Ridley J. R., 1990. Source of ore fluid and ore components: alteration assemblages. *In*: Ho, S. E., Groves, D. I. & Bennett, J. M. (editors) *Gold deposits of the Archaean Yilgarn Block, Western Australia: Nature, Genesis and Exploration guides*. Geology Department

(Key centre) and University Extension, The University of Western Australia, Publication, 20: 268 – 272.

Ridley J. R., Vearncombe J.R. and Jelsma H. A., 1997. Relations between greenstone belts and associated granitoids. *In:* de Wit and Ashwal (editors) *Greenstone belts.* Clarendon Press. Oxford. 376 – 397.

Rifman S. S., 1973. Digital rectification of ERTS multispectral imagery: Symposium on Significant Results Obtained from ERTS-1, NASA SP-**327**: 1131 – 1142.

Robert F., Phillips G.N., Kesler S. E., 1990. Introduction. Abstract volume, NUNA research conference on greenstone gold and crustal evolution, Geological Association of Canada/Society of Economic Geologists, Val d'Or, Quebec, Canada: 6-10.

Roberts A. E., 1979. A gold bearing felsite horizon near Umtali – Rhodesia. Geological Society of South Africa Special Publication. **5**: 61 –65.

Roberts D. A., Smith M. O. and Adams J. B. 1993. Green vegetation nonphotosynthetic vegetation, and soils in AVIRIS data. Remote sensing of Environment, **44**: 255 – 269.

Robertson I. D. M., 1976. The geology of the country around Battlefields, Gatooma District. Bull. Geological Survey of Rhodesia **76**.

Rollinson H. R. 1993. A terrane interpretation of the Archaean Limpopo belt. Geological Magazine, **130**: 755 - 765.

Rowan L. C. and Wetlaufer P. H., 1975. Iron absorption band analysis for the discrimination of iron rich zones: U. S. Geological Survey, Type III Final report, contract S-70243 – AG.

Rowan L. C., Goetz A. F. H. and Ashley R. P., 1979. Discrimination of hydrothermally altered and unaltered rocks in the visible and near infrared: Geophysics **42**: 533 – 535.

Saager R., Meyer M. and Muff R., 1982. Gold distribution in supracrustal rock from Archaean greenstone belts of Southern Africa and from Palaeozoic ultramafic complexes of the European Alps: metallogenetic and geochemical implications. Economic Geology, 77: 1 – 24.

Sabins Jr. F. F., 1987. Remote Sensing – Principles and interpretation; W.H. Freeman and Company; New York; 449p

Saeze U. A, 2000. Estudo de Inclusoes fluidas, paragenese e texturas de minerais de minerio da Mina Monarch sua relacao com o beneficiamento: Cinturao de Rochas verdes de Manica. Unpubl. Licenciatura (Hons.) Project. Geology Department; Eduard Mondlane University, 76p, Maputo.

Sahoo N.R., Jothimani P. and Tripathy G.K., 2000. Multi-criteria analysis in GIS environment for Natural Resource Development- A case study on gold exploration; ttp://www.gisdevelopment.net/magazine/gisdev/2000/may/gise.shtml

Sanderson D. J. & Zhang X., 1999. Critical stress localisation of flow associated with deformation of well-fractured rock masses, with implications for mineral deposits. *In*: McCaffrey, K. J. W., Lonergan, L. and Wilkinson, J. J. (editors) *Fractures, Fluid Flow and Mineralisation*; Geological Society special publication, **155**:69 - 81.

Sanderson D. J., Roberts S., and Gumiel P., 1994. A relationship between vein thickness and gold grades. Economic Geology **89**: 168 – 173.

Schmidt Mumm A., Chenjerai K. G., Blenkinsop T. G., Oberthur T., Vetter U. & Chatora D. R., 1994. The Redwing Gold Deposit, Mutare Greenstone Belt, Zimbabwe: Geology, mineralogy, geochemistry and fluid inclusion studies. Geol. Jahrbuch, Reihe D **100**, 423 – 478, German.

Schmidt R. G., 1975. Exploration for porphyry copper deposits in Pakistan using digital processing of ERTS-1 data: USGS open file report, 29p.

Schmidt R. G., Clark B. B. and Bernstein R., 1975. A search for sulphide-earning areas using Landsat-1 data and digital image-processing techniques: NASA Earth resources survey symposium, Abstracts, Houston, paper G-**26**: 150 – 151.

Shackleton R. M., 1995. Tectonic evolution of greenstone belts. *In:* Coward M. P. & Ries A. C. (editors), *Early Precambrian Processes*, Geological Society Special Publication No. **95**, 53 – 65. London.

Sheeran D. A and Vennter L. C., 1990. Final Report on Prospecting Lode Gold Agreement Areas. Unpubl. D.N.G., Maputo.

Sheeran D. A.; Gonçalves R. J. e Minnitt R. C., 1990. Regional Geology- Manica Area. Minas Auríferas de Manica. Escala 1: 25 000. Unpublished map. DNG., Maputo.

Sibson R. H., 1987. Earthquake rupturing as a hydrothermal mineralising agent in hydrothermal systems. Geology, **15**: 701 – 704.

Sibson R. H., 1990. Faulting and fluid flow. Mineralogical Society of Canada, Short Course Handbook, **18**: 93 – 132.

Sibson R. H., 1992. Fault valve behaviour and hydrostatic-lithostatic fluid pressure interface. Earth Science Reviws, **32: 141-144.**

Sibson R. H., 1996. Structural permeability of fluid-driven fault-fracture meshes. Journal of Structural Geology, **18**: 1031 – 1042.

Sibson R. H., Robert F. & Poulsen K. H., 1988. High-angle reverse faults, fluid –pressure cycling, and mesothermal gold deposits. Geology, **16**: 551 – 555.

Singer R. B. 1981. Near infrared spectral reflectance of mineral mixtures: Systematic combinations of pyroxenes, olivine, and iron oxides. J. Geophysical Research **86**: 7967 – 7982.

Singer R. B. and McCord T.B., 1979. Mars: Large scale mixing of bright and dark surface materials and implications for analysis of spectral reflectance. *In*: Proceedings of the 10th Lunar and Planetary Science Conference, 19-23 March, Houston, USA: pp. 1835 – 1848.

Sleep N. H. and Windley B. F., 1982. Archaean plate tectonics: constraints and inferences. Journal of Geology, **90**: 363 – 379.

Smith M. O., Adams J. B. and Sabol D. E., 1994. Spectral mixture analysis: New strategies for the analysis of Multispectral Resolution data. In: J. Hill and J. Mègier (Eds.), *Imaging Spectrometry – a Tool for Environmental Observations*. Kluwer Academic Publishers, Dordrecht: 125 – 143.

Smith M. O., Johnson P. E. and Adams J. B., 1985. Quantitative determination of mineral types and abundances from reflectance spectra using principal components analysis. In Proc. Lunar Planetary Science Conference 15th, part 2, J. of Geophysical Research, 90 (Suppl.): C797 – C804.

Snowden P. A. and Bickle M. J., 1976. The Chinamora batholith: diapiric intrusion or interference fold? Journal of Geological Society of London, **132**: 131 - 137.

Snowden P. A., 1984. Non-diapiric batholiths in the north of Zimbabwe schield. *In*: Kroner, A. and Greiling, R. (eds). *Precambrian Tectonics illustrated, E.Schweizerbart'sche Verlagsbuchhandlung, Stuttgart*; pp 135 - 146.

Spiegelhalter D.J. and Knill-Jones R.P., 1984. Statistical and knowledge-based approaches to clinical decision-support systems, with and application to gastroenterology. Journal of the Royal Statistical Society, A, Part 1: 35 – 77.

Spiegelhalter D.J., 1986. Uncertainty in expert systems. In: Gale W.A. (Editor), Artificial Intelligence and Statistics, Addison-Wesley, Reading, Massachusetts, 17 – 55.

Stagman J. G., 1978. An outline of the geology of Rhodesia. Bull. Geological Survey of Rhodesia **80**, 126p.

Stagman J. G., 1994. Geological Map of Zimbabwe. Geological Survey of Zimbabwe, 7th Edition; Harare.

Stockwell C. H., 1933. Great Slave Lake – Copper mine River area, Northwest Territories: Geological Survey of Canada Summary Report 1932, **Part C**: 37 – 63.

Stoner E. R. and Baumgartner M. F., 1981. Characteristic variations in reflectance of surface soils. Soil Science Society American Journal, **45**: 1161 – 1165.

Stott G.M., 1997. The Superior Province, Canada. *In:* de Wit and Ashwal (editors) *Greenstone belts*. Clarendon Press. Oxford. 480 – 507.

Stowe C. W., 1971. Summary of the tectonics of the Rhodesian Archaean craton. *In*: Glover J. E. (Editor) *Symposium on Archaean Rocks*. Special Publication of the Geological Society of Australia, **3**: 373 – 383.

Stowe C. W., 1974. Alpine type structures in the Rhodesian basement at Selukwe. Journal of the Geological Society, London, **130**: 411 – 425.

Stowe C. W., 1980. Wrench tectonic in the Archaean Rhodesian Craton. Trans. Geol. Soc. S. Africa, **83**: 193 – 205.

Stowe C. W., 1984. The early Archaean Selukwe nappe Zimbabwe. *In*: Kroner A. and Greiling R. (Editors), *Precambrian Tectonics Illustrated*. Schweitzerbart: Stittgart, 41 – 56.

Stowe K., Will T. M. & Zhou S., 1993. On the timing relationship between fluid production and metamorphism in metamorphic piles: some implications for the origin of post-metamorphic gold miralization. Earth Planetary Science Letters, **114**: 417 – 430.

Swager C. P. and Griffin T. J., 1990. An early thrust duplex in the Kalgoorlie-Kambalda greenstone belt, Eastern Goldfields Province, Western Australia. Precambrian Research, **48**: 63 – 73.
Swain, P.H. and Davis, S.M., 1979. Remote Sensing: The Quantitative Approach, McGraw-Hill, New York, 396p.

Swift W. H., 1956. The geology of the Odzi Gold Belt; Southern Rhodesia Geological Survey Bulletin No. **45**. Salisbury.

Taylor P. N. and Chadwick B., 1984. Petrography, chemistry, and isotopic ages of the Peninsular gneiss, Dharwar acid volcanic rocks and the Chitradurga Granite with special reference to the late Archaean evolution of the Karnataka craton, southern India. Precambrian Research, **23**: 349 – 375.

Tighe L.M., Akhavi M.S., and Hudgins A., 1995. Applications of synthetic aperture radar (SAR) to gold exploration in central Nova Scotia. In Radar Remote Sensing: A Tool for Real-Time Land Cover Monitoring and GIS Integration. 17th Canadian Symposium on Remote Sensing, Canada Centre for Remote Sensing, **2**: 721-726.

Townsend J. R. G. and Justice C. O., 1986. Analysis of the dynamics of African vegetation using normalised difference vegetation index. International Journal of Remote Sensing, 7 **(11)**: 1435 – 1452.

Treloar P. J. and Blenkinsop T. G., 1995. Archaean deformation patterns in Zimbabwe: true indicators of Tibetan-style crustal extrusion or not? *In:* Coward M. P. & Ries A. C. (editors.), *Early Precambrian Processes,* Geological Society Special Publication, **95**, 87 - 108. London.

Treloar P. J., Coward M. P. and Harris N. W., 1992. Himayan-Tibetan analogies for the evolution of the Zimbabwe craton and Limpopo Belt. Precambrian Research, **55**: 571 – 587.

Tsomondo J. M., Wilson J. F. and Blenkinsop T. G., 1992. Reassessment of the structure and stratigraphy of the early Archaean Selukwe nappe, Zimbabwe. *In:* Glover J. E. and Ho S. E. (editors), *The Archean Terrains, Processes and Metallogeny* (Proceedings volume 3rd International Archaean Symposium, Perth): Geology Department and Extension Service, University of Western Australia, 123 – 135.

Turcotte D. L., 1986. A fractal approach to the relationship between ore grade and tonnage. Econ. Geol. **81**: 1528 – 1532.

Turcotte D. L., 1991. Fractals in geology: What are they and what are they good for? GSA Today **1**: 1 – 4.

Turcotte D. L., 1992. Fractals and chaos in geology and geophysics. Cambridge University Press, UK. 221p.

USGS, 1998. Spectroscopy Laboratory, Spectroscopy of Rocks and Minerals, and Principles of Spectroscopy_files. Geological Society Bulletin.

van der Meer F., 1995. Imaging Spectrometry and the Ronda peridotites. PhD thesis. Wageningen, The Netherlands. 309p.

van der Meer F., 1999. Can we map swelling clays with remote sensing; JAG. **1**: 27 – 35.

Vane G. and Goetz A. F. H., 1993. Terrestrial Imaging Spectrometry: Current status, future trends. Remote Sensing Environment **44**: 117 – 126.

Vearncombe J. and Vearncombe S., 1999. The spatial distribution of mineralization: Applications of Autocorrelation Analysis; Economic Geology. **94**: 475 – 486.

Vicente A. and Camarinhas M.F., 1949. Mina Monarch: Ouro, Estudo, Projecto de Trabalho a Executar e Informação Sobre o Pedido de Financiamento, Rel. 2ª Brogada de Fundo de Fomento Mineiro. Unpubl. Repartição Téc. da Indus. e Geol., Lourenço Marques. **II**. 158p.

Viljoen M. J. and Viljoen R. P., 1970. Archaean volcanicity and continental evolution in the Barberton region, Transvaal. *In*: Clifford T. N. and Gass I. G. (Editors) *African Magmatism and Tectonics*. Oliver & Boyd, Edinburgh, 27 – 49.

Viljoen R. P., Saager R. and Viljoen M. J., 1970. Some thoughts on the origin and processes responsible for the concentration of gold in the early Precambrian of Southern Africa. Mineralium Deposita, **64**: 778 – 797.

Vinyu M. L., Frei R. and Jelsma H. A., 1996. Timing between granitoid emplacement and associated gold mineralization: Examples from the ca. 2.7 Ga Harare – Shamva greenstone belt, northern Zimbabwe. Canadian Journal of Earth Science **33**: 981 – 992.

Viswanatha M. N., Ramakrishnan M. and Swami Nath J., 1982. Angular unconformity between Sargur and Dharwar supracrustals in Shigegudda, Karnataka craton, South India, Journal of the Geological Society of India, **23**: 85 – 89.

Vlaar N. J., 1986. Archaean global dynamics. Geologieen Mijnboum, **65**: 91 – 101.
Wackernagel H., 1995. Multivariate geostatistics, an introduction with applications. Springer-Verlag, New Yor, pp. 144 – 151.

Walker P. A. and Lev J., 1953. Statistical Inference: Holt, Rinehart and Winston, New York, 510p.

Walsh J., Watterson J., and Yielding G., 1991. The importance of small-scale faulting in regional extension. Nature **351**: 391 – 393.

Wilks M. E. and Nisbet E. G., 1988. Stratigraphy of the Steep Rock Group, northwest Ontario: a major Archaean unconformity and Archaean stromatolites. Canadian Journal of Earth Sciences, **25**: 370 – 391.

Wilson J. F., 1979. A preliminary reappraisal of the Rhodesian basement complex. Special Publication of the Geological Society S. Africa, **5**: 1 – 23.

Wilson J. F., Jones D. L. and Kramers, J. D., 1987. Mafic dyke swarms in Zimbabwe. In H.C. Halls & W.F. Fahrig (Eds): Mafic dyke Swarms. Geological Association of Canada, Special Paper, **34**: 433 – 444.

Wilson J. F., Nesbitt R. W., and Fanning C. M, 1995. Zircon geochronology of Archaean felsic sequences in the Zimbabwe Craton: a revision of greenstone stratigraphy and a model for crustal growth – *In:* Coward M. P. & Ries A. C. (editors), *Early Precambrian Processes*, Geological Society Special Publication, **95**: 109 – 126, London.

Windley B. F., 1973. Uniformitarianism today: plate tectonics is the key to the past. Journal of the Geological Society, London, **150**: 7 – 19.

Windley B. F. and Brigwater D., 1971. The evolution of Archaean low-and high grade terrains. Geological Society of Australia, Special Publication, **3**: 33 – 46.

Wyborn L. A. I., Gallagher R, and Jagodzinski E.A., 1994. A conceptual approach to metallogenic modelling using GIS: examples from the Pine Creek Inlier. Proceedings of a Symposium on Australian Research in Ore Genesis, Australian Mineral Foundation, Adelaide, pp. 15.1 – 15.5.

Zhang X. and Sanderson D. J., 1994. Fractal structure and deformation of fractured rock masses. *In*: Kruhl (editor) *Fractals and Dynamic systems in Geoscience*. Springer, Berlin Heidelberg New York, pp 37 – 52.

Zhang X. and Sanderson D. J., 1995. Anisotropic features of geometry and permeability in fractured rock masses. Engineering Geology, **40**: 65 – 75.

Ziehlke D. V., 1975. Eagle-Wabigoon-Dinorwic-Manitou Lake volcanic belt. In: annual Report, Centre for Precambrian Studies, University of Manitoba. Pp. 35 – 48.

APPENDIXES

Location coordinate		Name	Shear Fault zone	Qz vein	Contact			First Order						Lithology									
											Intersection	Fabric		Sediments			Volcanic				Intrusives		
														Clastic	Fine graine	Chemical	Clastic		Lavas		Felsic	Mafic	
Y	Altitude m	Sample				Younging	S0	S1	S2	Lineation	Lin-	Shear sense	fold axis				Felsic	Mafic/Ultra mafic	Mafic	Ultra mafic			Remarks
7907561	1201						70/190	80/352		30-267				Conglomerate									Low strain (high ange between s0 and S1)
7907550	1203						70/190	80/352						Conglomerate									up-stream
7907620	1221						70/184	87/349							phyllite								
7907434	1199							86/356						ultramafic sediment									
7907600	1207							80/345		16-260				Conglomerate									Pebble size (8 - 10 cm)
7907627	1201							82/001		15-269				Conglomerate									Pebble are of mafic composition)
7907731	1231						80/182	80/180	28/012	12-261	17/258		05-096	Phillite									Intercalated with conglomerates
7909167	1243						65/350	85/000						Aglomerate (tuff)									
7908748	1294						65/200	80/195							Siltstone (phyllite)								
7908608	1297					NNW									Siltstone (phyllite)								Younging derived from cross bedding
7908510	1298						70/344	75/356							Siltstone (phyllite)								(?slumped)
7910154	1264	B21/00					67/011	86/194						Felsic Tuff									
7909173	1241	B22/00, B23/00						85/178							Phyllite								In contact with felsic porphyry
7910712	1223																						Farm
7910715	1202	B24/00					73/352	87/005			30-090												
7910880	1163		87/197				80/195	87/197		30-095				Conglomeratic BIF Breccia									80 - 90% BIF fragments in mafic-ultramafic matrix
7912078	1282															BIF							Laminated and mineralised
7913644	1285							87/183											Basalt				
7912908	1243		E-W																				Rapanda
7912317	1242		?					85/184												Talc-carbonate-schist			sericitic at places
7912207	1265		70/170				50/170	55/180		25-100		Sinistral			Sericitic shales	Chert (BIF)	Tuffs						Annastomosing foliation
7912278	1322				metasediments and talc		84/177	85/348		45-090										Talc-carbonate-schist			
7912137	1288							87/170		60-080									Basalt	Talc-carbonate-schist		mafic	Intrusive relationships (tcs-basalt) - iso-folding)
7908420	1093							85/182		58-280							Tuffs						
7908271	1082						88/182	85/210		35-320					Phyllitic schist	BIF				Talc-carbonate-schist			
7905997	1017				granite and ultramafics																granite		
7906984	1011		75/142					75/142														Serpentinite	horizontal slickenside lineation
7906285	999		75/168					75/168											meta-basalt				5 m wide shear zone
7909144	1017	B25/00	65/190					74/182		40-278		South UP							komatiitic l	Talc-carbonate-schist			
7912120	1287							74/320	64/110	45-080										Talc-carbonate-schist		mafic	
7912182	1307		85/010					85/010												Talc-carbonate-schist		Dolerite	Intrusive relationships (tcs-mafic dyke) - iso-folding)
7912178	1306							85/180												Talc-carbonate-schist		Dolerite	Intrusive relationships (tcs-mafic dyke) - iso-folding)
7912197	1293																			Talc-carbonate-schist		Basalt	Intense isoclinal folding
7912209	1296							60/170		30-100					Qz-sericitic carbonate laminated ironstone								wavy S1
7912280	1302		60/144		BIF and ultramafics				<10	30-080		South UP				BIF							wavy S1
7912304	1315						80/152	70/184								BIF							wavy S1
7912309	1302							66/174		25-090							Tuff						
7912283	1316			N-S				74/150	<0	45-260										Talc-carbonate-s dyke			complex folding and kink folds at cm scale
7912275	1340																			Talc-carbonate-schist			complex folding and kink folds at cm scale
7912294	1329							65/120		50-070										Talc-carbonate-schist		Dolerite	
7912236	1328																					Serpentinite	
7912229	1332							80/140												Talc-carbonate-schist			
7912205	1333							45/148												Talc-carbonate-schist			
7912203	1334							80/158		20-092										Talc-carbonate-schist			
7912140	1336		87/190																	Talc-carbonate-schist			Exploration Adit (N-S)
7912159	1342		80/160					80/184				South UP								Talc-carbonate-schist			
7912214	1345							50/218												Talc-carbonate-schist			Annastomosing S1
7912222	1359	B26/00						45/180												Talc-carbonate-schist		Dolerite	
7912338	1375																					Serpentinite	Orinated E-W
7912320	1362	B27/00																		Talc-carbonate-schist		Serpentinite	Intrusive relationships (TCS - serpentinite - gabbro)
7912292	1385							59/172												Talc-carbonate-schist		Chloritic dyke	mafic dyke in lenses (deformed)
7912198	1384		87/190	80/196				88/182		25-095										Talc-carbonate-schist			Qz veins with horizontal crenulation cleavage
7912127	1390		88/184	N-S, NE-SW				88/184		25-090						BIF				Talc-carbonate-schist			mineralised veinlets within the shear zone
7912100	1392		88/185													BIF							highly suphurdised stockwork with Qz veins
7911935	1400	B28/00																Chloritic rock					silicified and mineralised (w/ N-S exploration Adit)
7911938	1402	B29/00												Conglomeratic BIF Breccia									fresh breccia oriented NE-SW
7911940	1427	B30/00												Conglomeratic BIF Breccia									
7911987	1436							85/210		29/100										Talc-carbonate-schist			
7912057	1474																						Ground Control Point
7911957	1485													Conglomeratic BIF Breccia									General orientation of the BIF (120 - 300)
7914010	1293	B31/00				190													Basalt				
7913880	1291		85/020					85/020												Talc-carbonate-schist			
7913770	1278		75/028		Qz porphyry/TCS			75/028												Talc-carbonate-s	Qz Porphyry		
7913668	1273		75/190					75/190		28-100										Talc-carbonate-schist			S1 is annastomosing
7912089	1230		80/172					80/172								Silicified BIF							S1 is annastomosing and sulpurdised shear zone
7912077	1229							75/178		15-085										Talc-carbonate-schist			
7912041	1230							75/358												Talc-carbonate-schist			
7912025	1230		85/340					85/340				South UP								Talc-carbonate-schist		Serpentinite	
7911877	1302																			Talc-carbonate-schist			
7911767	1307							55/162												Talc-carbonate-schist			Adit (220 - 040)

911643	1315	B32/00	70/340					70/340											Serpentinite	Very close to Razende shear zone
911576	1330			124-306				70/330					Conglomeratic BIF Breccia							
911538	1333		340-160										Conglomeratic BIF Breccia							Razende shear/ mineralised breccia with iron sulphides
911046	1346																			Pinne and eucalipter plantation (GCP)
911388	1353																			Pinne and eucalipter plantation (GCP)
911821	1303																			Adit (N-S) with water
911812	1206												Conglomeratic BIF Breccia							The breccia has been ductily deformed
911830	1208																		Serpentinite	
911796	1220																		Serpentinite	
911817	1235												Conglomeratic BIF Breccia							*Mr.* Franklin's property (no permition to work)
911524	1295																		Dolerite	
911427	1292							70/168									Talc-carbonate-schist			At places the TCS is intercalated with chlorite schists
911387	1297							75/208									Talc-carbonate-schist			At places the TCS is intercalated with chlorite schists
911598	1298																Talc-carbonate-schist			
911669	1270												Conglomeratic BIF Breccia							
911730	1253												Conglomeratic BIF Breccia							
911777	1211																Talc-carbonate-schist			
912118	1164																		Dolerite	
910370	1167		60/184					60/184		30-100	South UP		Conglomeratic BIF Breccia							
910332	1150		65/176					65/176												
910158	1088																			Highly sheared
910069	1087										South UP		BIF		Qz sericitic schist (BIF?)					Sheared contact
910019	1088							72/334		35-080										
909984	1088		75/008					75/008												
909970	1089	B33/00																		
909825	1134																			
909945	1152	B34/00					190			05-090										Some pillows ? Showing younging south
910003	1202																		Serpentinite	Sheared
910140	1204																		Serpentinite	Intensely sheared and folded at cm scale
910445	1107																		Dolerite	
909763	1113							65/008	<0	25-100										
909693	1111	B35/00	85/170					85/170											Serpentinite	horizontal slickenside and mineralised with Py
909417	1083		90/190			90/190							Conglomeratic BIF Breccia							
912374	1435	B36/00														Basalt				highly silicified and mineralised by iron sulphides
912388	1434	B37/00														Basalt				Herbert-6 Peg (Iron Pyrite)
913278	1167															Basalt				
913144	1142															Basalt				
914755	1171					Basalt/granite										Basalt		Granite		sheared contact
914718	1176		80/100					80/100								Basalt				
914643	1171		75/100					75/100					agglomerate		tuff	Basalt				komatiitic basalt with spinifex structure
914558	1165									09-275						Basalt				komatiitic basalt with spinifex structure
913057	1366															Basalt				
914649	1443	B38/00				110 - 280												Granite		
914529	1450	B39/00																	Serpentinite	
914506	1448							65/184											Serpentinite	
914434	1432																Talc-carbonate-schist			
914373	1450		87/190					87/190		35-090									Serpentinite	
914338	1454						190									Basalt				With pillow lavas
914272	1450		75/010					75/010		09-100	North UP									
914244	1448		60/356					60/356		30-100										
914224	1456		65/350					65/350		15-090										
914193	1455		60/016					60/016		45-100							Talc-carbonate-schist			Main shear
914143	1449	B40/00				Tremolite sch/TCS											Talc-carbonate-schist			Sheared contact
914078	1446		75/190					75/190		60-280										Also 30 - 090, and Qz vein
913903	1465	B41/00														Basalt				
913509	1412				N-S											Basalt				
913236	1403	B42/00														Basalt				Silicified
913118	1270													BIF						Blocks (BIF)
912694	1214				E-W											Basalt				
911569	1225	B43/00						85/001	80/020	25-095										With S-C fabric
911522	1213				45/020			75/350												Exploration pit
911274	1220							80/170												
911341	1186				E-W															
911421	1215							80/012												
911494	1224	B44/00										35-310								
911082	1198		65/140	70/160				65/140									Talc-carbonate-schist			
911041	1189																		Serpentinite	
911006	1186																		Serpentinite	
911275	1188				E-W									BIF					Serpentinite	
914346	1207																	Granite		Northern granite
912934	754		80/220					80/220					Conglomeratic BIF Breccia							with chloritic schists (mineralised with iron sulphides)
912397	1130												Conglomeratic BIF Breccia							

7909665	1130	B33/00																		With sulphides
7912425	1131																	Granite		Northern granite
7910814	1057																	Granite		
7908917	1046	B46/00																	Serpentinite	
7908891	1036		85/140		chloritic sch/granite	85/140														
7908480	1035	B47/00	80/164			80/164													Serpentinite	
7908088	1031					70/010		50-270												Wavy S1
7908111	1024					85/210		50-280												
7908060	1032					86/342														
7908112	1045	B48/00																		Silicified - Old Mine (shaft and pit)
7908017	1046		87/180			87/180		50-280	South UP											
7908001	1046																		Serpentinite	
7907913	1048																		Serpentinite	Farm House, no permition to visit the outcrops
7907887	1031																		Serpentinite	
7907789	1032	B49/00				85/350													Serpentinite	
7906190	1064		70/200		Ultramafic/ granite	70/200		30-300										Granite		
7906136	1061																		Serpentinite	
7907735	1023																		Serpentinite	
7907486	1005															Basalt				Komatiitic
7907421	1045															Basalt				Komatiitic
7907313	1026															Basalt				Komatiitic
7907683	1070				070-250											Basalt		Granite		
7911142	1108				Granite/ ultramafic													Granite		
7911025	1120	B50/00																		
7910788	1098					83/184										Basalt				Silicified and interfingered in the ultramafics
7910507	1084					80/170		10-268												
7910116	1066																			
7909593	1106										Conglomeratic BIF Breccia									Old Mine
7909562	1095	B51/00				85/190					Conglomeratic BIF Breccia				Actinolite - tremolite					
7909528	1087		70/028			70/028									Actinolite - tremolite					slickenside 06-260
7909559	1068		N-S																Serpentinite	
7909587	1075																		Serpentinite	Blocks
7909937	1099		85/186			85/186		30-280											Serpentinite	
7910009	1104																		Serpentinite	
7909804	1076					80/330											Talc-carbonate-schist			Highly folded
7909652	1077					85/334									Mafic schist					
7909640	1073					85/350											Talc-carbonate-schist			with intercalations of mafic sch, highly folded
7909871	1067					83/142	50/000	28-240									Talc-carbonate-schist			
7909025	1080		75/318			75/318		35-040		30-250					Mafic schist					
7909869	1057					68/022											Talc-carbonate-schist			
7910001	1080																Talc-carbonate-schist			200 m shear zone,ductile-brittle deformation and folding
7910066	1072																Talc-carbonate-schist		Mafic dykes	Complex folding in flower structures
7906747	1043																			GCP (Ndemera Farm)
7906704	1056	B52/00													Actinolite - tremolite					
7906801	1085												BIF							
7906715	1035		70/050			70/050		35-310												
7906656	1015		60/000			60/000						Graphitic shal	BIF							
7906149	1086	B53/00	75/012			75/012													Serpentinite	
7906191	1106																		Serpentinite	
7906389	1026					75/016											Talc-carbonate-schist		Serpentinite	
7906467	1029		75/014			75/014			North UP										Serpentinite	
7906919	1008																		Serpentinite	
7905795	1023					80/172									Mafic schist					
7905476	1006		70/170			70/170			North UP						Actinolite schist					
7905413	1006			100 - 280											Actinolite schist					
7906158	1049		85/186			85/186													Serpentinite	S1 is wavy, slickenside (05 - 45 - 310 - 320)
7906137	1058		70/215			70/215		45-292											Serpentinite	
7906121	1067			60/186		75/350								Tuff						
7906104	1071	B54/00				30/188													Mafic dyke	
7906045	1072													Tuff						
7906052	1039		80/190		Ultramafic/phyllite	85/196						Phyllite								
7906097	1039					75/158		40-250				Ultramafic sed								
7906139	1022					80/220						Ultramafic sed								
7906173	1022		75/190			75/190			South UP			Ultramafic sed								
7906441	1029			100 - 280								Ultramafic sed								
7906266	1029					75/182		50-250							Mafic schist					
7906223	1030	B55/00										Interlayered								

45746	7905355	1105				Granite/basalt										Basalt		Granite		Komatiitic
45760	7905423	1099						70/220	35-290						Tuff					
45889	7905602	1092						70/170							Tuff					
45844	7905611	1098	B56/00												Tuff					Silicified
45955	7905701	1082						80/194						BIF						Recrystallised Qz sericitic schist
46553	7905891	1082			E-W									BIF						Several exploration pits oriented N-S
46688	7905951	1095		80/176				80/178	30-090							Serpentinite				
45949	7906232	1049		80/180				80/180								Serpentinite				
45945	7906253	1049						70/020	30-110								Talc-carbonate-schist			
45943	7906269	1037					70/012							BIF						
45942	7906283	1038						80/188									Talc-carbonate-schist			
45940	7906296	1040					80/040	85/028					Phyllite							
45961	7906322	1056						80/190								Serpentinite				
447628	7906689	1098														Serpentinite				
447845	7907498	1053										Conglomerate								Monomict
448279	7907074	1063	B57/00					87/172	35-270			Conglomerate								Monomict, size of the pebbles <20 X 10 and > 2 X 1 cm
448815	7907143	1068										Conglomerate								Continuous exposure for >700 m
448694	7907056	1082						86/178				Conglomerate								Monomict
448862	7906877	1091					87/180	85/170					Phyllite							
448967	7906434	1106		84/182				84/182											Serpentinite	
448990	7906305	1109												BIF						with Qz veins
448957	7906121	1119												BIF						with Qz veins
449494	7907084	1085						80/170					Ultramafic sed							Slumped ?
449132	7907089	1076		65/334				85/334	45-260			Conglomerate								Slumped ?
449150	7906890	1091																	Gabbro dyke	N-S
449232	7906821	1103																	Dolerite	
449296	7906964	1100						80/190					Ultramafic sed							
449292	7906977	1096		80/192				80/192				Conglomerate								Monomict
449317	7907020	1103																	Serpentinite	
449401	7907073	1074										Conglomerate								Monomict
449626	7907029	1086										Conglomerate								Monomict
449631	7907010	1068																	Gabbro dyke	striking 100 - 280
449633	7907584	1053					80/220	70/356	50-274				Phyllite							High strained siltstone
449698	7907613	1070	B58/00															Granite		Inner granite
449621	7907578	1062						78/000					Phyllite							
449660	7907097	1075																		
449689	7907101	1071						82/192					Ultramafic sed							
449611	7907087	1069				North		79/191					Ultramafic sed							Finning douwnwards
449877	7907087	1076					75/183	75/182					Ultramafic sed							S1 is parallel to S0
449941	7907072	1067										Conglomerate								Monomict
449994	7907092	1067					80/168	75/188			30-240		Interlayered							with crossbedding and intrafolial folding
450904	7907032	1081		30/210				30/210			40-138		Interlayered							complex folding and shearing
450882	7907087	1096					85/220	55/314					Interlayered							
450914	7907038	1111											Interlayered							Complex folding
450964	7906835	1110						70/194				Conglomerate								Monomict
451003	7906621	1115						65/230											Serpentinite	
451246	7906414	1151	B59/00		E-W														Serpentinite	Reliance Shaft (Au - Ag)
450981	7906582	1110		80/184				80/184												
451272	7906829	1092																		GEM mine
454143	7906815	1110			70/268															
454982	7905902	1177																	Serpentinite	
455075	7905786	1192												BIF						Blocks
455304	7905787	1166		85/186				65/186											Serpentinite	
455372	7905472	1194						80/190					Phyllite/ graphitic							
455325	7905518	1183																	Serpentinite	
455319	7905502	1147																	Serpentinite	
456045	7905596	1164	B60/00																	
456060	7906007	1139						74/182					Ultramafic sed							With tremolite overgrowing
456068	7905986	1134		85/334				65/334		South UP			Ultramafic sed							
456139	7906044	1131						75/190					Ultramafic sed							
456229	7906033	1144						70/192					Ultramafic sed							
456518	7906010	1144						75/190					Ultramafic sed							
457059	7906034	1176				Tremolite Sch./conglomerate						Conglomerate								
457726	7906285	1139					70/090	65/178					Ultramafic sed							Complex folding
458170	7906118	1170						65/176											Serpentinite	
458216	7905936	1181																	Dolerite	NE - SW

58332	7906143	1206																	Dolerite	NE - SW
58432	7906152	1239																	Dolerite	(NE - SW) 263 - 054
56210	7906125	1176								65/174							Talc-carbonate-schist		Dolerite	
58710	7906540	1174							50/200	65/185				Interlayered						Cross bedding and channeling
58732	7906537	1167							50/168	70/192				Interlayered						Cross bedding and channeling
58840	7906547	1163												Interlayered						
59033	7906890	1158								75/182	10 - 095			Interlayered						
59760	7906834	1181							55/196	65/196				Interlayered						at places tuffaceous and shally (greywacke ?)
59179	7906770	1182																	Dolerite	
59251	7906723	1186						North	70/182	60/162				Interlayered						tuffaceous silty claystones with cross bedding
59321	7906742	1192							55/180					Interlayered						
59327	7906746	1182					60/110													
59429	7906755	1196																	Dolerite	
59550	7906381	1231							65/192	75/198	05-097			Ultramafic sed						
59597	7906351	1213							65/186					Ultramafic sed						
59648	7906321	1193																	Serpentinite	
59649	7906383	1210								75/008				Ultramafic sed						
59800	7906370	1209							75/140	70/180	35-274		Conglomerate	Ultramafic sed						
59888	7906398	1211	B63/00							65/182	30-276		Conglomerate							Flattened pebbles (21 X 7 X 0,5 cm)
59850	7906056	1238																	Basalt	
59918	7906084	1244																	Dolerite	N-S
60497	7906019	1252																	Dolerite	
60557	7905869	1232								65/140					BIF				Serpentinite	
60608	7905941	1196				E-W														
60520	7905842	1264				E-W									BIF					
60462	7906033	1253								50/184					BIF					
60200	7906134	1235																		
60484	7906439	1207								60/186	30-260			Ultramafic sed						
61416	7906779	1239								50/192				Ultramafic sed						
61478	7906681	1242								55/192	35-330			Ultramafic sed						
61512	7906729	1237								75/186	30-272			Ultramafic sed						
61584	7906752	1237								50/186				Ultramafic sed						
61614	7906892	1274								50/178			Conglomerate							
61661	7906727	1267					Ultramafic sed / conglomerate						Conglomerate	Ultramafic sed						Sheared contact
61640	7906762	1238																	Gabbro	E - W
63302	7913933	1210		87/190						87/190							Talc-carbonate-schist			Slumped ?
63361	7913970	1218		65/186						65/186	30-100	South UP				Basalt			Serpentinite	
63313	7914024	1204	B64/00							60/192	40-098					Basalt			Serpentinite	
63252	7913954	1197						190		65/210						Basalt	Talc-carbonate-schist			Pillow lavas with chilled margins and carbonates
66797	7913882	1250								70/218	30-124					Basalt				
66799	7913869	1291				N-S				70/220						Basalt				Exploration pit or small mine (in Qz)
66808	7913713	1274								75/008						Basalt				
66814	7913730	1254								60/208						Basalt				
66832	7913776	1265														Basalt				
66848	7913801	1269								76/228							Talc-carbonate-schist			
66856	7913824	1266		60/232						60/232										With spinifex structures
66924	7913802	1273		76/336						76/336	20-238								Serpentinite	complex folding within the shear zone
66950	7913782	1269		75/006						75/006	35-274								Serpentinite	
66984	7913779	1278								55/326									Serpentinite	
67120	7913819	1283		65/356						65/356									Serpentinite	
67122	7913876	1269																	Serpentinite	Three sets of joints
67155	7913949	1298					Serpentinite/Qz porphyry											Qz porphy	Serpentinite	
67263	7914127	1300						z		60/182									Serpentinite	
67265	7914140	1301	B67/00															Rhyolite		
67339	7914326	1321			E-W															
67087	7914501	1298																Rhyolite		
66828	7914779	1336																Rhyolite		
66853	7914831	1337																	Dolerite	
66894	7914897	1335			E-W					80/190										Highly brecciated
66976	7915237	1328			E-W											Basalt				
66920	7915674	1321														Basalt				

466209	7918865	1457											Basalt			Gabbro	
466388	7919843	1463													Granite		Northern Granite
466764	7914734	1354															
466406	7914873	1436	B68/00												Qz Diorite		
466825	7914862	1312			Qz porphyry/TCS									Talc-carbonate-s	Qz porphyry		
461781	7906897	1222					65/180									Gabbro	
462155	7907048	1220								Conglomerate							Sheared
462245	7907038	1233									Ultramafic sed					Serpentinite	
462548	7907066	1231					65/180			Conglomerate	Ultramafic sed						
462579	7907034	1239				65/210	65/200				Interlayered						
462693	7907056	1246					70/190				Interlayered						
462705	7907068	1247					74/193				Ultramafic sed						
462739	7907044	1252					80/187				Interlayered						High strain and intensely foliated
462570	7908814	1306														Serpentinite	Toronto mine main shaft
462386	7908777	1302															
462525	7908610	1336										BIF				Serpentinite	
462566	7908539	1359				55/198						BIF				Serpentinite	
462728	7908454	1360		50/182			50/182										
462796	7908383	1376				50/180	50/180				Interlayered						S0 is parallel to S1
462924	7908384	1374		75/196			75/198		North UP							Serpentinite	
462981	7908453	1356		75/196			75/198									Serpentinite	Gogue marks indicating South down
463219	7908449	1330		55/182			65/182					BIF		Talc-carbonate-schist			
463336	7908461	1321	B69/00									BIF				Serpentinite	Highly sheared
463388	7908430	1337										BIF				Serpentinite	
462896	7907202	1260					75/192			Conglomerate							
462987	7907083	1225					70/182			Conglomerate	Utramafic sed						
462876	7907031	1241		75/180			75/180			Conglomerate							
462958	7906986	1249					65/179	30-080									
462969	7906947	1248														Serpentinite	
463217	7906865	1271										BIF					
463417	7908773	1298										BIF					
463550	7908785	1327										BIF				Serpentinite	
463822	7908830	1354														Serpentinite	Highly sheared
463906	7908843	1336		75/172			75/172									Serpentinite	Highly sheared
469428	7908767	1315				65/176	73/150	30-128			Phyllite						
469597	7908737	1313					65/180			Aglomerate							
469779	7908787	1309	B70/00				50/179			Aglomerate							
469860	7908843	1301					50/198				Phyllite						
470296	7908622	1371					55/190				Phyllite						
470224	7908558	1332				55/196	60/180				Phyllite						
469203	7909089	1392									Phyllite						Layers from mm to tens of cm
469348	7907753	1394					90/180	50-270		Conglomerate							Sheared
469560	7907682	1394								Conglomerate							Talc Carbonate rich
469509	7907485	1400		75/170			75/170			Conglomerate							Highly sheared
469560	7907410	1430														Serpentinite	
469791	7907209	1513														Serpentinite	
470647	7907080	1490					70/010					BIF					
470702	7907130	1471					60/350					BIF					
470422	7907808	1344															Breccia with some rounded clasts
470265	7908054	1343					80/178			Conglomerate							Highly sheared
470257	7908114	1230								Conglomerate							
470381	7909457	1232								Aglomerate							Highly wheathered
470343	7909644	1235								Aglomerate							
470220	7909631	1340								Aglomerate							Highly wheathered
469943	790969	1256								Aglomerate							Tuffacceous
469698	7909670	1240								Aglomerate							
469416	7909656	1226								Aglomerate							It weather to whitish soil to brown reddish
466927	7909887	1186								Aglomerate							
466968	7909698	1209								Aglomerate					Rhyolite		Rhyolite or fresh aglomerate ??
466475	7909299	1225								Aglomerate					Rhyolite		Rhyolite or fresh aglomerate ??
466562	7909134	1243														Dolerite	N-S
466069	7910002	1185								Aglomerate							
462085	7910862	1132					87/175										
462442	7912107	1152														Serpentinite	
461424	7910059	1128														Dolerite	E-W
461445	7910018	1129		85/190			85/190					BIF					Sheer zone
461445	7909992	1133					85/190	15-080		Conglomeratic BIF Breccia							
461416	7909935	1129					85/191	15-081		Conglomeratic BIF Breccia							
461400	7909917	1129		65/004			65/004							Talc-carbonate-schist			
461390	7909898	1125		80/002			80/002		North UP					Talc-carbonate-schist			Highly sheared (main shear ???)

61364	7909660	1129		85/357				85/357				Utramafic sed								
61421	7909601	1131		75/002				75/002				Utramafic sed								In contact with agglomerate
61293	7909789	1168		65/002	Ultramafic/aglomerate			65/002			Aglomerate						Talc-carbonate-schist			
59684	7909525	1133									Conglomeratic BIF Breccia									Highly sheared
59688	7909510	1134		75/004				75/004									Talc-carbonate-schist			
59699	7909492	1133						70/008			Conglomeratic BIF Breccia									
59707	7909481	1126		70/170	TCS/BIF Breccia			70/170			Conglomeratic BIF Breccia						Talc-carbonate-schist			
61093	7906174	1388	B72/00			North										Basalt				With iron sulphides
61291	7906184	1372											BIF				Talc-carbonate-schist			with BIF and Qz veins
61308	7906108	1344						80/330												
61687	7906384	1378						87/002								Basalt				
62190	7905466	1407				North										Basalt				with pillows younging upwards
62286	7905457	1407							45-292										Serpentinite	
62398	7905437	1409						50/008	45-252										Dolerite	
62863	7905490	1449		70/008				70/008									Talc-carbonate-schist			
63242	7905651	1480		80/060				80/060	40-164											Slumped??
64108	7905731	1622							50-132											Intensely folded
64156	7905681	1636																	Serpentinite	
53782	7906482	1153									Conglomerate									Monomict
53639	7906379	1202						70/182			Conglomerate									Monomict, conglomeratic and tremolitic-actinolitic
53781	7906261	1226						65/194			Conglomerate									
53852	7906653	1150											BIF							Blocks
53847	7906612	1136																	Serpentinite	
70087	7910074	1261									Aglomerate									
70092	7910919	1354									Aglomerate									
69759	7911112	1412									Aglomerate									
68535	7911470	1482									Aglomerate								Dolerite	
68377	7911612	1495									Aglomerate		BIF							BIF breccia making the Ultramafic-aglomerate contact
58356	7911637	1490			Aglomerate/BIF breccia						Conglomeratic BIF Breccia									
68356	7911683	1496			Ultramafic/BIF breccia						Conglomeratic BIF Breccia									
69266	7912298	1403		85/190				85/190												Alignment of old works (looking West)
62570	7913744	767															Talc-carbonate-schist			Au in TCS intruded by Qz veinlets of limited extension
62565	7913864	821												Tuff						Exploration pit
62667	7913894	869			E-W, NE-SW			30/360									Talc-carbonate-schist			Qz veins oriented E-W and NE-SW
62683	7914101	843					80/040	80/040					BIF							
67719	7908048	787																		GCP (Tete intersection)
67833	7908306	784																		GCP (Chimedzi intersection)
68369	7910691	710																		Bridge over Revue River
68446	7911172	711																		GCP intersection to Mucthinza
68870	7912073	730		82/056				82/056			Conglomeratic BIF Breccia		BIF				Talc-carbonate-schist			
68878	7912074	731		80/186				80/186		South UP	Conglomeratic BIF Breccia									In tercalations of schist in the shear zone
68885	7912125	738		80/188				80/188		South UP	Conglomeratic BIF Breccia									
68724	7912978	746						85/194					BIF							
68524	7912986	768																	Serpentinite	Serpentinite intruding TCS
68415	7913119	795						85/198					BIF							
68822	7913802	826	B02/00											Tuff						
69702	7914394	920																	Dolerite	strike 148 - 328
91772	7914747	1049						70/015											Serpentinite	
91796	7914738	1045	B03/00					70/326				Phyllite								
92492	7914623	1023		65/052	Chloritic Sch/serpentinite			65/052												
92479	7914669	1031						56/046											Serpentinite	
93391	7014667	1063						70/240											Serpentinite	Folded
93707	7915679	899		80/196	Phyllite/BIF			80/196				Phyllite								
93708	7915679	899		85/190				85/190		South UP			BIF							
93368	7916020	1022		75/190				75/190		South UP			BIF							with chloritic schists
93219	7916497	940						85/120				Phyllite/ back shale								intensely foliated
93103	7916528	930						64/178				Phyllite/ back shale								
92936	7916670	920						70/182				Phyllite/ back shale								
82674	7912244	739																		GCP - Intersection to the CAMP
82321	7912778	740																		GCP - Intersection to CHUA
81925	7913913	720																		GCP - Bridge over Revue River
81495	7914392	745																		GCP - Bridge over Chua River
81438	7914448	762																		GCP - Bifucartion to Chua
62965	7914579	1099	3/gr/Rw															Granite		
64290	7914295	1380	4/sp/Rw					85/002											Serpentinite	
64203	7914024	1416						86/010									Talc-carbonate-schist			
64114	7913977	1342	14/7/Rw		Granite/TCS												Talc-carbonate-s	Granite		
64142	7913900		15/7/Rw	89/070													Talc-carbonate-schist			
64092	7913822		18/7/Rw					80/350									Talc-carbonate-schist			
64074	7913632		22/7/Rw												Mafic schist					
64011	7913611		23/7/Rw													basalt				
63977	7913528		24/7/Rw													basalt				
62927	7912118	1200	23/BIF/Rw										BIF							
62834	7912238	1137	26/7/Rw														Talc-carbonate-schist		Serpentinite	
60402	7906313																			GCP- Hre HW - Penhalonga
76595	7909695																			GCP- Monarch - Manica - Chazuca
71259	7912177																			Monarch mine
71256	7912270	1491																		Adit 2 - Monarch mine
71152	7912273			87/060 45/320															Dolerite	Open pit

7910428		01/Man/99											BIF							Try Again Mine
7912835															Mafic schist					Ivone Mine
7912894	652		85/020									Conglomeratic BIF Breccia	BIF							
7913091		02/Man/99						45/200									Talc-carbonate-schist			
7913036	812		50/010														Talc-carbonate-schist			
7916527	771												BIF							
7917388	764															basalt			Dolerite	Two Fools mine
7917277	861															basalt				Adit at Two Fools Mine
7917578																				Chua Mine
7917771	868		87/335		87/335													Granite		Jhonson Mine
7917870	894																	Granite		Jhonson Mine - graisen
7916473	786																			GCP - Chua - Chimedzi Junction
7908360	886																	Qz porphyry		
7919948	891													Tuff						
7920129						Qz Diorite/Mafic sch		87/220							Mafic schist			Qz Diorite		
7919768	1150																			Adit
7913162	955	01/Muza/99														Peridotite			Serpentinite	
7912837	936																		Serpentinite	
7913873	1007	3, 4/Muza/	85/130		76/130											Basalt			Serpentinite	Muza Reef mine
7916672	820																			GCP - Tete - Melka - Manica
7918812	1056		80/300					50/150			North UP				Mafic schist				Serpentinite	
7913707	1095							40/170							Mafic schist					Cantao Mine (main)
7918712								40/180							Mafic schist					Adit (Cantao Mine)
7918749	1104																			Mine Dam
7919071	1236		48/150 N-S					48/150			South UP									
7919182	1650							80/310												
7918895	1708		85/170					30/170							Mafic schist		Talc-carbonate-schist			Marondo Mine
7918650		01/Marondo/99															Talc-carbonate-schist			Marondo Mine
7910725	760											Conglomeratic BIF Breccia								Boa Esperance Mine
7909916	818					Granite/Mafic Sch														
7917862	1066																			Adit
7917790	1106														Mafic schist					Excelsior Mine
7918149			70/060		87/04	Granite/TCS		70/060												
7911034	816		84/184					84/184	70-214				BIF				Talc-carbonate-schist			Dot's Lock Mine
7912863	1461		49/292					49/292	73-255	03/160	North UP						Talc-carbonate-schist			Monarch Mine (adit 5)
7912877	1494				330 - 150			80/154	74/053		South UP						Talc-carbonate-schist		Dolerite	Open pit
7912848	1511		69/090	74/095				75/039	21 - 010								Talc-carbonate-schist			Open pit (Monarch mine)
7910780			85/176		70/268			71/168	68 - 100		South UP		BIF		Mafic schist					Fair Bride
7916780					55/251								BIF		Mafic schist					Fair Bride
7910537								90/350					BIF		Mafic schist					Try Again
7910830			83/182				83/182		70 - 102				BIF		Mafic schist					
7914290			70/112					70/112	61 - 055	76 - 020					Mafic schist		Talc-carbonate-schist			
7913870								50/128									Talc-carbonate-schist			
7914330															Mafic schist					Old Work
7919050			58/242					70/120										Granite		Exploration trench (Morgan Mine)
7919019																		Granite		Exploration trench (Morgan Mine)
7918820			66/330						36 - 248	42 - 260								Granite		Graisen
7918780																		Granite		Old Work
7916610					70/163													Granite		Old Work
7916390																		Granite		Exploration trench (Chua Mine)
7916320					87/220													Granite		Exploration trench (Chua Mine)
7917470																			Dolerite	Two Fools
7913090					90/200															Guy Fawkes mine
7910891	1113		85/002					85/002	12 - 060			Conglomeratic BIF Breccia					Talc-carbonate-schist			
7910910			70/350									Conglomeratic BIF Breccia								
7910629																	Talc-carbonate-schist			
7910882						68/350		84/016	44 - 048			Conglomeratic BIF Breccia								
7918579								75/020	10 - 268						Mafic schist					
7916768					69/040										Mafic schist					
7916744									40 - 084						Mafic schist					
7918852								70/172							Mafic schist					Cantao Main Open Pit
7918471								60/184							Mafic schist					Cantao Main Open Pit
7918891															Mafic schist					Exploration thrench
7918852				70/066				30/154							Mafic schist					
7919666								49/192							Mafic schist					Cantao Main Adit
7919139																	Talc-carbonate-schist			Exploration Pit
7919619			30/202	87/090	50/310			30/202									Talc-carbonate-schist			Marondo Mine area
7919125			50/152					52/170									Talc-carbonate-schist			Marondo Mine area
7919681	1616	01/Maronc	80/170					80/170							Mafic schist		Talc-carbonate-schist			
7919671	1631		87/150			030 - 210		50/178							Mafic schist					
7919777															Mafic schist					Marondo Adit

78792	7919755					87/186											Mafic schist					
79605	7919078																Mafic schist					Exploration trench
77124	7907232	1051																			Serpentinite	Seymour Adit
76964	7907118	1535	SP3/08/99																		Serpentinite	
77626	7907047	1149																		Talc-carbonate-schist		Serpentinite	
77969	7907140	779																				Monduguara Mine (processing plant)
33160	7910692	762		75/190	87/040				75/190					Conglomerate			Mafic schist					Boa Esperance Mine
93151	7910697	767		80/180					80/180					Conglomerate								Boa Esperance Mine area
93151	7910743		SP7/03/99																Talc-carbonate-schist			Boa Esperance Mine area
93151	7910783		SP7/04/99	85/180					85/180	89/102	22 - 100			Conglomerate								Boa Esperance Mine area
81424	7910729	836		70/006					70/006		20 - 068		North UP			BIF						Dot's Lock Mine
81424	7910762	856																				Collapsed adit
81535	7910810	764																				Exploration trench
81546	7910848			60/160					70/160							BIF	Mafic schist					Edge of the Pit
81495	7910777	821															Mafic schist					Exploration Pit
93278	7910804	730			70/086				55/100		58 - 102			Conglomerate					Talc-carbonate-schist			Boa Esperance Mine
80534	7918841																			Granite		Old Wednesday
81167	7917762	1091																		Granite		Collapsed adit (Chua Mine)
81140	7917847																			Granite		Chua Mine
81232	7917854																			Granite		
84361	7917938																			Granite		Collapsed Adit
73272	7914068		37 - 41/MN/99												Agglomerate			basalt				Revue Mine
73291	7913768	838													Agglomerate							Collapsed Adit (Revue mine)
67857	7908402	711							90/120											Granite		Cross section S-N
67857	7908416	711		42/344		45/350			42/344		08 - 082									Granite		
67856	7908422	711		40/360					40/360											Granite		
67855	7908429	711		80/306					80/306											Granite		
67902	7908451					78/360														Granite		
67905	7908549			62/336					62/336											Granite		
67907	7908558						45/360		50/334										Talc-carbonate-s	Granite		
67909	7908584				45/350				65/336										Talc-carbonate-schist			
67912	7908592								70/340										Talc-carbonate-schist			
67915	7908598								89/136		47 - 052								Talc-carbonate-schist			Folded with Kink folds
67917	7908630								69/310						Interlayered							
67915	7908623																Mafic schist					
67916	7908804		MAP1/01/99														Mafic schist					
67862	7908749	733	MAP1/03/99														Mafic schist					
67837	7908813	790	MAP1/05/99						86/337		40 - 093						Mafic schist					
67837	7908817								89/136	60 - 140	22 - 053	47 - 062										
67839	7908825								87/319														
67839	7908831								69/134														
67840	7908840								75/317														
67835	7908656								69/310														
67837	7908658							72/327							Interlayered							
67836	7908660								85/320														
67840	7908662							12/272							Interlayered							
67838	7908665								80/294														
67837	7908668							17/300							Interlayered							
67837	7908669							63/240															
67838	7908672							63/324	72/094						Interlayered							
67836	7908681								85/290												Annestomosing foliation
67837	7908685								76/310														
67836	7908700								80/310														
67838	7908717								47/109														
67832	7908729		MAP1/07/99						89/114														
67835	7908732								80/275														
67836	7908736								82/286														
67862	7908749	733	MAP1/08/99																		
67860	7908761								90/287														
67858	7908762								79/294												Serpentinite	
67857	7908763								85/300												Serpentinite	
67834	7908764	782	MAP1/09/99					77/220	76/298										Talc-carbonate-schist			
67835	7908773							90/242	76/313														
67830	7908783								64/304														
67827	7908788								70/327														
67823	7908898	725																			
71153	7912250								30/334												Wester Adit (Monarch Mine)
71917	7912609	1412			45/300				44/062		36 - 270											Monarch Mine area (along the road)
71917	7912609	1412			45/170				30/56		40 - 090											Monarch Mine area (along the road)
71940	7912512	1774														BIF			Talc-carbonate-schist			Monarch Mine adit 3

471508	7912517	1396												BIF			Talc-carbonate-schist		Monarch Mine adit (Explosive magazin)
471153	7912250													BIF			Talc-carbonate-schist		Monarch Mine adit
471140	7912304			75/294	80/358		75/152				21 - 104			BIF			Talc-carbonate-schist		Monarch Mine Open Pit
471140	7912304				80/277						27 - 013			BIF			Talc-carbonate-schist		Monarch Mine Open Pit
471279	7912345																		Monarch Mine adit 5
471278	7912245					40/34:	34/356		40/358		09 - 110						Talc-carbonate-schist	Dolerite	Monarch Mine adit
486946	7912646	740												BIF			Talc-carbonate-schist		Guy Fawkes mine - adit
486937	7912659																		Guy Fawkes mine - Exploration Trench
487028	7912610							70/036	89/181		62 - 090	South UP		BIF					Guy Fawkes mine - Exploration Pit
486970	7912694	767						70/036									Talc-carbonate-schist		
487025	7912796																Talc-carbonate-schist		Guy Fawkes mine - Exploration Shaft
486925	7912817								54/033	62 - 029	40 - 090						Talc-carbonate-schist		Guy Fawkes mine - Main Open Pit
486925	7912817								52/012			South UP					Talc-carbonate-schist		
486760	7912737																Talc-carbonate-schist		Guy Fawkes mine - Exploration Shaft
486808	7912791								45/010								Talc-carbonate-schist		
486769	7912781			25/004	25/004				36/342		22 - 030						Talc-carbonate-schist		Guy Fawkes mine - adit
486769	7912781			25/004					51/358		22 - 030						Talc-carbonate-schist		Guy Fawkes mine - adit
486889	7912659				86/356		57/360		51/039				Conglomeratic BIF Breccia	BIF					Guy Fawkes mine - adit
487834	7908068	735	MAP1/10/99						54/344								Talc-carbonate-schist		Cross section South - North
487834	7908886	735							52/344								Talc-carbonate-schist		
487834	7908907								80/158								Talc-carbonate-schist		
487834	7908908						71/206		80/168								Talc-carbonate-schist	Serpentinite	
487835	7908931								64/330									Serpentinite	
487834	7908939					64/348			63/346									Serpentinite	
487836	7909007	683							83/166										
487834	7909009	683				64/348													
487844	7909010		MAP1/11/99						86/322								Talc-carbonate-schist		
487850	7909016															basalt			with spinifex structures
487851	7909039																	Serpentinite	
487851	7909040								89/075								Talc-carbonate-schist		
487835	7909020		MAP1/134	78/056					78/056										
487836	7909022								62/064										
487834	7909028								77/103										
487835	7909034								64/346										
487834	7909039								35/002										
487839	7909045								57/340										
487945	7909061		MAP1/14/99						67/332										
487946	7909077								42/317										
487946	7909081								65/012										
487945	7909085								74/352										
487944	7909088								68/006										
487948	7909090								86/296										
487956	7909096								80/346										
487957	7909106								80/341										
487957	7909109								70/358										
487967	7909119								81/358										
487967	7909121								52/164										
487962	7909158								70/162										
487961	7909160								67/006										
487962	7909166								88/352		32 - 072								
487847	7909183								38/353										
487842	7909158								54/153										
497843	7909161								59/170		62 - 078								
497844	7909163								72/340										
497843	7909164								63/356										
497844	7909165								66/012										
497846	7909166								74/170										
497847	7909169								36/170										
487891	7909273	661																	
487856	7909514								52/009						Mafic schist				
487868	7909636	709							75/342							basalt			
487868	7909677		MAP1/15/99						77/340		25 - 094				Mafic schist				
487914	7909690								80/002		44 - 056				Mafic schist				
487914	7909696		MAP1/16/99						53/009		45 - 056				Mafic schist				
487915	7909698								57/343										
487914	7909699								67/350										
487916	7909704				14/067				74/342						Mafic schist				
487914	7909719					45/170													
488022	7909794								83/358										
487977	7909790	798							76/162					BIF	Mafic schist			Serpentinite	
488080	7909843								62/137		42 - 070							Serpentinite	
488082	7909850								81/042						Mafic schist				
488081	7909855			84/170					84/170						Mafic schist				
488087	7909872								78/184						Mafic schist				
488085	7909880								84/350										
488084	7909840		MAP1/19/99																
488075	7909914	709					64/196				26 - 276				Mafic schist			amphibolite	
488080	7909924								82/202		10 - 290				Mafic schist			amphibolite	
488088	7909946								52/222								Talc-carbonate-schist	amphibolite	
488089	7909954						70/224		87/347								Talc-carbonate-schist	amphibolite	
488138	7909923								80/196		60 - 130								

APPENDIX IV-A

DATABASE STRUCTURE

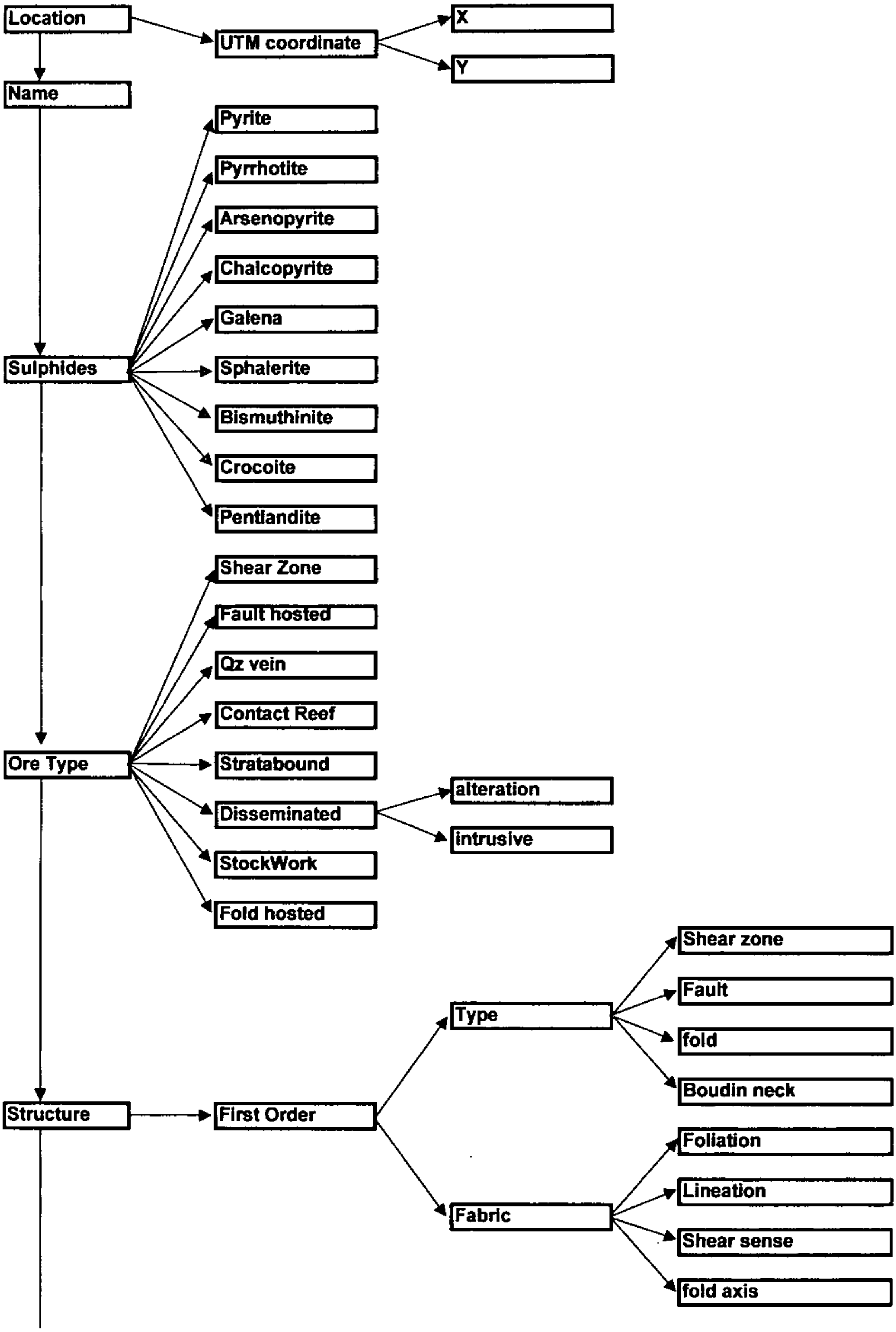

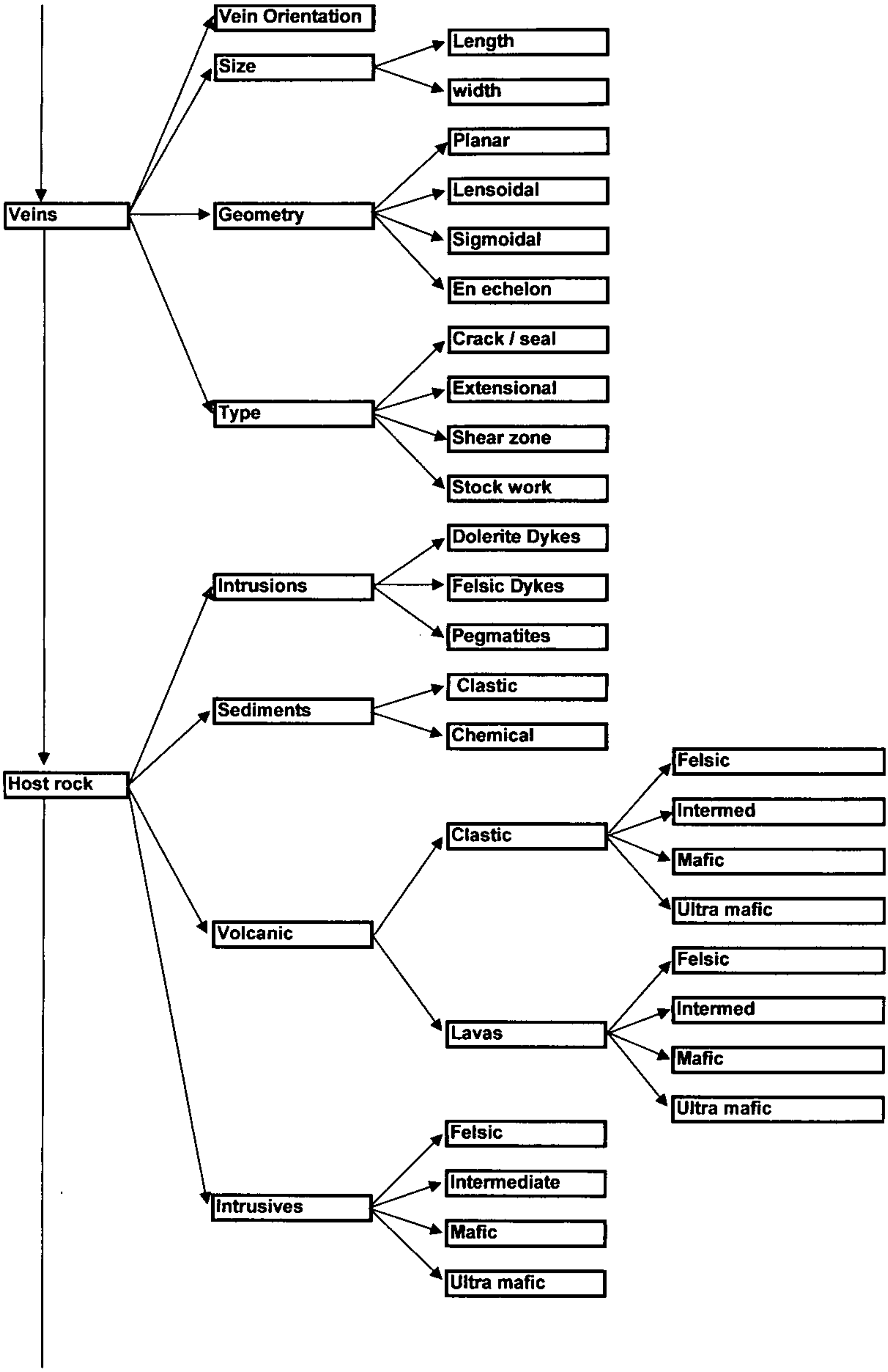
Vein Orientation
Size
Length
width
Planar
Lensoidal
Veins
Geometry
Sigmoidal
En echelon
Crack / seal
Extensional
Type
Shear zone
Stock work
Dolerite Dykes
Intrusions
Felsic Dykes
Pegmatites
Clastic
Sediments
Chemical
Felsic
Host rock
Intermed
Clastic
Mafic
Ultra mafic
Volcanic
Felsic
Intermed
Lavas
Mafic
Ultra mafic
Felsic
Intermediate
Intrusives
Mafic
Ultra mafic

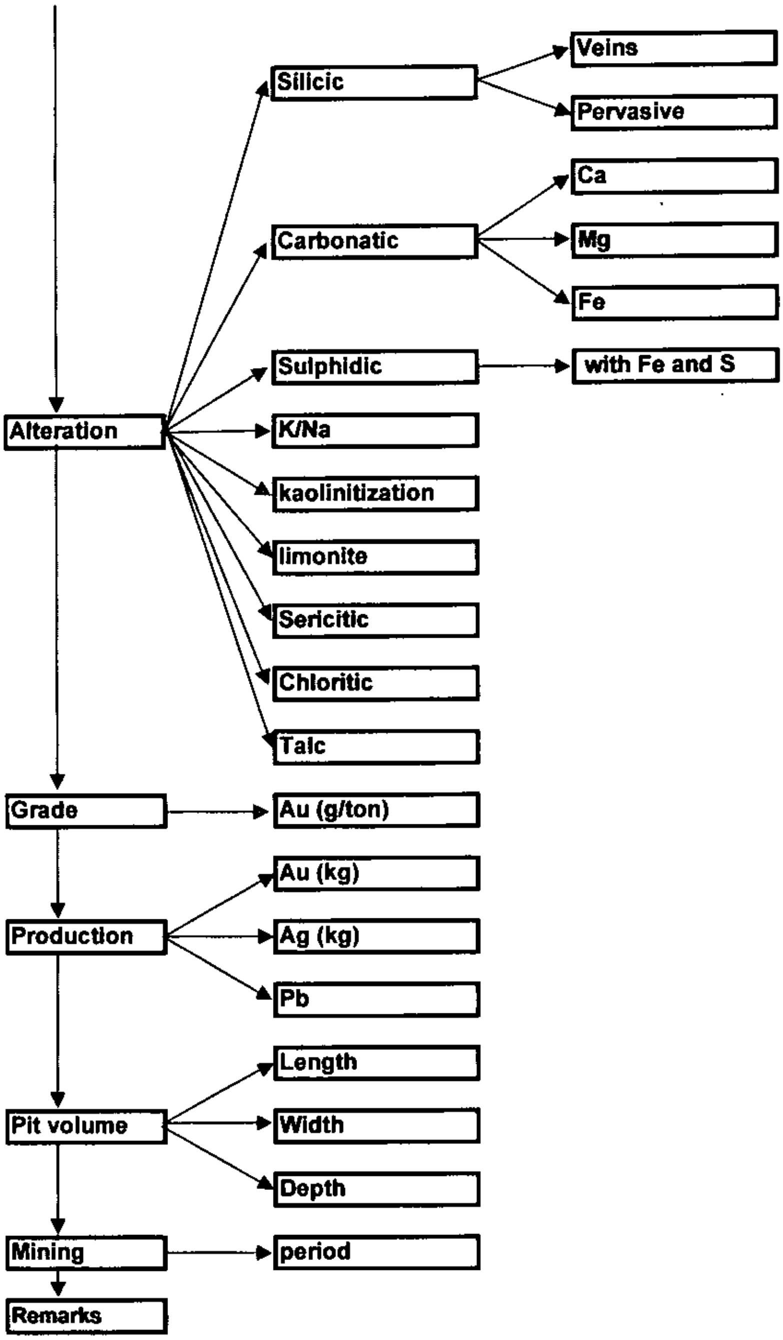
Silicic
Veins
Pervasive
Carbonatic
Ca
Mg
Fe
Sulphidic
with Fe and S
Alteration
K/Na
kaolinitization
limonite
Sericitic
Chloritic
Talc
Grade
Au (g/ton)
Production
Au (kg)
Ag (kg)
Pb
Pit volume
Length
Width
Depth
Mining
period
Remarks

Appendix IV-B

Percentage of Deposits

Type	Percentage	No. Deposits
Shear Zone	32.73809524	110
Quart vein hosted	50.29761905	169
Stockwork	4.166666667	14
Stratabound	3.869047619	13
Contact reefs	3.273809524	11
Fault hosted	2.976190476	10
Disseminated Intrusion	1.19047619	4
Disseminated alteration	1.19047619	4
Fold haotes	0.297619048	1
		336

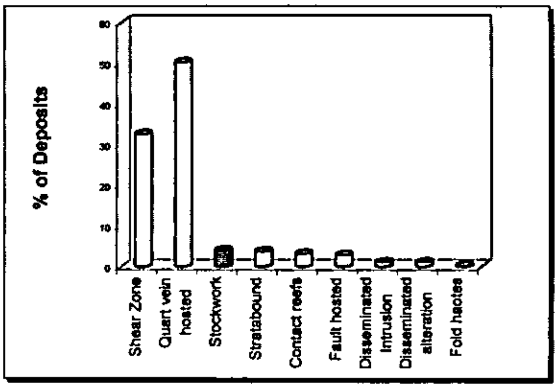

Production X Deposit Type

1384299.2	Shear Zone
1354996.3	Quart vein hosted
1037161	Stockwork
18122.9	Stratabound
26969	Contact reefs
60972	Fault hosted
7350	Disseminated Intrusion
12530	Disseminated alteration
2142	Fold hosted

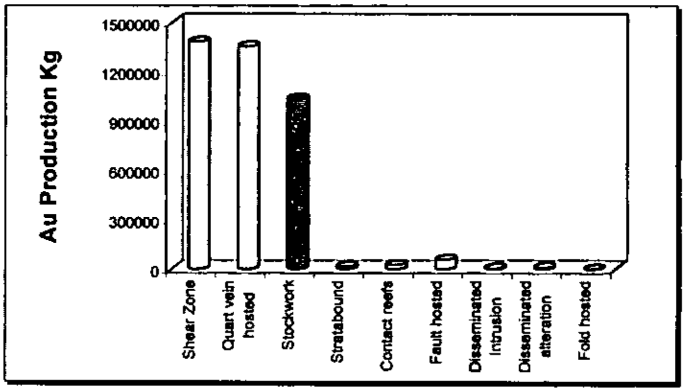

Size of the deposit X Type (considered the largest deposit)

839455	Shear Zone
179746	Quart vein hosted
1037000	Stockwork
10605	Stratabound
9171	Contact reefs
30351	Fault hosted
2767	Disseminated Intrusion
7089	Disseminated alteration
2142	Fold hosted

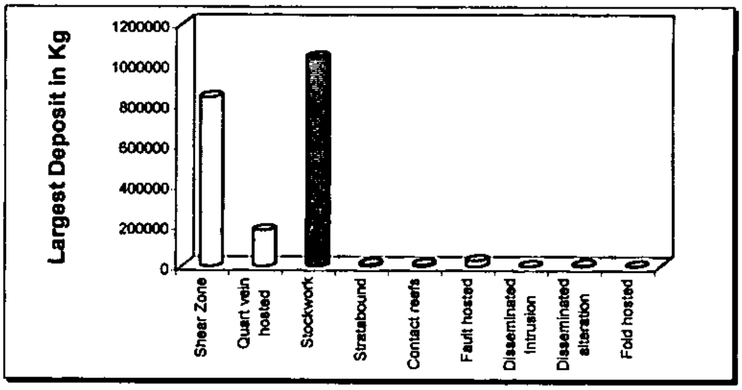

Average grade

12.36	Shear Zone
10.07	Quart vein hosted
5.9	Stockwork
4.84	Stratabound
5.35	Contact reefs
23.5	Fault hosted
7.1	Disseminated Intrusion
7.68	Disseminated alteration
4.51	Fold hosted

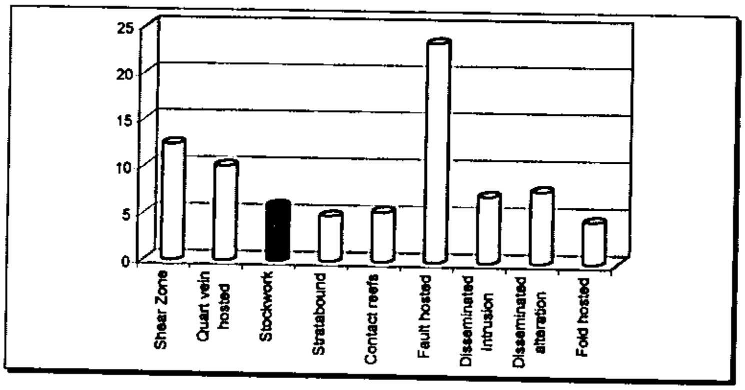

Highest Grade X Deposit type

115.67	Shear Zone
260.82	Quart vein hosted
10.61	Stockwork
10.17	Stratabound
9.3	Contact reefs
148.27	Fault hosted
10.61	Disseminated Intrusion
8.19	Disseminated alteration
4.51	Fold hosted

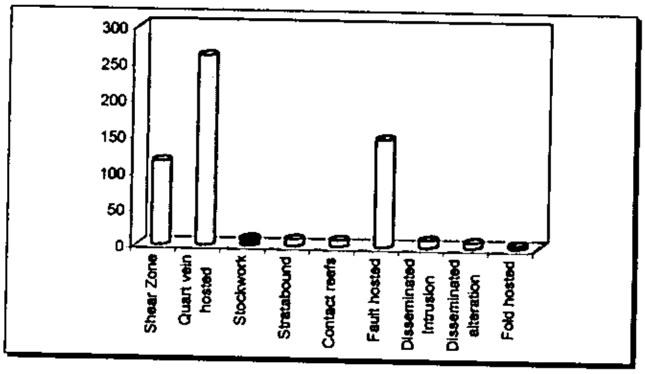

Total Production X Lithology

261380.99	Mafic Intrusions
1203513.30	Felsic Intrusions
232806.26	Clastic and fine grain sediments
243556.41	BIF
48502	Felsic volcanics
67.1	Intermediate volcanics
996811.19	Mafic volcanics
122735.76	Ultramafic units
118208.54	Felsic intrusives
991706.1	Intermediate intrusives
8808.81	Mafic Intrusives

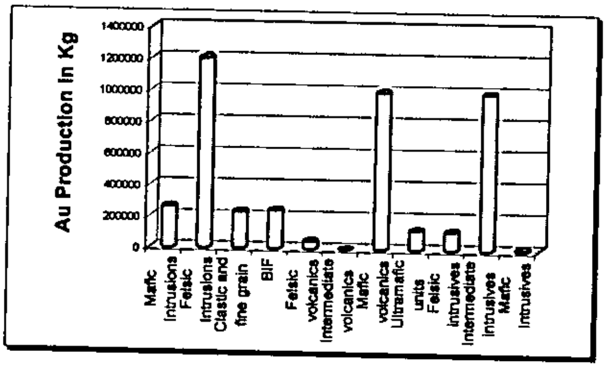

Grade X Lithology

19.3	Mafic Intrusions
10.1	Felsic Intrusions
11.41	Clastic and fine grain sediments
14.62	BIF
5.07	Felsic volcanics
5.97	Intermediate volcanics
12.41	Mafic volcanics
10.73	Ultramafic units
7.87	Felsic intrusives
11.79	Intermediate intrusives
13.22	Mafic Intrusives

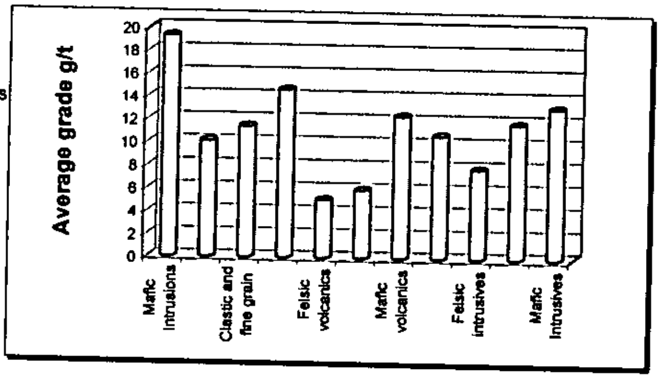

Hihest Grade X Lithology

85.9	Mafic Intrusions
41.82	Felsic Intrusions
113.4	Clastic and fine grain sediments
260.82	BIF
13.89	Felsic volcanics
9.65	Intermediate volcanics
115.67	Mafic volcanics
10.61	Ultramafic units
44.23	Felsic intrusives
85.9	Intermediate intrusives
46.41	Mafic Intrusives

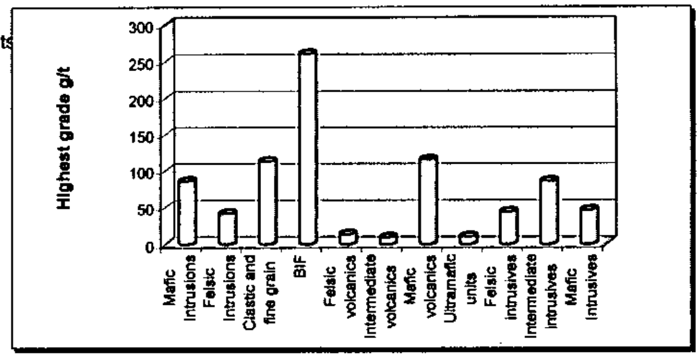

Largest Deposit X Lithology

179746	Mafic Intrusions
839455	Felsic Intrusions
179746	Clastic and fine grain sediments
9171.076	BIF
10605	Felsic volcanics
61	Intermediate volcanics
839455	Mafic volcanics
80489	Ultramafic units
32412	Felsic intrusives
839455	Intermediate intrusives
3055	Mafic Intrusives

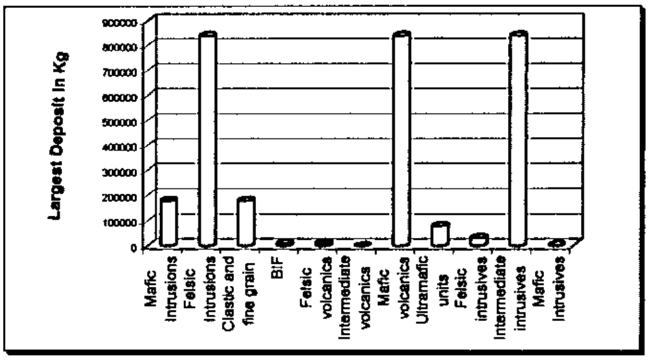

Lithology-Production [oz] per Km^2

31491.69	Mafic Intrusions
103394.61	Felsic Intrusions
2675.32	Clastic and fine grain sediments
17465.5	BIF
639.7	Felsic volcanics
1.52	Intermediate volcanics
9384.4	Mafic volcanics
520.57	Ultramafic units
9300.44	Felsic intrusives
52030.75	Intermediate intrusives
0	Mafic Intrusives

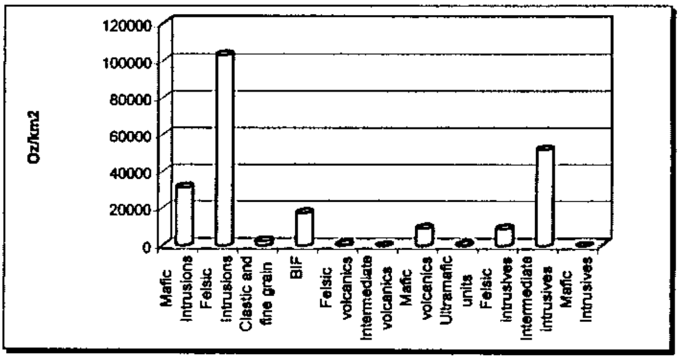

APPENDIX V-A

Fry Analysis (autocorrelation analysis) applied to gold deposits in MMO

The following sections describe the results of Autocorrelation analysis for the above subsets and the results are summarised in the Table 5 – 6.

Manica Sector

The Manica sector trends towards north-northeast and is bordered to the east by the gneissic Barue Complex. A total of 44 gold deposits were recorded in the Manica sector and were all used in the analysis. A gold deposit was considered as a whole and the presence of several adits and shafts were regarded as a single deposit and the position considered to be the main (usually the first) shaft or adit (entrance).

Results of the Autocorrelation analysis of the Manica sector is presented in the Fig. VA - 1.

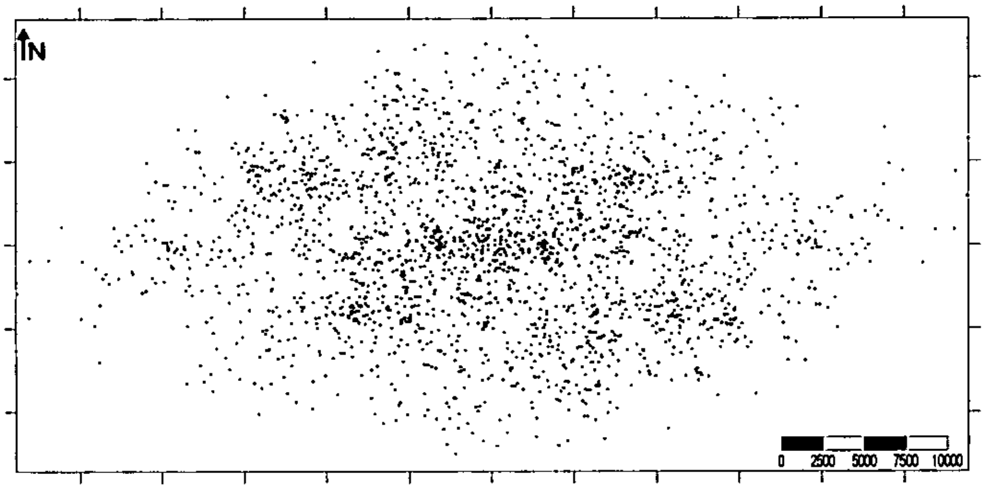

Figure VA – 1. Fry plot – translations of the gold deposits in the Manica sector of the MMO

Rose diagram of the Manica part of the MMO belt is presented in Fig. VA-1.

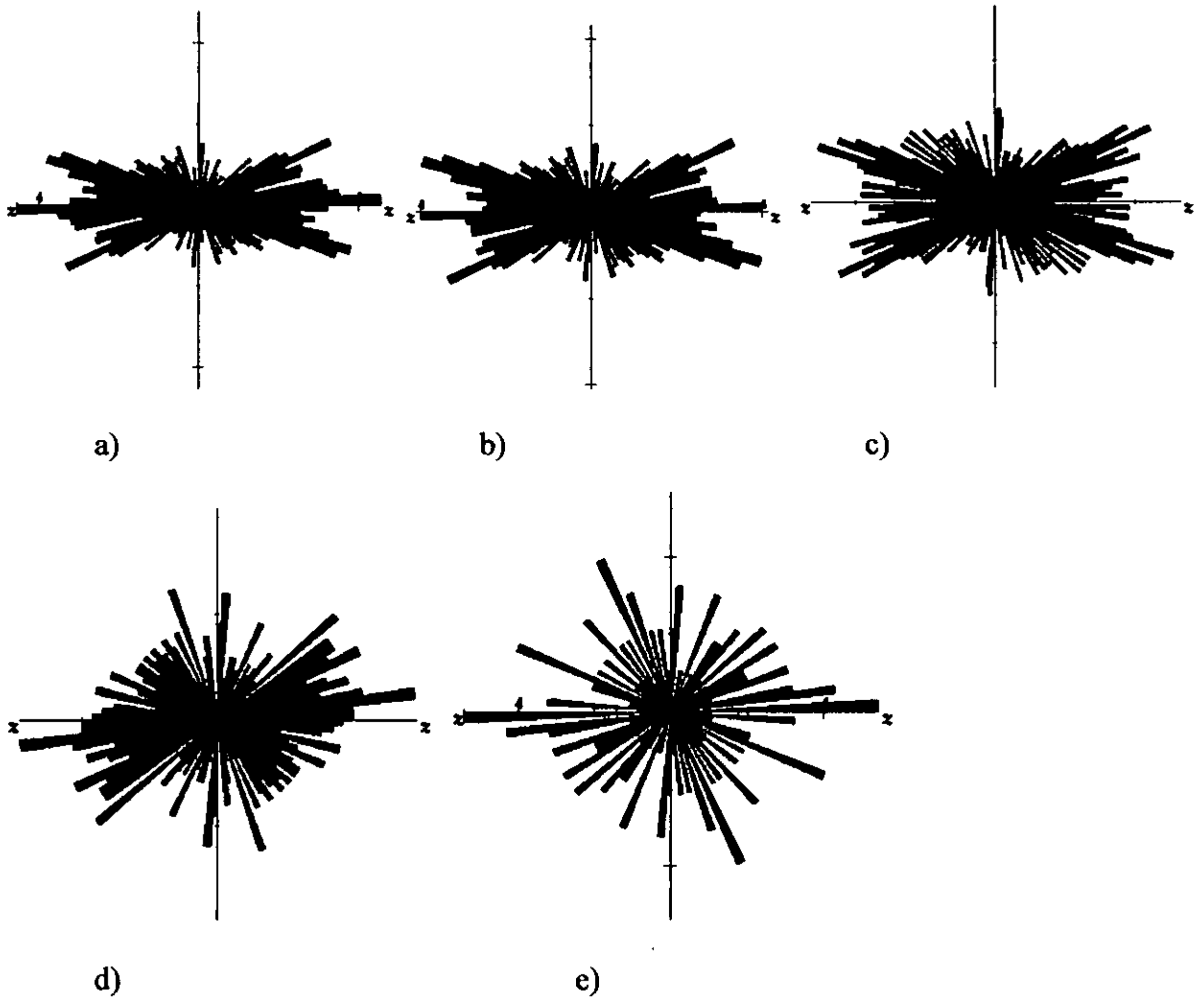

a) b) c)

d) e)

Figure VA – 2 Rose diagrams for Manica sector of the MMO belt;
a) Rose diagram of all deposits in the Manica sector (1980 points); b) Rose diagram showing all deposits within 20 km distance search (1899 points); c) Rose diagram showing all deposits within 15 km distance search (1669 points); d) Rose diagram showing all deposits within 9 km distance search (993 points); e) Rose diagram showing all deposits within 3 km distance search (185 points)

Data Analysis and Interpretation

The translations map in Fig.VA-1, shows broad linear zones defined by gold deposits positions, and are oriented in three key directions, ENE – WSW, WNW – ESE and W - E. The rose diagrams of the azimuth-frequency (Fig. VA-2) also confirms these directions.

The ENE – WSW direction is interpreted as related to the continuity of the MMO Archaean greenstone belt. The NW – SE and N-S directions are invoked here as representing directions controlling gold mineralisation in the Manica sector of the MMO greenstone belt. These directions are not evident on structural maps of the area. The NW-SE and N-S direction controlling gold distribution in the Archaean greenstone belt have also been identified in Mashava area in the Zimbabwe Craton (Blenkinsop, 1991).

Mutare Sector

The Mutare sector of the MMO Archaean greenstone belt stretches from the border of Mozambique – Zimbabwe which is approximately up to the 32°30' parallel to the west. The area was mapped by Phaup (1937). The positions of the gold deposits were extracted from his map by Dirks et al. (1999). In this study some sectors of this area were checked and remapped structurally (see also chapter 3).

A total of 137 deposits were entered as input data to autocorrelation analysis and translations map was generated (Fig. VA - 3).

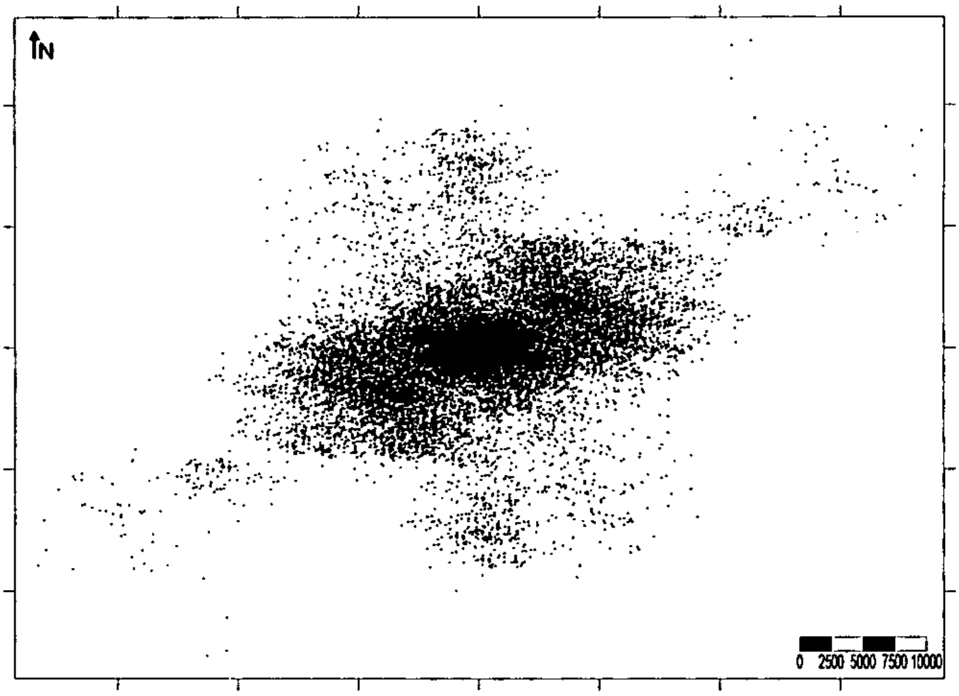

Figure VA – 3. Fry plot – translations map of the Mutare sector

Rose diagrams of the azimuth-frequency of the Mutare area are shown on Fig.VA - 4.

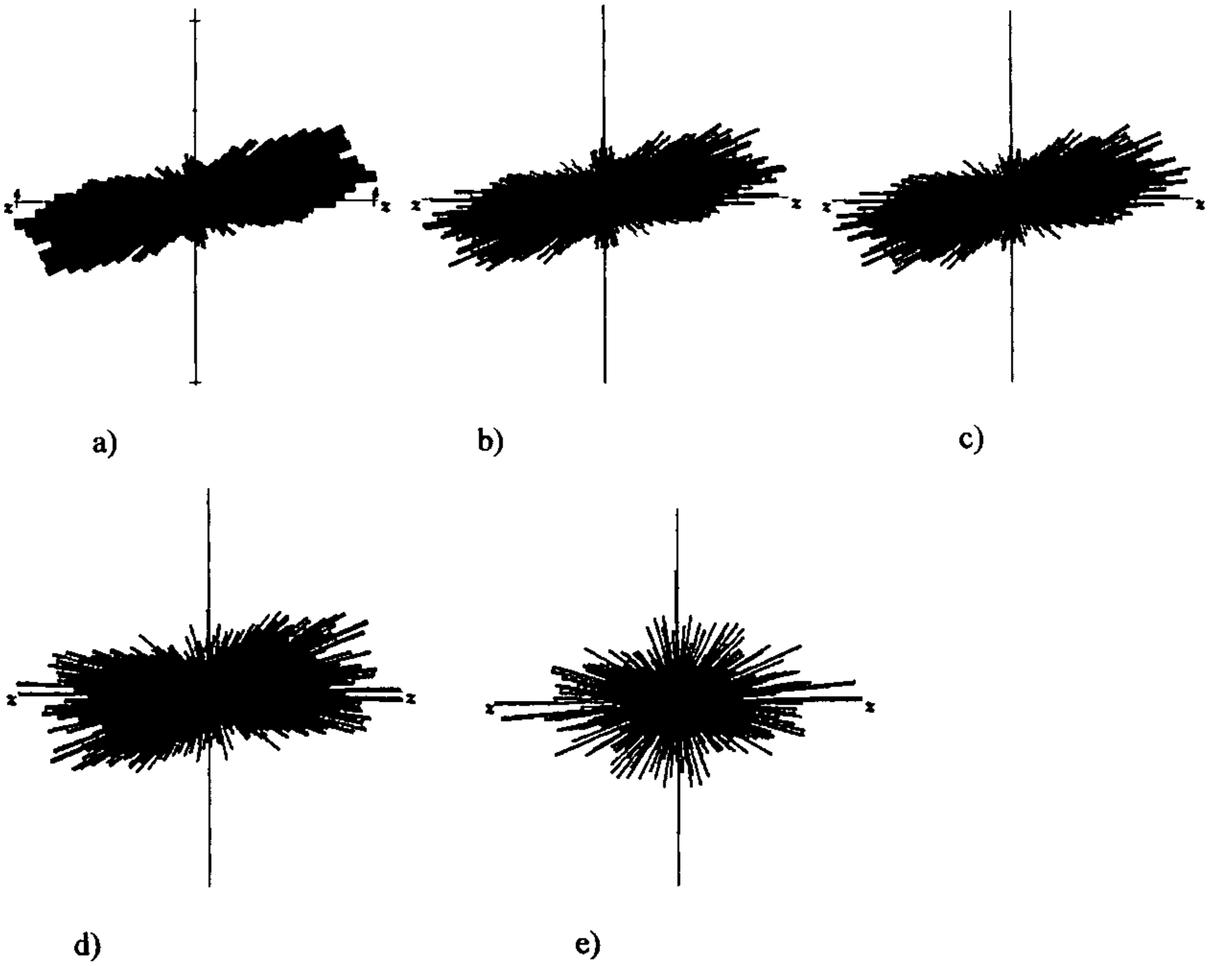

Figure VA – 4. Rose diagrams for Mutare sector of the MMO belt;
a) Rose diagram of all deposits in the Mutare sector (18632 points); b) Rose diagram showing all deposits within 20 km distance search (18292 points); c) Rose diagram showing all deposits within 15 km distance search (17118 points); d) Rose diagram showing all deposits within 9 km distance search (12558 points); e) Rose diagram showing all deposits within 3 km distance search (4442 points)

Data Analysis and interpretation

The distribution of gold deposits in the Mutare sector revealed highest concentration of deposits around Penhalonga granodiorite.

The pattern of gold distribution (Fig. VA - 4), suggests that at least three main directions of high population of deposits can be found and are ENE – WSW, N – S and WNW – ESE.

The ENE – WSW was interpreted as a reflection of the continuity of the geometry of the greenstone belt, thus it was disregarded for the purpose of mineralisation control.

The N - S and the WNW – ESE direction are the main corridor direction that reflect the clustering of gold deposits. As mentioned earlier, these corridors are not shown in any structural map of the area.

Odzi Sector

The Odzi sector comprises the rest of the MMO belt to the west from the longitude 32°30' up to longitude 31°55' and contain 58 gold deposits. The translation map in Fig. VA - 5 represents the results of the Autocorrelation analysis for the Odzi sector.

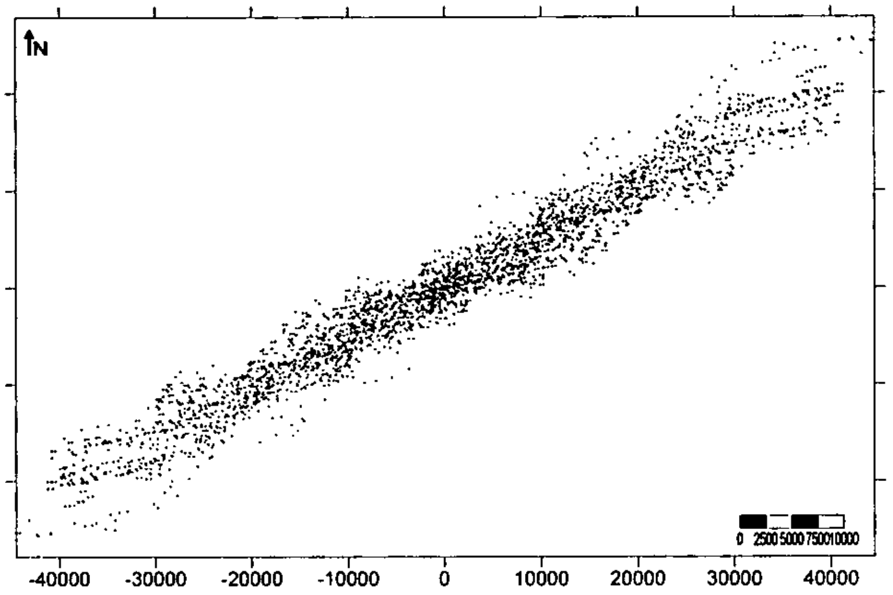

Figure VA – 5. Fry analysis translation map of the Odzi sector

An additional and different view of the data is given by plotting a rose diagram of the azimuth-frequency as presented in Fig. VA - 6.

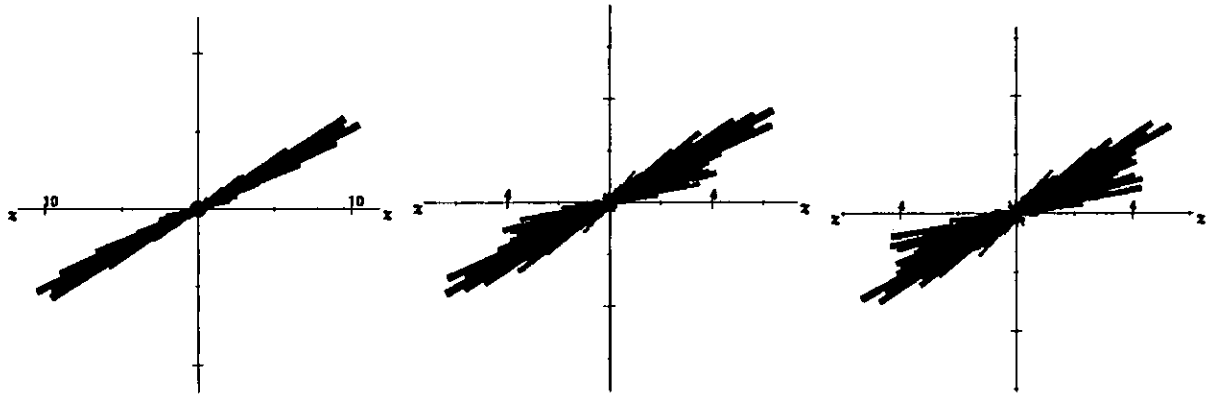

a) b) c)

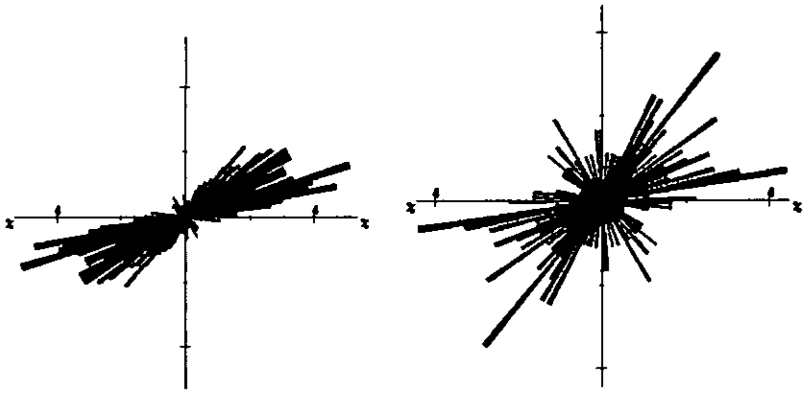

d) e)

Figure VA – 6. Rose diagrams – azimuth frequency of the segments that link every two points generated from the Autocorrelation analysis for Odzi sector of the MMO belt;
a) Rose diagram of all deposits in the Odzi sector (3422 points); b) Rose diagram showing all deposits within 20 km distance search (2040 points); c) Rose diagram showing all deposits within 15 km distance search (1644 points); d) Rose diagram showing all deposits within 9 km distance search (1128 points); e) Rose diagram showing all deposits within 3 km distance search (360 points)

Data Analysis and Interpretation

The results of autocorrelation analysis are presented in Fig. VA - 5 (translations map) and show that the three directions identified on the previous sectors (Manica and Mutare) are not clearly defined mainly due to linearity of this section. The N – S direction is not present and therefore is not expressed on the rose diagram of the azimuth frequency (Fig.VA – 6).

Deposit type

The grouping of deposits is discussed in chapter 4 section 4.2.

Deposits associated with shear zones/faults and sheared contacts (Fig. 4-1) produced the autocorrelation plot presented in Fig. VA – 7 and the rose diagram in Fig. VA – 8.

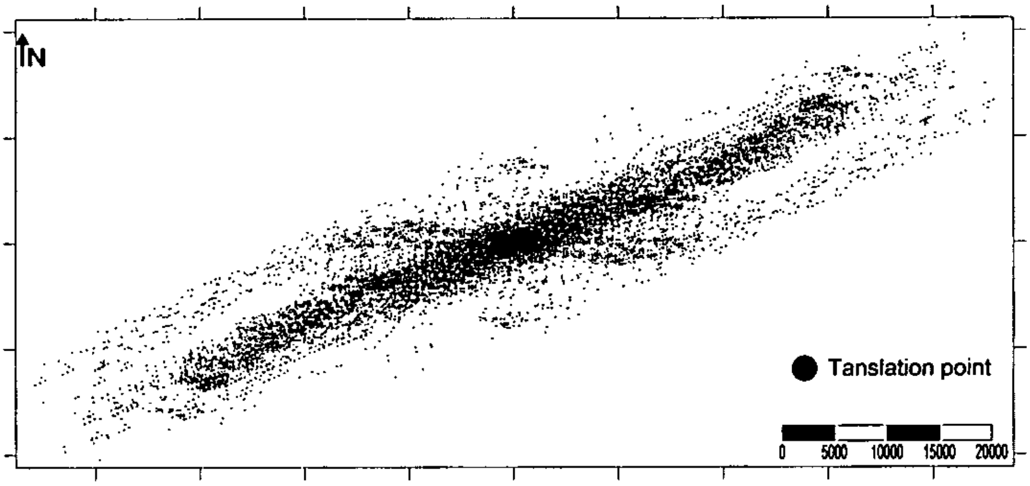

Figure VA - 7. Fry analysis – translations map of the shear zone and fault hosted deposits;

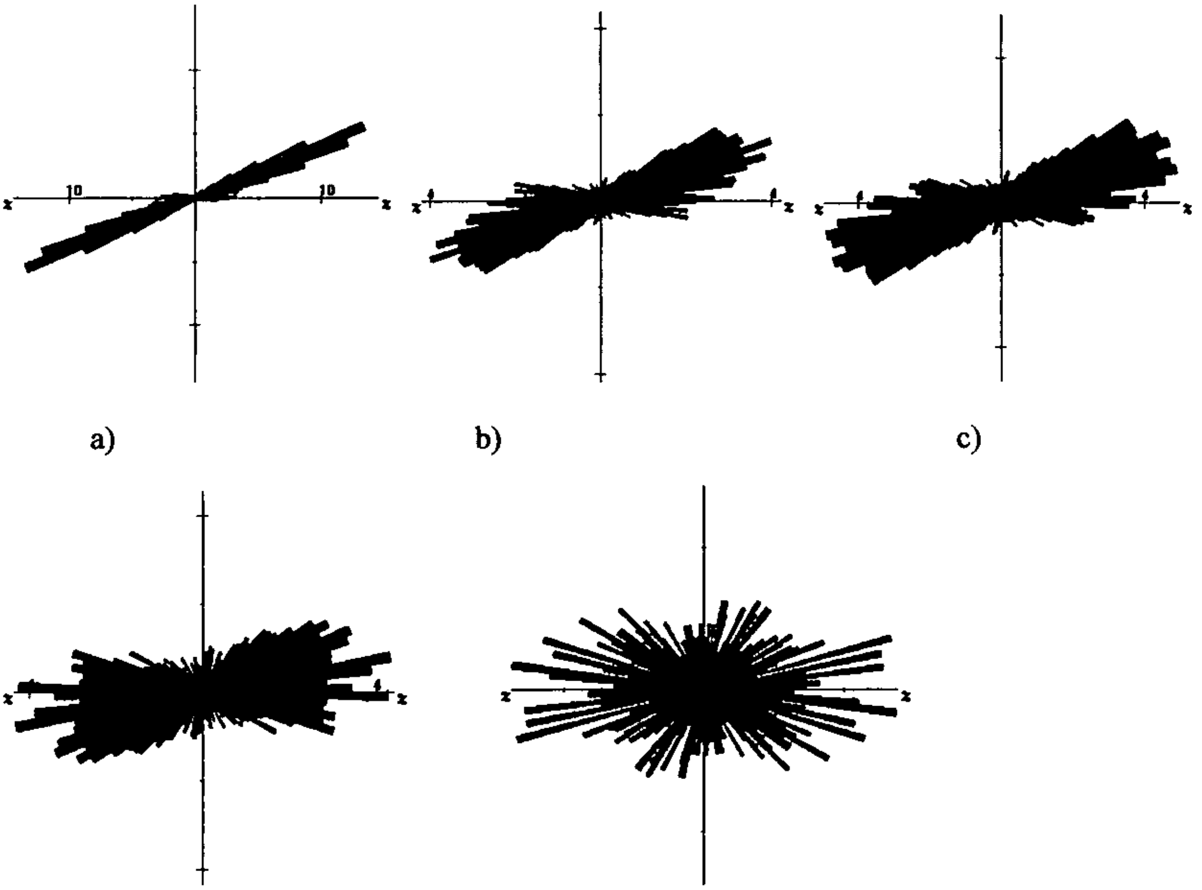

a) b) c)

d) e)

Figure VA – 8. Rose diagrams – azimuth frequency of the segments that link every two points generated from the Autocorrelation analysis for Shear zone and fault hosted deposits in the MMO belt; a) Rose diagram of all shear zone and fault hosted deposits in the MMO belt (12432 points); b) Rose diagram showing all deposits within 20 km distance search (6167 points); c) Rose diagram showing all deposits within 15 km distance search (5080 points); d) Rose diagram showing all deposits within 9 km distance search (3381 points); e) Rose diagram showing all deposits within 3 km distance search (1091 points)

The deposits associated to quartz veins show the distribution presented in Fig. VA – 9, the Autocorrelation plot is shown in Fig. VA – 10 and the rose diagrams on Fig. VA – 11.

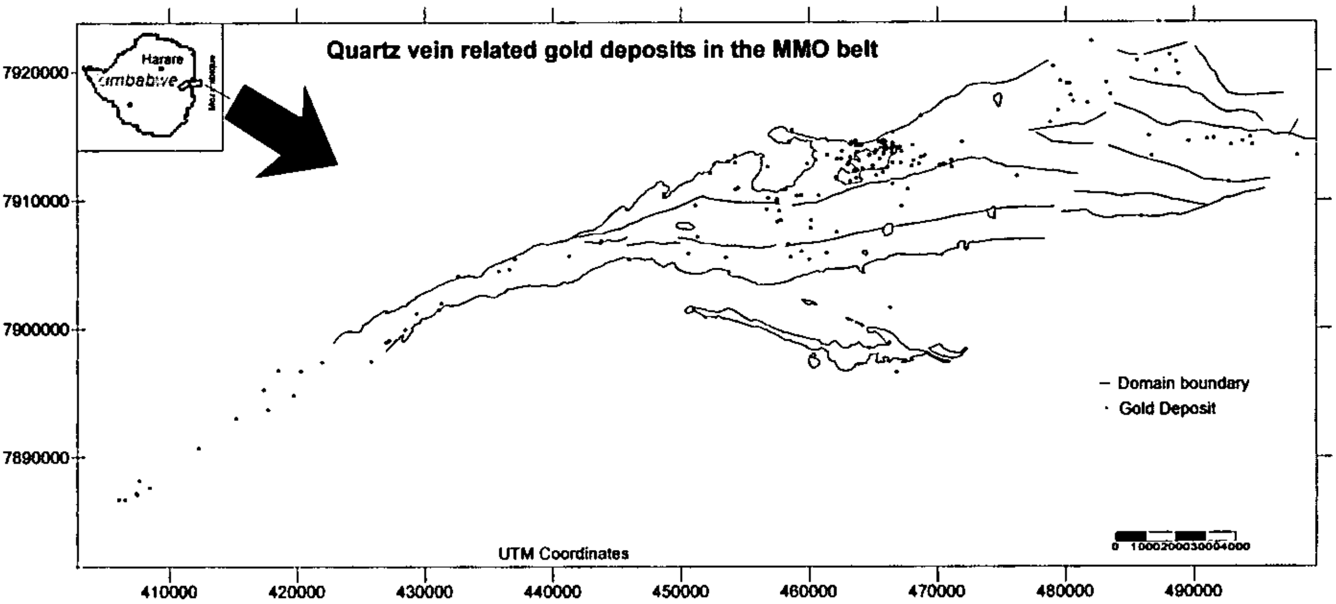

Figure VA – 9. Distribution of quartz vein related gold deposits in the MMO belt.

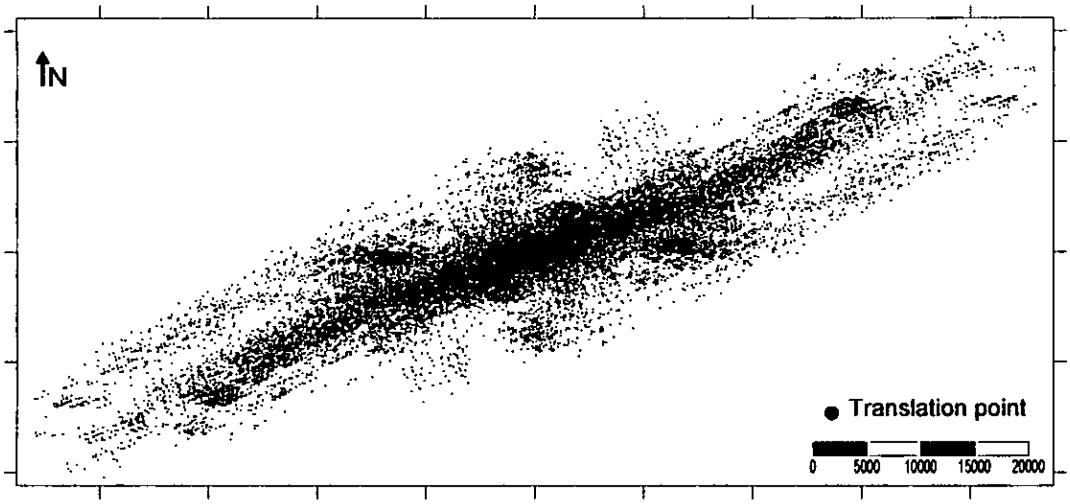

Figure VA - 10 - Fry analysis – translations map of the quartz vein deposits

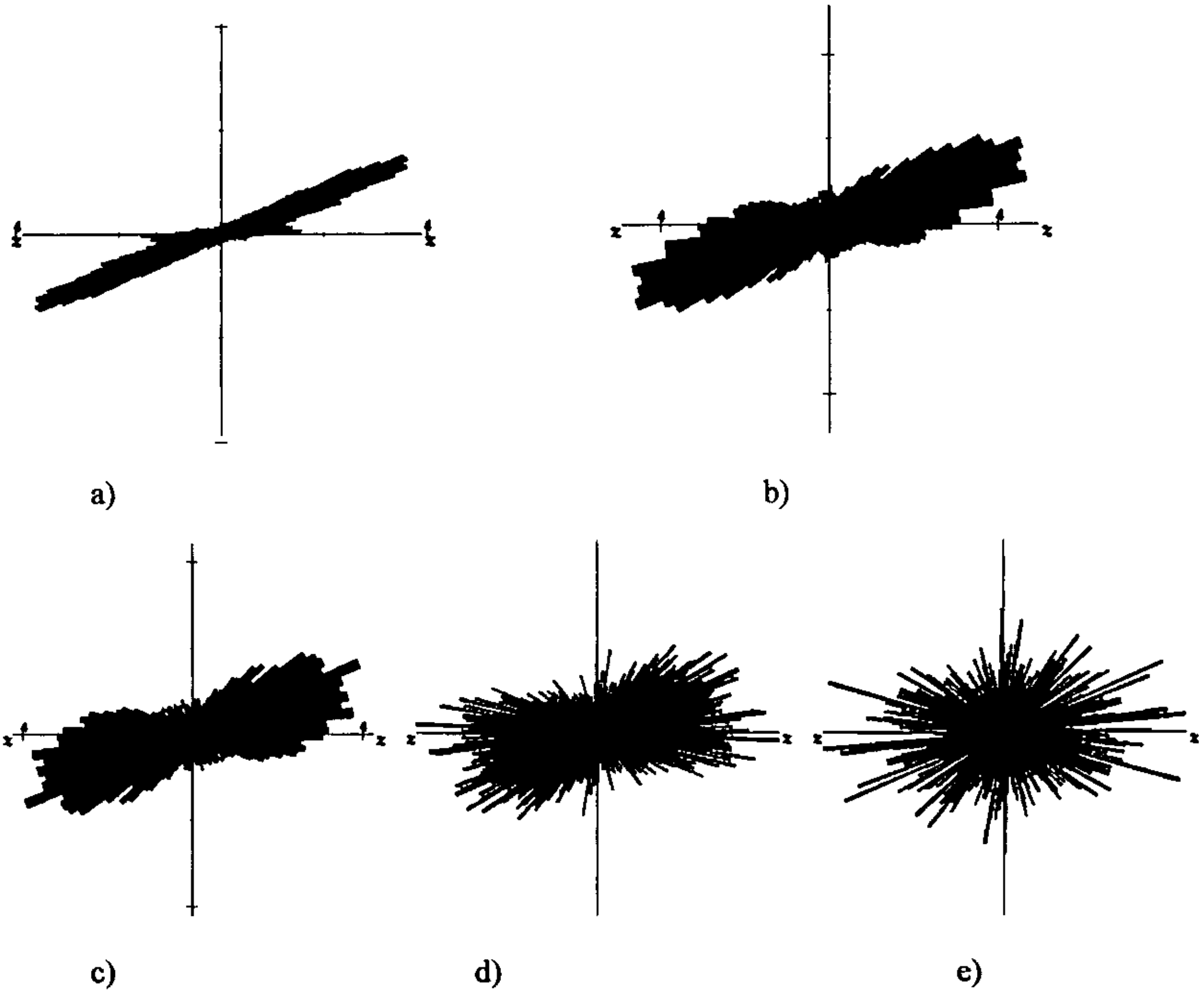

Figure VA – 11. Rose diagrams for the deposits related to quart veins;
a) Rose diagram of all deposits in the MMO belt (28730 points); b) Rose diagram showing all deposits within 20 km distance search (15388 points); c) Rose diagram showing all deposits within 15 km distance search (12820 points); d) Rose diagram showing all deposits within 9 km distance search (8634 points); e) Rose diagram showing all deposits within 3 km distance search (2966 points).

Deposits related to felsic and intermediate intrusions (Fig. VA – 12) generated the Autocorrelation plot shown in Fig. VA – 13 and the rose diagram in Fig. VA – 14.

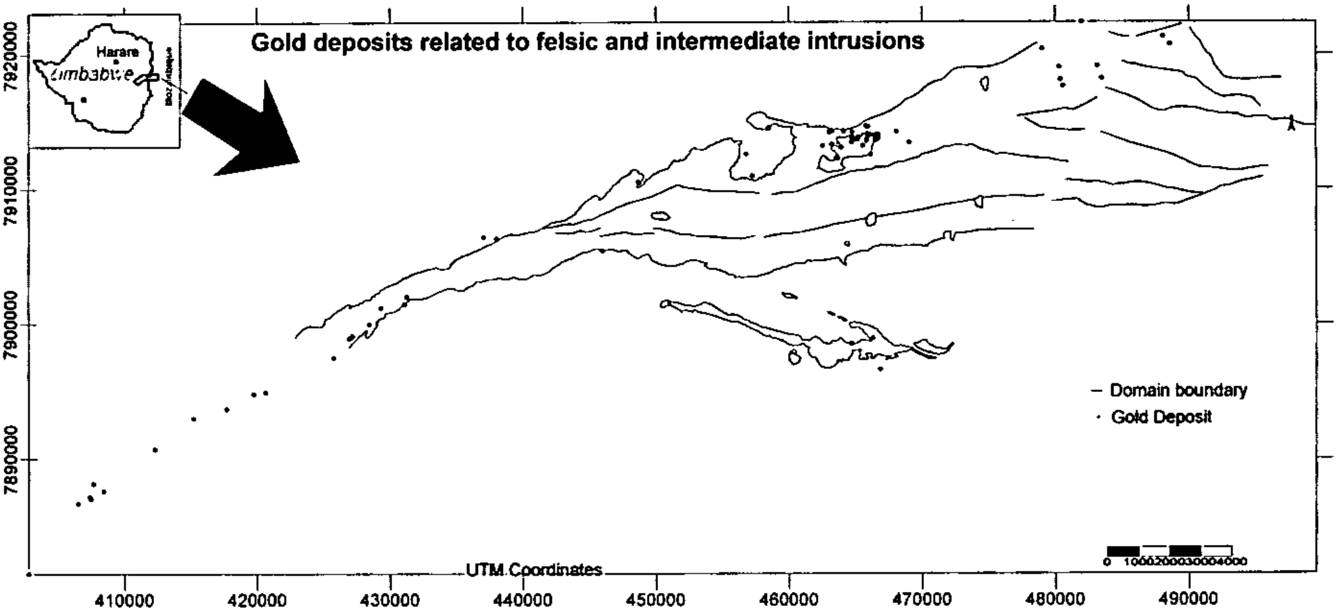

Figure VA – 12. Distribution of gold deposits related to felsic and intermediate intrusions in the MMO belt.

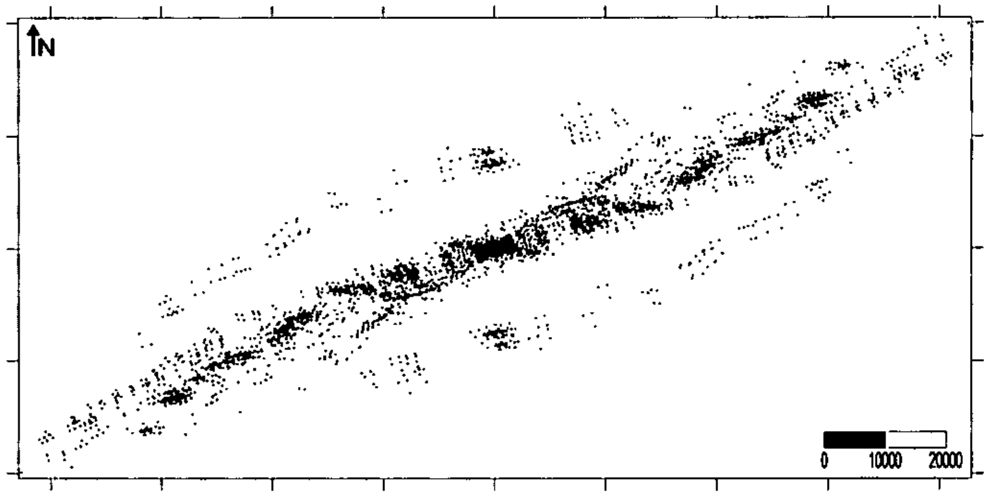

Figure VA – 13. Autocorrelation plot of the deposits related to felsic and intermediate intrusions in the MMO belt.

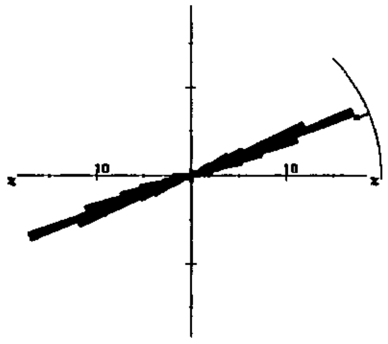

a)

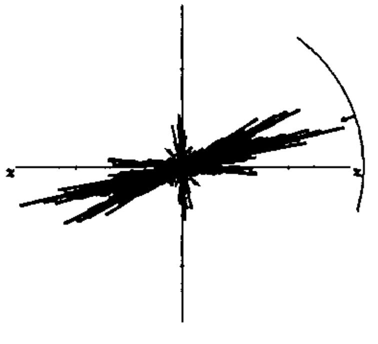

b)

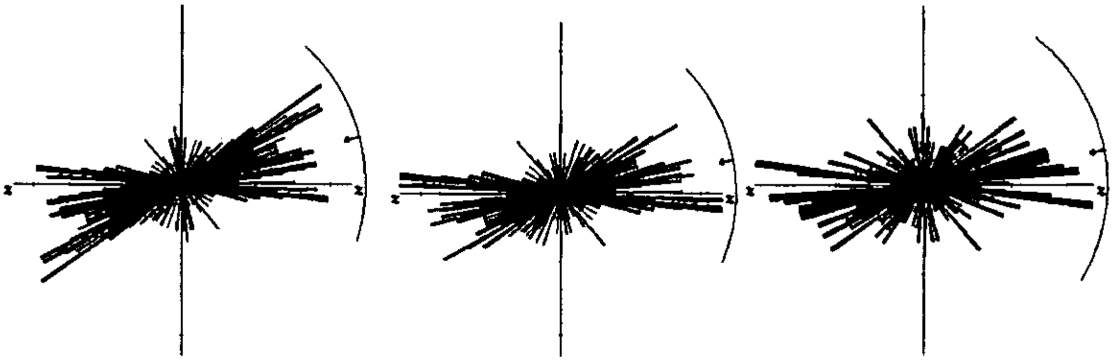

c) d) e)

Figure VA – 14. Rose diagrams for the deposits related to felsic and intermediate intrusions;
a) Rose diagram of all deposits in the MMO belt (4160 points); b) Rose diagram showing all deposits within 20 km distance search; c) Rose diagram showing all deposits within 15 km distance search (1324 points); d) Rose diagram showing all deposits within 9 km distance search (1044 points); e) Rose diagram showing all deposits within 3 km distance search (620 points).

Deposits associated to BIF rocks generated the Autocorrelation plot shown in Fig. VA – 15 and the rose diagram in Fig. VA – 16.

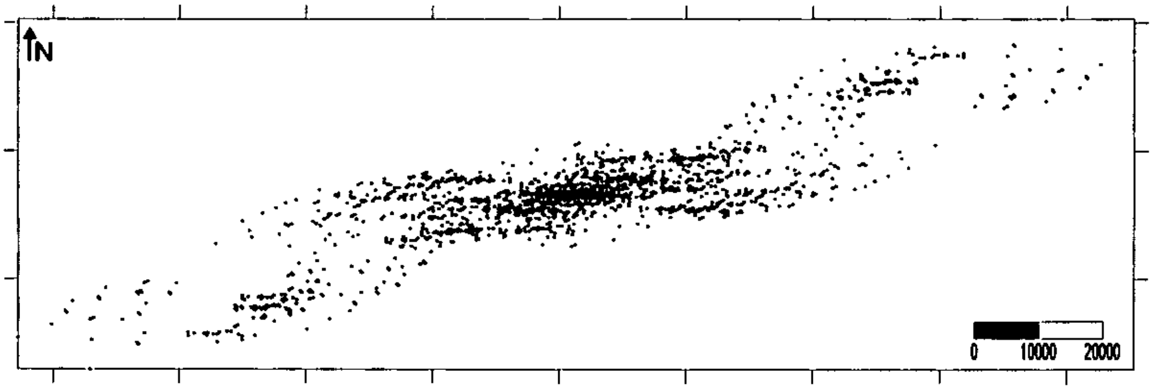

Figure VA – 15. Autocorrelation plot of the deposits associated with BIF in the MMO belt.

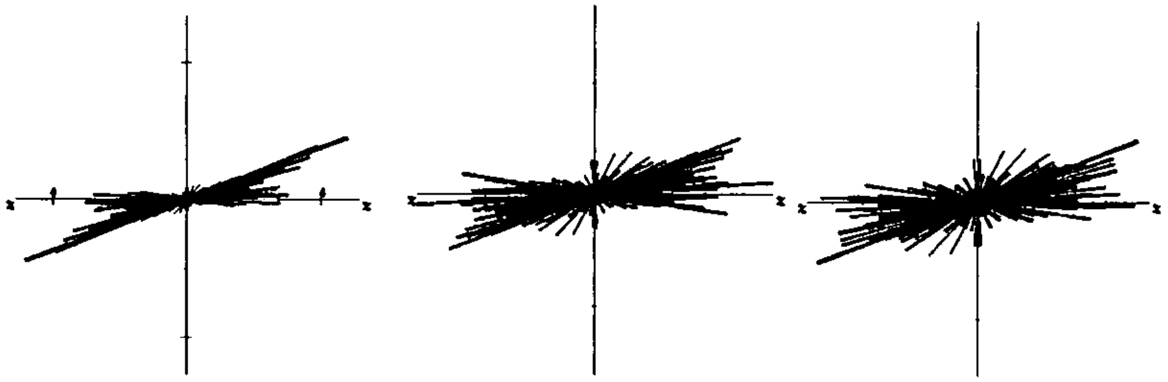

a) b) c)

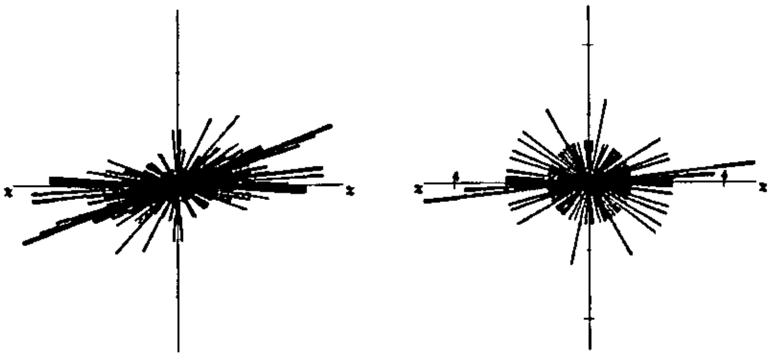

d) e)

Figure VA – 16. Rose diagrams for the deposits related to BIF;
a) Rose diagram of all deposits in the MMO belt (1722 points); b) Rose diagram showing all deposits within 20 km distance search (990 points); c) Rose diagram showing all deposits within 15 km distance search (810 points); d) Rose diagram showing all deposits within 9 km distance search (600 points); e) Rose diagram showing all deposits within 3 km distance search (162 points).

Figure VA – 17 show the Autocorrelation plot for the deposits hosted by Shamvaian rocks and, the rose diagram is shown in Fig. VA – 18.

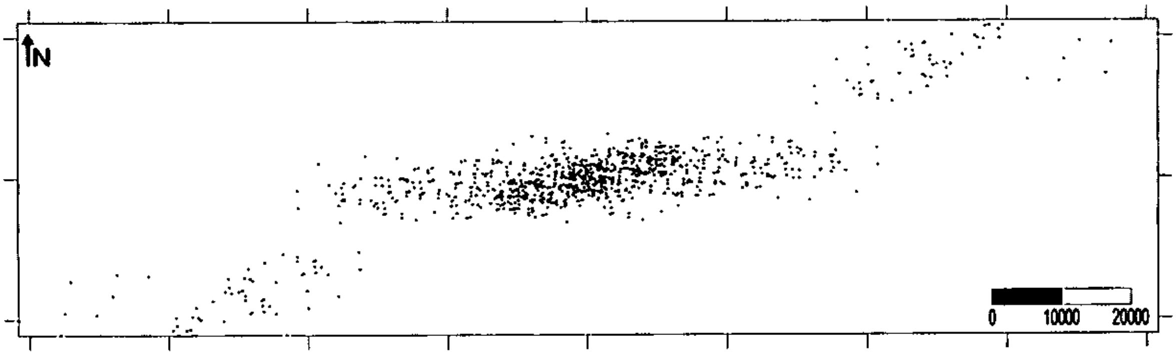

Figure VA – 17. Autocorrelation plot of the deposits associated with Shamvaian sediments in the MMO belt.

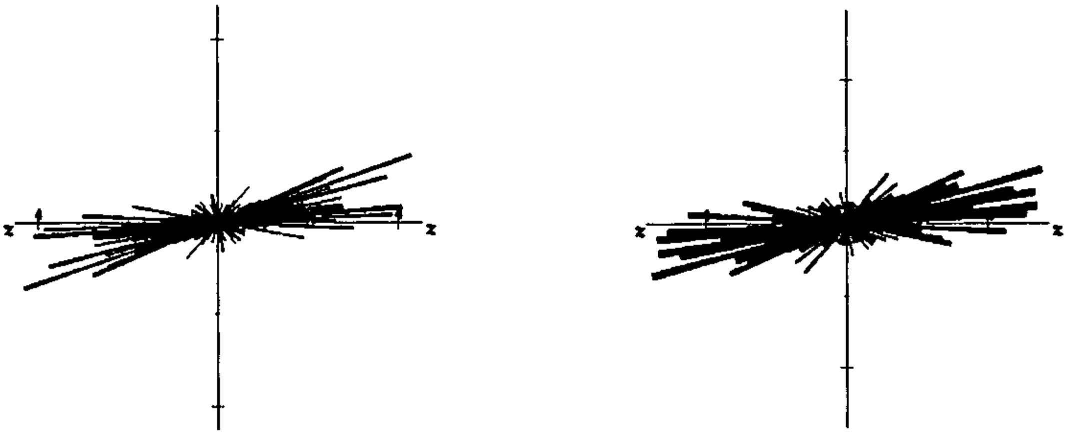

a) b)

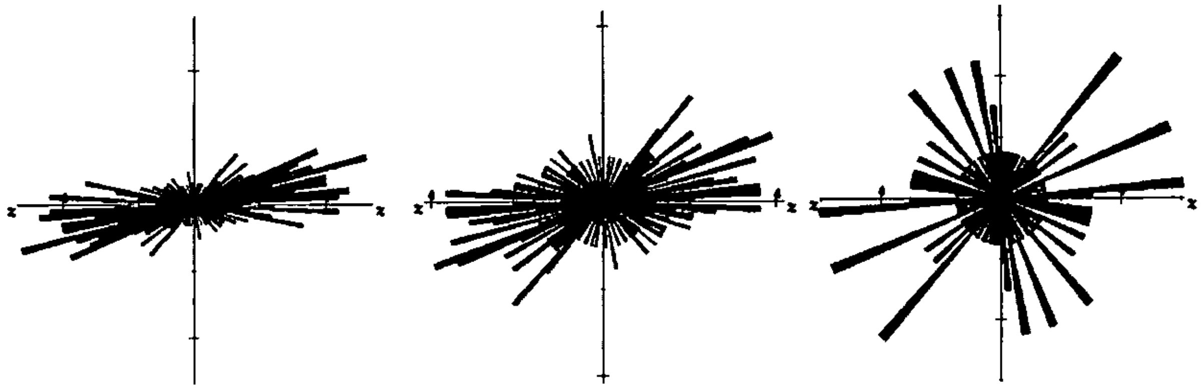

c) d) e)

Figure VA – 18. Rose diagrams for the deposits associated to Shamvaian sediments;

a) Rose diagram of all deposits in the MMO belt (930 points); b) Rose diagram showing all deposits within 20 km distance search (670 points); c) Rose diagram showing all deposits within 15 km distance search (590 points); d) Rose diagram showing all deposits within 9 km distance search (384 points); e) Rose diagram showing all deposits within 3 km distance search (132 points).

Gold deposits hosted by Upper Bulawayan rocks (Fig. VA – 19) produced the Autocorrelation plot (Fig. VA – 20) and the rose diagram shown in Fig. VA – 21.

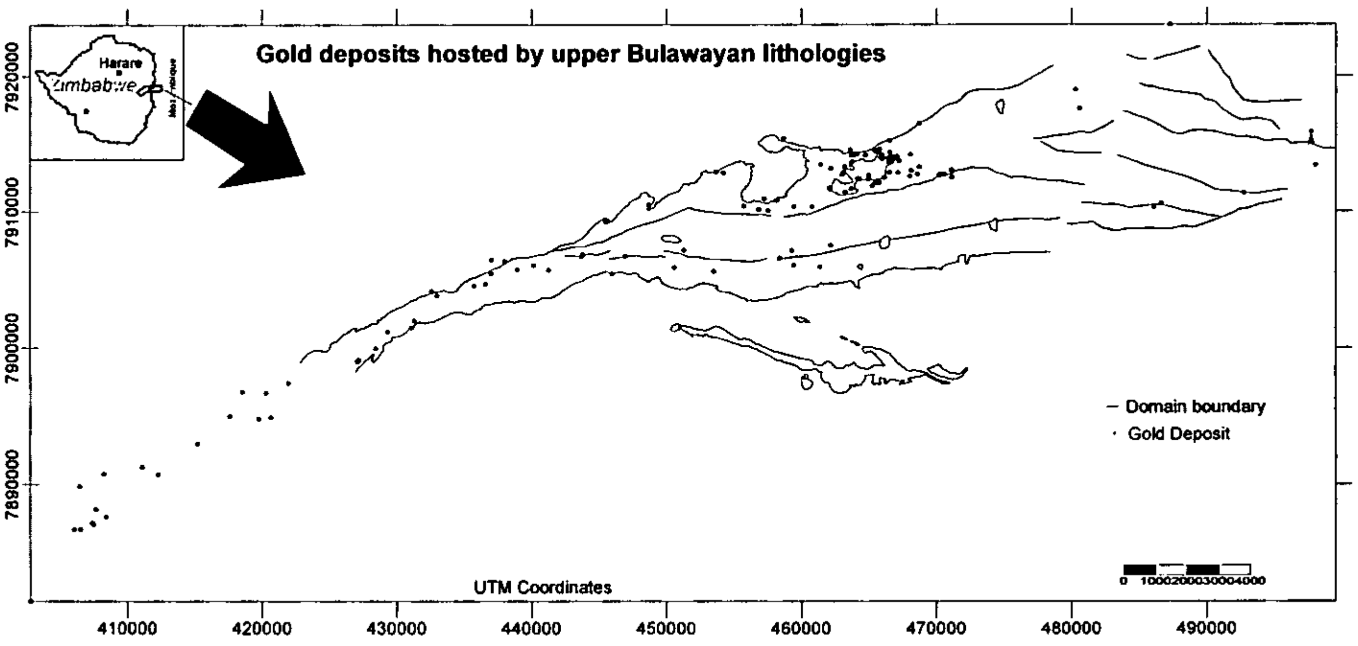

Figure VA – 19. Spatial distribution of the gold deposits hosted by Upper Bulawayan rocks.

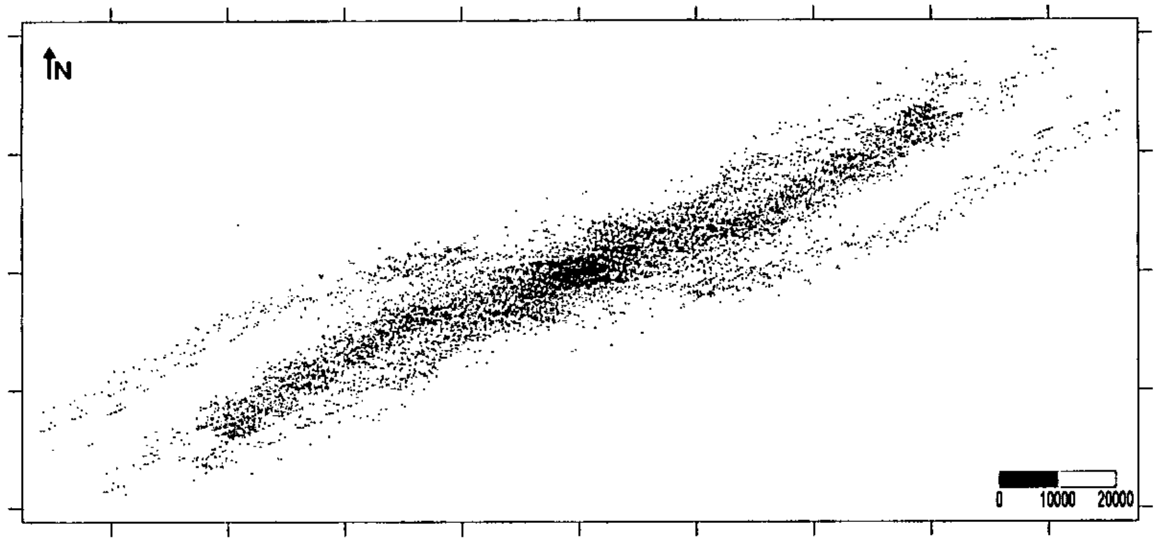

Figure VA – 20. Autocorrelation plot of the deposits associated with Upper Bulawayan rocks in the MMO belt.

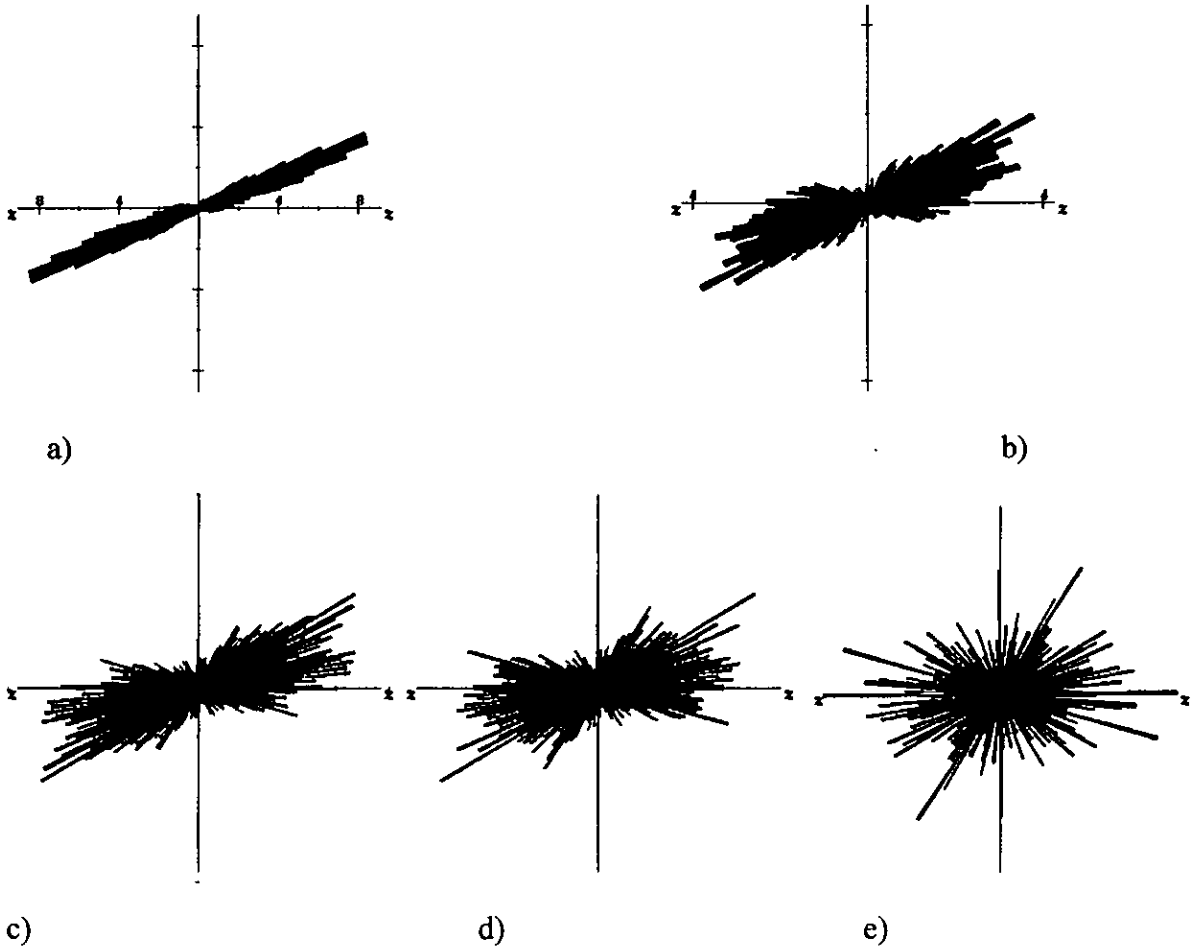

a)

b)

c)

d)

e)

Figure VA – 21. Rose diagrams for the deposits associated to Upper Bulawayan lithologies;
a) Rose diagram of all deposits in the MMO belt (12882 points); b) Rose diagram showing all deposits within 20 km distance search (6186 points); c) Rose diagram showing all deposits within 15

km distance search (5262points); d) Rose diagram showing all deposits within 9 km distance search (4112points); e) Rose diagram showing all deposits within 3 km distance search (1432points).

The gold deposits of high grade (>5 g/t) produced the Autocorrelation plot and rose diagram shown in Figs. VA – 22 and 23, whereas the low grade (<5 g/t) deposits' are presented in Figs. VA – 24 and 25.

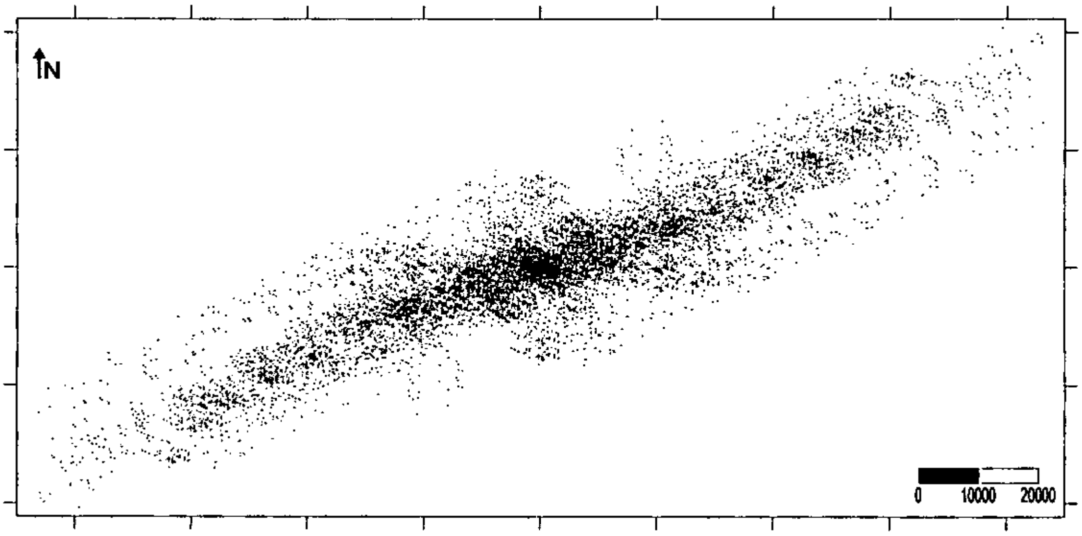

Figure VA – 22. Autocorrelation plot of the high-grade (> 5 g/t) deposits in the MMO belt.

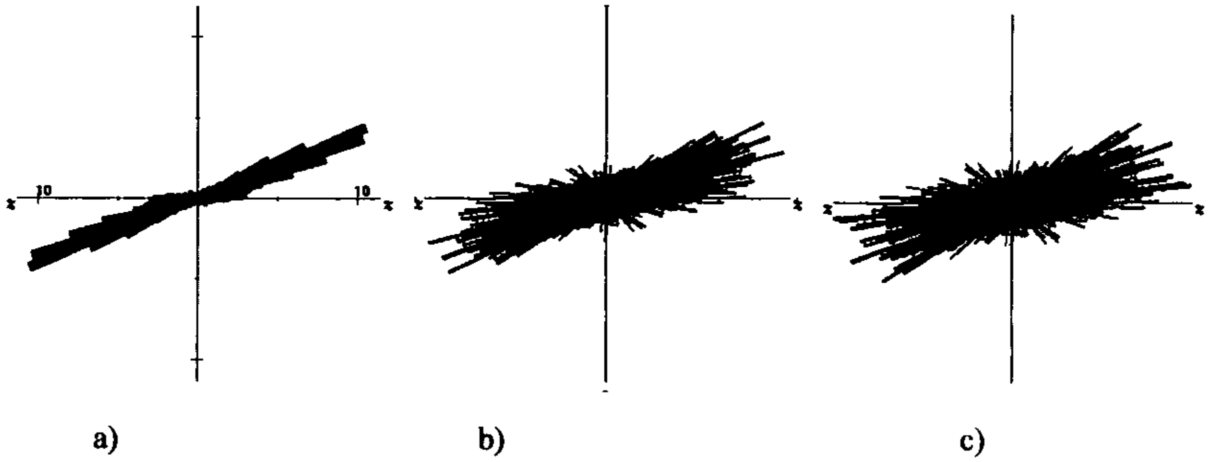

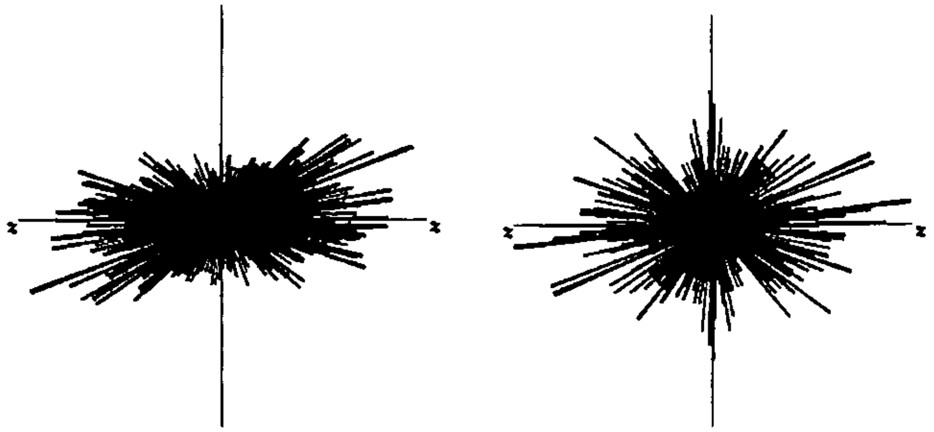

d) e)

Figure VA – 23. Rose diagrams for high-grade deposits in the MMO belt;

a) Rose diagram of all deposits in the MMO belt (15500 points); b) Rose diagram showing all deposits within 20 km distance search (9016 points); c) Rose diagram showing all deposits within 15 km distance search (7788 points); d) Rose diagram showing all deposits within 9 km distance search (5067 points); e) Rose diagram showing all deposits within 3 km distance search (1868 points).

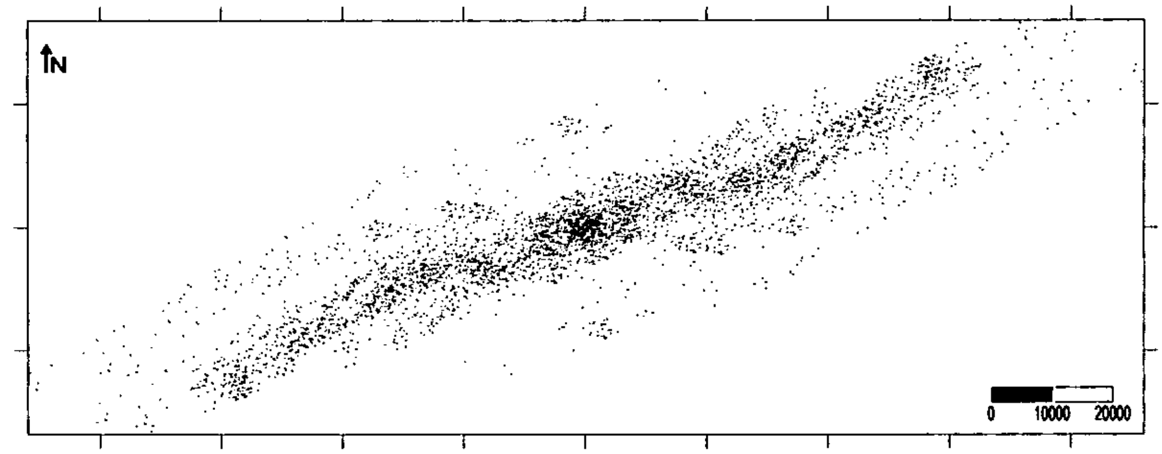

Figure VA – 24. Autocorrelation plot of the low-grade (< 5 g/t) deposits in the MMO belt.

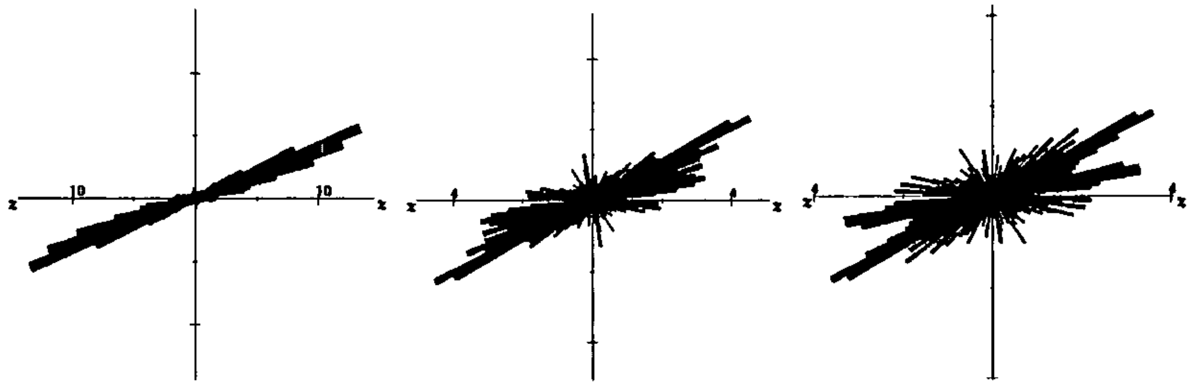

a) b) c)

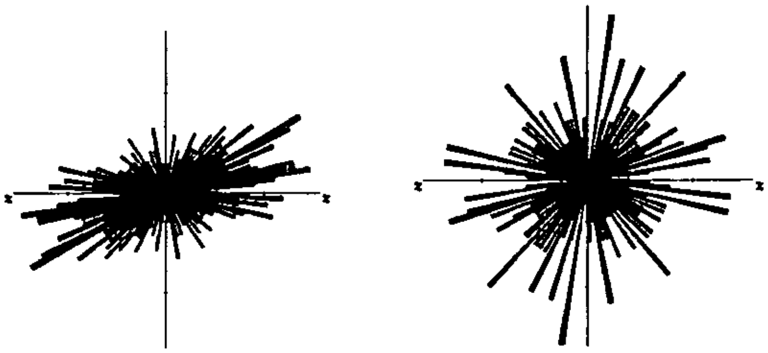

d) e)

Figure VA – 25. Rose diagrams for low-grade deposits in the MMO belt;

a) Rose diagram of all deposits in the MMO belt (4830 points); b) Rose diagram showing all deposits within 20 km distance search (2252 points); c) Rose diagram showing all deposits within 15 km distance search (1734 points); d) Rose diagram showing all deposits within 9 km distance search (1344 points); e) Rose diagram showing all deposits within 3 km distance search (512 points).

The low, medium and high production gold deposits generated the Autocorrelation plots and rose diagrams shown in figures VA – 26 and 27, VA – 28 and 29 and VA – 30 and 31 respectively.

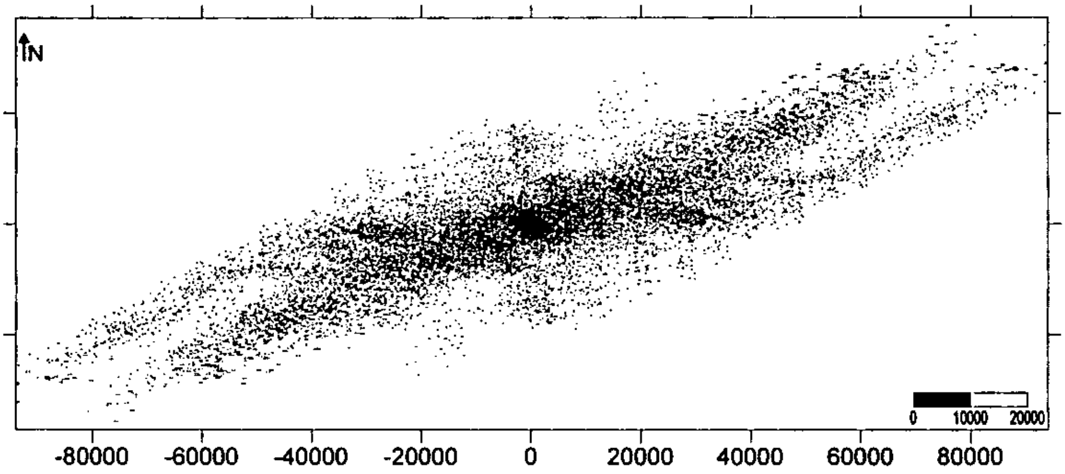

Figure VA – 26. Autocorrelation plot of the low-production deposits in the MMO belt.

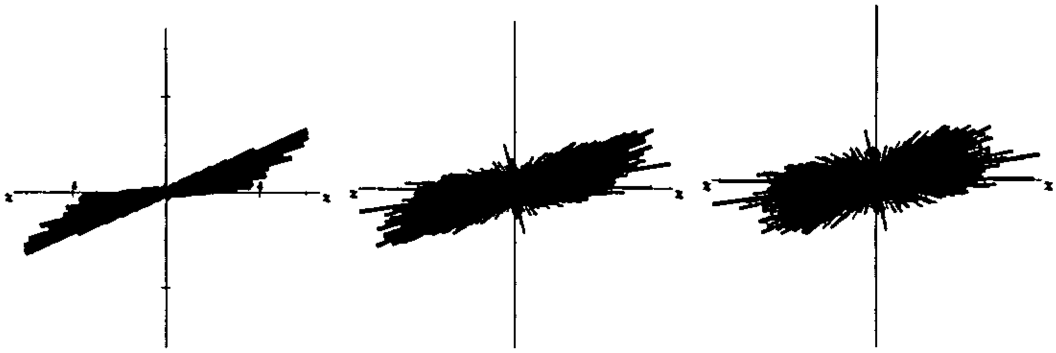

a) b) c)

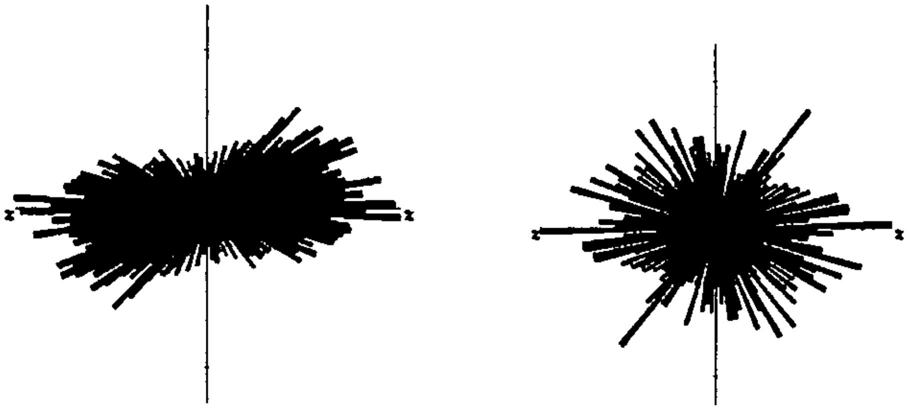

d) e)

Figure VA – 27. Rose diagrams for low-production deposits in the MMO belt;
a) Rose diagram of all deposits in the MMO belt (23870 points); b) Rose diagram showing all deposits within 20 km distance search (12232 points); c) Rose diagram showing all deposits within 15 km distance search (9822 points); d) Rose diagram showing all deposits within 9 km distance search (6304 points); e) Rose diagram showing all deposits within 3 km distance search (1760 points)

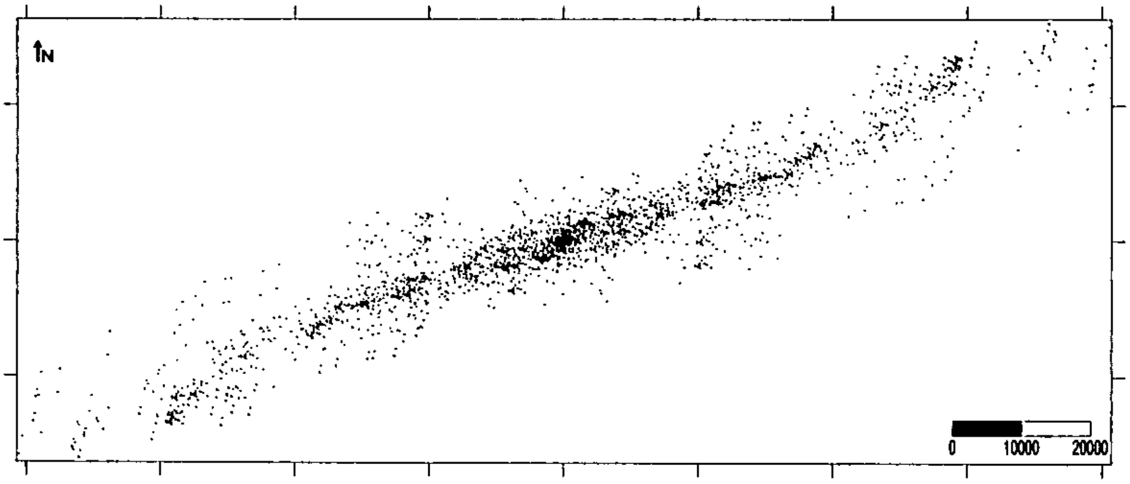

Figure VA – 28. Autocorrelation plot of the medium-production deposits in the MMO belt.

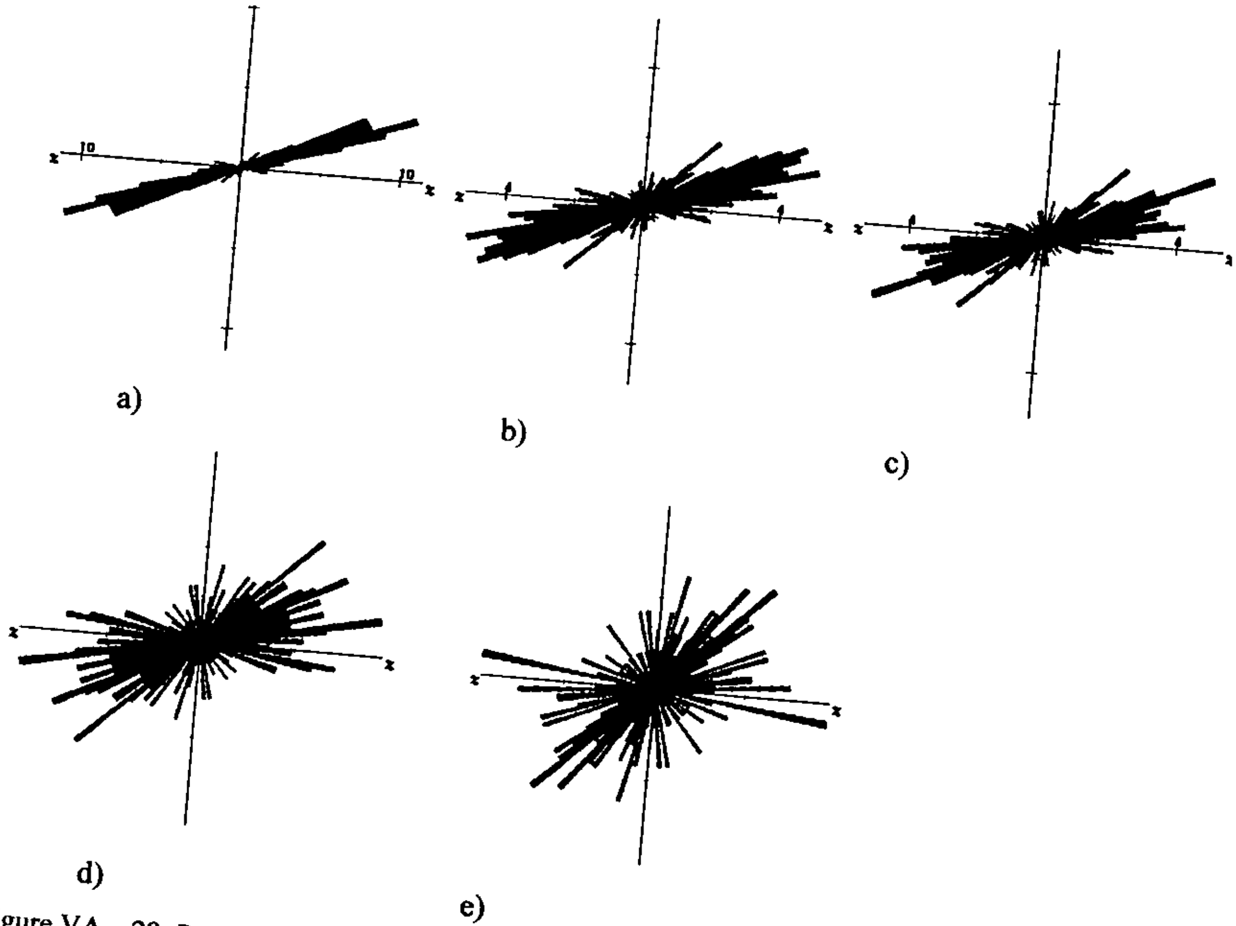

Figure VA – 29. Rose diagrams for medium-production deposits in the MMO belt; a) Rose diagram of all deposits in the MMO belt (2756 points); b) Rose diagram showing all deposits within 20 km distance search (1384 points); c) Rose diagram showing all deposits within 15 km distance search (1228 points); d) Rose diagram showing all deposits within 9 km distance search (836 points); e) Rose diagram showing all deposits within 3 km distance search (470 points).

Figure VA – 30. Autocorrelation plot of the high-production deposits in the MMO belt.

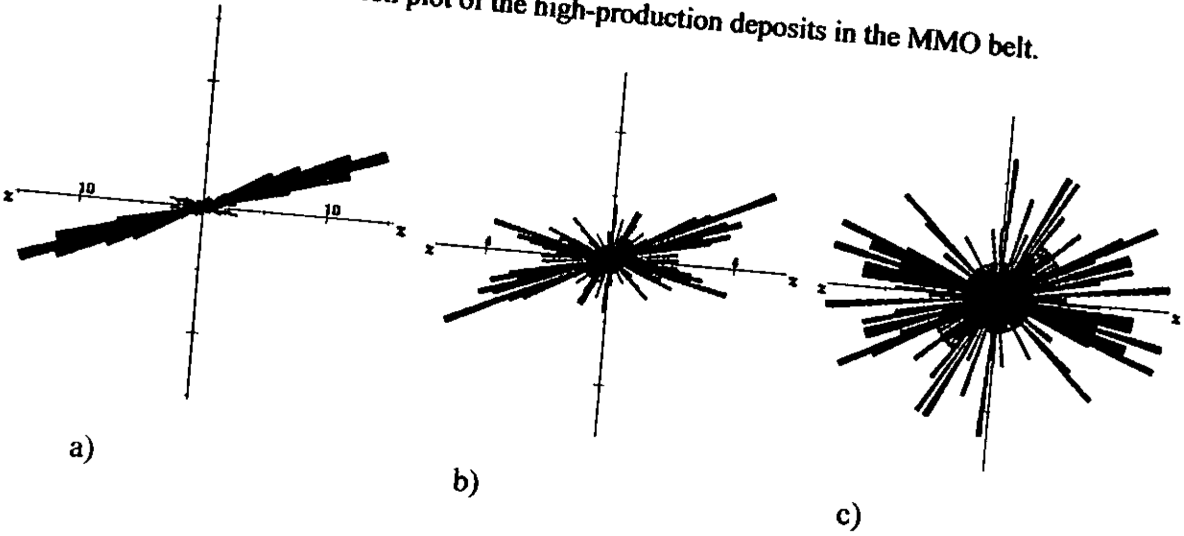

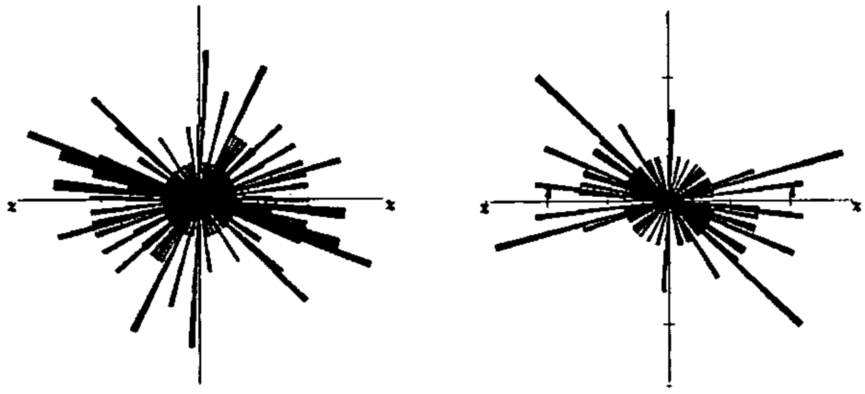

d) e)

Figure VA – 31. Rose diagrams for high-production deposits in the MMO belt;
a) Rose diagram of all deposits in the MMO belt (1056 points); b) Rose diagram showing all deposits within 20 km distance search (459 points); c) Rose diagram showing all deposits within 15 km distance search (330 points); d) Rose diagram showing all deposits within 9 km distance search (270 points); e) Rose diagram showing all deposits within 3 km distance search (470 points).

Data analysis and interpretation

The results of Autocorrelation analysis for the different types of deposits show that N-S is usually negligible at belt scale, 20 km, and 15 km distance search. It is only at 9 and 3 km distance search that the N-S direction is accountable. This can be explained by the fact that the N-S direction is characteristic of quartz veins which cluster ate small radius and are a result of N-S maximum compression. This fact is supported by field evidence at Dot's Luck mine (see also Chapter 3).

The BIF deposits are dominated by E-W trend, which is not unusual because of their relationship with early shear zones as already discussed in chapter 3.

Appendix VI – A

PIMA SP principles, the PIMA spectrum, PIMA measurements and data processing, and mineral identification and feature extraction from PIMA

The PIMA Spectrometer

The Portable Infrared Mineral Analyser (PIMA) shown in Fig. VIA - 1 is a short wave infrared reflectance spectrometer that operates in the wavelength region between 1300 and 2500 nm. The PIMA spectrometer, similar to all other high spectral resolution ("hyperspectral") spectrometers, provides a complete spectrum for the full SWIR range at ~7nm spectral resolution. This has an advantage when compared to broadband multispectral scanners such as Landsat Thematic Mapper (TM) or Enhanced Thematic Mapper (ETM) which have only two spectral wavelength bands (bands 5 (1,55 – 1,75 µm) and 7 (2,05 – 2,35 µm) in the SWIR and spectral resolution on the order of 100 to 200nm (van der Meer, 1999). The comparison between the ETM and TM reflectance and the PIMA spectrum is only valid for the infrared bands (bands 5 and 7); thus, its importance in the mapping of alteration and clay minerals.

The produced spectrum results from a sample area of about 10mm by 2 mm and the spectra have a 2 nm wavelength-sampling interval (PIMA SP users manual, 1999). Soil, powder, rock chip or solutions can be measured, in the field or in the laboratory (e.g. Fig. VIA - 1), using PIMA.

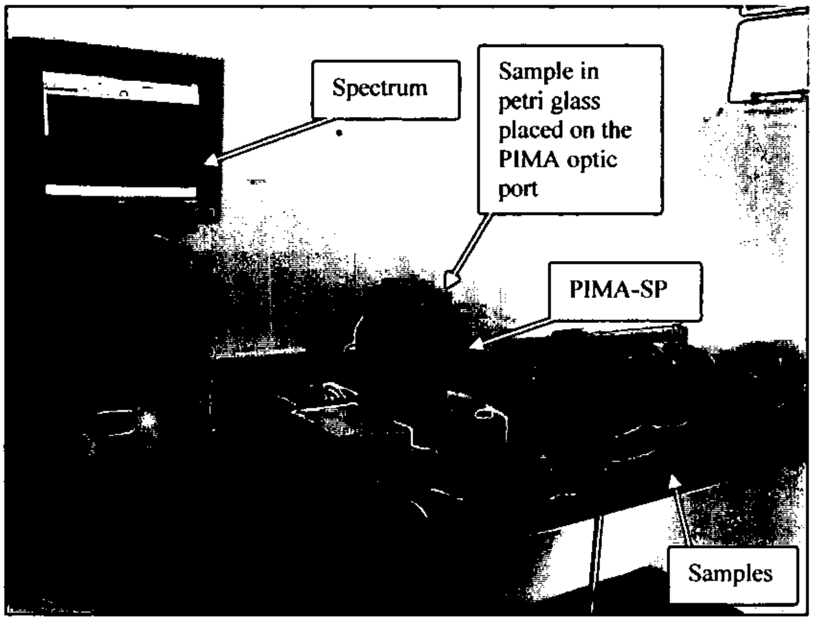

Figure VIA - 1. PIMA Spectrometer set for laboratory analysis and connected to a PC. De Beers laboratory, Johannesburg, South Africa in 2001.

The PIMA SP spectrum is characterised mathematically by spectral parameters, which describe spectral features on the basis of depth, width, asymmetry, size and wavelength position of a particular absorption feature as indicated in Fig. VIA - 2.

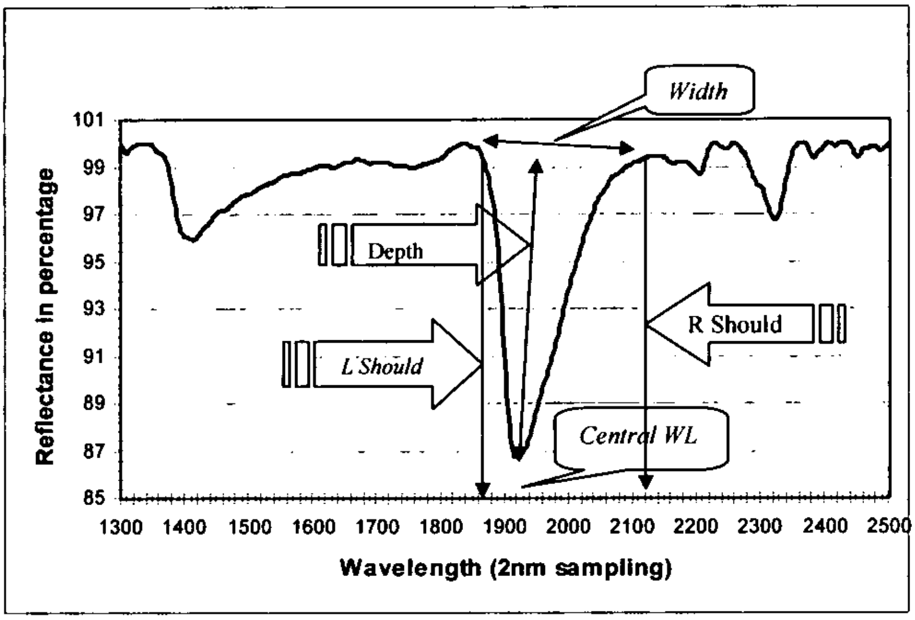

Figure VIA - 2. Main spectral parameters; the spectrum is Fourier Smoothed at 1% and is Hull Quotient applied (L = left, R = right and WL = wavelength), width is the distance between the two shoulders, Depth is the minimum in the spectra anomaly

The absorption wavelength is defined as the wavelength of minimum reflectance of an absorption feature (van der Meer, 1995). The width of an absorption feature can be calculated as

$$\mathbf{Width} = \frac{(\mathbf{A}_{left} + \mathbf{A}_{right})}{\mathbf{2D}} \qquad \text{(VIA - 1)}$$

where: **D** is the depth of the feature relative to hull (Green & Graig, 1985; see Fig. VIA - 3); **A** (left and right are the wavelength to the left and right shoulders of the absorption feature as start and end points of the areas).

The depth of an absorption feature, **D**, is usually defined relative to the "background absorption", $\mathbf{R_c}$, and it depends on the abundance of the absorber and the grain size of the material.

$$\mathbf{D} = 1 - \frac{\mathbf{R_b}}{\mathbf{R_c}} \qquad \text{(VIA – 2)}$$

Where: $\mathbf{R_b}$ is the reflectance at the band centre, and $\mathbf{R_c}$ is the reflectance of the background at the same wavelength as $\mathbf{R_b}$ (Clark and Roush, 1984).

The asymmetry of an absorption feature, S, is defined as the ratio of the area left ($\mathbf{A'_{left}}$) of the absorption central wavelength to the area right ($\mathbf{A'_{right}}$) of the central wavelength (Fig. 6 - 5) as (see also table VIA - 1)

$$S = \frac{\mathbf{A'_{left}}}{\mathbf{A'_{right}}} \qquad \text{(VIA – 3)}$$

PIMA measurements and Data Processing

The petri dish with soil sample is placed on top of the optical port of the PIMA SP so that the port is completely covered by the sample in the petri dish. The sample is measured and a reflectance spectrum is produced. The spectrum and the parameters are saved as a binary file.

For measuring the rock samples the configuration has to be calibrated to normal wavelength (without petri dish). The rock samples were cut and not polished to avoid extra reflectance due to smooth surface. The relatively flat surface of the rock sample is placed against the optical port of the PIMA instrument so that the optical port is covered completely.

The acquisition of the readings was done by PIMA SP PC Acquisition software version 2.2. The instrument was recalibrated at every 10°C variation. All measurements were performed at integration 8 and quality/speed setting; "Quality" which was labelled speed 1 for convenience.

Reflectance spectra were loaded into a software package (De Beers/AAC in house SpectNT 1.63) where data quality control for checking the file names and configuration, exporting of files FOS into DSP extensions, generating library files was done. Spectra were Fourier-Smoothed using two settings (0,5 %, and 1%), and a "Hull Quotient" was applied to each of the resulting sets of spectra.

The hull correction is a baseline or hull, which is calculated to touch the maximum number of points on the spectrum whilst remaining convex and not crossing the spectrum line (Pontual et al., 1997a). The result is that in both quotient and difference correction the spectrum should have reflectance values of 100% at the beginning and at the end of the spectrum (Fig. VIA - 3). Clark and Roush (1984) suggested that dividing the hull into the reflectance spectrum or subtracting it from the apparent absorbance should remove a hull. Thus, the hull quotient calculation involves multiplying by 100 the value given by the division of the reflectance value for each wavelength on the spectrum by the reflectance value for the same wavelength on the calculated hull line (Fig. VIA - 3). On the other hand, the hull difference is obtained by subtracting from 100 the value of the subtraction of the reflectance value for each wavelength on the spectrum and the reflectance value for the same wavelength on the calculated hull line (Fig. VIA - 3).

The fast Furrier smoothing is a mathematically complex way of averaging the spectra as frequencies of DN (radiance or reflectance) values and are modelled by sine/cosines to separate the amplitude and the phase of the signal

$$f(t) = A_0 + \Sigma A_n \mathrm{Cos}\, n\varpi t + \Sigma B_n \mathrm{Sin}\, n\varpi t \qquad \text{(VIA – 4)}$$

where: A_0 = mean level of the function
A_n and B_n are the coefficients of the sine/cosine waves
$\varpi = 2\pi/T$ the frequency is proportional to the length T of the series

After the hull correction and Furrier smoothing of the spectra a macro program (pers. comm. Harris P., 2000) extracts the main spectral parameters (Table VIA - 1). Resulting spectra and summary of extracted features were exported to Excel in an "XYYY" format.

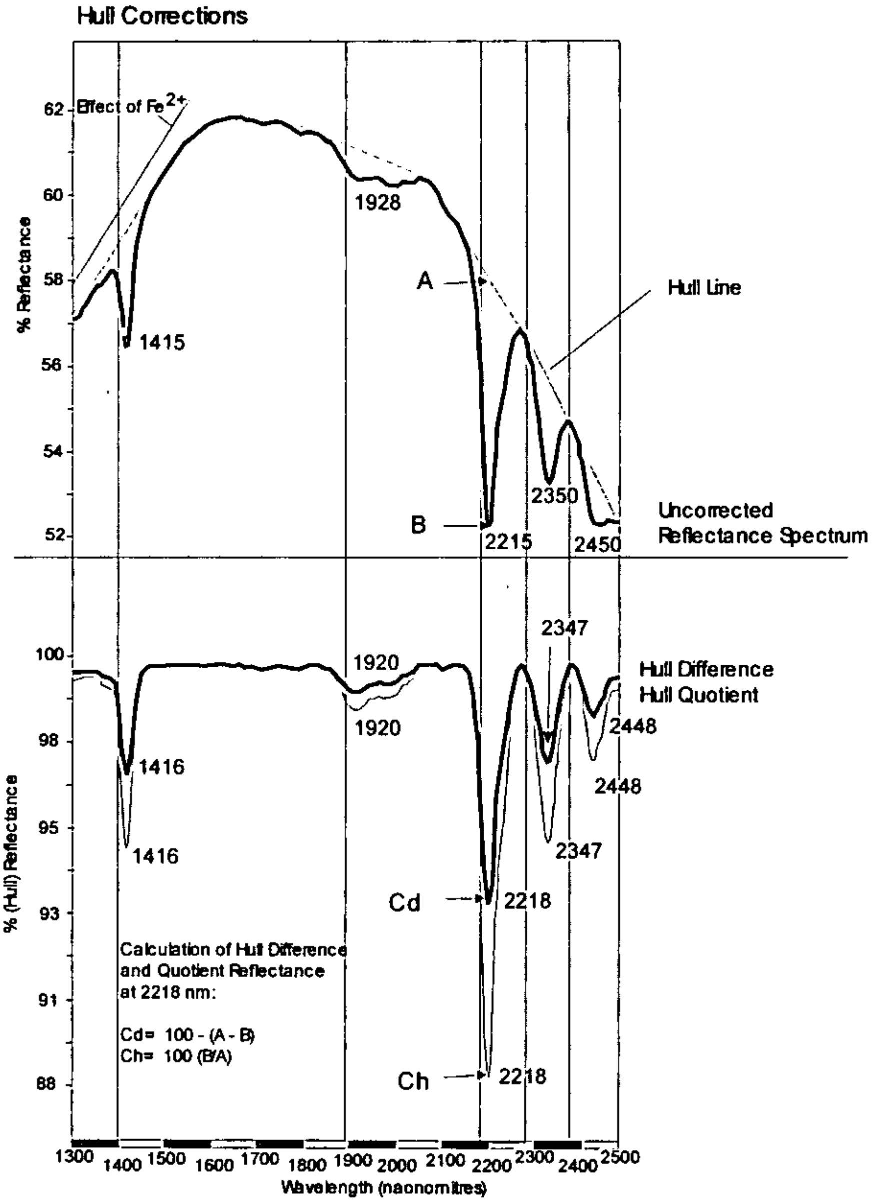

Figure VIA - 3. Illustration of Hull correction. The convex Hull is an envelope curve fitted over the original reflectance spectrum having no absorption features. (Source: Pontual et al. 1997a)

All data are further processed and reflectance spectra are produced from Excel data sets using PIMAVIEW 3.1. The reference library data are hull quotient corrected and Fourier-smoothed at 1%.

Table VIA – 1. Example of results of feature extraction from powder spectra library, profile B in the MMO belt (for explanation of abbreviations see Appendix VI – C and Fig. VIA - 2, for sample location refer to Fig. 6 - 1)

```
Results of extracting features from Library : P_Spectra

Processes Performed :                                          Abbreviations
====================                                           Rnk - rank
FourierSmoothing , Smoothing = 1.00%                           Asym - asymetry

Feature Extraction Settings:
===========================
Sort Key : Sort by Depth
Sorted in Descending Order? : TRUE
Maximum # of features to Keep : 10
Feature Extraction Mode : Use 100% Intensity Line
```

Spectrum	L Should	Cent. WL	R Should	Depth	Asym.	Rnk	L. FWHM	R. FWHM	FWHM BW	FWHM BC	Sh BndW
P_B01_00	2230	2500	2500	55.1	99	1	2399.75	0.1	0	0	270
P_B01_00	2100	2210	2230	50.93	5.35	2	2180.07	2216.93	36.87	2198.5	130
P_B01_00	1300	1300	1366	50.32	0	3	0.1	1322.24	1322.14	661.17	66
P_B01_00	1838	1932	2100	50.25	0.55	4	1896.07	2002.5	106.42	1949.29	262
P_B01_00	1366	1416	1638	49.93	0.23	5	1389.37	1483.08	93.71	1436.22	272
P_B01_00	1784	1790	1822	47.4	0.19	6	1787.13	1811.37	24.25	1799.25	38
P_B01_00	1762	1778	1784	47.4	2.67	7	1770.85	1781.11	10.27	1775.98	22
P_B01_00	1744	1754	1762	47.37	1.25	8	1748.85	1758.01	9.17	1753.43	18
P_B01_00	1698	1740	1744	47.36	10.48	9	1720.21	1742.28	22.07	1731.24	46
P_B01_00	1822	1826	1838	47.3	0.33	10	1823.85	1832.13	8.28	1827.99	16
P_B03_00	2144	2316	2358	75.64	3.84	1	2272.79	2331.22	58.43	2302.01	214
P_B03_00	2414	2500	2500	75.11	99	2	2448.47	0.1	0	0	86
P_B03_00	2358	2390	2414	73.95	1.33	3	2376.64	2400.48	23.84	2388.56	56
P_B03_00	1700	1916	2092	69	1.16	4	1889.17	1999.55	110.38	1944.36	392
P_B03_00	1368	1396	1664	67.6	0.11	5	1386.93	1445.85	58.92	1416.39	296
P_B03_00	1300	1300	1368	65.63	0	6	0.1	1325.36	1325.26	662.73	68
P_B03_00	2092	2134	2144	65.51	4.19	7	2109.54	2137.91	28.37	2123.73	52
P_B03_00	1664	1666	1678	61.64	0.17	8	1665.01	1671.77	6.76	1668.39	14
P_B03_00	1678	1684	1700	61.63	0.38	9	1680.58	1692.16	11.58	1686.37	22

External (room) and internal (instrument) temperature changes affect the results from PIMA Spectrometer measurement. The effect of temperature is minimised by keeping an air conditioner at coolest for 24 hours and seven days a week. The effects of temperature of the detector (instrument) is controlled by recalibrating the instrument at every 10° C increase and by discontinuing measurements for at least half an hour when temperature of the detector reaches 55°C. The quality of measurement is monitored and controlled by plotting all the calibration spectra and checking for any changes on the shape and position of the calibration spectra as shown in Fig. VIA - 4. The shape and position of the spectra show that there is no change due to instrument drifts mainly related to temperature changes.

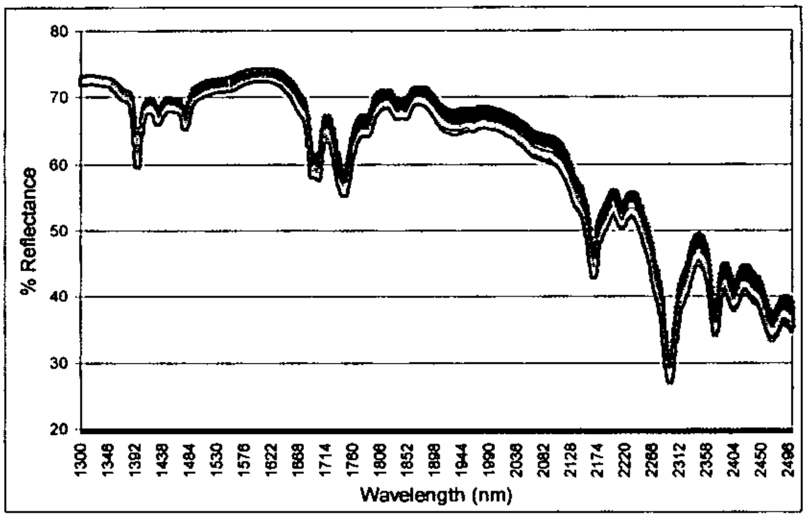

Figure VIA - 4. Instrument calibration. Reflectance spectra of 44 PIMA SP calibration samples vs wavelength

6.1 Mineral Identification and feature extraction from PIMA Data

Pontual et al. (1997a) considers PIMA analysis semi-quantitative because the spectral response of a mineral mixture is mainly influenced by varying *absorption coefficients* between different minerals. Absorption features out of the range of the PIMA also influence PIMA reflectance spectra. These features include the ferrous iron absorptions around 1000 nm and strong water and carbonate absorptions around 2700 nm. Pontual et al. (1997a) showed that the influence of ferrous iron on the reflectance spectrum provide an added dimension of spectral information (reflectance hull) that allows distinction of iron-bearing minerals from non-iron-bearing minerals. Although the importance of this information contained on the "reflectance hull", makes the determination of the other absorption features difficult, particularly those on the steepest parts of the reflectance spectrum. Therefore, it is recommended to remove the "reflectance hull" and to enhance the spectral absorption features (Pontual et al., 1997a and Clark and Roush, 1984).

The main advantage of hull correction is to improve the absorption features or minima not easily detectable in the uncorrected reflectance spectrum. But the hull correction has the disadvantage of removing largely the effect of iron (Pontual et al., 1997a). The next section discusses the mineral identification using spectra from PIMA.

Mineral identification by spectral interpretation (methods and procedures)

The method presented here is not unique for mineral identification and mapping, however, is comparatively advantageous due to its fast result and its ability to be used directly in the field, especially when quick indicative results are needed in regional exploration.

The diagnostic characteristics of each mineral are ideal in pure (no mixing) minerals. In general, spectra of a sample present features of more than one mineral at specific conditions. Therefore it is recommended that the interpretation of spectra be based in comparison with a spectral library (spectra resulting from analyses and tests under different conditions such as differing grain sizes or mixtures of various materials) (Fig. VIA - 5). This approach is sensitive enough to map different regions of the spectrum such as a kaolinite versus a halloysite-like feature. The result can then be compared with results from other identification methods such as chemistry and petrography.

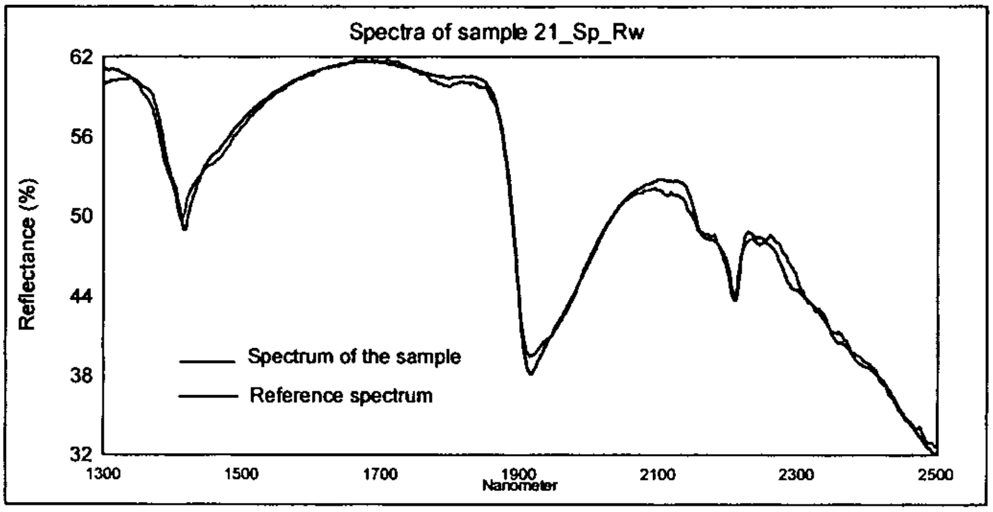

Figure VIA - 5. Reference spectrum against the spectrum of the sample.
The spectra reconcile the mixture of anhydrite, montmorillonite and halloysite at proportions of 37:32:30 percent.

Most minerals generally have major diagnostic absorption wavelengths between 2050 and 2450 nm due to Al-OH, Fe-OH, Mg-OH and CO_3 absorption bonds and can be grouped spectrally according to the wavelength position of their deepest absorption feature.

The interpretation of spectra using a spectral library can be summarised in the seven steps suggested by Pontual et al. (1997a), (see Appendix VI – D).

After these steps most single minerals would have been identified and if not that would imply that the unknown spectrum is a result of mixture of more than one mineral. The spectral mixing can be considered in a simplistic way as a linear process where spectral signatures of different minerals are added together in one spectrum. For example;

Mixed Spectrum = X% Mineral 1 + Y% Mineral 2 + Z% Mineral 3 +...+ ε% Mineral n (VIA – 5)

Where: "Percentage (%)" of each contributing mineral (e.g. X) to the strength of its spectral signature and not necessarily its actual proportion in the target sample.

The contribution of each component to the final spectrum is expressed as relative proportion to the whole spectrum. Consequently the intensity of absorption features usually does not correspond to the proportion of a particular mineral in the mixture. Mathematically the linear combination of spectral end-members is as defined in the equation VIA – 4.

Johnson et al. (1983), Mustard and Pieters (1987) and Smith et al. (1994) regarded spectral unmixing as a convolution technique that aims at estimating the fractions of spectral components that together cause the observed mixed spectra.

The spectral interpretation of a simple mixture can be performed following the steps suggested by Pontual et al. (1997a) (Appendix VI-D). He proposed the use of area one (2050 nm – 2450 nm) as the main one for searching diagnostic features followed by the areas 2 to 4 (1300 nm – 2050 nm) and comparing the unknown spectrum with best match from the pre-defined spectrum from the spectra library. Comparing the reference library spectra and the sample spectra in the PimaView 3.1 software, the main minerals in the MMO greenstone belt were identified and, the important remarks for their identification are summarised in Appendix VI-E.

The second method for identification of minerals using PIMA consists of plotting a scattergram of the deepest absorption feature of the sample against the wavelength. This method allows identification of mineral fields according to the position of the sample in the scatter plot as seen in the Fig. VIA – 6 for the USGS - reference library samples.

As shown in Fig. VIA – 6 each mineral has its unique position in the scatter plot, which depends mainly on its chemical composition.

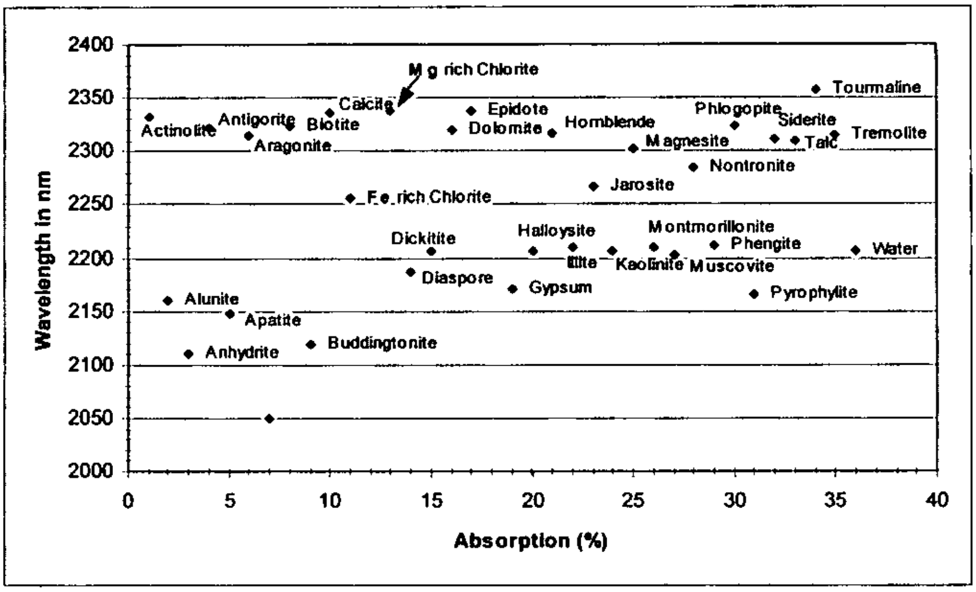

Figure VIA - 6. Representation of deepest absorption features in the area 1 as function of central wavelength and mineral ID from the reference library (Library was Fourier Smoothed at 1% and Quotient Hull).

The third and last method is similar to the previous method where the asymmetry is used instead of deepest absorption feature (Fig. VIA - 7). This method proved to be powerful tool for discrimination of mineral field that usually overlap in the scatter plot of deepest absorption feature.

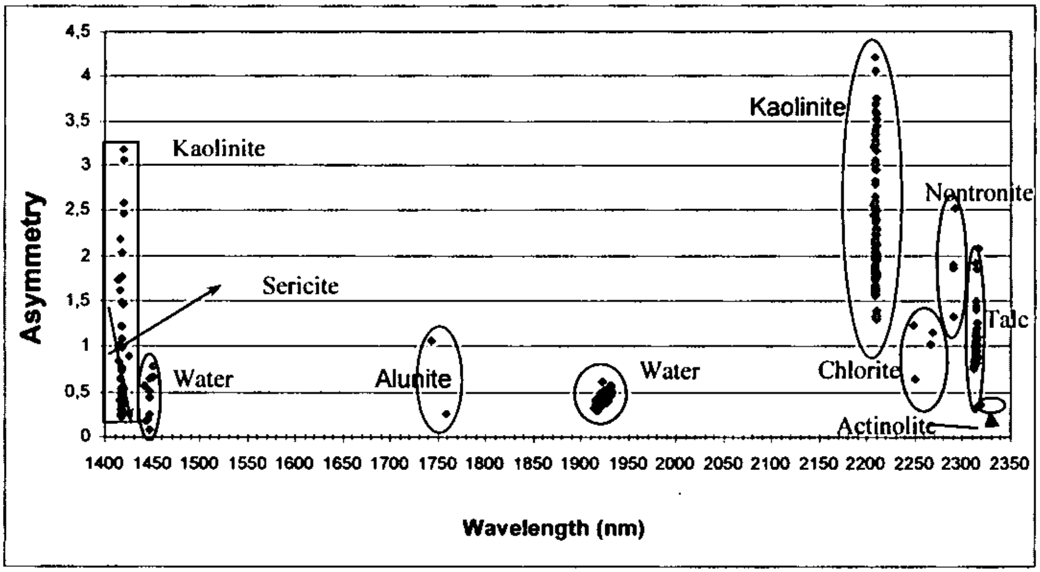

Figure VIA - 7. Central wavelength of the deepest absorption feature versus asymmetry of the absorption feature for the SWIR. Note the groups of minerals that can be separated for the soil samples from the MMO greenstone belt.

Similar results obtained from plotting the deepest absorption feature against the wavelength were in general achieved by plotting the asymmetry of the absorption feature versus the wavelength position in the SWIR as shown in the Fig. VIA - 7. Pontual et. al., 1997c obtained the same magnitude of results and separated mineral groups (actinolite and Fe-carbonate) by plotting the Fe^{2+} slope (between 1350 and 1700nm) versus the sample number.

In general the main mineral groups in the MMO greenstone belt were identified by description of their deepest absorption feature and their asymmetry in area 1 (2050 – 2450 nm). However, these groups could not conclusively characterise the mineralised shear zones mainly due to presence of weathering products that interfere in the spectrum. Thus an analysis per shear zone was performed and is described in the next sections.

6.2 *Appendix VI - B*

Table VIB-1. Sample location in UTM, including the observations

Position	***in UTM***	***Code***		
X	**Y**	**Designation**	**Sample type**	**Observations**
462825	7912607	01/L/Rw	Top soil - wall face	Redwing Mine
462985	7914579	02/ore/Rw	Ore from the Dump	Redwing Mine
464280	7914290	03/Gr/Rw		Redwing Mine
464291	7914265	04/Sp/Rw	Top soil	Redwing Mine
464291	7914265	05/Sp/Rw	Top soil	Redwing Mine
464291	7914265	05A/Sp/Rw	Top soil	Redwing Mine
464289	7914255	06/S-Sp/Rw	Top soil	Redwing Mine
464290	7914245	07/S-Sp/Rw	Top soil	Redwing Mine
464288	7914235	08/Sp/Rw	Top soil	Redwing Mine
464289	7914225	09/ /Rw	Top soil	Redwing Mine
464287	7914215	10/S. Gr/Rw		Redwing Mine
464285	7914205	11/S.Gr/Rw		Redwing Mine
464280	7914190	12/Sp/Rw	Top soil	Redwing Mine
464300	7914100	13/?/Rw		Redwing Mine
464114	7914050	14/?/Rw		Redwing Mine
464130	7914000	15/?/Rw		Redwing Mine
464135	7913950	16/?/Rw		Redwing Mine
464142	7913920	17/?/Rw		Redwing Mine
464100	7913895	18/?/Rw		Redwing Mine
464092	7913822	19/sch/Rw		Redwing Mine
464090	7913780	20/Talc/Rw		Redwing Mine
464080	7913720	21/Qz/Rw		Redwing Mine
464074	7913632	22/Seric.sch/Rw		Redwing Mine
464011	7913611	23/BIF/Rw		Redwing Mine
463977	7913526	24/Soil/Rw	Top soil	Redwing Mine
463890	7913390	25/?/Rw		Redwing Mine
462854	7912539	26/Mrock./Rw		Redwing Mine
463016	7912459	27/chl./Rw		Redwing Mine
463016	7912429	28/Sp/Rw	Top soil	Redwing Mine
463016	7912399	29/Sp/Rw	Top soil	Redwing Mine
463062	7912374	30/Sp/Rw	Top soil	Redwing Mine
463108	7912350	31/Sp/Rw	Top soil	Redwing Mine
463157	7912329	32/Sp/Rw	Top soil	Redwing Mine
463094	7912307	33/Sp/Rw	Top soil	Redwing Mine
463150	7912280	34/Sp/Rw	Top soil	Redwing Mine
463197	7912255	35/Sp/Rw	Top soil	Redwing Mine
463245	7912235	36/Sp/Rw	Top soil	Redwing Mine
463264	7912210	37/Sp/Rw	Top soil	Redwing Mine
463315	7912185	38/Sp/Rw	Top soil	Redwing Mine
463338	7912160	39/Sp/Rw	Top soil	Redwing Mine
463325	7912135	40/Sp/Rw	Top soil	Redwing Mine
463386	7912110	41/Sp/Rw	Top soil	Redwing Mine
463428	7912085	42/Sp/Rw	Top soil	Redwing Mine
479586	7918612	01/Cantao/99	Rock	Cantao
479603	7918707	02/Cantao/99	Rock	Cantao

479603	7918707	03/Cantao/99	Rock	Cantao
479605	7918749	04/Cantao/99	Rock	Cantao
479605	7918749	05/Cantao/99	Rock	Cantao
499728	7918488	99MN011	Rock	Cantao
479882	7918752	Sp1/1/001	Top soil	Cantao
479837	7918744	Sp1/1/002	Top soil	Cantao
479690	7918695	Sp1/1/004	Top soil	Cantao
479680	7918685	Sp1/1/005	Top soil	Cantao
479650	7918680	Sp1/1/006	Top soil	Cantao
479600	7918682	Sp1/1/007	Top soil	Cantao
479590	7918680	Sp1/1/008	Top soil	Cantao
479550	7918679	Sp1/1/009	Top soil	Cantao
479490	7918676	Sp1/1/010	Top soil	Cantao
479480	7918678	Sp1/1/011	Top soil	Cantao
479462	7918665	Sp1/1/012	Top soil	Cantao
488170	7920414	01/Braga/99	Rock	Felsic tuff
480534	7918841	99MN034	Rock	Old-Wednesday U/G
481140	7917847	01/Chua/99	Rock	Chua
481166	7917762	99MN035	Rock	Chua
481140	7917847	99MN036	Rock	Chua
493151	7910697	Sp7/01/99	Top soil	B. Esperanca
493151	7910723	Sp7/02/99	Top soil	B. Esperanca
493151	7910743	SP7/03/99	Top soil	B. Esperanca
493151	7910783	Sp7/04/99	Top soil	B. Esperanca
493151	7910793	SP7/05/99	Top soil	B. Esperanca
493151	7910803	SP7/06/99	Top soil	B. Esperanca
493151	7910818	SP7/07/99	Top soil	B. Esperanca
493151	7910838	SP7/08/99	Top soil	B. Esperanca
493151	7910858	SP7/09/99	Top soil	B. Esperanca
493151	7910873	SP7/10/99	Top soil	B. Esperanca
493071	7910626	99MN027	Rock	B. Esperanca
477124	7907232	99MN017	Rock	Saymour U/G
477124	7907232	99MN018	Rock	Saymour U/G
477124	7907232	99MN019	Rock	Saymour U/G
477124	7907232	99MN020	Rock	Saymour U/G
477124	7907232	99MN021	Rock	Saymour U/G
476832	7910713	Sp5/01/99	Top soil	Fair Bride
486832	7910696	Sp5/02/99	Top soil	Fair Bride
486832	7910680	Sp5/03/99	Top soil	Fair Bride
486832	7910665	Sp5/04/99	Top soil	Fair Bride
486832	7910645	Sp5/05/99	Top soil	Fair Bride
486905	7910626	Sp5/06/99	Top soil	Fair Bride
486905	7910608	Sp5/07/99	Top soil	Fair Bride
486922	7910554	Sp5/08/99	Top soil	Fair Bride
486830	7910542	Sp6/01/99	Top soil	Fair Bride
486830	7910567	Sp6/02/99	Top soil	Fair Bride
486830	7910592	Sp6/03/99	Top soil	Fair Bride
486846	7910606	Sp6/04/99	Top soil	Fair Bride
486795	7910640	Sp6/05/99	Top soil	Fair Bride
486795	7910665	Sp6/06/99	Top soil	Fair Bride
486795	7910690	Sp6/07/99	Top soil	Fair Bride

486784	7910723	Sp6/08/99	Top soil	Fair Bride
486063	7910275	Sp4/01/99	Top soil	Try Again
486063	7910290	Sp4/02/99	Top soil	Try Again
486063	7910305	Sp4/03/99	Top soil	Try Again
486063	7910320	Sp4/04/99	Top soil	Try Again
486063	7910335	Sp4/05/99	Top soil	Try Again
486050	7910408	Sp4/06/99	Top soil	Try Again
486050	7910423	Sp4/07/99	Top soil	Try Again
486050	7910438	Sp4/08/99	Top soil	Try Again
481424	7910584	Sp8/01/99	Top soil	Dot's Luck
481515	7910599	Sp8/02/99	Top soil	Dot's Luck
481515	7910614	Sp8/03/99	Top soil	Dot's Luck
481535	7910629	Sp8/04/99	Top soil	Dot's Luck
481546	7910618	Sp8/05/99	Top soil	Dot's Luck
481546	7910633	Sp8/06/99	Top soil	Dot's Luck
481546	7910648	Sp8/07/99	Top soil	Dot's Luck
481546	7910648	Sp8/08/99	Top soil	Dot's Luck
481509	7910755	Sp8/09/99	Top soil	Dot's Luck
481521	7910765	Sp8/10/99	Top soil	Dot's Luck
481453	7910877	Sp8/11/99	Top soil	Dot's Luck
493261	7910964	99/MN023	Rock	Dot's Luck
480414	7917700	Sp9/TF/01	Top soil	Two Fools
480424	7917650	Sp9/TF/02	Top soil	Two Fools
480435	7917600	Sp9/TF/03	Top soil	Two Fools
480462	7917577	Sp9/TF/04	Top soil	Two Fools
480470	7917550	Sp9/TF/05	Top soil	Two Fools
480475	7917500	Sp9/TF/06	Top soil	Two Fools
480487	7917475	Sp9/TF/07	Top soil	Two Fools
480490	7917450	Sp9/TF/08	Top soil	Two Fools
480495	7917430	Sp9/TF/09	Top soil	Two Fools
480485	7917404	Sp9/TF/10	Top soil	Two Fools
486970	7912944	99MN054	Mine	Guy Fawkes
486970	7912994	99MN055	Mine	Guy Fawkes
487035	7913144	Sp/GF/01	Top soil	Guy Fawkes
487000	7913110	Sp/GF/02	Top soil	Guy Fawkes
486984	7913099	Sp/GF/03	Top soil	Guy Fawkes
486860	7913037	Sp/GF/04	Top soil	Guy Fawkes
486830	7913000	Sp/GF/05	Top soil	Guy Fawkes
486971	7913051	Sp/GF/06	Top soil	Guy Fawkes
486800	7913010	Sp/GF/07	Top soil	Guy Fawkes
471940	7912512	99MN049	Rock	Monarch
471508	7912517	99MN050	Rock	Monarch
471153	7912550	99MN052	Rock	Monarch
471140	7912604	99MN053	Rock	Monarch
471259	7912637	01/monarch/99	milling site	Monarch
471140	7912754	Sp10/01/99	Top soil	Monarch
471135	7912670	Sp10/02/99	Top soil	Monarch
471152	7912695	Sp10/03/99	Top soil	Monarch
471283	7912695	Sp10/04/99	Top soil	Monarch
473282	7914316	99MN037	Rock	Revue
473275	7914314	99MN038	Rock	Revue

473270	7914312	99MN039	Rock	Revue
473259	7914310	99MN040	Rock	Revue
473325	7914094	99MN041	Rock	Revue
473324	7914074	99MN042	Rock	Revue
473323	7914063	99MN043	Rock	Revue
473320	7914050	99MN044	Rock	Revue
473323	7914040	99MN045	Rock	Revue
473322	7914030	99MN046	Rock	Revue
473323	7914028	99MN047	Rock	Revue
473290	7914027	99MN048	Rock	Revue
487882	7908690	MAP1/01/99	Rock	Profile S-N
487879	7908729	MAP1/02/99	Rock	Profile S-N
487880	7908749	MAP1/03/99	Rock	Profile S-N
487880	7908749	MAP1/03b/99	Rock	
487882	7908769	MAP1/04/99	Rock	Profile S-N
487881	7908789	MAP1/05/99	Rock	Profile S-N
487883	7908800	MAP1/06/99	Rock	Profile S-N
487880	7908820	MAP1/07/99	Rock	Profile S-N
487885	7908850	MAP1/08/99	Rock	Profile S-N
487886	7908870	MAP1/09/99	Rock	Profile S-N
487883	7908888	MAP1/10/99	Rock	Profile S-N
487884	7909010	MAP1/11/99	Rock	Profile S-N
487880	7909016	MAP1/12/99	Rock	Profile S-N
487880	7909020	MAP1/13/99	Rock	Profile S-N
487882	7909061	MAP1/14/99	Rock	Profile S-N
487883	7909690	MAP1/15/99	Rock	Profile S-N
487885	7909695	MAP1/16/99	Rock	Profile S-N
487886	7909720	MAP1/17/99	Rock	Profile S-N
487888	7909780	MAP1/18/99	Rock	Profile S-N
487888	7909780	MAP1/18b/99	Rock	
487888	7909780	MAP1/18c/99	Rock	
487880	7909898	MAP1/19/99	Rock	Profile S-N
487885	7909997	MAP1/20/99	Rock	Profile S-N
467346	7914336	RED3/001/99	Top soil	Redwing
467364	7914309	RED3/002/99	Top soil	Redwing
467454	7914292	RED3/003/99	Top soil	Redwing
467354	7914230	RED3/004/99	Top soil	Redwing
467343	7914126	RED3/005/99	Top soil	Redwing
467229	7914159	RED3/006/99	Top soil	Redwing
467165	7914045	RED3/007/99	Top soil	Redwing
467205	7913952	RED3/008/99	Top soil	Redwing
467190	7913957	RED3/009/99	Top soil	Redwing
467126	7913850	RED3/010/99	Top soil	Redwing
467127	7913820	RED3/011/99	Top soil	Redwing
467184	7913799	RED3/012/99	Top soil	Redwing
467179	7913749	RED3/013/99	Top soil	Redwing
467230	7913668	RED3/014/99	Top soil	Redwing
467292	7913624	RED3/015/99	Top soil	Redwing
467292	7913624	RED3/016/99	Top soil	Redwing
466937	7913740	RED3/017/99	Top soil	Redwing
467495	7913265	RED3/018/99	Top soil	Redwing

467625	7913234	RED3/019/99	Top soil	Redwing
467709	7912811	RED3/020/99	Top soil	Redwing
467729	7912779	RED3/021/99	Top soil	Redwing
467735	7912564	RED3/022/99	Top soil	Redwing
467788	7912544	RED3/023/99	Top soil	Redwing
464306	7914044	RED2/01/99	Top soil	Redwing
464755	7914128	RED2/02/99	Top soil	Redwing
464755	7914128	RED2/03/99	Top soil	Redwing
465027	7914142	RED2/04/99	Top soil	Redwing
465028	7914153	RED2/05/99	Top soil	Redwing
465026	7914167	RED2/06/99	Top soil	Redwing
465026	7914142	RED2/07/99	Top soil	Redwing
465026	7914117	RED2/08/99	Top soil	Redwing
465026	7914100	RED2/09/99	Top soil	Redwing
465037	7914090	RED2/10/99	Top soil	Redwing
465077	7914070	RED2/11/99	Top soil	Redwing
465059	7914022	RED2/12/99	Top soil	Redwing
465071	7913955	RED2/13/99	Top soil	Redwing
465097	7913865	RED2/14/99	Top soil	Redwing
465097	7913835	RED2/15/99	Top soil	Redwing
465127	7913818	RED2/16/99	Top soil	Redwing
465167	7913750	RED2/17/99	Top soil	Redwing
465182	7913625	RED2/18/99	Top soil	Redwing
465193	7913526	RED2/19/99	Top soil	Redwing
465419	7913454	RED2/20/99	Top soil	Redwing
465203	7913366	RED2/21/99	Top soil	Redwing
465281	7913239	RED2/22/99	Top soil	Redwing
465316	7913196	RED2/23/99	Top soil	Redwing
465320	7913180	RED2/24/99	Top soil	Redwing
465325	7913142	RED2/25/99	Top soil	Redwing
465325	7913127	RED2/26/99	Top soil	Redwing
465394	7913015	RED2/27/99	Top soil	Redwing
465434	7913006	RED2/28/99	Top soil	Redwing
465409	7912964	RED2/29/99	Top soil	Redwing
465409	7912900	RED2/30/99	Top soil	Redwing
465519	7912885	RED2/31/99	Top soil	Redwing
465519	7912879	RED2/32/99	Top soil	Redwing
465519	7912869	RED2/33/99	Top soil	Redwing
465593	7912856	RED2/34/99	Top soil	Redwing
465712	7912687	RED2/35/99	Top soil	Redwing
465590	7912152	RED2/36/99	Top soil	Redwing
466163	7911838	RED2/37/99	Top soil	Redwing
466108	7911793	RED2/38/99	Top soil	Redwing
465935	7911710	RED2/39/99	Top soil	Redwing
465839	7911685	RED2/40/99	Top soil	Redwing
465746	7911660	RED2/41/99	Top soil	Redwing
465746	7911635	RED2/42/99	Top soil	Redwing
465594	7911585	RED2/43/99	Top soil	Redwing
481825	7909041	SP2_01	Soil profile	Road to Mondungwara
481825	7909041	SP2_02	Soil profile	Road to Mondungwara
481825	7909041	SP2_03	Soil profile	Road to Mondungwara

481825	7909041	SP2_04	Soil profile	Road to Mondungwara
481825	7909041	SP2_05	Soil profile	Road to Mondungwara
481826	7909075	SP2_06	Top soil	Road to Mondungwara
481824	7909065	SP2_07	Top soil	Road to Mondungwara
481826	7909055	SP2_08	Mafic schist	Road to Mondungwara
481824	7909045	SP2_09	Quartz vein	Road to Mondungwara
476936	7907104	SP3_01	Bear soil	Isitaca Mountain
476940	7907106	SP3_02	Bear soil	Isitaca Mountain
476944	7907108	SP3_03	Bear soil	Isitaca Mountain
476948	7907110	SP3_04	Bear soil	Isitaca Mountain
476952	7907112	SP3_05	Bear soil	Isitaca Mountain
476956	7907114	SP3_06	Bear soil	Isitaca Mountain
476960	7907116	SP3_07	Bear soil	Isitaca Mountain
476964	7907118	SP3_08	Bear soil	Isitaca Mountain
476954	7907152	SP3_09	Serpentinite	Isitaca Mountain
477093	7907219	SP3_10	Serpentinite	Isitaca Mountain
477042	7907051	SP3_11	Serpentinite	Isitaca Mountain
477307	7907562	SP3_12	Serpentinite	Isitaca Mountain
477248	7907429	SP3_13	Serpentinite	Isitaca Mountain
477348	7907429	SP3_14	Serpentinite	Isitaca Mountain
477628	7907047	SP3_15	Serpentinite	Isitaca Mountain
477628	7907045	SP3_16	Serpentinite	Isitaca Mountain
476431	7907889	RED3/001/100	Top soil	Redwing
476581	7907802	RED3/002/100	Top soil	Redwing
476730	7907716	RED3/003/100	Top soil	Redwing
476880	7907630	RED3/004/100	Top soil	Redwing
477030	7907543	RED3/005/100	Top soil	Redwing
477180	7907457	RED3/006/100	Top soil	Redwing
477330	7907371	RED3/007/100	Top soil	Redwing
477480	7907284	RED3/008/100	Top soil	Redwing
477630	7907198	RED3/009/100	Top soil	Redwing
477779	7907112	RED3/010/100	Top soil	Redwing
477929	7907025	RED3/011/100	Top soil	Redwing
478079	7906939	RED3/012/100	Top soil	Redwing
464280	7914190	R_12c_SP_RW	Float	
488822	7913802	R_B01_00	Rock	
491796	7914736	R_B03_00	Rock	
466325	7910154	R_B21_00	Rock	
443065	7906144	R_B25_00	Rock	
468260	7912222	R_B26_00	Rock	
468288	7912320	R_B27_00	Rock	
468748	7911935	R_B28_00	Rock	
468813	7911938	R_B29_00	Rock	
468881	7911940	R_B30_00	Rock	
465405	7914010	R_B31_00	Rock	
467517	7911643	R_B32_00	Rock	
457045	7909970	R_B33_00	Rock	
456844	7909945	R_B34_00	Rock	
454705	7912386	R_B37_00	Rock	
461358	7914549	R_B38_00	Rock	
461338	7914143	R_B40_00	Rock	

461159	7913903	R_B41_00	Rock	
461113	7913236	R_B42_00	Rock	
447766	7908917	R_B46_00	Rock	
446990	7908480	R_B47_00	Rock	
445615	7908112	R_B48_00	Rock	
444977	7907789	R_B49_00	Rock	
450896	7911025	R_B50_00	Rock	
454277	7909562	R_B51_00	Rock	
444632	7906704	R_B52_00	Rock	
444856	7906149	R_B53_00	Rock	
445113	7906104	R_B54_00	Rock	
443771	7906223	R_B55_00	Rock	
445844	7905611	R_B56_00	Rock	
451246	7906414	R_B59_00	Rock	
456045	7905598	R_B60_00	Rock	
459888	7906398	R_B63_00	Rock	
463313	7914024	R_B64_00	Rock	
467265	7914140	R_B67_00	Rock	
466406	7914973	R_B68_00	Rock	
463336	7906461	R_B69_00	Rock	
469779	7908767	R_B70_00	Rock	
461093	7905174	R_B72_00	Rock	
493242	7910879	R_BoaEsperan	Main pit	
488170	7920414	R_Braganca_1	Shaft	
488236	7920460	R_Braganca_3	Small adit	
488150	7920514	R_Braganca_5	Small adit	
479959	7918805	R_Cantao_1	Adit	
483715	7918130	R_Excelsior_1	Adits	
483429	7917999	Excelsior_2		
487050	7913090	R_Guy Fawkes	Open pit (main)	
486796	7912635	R_Ivone_1	Dump	
486796	7912635	R_Ivone_2	Dump	
486796	7912635	R_Ivone_4	Dump	
478790	7920250	R_Marondo_1	Adit	
471152	7912273	R_Monarch_3	Open pit	
471182	7912346	R_Monarch_4	Open pit	
471279	7912345	R_Monarch_5	Adit 5	
473291	7913765	R_Revue_3	Adit	
473391	7913916	R_Revue_4	Exploration adit	
480431	7917374	R_Two Fools_2	Open pit	
480430	7917290	R_Two fools _3	Adit 7	
481449	7910666	99/MN024	Dots Luck 4	Dot's Luck
481458	7910684	99MN029	Dots Luck 6	Dot's Luck

6.3 Appendix VI – C

Table VIC-1. Spectrum feature extraction explanation and comments

Field	Explanation	Cut off limits	NOTES
Spectrum	The name of the spectrum to which processes have been applied	-	All spectra have been smoothed to the 1% setting, using a Fourier smoothing algorithm, prior to any other process being performed.
maxy	The maximum albedo of the spectrum, after smoothing 1%	-	All spectra with HQ in the result header (through the complete wavelength range) have had a background removal process applied in the form of a convex hull quotient removal.
y1320	The reflectance value at wavelength 1320,	-	Results with "gr" in the name have been resampled to a grid after smoothing, before the hull quotient has been removed. Grid range is specified in the explanation.
y1650	The reflectance value at wavelength 1650, combined with y1320 provides a measure of the slope towards a Fe2+ absorption at 1000nm, present in e.g. clinopyroxene, olivine.	-	Cut off limits represent the wavelength limits beyond which the selected feature can not occur. The extraction process looks for the nearest feature to the specified wavelength, and this could be quite far away, so the clip limits test the results and return a 0 for features outside the specified range.
y2162HQ	Reflectance value after hull removal, this is a point along kaolinite/halloysite shoulder feature, and can be used to calculate crystallinity of the kaolinite, according to the G-Mex method	-	Extractions have been done using a macro written by P.D. Harris within the proprietary software SpectNT 1.63d developed at Anglo American and jointly owned by DeBeers Consolidated Mines and Anglo American Geophysical Services Department, a part of AAC plc.
y2178HQ	Reflectance value after hull removal, this is a point along kaolinite/halloysite shoulder feature, and can be used to calculate crystallinity of the kaolinite, according to the G-Mex method	-	
y2184HQ	Reflectance value after hull removal, this is a point along kaolinite/halloysite shoulder feature, and can be used to calculate crystallinity of the kaolinite, according to the G-Mex method	-	
y2190HQ	Reflectance value after hull removal, this is a point along kaolinite/halloysite shoulder feature, and can be used to calculate crystallinity of the kaolinite, according to the G-Mex method	-	
n1380HQ	The wavelength of the nearest feature to 1380nm, represents O-H bonds	1395-1405	
d1380HQ	Depth of the nearest feature to 1380nm, represents O-H bonds,		
n1410HQ	The wavelength of the nearest feature to 1410nm, represents O-H bonds	1405-1410	
d1410HQ	Depth of the nearest feature to 1410nm, represents O-H bonds,		
n1750HQ	The wavelength of the nearest feature to 1750nm, represents sulphate minerals	1699-1881	

d1750HQ	Depth of the nearest feature to 1750nm, represents sulphate minerals	
n1910HQ	Wavelength of the nearest feature to 1910nm, represents H_2O normally crystalline/interlayer water, free water tends toward longer wavelengths 1956 for atmospheric water.	1881-1999
d1910HQ	Depth of the water feature.	
n2165HQ	The wavelength of the Kaolinite shoulder feature/Pyrophyllite/Alunite major feature	2159-2179
d2165HQ	Depth of the kln shoulder, useful for kaolinite abundance and crystallinity	
n2210HQ	Wavelength of the nearest feature to 2210, represents the Al-OH bond, present in Illite, sericite, kaolinite, muscovite and other Al-OH bearing minerals.	2179-2229
d2210HQ	Depth of the Al-OH feature	
n2250HQ	Wavelength of the nearest feature to the 2250nm position, this represents an Fe_2+ bond (unconfirmed in literature) and is common in chlorites, biotites, epidotes, some amphiboles, etc.	2229-2261
d2250HQ	Depth of the 2250nm feature	
n2280HQ	Wavelength of the nearest feature to 2280nm, this feature will normally collect a 2290nm absorption for nontronite, or a talc shoulder feature at the same position. This is thought to represent the Fe_3+ in nontronite.	2261-2299
d2280HQ	Depth of the 2280nm feature	
n2320HQ	Wavelength of the main Mg-OH absorption feature, this is common for actinolite, tremolite, talc, Mg-rich chlorite, biotite, phlogopite, some epidotes	2299-2331
d2320HQ	Depth of the Mg-OH feature	
n2350HQ	Wavelength of the nearest feature to 2350nm, this feature is present as the dominant feature in most carbonates, intermediate and Fe-rich chlorites, some epidotes, and as a secondary but still large feature in sericite, muscovite, illite.	2331-2361
d2350HQ	The depth of the nearest feature to 2350nm	
n2390HQ	Wavelength of the nearest feature to 2390nm, this feature is a common secondary feature in most Mg-OH bearing minerals such as amphibole and talc, and has been used to track their abundance	2361-2401
d2390HQ	Depth of the nearest feature to 2390nm	
n2440HQ	Wavelength of the nearest feature to 2440nm, this represents the position of a carbonate absorption feature. The quality of data beyond 2400nm is often poor (low signal levels0 therefore treat this with caution.	2401-2475
d2440HQ	The depth of the nearest feature to 2440nm	grid
d2165gr	The gridded before being hulled feature Depth of the 2165nm absorption. This feature is often a shoulder or inflection, representing kaolinite abundance and crystallinity - gridding removes the local background and provides a more precise measure of the feature. Grid range is 2128 to 2194nm at 2nm spacing.	grid

d2210gr	The gridded before being hulled feature Depth of the Al-OH 2210nm absorption. This feature often falls on a slope not fully represented by the full hull line, therefore gridding provides a more precise background model and therefore removal. Grid range is 2120 to 2260nm at 2nm	grid
d2340gr	The gridded before being hulled feature Depth of the carbonate/chlorite 2340/2350nm absorption. This feature often falls on a slope not fully represented by the full hull line, therefore gridding provides a more precise background model and therefore removal. Grid range is 2260 to 2420 at 2nm	grid
w2210HQ	This extraction is the Width at Half Depth of the Al-OH feature at 2210nm, the same feature as the d2210HQ and n2210HQ as above. The width provides an alternative measure of the effects of the 2165nm feature, and may represent a measure of the relative proportions of kaolinite and illite/sericite/mica as the latter have narrower features with less kaolinite also present.	no clip check!

6.4 Appendix VI – D

Steps for mineral identification using its spectrum (Pontual et al. (1997a)

1. Obtain the best spectrum of the data (hull corrected and smoothed if necessary) and get the best display of the spectrum on paper or on PC screen.

2. Look at the 2050-2450nm spectral region (area 1)

3. Identify the deepest absorption in the 2050-2450nm spectral region and note its wavelength position.

4. Look this wavelength up in the spectral library index and identify which spectral group the spectrum belongs to.

5· Go to that spectral group page in the spectral library.

6. Looking at 2050-2450nm spectral region, take into account other absorption features and compare the unknown spectrum with each of the spectra of this spectral group. Identify the spectrum with the closest match to your unknown.

7. Turn to the page of the closest match. Take into account other absorption features between 1300-2050nm (areas 2 to 4 as shown on Fig. VID - 1) and cross check your identification to confirm similarities with the library spectrum, and to make a final distinction between spectrally similar minerals.

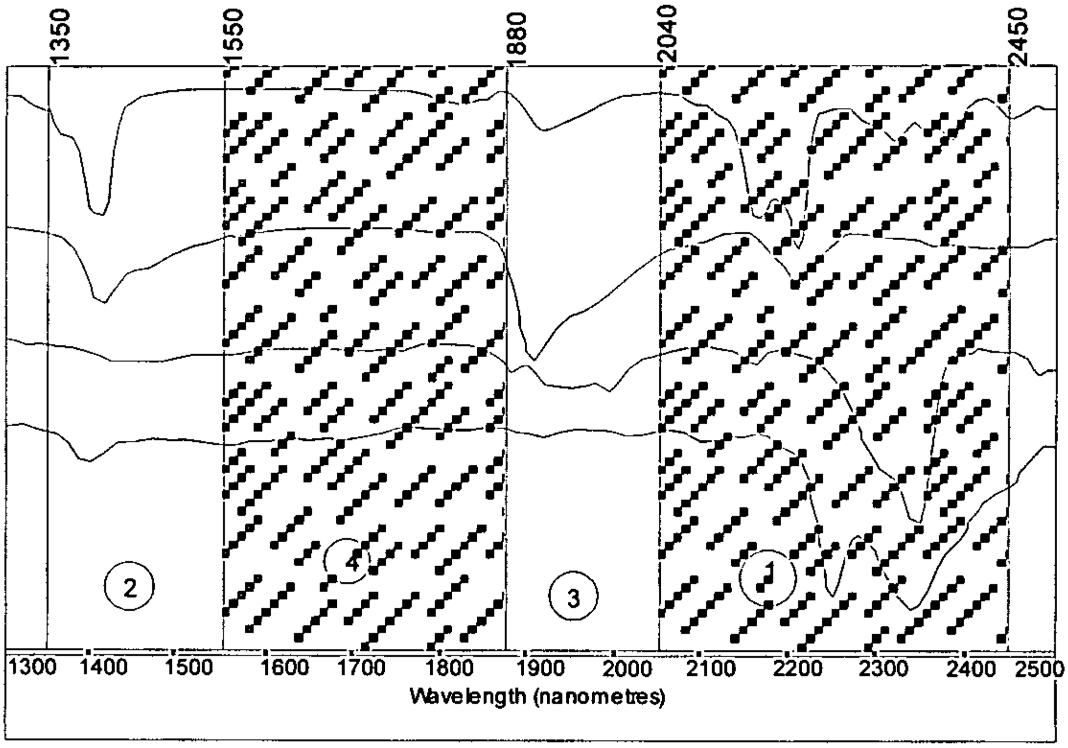

② Compare the absorptions (shapes and wavelengths) in this part of spectrum to help/confirm identification

④ Look at this wavelength region last for other diagnostic absorptions of sulphates and diaspore

③ Look at the depth & shape of any water absorption to identify water-bearing minerals

① Most diagnostic wavelength region
Look here first to make interpretation
1. Pick out DEEPEST absorption
2. Note wavelength
3. Search in spectral library
4. Compare shapes/wavelengths of other features in this spectral region

Figure VID - 1. Structured approach to spectral interpretation (source: Pontual et al., 1997a)

6.5 *Appendix VI – E*

Mineral identification using PIMA spectrometer

The following minerals are the most common in the study area. The following description of the absorption features and the albedo are summarised from the Spectra file information at the PimaView software.

Anhydrite spectra are typically noisy with a highly variable albedo. Trace water absorption is often noted at 1450nm and 1940nm. Weak absorption is noted in the vicinity of 2325nm.

Anhydrite is a principal component of evaporite sequences, and is also found as an accessory mineral in carbonate facies. It may also be found as an alteration product of carbonates and in high sulphidation environments.

Halloysite spectra are very similar to those of kaolinite, with the following differences:

Halloysite bears a large water feature at 1912nm

The 1400nm doublet of halloysite has rounded shoulders in comparison to kaolinite.

The sharpness of the 1400nm and 2200nm doublets of halloysite is weak in comparison to those of kaolinites.

The definition of halloysite auxiliary absorptions in the 2320nm - 2400nm range is very weak in comparison to those noted in kaolinite spectra.

Halloysite is a hydrated pseudomorph of kaolinite, typically found as a weathering product of aluminous minerals

Hornblende spectra show strong Fe {+2} absorption, coupled with 2316nm and 2380nm absorptions. Significant amounts of Fe may be identified by the shoulder at 2250nm.

Hornblende occurs in a wide range of igneous environments ranging from ultra-basic to acid and alkali, but is characteristic of plutonic rocks of intermediate composition. It is also a common constituent of regional metamorphic environments.

Kaolinite is identified by distinctive doublets at:

1395nm and 1412nm

2160nm and 2208nm

Supplementary absorptions are also noted in the 2320nm - 2400nm range.

An indication of kaolinite crystallinity may be gained by an assessment of the doublets. In crystalline kaolinite, these features are well defined as separate absorptions, whereas in poorly crystalline (and halloysite), the shorter wavelength feature tends to appear as a shoulder to the longer wavelength feature.

Kaolinite has two major modes of occurrence; as an alteration product of hydrothermal systems, and as a weathering product of aluminous mineralogies.

Montmorillonite is identified by strong asymmetric 1418nm absorption and a large asymmetric water feature at 1910nm. Al absorption is noted at 2208nm.

Montmorillonite is a weathering product of ferro-magnesian minerals with the retention of Mg.

Nontronite is identified by strong asymmetric 1430nm absorption and a large asymmetric water feature at 1910nm. Major absorption is noted at 2280nm.

Nontronite is a Mg rich member of the smectitic clays, and occurs in weathering of strongly magnesian minerals with the retention of Mg.

Phengitic muscovite spectra tend to bear broad Fe{+2} absorption at shorter wavelengths. The main muscovite absorption is noted in the vicinity of 2210nm-2240nm.

Accessory absorptions are noted at 2345nm and 2435nm, with a variably developed minor absorption at 2115nm.

Phengite is a Fe-Mg rich muscovite, which is typically found inn hydrothermal alteration environments.

Talc has a well defined 1390nm feature, with a diagnostic doublet at 2290nm and 2310nm.

Accessory features are noted at 2390nm and 2460nm, and in the range 2080nm - 2230nm.

Talc occurs as a hydrothermal alteration product or a hydrated metamorphic product of ultramafic lithologies.

Tremolite spectra lack the broad Fe {2+} absorption at shorter wavelengths noted in other amphiboles. Moderate to strong 1400nm absorption is noted, and the 1900nm water absorption is weak to absent. Major mineralogical absorptions are noted in the vicinity of 2335nm and 2400nm.

Tremolite is typically identified in metamorphic assemblages of calc-silicate lithologies.

The table VIE – 1 show the main three minerals in each sample, the proportion of mixture in percentage and the confidence percentage of the spectral analysis. The analyses with confidence percentage less than 90 were rejected.

Table VIE -1. Summary of the mineral identification using spectral analysis

Sample no.	**Minerals**			**Mixture %**	**Confidence%**
Shear zones near the contact between the Bulawayan and Shamvaian					
Sp8/01/99	Anhydrite	Talc	Halloysite	53-24-24	94.55
Sp8/02/99	Anhydrite	Talc	Kaolinite	52-28-20	90.37
Sp8/03/99	Anhydrite	Talc	Kaolinite	61-23-17	94.25
Sp8/04/99	Talc	Kaolinite		64-36	53.92
Sp8/05/99	Anhydrite	Talc	Kaolinite	49-34-17	91.48
Sp8/06/99	Anhydrite	Kaolinite	Talc	57-26-17	91.55
Sp8/07/99	Anhydrite	Halloysite	Talc	48-36-16	94.42
Sp8/08/99	Kaolinite	Talc	Hornblende	51-35-14	37.53
Sp8/09/99	Anhydrite	Kaolinite		52-48	83.36
Sp8/10/99	Halloysite	Anhydrite	Kaolinite	55-44-1	96.20
Sp8/11/99	Anhydrite	Halloysite	Kaolinite	56-43-2	96.04
Sp/GF/01	Anhydrite	Water	Kaolinite	48-34-18	97.26
Sp/GF/02	Anhydrite	Talc	Halloysite	54-28-18	95.13
Sp/GF/03	Anhydrite	Talc	Kaolinite	64-24-12	94.21
Sp/GF/04	Water	Talc	Kaolinite	64-23-13	88.35
Sp/GF/05	Anhydrite	Halloysite	Talc	59-24-18	95.60
Sp/GF/06	Anhydrite	Talc	Kaolinite	60-27-13	92.96
Sp/GF/07	Anhydrite	Halloysite	Talc	55-27-17	96.63
Sp6/01/99	Anhydrite	Halloysite	Talc	58-26-16	97.26
Sp6/02/99	Water	Halloysite	Talc	60-22-17	91.76
Sp6/03/99	Anhydrite	Water	Talc	53-31-16	94.81
Sp6/04/99	Anhydrite	Halloysite	Water	61-20-19	95.76
Sp6/05/99	Anhydrite	Halloysite		69-31	95.30
Sp6/06/99	Anhydrite	Halloysite	Water	61-21-17	96.81
Sp6/07/99	Anhydrite	Halloysite	Talc	64-22-14	96.84
Sp6/08/99	Anhydrite	Halloysite	Water	62-20-18	96.51
Sp4/01/99	Anhydrite	Talc	Halloysite	55-31-14	95.75
Sp4/02/99	Anhydrite	Talc	Halloysite	53-32-16	95.34
Sp4/03/99	Anhydrite	Halloysite	Talc	62-20-18	96.59
Sp4/04/99	Anhydrite	Halloysite	Talc	61-22-17	96.86
Sp4/05/99	Anhydrite	Water	Halloysite	58-30-12	97.14
Sp4/06/99	Anhydrite	Halloysite		75-25	94.45
Sp4/07/99	Anhydrite	Halloysite	Tremolite	56-35-9	90.92
Sp4/08/99	Anhydrite	Water	Halloysite	54-30-16	97.99
Shear zones near the contact between Bulawayan and granites					
Sp1/1/001	Anhydrite	Halloysite		51-49	91.97
Sp1/1/002	Anhydrite	Halloysite	Kaolinite	54-33-13	92.37
Sp1/1/003	Halloysite	Anhydrite	Kaolinite	43-41-17	92.90
Sp1/1/004	Anhydrite	Halloysite	Kaolinite	56-36-9	93.25
Sp1/1/005	Anhydrite	Kaolinite		52-48	88.11
Sp1/1/006	Halloysite	Anhydrite	Kaolinite	56-26-19	94.28

Sp1/1/007	Halloysite	Anhydrite	Kaolinite	48-33-20	93.87
Sp1/1/008	Water	Anhydrite	Halloysite	54-28-17	98.68
Sp1/1/010	Water	Anhydrite	Halloysite	52-29-18	98.79
Sp1/1/011	Anhydrite	Halloysite	Kaolinite	46-35-19	91.67
Sp1/1/012	Anhydrite	Halloysite	Kaolinite	55-36-9	94.36
Shear zones near the Penhalonga granodiorite					
026/Sp/Rw	Halloysite	Anhydrite		56-44	92.36
027/Sp/Rw	Anhydrite	Halloysite	Talc	50-28-22	94.64
028/Sp/Rw	Anhydrite	Halloysite	Talc	42-42-16	94.16
029/Sp/Rw	Anhydrite	Halloysite		52-48	94.07
030/Sp/Rw	Anhydrite	Halloysite	Talc	46-38-16	95.00
031/Sp/Rw	Anhydrite	Halloysite	Talc	48-37-15	95.29
032/Sp/Rw	Anhydrite	Halloysite		54-46	93.24
033/Sp/Rw	Anhydrite	Halloysite		51-49	94.12
034/Sp/Rw	Anhydrite	Halloysite	Hornblande	49-27-24	94.09
035/Sp/Rw	Anhydrite	Hornblande	Halloysite	44-30-26	93.52
036/Sp/Rw	Anhydrite	Halloysite	Nontronite	49-33-18	92.68
037/Sp/Rw	Anhydrite	Halloysite		53-47	92.68
038/Sp/Rw	Anhydrite	Halloysite	Tremolite	47-33-20	94.37
039/Sp/Rw	Talc	Halloysite	Anhydrite	36-33-31	92.97
040/Sp/Rw	Halloysite	Anhydrite		58-42	93.82
041/Sp/Rw	Halloysite	Anhydrite		58-42	94.40
042/Sp/Rw	Anhydrite	Halloysite	Nontronite	49-39-12	95.07
Felsic intrusion within the Bulawayan e.g. the Penhalonga Granodiorite					
RED2/01/99	Anhydrite	Talc	Halloysite	46-35-19	93.67
RED2/02/99	Anhydrite	Halloysite	Tremolite	54-25-21	95.65
RED2/04/99	Anhydrite	Halloysite	Kaolinite	52-37-11	92.85
RED2/05/99	Anhydrite	Halloysite	Kaolinite	52-41-7	93.86
RED2/06/99	Anhydrite	Halloysite		52-48	95.71
RED2/07/99	Halloysite	Anhydrite	Kaolinite	41-31-28	91.22
RED2/08/99	Anhydrite	Halloysite	Kaolinite	38-32-29	86.98
RED2/09/99	Anhydrite	Halloysite	Kaolinite	38-37-24	91.55
RED2/10/99	Halloysite	Anhydrite	Kaolinite	48-41-11	94.43
RED2/11/99	Anhydrite	Halloysite	Tremolite	43-42-14	96.86
RED2/12/99	Halloysite	Anhydrite		55-45	96.93
RED2/13/99	Not	Identifiable			?Alunite
RED2/14/99	Anhydrite	Halloysite	Tremolite	64-31-5	87.44
RED2/15/99	Anhydrite	Halloysite	Tremolite	63-19-18	89.38
RED2/16/99	Anhydrite	Talc		54-46	80.08
RED2/17/99	Anhydrite	Halloysite	Kaolinite	55-35-9	92.54
RED2/18/99	Halloysite	Water	Anhydrite	40-34-27	98.99
RED2/19/99	Anhydrite	Halloysite	Kaolinite	43-40-17	92.24
RED2/20/99	Halloysite	Anhydrite	Kaolinite	46-35-18	92.99
RED2/21/99	Water	Halloysite	Kaolinite	55-39-6	96.23
RED2/22/99	Anhydrite	Halloysite	Kaolinite	48-40-13	92.52
RED2/23/99	Anhydrite	Halloysite	Kaolinite	52-37-11	93.53
RED2/24/99	missing				
RED2/25/99	Halloysite	Anhydrite	Kaolinite	45-33-23	92.64
RED2/26/99	Halloysite	Anhydrite	Kaolinite	51-26-23	91.68
RED2/27/99	Anhydrite	Halloysite	Water	50-40-10	97.31
RED2/28/99	Halloysite	Anhydrite	Kaolinite	46-29-25	92.62
RED2/29/99	Halloysite	Anhydrite	Kaolinite	50-40-10	95.10
RED2/30/99	Anhydrite	Halloysite	Kaolinite	43-43-14	93.16
RED2/31/99	Anhydrite	Water	Halloysite	44-31-25	98.75
RED2/32/99	Water	Anhydrite	Halloysite	40-32-28	98.92
RED2/33/99	Anhydrite	Halloysite	Water	50-29-21	98.46
RED2/34/99	missing				

RED2/35/99	missing				
RED2/36/99	missing				
RED2/37/99	Halloysite	Anhydrite	Kaolinite	37-35-28	90.79
RED2/38/99	Missing				
RED2/39/99	Halloysite	Anhydrite	Kaolinite	50-33-16	87.01
RED2/40/99	Halloysite	Anhydrite	Kaolinite	48-32-20	91.14
RED2/41/99	Kaolinite	Prengite		78-22	86.70
RED2/42/99	Anhydrite	Halloysite	Kaolinite	45-38-17	93.03
RED2/43/99	Anhydrite	Halloysite	Kaolinite	44-36-20	89.90
Shear Zones within the Shamvaian					
Sp7/01/99	Anhydrite	Kaolinite		71-29	83.01
Sp7/02/99	Anhydrite	Water	Halloysite	55-24-21	97.62
SP7/03/99	Anhydrite	Hornblende	Halloysite	49-27-25	94.20
Sp7/04/99	Water	Anhydrite	Tremolite	62-30-7	98.06
SP7/05/99	Anhydrite	Halloysite	Tremolite	70-20-10	97.01
SP7/06/99	Anhydrite	Water	Halloysite	61-27-12	96.30
SP7/07/99	Anhydrite	Halloysite		77-23	96.38
SP7/08/99	Anhydrite	Halloysite	Tremolite	53-38-9	94.35
SP7/09/99	Anhydrite	Halloysite	Tremolite	64-25-11	96.39
SP7/10/99	Anhydrite	Water	Tremolite	46-40-14	96.10

Appendix VII

On this appendix more results of the comparison between the PIMA reflectance values and the TM and ETM reflectance values on the band 5 and 7 are present.

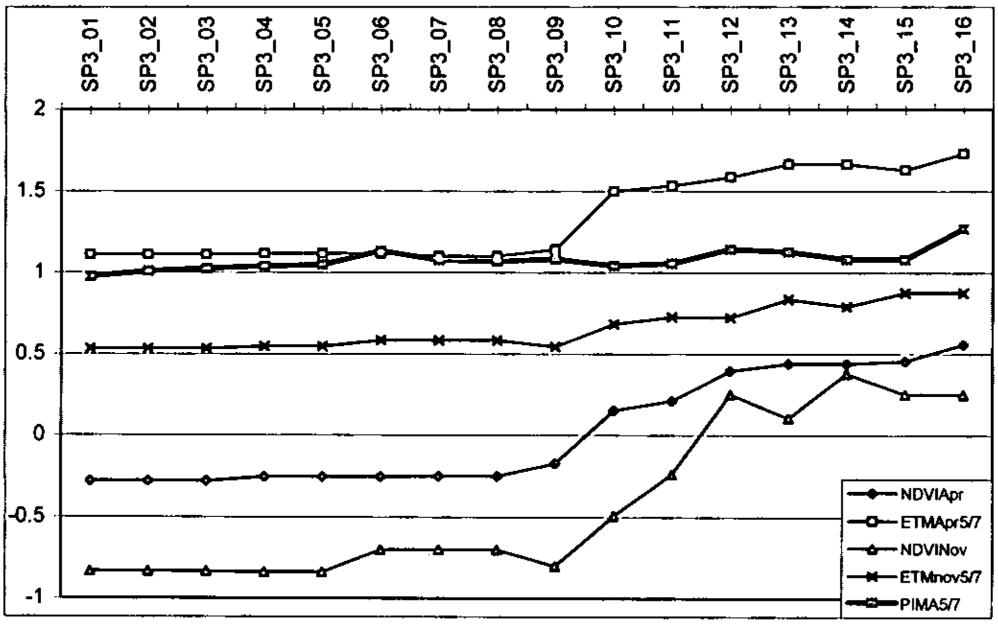

Figure VIIA – 1. Graphical representation of the ratios ETM Nov., ETM Apr. and PIMA bands 5 and 7 and, NDVI April and November for the soil profile SP3

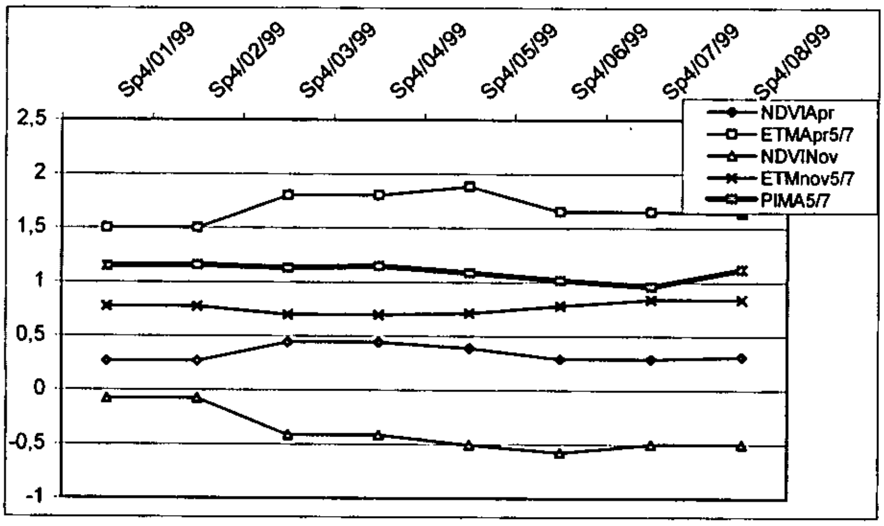

Figure VIIA - 2 - Graphical representation of the ratios ETM Nov., ETM Apr. and PIMA bands 5 and 7 and, NDVI April and November for the soil profile SP4

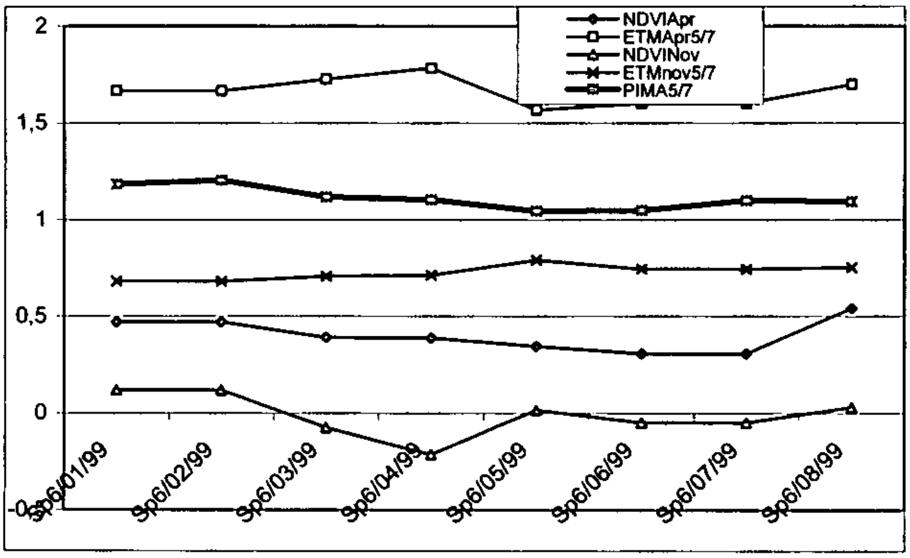

Figure VIIA – 3. Graphical representation of the ratios ETM Nov., ETM Apr. and PIMA bands 5 and 7 and, NDVI April and November for the soil profile SP6

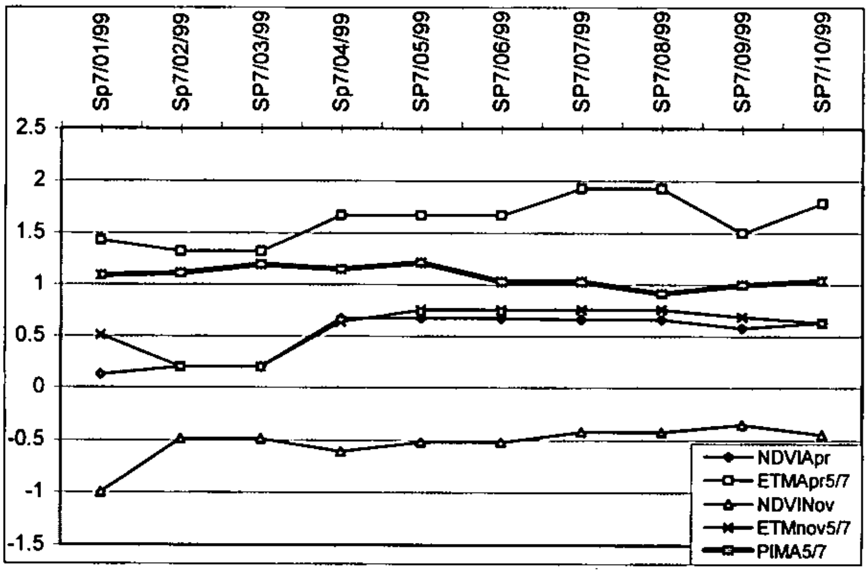

Figure VIIA – 4. Graphical representation of the ratios ETM Nov., ETM Apr. and PIMA bands 5 and 7 and, NDVI April and November for the soil profile SP7

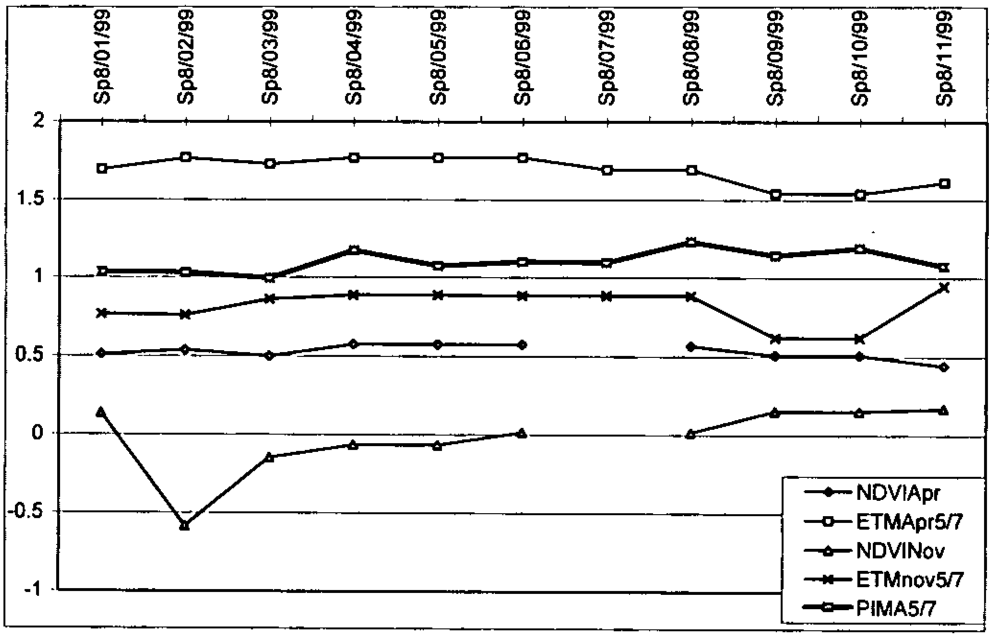

Figure VIIA – 5. Graphical representation of the ratios ETM Nov., ETM Apr. and PIMA bands 5 and 7 and, NDVI April and November for the soil profile SP8

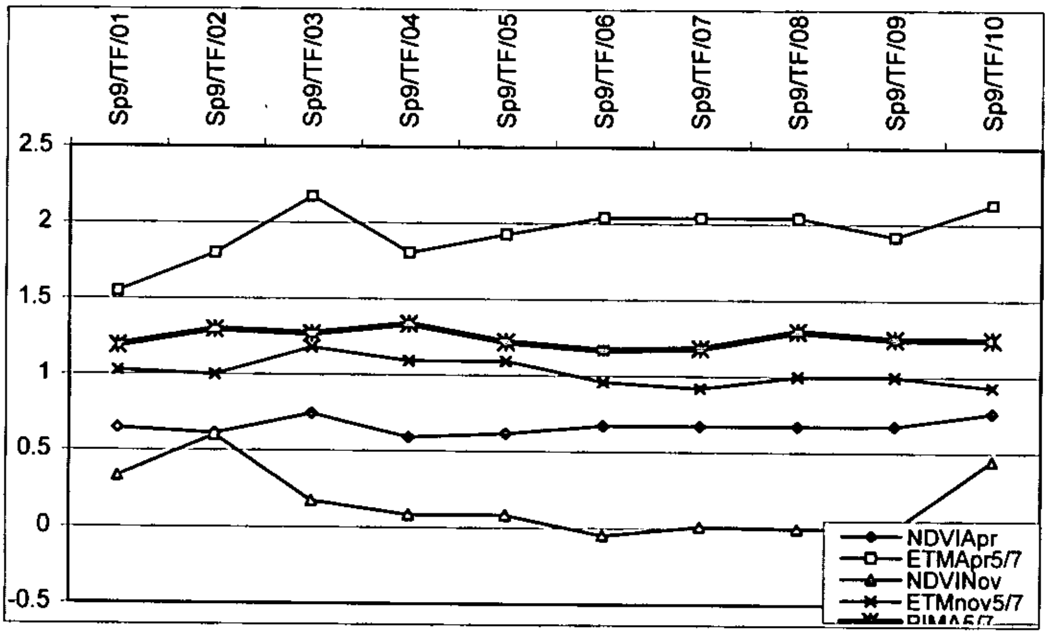

Figure VIIA – 6. Graphical representation of the ratios ETM Nov., ETM Apr. and PIMA bands 5 and 7 and, NDVI April and November for the soil profile SP9

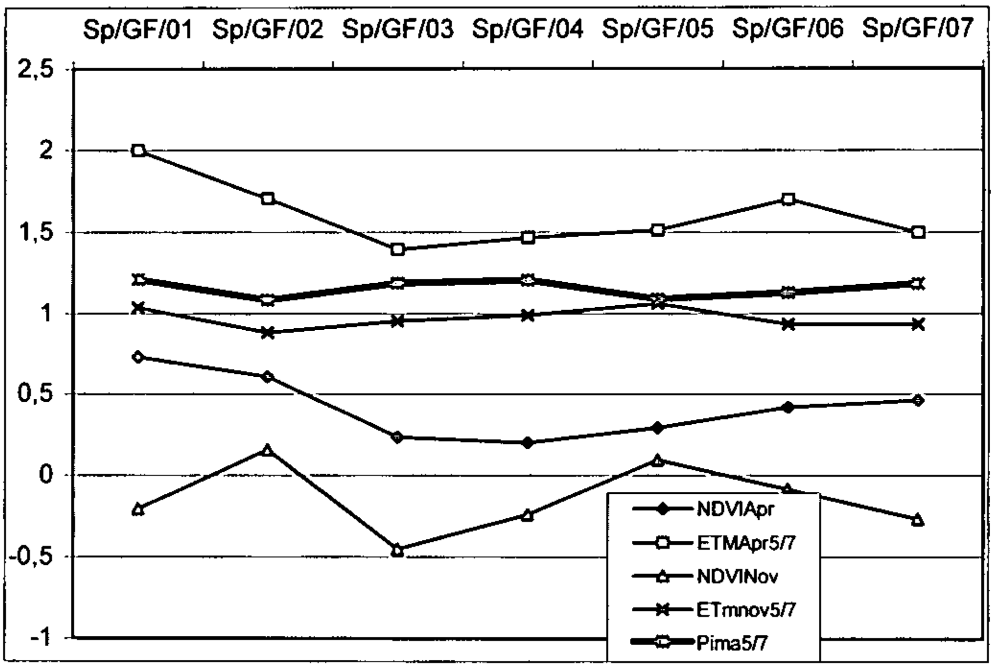

Figure VIIA – 7. Graphical representation of the ratios ETM Nov., ETM Apr. and PIMA bands 5 and 7 and, NDVI April and November for the soil profile SPGF

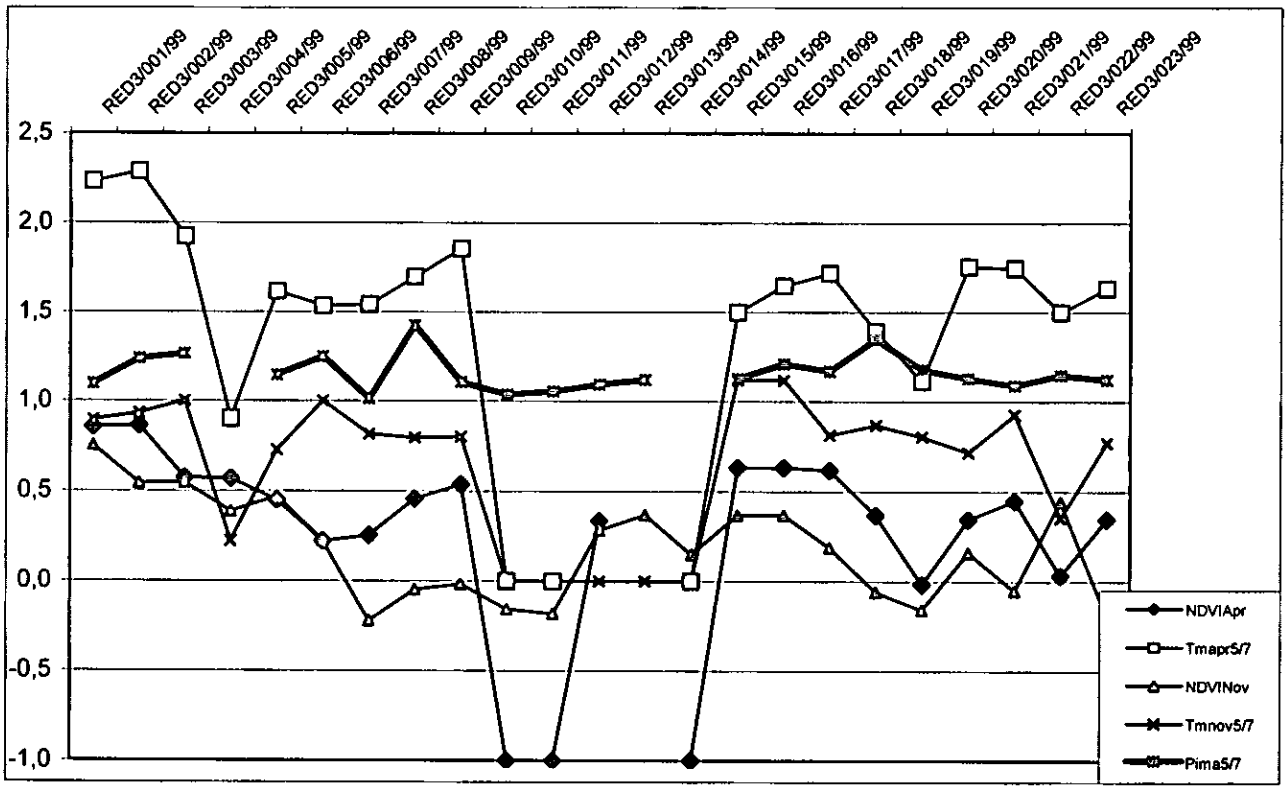

Figure VIIA – 8. Graphical representation of the ratios ETM Nov., ETM Apr. and PIMA bands 5 and 7 and, NDVI April and November for the soil profile SPRW3

APPENDIX VIIB

LIST OF SAMPLES

Position	In UTM	Code			25-Apr-00				17-Nov-99				Soils PIMA-	Soils 1%smooth		Rocks	Rocks		Powders	Powders	
X	Y	Designation	Sample type	Observations	ETM7	ETM5	NDVI	ETM5/ETM7	ETM7	ETM5	NDVI	ETM5/ETM7	2225	1650	1650/2225	2225.00	1650.00	1650/2225	2225.00	1650.00	1650/2225
462825	7912607	001/A/Rw	Top soil - wall face	Redwing Mine	18	29	0	1.61	41	30	0	0.73									
462825	7912607	001/B/Rw	Top soil - wall face	Redwing Mine	18	29	0	1.61	41	30	0	0.73									
462825	7912607	001/C/Rw	Top soil - wall face	Redwing Mine	18	29	0	1.61	41	30	0	0.73									
462825	7912607	001/D/Rw	Top soil - wall face	Redwing Mine	18	29	0	1.61	41	30	0	0.73									
462825	7912607	001/E/Rw	Top soil - wall face	Redwing Mine	18	29	0	1.61	41	30	0	0.73									
462825	7912607	001/F/Rw	Top soil - wall face	Redwing Mine	18	29	0	1.61	41	30	0	0.73									
462825	7912607	001/G/Rw	Top soil - wall face	Redwing Mine	18	29	0	1.61	41	30	0	0.73									
462825	7912607	001/H/Rw	Top soil - wall face	Redwing Mine	18	29	0	1.61	41	30	0	0.73									
462825	7912607	001/I/Rw	Top soil - wall face	Redwing Mine	18	29	0	1.61	41	30	0	0.73									
462825	7912607	001/J/Rw	Top soil - wall face	Redwing Mine	18	29	0	1.61	41	30	0	0.73									
462825	7912607	001/K/Rw	Top soil - wall face	Redwing Mine	18	29	0	1.61	41	30	0	0.73									
462825	7912607	001/L/Rw	Top soil - wall face	Redwing Mine	18	29	0	1.61	41	30	0	0.73	47	53	1.14						
462985	7914579	002/ore/Rw	Ore from the Dump	Redwing Mine				#DIV/0!				#DIV/0!			#DIV/0!						
462985	7914579	002/Ore/Rw	Ore from the Dump	Redwing Mine				#DIV/0!				#DIV/0!			#DIV/0!						
462985	7914579	002/Ore/Rw	Ore from the Dump	Redwing Mine				#DIV/0!				#DIV/0!	52	62	1.18						
464280	7914290	003/Gr/Rw		Redwing Mine	22	31	0	1.41	79	68	0	0.86	41	66	1.62						
464291	7914265	004/Sp/Rw	Top soil	Redwing Mine	25	35	0	1.40	73	64	0	0.88			#DIV/0!						
464291	7914265	005/Sp/Rw	Top soil	Redwing Mine	25	35	0	1.40	73	64	0	0.88			#DIV/0!						
464291	7914265	005A/Sp/Rw	Top soil	Redwing Mine	25	35	0	1.40	73	64	0	0.88			#DIV/0!						
464289	7914255	006/S-Sp/Rw	Top soil	Redwing Mine	25	35	0	1.40	73	64	0	0.88	28	27	0.96						
464290	7914245	007/S-Sp/Rw	Top soil	Redwing Mine	24	36	0	1.50	73	64	0	0.88	27	28	0.96						
464288	7914235	008/Sp/Rw	Top soil	Redwing Mine	24	36	0	1.50	70	65	0	0.93			#DIV/0!						
464289	7914225	009/ /Rw	Top soil	Redwing Mine	24	36	0	1.50	70	65	0	0.93			#DIV/0!						
464287	7914215	010/S. Gr/Rw		Redwing Mine	27	43	0	1.59	70	65	0	0.93	31	28	0.90						
464285	7914205	011/S.Gr/Rw		Redwing Mine	27	43	0	1.59	66	65	0	0.98	26	26	1.00						
464280	7914190	012/Sp/Rw	Top soil	Redwing Mine	26	40	0	1.54	66	64	0	0.97			#DIV/0!						
464300	7914100	013/?/Rw		Redwing Mine	20	32	0	1.60	65	58	0	0.89	36	38	1.04						
464114	7914050	014/?/Rw		Redwing Mine	35	49	0	1.40	63	61	0	0.96	28	27	0.96						
464130	7914000	015/?/Rw		Redwing Mine	35	51	0	1.46	80	76	0	0.95			#DIV/0!						
464135	7913950	016/?/Rw		Redwing Mine	27	44	0	1.63	84	70	0	0.83			#DIV/0!						
464142	7913920	017/?/Rw		Redwing Mine	21	36	0	1.71	75	67	0	0.89	33	35	1.03						
464100	7913895	018/?/Rw		Redwing Mine	35	54	0	1.54	82	73	0	0.89	37	37	1.02						
464092	7913822	019/sch/Rw		Redwing Mine	19	37	0	1.95	72	57	0	0.79	45	49	1.10						
464090	7913780	020/Talc/Rw		Redwing Mine	22	34	0	1.55	65	52	0	0.80	41	43	1.06						
464080	7913720	021/Qz/Rw		Redwing Mine	19	32	0	1.68	58	40	-1	0.69	47	61	1.29						
464074	7913632	22/Seric.sch/Rw		Redwing Mine	49	57	0	1.16	84	79	0	0.94	40	40	1.02						
464011	7913611	023/BIF/Rw		Redwing Mine	44	52	0	1.18	71	70	0	0.99	30	47	1.54						
463977	7913526	024/Soil/Rw	Top soil	Redwing Mine	54	69	0	1.28	70	78	0	1.11	28	27	0.97						
463890	7913390	025/?/Rw		Redwing Mine	56	62	0	1.11	81	68	0	0.84	37	52	1.38						
462854	7912539	026/Mrock./Rw		Redwing Mine	29	43	0	1.48	43	40	0	0.93	36	36	1.01						
463016	7912459	027/chl./Rw		Redwing Mine	33	52	0	1.58	40	37	0	0.93	32	31	0.99						
463016	7912429	028/Sp/Rw	Top soil	Redwing Mine	28	46	0	1.64	41	32	0	0.78	32	32	1.01						
463016	7912399	029/Sp/Rw	Top soil	Redwing Mine	20	29	0	1.45	43	27	0	0.63	36	37	1.03						
463062	7912374	030/Sp/Rw	Top soil	Redwing Mine	22	35	0	1.59	42	29	0	0.69	36	37	1.04						
463108	7912350	031/Sp/Rw	Top soil	Redwing Mine	35	57	0	1.63	50	48	0	0.96	34	35	1.03						
463157	7912329	032/Sp/Rw	Top soil	Redwing Mine	41	61	0	1.49	60	63	0	1.05			#DIV/0!						
463094	7912307	033/Sp/Rw	Top soil	Redwing Mine	22	35	0	1.59	60	51	0	0.85	32	33	1.03						
463150	7912280	034/Sp/Rw	Top soil	Redwing Mine	35	55	0	1.57	69	66	0	0.96	42	43	1.03						
463197	7912255	035/Sp/Rw	Top soil	Redwing Mine	38	61	0	1.61	54	49	0	0.91	44	47	1.07						
463245	7912235	036/Sp/Rw	Top soil	Redwing Mine	36	56	0	1.56	73	64	0	0.88	38	41	1.08						
463264	7912210	037/Sp/Rw	Top soil	Redwing Mine	34	54	0	1.59	60	52	0	0.87	37	39	1.04						
463315	7912185	038/Sp/Rw	Top soil	Redwing Mine	31	55	0	1.77	67	58	0	0.87	39	41	1.06						
463338	7912160	039/Sp/Rw	Top soil	Redwing Mine	32	54	0	1.69	59	49	0	0.83	35	38	1.08						
463325	7912135	040/Sp/Rw	Top soil	Redwing Mine	32	54	0	1.69	59	49	0	0.83	34	35	1.04						
463386	7912110	041/Sp/Rw	Top soil	Redwing Mine	30	50	0	1.67	57	51	0	0.89	33	35	1.04						
463428	7912085	042/Sp/Rw	Top soil	Redwing Mine	31	52	0	1.68	48	39	0	0.81	36	37	1.03						
479686	7918612	01/Cantao/99		Cantao	33	62	1	1.88	93	82	0	0.88									
479603	7918707	02/Cantao/99		Cantao	14	28	1	2.00	29	29	1	1.00									
479603	7918707	03/Cantao/99		Cantao	14	28	1	2.00	29	29	1	1.00									
479605	7918749	04/Cantao/99		Cantao	17	35	1	2.06	38	36	0	0.95									
479605	7918749	05/Cantao/99		Cantao	17	35	1	2.06	38	36	0	0.95									

499728	7918488	99MN011		Cantao	8	6	0	1.00	69	34	-1	0.49			
479882	7918752	Sp1/1/001	Top soil	Cantao	31	46	0	1.48	96	83	0	0.86	42	49	1.17
479837	7918744	Sp1/1/002	Top soil	Cantao	27	49	1	1.81	77	79	0	1.03	36	41	1.13
479690	7918695	Sp1/1/004	Top soil	Cantao	10	13	1	1.30	38	41	0	1.08	36	44	1.21
479680	7918685	Sp1/1/005	Top soil	Cantao	10	13	1	1.30	51	52	0	1.02	40	44	1.10
479650	7918680	Sp1/1/006	Top soil	Cantao	18	34	1	1.89	51	50	0	0.98	38	45	1.19
479600	7918682	Sp1/1/007	Top soil	Cantao	18	38	1	2.11	32	34	1	1.06	47	63	1.35
479590	7918660	Sp1/1/008	Top soil	Cantao	18	38	1	2.11	32	34	1	1.06	41	52	1.29
479560	7918679	Sp1/1/009	Top soil	Cantao	17	39	1	2.29	47	48	0	1.02	19	26	1.38
479490	7918676	Sp1/1/010	Top soil	Cantao	37	59	0	1.59	63	75	0	0.90	20	27	1.33
479480	7918678	Sp1/1/011	Top soil	Cantao	41	58	0	1.41	60	42	0	0.84	33	39	1.18
479462	7918665	Sp1/1/012	Top soil	Cantao	35	56	0	1.60	69	62	0	0.88	34	40	1.18
478267	7919071	01/Wed-Maro/99			29	46	1	1.59	96	68	-1	0.71			
488170	7920414	01/Braga/99		Felsic tuff	27	48	1	1.78	59	47	0	0.80			
480534	7918841	99MN030		Old-Wednesday U/G	9	11	0	1.22	96	93	0	0.97			
480534	7918841	99MN031		Old-Wednesday U/G	9	11	0	1.22	96	93	0	0.97			
480534	7918841	99MN032		Old-Wednesday U/G	9	11	0	1.22	96	93	0	0.97			
480534	7918841	99MN033		Old-Wednesday U/G	9	11	0	1.22	96	93	0	0.97			
480534	7918841	99MN034		Old-Wednesday U/G	9	11	0	1.22	96	93	0	0.97			
481140	7917847	01/Chua/99		Chua	4	3	0	0.75	10	0	0	0.00			
481166	7917762	99MN035		Chua	18	30	0	1.67	65	64	0	0.83			
481140	7917847	99MN036		Chua	4	3	0	0.75	10	0	0	0.00			
493151	7910697	Sp7/01/99	Top soil	B. Esperance	35	50	0	1.43	69	35	-1	0.51	42	46	1.09
493151	7910723	Sp7/02/99	Top soil	B. Esperance	25	33	0	1.32	30	6	0	0.20	23	26	1.11
493151	7910743	SP7/03/99	Top soil	B. Esperance	25	33	0	1.32	30	6	0	0.20	29	35	1.19
493151	7910783	Sp7/04/99	Top soil	B. Esperance	15	25	1	1.67	69	44	-1	0.64	48	55	1.15
493151	7910793	SP7/05/99	Top soil	B. Esperance	15	25	1	1.67	73	55	-1	0.75	21	25	1.21
493151	7910803	SP7/06/99	Top soil	B. Esperance	15	25	1	1.67	73	55	-1	0.75	31	32	1.03
493151	7910818	SP7/07/99	Top soil	B. Esperance	14	27	1	1.93	70	53	0	0.76	24	25	1.03
493151	7910838	SP7/08/99	Top soil	B. Esperance	14	27	1	1.93	70	53	0	0.76	32	29	0.92
493151	7910858	SP7/09/99	Top soil	B. Esperance	16	24	1	1.50	61	42	0	0.69	32	32	1.00
493151	7910873	SP7/10/99	Top soil	B. Esperance	14	25	1	1.79	60	38	0	0.63	30	31	1.04
493071	7910626	99MN027		B. Esperance	26	43	0	1.65	66	39	-1	0.59			
477124	7907232	99MN017		Saymour U/G	47	72	0	1.53	56	39	0	0.70			
477124	7907232	99MN018		Saymour U/G	47	72	0	1.53	56	39	0	0.70			
477124	7907232	99MN019		Saymour U/G	47	72	0	1.53	56	39	0	0.70			
477124	7907232	99MN020		Saymour U/G	47	72	0	1.53	56	39	0	0.70			
477124	7907232	99MN021		Saymour U/G	47	72	0	1.53	56	39	0	0.70			
476832	7910713	Sp5/01/99	Top soil	Fair Bride	20	36	0	1.80	43	33	0	0.77	31	32	1.04
486832	7910696	Sp5/02/99	Top soil	Fair Bride	20	36	0	1.80	43	33	0	0.77	22	23	1.01
486832	7910680	Sp5/03/99	Top soil	Fair Bride	24	42	0	1.76	48	35	0	0.73	29	30	1.05
486832	7910665	Sp5/04/99	Top soil	Fair Bride	24	42	0	1.76	48	35	0	0.73	28	29	1.03
486832	7910645	Sp5/05/99	Top soil	Fair Bride	26	45	0	1.73	72	53	0	0.74	33	35	1.06
486905	7910626	Sp5/06/99	Top soil	Fair Bride	24	45	0	1.88	52	40	0	0.77	32	36	1.12
486905	7910608	Sp5/07/99	Top soil	Fair Bride	24	45	0	1.88	62	40	0	0.77	36	42	1.17
486922	7910554	Sp5/08/99	Top soil	Fair Bride	17	33	1	1.94	42	28	0	0.67	33	36	1.10
486830	7910542	Sp6/01/99	Top soil	Fair Bride	18	30	0	1.67	44	30	0	0.68	32	38	1.18
486830	7910567	Sp6/02/99	Top soil	Fair Bride	18	30	0	1.67	44	30	0	0.68	30	36	1.21
486830	7910592	Sp6/03/99	Top soil	Fair Bride	22	38	0	1.73	62	44	0	0.71	29	32	1.12
486846	7910606	Sp6/04/99	Top soil	Fair Bride	23	41	0	1.76	63	45	0	0.71	28	30	1.10
486795	7910640	Sp6/05/99	Top soil	Fair Bride	30	47	0	1.57	53	42	0	0.79	34	36	1.05
486795	7910665	Sp6/06/99	Top soil	Fair Bride	25	40	0	1.60	63	47	0	0.75	24	25	1.05
486795	7910690	Sp6/07/99	Top soil	Fair Bride	25	40	0	1.60	63	47	0	0.75	25	28	1.10
486784	7910723	Sp6/08/99	Top soil	Fair Bride	20	34	1	1.70	63	40	0	0.75	26	28	1.10
486063	7910275	Sp4/01/99	Top soil	Try Again	12	18	0	1.50	44	34	0	0.77	24	28	1.15
486063	7910290	Sp4/02/99	Top soil	Try Again	12	18	0	1.50	44	34	0	0.77	27	31	1.16
486063	7910305	Sp4/03/99	Top soil	Try Again	15	27	0	1.80	73	51	0	0.70	26	30	1.13
486063	7910320	Sp4/04/99	Top soil	Try Again	15	27	0	1.80	73	51	0	0.70	28	32	1.16
486063	7910335	Sp4/05/99	Top soil	Try Again	17	32	0	1.88	84	60	-1	0.71	16	16	1.09
486050	7910408	Sp4/06/99	Top soil	Try Again	26	43	0	1.65	102	80	-1	0.78	32	32	1.02
486050	7910423	Sp4/07/99	Top soil	Try Again	26	43	0	1.65	100	84	-1	0.84	34	32	0.97
486050	7910438	Sp4/08/99	Top soil	Try Again	25	41	0	1.64	100	84	-1	0.84	28	31	1.12
481424	7910584	Sp8/01/99	Top soil	Dot's Luck	23	39	1	1.70	30	23	0	0.77	39	41	1.03
481515	7910599	Sp8/02/99	Top soil	Dot's Luck	26	46	1	1.77	67	51	-1	0.76	41	42	1.03
481515	7910614	Sp8/03/99	Top soil	Dot's Luck	26	45	1	1.73	51	44	0	0.86	38	37	0.99
481535	7910629	Sp8/04/99	Top soil	Dot's Luck	22	39	1	1.77	54	48	0	0.89	48	56	1.17

481546	7910618	Sp8/05/99	Top soil	Dot's Luck	22	39	1	1.77	54	48	0	0.89	44	47	1.08						
481546	7910633	Sp8/06/99	Top soil	Dot's Luck	22	39	1	1.77	44	39	0	0.89	43	47	1.10						
481546	7910648	Sp8/07/99	Top soil	Dot's Luck	23	39		1.70	44	39		0.89	42	46	1.10						
481546	7910648	Sp8/08/99	Top soil	Dot's Luck	23	39	1	1.70	44	39	0	0.89	44	54	1.23						
481509	7910755	Sp8/09/99	Top soil	Dot's Luck	24	37	1	1.54	29	18	0	0.62	47	54	1.14						
481521	7910766	Sp8/10/99	Top soil	Dot's Luck	24	37	1	1.54	29	18	0	0.62	31	37	1.19						
481453	7910877	Sp8/11/99	Top soil	Dot's Luck	13	21	0	1.62	40	38	0	0.95	25	26	1.08						
493261	7910964	99/MN023		Dot's Luck	10	16	1	1.60	61	28	-1	0.46			#DIV/0!						
480414	7917700	Sp9/TF/01	Top soil	Two Foots	31	48	1	1.55	40	41	0	1.03	28	34	1.19						
480424	7917650	Sp9/TF/02	Top soil	Two Foots	30	54	1	1.80	28	28	1	1.00	33	43	1.30						
480435	7917600	Sp9/TF/03	Top soil	Two Foots	23	50	1	2.17	72	85	0	1.18	26	32	1.27						
480462	7917577	Sp9/TF/04	Top soil	Two Foots	31	56	1	1.81	75	82	0	1.09	31	42	1.34						
480470	7917550	Sp9/TF/05	Top soil	Two Foots	27	52	1	1.93	75	82	0	1.09	29	35	1.22						
480475	7917500	Sp9/TF/06	Top soil	Two Foots	24	49	1	2.04	75	72	0	0.96	37	44	1.17						
480487	7917475	Sp9/TF/07	Top soil	Two Foots	24	49	1	2.04	76	70	0	0.92	37	44	1.18						
480490	7917450	Sp9/TF/08	Top soil	Two Foots	24	49	1	2.04	71	71	0	1.00	28	37	1.30						
480495	7917430	Sp9/TF/09	Top soil	Two Foots	25	48	1	1.92	71	71	0	1.00	30	37	1.25						
480485	7917404	Sp9/TF/10	Top soil	Two Foots	23	49	1	2.13	43	40	0	0.93	29	35	1.24						
486970	7912944	99MN054	Mine	Guy Fawkes	18	36	1	2.00	55	57	0	1.04									
486970	7912994	99MN055	Mine	Guy Fawkes	17	29	1	1.71	42	37	0	0.88									
487035	7913144	Sp/GF/01	Top soil	Guy Fawkes	38	53	0	1.39	104	99	0	0.95	26	31	1.21						
487000	7913110	Sp/GF/02	Top soil	Guy Fawkes	45	66	0	1.47	102	101	0	0.99	33	35	1.06						
486984	7913099	Sp/GF/03	Top soil	Guy Fawkes	37	56	0	1.51	48	51	0	1.06	34	41	1.19						
486860	7913037	Sp/GF/04	Top soil	Guy Fawkes	10	17	0	1.70	45	42	0	0.93	29	35	1.21						
486830	7913000	Sp/GF/05	Top soil	Guy Fawkes	12	18	0	1.50	45	42	0	0.93	31	34	1.09						
486971	7913051	Sp/GF/06	Top soil	Guy Fawkes	26	45	0	1.73	52	55	0	1.06	36	41	1.13						
486800	7913010	Sp/GF/07	Top soil	Guy Fawkes	11	14	0	1.27	71	49	-1	0.69	34	41	1.19						
471940	7912512	99MN049		Monarch	11	16	1	1.45	16	0	0	0.00	48	59	1.22						
471506	7912517	99MN050		Monarch	11	18	1	1.64	10	0	1	0.00									
471153	7912550	99MN052		Monarch	2	1	1	0.50	22	17	1	0.77									
471140	7912604	99MN053		Monarch	7	14	1	2.00	42	34	0	0.81									
471259	7912637	01/monarch/99	milling site/several bl	Monarch	8	6	1	0.75	16	8	1	0.50									
471140	7912754	Sp10/01/99	Top soil	Monarch	0	0	-1	#DIV/0!	7	0	1	0.00	17	21	1.27						
471135	7912670	Sp10/02/99	Top soil	Monarch	1	1	1	1.00	20	9	1	0.45	17	25	1.43						
471152	7912695	Sp10/03/99	Top soil	Monarch	1	1	1	1.00	10	0	1	0.00	18	22	1.28						
471263	7912695	Sp10/04/99	Top soil	Monarch	17	35	1	2.06	15	2	1	0.13	16	23	1.41						
473282	7914316	99MN037		Revue	11	18	1	1.64	5	0	1	0.00	41	51	1.25						
473276	7914314	99MN038		Revue	11	18	1	1.64	6	0	1	0.00									
473270	7914312	99MN039		Revue	11	18	1	1.64	6	0	1	0.00									
473259	7914310	99MN040		Revue	10	15	1	1.50	6	0	1	0.00									
473325	7914094	99MN041		Revue	18	30	1	1.68	48	33	0	0.69									
473324	7914074	99MN042		Revue	12	21	1	1.75	16	3	0	0.19									
473323	7914063	99MN043		Revue	16	30	1	1.88	16	3	0	0.19									
473320	7914050	99MN044		Revue	14	26	1	1.86	22	14	1	0.64									
473323	7914040	99MN045		Revue	17	33	1	1.94	22	14	1	0.64									
473322	7914030	99MN046		Revue	17	33	1	1.94	22	14	1	0.64									
473323	7914028	99MN047		Revue	17	33	1	1.94	14	0	1	0.00									
473290	7914027	99MN048		Revue	19	35	1	1.84	10	0	0	0.00									
487882	7908690	MAP1/01/99		Profile S-N	32	54	0	1.69	121	128	0	1.06									
487879	7908729	MAP1/02/99		Profile S-N	64	110	0	1.31	124	128	0	1.03	41	52	1.28						
487880	7908749	MAP1/03/99		Profile S-N	64	110	0	1.31	113	115	0	1.02	49	57	1.18	11.94	23.67	1.98	45.96	57.33	
487880	7908749	MAP1/03b/99			63	108	0	1.30	154	156	0	1.01				14.90	25.72	1.73			
487882	7908769	MAP1/04/99		Profile S-N	63	108	0	1.30	154	156	0	1.01									
487881	7908789	MAP1/05/99		Profile S-N	71	92	0	1.30	154	156	0	1.01									
487883	7908800	MAP1/06/99		Profile S-N	71	92	0	1.30	116	116	0	0.98									
487880	7908820	MAP1/07/99		Profile S-N	110	134	0	1.22	116	116	0	0.98									
487885	7908850	MAP1/08/99		Profile S-N	114	134	0	1.18	74	51	-1	0.69									
487886	7908870	MAP1/09/99		Profile S-N	66	87	0	1.32	73	38	-1	0.52									
487883	7908888	MAP1/10/99		Profile S-N	66	87	0	1.32	73	38	-1	0.52									
487884	7909010	MAP1/11/99		Profile S-N	40	57	0	1.43	82	58	-1	0.71									
487880	7909016	MAP1/12/99		Profile S-N	40	57	0	1.43	82	58	-1	0.71				17.36	23.89	1.38	45.53	49.27	1.08
487880	7909016	MAP1/12b/99			40	57	0	1.43	82	58	-1	0.71				12.94	18.04	1.39			
487880	7909020	MAP1/13/99		Profile S-N	32	51	0	1.59	82	58	-1	0.71									
487882	7909061	MAP1/14/99		Profile S-N	27	44	0	1.63	80	62	-1	0.78									
487883	7909690	MAP1/15/99		Profile S-N	38	56	0	1.53	89	94	0	1.06									
487885	7909695	MAP1/16/99		Profile S-N	38	56	0	1.53	89	94	0	1.06									

487686	7909720	MAP1/17/99		Profile S-N	32	51	0	1.59	93	96	0	1.03									
487688	7909760	MAP1/18/99		Profile S-N	35	49	0	1.40	59	61	0	1.03				23.63	24.92	1.05	45.43	44.67	0.98
487686	7909760	MAP1/18b/99			35	49	0	1.40	59	61	0	1.03				14.89	16.06	1.08			
487686	7909760	MAP1/18c/99			35	49	0	1.40	59	61	0	1.03				19.61	21.68	1.09			
487680	7909698	MAP1/19/99		Profile S-N	37	50	0	1.38	46	51	0	1.11									
487685	7909997	MAP1/20/99		Profile S-N	29	41	0	1.41	32	34	0	1.06									
467346	7914336	RED3/001/99	Top soil	Redwing	13	29	1	2.23	19	17	1	0.89	36	40	1.10						
467364	7914309	RED3/002/99	Top soil	Redwing	7	16	1	2.29	29	27	1	0.93	43	54	1.24						
467454	7914292	RED3/003/99	Top soil	Redwing	26	50	1	1.92	31	31	1	1.00	38	48	1.26						
467354	7914230	RED3/004/99	Top soil	Redwing	10	9	1	0.90	18	4	0	0.22			#DIV/0!						
467343	7914126	RED3/005/99	Top soil	Redwing	13	21	0	1.62	22	16	0	0.73	38	44	1.15						
467229	7914159	RED3/006/99	Top soil	Redwing	28	43	0	1.54	36	36	0	1.00	34	42	1.25						
467165	7914045	RED3/007/99	Top soil	Redwing	24	37	0	1.54	66	54	0	0.82	26	26	1.01						
467205	7913952	RED3/008/99	Top soil	Redwing	20	34	0	1.70	54	43	0	0.80	51	72	1.43						
467190	7913957	RED3/009/99	Top soil	Redwing	21	39	1	1.86	51	41	0	0.80	37	41	1.11						
467126	7913850	RED3/010/99	Top soil	Redwing	2	0	-1	0.00	5	0	0	0.00	23	24	1.04						
467127	7913820	RED3/011/99	Top soil	Redwing	1	0	-1	0.00	9	0	0	0.00	26	27	1.05						
467184	7913799	RED3/012/99	Top soil	Redwing	0	0	0	#DIV/0!	11	0	0	0.00	25	27	1.09						
467179	7913749	RED3/013/99	Top soil	Redwing	0	0 ?		#DIV/0!	8	0	0	0.00	26	30	1.12						
467230	7913668	RED3/014/99	Top soil	Redwing	3	0	-1	0.00	13	0	0	0.00			#DIV/0!						
467292	7913624	RED3/015/99	Top soil	Redwing	20	30	1	1.50	42	47	0	1.12	26	29	1.13						
467292	7913624	RED3/016/99	Top soil	Redwing	20	33	1	1.65	42	47	0	1.12	33	40	1.21						
466937	7913740	RED3/017/99	Top soil	Redwing	26	43	1	1.72	43	35	0	0.81	26	30	1.17						
467495	7913265	RED3/018/99	Top soil	Redwing	23	32	0	1.39	69	60	0	0.87	41	55	1.36						
467625	7913234	RED3/019/99	Top soil	Redwing	45	50	0	1.11	82	66	0	0.80	35	41	1.18						
467709	7912811	RED3/020/99	Top soil	Redwing	25	44	0	1.76	32	23	0	0.72	37	41	1.13						
467729	7912779	RED3/021/99	Top soil	Redwing	24	42	0	1.75	41	38	0	0.93	34	36	1.09						
467735	7912564	RED3/022/99	Top soil	Redwing	24	36	0	1.50	17	6	0	0.35	35	41	1.15						
467768	7912544	RED3/023/99	Top soil	Redwing	22	36	0	1.64	66	51	0	0.77	33	37	1.12						
464306	7914044	RED2/01/99	Top soil	Redwing	22	34	0	1.55	64	60	0	0.94	32	32	1.02						
464755	7914128	RED2/02/99	Top soil	Redwing	20	32	0	1.60	54	52	0	0.96	30	30	1.02						
464755	7914128	RED2/03/99	Top soil	Redwing	20	32	0	1.60	54	52	0	0.96			#DIV/0!						
465027	7914142	RED2/04/99	Top soil	Redwing	22	25	-1	1.14	66	51	-1	0.78	37	39	1.06						
465028	7914183	RED2/05/99	Top soil	Redwing	22	25	-1	1.14	66	51	-1	0.78	31	32	1.00						
465026	7914167	RED2/06/99	Top soil	Redwing	14	12	-1	0.86	65	51	-1	0.78	34	39	1.14						
465026	7914142	RED2/07/99	Top soil	Redwing	14	12	-1	0.86	69	53	-1	0.77	40	48	1.21						
465026	7914117	RED2/08/99	Top soil	Redwing	15	20	-1	1.33	69	53	-1	0.77	39	47	1.20						
465026	7914100	RED2/09/99	Top soil	Redwing	21	34	0	1.62	69	53	-1	0.77	38	44	1.16						
465037	7914090	RED2/10/99	Top soil	Redwing	15	21	-1	1.40	60	45	-1	0.75	40	45	1.15						
465077	7914070	RED2/11/99	Top soil	Redwing	13	17	-1	1.31	63	51	0	0.81	40	49	1.23						
465059	7914022	RED2/12/99	Top soil	Redwing	12	19	0	1.58	50	37	0	0.74	37	44	1.18						
465071	7913958	RED2/13/99	Top soil	Redwing	15	27	0	1.80	52	38	0	0.73	20	19	0.91						
465097	7913865	RED2/14/99	Top soil	Redwing	22	36	0	1.64	55	49	0	0.89	27	26	0.97						
465097	7913835	RED2/15/99	Top soil	Redwing	19	29	0	1.53	57	51	0	0.89	28	27	0.97						
465127	7913818	RED2/16/99	Top soil	Redwing	17	28	0	1.63	57	46	0	0.81	34	35	1.04						
465167	7913750	RED2/17/99	Top soil	Redwing	14	21	0	1.50	36	36	0	1.00	32	33	1.01						
465182	7913625	RED2/18/99	Top soil	Redwing	20	37	0	1.85	45	43	0	0.96	25	28	1.12						
465193	7913526	RED2/19/99	Top soil	Redwing	24	44	0	1.83	86	76	0	0.88	42	44	1.05						
465419	7913454	RED2/20/99	Top soil	Redwing	21	27	0	1.29	59	47	0	0.80	35	40	1.13						
465203	7913366	RED2/21/99	Top soil	Redwing	80	76	-1	0.95	123	98	0	0.80	34	42	1.25						
465281	7913239	RED2/22/99	Top soil	Redwing	57	68	0	1.19	88	86	0	0.98	33	36	1.07						
465316	7913196	RED2/23/99	Top soil	Redwing	20	33	1	1.65	70	68	0	0.97	39	41	1.04						
465320	7913180	RED2/24/99	Top soil	Redwing	20	33	1	1.65	74	74	0	1.00			#DIV/0!						
465325	7913142	RED2/25/99	Top soil	Redwing	30	50	0	1.67	91	87	0	0.96	38	43	1.11						
465325	7913127	RED2/26/99	Top soil	Redwing	30	50	0	1.67	91	87	0	0.96	35	38	1.09						
465394	7913015	RED2/27/99	Top soil	Redwing	27	44	0	1.63	75	62	0	0.83	34	35	1.03						
465434	7913006	RED2/28/99	Top soil	Redwing	25	41	0	1.64	59	49	0	0.83	38	43	1.13						
465409	7912964	RED2/29/99	Top soil	Redwing	29	49	0	1.69	86	74	0	0.86	35	39	1.11						
465409	7912900	RED2/30/99	Top soil	Redwing	25	42	0	1.68	89	82	0	0.92	34	36	1.06						
465519	7912885	RED2/31/99	Top soil	Redwing	32	54	0	1.69	80	83	0	1.04	21	21	1.00						
465519	7912879	RED2/32/99	Top soil	Redwing	32	54	0	1.69	80	83	0	1.04	21	24	1.12						
465519	7912869	RED2/33/99	Top soil	Redwing	42	67	0	1.60	80	83	0	1.04	27	29	1.06						
465593	7912856	RED2/34/99	Top soil	Redwing	22	39	1	1.77	92	82	0	0.89			#DIV/0!						
465712	7912687	RED2/35/99	Top soil	Redwing	24	41	1	1.71	23	14	1	0.61			#DIV/0!						
465590	7912152	RED2/36/99	Top soil	Redwing	24	47	1	1.96	85	73	0	0.86			#DIV/0!						
466163	7911838	RED2/37/99	Top soil	Redwing	14	24	1	1.71	17	7	1	0.41	41	45	1.11						

465106	7911793	RED2/38/99	Top soil	Redwing	13	26	1	2.00	12	5	1	0.42			#DIV/0!						
465935	7911710	RED2/39/99	Top soil	Redwing	17	30	1	1.76	22	16	1	0.73	36	37	1.01						
465639	7911685	RED2/40/99	Top soil	Redwing	29	46	0	1.59	28	21	0	0.75	37	40	1.09						
465746	7911660	RED2/41/99	Top soil	Redwing	22	41	0	1.86	38	29	0	0.76	52	70	1.35						
465746	7911635	RED2/42/99	Top soil	Redwing	24	40	0	1.67	26	18	0	0.69	37	41	1.11						
465594	7911585	RED2/43/99	Top soil	Redwing	22	36	0	1.64	30	20	0	0.67	40	42	1.05						
481625	7909041	SP2_01	Soil profile	Road to Mondungwara	45	61	0	1.36	72	71	0	0.99	38	43	1.12						
481625	7909041	SP2_02	Soil profile	Road to Mondungwara	45	61	0	1.36	72	71	0	0.99	34	43	1.26						
481625	7909041	SP2_03	Soil profile	Road to Mondungwara	45	61	0	1.36	72	71	0	0.99	34	46	1.34						
481625	7909041	SP2_04	Soil profile	Road to Mondungwara	45	61	0	1.36	72	71	0	0.99	40	58	1.47						
481625	7909041	SP2_05	Soil profile	Road to Mondungwara	45	61	0	1.36	72	71	0	0.99	38	56	1.48						
481626	7909075	SP2_06	Top soil	Road to Mondungwara	28	46	0	1.64	49	45	0	0.92	42	44	1.05						
481624	7909065	SP2_07	Top soil	Road to Mondungwara	28	46	0	1.64	72	71	0	0.99	36	43	1.20						
481626	7909055	SP2_08	Mafic schist	Road to Mondungwara	28	46	0	1.64	72	71	0	0.99			#DIV/0!						
481624	7909045	SP2_09	Quartz vein	Road to Mondungwara	45	61	0	1.36	72	71	0	0.99			#DIV/0!						
476936	7907104	SP3_01	Bear soil	Isltaca Mountain	48	51	0	1.11	62	33	-1	0.53	21	20	0.97						
476940	7907106	SP3_02	Bear soil	Isltaca Mountain	48	51	0	1.11	62	33	-1	0.53	22	22	1.01						
476944	7907108	SP3_03	Bear soil	Isltaca Mountain	48	51	0	1.11	62	33	-1	0.53	20	21	1.02						
476948	7907110	SP3_04	Bear soil	Isltaca Mountain	52	58	0	1.12	64	35	-1	0.55	24	25	1.04						
476952	7907112	SP3_05	Bear soil	Isltaca Mountain	52	58	0	1.12	64	35	-1	0.55	23	24	1.05						
476956	7907114	SP3_06	Bear soil	Isltaca Mountain	52	58	0	1.12	65	38	-1	0.58	26	30	1.13						
476960	7907116	SP3_07	Bear soil	Isltaca Mountain	50	55	0	1.10	65	38	-1	0.58	26	27	1.07						
476964	7907118	SP3_08	Bear soil	Isltaca Mountain	50	55	0	1.10	65	38	-1	0.58	23	25	1.07						
476954	7907152	SP3_09	Serpentinite	Isltaca Mountain	50	57	0	1.14	66	36	-1	0.55	25	27	1.08						
477093	7907219	SP3_10	Serpentinite	Isltaca Mountain	48	72	0	1.50	54	37	0	0.69	18	18	1.04						
477042	7907051	SP3_11	Serpentinite	Isltaca Mountain	45	69	0	1.53	48	35	0	0.73	19	21	1.05						
477307	7907562	SP3_12	Serpentinite	Isltaca Mountain	34	54	0	1.59	40	29	0	0.73	35	40	1.14						
477248	7907429	SP3_13	Serpentinite	Isltaca Mountain	36	60	0	1.67	43	36	0	0.84	30	33	1.13						
477348	7907429	SP3_14	Serpentinite	Isltaca Mountain	36	60	0	1.67	29	23	0	0.79	26	28	1.08						
477628	7907047	SP3_15	Serpentinite	Isltaca Mountain	38	62	0	1.63	41	36	0	0.88	28	31	1.08						
477628	7907045	SP3_16	Serpentinite	Isltaca Mountain	30	52	1	1.73	41	36	0	0.88	31	40	1.27						
476431	7907889	RED3/001/100	Top soil	Redwing	13	29	1	2.23	19	17	1	0.89									
476581	7907802	RED3/002/100	Top soil	Redwing	7	16	1	2.29	29	27	1	0.93	45	64	1.43						
476730	7907716	RED3/003/100	Top soil	Redwing	26	50	1	1.92	31	31	1	1.00	36	51	1.35						
476880	7907630	RED3/004/100	Top soil	Redwing	10	9	1	0.90	18	4	0	0.22	34	53	1.53						
477030	7907543	RED3/005/100	Top soil	Redwing	13	21	0	1.62	22	16	0	0.73	17	25	1.43						
477180	7907457	RED3/006/100	Top soil	Redwing	28	43	0	1.54	36	36	0	1.00	34	31	0.90						
477330	7907371	RED3/007/100	Top soil	Redwing	24	37	0	1.54	66	54	0	0.82	36	37	0.99						
477480	7907284	RED3/008/100	Top soil	Redwing	20	34	0	1.70	54	43	0	0.80				28.34	27.80	0.98			
477630	7907198	RED3/009/100	Top soil	Redwing	21	39	1	1.86	51	41	0	0.80				59.62	64.62	1.08			
477779	7907112	RED3/010/100	Top soil	Redwing	2	0	-1	0.00	6	0	0	0.00				50.04	50.93	1.02			
477929	7907026	RED3/011/100	Top soil	Redwing	1	0	-1	0.00	9	0	0	0.00				5.66	6.00	1.06			
478079	7906939	RED3/012/100	Top soil	Redwing	0	0	0	#DIV/0!	11	0	0	0.00				7.25	7.90	1.09			
464250	7914190	R_12c_SP_RW	Float		26	40	0	1.54	66	64	0	0.97				6.55	5.49	0.99			
488822	7913802	R_B01_00			17	34	1	2.00	59	46	0	0.78				56.79	69.27	1.18	50.07	52.75	1.05
488822	7913802	R_B01b_00			17	34	1	2.00	59	46	0	0.78				54.74	64.34	1.18			#DIV/0!
491796	7914736	R_B03_00			22	45	1	2.05	36	32	1	0.89				6.05	9.44	1.56	31.36	38.16	1.22
491796	7914736	R_B03b_00			22	45	1	2.05	36	32	1	0.89				6.21	9.82	1.58	40.16	51.04	1.27
491796	7914736	R_B03c_00			22	45	1	2.05	36	32	1	0.89				21.69	35.25	1.63			#DIV/0!
466325	7910154	R_B21_00			25	48	1	1.92	55	53	0	0.96				15.88	15.96	1.00			#DIV/0!
466325	7910154	R_B21b_00			25	48	1	1.92	55	53	0	0.96				20.49	18.80	0.92			#DIV/0!
443065	7906144	R_B25_00			31	47	0	1.52	95	82	-1	0.86				10.53	12.91	1.23	45.72	52.26	1.14
443065	7906144	R_B25b_00			31	47	0	1.52	95	82	-1	0.86				10.99	13.52	1.23			#DIV/0!
466260	7912222	R_B26_00			29	45	0	1.55	51	38	0	0.75				20.52	29.07	1.42	49.58	58.64	1.18
466260	7912222	R_B26b_00			29	45	0	1.55	51	38	0	0.75				24.32	32.75	1.35			#DIV/0!
466288	7912320	R_B27_00			16	25	0	1.39	46	27	0	0.59				12.60	10.91	0.87	31.19	23.09	0.74
466288	7912320	R_B27b_00			16	25	0	1.39	46	27	0	0.59				11.03	10.94	0.99			#DIV/0!
466748	7911935	R_B28_00			9	24	1	2.67	6	0	1	0.00				8.28	7.82	0.94	16.12	15.73	0.98
466748	7911935	R_B28b_00			9	24	1	2.67	6	0	1	0.00				6.50	6.32	0.98			#DIV/0!
466813	7911938	R_B29_00			17	26	1	1.53	11	0	0	0.00						#DIV/0!	16.29	16.59	1.02
466881	7911940	R_B30_00			16	32	1	2.00	13	0	1	0.00				11.63	10.32	0.89			#DIV/0!
466881	7911940	R_B30b_00			16	32	1	2.00	13	0	1	0.00				14.59	13.19	0.90			#DIV/0!
465405	7914010	R_B31_00			26	46	0	1.77	54	49	0	0.91				8.39	8.54	1.02			#DIV/0!
465405	7914010	R_B31b_00			26	46	0	1.77	54	49	0	0.91				7.90	7.58	0.96			#DIV/0!
467517	7911643	R_B32_00			6	14	1	2.33	2	0	1	0.00				17.78	27.54	1.55	41.22	49.52	1.20

467517	7911643	R_B32b_00		6	14	1	2.33	2	0	1	0.00	11.81	13.85	1.17			#DIV/0!
457045	7909970	R_B33_00		14	23	1	1.64	29	22	0	0.76	25.43	39.89	1.57	42.62	47.66	1.11
457045	7909970	R_B33b_00		14	23	1	1.64	29	22	0	0.76	21.98	35.57	1.62			#DIV/0!
456844	7909945	R_B34_00		26	46	0	1.77	52	50	0	0.96	9.12	10.26	1.13			#DIV/0!
456844	7909945	R_B34b_00		26	46	0	1.77	52	50	0	0.96	9.25	10.51	1.14			#DIV/0!
454705	7912386	R_B37_00		18	30	0	1.67	51	45	0	0.88	6.65	8.46	1.27			#DIV/0!
454705	7912386	R_B37b_00		18	30	0	1.67	51	45	0	0.88	7.00	8.73	1.25			#DIV/0!
461358	7914549	R_B38_00		17	18	-1	1.06	57	47	0	0.82	21.98	29.45	1.34	43.31	48.23	1.11
461358	7914549	R_B38b_00		17	18	-1	1.06	57	47	0	0.82	27.51	36.46	1.33			#DIV/0!
461338	7914143	R_B40_00		22	36	1	1.64	69	56	0	0.81	13.22	16.10	1.22	44.60	50.41	1.13
461159	7913903	R_B41_00		19	24	0	1.26	63	48	0	0.76	15.69	17.66	1.11	32.01	33.73	1.06
461159	7913903	R_B41b_00		19	24	0	1.26	63	48	0	0.76	17.97	20.65	1.15			#DIV/0!
461113	7913236	R_B42_00		30	32	-1	1.07	66	45	0	0.68	8.45	9.57	1.13			#DIV/0!
461113	7913236	R_B42b_00		30	32	-1	1.07	66	45	0	0.68	8.91	10.12	1.14			#DIV/0!
447766	7908917	R_B46_00		27	38	0	1.41	62	60	0	0.97	6.99	6.51	0.93			#DIV/0!
447766	7908917	R_B46b_00		27	38	0	1.41	62	60	0	0.97	6.24	5.61	0.90			#DIV/0!
446990	7908480	R_B47_00		53	68	-1	1.28	88	63	-1	0.72	7.38	8.26	1.12	18.70	21.23	1.14
446990	7908480	R_B47b_00		53	68	-1	1.28	88	63	-1	0.72	8.08	10.83	1.34			#DIV/0!
445615	7908112	R_B48_00		19	31	0	1.63	40	34	0	0.85			#DIV/0!	31.43	35.04	1.11
444977	7907789	R_B49_00		13	20	0	1.54	92	74	-1	0.80	12.78	12.60	1.00			#DIV/0!
444977	7907789	R_B49b_00		13	20	0	1.54	92	74	-1	0.80	8.50	9.44	1.11			#DIV/0!
450696	7911025	R_B50_00		26	40	0	1.54	70	69	0	0.99	28.59	39.48	1.38	46.40	51.39	1.11
450696	7911025	R_B50b_00		26	40	0	1.54	70	69	0	0.99	29.33	39.84	1.36			#DIV/0!
454277	7909562	R_B51_00		27	39	0	1.44	63	63	0	1.00	17.61	24.07	1.37	40.49	46.57	1.15
454277	7909562	R_B51b_00		27	39	0	1.44	63	63	0	1.00	6.26	6.95	1.11			#DIV/0!
444632	7906704	R_B52_00		21	35	0	1.67	53	45	0	0.85	6.26	6.95	1.11	36.44	41.88	1.15
444632	7906704	R_B52b_00		21	35	0	1.67	53	45	0	0.85	8.85	10.70	1.21			#DIV/0!
444856	7906149	R_B53_00		27	42	0	1.56	68	32	-1	0.47	10.50	12.97	1.24	43.50	52.32	1.20
444856	7906149	R_B53a_00		27	42	0	1.56	68	32	-1	0.47	16.92	25.90	1.53	40.12	45.38	1.13
444856	7906149	R_B53ab_00		27	42	0	1.56	68	32	-1	0.47	19.32	29.53	1.53			#DIV/0!
444856	7906149	R_B53b_00		27	42	0	1.56	68	32	-1	0.47	13.14	16.52	1.26			#DIV/0!
445113	7906104	R_B54_00		27	38	0	1.41	61	46	-1	0.57	8.33	8.03	0.97	17.43	19.81	1.14
445113	7906104	R_B54a_00		27	38	0	1.41	61	46	-1	0.57	5.93	5.24	0.88			#DIV/0!
445113	7906104	R_B54ab_00		27	38	0	1.41	61	46	-1	0.57	6.93	7.35	0.82			#DIV/0!
445113	7906104	R_B54b_00		27	38	0	1.41	61	46	-1	0.57	8.88	8.61	0.97			#DIV/0!
443771	7906223	R_B55_00		27	42	0	1.56	66	61	0	0.92	27.78	42.74	1.54	51.62	58.84	1.14
443771	7906223	R_B55b_00		27	42	0	1.56	66	61	0	0.92	14.37	18.67	1.30			#DIV/0!
445844	7905611	R_B56_00		17	20	-1	1.18	61	63	0	1.02	21.60	22.93	1.06	16.17	16.12	1.00
445844	7905611	R_B56b_00		17	20	-1	1.18	61	63	0	1.02	20.91	20.90	1.00			#DIV/0!
451246	7906414	R_B59_00		21	38	0	1.81	51	43	0	0.84	12.93	11.18	0.87	16.17	16.12	1.00
456045	7905598	R_B60_00		28	43	0	1.54	33	27	0	0.82	14.30	11.73	0.82			#DIV/0!
456045	7905598	R_B60b_00		28	43	0	1.54	33	27	0	0.82	11.49	9.62	0.84			#DIV/0!
459668	7906398	R_B63_00		31	40	0	1.29	41	41	0	1.00	21.05	29.36	1.40	39.47	47.46	1.20
459668	7906398	R_B63b_00		31	40	0	1.29	41	41	0	1.00	15.63	16.07	1.03			#DIV/0!
463313	7914024	R_B64_00		24	39	0	1.63	76	47	-1	0.62	9.00	9.39	1.04	32.25	34.96	1.08
463313	7914024	R_B64b_00		24	39	0	1.63	76	47	-1	0.62	7.99	8.37	1.05			#DIV/0!
467265	7914140	R_B67_00		13	21	1	1.62	38	36	0	0.95	10.13	12.58	1.24			#DIV/0!
467265	7914140	R_B67b_00		13	21	1	1.62	38	36	0	0.95	13.76	17.40	1.26			#DIV/0!
466406	7914973	R_B68_00		1	0	1	0.00	5	0	1	0.00	8.61	9.31	1.08			#DIV/0!
466406	7914973	R_B68b_00		1	0	1	0.00	5	0	1	0.00	8.19	7.29	0.89			#DIV/0!
463336	7906461	R_B69_00		28	44	0	1.57	35	30	0	0.86	24.48	29.34	1.20	21.95	20.40	0.93
463336	7906461	R_B69b_00		28	44	0	1.57	35	30	0	0.86	12.06	11.36	0.94			#DIV/0!
469779	7908767	R_B70_00		4	2	1	0.50	13	3	1	0.23	35.21	48.69	1.39	47.55	56.14	1.18
469779	7908767	R_B70b_00		4	2	1	0.50	13	3	1	0.23	35.79	47.33	1.32			#DIV/0!
461093	7905174	R_B72_00		24	43	0	1.79	69	63	0	0.91	11.41	11.30	0.99	35.97	36.47	1.01
461093	7905174	R_B72b_00		24	43	0	1.79	69	63	0	0.91	17.08	17.62	1.03			#DIV/0!
493242	7910879	R_BoaEsperan	Main pit	20	35	1	1.75	52	38	0	0.73	27.47	39.45	1.44			#DIV/0!
488170	7920414	R_Braganca_1	Shaft	27	48	1	1.78	59	47	0	0.80	23.32	30.29	1.30	62.11	66.99	1.08
488236	7920460	R_Braganca_3	Small adit	21	36	1	1.71	82	93	0	1.13	14.44	21.01	1.46	42.25	44.98	1.06
488150	7920514	R_Braganca_5	Small adit	18	35	1	1.94	42	39	0	0.93	12.67	12.42	0.98			#DIV/0!
479959	7918805	R_Cantao_1	Adit	14	28	1	2.00	38	36	0	0.95	16.82	20.63	1.23			#DIV/0!
479959	7918805	R_Cantao_1b	Adit	14	28	1	2.00	38	36	0	0.95	13.95	17.05	1.22			#DIV/0!
479959	7918805	R_Cantao_1c	Adit	14	28	1	2.00	38	36	0	0.95	19.40	29.62	1.53			#DIV/0!
479959	7918805	R_Cantao_1d	Adit	14	28	1	2.00	38	36	0	0.95	15.93	19.46	1.22			#DIV/0!
479959	7918805	R_Cantao_1e	Adit	14	28	1	2.00	38	36	0	0.95	20.52	23.69	1.15			#DIV/0!
483715	7918130	R_Excelsior_1	Adits	6	6	1	1.00	8	0	0	0.00	51.58	62.24	1.21			#DIV/0!

483429	7917999	Excelsior_2			2	1	-1	0.50	7	0	1	0.00						
487050	7913090	R_Guy Fawkes	Open pit (main)		38	61	0	1.61	87	90	0	1.03	40.66	46.19	1.13			#DIV/0!
486796	7912635	R_Ivone_1	Dump		27	44	1	1.63	48	48	0	1.00			#DIV/0!	48.46	48.48	1.00
486796	7912635	R_Ivone_2	Dump		27	44	1	1.63	48	48	0	1.00	10.54	9.94	0.94	50.95	47.34	0.93
486796	7912635	R_Ivone_2b	Dump		27	44	1	1.63	48	48	0	1.00	15.88	16.99	1.07			#DIV/0!
486796	7912635	R_Ivone_2c	Dump		27	44	1	1.63	48	48	0	1.00	10.01	10.96	1.09			#DIV/0!
486796	7912635	R_Ivone_4	Dump		27	44	1	1.63	48	48	0	1.00	15.22	19.75	1.30	49.09	50.00	1.02
486796	7912635	R_Ivone_4b	Dump		27	44	1	1.63	48	48	0	1.00	13.27	15.13	1.14			#DIV/0!
486796	7912635	R_Ivone_4c	Dump		27	44	1	1.63	48	48	0	1.00	11.72	13.24	1.13			#DIV/0!
478790	7920250	R_Marondo_1	Adit		33	41	-1	1.24	14	0	0	0.00	29.62	50.73	1.71	51.14	66.33	1.30
478790	7920250	R_Marondo_1b	Adit		33	41	-1	1.24	14	0	0	0.00	13.59	22.81	1.68	24.39	27.61	1.13
478790	7920250	R_Marondo_1c	Adit		33	41	-1	1.24	14	0	0	0.00	16.82	27.70	1.65			#DIV/0!
478790	7920250	R_Marondo_1d	Adit		33	41	-1	1.24	14	0	0	0.00	13.15	22.83	1.74			#DIV/0!
471152	7912273	R_Monarch_3	Open pit		15	24	1	1.60	22	17	1	0.77	19.90	25.42	1.28	26.04	25.65	0.99
471152	7912273	R_Monarch_3b	Open pit		15	24	1	1.60	22	17	1	0.77	14.79	16.17	1.09			#DIV/0!
471152	7912273	R_Monarch_3c	Open pit		15	24	1	1.60	22	17	1	0.77	16.77	19.32	1.15			#DIV/0!
471182	7912346	R_Monarch_4	Open pit		10	15	1	1.50	12	4	1	0.33	11.69	16.34	1.37	27.29	26.66	0.98
471182	7912346	R_Monarch_4b	Open pit		10	15	1	1.50	12	4	1	0.33	11.74	13.75	1.17			#DIV/0!
471182	7912346	R_Monarch_4c	Open pit		10	15	1	1.50	12	4	1	0.33	11.43	12.07	1.06			#DIV/0!
471182	7912346	R_Monarch_4d	Open pit		10	15	1	1.50	12	4	1	0.33	9.96	10.60	1.06			#DIV/0!
471279	7912345	R_Monarch_5	Adit 5		8	10	1	1.25	12	4	1	0.33	7.30	7.65	1.05	17.56	15.64	0.89
471279	7912345	R_Monarch_5b	Adit 6		8	10	1	1.25	12	4	1	0.33	6.81	6.76	1.00			#DIV/0!
471279	7912345	R_Monarch_5c	Adit 7		8	10	1	1.25	12	4	1	0.33	6.40	6.27	0.98			#DIV/0!
473291	7913765	R_Revue_3	Adit		11	18	1	1.64	31	24	0	0.77	38.81	36.66	0.95			#DIV/0!
473291	7913765	R_Revue_3b	Adit		11	18	1	1.64	31	24	0	0.77	36.03	35.14	0.98			#DIV/0!
473391	7913916	R_Revue_4	Exploration adit		23	43	1	1.87	68	64	0	0.94	13.74	15.75	1.15	46.66	46.21	0.99
473391	7913916	R_Revue_4b	Exploration adit		23	43	1	1.87	68	64	0	0.94	22.67	22.68	1.00			#DIV/0!
480431	7917374	R_Two Foots_2	Open pit		20	44	1	2.20	39	40	0	1.03	23.79	26.27	1.10			#DIV/0!
480430	7917290	R_Two fools _3	Adit 7		21	44	1	2.10	30	31	1	1.03	47.11	48.76	1.04			#DIV/0!
481449	7910666	99/MN024	Dots Luck 4	Dot's Luck	23	47	1	2.04	56	41	-1	0.73						
481456	7910664	99MN029	Dots Luck 6	Dot's Luck	23	47	1	2.04	56	41	-1	0.73						

Appendix VIII-A

Digital Image Data Processing flow chart

Schematic represantation of data flow

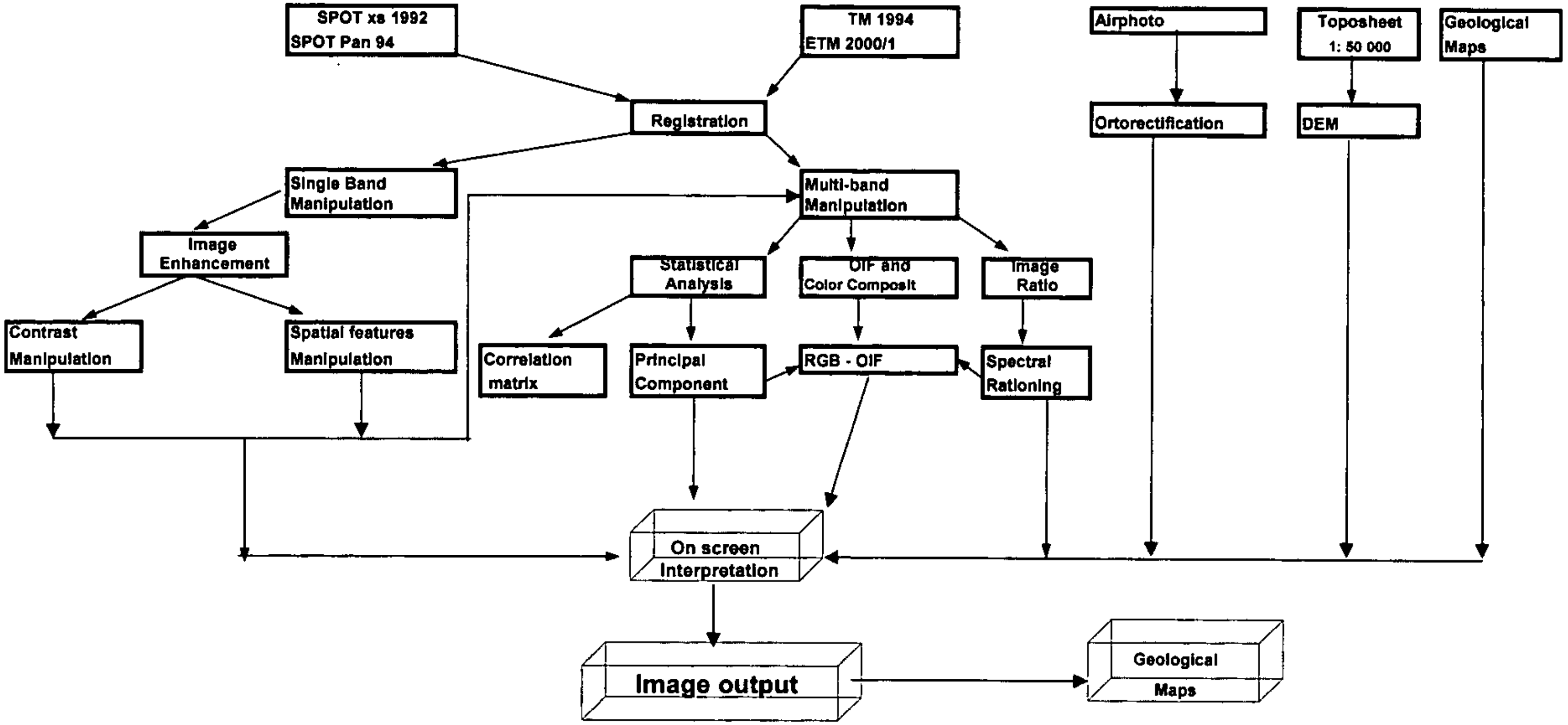

Figure VIIIA-1. Schematic representation of the different phases of data processing

(Appendix VIII-B)

Digital Image and Data Processing

In this appendix, digital image processing of the Manica Mutare Odzi greenstone belt is discussed with aim of defining the means of application of procedures in feature recognition and data integration.

Geometric correction

The raw images need to be geometrically corrected in order to allow correct overlap and match of topographic and other geographic information that are based on the coordinate system position.

The process of registration (geometric correction or georeferencing) of the SPOT images involves the use of topographic maps (1: 50 000) as reference maps coupled by ground control points (GCP) collected from features that can be accurately located on the digital image. The GCP were collected using a Garmin 12XS global position system (GPS) in Universal Transverse Mercator (UTM) WGS84, Clarke 1886 datum.

Geometric correction involves the assignment of reasonably well-distributed GCP coordinates to the equivalent features on the non-corrected (distorted) satellite image. Afterwards, the difference between the corrected and the non-corrected images is calculated by a least-squares regression analyses. These differences are used as transformation coefficients for the resampling of the non-corrected image, thus:

$x = f_1 (X,Y)$

$Y = f_2 (X,Y)$

Where

(x, y) are the distorted image coordinates (column, row)

(X, Y) are the correct (map) coordinates

(f_1, f_2) are the transformation functions

The resampling techniques have been extensively described by Rifman (1973), and Goetz et al., (1975). These techniques include the nearest neighbour, the bilinear interpolation and the cubic convolution. After testing the three methods for the satellite imagery and air photograph mosaic of the MMO area, the one that gave best results was the cubic convolution and it was used to build up the rectified image on the new grid defined over the map.

Image Enhancement

Satellite images are recorded in wide range of grey tones, which ideally should occupy the whole grey scale from 0 to 255. Very few images use the full range of grey scale due to differences in the surface cover material. Thus the best contrast of an image would be the one using the full range of the grey scale i.e. 0 to 255. The image enhancement aims at improving the visual interpretability of an image by increasing the apparent contrast between the features on it.

The contrast manipulation, spatial feature manipulation and multi-image manipulation are the main enhancement methods used.

Contrast manipulation

The contrast manipulation involves the alteration of grey level in the input image in order to obtain the best contrast. It is performed in three different ways; the contrast stretching, the level slicing and the grey-level thresholding. The description of these techniques can be found in any introductory book on Remote Sensing principles e.g. Lillesand and Kiefer (1994), Sabins (1987).

For the Manica Mutare Odzi greenstone belt after testing the three techniques it was decided to use the linear contrast stretching. The range in which the values of the input image is distributed is determined by plotting an histogram of the number of pixels or percentage of pixels versus pixel values (Digital Numbers, DN) (see Fig.VIII – 1a and VIII - 1b).

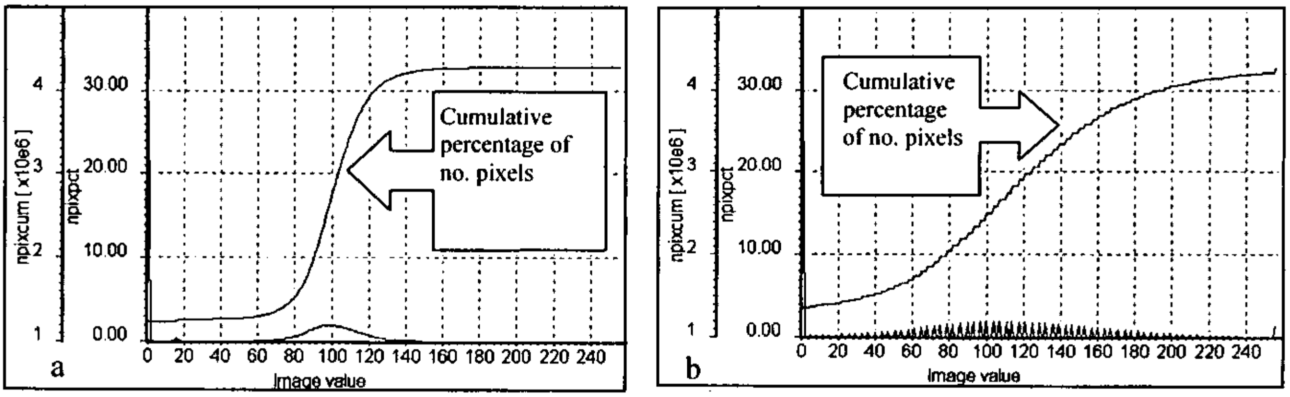

Figure VIII - 1a – Histogram of the Landsat ETM band 4 April (Manica Mutare Odzi region) – Note that 30 percent of the pixels occupy only 0 to 2 DN, between 2 and 68 there is c. 0% of pixels and less than 1 % are distributed from 145 to 155 DN; this leaves 70% of all data and 90% of DN not zero distributed between 68 and 145. The Fig VIII-1b shows the same image after linear contrast stretching (images values between 68 and 145 only). Note that the image values are linearly distributed in a Gaussian profile throughout the whole range (0 – 255).

Spatial Feature Manipulation

The filter operations are local image transformations in which each pixel depends on its neighbours multiplied by a filter kernel. The kernel[1] defines the output pixel value as a linear combination of pixel values in a neighbourhood covered by the kernel on the original image.

Filter operations can be specifically designed to enhance specific information, and are called directional when the objective is to enhance features with specific linear orientation, or non-directional if the objective is to enhance linear information at any direction. The Filter operations are extensively explained in most books of remote sensing (e.g. Lillesand and Kiefer (1994), Sabins (1987)).

Several filters (edge enhancement and Laplacian kernel, Fourier transform) were tested for the study area and the best results were achieved on the application of Edge enhancement filter (table 1). This filter enhances spatial details related to linear features such as roads, faults, and lithological boundaries. It calculates the difference between the central

---

[1] Filter kernel is the window of odd number of rows by same number of columns

pixel and its neighbours in such a way that the light features become lighter and the dark features become darker.

-1	**-1**	**-1**
-1	16	-1
-1	-1	-1

Table 1 – Filter kernel used for edge enhancement

Multi-band Manipulation

The Multi-band operations include band ratio, band difference, band addition, band multiplication, band fusion, band combination (colour composite), vegetation index, and decorrelation stretching. The present discussion will be restricted to operation that gave good results when applied in the study area.

Band Ratioing

Band ratio has been used for compensating the variations in illumination due to variation in topography and is also commonly used in index calculations (TM3/TM1). It is achieved by dividing the DN in one band by the corresponding DN in another band for each pixel. The result is plotted in an image after stretching. The ratio operation can be performed on the spectrum of the image or any reflectance data (see also chapter 7).

In this study several ratio images were created and assessed for lithological and alteration mapping. The ratio images were combined in colour composite RGB or they were density sliced for better visualisation.

Colour Composite and Optimum Index Factor (OIF)

Colour composite is an operation by which three primary colours (red, green and blue (RGB)) are combined for the purpose of display on screen. There are two methods used to create colour composite images: the standard and the dynamic colour composites.

The standard colour composite involves a linear stretching of interval or a histogram equalisation. In both linear stretching and histogram equalisation the intervals are user defined.

The dynamic colour composite is created from the Heckbert Quantization Algorithm (HQA), which is based on the amount of variations in the input pixel value. The principle is illustrated in Fig. VIII - 2a and VIII – 2b.

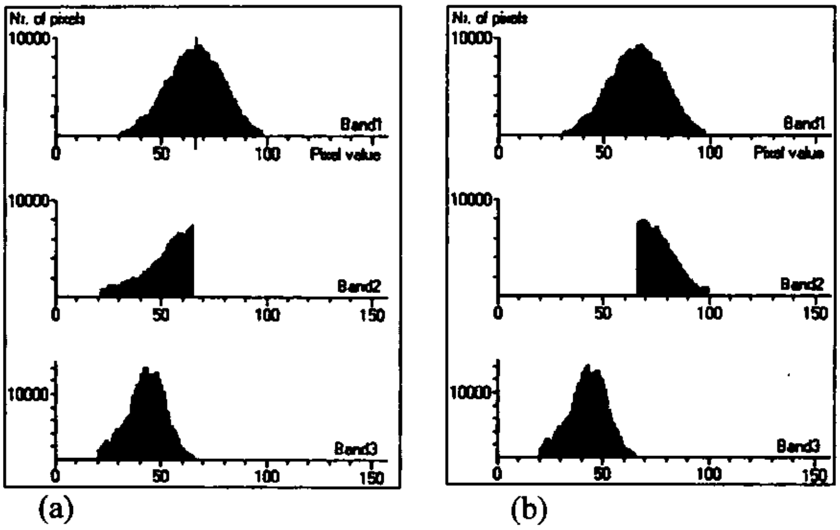

Figure VIII - 2a – Pixel values range in box1: from 31 to 98 in the band1; from 22 to 65 in the band2; and from 21 to 66 in the band3. Fig. VIII -2b – Represents pixel values range in box2: from 31 to 98 in the band 1; from 66 to 100 in the band 2; and from 21 to 66 in the band 3 (modified from ILWIS 2.1, Reference Guide)

The *Optimum Index Factor* (OIF) is a statistical operation developed by Chavez et al. (1982) that can be used for band selection of optimum combination of three bands to be used in the creation of a colour composite image. Statistically optimum combination means the one with highest amount of information. The use of bands with high OIF for colour composite does not mean necessarily that the best colour composite image is produced, hence this depend on the purpose of the study. In the present study the best OIF ranked colour composite image was not useful for geological studies.

Statistical Analyses

In this chapter, the principal component and the correlation matrix for image data compression and test of usefulness of the resulting images was used for geologic structural mapping.

Principal component analyses

Principal Component Analyses (PCA) is a statistical linear transformation used to reduce or remove the redundancy derived from different bands capturing the same information although in different wavelength.

Loéve (1955), developed PCA and the concepts can be expressed graphically by two bands of data in Fig. 6 – 18. The transformation defines a new axis (y_1) oriented in the long dimension of the distribution and the second axis (y_2) perpendicular to y_1 (Sabins, 1987). The original pixel values are transformed into new coordinate system in a linear mathematical expression as

$$Y_1 = \alpha_{11}x_1 + \alpha_{12}x_2 \qquad (1)$$

$$Y_2 = \alpha_{21}x_1 + \alpha_{22}x_2 \qquad (2)$$

Where: x_1 and x_2 are the pixel coordinates in the original system; Y_1 and Y_2 are the coordinates in the new system; and α_{11}, α_{21}, and α_{22} are coefficients of the first and second component

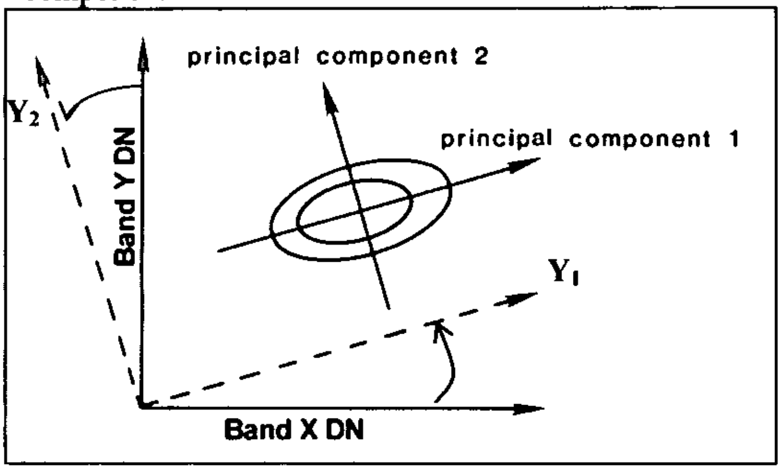

Figure VIII – 3. Scatter plot of Landsat TM band X (x_1 axis) and band Y (x_2 axis) showing correlation between these bands. The principal component transformation was used to generate a new coordinate system (Y_1, Y_2) (modified after Swain and Davis, 1978; Sabins, 1987)

For more than two bands each additional band will add an extra component, which is perpendicular to all others.

A principal component transformation was performed on the three visible bands and the three reflected infrared band of Landsat TM and ETM, all bands of Landsat TM and ETM, and the SPOT-xs data for the Manica Mutare Odzi area. The PCA images were combined to create a colour composite where PC1, PC2 and PC3 were assigned the RGB respectively.

Correlation Matrix

The satellite images in general had a degree of correlation. This means that information in one band can be repeated proportionally in another band. The correlation matrix is calculated in order to assess the degree of redundancy in the satellite images bands. It is useful for band selection in colour composite exercise.

Correlation matrix is calculated after the determination of the covariance and then the covariance matrix is normalised as

$$\mathbf{Corr}_{b1,b2} = \frac{\mathbf{Covar}_{b1,b2}}{\sqrt{\mathbf{Var}_{b1}} * \mathrm{Var}b2} \qquad (3)$$

Where: $\mathbf{Corr}_{b1,b2}$ is the covariance calculated for two input raster maps (b1 and b2)

$\mathbf{Var}_{b1}$ is the variance calculated for the band b1

Image Classification

Digital image classification is the process in which the computer performs the recognition of certain classes based on pre-set conditions (supervised) or on the basis of spectral similarities of the pixels. The principle of digital image classification is that a pixel is assigned to class based on its feature vector[2], by comparing it to pre-defined clusters in the feature space[3] (Janssen, 2000).

Digital image classification is divided into supervised and unsupervised. It is supervised when the clusters are interactively selected on the basis of previous knowledge of the area, and supplied to the computer by the analyst. While the unsupervised classification does not require any knowledge of the area and the clusters are defined on the basis of spectral similarities by clustering algorithms.

Several classification algorithms exist and its choice depends mainly on the purpose of the study and on the data available. The box, the minimum distance to mean and the maximum likelihood classifiers are the most commonly used.

The maximum likelihood classifier (MLC) was used to the Manica Mutare Odzi region because it gave better results than the other classifiers. The MLC algorithm calculates for each feature vector, the distances towards class means and for each class, variance - covariance matrixes are calculated. The following formula is used in Maximum Likelihood algorithm:

$$D_i(x) = \ln | V_i | + Y^T V_i^{-1} Y \qquad (4)$$

Where:

D_i is the distance between feature vector (x) and a class mean based on possibilities
V_i is the M x M variance-covariance matrix of a class
M is the number of band
$| V_i |$ is the determinant of V_i
Y is x-m_i; is the distance towards a class mean
Y^T is the transposed Y

The shortest distance D to a class is found if D is smaller than the user defined threshold, then this class is assigned to the output pixel otherwise the pixel is assigned as undefined.

---

[2] two or more dimensional vector where each vector represent an image band

[3] a graph that shows the values of the feature vectors

Appendix IX-A

Bayesian Probability Model

The Bayesian probability model or weights of evidence model was first developed for medical diagnosis (Lusted, 1968; Spiedelhalter and Knill-Jones, 1984; Spiegelhalter, 1986). It was first applied for mineral potential mapping by Agterberg (1989). Bonham-Carter et al. (1989), Bonham-Carter (1997) and Caranza (2002) described the way Bayesian probability model can be used for mineral potential recognition criteria.
The following formulation of the weights of evidence is summarised from Bonham-Carter et al. (1989), Bonham-Carter (1997) and Caranza (2002).

It an area is captured in raster form or any other model that divide it in picture units (pixels) of fixed size, s, and the total area equivalent to t, then N{T}=t/s is the total number of pixels in the area. In mineralised area some pixels will be occupied by mineral deposits D, equal to the number of deposits if the s is small enough that only one can occupy the pixel, then the prior probability of a mineral deposit is:

$P\{D\} = N\{D\}/N\{T\}$ Eq. IX - 1

Assuming that there is binary predictor pattern B (e.g. shear zone), occupying N{B} pixels, occurs in the region and that a number of mineral deposits are known to be associated with predictor pattern, i.e., $N\{D \cap B\}$. The probability of a mineral deposit occurring within the predictor pattern is greater than the prior probability. The probability of finding a mineral deposit given a predictor pattern can be expressed by the conditional probability:

$P\{D|B\} = P\{D \cap B\}/P\{B\} = P\{D\}(P\{B|D\}/P\{B\},$ Eq. IX - 2

Where P{D| } is the conditional or posterior probability of a mineral deposit given the presence of the predictor pattern, P{B| D} is the posterior probability of being in the predictor pattern B, given the presence of a mineral deposit D, and P{B} is the prior probability of the predictor pattern. The probability of finding a mineral deposit in the absence of a predictor pattern can be expressed by the following conditional probability

$$P\{D^{\cdot}\cdot.\overline{B}\} = \frac{P\{D \cap \overline{B}\}}{P\{\overline{B}\}} = P\{D\}\frac{P\{\overline{B}^{\cdot}\cdot.D\}}{P\{\overline{B}\}} \qquad \text{Eq. IX -3}$$

Where P{D is posterior probability of a mineral deposit given the absence of a predictor pattern, P{B is the posterior probability of being outside the predictor B, given the presence of a mineral deposit D, and P{ is the prior probability of the area outside the predictor pattern.

The equations 6-2 and 6 – 3 satisfy the Bayes' rule. The same model can be expressed in an odds formulation, where odds, O, are defined as O =P/(1 – P).
Expressed as odds, equations 6 – 2 and 6 – 3 become 6 – 4 and 6 – 5, respectively

$$O\{D^{\cdot}\cdot.B\} = O\{D\}\frac{P\{B^{\cdot}\cdot.D\}}{P\{B^{\cdot}\cdot.\overline{D}\}} \qquad \text{Eq. IX – 4}$$

$$O\{D^{\cdot}\cdot.\overline{B}\} = O\{D\}\frac{P\{\overline{B}^{\cdot}\cdot.D\}}{P\{\overline{B}^{\cdot}\cdot.\overline{D}\}} \qquad \text{Eq. IX} - 5$$

Where O{D and O{D are the posterior odds of a mineral deposit given the presence and absence of a binary predictor pattern, and O{D} is the prior odds of a mineral deposit. The terms P{B| D}/P{B| D} and P{ are known as the likelihood sufficiency ratio (LS) and likelihood necessity ratio (LN), respectively (Bonham-Carter, 1997).

The values of LS and LN, in the weights of evidence model, are calculated using the mineral deposit data and by taking natural logarithms of both sides of Equations 6 – 4 and 6 – 5. The weights for the binary predictor pattern, or the log$_e$ of LS and LN, are as follows:

$$W^{+} = \log_e \frac{P\{B^{\cdot}\cdot.D\}}{P\{B^{\cdot}\cdot.\overline{D}\}} \qquad \text{Eq. IX} - 6$$

$$W^{-} = \log_e \frac{P\{\overline{B}^{\cdot}\cdot.D\}}{P\{\overline{B}^{\cdot}\cdot.\overline{D}\}} \qquad \text{Eq. IX} - 7$$

Where W^+ and W^- are the positive and negative weights of evidence when a binary predictor pattern is present and absent, respectively. Thus, Equations 6 –4 and 6 – 5 become

$$\log_e O:\{D^{\cdot}\cdot.B\} = \log_e O\{D\} + W^{+} \qquad \text{Eq. IX} - 8$$

$$\log_e O:\{D^{\cdot}\cdot.\overline{B}\} = \log_e O\{D\} + W^{-} \qquad \text{Eq. IX} - 9$$

The variances of the weights can be calculated by the following expressions (Bishop et al., 1975; Agterberg et al., 1990)

$$S^2(W^{+}) = \frac{1}{N\{B \cap D\}} + \frac{1}{N\{B \cap \overline{D}\}} \qquad \text{Eq. IX} - 10$$

$$S^2(W^{-}) = \frac{1}{N\{\overline{B} \cap D\}} + \frac{1}{N\{\overline{B} \cap \overline{D}\}} \qquad \text{Eq. IX} - 11$$

The contrast, C, defined as

$C = W^+ - W^-$

Provides a useful measure of the spatial association between a binary predictor pattern and mineral deposit points. For a positive spatial association, C is positive; C is negative in the case of negative association. The Studentised C, calculated as the ratio of C to its standard deviation, C/C_S, serves as a guide to the statistical significance of the spatial association (Bonham-Carter (1997). The standard deviation of C is given by:

$$S(C) = \sqrt{S^2(W^{+}) + S^2(W^{-})} \qquad \text{Eq. IX} - 13$$

Bonham-Carter et al. (1989) and Bonham-Carter (1997) showed that when Studentised C is greater than 2 implies that C is statistically significant.

Conditional probability for multiple binary patterns

If it is assumed that there are two binary predictor patterns, B_1 and B_2. from probability theory, it can be shown that the conditional probability of a mineral deposit given the presence of two predictor patterns is,

$$P\{D^{\cdot}\cdot.B_1 \cap B_2\} = \frac{P\{B_1 \cap B_2{}^{\cdot}\cdot.D\}P\{D\}}{P\{B_1 \cap B_2{}^{\cdot}\cdot.D\}P\{D\} + P\{B_1 \cap B_2{}^{\cdot}\cdot.\overline{D}\}P\{\overline{D}\}} \qquad \text{Eq IX} - 14$$

If B_1 and B_2 are conditionally independent of each other with respect to a set of points, it means that the following relation is satisfied:

$$P\{B_1 \cap B_2{}^{\cdot}\cdot.D\} = P\{B_1{}^{\cdot}\cdot.D\}P\{B_2{}^{\cdot}\cdot.D\} \qquad \text{Eq. IX} - 15$$

Equation 6 – 15 allows Equation 6 – 14 to be simplified, thus

$$P\{D^{\cdot}\cdot.B_1 \cap B_2\} = P\{D\}\frac{P\{B_1{}^{\cdot}\cdot.D\}P\{B_2{}^{\cdot}\cdot.D\}}{P\{B_1\}P\{B_2\}} \qquad \text{Eq. IX} - 16$$

Equation 6 – 16 is similar to equation 6 –2, except that multiplication factors for two binary predictor patterns are used to update the prior probability to give the posterior probability. Using the odds formulation, it can be shown that

$$\log_e O\{D^{\cdot}\cdot.B_1 \cap B_2\} = \log_e O\{D\} + W_1^{+} + W_2^{+}\cdot \qquad \text{Eq. IX} - 17$$

$$\log_e O\{D^{\cdot}\cdot.B_1 \cap \overline{B_2}\} = \log_e O\{D\} + W_1^{-} + W_2^{+} \qquad \text{Eq. IX} - 18$$

$$\log_e O\{D^{\cdot}\cdot.\overline{B_1} \cap \overline{B_2}\} = \log_e O\{D\} + W_1^{-} + W_2^{+}, \qquad \text{Eq. IX} - 19$$

$$\log_e O\{D^{\cdot}\cdot.\overline{B_1} \cap \overline{B_2}\} = \log_e O\{D\} + W_1^{-} + W_2^{-} \qquad \text{Eq. IX} - 20$$

Similarly, if more than two binary patterns are used, they can be added provided they are also conditionally independent of one another with respect to the mineral deposit point position. Thus, with $B_j(j= 1,2,\ldots,n)$ binary predictor patterns, the $\log_e$ posterior odds are:

$$\log_e O\{D^{\cdot}\cdot.B_1^k \cap B_2^k \cap B_3^k \cdots B_n^k\} = \sum_{j=1}^{n} W_j^k + \log_e O\{D\} \qquad \text{Eq. IX} - 21$$

where the superscript k is positive (+) or negative (-) if the binary predictor pattern is present or absent, respectively. The posterior odds can then be converted to posterior probabilities, based on the relation P=O/(1+O), which represent mineral potential.

Appendix IX - B

	Calculation of Chi Square in the MMO Greenstone belt				Chi Square
Observed	bmpbif X bmpgr	bmpbif	bmpgr	all absent	
	14	48	14	42	
	0.466666667	-10	-14	-5.533333333	
	0.016091954	1.724137931	7	0.644132772	9.38436266
Expected	bmpbif X bmpgr	bmpbif	bmpgr	all absent	
	13.53333333	58	28	47.53333333	
	bmpbif X bmpshear	bmpbif	bmpshear	all absent	
Observed	32	30	28	28	
	bmpbif X bmpshear	bmpbif	bmpshear	all absent	
Expected	24.16666667	58	50	36.16666667	
	7.833333333	-28	-22	-8.166666667	
	2.53908046	13.51724138	9.68	1.844086022	27.5804079
	bmpbif X bmpgrgr	bmpbif	bmpgrgr	all absent	
Observed	19	43	28	28	
	bmpbif X bmpgrgr	bmpbif	bmpgrgr	all absent	
Expected	22.71666667	58	47	37.71666667	
	-3.716666667	-15	-19	-9.716666667	
	0.608082661	3.879310345	7.680851064	2.503233171	14.6714772
	bmpbif X bmpshabu	bmpbif	bmpshabu	all absent	
Observed	22	40	6	50	
	bmpbif X bmpshabu	bmpbif	bmpshabu	all absent	
Expected	13.53333333	58	28	47.53333333	
	8.466666667	-18	-22	2.466666667	
	5.296880131	5.586206897	17.28571429	0.12800374	28.2968051
	bmpgr X bmpgrgr	bmpgr	bmpgrgr	all absent	
Observed	4	24	43	47	
	bmpgr X bmpgrgr	bmpgr	bmpgrgr	all absent	
Expected	10.96666667	28	47	55.96666667	
	-6.966666667	-4	-4	-8.966666667	
	4.425633232	0.571428571	0.340425532	1.43658924	6.77407657
	bmpgr X bmpshabu	bmpgr	bmpshabu	all absent	
Observed	4	24	24	66	
	bmpgr X bmpshabu	bmpgr	bmpshabu	all absent	
Expected	6.533333333	28	28	70.53333333	
	-2.533333333	-4	-4	-4.533333333	
	0.982312925	0.571428571	0.571428571	0.29136736	2.41653743
	bmpgr X bmpshear	bmpgr	bmpshear	all absent	
Observed	15	13	45	45	
	bmpgr X bmpshear	bmpgr	bmpshear	all absent	
Expected	11.66666667	28	50	53.66666667	
	3.333333333	-15	-5	-8.666666667	
	0.952380952	8.035714286	0.5	1.399585921	10.8876812
	bmpgrgr X bmpshabu	bmpgrgr	bmpshabu	all absent	
Observed	0	47	28	43	
	bmpgrgr X bmpshabu	bmpgrgr	bmpshabu	all absent	
Expected	10.96666667	47	28	55.96666667	
	-10.96666667	0	0	-12.96666667	
	10.96666667	0	0	3.004189001	13.9708557

	bmpgrgr X bmpshear	bmpgrgr	bmpshear	all absent	
Observed	22	25	38	33	
	bmpgrgr X bmpshear	bmpgrgr	bmpshear	all absent	
Expected	19.58333333	47	50	42.58333333	
	2.416666667	-22	-12	-9.583333333	
	0.29822695	10.29787234	2.88	2.156718852	15.6328181
	bmpshabu X bmpshear	bmpshabu	bmpshear	all absent	
Observed	21	7	39	51	
	bmpshabu X bmpshear	bmpshabu	bmpshear	all absent	
Expected	11.66666667	28	50	53.66666667	
	9.333333333	-21	-11	-2.666666667	
	7.466666667	15.75	2.42	0.132505176	25.7691718
	bmpfryX bmpshear	Fry	bmpshear	all absent	
Observed	32	30	28	28	
	bmpfry X bmpshear	Fry	bmpshear	all absent	
Expected	25.83333333	62	50	33.83333333	
	6.166666667	-32	-22	-5.833333333	
	1.472043011	16.51612903	9.68	1.005747126	28.6739192
	bmpfryX bmpshabu	Fry	bmpshabu	all absent	
Observed	17	45	11	45	
	bmpfry X bmpshabu	Fry	bmpshabu	all absent	
Expected	14.46666667	62	28	44.46666667	
	2.533333333	-17	-17	0.533333333	
	0.443625192	4.661290323	10.32142857	0.006396802	15.4327409
	bmpfryX bmpgrgr	Fry	bmpgrgr	all absent	
Observed	21	41	26	30	
	bmpfry X bmpgrgr	Fry	bmpgrgr	all absent	
Expected	24.28333333	62	47	35.28333333	
	-3.283333333	-21	-21	-5.283333333	
	0.443937314	7.112903226	9.382978723	0.791127382	17.7309466
	bmpfryX bmpgr	Fry	bmpgr	all absent	
Observed	20	42	8	48	
	bmpfry X bmpgr	Fry	bmpgr	all absent	
Expected	14.46666667	62	28	44.46666667	
	5.533333333	-20	-20	3.533333333	
	2.116436252	6.451612903	14.28571429	0.28075962	23.1345231
	bmpfryX bmpbif	Fry	bmpbif	all absent	
Observed	40	22	22	34	
	bmpfry X bmpbif	Fry	bmpbif	all absent	
Expected	29.96666667	62	58	29.96666667	
	10.03333333	-40	-36	4.033333333	
	3.359325176	25.80645161	22.34482759	0.54286244	52.0534668